MODELING THE DISPERSION AND EVAPORATION OF SPRAYS IN AERONAUTICAL COMBUSTION CHAMBERS

Patricia Sierra Sanchez

THESE

En vue de l'obtention du

DOCTORAT DE L'UNIVERSITÉ DE TOULOUSE

Délivré par Institut National Polytechnique de Toulouse
Discipline ou spécialité : Enérgetique et Transferts

Par Patricia SIERRA SÁNCHEZ
Soutenue le : 23 janvier 2012

MODELING THE DISPERSION AND EVAPORATION OF SPRAYS IN AERONAUTICAL COMBUSTION CHAMBERS

JURY

R. O. FOX	Professeur à l'Université d'Iowa	Rapporteur
J. REVEILLON	Professeur à l'Université de Rouen	Rapporteur
O. SIMONIN	Professeur à l'INP de Toulouse	Examinateur
S. JAY	Docteur (IFPEn)	Examinateur
A. ROUX	Docteur (Turbomeca)	Examinateur
L. GICQUEL	Chercheur Senior au CERFACS	Directeur de thèse

École doctorale : Mécanique, Energétique, Génie civil, Procédés
Unité de recherche : CERFACS
Directeur de Thèse : Laurent GICQUEL
Co-Directeur de Thèse : Eleonore RIBER

THÈSE

présentée pour obtenir le titre de

DOCTEUR DE
L'INSTITUT NATIONAL POLYTECHNIQUE DE TOULOUSE

Ecole doctorale:	MeGeP
Spécialité:	Enérgetique et Transferts
Directeur:	Laurent GICQUEL
Co-directeur:	Eleonore RIBER

Par **Patricia SIERRA SÁNCHEZ**

MODELING THE DISPERSION AND EVAPORATION OF SPRAYS IN AERONAUTICAL COMBUSTION CHAMBERS

Soutenue le 23 Janvier 2012 devant le jury composé de:

R. O. FOX	Professeur à l'Université d'Iowa	Rapporteur
J. REVEILLON	Professeur à l'Université de Rouen	Rapporteur
O. SIMONIN	Professeur à l'INP de Toulouse	Examinateur
S. JAY	Docteur (IFP-EN)	Examinateur
A. ROUX	Docteur (Turbomeca)	Examinateur
L. GICQUEL	Chercheur au CERFACS	Directeur de thèse

Réf. CERFACS : TH/CFD/12/??

Contents

List of symbols

Roman letters

Symbol	Description	Units
b	Exponent of the Power law	
$b^*_{p,ij}$	RUM anisotropy stress tensor	
$\mathbf{c}_p$	Particle velocity	[m/s]
C_D	Drag coefficient	[-]
C_m	Added-mass force constant	[-]
C_p	Specific heat capacity at constant pressure of the fluid	[J/(kgK)]
C_v	Specific heat capacity at constant volume of the fluid	[J/(kgK)]
C_w	Constant of the Smagorinsky model	[-]
D_k	Molecular diffusivity of the species k	[m^2/s]
e_s	Specific sensible energy of the fluid phase	[J/kg]
E	Total non-chemical energy	[J/kg]
$E(\kappa)$	Energy spectrum	
f_i	Component (i) of the volumetric force vector	[kg/(ms^2)]
f_p	PDF function	
F_{AM}	Added-mass force	[N]
F_D	Drag force	[N]
F_H	Basset force	[N]
F_L	Lift force	[N]
$F_{p,i}$	Component (i) of the vector of forces acting upon a particle	[kg/(ms^2)]
$F^u_{p,i}$	Component (i) of the vector of forces that would act on a fluid particle occupying the position of the particle	[kg/(ms^2)]
$F^p_{p,i}$	Component (i) of the vector of forces acting upon a particle due to perturbations on the fluid field due to the presence of the particle	[kg/(ms^2)]
$\mathcal{F}^{\mathcal{I}}$	Inviscid flux tensor of conservative variables	[kg/(m^2s^2)]
$\mathcal{F}^{\mathcal{V}}$	Viscous flux tensor of conservative variables	[kg/(m^2s^2)]
$\mathcal{F}_p$	Particle flux tensor	
$\mathcal{F}^{\mathcal{U}}_p$	Particle flux tensor due to the uncorrelated motion	
$\mathcal{F}^{\mathcal{M}}_p$	Particle flux tensor due to convection of the mesoscopic motion	
g_i	Component (i) of the gravity vector	[kg/(ms^2)]
G_Δ	Low-pass filter	
h_s	Sensible enthalpy of the fluid/ gas phase	[J/(kg)]
$h_{s,l}$	Sensible enthalpy of the liquid/ particle	[J/(kg)]
h_p	Particle enthalpy	[J/(kg)
$\mathcal{H}_f$	Carrier fluid realization	
$\mathcal{H}_p$	Particle phase realization	
$\mathbf{I}$	Identity matrix	
$J_{j,k}$	Component (j) of the diffusive flux vector of the species k	[kg/(ms^2)]
k	Turbulent kinetic energy	[m^2/s^2]
$\mathcal{L}$	Characteristic length scale	[m]
L_{evap}	Latent heat of evaporation	[J/(kg)]
m_p	Particle mass	[kg]
$\dot{m}_F$, $\dot{m}_p$	Mass transfer rate	[kg/m^3s]
$\delta\breve{M}_{p,ijmn}$	4^{th} order particle uncorrelated velocity correlations tensor	
n_p	Number of particles per unit volume	[$1/m^3$]
N_p	Number of particles	
P_g	Pressure	[N/m^2]

q_f^2	Fluid turbulent kinetic energy	[J]
q_{fp}	Fluid-particle correlation	[J]
$q_{f@p}^2$	Fluid turbulent kinetic energy sampled along particle trajectories	[J]
$q_{g,i}$	Component (i) of the heat flux vector	[J/(m^{2}s)]
q_p^2	Particle kinetic energy	[J]
δq_p^2	Particle Random Uncorrelated Energy	[J]
$\delta \mathring{Q}_{p,ijm}$	3^{rd} order particle uncorrelated velocity correlations tensor	
r	Gas constant of a mixture (mass)	[J/(kg K)]
$r_p(d_p)$	Particle radius (diameter)	[m]
$\mathcal{R}$	Universal gas constant (molar)	[J/(mol K)]
$\breve{\mathbb{R}}_{p,ij}$	Mean mesoscopic stress tensor	
$\delta\breve{\mathbb{R}}_{p,ij}$	Mean RUM stress tensor	
$\delta\breve{R}_{p,ij}$	Component (i,j) of the uncorrelated motion stress tensor	[m^2/s^2]
$\delta\breve{R}^*_{p,ij}$	Component (i,j) of the uncorrelated motion deviatoric stress tensor	[m^2/s^2]
s	Specific entropy of the fluid phase	[J/kg]
$\mathbf{s_{l-g}}$	Source term vector (liquid to gaseous phase)	
$\mathbf{s_{p-g}}$	Source term vector (particle to gaseous phase)	
$\mathbf{s_p}$	Source term vector (particle phase)	
$\mathbf{s_{g-p}}$	Source term vector (gaseous to particle phase)	
$\mathbf{s}_\theta$	Source term vector (linked to the uncorrelated motion)	
s_{ij}	Component (i,j) of the velocity deformation tensor	[m/s^2]
$S_{g,ij}$, $S_{p,ij}$	Rate of strain tensor in the gas/dispersed phase	[1/s]
$\mathbf{S}$	Particle rate-of-strain tensor	[s^{-1}]
T	Temperature of the fluid/ gas	[K]
T_p	Temperature of the particle	[K]
$\mathbf{u}, u_i$	Fluid velocity vector/ component (i)	[m/s]
$u_{p,i}$	Component (i) of the particle velocity vector	[m/s]
$\mathbf{u}_{f@p}$, $\mathbf{u}_{f@p,i}$	Undisturbed fluid velocity vector at the position of the particle/ component (i)	[m/s]
$\mathcal{U}$	Characteristic velocity	[m/s]
$\mathbf{v_p}$, $\mathbf{v_{p,i}}$	Particle velocity vector/ component (i)	[m/s]
V_i^c	Component (i) of the correction diffusion velocity	[m/s]
$V^{k,i}$	Component (i) of the diffusion velocity of the species k	[m/s]
$\mathbf{w}$	Conservative variables vector for the carrier fluid	
$\mathbf{w}_p$	Conservative variables vector for the dispersed phase	
$\mathcal{W}$, $\mathcal{W}_k$	Molecular weight of gaseous mixture/ of species k	[kg/m^3]
W_θ	Drag force source term	
$x_{p,i}$	Component (i) of the particle position vector	[m]
X_k	Molar fraction of the species k	[-]
Y_k	Mass fraction of the species k	[-]

Greek letters

Symbol	Description	Units
α_l, α_p	Liquid (particle) volume fraction	[-]
$\delta(\cdot)$	Dirac delta function	[-]
δ_{ij}	Component (i,j) of the Kronecker delta	[-]
$\delta\theta_p$	Random Uncorrelated Energy	[J]
Δ	Characteristic filter width	[m]
$\Delta h^0_{f,k}$	Formation enthalpy of the species k	[J/kg]

ϵ	Turbulent dissipation rate	
η_k, η	Kolmogorov length scale	[m]
Γ	Mass evaporation rate	[kg/m^3s]
κ_{RUM}	Uncorrelated diffusion coefficient	[kgm^2/s]
λ_g	Thermal conductivity of the fluid/ gas	[J/(mKs)]
μ_g	Dynamic viscosity	[kg/(ms)]
μ_p	Particle mass	[kg]
ν_g	Kinematic viscosity	[m^2/s]
ν_{RUM}	RUM viscoisty	[Js]
ν_t	Turbulent kinematic viscosity	[m^2/s]
Ω_g	Fluid vorticity	[s^{-1}]
$\mathbf{\Omega}$	Particle mesoscopic rotation tensor	[s^{-1}]
Φ_p	Heat transfer rate	[W/m^3]
Φ^c	Particle conductive heat flux	[J/s]
Φ^{cv}	Particle convective heat flux	[J/s]
Π_g	Sensible energy transfer rate due to evaporation and thermal conduction	[W/m^3]
ρ_g	Fluid/ gas density	[kg/m^3]
ρ_k	Partial density of the species k	[kg/m^3]
ρ_l, ρ_p	Particle/ liquid density	[kg/m^3]
u_η	Kolmogorov velocity scale	[m/s]
τ_η	Kolmogorov timescale	[s]
τ_{cv}	Characteristic convective time scale	[s]
τ_{ev}	Droplet evaporation time scale	[s]
τ_f^t	Lagrangian turbulent time-scale	[s]
τ_{fp}^F	Mean particle relaxation time	[s]
$\tau_{g,ij}$	Component (i, j) of the stress tensor	[N/m^2]
τ_p	Particle relaxation time scale	[s]
θ_S	Spray angle	[°]
ζ	Artificial viscosity sensor	[-]
ζ_p	Particle temperature	[K]

Non-dimensional numbers

Symbol	Description
B_M	Spalding number for mass transfer
B_T	Spalding number for heat transfer
Kn	Knudsen number
Le	Lewis number
Nu	Nusselt number
Pr	Prandtl number
Re	Reynolds number
Re_p	Particle Reynolds number
St	Stokes number
Sc	Schmidt number
Sh	Sherwood number
We	Weber number

Subscripts

Symbol	Description
0	Plane of the atomizer orifice
0	Thermodynamic reference state

∞	State in the far-field
ζ	Interface between particle and fluid
cc	Point on the saturation curve
f	Index of the carrier fluid
F	Index of gaseous fuel
g	Index of the gaseous phase
k	General index of the species
l	Index of the liquid phase
lam	Laminar component
p	Index of the particle phase
ref	Index of the reference state
t	Turbulent component
v	Index of the vapor species
wb	Wet-bulb

Superscripts

Symbol	Description
f	Filtered quantity
$\hat{f}$	Density weighted filtered quantity
$\breve{f}$	Ensemble averaged quantity
$\breve{f}$	Mesoscopic liquid quantity in the Eulerian framework
f'	Fluctuation
f^i	Invscid component
f^{sgs}	Subgrid-scale contribution
f^v	Viscous component
(k)	Index of the k^{th} particle
δf	Uncorrelated part of a quantity
$*$	Traceless tensor

Abreviations

Acronym	Description
CPS	Computational Fluid Dynamics
DNS	Direct Numerical Simulation
DQMOM	Direct Quadrature Method Of Moments
DPS	Discrete Particle Simulation
EE	Euler-Euler
EL	Euler-Lagrange
EMSM	Eulerian Multi Size Moment
EMVM	Eulerian Multi Fluid Multi Velocity
HIT	Homegenous Isotropic Turbulence
IMFT	Institut de Mécanique de Fluides de Toulouse
LES	Large-Eddy Simulation
MEF	Mesoscopic Eulerian Formalism
MERCATO	Moyen d'Étude et de Recherche en Combustion Aérobie par Techniques Optiques
MYPLANET	Massively Parallel Computations of Combustion and Emissions Simulations
NS	Navier-Stokes
NSCBC	Navier-Stokes Characteristic Boundary Condition
PDF	Probability Density Function
PTC	Particle Trajectory Crossing
RANS	Reynolds Averaged Navier-Stokes

RMS	Root Mean Square
RUE	Random Uncorrelated Energy
RUM	Random Uncorrelated Motion
WALE	Wall-Adapting Local Eddy-viscosity

Chapter 1

General Introduction

In today's industrial society more than 80% of the energy consumed on earth is produced by burning fossil fuels. However, the progressive exhaustion of fossil fuels and the ecological problems derived require an important technological progress in order to optimize the combustion processes. In this context of fuel depletion, growing pollution and global earth warming, this statement is globally recognized. Indeed, regulations on pollutant emissions recently adopted by many countries oblige a drastic reduction of emissions and fuel consumption. Many other energy sources, alternatives to combustion, exist such as nuclear, wind, solar and hydraulic power, biomass, etc. However, in the domain of aeronautical transport, few other sources of energy other than hydrocarbons start to be considered nowadays. This limited impact is mainly due to the necessity of a high power/weight ratio that only combustion of liquid fuels can provide due to their high specific energy content and high volumetric energy density.

Many chemical components are produced during combustion. Some, like H_2O or CO_2, are intrinsic to the process itself and cannot be avoided. Some others, like NO_x, CO, unburnt hydrocarbons and soot are also produced when burning hydrocarbon fuels. All these components can be grouped under the term "pollutant emissions". In order to reduce the quantity of these species produced during combustion, several strategies may be adopted. The production of CO_2 is directly linked to the quantity of fuel burnt. For this reason, in order to reduce CO_2 production, fuel comsumption must be reduced meaning that more efficient engines must be designed. The formation of other pollutants is mainly linked to the combustion mode. High temperature combustion increases the emissions of NO_x, lean combustion promotes the formation of CO and unburnt hydrocarbons. Pureness of the fuel itself has also a direct impact on particle emissions.

Therefore, an improvement of the combustion process used in current aeronautical engines is necessary both to increase the efficiency of combustion process and to reduce derived pollutant emissions. For this reason, many efforts are being invested in research and development of new, more efficient and less pollutant engines. Numerical simulations have become very important tools in this framework. Indeed, during the past decades, the advances in computing resources and simulation methods allow sophisticated simulations at industrial scale (Boileau (2007), Wolf *et al.* (2010)). This work is situated in this context since the improvement of the actual techniques can only be achieved through a better comprehension of the processes and phenomena taking place inside the engines.

1.1 The Numerical Simulation as a powerful tool

As an illustrative example, Figure 1.1 displays a cut of an aircraft engine showing its main parts. Despite the specificity of this choice, the same general statements (with some modifications, especially regarding the configuration and the thermodynamic cycle) may be applied to piston engines and other applications.

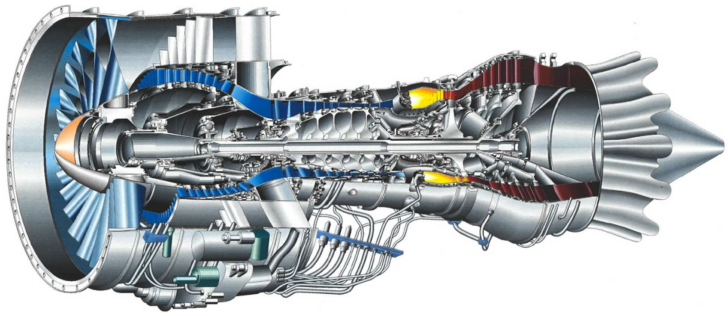

Figure 1.1: *Mid-plane cut of an aircraft engine. (Source http://web.engr.oregonstate.edu).*

The process to generate power is as follows: air enters the engine through the compressor, where the pressure of the flow is increased. Then it enters the combustion chamber where it is mixed with the liquid fuel injected in spray form. The spray evaporates, mixes with air and then burns. The exhaust gases exit the engine through the turbine where the flow energy is transformed into work. The burnt gases may be diluted with some air to decrease their temperature in order to reduce possible damages to the first stages of the turbine. From the thermodynamic point of view, three main processes take place (Fig. 1.2):

1. Isentropic compression in the compressor
2. Isobaric combustion in the combustion chamber
3. Isentropic expansion in the turbine

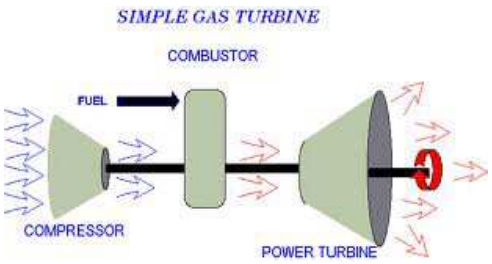

Figure 1.2: *Simplified sketch of the thermodynamic cycle of a gas turbine. Source Wikipedia.*

In this work, only the processes taking place in the combustion chamber are of interest, and more precisely the phenomena related to liquid fuel spray. For this reason, the compressor and the turbine will not be taken into account. Moreover, since the phenomena involving the spray are of a high complexity, the scope of this work is reduced to non-reactive cases.

In the past decades, Computational Fluid Dynamics (CFD) has become a very powerful tool both in academic research and industrial applications. On one side, it permits the validation of analytical models in a simple and fast manner. On the other side, they have partly replaced experiments in the industrial field for the design of new components. Indeed, simulations are faster and much cheaper than experiments when complex geometries are taken into account. This is due to the difficulties related to the simultaneous

characterization of the different phenomena occuring in the flow (such as in two-phase reacting flows) and to access the flow field in complex geometries. Moreover, it is rather simple to perform parametric studies using CFD which allows to study the influence of individual parameters on the industrial device performances.

There are three main strategies regarding CFD simulations:

- Direct Numerical Simulation (DNS), which completely solves flow dynamics up to the smallest scales, requiring no modeling (i.e. all turbulence scales are explicitly determined), but is computationally very expensive. Furthermore, when including two-phase flows, it can quickly become prohibitive and it is certainly not applicable today to real industrial configurations. For this reason, its use is limited to canonical test cases, where it greatly contributes to the understanding and related modeling efforts of many different types of flows.
- Reynolds Averaged Navier-Stokes (RANS) simulations (Jameson (1991), Lathouwers & Bellan (2001)), which only solve the mean flow field (Chassaing (2000), Pope (2000)). The balance equations for mass-weighted averaged quantities are obtained by averaging the instantaneous balance equations. The average equations require closure models for the turbulent dynamics of the flow. The greatest advantage of RANS is its low computational cost and the years of research and development invested in this approach. However, this approach is not suitable for the simulation of unsteady or transient flows.
- Large Eddy Simulation (LES) (Smagorinsky (1963), Lilly (1967), Deardorff (1974)), in the middle between DNS and RANS simulations, solves the largest scales of the flow up to a certain length-scale and the scales smaller than that are modeled by means of subgrid models. The balance equations are obtained by spatially filtering the instantaneous equations. The size of this filter determines the size of the scales that are solved and those that are modeled. This approach provides information about transient phenomena and is very suitable to perform unsteady flows simulations. Most developments on LES derive from the study of academic configurations such as Homogeneous Isotropic Turbulence (Kraichnan (1976), Chasnov (1991)) or turbulent channel flow (Deardorff (1970), Schumann (1975), Moin & Kim (1982)). However, it has also been used in industrial configurations (Haworth *et al.* (2000)). The computational cost of LES is bigger than that of RANS simulations and moderate compared to DNS (depending on the size of the scales that are solved), but affordable in most cases. It is in fact a very good compromise between accuracy and computational time.

Nowadays CFD uses DNS for the validation of numerical models in canonical test cases. In real industrial applications RANS is a suitable approach for the simulation of the compressor and the turbine in aircraft engines. Due to the unsteady nature of the phenomena occuring in the combustion chamber, LES is the most suitable approach for the simulations of this part of the engine. In the context of this work, stress is applied to model validation in a first part. DNS of academic configurations is used to assess the validity of algebraic models. On a second part, where the application to more complex configurations is studied, LES is used.

1.2 The role of the liquid sprays

Many industrial applications involve liquid sprays. Most of them are used for power generation (liquid rocket engines, diesel engines, jet engines, etc.), but there are many other applications involving droplet/particle laden flows (refrigeration, fluidized beds, etc.). The study of turbulent gaseous flows is a timely research topic. The study of liquid sprays in turbulent flows is more recent. For this reason, there is still a long path to propose models for the simulation of two-phase turbulent flows which account for all the phenomena involved in the dynamics of sprays in turbulent gaseous flows. The lack of experimental data in industrial configurations at real conditions is an important impediment for the validation of models and numerical results. This is due to the high complexity of this type of systems. The measuring techniques used nowadays to perform experiments need further developpement. It is crucial to obtain simultaneous data on different quantities (related to the gaseous and the dispersed phase) to characterize the flow. Indeed, two-phase flows include a number of processes involving very different time and length scales. Simplifications must be done in order to be able to reproduce part of these phenomena. The characteristic length-scales of an evaporating two-phase flow range from the size of the smallest droplets of the spray (of the order of a micrometer) to the size of the combustion chamber (of several centimeters). The characteristic time-scales of the flow depend on the size of the droplet, which has a major impact on the inertia and the lifetime of the droplets.

Here, a brief overview of the principal processes involving the dispersed phase is provided.

1.2.1 Injection

The injection system represents one of the essential components of the combustion chamber. It provides the liquid fuel and plays an important part in internal reacting flow aerodynamics. The liquid fuel is injected in the form of a cylindrical column or a thin liquid sheet that due to an aerodnamic destructive effect is atomized into a cloud of droplets. The characteristics of this cloud, such as the droplet density and size, strongly depend on the injection parameters and geometry.

There are many types of injectors. Here, only three types are recalled:

- Rotary atomizers. The liquid flow is forced into a rotating device before entering the combustion chamber. The rotation velocity of this device determines the size of the droplets that are formed. These devices can control very tightly the final diameter of the droplets and generate very fine clouds. However, they are too complex to be employed in aeronautical combustion chambers.
- Airblast atomizers. The shear effect of accelerated air flow parallel to the the fuel injection is used to atomize the liquid fuel. A complex interaction between the air and the fuel produces the formation of the droplet cloud. These mechanisms work at low relative speed and high air flow. The configuratio of the injection streams can be planar or annular.
- Pressure atomizers. The liquid is forced to flow through a small hole by means of a strong pressure force, generating a conical spray. The inlet can have a planar or annular geometry, combined or not with a swirl diffusor. The liquid sheet is subjected to strong shear on both sides, which provokes its disintegration into small droplets.

In aircraft engines, fuel is generally injected by means of pressure swirl atomizers. The characteristics of the spray pattern highly depends not only on the parameters of the injection device, but also on the gaseous flow inside the combustion chamber and the properties of the liquid fuel: for example the viscosity (directly influencing the droplet size) and the fuel volatility (which impacts the vaporization process). Pressure swirl atomizers and the influence of the different parameters on the resulting droplet cloud have been extensively studied in the literature (Lefebvre (1989), Taylor (1948), Bayvel & Orzechowski (1993), Jones & Whitelaw (1982)).

1.2.2 Atomization

Fuels used in aircraft engines are not volatile enough to be ignited and burnt if the surface in contact with the oxydizer is not augmented by pulverization. The liquid sheet exiting the injector must be atomized into a cloud of droplets. The atomization process can be described as the ensemble of mechanisms that occur in the injection of a high pressure liquid through a small fence. Two different phenomena can be distinguished in this process: the primary atomization takes place in the region near the orifice, the secondary atomization usually extends much further.

The mechanisms of liquid sheet disintegration have been widely studied. Several studies focus on the linear stability analysis of the sheet oscillation by means of Navier-Stokes temporal stability analysis of liquid sheets injected into still gaseous flow (Squire (1953), Taylor (1959)). These studies conclude that the atomization process is caused by two types of instabilities (Reitz (1978)) formed in the liquid sheet interface (sinusoidal antisymmetrical oscillations and symmetrical dilatation instabilities). The waves caused by the sinusoidal mode are not strong enough to cause the liquid sheet break-up. Rangel & Sirignano (1991) stated that the sheet may disintegrate following the growth of the amplitude of the dilatation waves, producing a pinch resulting in the sheet break-up. Very fine liquid ligaments are formed that suffer further disintegration into droplets of different sizes (secondary breakup). The primary atomization has been studied experimentally by Stapper & Samuelsen (1990), Marmottant & Villermaux (2004), Carvalho *et al.* (2002), Lefebvre (1989) and Lozano *et al.* (2001) amongst others.

The numerical simulation of the primary atomization process requires the explicit resolution of the Navier-Stokes (NS) equations for both phases and the coupling between them through jump relations at the interface. In addition, the position and motion of the interface must be accurately described (Couderc & J.-L. (2003), Trontin (2009)). DNS of the primary atomization process needs extremely high resolution meshes since the length scale of the smallest liquid structures can become very small as the liquid ligaments approach their breakup. In general the mesh size is determined by the smallest droplet diameter. At least two to five computational cells per droplets are needed (Gorokhovski & Herrmann (2008)). This feature prevents the numerical simulations of the primary atomization at industrial scale. However, as small droplets are only present at the periphery of the liquid sheet, mesh adaptation techniques (Berger (1982), Almgren *et al.* (1993), Sussman *et al.* (1999), Zuzio (2010)) can be used in order to reduce the computational cost. Level-Set (Osher & Fedwik (2003)) and Volume of Fluid (VOF, DeBar (1974)) methods are suitable approaches for this task (Menard *et al.* (2007)). Desjardins *et al.* (2008) developped a Level-Set method combined with high-order implicit transport schemes to preserve mass conservation. Moreau & Desjardins (2008) implemented a high-order Ghost Fluid method. Both approaches show accurate results. Due to the large range of length and timescales involved in the process, direct and detailed numerical predictions of the primary atomization process are computationally very expensive and not affordable at large scales. Their application is limited in terms of Reynolds number and geometry complexity. However, RANS and LES approaches for the simulation of the primary atomisation exist (Beau *et al.* (2006, Paper 98166), Chesnel (2010)).

Once the liquid sheet has decomposed into fine liquid ligaments, further disintegration occurs and droplets of different sizes arise due to air entrainment and aerodynamical forces acting on the ligaments. This process is called secondary breakup. Several regimes, depending on the Weber number, exist. The Weber number is a dimensionless number relating the aerodynamic forces acting on the droplet and its surface tension. Those two forces have opposite effects on a droplet: the surface tension stabilizes the droplet and the aerodynamic force tends to break it. This is a process of high difficulty in terms of modeling and simulation. Indeed, there are many effects that must be taken into account, such as the droplet deformations prior to breakup (which modifies the drag force law) and collisions and coalescence which are predominant in this zone of the spray. Indeed, in the secondary breakup zone, the spray is very dense, which increases the probability of collision between droplets. Numerical studies of this problem may rely on different approaches (Fig 1.3 is an example for the case of the atomization of a liquid column). DNS using an interface tracking method being out of reach for realistic applications, simplifications have been proposed in literature. Apte *et al.* (2003*a*) use a Lagrangian method, neglecting the liquid column and taking into account secondary breakup only. Rachner *et al.* (2002) use a Lagrangian method combined

with modified laws for drag force and models for the column breakup based on empirical correlations. Finally, a common solution consists on considering the primary atomization as a boundary condition for the dispersed phase from which a distribution of droplets is directly injected.

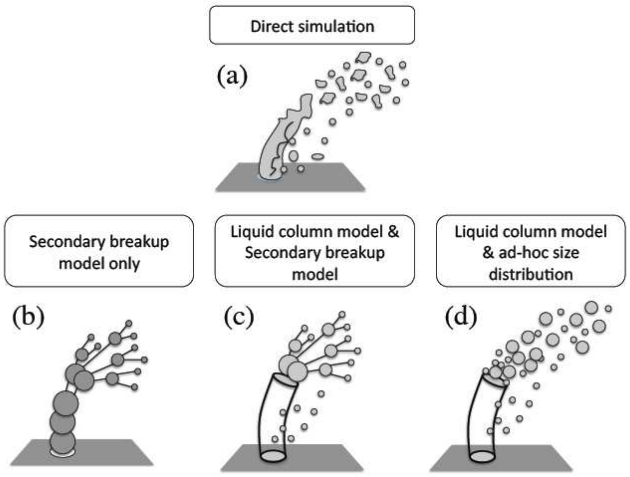

Figure 1.3: *Schematic of the modeling approaches for a liquid jet-in-cross-flow case. (Extracted from Jaegle (2009)).*

Figure 1.4 shows a sketch of the main phenomena following the liquid injection. The secondary atomization produces a cloud of droplets of different sizes. In this zone, far from the injection where the spray is much denser, the volume fraction of droplets is very small compared to that of the gas phase. Droplet/particle laden two-phase flows can be classified taking into account the particle volume (α_p) and mass fractions (M_p) of the spray (Fede *et al.* (2004)):

- $\alpha_p < 10^{-4}$ and $M_p < 10^{-2}$: very diluted flows. Inter-particle collisions and effects of particles on the carrier fluid phase can be neglected due to the low inertia of the particles.
- $\alpha_p < 10^{-4}$ and $M_p > 10^{-2}$: diluted flows. Two-way coupling between the gaseous and the dispersed phases must be taken into account.
- $10^{-4} < \alpha_p < 10^{-1}$: moderately dense sprays. Inter-particle collisions become important in this type of flows. However, the carrier phase flow remains the main contribution to particle motion
- $\alpha_p > 10^{-1}$: very dense sprays. Inter-particle collisions are the most important contribution to the particle motion.

This work focuses on the diluted regime zone located after the secondary breakup zone. Only diluted and very diluted flows are considered. Thus, inter-particle collisions are ignored and one-way or two-way coupling with the carrier fluid is considered depending on the configuration. In this type of flows, the principal physical phenomena is the particle dispersion due to the gaseous turbulence. If two-way coupling is considered, the fluid turbulent energy tends to decrease due to the presence of the dispersed phase. Note that throughout this work particle phase refers to a dispersed phase composed by solid particles, liquid phase to a dispersed phase composed by liquid droplets and the term dispersed phase is used indistinctly for both.

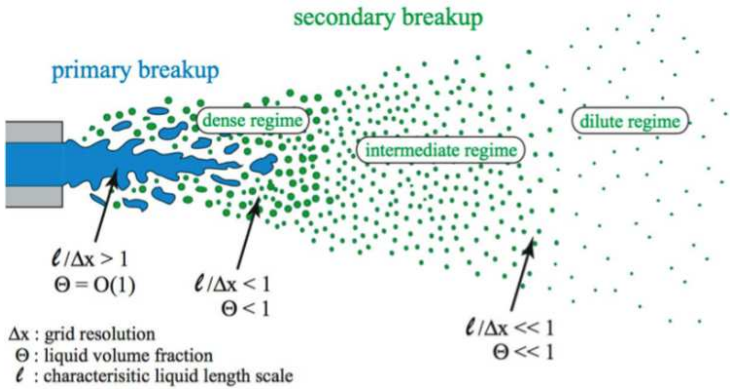

Figure 1.4: *Phenomenology of the atomization of a spray. (Source M. Hermann, Summer Program of the CTR, Stanford).*

1.2.3 Dipersion and Evaporation

In the diluted regime, dispersion and evaporation become predominant. In this case, particle trajectories are directly influenced by the carrier flow turbulence. However, their response to the gaseous flow depends also on their inertia. The Stokes number (St) relates the characteristic particle response timescale (τ_p) to the characterisitc fluid timescale (τ_f), giving a measure of the particle inertia. Very inertial particles ($St >> 1$) have trajectories quite independent from the carrier fluid flow. On the contrary, very low inertial particles ($St << 1$) quickly respond to changes in the gaseous flow. In industrial applications, the inertia of the particles varies because their size and mass change due to evaporation and polydispersion effects. Very different behaviors take place at the same time. When the evaporation timescale of the droplets (τ_{ev}) is very short, droplets evaporate very quickly and very few droplets are present far from the injection zone. If, on the contrary, the droplet lifetime is long, droplets are present further downstream.

The dispersion of particles has been deeply studied. The first studies on particle motion date from the nineteenth century. Later on, Tchen (1947) and Reeks (1991), amongst others, performed theoretical analysis of particle dispersion which led to the definition of the main length and time-scales of the particle motion in gaseous turbulence. Maxey (1987) proposed analytical methods able to predict complex phenomena such as preferential concentration effects (i.e. cummulation of particles in low-vorticity and high-strain regions, also called particle segragation (Squires & Eaton (1991*a*)), Eaton & Fessler (1994)) or particle trajectory crossing (Wells & Stock (1983)), which characterise the interactions of the particles with the gaseous turbulence. The modulation of the turbulence by the presence of the particles is also a process of interest. It is often assumed that the carrier fluid flow turbulence is not affected by the presence of the particles (one-way coupling). This hypothesis is valid in very diluted regime. However, in diluted regime inverse coupling in not negligible and the effects of the dispersed phase on the fluid turbulence must be accounted for (Fede *et al.* (2004)). Turbulence modification due to the presence of particles has been widely studied in particle-laden Homogeneous Isotropic Turbulence (HIT) flows (Squires & Eaton (1990), Elghobashi & Truesdell (1993) (accounting for two-way coupling), Boivin *et al.* (1998) (using DNS of the gaseous phase), Sundaram & Collins (1999)) and mean sheared configurations (Vermorel *et al.* (2003), Vermorel (2003)).

Particle dipersion in gaseous turbulence has been widely studied experimentally (Snyder & Lumley (1971)) and numerically (Squires & Eaton (1991*a*), Deutsch (1992), Mei *et al.* (1991) (accounting for Basset force and gravity settling effects), Laviéille (1997) (taking into account interparticle collisions), Elghobashi & Truesdell (1992) (using DNS) and Boivin *et al.* (2000) (using LES and accounting for two-way coupling) in HIT, Reeks (1993) in simple shear flows, Simonin (1991) in particle-laden jets, Vance *et al.* (2006), Wang & Pletcher (1996) (using LES), Yamamoto *et al.* (2001) (in vertical channel configuration using LES and accounting for collisions) in particle-laden turbulent channel flows, Apte *et al.* (2003*a*) in swirling flows, etc).

Regarding the vaporization process many models exist. Models are mainly based on empirical results on single isolated droplets, which have been modified to include the effects of neighbouring droplets, convection, multicomponent fuels, etc. (cf Part III). Many parameters have an influence on the vaporization process. Indeed, the characteristics of the fuel, the spray and the carrier flow play an important role and directly influence the evaporation of droplets inside the combustion chamber. An exhaustive review of the theoretical models for droplet vaporization can be found in Sazhin (2006) or in classical textbooks such as Sirignano (1999), Kuo (2005) or Williams (1985).

Experimental studies on droplet vaporization are often performed on isolated droplets, taking into account or not the effects of convection (Wong & Lin (1992)), radiation, heat conduction through the support fiber (Yang & Wong (2002), Chauveau *et al.* (2008)), multicomponent fuels (Ghassemi *et al.* (2006)) and for high pressure and temperature (Matlosz *et al.* (1972), Kadota & Hiroyasu (1976), Nomura *et al.* (1996) Morin *et al.* (2004)).

From the numerical point of view, the effect of ambient gas and fuel properties has been studied by Hubbard *et al.* (1975). Yang & Chang (2001) performed a numerical study on the effects of the heat conduction through the support fiber and the radiation of the furnace in the experiments of Nomura

et al. (1996).

Evaporation has an important effect on the dispersion of particles in turbulent flows. Albrecht *et al.* (1999) studied the dispersion of evaporating droplets in HIT flow, Réveillon & Vervisch (2004) studied the dispersion of evaporating droplets in turbulent flows taking into account polydispersion effects.

1.2.4 Combustion of droplets

The combustion process considered often involves chemical reactions that only take place in the gaseous phase (Williams (1971)). Thus, the evaporation of liquid fuel droplets is a necessary step for the combustion to take place. However, two main types of combustion exist: single-phase combustion and two-phase combustion. These two regimes depend on the ratio between the characteristic evaporation time and the convection time of the carrier phase. When the characteristic evaporation time of the droplets is very small compared to the convection time, the droplets completely evaporate before reaching the flame front. Combustion taking place in the single-phase regime, it only depends on the gaseous fuel repartition in the chamber. The gaseous fuel field will however depend on the characteristics of the evaporation process and the dispersion of the droplets. On the other hand, when the evaporation time is longer than the convection time, flame and spray are coupled. The droplets may reach the flame front and the characteristics of the flame strongly depends on the spray parameters.

Isolated droplet combustion studies can be found in the work of Godsave (1953)

Numerical results obtained using DNS of sprays in different combustion regimes provide an extra classification of the phenomena coupling spray and reaction (Réveillon & Vervisch (2005)). Two-phase flow combustion has different characteristics than gaseous phase combustion. The characteristics of the flame are modified due to the presence of liquid droplets and strongly depend on the quantity of fuel that has been evaporated before reaching the flame front. Indeed, the gaseous field is modified by the presence of droplets upstream from the flame which may lead to flame instabilities. Note also that the evaporation rate depends, amongst other things, on the concentration of droplets. This may create zones of very high concentration of gaseous fuel and very lean zones too. The mixing is then different from the case where gaseous fuel is directly injected into the chamber.

Furthermore, if the droplets reach the flame front, the evaporation and combustion zones overlap, leading to different combustion regimes. Réveillon & Vervisch (2005) give a symmetric description of the spray flame structures that is recalled here. They classify the different modes depending on a dimensionless number, G, which is the ratio between the droplet evaporation rate and the diffusion rate of hot gases within the droplet cloud. When convection is more important than diffusion, G is approximated as follows:

$$G \approx \frac{5N_p^{\frac{2}{3}}}{S} \tag{1.1}$$

where N_p is the number of droplets in the cloud and S is a mean doplet spacing parameter linking the characteristic average distance between droplets to the diffusion flame radius.

For large G numbers, the spray is very dense and diffusion inside the cloud is low, only the droplets located at the periphery of the cloud evaporate. The flame enveloppes the whole cloud of droplets. It is referred to as external sheath combustion. For diluted spray regimes, where $G << 1$ droplets are far from each other and the evaporation rate increases due to hot gases diffusion. Separated flames surround each droplet, which burn individually. Intermediate regimes exist between these two extremes: for G numbers slightly larger than one, the flame surrounds the whole cloud of droplets but hot gases diffusion is high enough, thus the droplets in the center of the cloud vaporize. When $G < 1$, the center of the cloud burns in an external combustion regime and the droplets located at the periphery burn in an isolated manner. Figure 1.5, taken from Réveillon & Vervisch (2005), illustrates four distinct modes of spray combustion regimes depending on G.

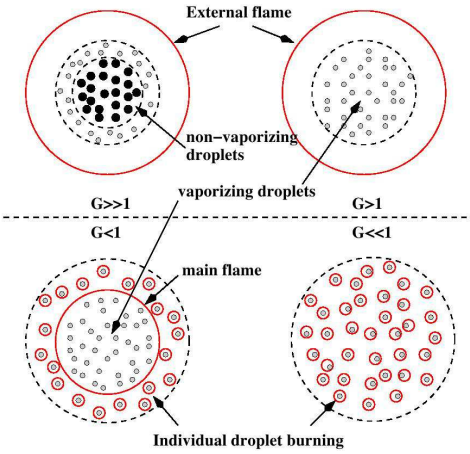

Figure 1.5: *Classification of different spray combustion regimes. Extracted from Réveillon & Vervisch (2005).*

Borghi (1996*a*) and Borghi & Champion (2000) propose another classification based on the characteristic evaporation time τ_{ev}, the characteristic time of the flame τ_f and the flame thickness δ_f. When $\tau_{ev} << \tau_f$, droplets evaporate in the preheating zone upstream from the flame which burns in a premixed regime. In this case, spray characteristics fluctuations may lead to partially-premixed flames. When the evaporation time is longer than the flame characteristic timescale, two distinct regimes are possible depending on the ration between the flame thickness and the droplet flame radius. If the radius of the flame surrounding the droplets is small compared to the flame thickness, burning droplets cross the flame front and burn in a secondary reaction zone. On the contrary, for flame thicknesses smaller than the radius of the flame surrounding the droplet, the presence of the last modify the behavior of the flame front, thicknening it. This classification does not take into account turbulence effects and equivalence ratio variations. Réveillon & Vervisch (2005) provide a different classification based on numerical results of two-dimensional spray flames in counterflow:

- External combustion regime: in a case of low equivalence ratio, the premixed flame consumes the totality of the fuel (liquid and gaseous). When the equivalence ratio is high, the fuel burns in diffusion regime.
- Group combustion regime: droplet clusters individually burn on rich premixed flames ussually followed by diffusion flames.
- Hybrid combustion regime: intermediate conditions between the external and the group combustion regimes.

Reviews on droplet and spray combustion can be found in Faeth (1983), Faeth (1987), Law (1982) or Sirignano (1983).

1.2.5 Numerical simulation of sprays

Two-phase flows involve complex physical phenomena, such as liquid-gas, or liquid-surface interactions, atomization process, droplet dynamics and heat and mass transfer. Up to date, no analytical treatment exist for a general representation of the complete set of processes involving particle/droplet laden flows. Therefore, numerical modeling and simulations have been increasingly employed. Numerical simulations are often preferred over experiments because they can usually be carried out faster due to a shorter lead-time and with less expense. Aditionally, control is easier and they can be used to study a much wider range of conditions, some of which are physically inaccesible (Liu (2000)). DNS of two-phase flows

are not accesible for realistic configurations. Indeed, a direct simulation of the dispersed phase implies the resolution of the flow field around each individual droplet and, in the case of liquid droplets, inside the droplet too. In realistic configurations, where evaporation of liquid sprays is usually accounted for, droplets can reach very small sizes (less than a micrometer), which need very fine computational grids. The computational cost related is very high, both in time and memory requirements. Therefore, DNS of two-phase flows is limited to canonical test cases in academical research. However, several options for the modelisation of the dispersed phase exist. They can be coupled with DNS or LES of the gaseous phase. An exhaustive review on LES approaches for the dispersed phase can be found in Fox (2012).

In this work, two modeling frameworks to simulate sprays in diluted regimes are used. The developments presented in this work concern the Euler-Euler approach. The Euler-Lagrange approach is used for validation when no experimental data are available:

- In the Lagrangian approach (Sankaran & Menon (2002), Apte *et al.* (2003*a*)), the individual trajectory of each particle is tracked in its own frame of reference. Droplets are treated through the point source approximation and their trajectories are evaluated through force balance at each point (Maxey & Patel (2001)). The carrier fluid flow is usually computed by solving the Navier-Stokes (NS) equations. In the Lagrangian computations, the location of the discrete particle not necessarily coincide with the computational grid. Therefore, in order to account for coupling between the gaseous and the dispersed phases, the properties of the carrier fluid must be interpolated at the location of the droplet or particle. An accurate numerical algorithm is needed for this task, which increases the numerical complexity of this method. Moreover, the difficulty increases when the gaseous flow is computed with a LES approach, since not all the scales of the carrier phase are resolved, and the effects of the unresolved scales on the particle motion must be taken into account (Dukowicz (1980)). On the other hand, polydispersity can easily be accounted for. The Lagrangian methods may become computationally very expensive when the number of particles to be followed increases. However, physical particles can be substituted by numerical particles representing a cluster of various real particles, which reduces the computational cost. On the other hand, parallelization tasks must be carefully handled, since in configurations where particle cummulation takes place (e.g. zones close to the injector), a bad load balance between processors takes place, for which adapted partitioning algorithms should be used (García (2009)).
- Another alternative approach is the Eulerian method, which considers both phases (the carrier and the dispersed phase) as continuum and captures only averaged quantities of the dispersed phase (Ferry & Balachandar (2002)). Depending on the formalismm used, the spray properties are averaged in a volumetric (Whitaker (1999)) or ensemble (Zhang & Prosperetti (1994), Simonin (1991)) sense and calculated through the evolution of a probability density function (pdf) equation. In general, the dispersed phase is solved using a set of conservation equations for the moments of the pdf equation. Accounting for polydispersity is less obvious in this case. However, it may be reproduced by discretizing the droplet size distribution leading the so called sectional methods (Greenberg *et al.* (1993), Laurent *et al.* (2004), Vié (2010)); a complete set of transport equations is solved for each section, which increases the computational cost and the complexity due to the exchanges between each section when phenomena such as evaporation are taken into account.

Both methods have advantages and drawbacks. Table 1.1 displays a non-exhaustive comparison between both approaches. Here, the supplementary modeling effort and the special treatment for particle trajectory crossing (PTC) are stressed. Indeed, the Mesoscopic Eulerian Formalism (MEF) used in this work needs closure for some terms appearing in the transport equations for the dispersed phase. These terms are linked to the modelisation of PTC related phenomena. On the same way, the coupling terms between phases, such as drag force and evaporation source terms also need modeling.

The CFD code used in this work, AVBP, has two different solvers for the dispersed phase, a Lagrangian one and an Eulerian one. Here, only the Eulerian solver is used. It is based on the Mesoscopic Eulerian Formalism (MEF, Février *et al.* (2005)) defined in Chapter 2. The basic idea is the distinction between two different contributions in the particle velocity: an ensemble velocity, shared by all the particles

Euler-Euler	Euler-Lagrange
Advantages	
⊕ Numerical straightforward treatment of dense zones. ⊕ Similarity with gaseous equations. ⊕ Direct transport of Eulerian quantities. ⊕ Similarity with gaseous computer paralelism	⊕ Numerically straightforward modeling of particle movements and interations. ⊕ Robust and accurate if enough particles are used. ⊕ Size distributions are easy to describe. ⊕ Numerically straightforward to implement physical phenomena (e.g heat and mass transfer, wall-particle interaction).
Drawbacks	
⊖ Difficult description of polydispersion. ⊖ Difficulty of droplet crossing treatment. ⊖ Limitation of the method in very diluted zones.	⊖ Delicate coupling with combustion. ⊖ Difficult parallel implementation. ⊖ CPU time spent in locating particles on unstructured grids.

Table 1.1: *Advantages and drawbacks of Euler-Euler and Euler-Lagrange approches. Extracted from García (2009).*

and an uncorrelated part, which is specific to each individual particle. Due to the contribution of the uncorrelated part of the particle velocity field, unclosed terms appear in the transport equations for the dispersed phase. These terms are closed by means of algebraic models.

1.3 Objectives of the present work

This thesis has been supported by CERFACS (Centre Européen de Recherche et Formation Avancée en Calcul Scientifique) and the European Union in the framework of the MYPLANET project (Massively Parallel Computations of Combustion and Emission Simulations) in an initiative to train a new generation of engineers in the field of high performance computing applied to the numerical combustion simulation, energy conversion processes and related atmospheric pollution issues.

This work proposes to improve the modeling of the dispersion and evaporation phenomena for diluted regimes oriented to the pre-vaporised combustion of sprays on industrial aeronautical chambers. Several models are implemented in the AVBP code, dedicated to LES in complex geometries and tested on academic and semi-industrial configurations. The results obtained are compared with reference data (either Lagrangian simulations or experimental measurements) in order to assess the validity of the models.

Combustion, both purely gaseous as well as spray combustion, is out of the scope of this study. This brief overview of the main phenomena related to the dispersed phase in aeronautical combustion chambers helps limiting the phenomena adressed in this work. Figure 1.6 displays a sketch of the processes followed by the dispersed phase after the injection of the fuel in the combustion chamber. Here, only the dispersion and the evaporation of droplets in non-reactive flows are taken into account.

Section 1.3.1 briefly recalls the previous developements performed on dispersed phase modeling with the MEF for the Eulerian approach. Section 1.3.2 presents the global outline of this manuscript.

1.3.1 Previous developments

The main tool used during this work is the code AVBP. This finite-volume and finite-element unstructured hybrid solver has been jointly developped by CERFACS and IFP-EN (Institut Francais du Pétrole -

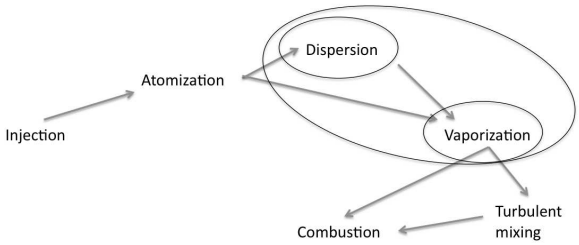

Figure 1.6: *Sketch of the principal phenomena related to the dispersed phase in combustion chambers.*

Energies Nouvelles) over the last 20 years. AVBP is a massively parallel code that explicitely solves both DNS and LES Navier-Stokes equations in compressible form. It is based on the cell-vertex approach (Schønfeld & Poinsot (1999)). High-order numerical schemes and characteristics boundary conditions (Poinsot & Lele (1992)) are available. More information on AVBP can be found in Lamarque (2007).

Several studies involving the MEF for Eulerian approach for the simulation of two-phase flows have been conducted until now. Février *et al.* (2005) introduced the MEF that allows the simulation of the dispersed phase coupled with DNS or LES of the gaseous phase. Closure models for the transport equations for the dispersed phase were firstly proposed by Simonin (2002) and Kaufmann *et al.* (2005). Kaufmann (2004) implemented the MEF in AVBP and performed the first numerical simulations in particle-laden HIT using DNS for the simulation of the carrier fluid flow. Validation of the implementation was performed through comparisons with reference data from Lagrangian computations. Moreau (2006) and Riber (2007) extended the MEF, until that time available only in the context of DNS, to LES. Closure models for the subgrid-scale terms were *a priori* developped in the particle-laden decaying HIT (already studied by Kaufmann (2004)) and Moreau (2006) and *a posteriori* validated in the same configuration by Riber (2007). Riber (2007) alse performed studies on more complex configurations (Hishida *et al.* (1987), Borée *et al.* (2001)). Mossa (2005) extended the MEF in order to take into account polydispersion. The MEF has also been employed in industrial configurations taking into account gaseous combustion (Pascaud (2006)). Boileau (2007) demonstrated the capability of this approach to simulate complex industrial configurations in real conditions presenting a LES of the two-phase reacting flow of a complete helicopter annular combustion chamber. Sanjosé (2009) implemented the FIM-UR methodology for the modelisation of the spray injection. Roux *et al.* (2009) developped new numerical schemes more adapted to the simulation of the dispersed phase. Masi (2010) recently proposed new algebraic equations for the modelisation of the unclosed terms appearing in the transport equations of the dispersed phase for DNS and LES and for the modelisation of the uncorrelated part of the particle temperature field from *a priori* simulations of a mean-sheared particle-laden flow (Vermorel (2003)). Vié (2010) included the possibility of taking into account polydispersion effects using a multi-section method. Recently Dombard (2011) studied the effects of the uncorrelated motion in anisothermal mean-sheared configurations.

The MEF is currently used for the simulation of reactive flows in complex geometries. Polydispersion effects can be accounted for. However, spray combustion is not taken into account and reactions occur only in the gaseous phase. Regarding the modelisation of the unclosed terms related to the uncorrelated motion (RUM, Février *et al.* (2005)), only one model (Simonin *et al.* (2001)) has been tested until now in complex geometries. The studies performed on particle-laden HIT showed that the RUM must be taken into account when low and high inertia particles are simulated. Otherwise, the simulation is numerically unstable. However, the viscosity-type model proposed by Simonin *et al.* (2001) based on a local-equilibrium assumption, leads to a re-laminarization of the dispersed phase flow in configurations with mean-shear (Riber (2007)). Several studies have revealed the importance of the mesh resolution in dispersed phase simulations. Indeed, a high resolution is needed in order to capture phenomena such as the preferential concentration. Eulerian simulations of complex geometries not accounting for the RUM show accurate mean particle velocity distributions but lead to an underestimation of the velocity fluctuations.

1.3.2 Plan of the manuscript

This work is organized as follows:

- Part I describes the governing equations for both the gaseous and the liquid phases in the context of non-reactive two-phase flows. Chapter 2 presents the Navier-Stokes (NS) equations for the gaseous phase in DNS as well as the equations for the dispersed phase in the Euler-Lagrange and the Euler-Euler approaches. The Mesoscopic Eulerian Formalism is presented and the transport equations and coupling terms with the gas phase described.

  Chapter 3 presents the concept of LES and briefly describes the filtering process underneath the approach. It presents the filtered governing equations for the gas and the dispersed phases. The WALE model for gaseous phase and the filtered equations for the dispersed phase (Moreau (2006)) used for the simulation of the MERCATO configuration in Part IV are summarized.

- Part II is dedicated to the analysis and validation of different closure models for the deviatoric part of the RUM stress tensor. First, Chapter 4 presents the different models (Masi (2010)) retained for their evaluation in AVBP. These models have been proposed by Masi (2010) during her thesis performed at IMFT (Institut de Mécanique de Fluides de Toulouse). Masi developped several closure models and performed an *a priori* analysis in the configuration of a particle-laden slab (Vermorel (2003)). Nine out of the eleven models developped by Masi along with the classic viscosity-type model already implemented in AVBP (Simonin *et al.* (2001)) have been implemented in AVBP and *a posteriori* validated against the Euler-Lagrange results of Masi (2010) in the same configuration (Fig. 1.7). A classification of the models following two criteria (the order of the model and the characteristic time scale used) as proposed by Masi (2010) is provided.

  Chapter 5 presents the results obtained for the configuration of Fig. 1.7. This academic configuration aims at being representative of the phenomena encountered in a hollow-cone type spray injection, where the liquid fuel droplets are subject to very strong shear due to the effect of air entrainment. Two different levels of turbulence and three levels of particle inertia have been tested. The models have been evaluated using the same numerical setup in order to simplify the comparisons. Low-order and high-order statistics have been compared as well as instantaneous fields of the droplet number density, droplet velocity and Random Uncorrelated Energy (RUE). The results obtained distinguish one model as the one giving the best performances (2ΦEASM3). This model has been retained for the simulation of the configuration presented in Part IV.

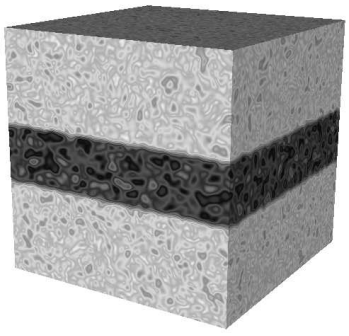

Figure 1.7: *Sketch of the case studied in Part II corresponding to the configuration initialy studied by Vermorel (2003).*

- Part III focuses on the development of a new model for the simulation of the evaporation process of liquid fuel droplets. This part is motivated by the recent publication of experimental results on

isolated droplet evaporation (Chauveau *et al.* (2008)) which are very different from the classical results (Nomura *et al.* (1996).

Chapter 6 proposed a classification of the different evaporation models and introduces the assumptions employed in the model implemented in AVBP. The equations used for the calculation of the main thermodynamic and transport properties are presented. A comparison between simulations performed with two different calculations of the transport and thermodynamic properties (as previously done by Sanjosé (2009)) allowed the identification of the parameters having a major influence on the process. Taking this into account, a new approach for the simulation of the evaporation process is proposed. Chapter 7 shows the results obtained with the classical approach implemented in AVBP and the new approach for both the Spalding and the Abramzon-Sirignano models for the evaporation of single isolated droplets. The results are presented for two fuels for a wide range of conditions (temperature and pressure).

- Finally, Part IV presents the simulations performed in the MERCATO configuration (Fig. 1.8) in order to assess the applicability of RUM and evaporation models to complex configurations. The MERCATO test rig is a semi-industrial configuration used for the study of spray autoignition at high altitude conditions. Four cases are presented, they are issued by the combination between two evaporation approaches and two RUM strategies (noRUM, which does not take into account the RUM contribution and 2ΦEASM3 model). The mean and instantaneous gaseous and liquid fields are studied. Both the gaseous and the liquid mean and root mean sqaure (RMS) velocity profiles are analyzed, as well as the mean and RMS droplet diameter profiles. Particle velocity fields are validated against the experimental data of García-Rosa (2008). For those quantities such as the particle volume fraction, for which experimental data is not available, comparison with the classical models implemented in AVBP are performed. The effects of the evaporation approach and the RUM model are assessed separately.

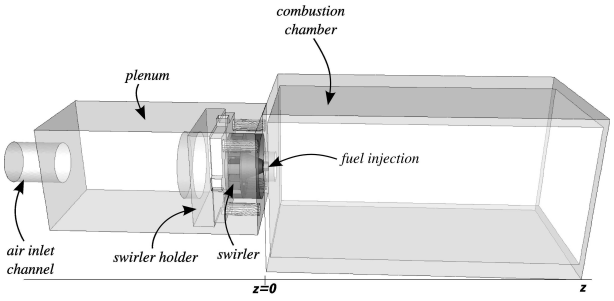

Figure 1.8: *Sketch of the MERCATO configuration studied in Part IV. Extracted from Senoner (2010).*

- Chapter presents the main conclusions obtained and proposes new paths for the continuation of this work.
- The Appendices include additional data which may be useful for a deeper analysis of the RUM models but have not been included in the manuscript itself for the sake of simplicity.

Part I

Equations and models for turbulent two-phase flows

Chapter 2

Transport equations for dispersed two-phase flows

This part aims at describing the compressible Navier-Stokes (NS) equations as found in many text books (Anderson (1990), Hirsch (2007)). Section 2.1 presents the NS equations for the gaseous phase. Reactive terms are not be considered as combustion is not studied in this work. Section 2.2 presents the conservation equations for the dispersed phase, both in the Euler-Lagrange (EL) and in the Euler-Euler (EE) frameworks as implemented in AVBP. The implementation retained in AVBP is based on the Mesoscopic Eulerian Formalism (MEF) for the Euler-Euler framework. It is described in Section 2.2.4. As comparisons with the Euler-Lagrange approach are needed for validation and assessment of the Eulerian closure models, the Euler-Lagrange approach is briefly described in Section 2.2.2. Coupling terms between both phases which are common to both formalismsare finally described in Section 2.3.

2.1 Conservation equations for compressible gaseous flows

Assuming no chemical reaction, one may write the set of conservation equations that describes a compressible gas flow as follows:

$$\frac{\partial}{\partial t}\rho_k + \frac{\partial}{\partial x_j}\rho_k u_{g,j} = -\frac{\partial}{\partial x_j}J_{j,k} \tag{2.1}$$

$$\frac{\partial}{\partial t}\rho_g u_{g,i} + \frac{\partial}{\partial x_j}\rho_g u_{g,i}u_{g,j} = -\frac{\partial}{\partial x_j}\left[P_g\delta_{ij} - \tau_{g,ij}\right] \tag{2.2}$$

$$\frac{\partial}{\partial t}\rho_g E_g + \frac{\partial}{\partial x_j}\rho_g E_g u_{g,j} = -\frac{\partial}{\partial x_j}\left[u_{g,i}(P_g\delta_{ij} - \tau_{g,ij}) + q_{g,j}\right]. \tag{2.3}$$

Equations (2.1) - (2.3) describe the conservation laws for species, momentum and total energy respectively, where ρ_k is the density of each species k composing the gaseous mixture ($\rho_k = \rho_g Y_k$, T_k is the mass fraction of species k), ρ_g is the gaseous mixture density ($\rho_g = \sum_{k=1}^{N}\rho_k$), $J_{j,k}$ is the mass diffusive flux of species k (Eq. (2.26)), $u_{g,i}$ is the $i-th$ component of the gaseous velocity, E_g denotes the gaseous total non-chemical energy, $\tau_{g,ij}$ denotes the viscous stress tensor and $q_{g,j}$ is the diffusive heat flux vector (Eq. (2.27)). The species conservation imposes $\sum_{k=1}^{N} Y_k = 1$.

This set of equations can be written in compressed form:

$$\frac{\partial}{\partial t}\mathbf{w} + \nabla\cdot\mathcal{F} = \mathbf{s_{l-g}}, \tag{2.4}$$

where $\mathbf{w} = (\rho_k, \rho_g u_{g,i}, \rho_g E_g)^T$ is the vector of conservative variables, $\mathcal{F}$ is the flux tensor and $\mathbf{s_{l-g}}$ is the source term vector due to the influence of the dispersed phase on the gaseous phase. The flux tensor can be decomposed into an inviscid $\mathcal{F}^{\mathcal{I}}$ and a viscous $\mathcal{F}^{\mathcal{V}}$ part which read:

$$\mathcal{F}^{\mathcal{I}} = \begin{pmatrix} \rho_k u_{g,j} \\ \rho_g u_{g,i} u_{g,j} + P_g \delta_{ij} \\ (\rho_g E_g + P_g \delta_{ij}) u_{g,j} \end{pmatrix}, \qquad \mathcal{F}^{\mathcal{V}} = \begin{pmatrix} J_{j,k} \\ -\tau_{g,ij} \\ -(u_{g,i}\tau_{g,ij}) + q_{g,j} \end{pmatrix}. \tag{2.5}$$

The hydrostatic pressure (P_g) is determined by the equation of state for perfect gases:

$$P_g = \rho_g \frac{\mathcal{R}}{\mathcal{W}_g} T_g \tag{2.6}$$

where $\mathcal{R} = 8.3143 J/(mol \cdot K)$ is the universal gas constant, $\mathcal{W}_g$ is the molecular weight of the gaseous mixture and T_g its temperature. The gaseous phase is usually composed by multiple species. It is considered as a perfect mixture of N perfect gases, whose state is defined by Eq. (2.6), where, $\mathcal{W}_g$ is the molecular weight of the mixture:

$$\frac{1}{\mathcal{W}_g} = \sum_{k=1}^{N} \frac{Y_k}{\mathcal{W}_k}. \tag{2.7}$$

The set of equations Eqs. (2.1) - (2.3) are closed provided the viscous flux tensor is modeled. In practical situations, all fluids are assumed to be Newtonian, so the stress tensor is given by a Newton law (Eq. (2.8)):

$$\tau_{g,ij} = 2\mu_g \left(S_{g,ij} - \frac{1}{3}\delta_{ij} S_{g,ll} \right), \tag{2.8}$$

where μ_g is the dynamic viscosity of the gaseous mixture. $S_{g,ij}$ is the gaseous rate-of-strain tensor:

$$S_{g,ij} = \frac{1}{2} \left(\frac{\partial u_{g,j}}{\partial x_i} - \frac{\partial u_{g,i}}{\partial x_j} \right). \tag{2.9}$$

2.1.1 Thermodynamical laws for the gaseous phase

The thermodynamical properties of the gaseous mixture are calculated as a mass average of the properties of each individual species. Thus, the mixture constant r and the heat capacities at constant pressure or volume depend on the local composition of the mixture and are written as follows:

$$\overline{r} = \frac{\mathcal{R}}{\mathcal{W}_g} = \sum_{k=1}^{N} \mathcal{R} \frac{Y_k}{\mathcal{W}_k} = \sum_{k=1}^{N} Y_k r_k, \tag{2.10}$$

$$\overline{C_p} = \sum_{k=1}^{N} Y_k C_{p,k}, \tag{2.11}$$

$$\overline{C_v} = \sum_{k=1}^{N} Y_k C_{v,k}. \tag{2.12}$$

For the sake of clarity, the subscript g for the gas phase has been omitted; the superscript m denotes molar quantities.

In AVBP, the thermodynamical properties (sensible enthalpy $h_{s,k}$ and sensible entropy s_k) are tabulated for each species. The tables include values from $0K$ to $5000K$ every $100K$. They are referenced at $T_0 = 0K$ and $1bar$. The values in the tables are extracted from the JANAF tables (Stull & Prophet

(1971)). The sensible enthalpy of each species is calculated from the tabulated values as in Eq. (2.13), as well as the sensible entropy as in Eq. (2.14). Finally the sensible energy is calculated using Eq. (2.15).

$$h_{s,k}(T) = \int_{T_0}^{T} C_{p,k}\,\mathrm{d}T = \frac{h^m_{s,k}(T) - h^m_{s,k}(T_0)}{\mathcal{W}_k}, \tag{2.13}$$

$$s_k(T) = \frac{s^m_k(T) - s^m_k(T_0)}{\mathcal{W}_k}, \tag{2.14}$$

$$e_{s,k}(T) = \int_{T_0}^{T} C_{v,k}\,\mathrm{d}T = h_{s,k}(T) - r_k T. \tag{2.15}$$

The sensible enthalpy (h_s) and sensible energy (e_s) are defined as follows:

$$h_s = \sum_{k=1}^{N} Y_k h_{s,k}, \tag{2.16}$$

$$e_s = \sum_{k=1}^{N} Y_k e_{s,k}. \tag{2.17}$$

The heat capacities are considered as constant on each interval of $100K$ corresponding to the gap between two consecutive values in the tables. They are evaluated as:

$$C_{p,k} = \frac{\partial h_{s,k}}{\partial T}, \qquad C_{v,k} = \frac{\partial e_{s,k}}{\partial T}. \tag{2.18}$$

2.1.2 Transport laws for the gaseous phase

In gaseous flow, there are two main mechanisms involving diffusion: the molecular diffusion due to local differences in composition, and the heat diffusion due to local differences in temperature.

Diffusion coefficients for mass and heat transport

Molecular and heat diffusion laws depend on several transport properties, such as the dynamic viscosity of the mixture (μ_g), its thermal conductivity (λ_g) or the diffusion coefficient of species k in the mixture (D_k).

The dynamic viscosity is assumed independent of the composition. It is calculated using a Power law which takes into account the variations of temperature. μ_{ref} and T_{ref} are the reference viscosity and temperature whereas b is the Power law exponent:

$$\mu_g = \mu_{ref}\left(\frac{T}{T_{ref}}\right)^b. \tag{2.19}$$

The thermal conductivity of the mixture is evaluated assuming a constant value for the Prandtl number (Pr), it depends on the dynamic viscosity and the heat capacity of the mixture:

$$\lambda_g = \frac{\mu_g \overline{C_p}}{Pr}. \tag{2.20}$$

The Prandlt number is a dimensionless number representing the ratio of momentum diffusivity to thermal diffusivity:

$$Pr = \frac{\nu}{\alpha} = \frac{\textit{viscous diffusion rate}}{\textit{thermal diffusion rate}}. \tag{2.21}$$

The molecular diffusion of each species k into the mixture is calculated assuming that the Schmidt number of each species (Sc_k) is constant; it depends on the dynamic viscosity and the density of the mixture:

$$D_k = \frac{\mu_g}{\rho_g Sc_k}. \tag{2.22}$$

The Schmidt number is a dimensionless number representing the ratio of momentum diffusivity and mass diffusivity. It relates the relative thickness of the hydrodynamic layer and the mass-transfer boundary layer:

$$Sc_k = \frac{\nu_k}{D_k} = \frac{viscous\ diffusion\ rate}{molecular\ diffusion\ rate}. \tag{2.23}$$

Mass transport law

When the gaseous phase is composed of several species, the conservation equation (2.24) must be satisfied. The species diffusion velocity $V_{k,i}$ is approximated by the Hirschfelder-Curtis relation (Hirsch (1990)):

$$Y_k V_{k,i} = -D_k \frac{\mathcal{W}_k}{\mathcal{W}} \frac{\partial X_k}{\partial x_i}, \tag{2.24}$$

where D_k is the diffusion coefficient of the species k into the mixture given by Eq. (2.22). This approximation does not ensure the conservation of total mass for mixtures composed of more than two species. A correction velocity V_i^c is thus introduced to ensure mass conservation (Poinsot & Veynante (2005)):

$$V_i^c = \sum_{k=1}^{N} D_k \frac{\mathcal{W}_k}{\mathcal{W}} \frac{\partial X_k}{\partial x_i}. \tag{2.25}$$

The diffusive flux taking into account this correction reads:

$$J_{i,k} = -\rho_g \left(D_k \frac{\mathcal{W}_k}{\mathcal{W}} \frac{\partial X_k}{\partial x_i} - Y_k V_i^c \right). \tag{2.26}$$

Heat transport law

The total heat flux $\mathbf{q}$ is composed of two contributions: the conductive heat flux and the heat flux through species diffusion. The conductive heat flux is modeled by Fourier's law. λ_g is the thermal conductivity of the mixture given by Eq. (2.20):

$$q_i = -\lambda_g \frac{\partial T}{\partial x_i} + \sum_{k=1}^{N} J_{i,k} h_{s,k}. \tag{2.27}$$

2.2 Conservation equations for the dispersed phase

While the gaseous phase is usually described as a continuum iwith an Eulerian approach, there are different approaches for the description of the dispersed phase. Recently, Fox (2012) has provided a classification of the different approaches for the DNS of two-phase flows (Fig. 2.1).

Two main frameworks for the simulation of the dispersed phase are used in this work: the Euler-Lagrange approach and the so-called Mesoscopic Eulerian Formalism (MEF). Whatever the approach used, to describe the behavior of droplets or particles in a gaseous flow, the first step os to determine the forces acting on them (Section 2.2.1). Generally, then the conservation equations taking into account those forces can be written. Section 2.2.2 briefly describes the Euler-Lagrange approach, introducing the quantities of interest for this work. Section 2.2.3 positions the MEF among the multiple Euler-Euler approaches. Finally, Section 2.2.4 describes the MEF itself and the transport equations which will be solved.

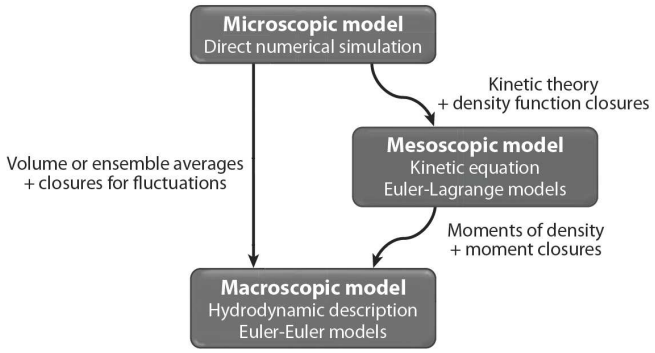

Figure 2.1: *Classification of modeling approaches for DNS of two-phase flows. Extracted from Fox (2012).*

2.2.1 Review of forces acting on an isolated particle

The first descriptions of the forces acting on an isolated particle date from the end of the 19^{th} century. Boussinesq (1885), Basset (1888) and Oseen (1927) studied the settling motion of particles in a quiescent flow due to the action of gravity. However, it was Tchen (1947) who applied their conclusions to particles in turbulent flows for the first time. He extended their work to the motion of rigid spherical particles in Homogeneous Isotropic Turbulence (HIT). Tchen took into account the main forces described by Boussinesq, Basset and Oseen, namely the Stokes drag, the pressure gradient force, the added mass, the Basset force and the lift force. More recently, the work of Tchen has been revisited by Maxey & Riley (1983). They considered isolated rigid spherical particles, with constant diameter d_p and density ρ_p.

The kinematic equation for a particle that translates at velocity (rotation is excluded) $\mathbf{v}_{p,i}$ reads:

$$\frac{d}{dt}x_{p,i} = \mathbf{v}_{p,i}. \tag{2.28}$$

The momentum conservation equation is written as:

$$m_p \frac{d}{dt}\mathbf{v}_{p,i} = F_{p,i} = F^u_{p,i} + F^p_{p,i}. \tag{2.29}$$

The total force $F_{p,i}$ is the sum of two contributions: $F^u_{p,i}$ is the force that would act on a fluid particle occupying the position of the particle; $F^p_{p,i}$ denotes the force exerted upon the particle due to the perturbation of the fluid velocity fields caused by the presence of the particle.

It is assumed that the particle diameter is small compared to the smallest scales of the fluid motion (the Kolmogorov scale η_k in a turbulent flow as described in Chapter 3):

$$d_p \ll \eta_k \ , \tag{2.30}$$

and a small particle Reynolds number Re_p which reads:

$$Re_p = \frac{d_p|\mathbf{u}_{f@p} - \mathbf{v}_p|}{\nu_g} \ , \tag{2.31}$$

where ν_g stands for the gaseous kinematic viscosity.

The term $F^u_{p,i}$ assumes that the forces due to pressure and viscous stress, that would have acted on a fluid particle occupying the volume where the particle is actually located, are transmitted to the particle. Maxey & Riley (1983) and Gatignol (1983) suggest:

$$F^u_{p,i} = \frac{\pi d_p^3}{6}\left[\rho_g \frac{D}{Dt}\mathbf{u}_{f@p,i} + (\rho_p - \rho_g)g_i\right], \tag{2.32}$$

where g_i denotes the $i-th$ component of the gravity vector, $\mathbf{u}_{f@p}$ is the undisturbed fluid velocity at the particle location, ρ is the density. The subscript g and p stands for the gas (or fluid) and the particle respectively. D/Dt represents the total derivative along particle trajectories:

$$\frac{D}{Dt} = \frac{\partial}{\partial t} + \mathbf{u}_{f@p,i}\frac{\partial}{\partial x_i}. \tag{2.33}$$

The first term in the Right-Hand-Side (RHS) of Eq. (2.32) accounts for pressure and viscous stresses and the second one for buoyancy effects.

The term $F^p_{p,i}$ stands for the aerodynamic forces acting on the particle: drag force, added-mass force, Basset force and lift force.

Drag force

The drag force F_D accounts for pressure and viscous stresses exerted on the particle surface. It corresponds to the force originally derived by Stokes (1851) in quiescent fluid for small Re_p, which allows to neglect inertial effects of the fluid flow.

$$F_D = \frac{3}{4}\rho_g\frac{\pi d_p^3}{6}\frac{1}{d_p}C_D|\mathbf{u}_{f@p} - \mathbf{v}_p|(\mathbf{u}_{f@p} - \mathbf{v}_p). \tag{2.34}$$

where C_D is the Stokes drag coefficient. Another definition introduces the particle response time τ_p to describe the drag force:

$$F_D = \frac{m_p}{\tau_p}(\mathbf{u}_{f@p} - \mathbf{v}_p)\ , \tag{2.35}$$

where:

$$\tau_p = \frac{4}{3}\frac{\rho_p}{\rho_g}\frac{d_p}{C_D}|\mathbf{u}_{f@p} - \mathbf{v}_p|^{-1}. \tag{2.36}$$

There are three main formulations for the Stokes drag coefficient C_D, depending on the particle Reynolds number. Stokes (1851) developped an analytical solution for $Re_p \ll 1$:

$$C_D = \frac{24}{Re_p}, \tag{2.37}$$

Oseen (1927) proposed a correction of the Stokes' relation to take into account inertial effects which is valid for $1 \leq Re_p \leq 5$:

$$C_D = \frac{24}{Re_p}\left(1 + \frac{3}{16}Re_p\right) \tag{2.38}$$

For larger Re_p, semi-empirical correlations are available. Up to $Re_p = 1000$, the correlation proposed by Schiller & Nauman (1935) is widely accepted (this is, in fact, the correlation inplemented in AVBP and used in this work):

$$C_D = \frac{24}{Re_p}(1 + 0.15Re_p^{0.687}). \tag{2.39}$$

For applications where $Re_p > 1000$, following Clift *et al.* (1978), the drag coefficient remains unaffected by the wake behind the particle and stays constant:

$$C_D = 0.44. \tag{2.40}$$

Added-mass force

The added-mass force accounts for the acceleration of the fluid due to the particle motion. When a particle accelerates in a fluid, it implies an acceleration of the surrounding fluid at the expense of the work exerted by the particle. It is usually written as:

$$F_{AM} = \frac{\pi d_p^3}{6}\rho_g C_m \left(\frac{D}{Dt}\mathbf{u}_{f@p} - \frac{d}{dt}\mathbf{v}_p\right). \tag{2.41}$$

where C_m is the added-mass force constant: $C_m = 0.5$.

Since the added-mass froce depends on the fluid density, it is often neglected for particles much denser than the fluid (Hinze (1975), Desjonqueres *et al.* (1986)). In this work, it is assumed that the ratio between the particle's density and the density of the fluid is larger than 10^3 ($\rho_p/\rho_g > 1000$), so that the added-mass force can be neglected. In those cases where the fluid is denser than the particles (or their densities are comparable), neglecting the added-mass force may lead to significant errors, since the virtual added-mass may become larger than the particle mass itself.

Basset force

The History or Basset force is linked to the memory of the particle, the history of its past accelerations. It accounts for the temporal delay in the boundary layer development due to the changes in the relative velocity between the particle and the fluid (Crowe *et al.* (1998)):

$$F_H = \frac{\pi d_p^3}{6}\frac{9\rho_g}{d_p}\left(\frac{\nu_g}{\pi}\right)^{1/2}\int_\infty^t \frac{d}{d\tau}(\mathbf{u}_{f@p} - \mathbf{v}_p)\frac{d\tau}{\sqrt{t-\tau}}. \tag{2.42}$$

It is usually neglected due to the dificulties of implementation (that is the case in this work). However, neglecting it may lead to significant errors when the particle is accelerated at high rate (Thomas (1992), Johnson (1998)), which is not the case in the configurations studied in this work.

Lift force

The lift force is due to the fluid vorticity Ω_g, it is non-negligible for large particles where the fluid velocity gradient differs significantly from one side of the particle to the other. It usually reads:

$$F_L = \frac{\pi d_p^3}{6}\rho_g C_L(\mathbf{u}_{f@p} - \mathbf{v}_p) \times \Omega_g. \tag{2.43}$$

Hinze (1975) and Desjonqueres *et al.* (1986) showed that not only the added-mass force, but also the pressure gradient and the Basset forces can be neglected when $\rho_p/\rho_g > 1000$, since they are small compared to the particle agitation and dispersion mechanisms. In HIT, Elghobashi & Truesdell (1993) showed that those two mechanisms are mainly due to Stokes drag and gravity.

2.2.2 Euler-Lagrange

The Lagrangian approach for the simulation of two-phase flows considers that the discrete phase is composed of an ensemble of particles (physical individual particles or numerical particles representing a cluster of real particles) each one with its own velocity. The individual trajectory of each particle is tracked and the point mechanics equations are solved with momentum, mass and heat coupling with the gas phase (treated with an Eulerian approach).

This method is also referred as Discrete Particle Simulation (DPS). It has been widely used for the simulation of gas-solid flows (Tchen (1947), Hinze (1975), Desjonqueres *et al.* (1986), Squires & Eaton (1990), Deutsch & Simonin (1991), Druzhinin (1995), Boivin *et al.* (1998), Février *et al.* (2005), Moreau (2006)), Masi (2010) in academic configurations. Following Boivin *et al.* (2000), this approach is limited to weakly loaded flows ($\alpha_p \leq 0.001$, where α_p is the particle volume fraction, i.e. the ratio between the total mass of the particles and the total mass of the gas) and particle response times larger than the characteristic time of the gaseous flow. Indeed, a large amount of particles implies that the individual equations of each particle must be solved, considerably increasing the computational cost of this approach.

The Euler-Lagrange (EL) approach has, however, an important advantage: it requires few modeling efforts. The treatment of polydispersion, for example, is straightforward. This method is commonly employed in Reynolds-Averaged-Navier-Stokes (RANS) codes and its potential in LES has been stated (Mahesh *et al.* (2002), Mashayek & Pandya (2003), Pandya & Mashayek (2002), García (2009)). It has also been applied to LES of industrial configurations (Senoner (2010)). There are still numerical issues to be handled: the location of particles in the Eulerian mesh needs very efficient algorithms. Another issue is the interpolation of the coupling terms from the Eulerian mesh nodes to the particle position and vice-versa. In order to avoid numerical errors, high-order numerical schemes are requested, which notably increases the computational cost. In parallel computing, the transfer of particles exiting the domain of one processor and entering a different one is crucial and very efficient domain partitioning algorithms are needed in order to avoir load balancing problems due to inhomogeneous repartition of the particles in the computational domain (García (2009)).

Equations for the Euler-Lagrange approach:

In the EL approach, the gas phase is described by means of the Navier-Stokes equations described in Section 2.1. Assuming that the only forces acting on a particle are the Stokes-drag and the gravity, the position $\mathbf{x}_p^{(k)}$ and the velocity $\mathbf{v}_p^{(k)}$ of particle k are calculated at each time step as follows:

$$\frac{d}{dt}\mathbf{x}_p^{(k)} = \mathbf{v}_p^{(k)} \tag{2.44}$$

$$\frac{d}{dt}(m_p^{(k)}\mathbf{v}_p^{(k)}) = F_{p,i}^{(k)} \tag{2.45}$$

$$\frac{d}{dt}m_p^{(k)} = \dot{m}_p^{(k)} \tag{2.46}$$

$$\frac{d}{dt}(m_p^{(k)}C_p^{(k)}T_p^{(k)}) = \dot{Q}_p^{(k)} \ , \tag{2.47}$$

where $m_p^{(k)}$ is the mass of the particle k, $C_p^{(k)}$ is its specific heat at constant pressure, $T_p^{(k)}$ is its temperature, $\dot{m}_p^{(k)}$ is the mass transfer rate due to evaporation (otherwise the mass of the particle remains constant) and $\dot{Q}_p^{(k)}$ is the heat transfert rate from the gas phase to the particle.

Useful Lagrangian quantities

The averaging operator associated with the particle-phase is noted $\langle\cdot\rangle_p$, it is defined, for every Lagrangian quantity $\Phi^{(k)}$, as:

$$\langle\Phi^{(k)}(\mathbf{x}_p^{(k)})\rangle_p = \frac{1}{N_p}\sum_{k=1}^{k=N_p}\Phi^{(k)}(\mathbf{x}_p^{(k)} - \delta\mathbf{x}_p) \tag{2.48}$$

where N_p is the total number of particles.

Then, the particle kinetic energy q_p^2, and the fluid-particle correlation q_{fp} (where the subscript $_f$ is used to denote the carrier fluid) yield:

$$q_p^2 = \frac{1}{2}\langle\mathbf{v}_p^{(k)}\cdot\mathbf{v}_p^{(k)}\rangle_p \tag{2.49}$$

$$q_{fp} = \langle \mathbf{v}_p^{(k)} \cdot \mathbf{u}_f(x_p^{(k)}) \rangle_p. \tag{2.50}$$

For the gas phase, the fluid turbulent kinetic energy q_f^2 can be defined using the classical Reynolds average operator (Hinze (1975)), noted $\langle \cdot \rangle_f$ and corresponding to a statistical mean of N flow realizations:

$$q_f^2 = \frac{1}{2} \langle \mathbf{u}'_f \cdot \mathbf{u}'_f \rangle_f \ , \tag{2.51}$$

where $\mathbf{u}'_f$ is the fluctuating part of the fluid velocity.

Tchen's theory

Tchen (1947) proposed, for stationnary particle-laden HIT flows, a link between the previous quantities through Eqs. (2.52)-(2.53), needed to have correspondance between the two operators applied to the fluid and particle fields. These relations require two main assumptions: first, the aerodynamic force acting on the particle must consist only of Stokes drag given by Eq. (2.35). Secondly, the relative velocity between the particle and the fluid must be very small.

$$q_{fp} = \frac{2}{1+St} q_f^2, \tag{2.52}$$

$$2q_p^2 = q_{fp} \tag{2.53}$$

where $St = \tau_p / \tau_f^t$ stands for the Stokes number, and τ_f^t is the Lagrangian turbulent time-scale (Haworth & Pope (1986)).

Deutsch & Simonin's extended theory

In order to relax the second assumption in Tchen's theory, Deutsch & Simonin (1991) proposed an extension of Tchen's theory using the fluid velocity along particle trajectories $\mathbf{u}_{f@p}$ introduced in Section 2.2.1. Consequently, the fluid turbulent kinetic energy sampled along particle trajectories $q_{f@p}^2$ reads:

$$q_{f@p}^2 = \frac{1}{2} \langle \mathbf{u}'_{f@p} \cdot \mathbf{u}'_{f@p} \rangle_p, \tag{2.54}$$

$$q_{fp} = \frac{2}{1+St'} q_{f@p}^2, \tag{2.55}$$

$$2q_p^2 = q_{fp}. \tag{2.56}$$

where $St' = c/\tau_p$ is a modified Stokes number. In the limit of very small Stokes numbers, $\tau_{f@p}^t \to \tau_f^t$. Since $\tau_{f@p}^t$ and $q_{f@p}^2$ are difficult to quantify, Eqs. (2.52) and (2.53) are often used as a first approximation to evaluate q_p^2.

2.2.3 Euler-Euler approach

In the Euler-Euler approach (EE), the dispersed phase is treated as a continuous phase, and instead of computing the properties of each individual particle, the local average properties are calculated. There are two main types of average operator: the volume average and the statistical average. For these approaches, the same numerical approach used for the gaseous phase may be applied to the dispersed phase, which greatly simplifies its implementation in parallel CFD codes. Moreover, no interpolation procedure is needed for the coupling between phases, since the information for both liquid and gaseous phases are stored at the same nodes of the grid. However, an important modeling effort is required which nowadays remains the main challenge.

For very low-inertial particles, the modeling effort is reduced, since the particles behave like tracers and almost follow the fluid flow. The equilibrium approach (Ferry & Balachandar (2002), Rani & Balachandar (2004)) has proved its efficiency and accuracy in the simulation of this type of flows. It consists in the solution of one transport equation for the particle number density (n_p, the number of particles per unit volume) and a Taylor expansion of the fluid velocity in particle relaxation time τ_p to predict the particle velocity (Maxey (1987)). When heavier particles are to be modeled, their response time become larger and the method reaches its applicability limits.

The two-fluid approach, originally developped by Druzhinin & Elghobashi (1998), is based on a spatial average of the instantaneous equations for the gaseous and dispersed phases over a length scale of the order of the Kolmogorov length scale (assuming that the particle diameter and the smallest length scale of the particle velocity are significantly smaller than the Kolmogorov length scale, so the unity of the particle velocity in the filtering volume is ensured). The two-fluid approach shows good results in the simulation of particle-laden decaying HIT flow for particles with small Stokes number.

In configurations where the average values are not sufficient for a realistic representation of the dispersed phase, the complexity of modeling increases. This is the case, for example, for polydispersed sprays. Following Greenberg *et al.* (1993), Laurent & Massot (2001) proposed to divide the dispersed phase into different sections, each one containing one class of diameter. Then, a different set of Eulerian equations needs to be solved for each of the sections. This increases notably the computational cost, but, the authors showed that a few sections are sufficient to obtain an accurate representation of a spray with a wide distribution of diameters. Another challenge of this approach, called Eulerian Multi Size Moment (EMSM), is the treatment of the exchanges between different classes of diameters; when including evaporation, the droplet diameter reduces as they evaporate and they must be transferred to a lower diameter class. Mossa (2005) proposed another approach where the addition of one equation for the particle droplet surface allows the representation of polydispersion effects.

Collision and crossing trajectories are difficult to model in the Eulerian approach. Indeed, Eulerian models derived from the Williams-Boltzmann equation through a near-equilibrium assumption along with closures for the second-order velocity moments are unable to capture the multiple values of particle velocity at the same time and location when particle trajectory crossing (PTC) takes place. The near-equilibrium assumption is a strong hypothesis, and although those methods may be able to capture when PTC takes place, they lead to singularities called δ-shocks (de Chaisemartin *et al.* (2008), de Chaisemartin (2009)). However, it has been stated (Desjardins *et al.* (2006)) that it is possibe to predict the crossing of particle trajectories in an Eulerian framework using the DQMOM approach (Marchisio & Fox (2005), Fox *et al.* (2008)). More recently, Kah (2010) proposed a new method called Eulerian Multi-Fluid Multi-Velocity (EMVM), using quadrature-based moment methods (Fox *et al.* (2008), Fox (2008), Fox (2009)), preserving the moment phase-space realizability. Indeed, Wright (2007) showed that, in general, high-order, finite-volume schemes do not guarantee realizable moments (i.e. the independent transport of the moments with schemes of order greater than one, may lead to invalid moment sets), and thus new realizable high-order algorithms must be used (Kah *et al.* (2011)). More details about this high-order algorithm as well as EMSM and EMVM methods can be found in Kah (2010).

Finally, it is to be noted that the Eulerian approach implies some difficulties from the numerical point of view due to high compressibility effects that require to transport very stiff gradients difficult to handle numerically. Riber *et al.* (2006) showed that the use of low dispersion numerical schemes along with an adapted artificial viscosity operator may be a solution.

The methods based on volume filtering show important limits when simulating flows with high inertial particles. The reasons for this failure were first pointed out by Février *et al.* (2005). The authors proposed a new method where the paticle velocity is split into two different contributions: a spatially correlated part and a spatially uncorrelated part, which becomes negligible for very low inertial particles. The Mesoscopic Eulerian Formalism (MEF) is based on a conditional ensemble averaging (Section 2.2.4). This average operator leads to unclosed terms that need to be modeled (Part II). The resulting set of equations is presented in Section 2.3. Figure 2.2 shows a classification of all these Euler-Euler formalisms.

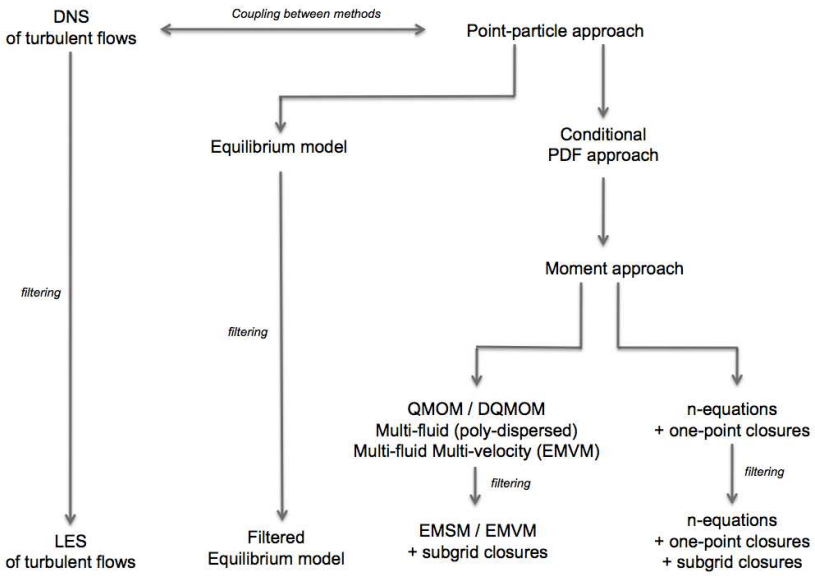

Figure 2.2: *Classification of EE modelling approaches for the dispersed phase interacting with turbulent flows. Modified from Masi (2010).*

2.2.4 Mesoscopic Eulerian approach

The MEF is the approach that has been implement in AVBP (Kaufmann (2004)). The main idea in the MEF is the distinction made between the properties of an ensemble of particles and the properties of an individual particle. The statistically averaged Euler-Euler (EE) equations are obtained from a Probability Density function (PDF) used to define a set of transport equations based on the kinetic theory of gases of Boltzmann (Chapman & Cowling (1939 (digital reprint 1999), Reeks (1991)). Based on this PDF evolution equation, direct integrations yield the transport equations of the desired moments for which unknowns naturally arise. Once the set of equations has been established, models are to be supplied. Contrary to the volume filtering of the equilibrium and two-fluid approaches, no assumption regarding the size of the filter is required at this stage.

The main steps in the procedure for the development of the MEF transport equations are:

1. The function $W_p^{(k)}$ describes the dynamics of the particles with respect to time and space. Each particle is identified by its position $\mathbf{x}$ at time t, its mass μ_p, its velocity $\mathbf{c}_p$ and its temperature ζ_p:

$$W_p^{(k)}(\mathbf{c}_p, \zeta_p, \mu_p, \mathbf{x}, t) = \delta\left(\mathbf{c}_p - \mathbf{u}_p^{(k)}(t)\right)\delta\left(\zeta_p - \zeta_p^{(k)}(t)\right)\delta\left(\mu_p - \mu_p^{(k)}(t)\right)\delta\left(\mathbf{x} - \mathbf{x}_p^{(k)}(t)\right) \quad . \tag{2.57}$$

2. Applying an ensemble averaging over a large number of particle realisations $\mathcal{H}_p$, conditioned by one realisation of the carrier fluid $\mathcal{H}_f$, a PDF for the particle presence is defined as:

$$\breve{f}_p(\mathbf{c}_p, \zeta_p, \mu_p, \mathbf{x}, t|\mathcal{H}_f) = \lim_{N_p\to\infty}\left[\frac{1}{N_p}\sum_{N_p}\sum_{k=1}^{N_p} W_p^{(k)}(\mathbf{c}_p, \zeta_p, \mu_p, \mathbf{x}, t, \mathcal{H}_p|\mathcal{H}_f)\right] \quad . \tag{2.58}$$

3. The Boltzmann type equation that describes the evolution of this PDF yields:

$$\frac{\partial}{\partial t}\breve{f}_p + \frac{\partial}{\partial x_j}\left[c_{p,j}\breve{f}_p\right] + \frac{\mathrm{d}}{\mathrm{d}c_{p,j}}\left[\frac{du_{p,j}}{dt}\breve{f}_p\right] + \frac{\mathrm{d}}{\mathrm{d}\zeta_p}\left[\frac{dT_p}{dt}\breve{f}_p\right] + \frac{\mathrm{d}}{\mathrm{d}\mu_p}\left[\frac{dm_p}{dt}\breve{f}_p\right] = \left(\frac{\mathrm{d}\breve{f}_p}{\mathrm{d}t}\right)_{coll} \quad . \tag{2.59}$$

4. A statistical average operator is defined to decribe the average properties of the dispersed phase. The mesoscopic quantities Ψ are defined by their mass ensemble average and correspond to the moments of the PDF.

$$\breve{\mathbf{\Psi}} = \langle \mathbf{\Psi} \rangle_p = \frac{1}{\rho_p \breve{\alpha}_p} \int \mu_p \mathbf{\Psi}(\mathbf{c}_p, \zeta_p, \mu_p) \breve{f}_p(\mathbf{c}_p, \zeta_p, \mu_p, \mathbf{x}, t | \mathcal{H}_f) d\mathbf{c}_p d\zeta_p d\mu_p. \tag{2.60}$$

In AVBP, the first five moments are transported, they correspond to the following mesoscopic quantities: $\breve{n}_p$ is the particle number density (number of particles per unit volume), $\breve{\alpha}_p$ is the volume fraction of particles, $\breve{\mathbf{u}}_p$ is the particle velocity, $\delta\breve{\theta}_p$ is the uncorrelated energy and $\breve{h}_p$ is the enthalpy.

5. The substitution of $\mathbf{\Psi}$ by the transported quantities produces a system of conservation equations that describes the mean mesoscopic field.

Definiton of correlated and uncorrelated motions.

The phenomenon of preferential concentration of particles in regions of low vorticity and/or high strain rate has been widely studied (Squires & Eaton (1991*b*), Rouson & Eaton (2001), Rani & Balachandar (2004)). The origin resides in the interactions between the particle phase and the carrier fluid and relates to the particle Stokes number. For low Stokes numbers, the particles follow the fluid flow and their velocity vectors are close to those of the carrier phase. Moreover, neighbouring particles have similar velocity vectors. On the contrary, for larger Stokes numbers, the particles do no follow the carrier fluid flow and the velocities of neighboring particles are not similar. This difference is due to the particle response time τ_p compared to a characteristic time of the fluid flow. For small Stokes numbers, τ_p is small, which means that the particles react rapidly to the velocity changes that take place in the carrier fluid flow. When τ_p increases, the particles are less sensitive to the surrounding changes, and the velocity samples obtained at a certain location correspond to particles coming from very distant regions of the flow.

Such observations are at the origin of the formalism proposed by Février *et al.* (2005). The Lagrangian velocity of each particle is splitted into a spatially correlated part and an uncorrelated part, sketched in Fig. 2.3, as follows:

$$\mathbf{u}_p^{(k)}(t) = \breve{\mathbf{u}}_p(\mathbf{x}_p^{(k)}(t), t) + \delta\mathbf{u}_p^{(k)}(t), \tag{2.61}$$

where $\breve{\mathbf{u}}_p$ is the mesoscopic velocity defined in the Eulerian framework, which corresponds to the velocity shared by all the particles. It provides a description of the structure of the velocity distribution and is often called correlated velocity and $\delta\mathbf{u}_p^{(k)}(t)$ is the residual velocity component of the particle, or Random Uncorrelated Velocity (RUV), defined for each individual particle along particle trajectories.

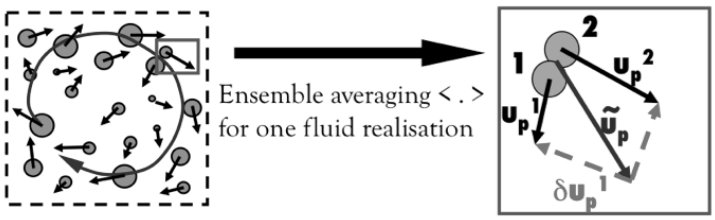

Figure 2.3: *Sketch of the correlated and uncorrelated motions in the MEF. Extracted from Riber (2007).*

The particle velocity may also be split in a mean and a fluctuating parts. As the Lagrangian mean field and the mesoscopic mean field are identical (Février *et al.* (2005)), fluctuating velocity contributions may also be written in terms of mesoscopic and residual contributions as follows:

$$\mathbf{u}'_p(t) = \breve{\mathbf{u}}'_p(\mathbf{x}_p^{(k)}(t), t | \mathcal{H}_f) + \delta\mathbf{u}'^{(k)}_p(t). \tag{2.62}$$

Using the properties of the statistical average operator $\langle\cdot\rangle$, several relations for the Eulerian equivalent of the quantities defined in Section 2.2.2 can be obtained:

- the ensemble average of the particle uncorrelated velocity is zero:

$$\langle \delta \mathbf{u}_p^{(k)} | \mathcal{H}_f \rangle = 0; \tag{2.63}$$

- the particle uncorrelated velocity is spatially decorrelated from the fluid velocity:

$$\langle \breve{\mathbf{u}}_f \cdot \delta \mathbf{u}_p^{(k)} | \mathcal{H}_f \rangle = 0; \tag{2.64}$$

- the particle uncorrelated velocity component is spatially decorrelated from the particle mesoscopic velocity:

$$\langle \breve{\mathbf{u}}_p \cdot \delta \mathbf{u}_p^{(k)} | \mathcal{H}_f \rangle = 0. \tag{2.65}$$

Using these properties, the mean mesoscopic stress tensor $\breve{\mathbb{R}}_{p,ij}$ and the mean Random Uncorrelated Motion (RUM) $\delta\breve{\mathbb{R}}_{p,ij}$ stress tensor are defined as:

$$\breve{\mathbb{R}}_{p,ij}(\mathbf{x},t) = \frac{\langle \breve{n}_p(\mathbf{x},t)\breve{u}'_{p,i}(\mathbf{x},t)\breve{u}'_{p,j}(\mathbf{x},t)\rangle}{\langle \breve{n}_p(\mathbf{x},t)\rangle}, \tag{2.66}$$

$$\delta\breve{\mathbb{R}}_{p,ij}(\mathbf{x},t) = \frac{\langle \breve{n}_p(\mathbf{x},t)\delta u_{p,i}(\mathbf{x},t)\delta\breve{R}_{p,ij}(\mathbf{x},t)\rangle}{\langle \breve{n}_p(\mathbf{x},t)\rangle}. \tag{2.67}$$

From this correlations, the definition of the turbulent kinetic energy q_p^2, the correlated kinetic energy $\breve{q}_p^2$ and the Random Uncorrelated Energy δq_p^2 is straightforward:

$$q_p^2 = \breve{q}_p^2 + \delta q_p^2, \tag{2.68}$$

$$\breve{q}_p^2 = \frac{1}{2}\frac{\langle \breve{n}_p \breve{u}'_{p,i}\breve{u}'_{p,i}\rangle}{\langle \breve{n}_p\rangle}, \tag{2.69}$$

$$\delta q_p^2 = \frac{\langle \breve{n}_p \delta\breve{\theta}_p\rangle}{\langle \breve{n}_p\rangle}, \tag{2.70}$$

where $\delta\breve{\theta}_p$ is the Random Uncorrelated Energy (RUE) that will be defined later in this section. Dependencies of $\breve{n}_p$, $\breve{u}'_{p,i}$ and $\delta\breve{\theta}_p$ with space and time have been omitted in Eqs. (2.69) and (2.70) and summation convention is adopted for Latin indices other than p.

A first attempt to evaluate the two contributions (mesoscopic and uncorrelated) was made by Février *et al.* (2005) in a DPS of a particle-laden stationnary HIT flow. He found that the ratio of kinetic RUE to total particle kinetic energy increased with the particle inertia. Vance *et al.* (2006) showed the same trend in a fully-developped channel flow for both colliding and non-colliding particles.

Particle mesoscopic transport equations

The transport equations for the mesoscopic variables are given in Eqs. (2.71)-(2.74). Γ denotes the mass transfer rate from the liquid to the gas phase, Φ_p is the enthalpy transfer rate from the gaseous to the liquid phase, $\mathbf{F}_D$ is the drag force exerted by the fluid on the particles and $\delta\breve{R}_{p,ij}$ denotes the 2^{nd} order particle uncorrelated velocity correlations tensor, $\delta\breve{R}_{p,ij}(\mathbf{x},t) = \langle \breve{u}_{p,i}(t)\breve{u}_{p,j}(t)|\mathbf{x}_p(t) = \mathbf{x}, \mathcal{H}_f\rangle$.

$$\frac{\partial}{\partial t}\breve{n}_p + \frac{\partial}{\partial x_j}\breve{n}_p\breve{u}_{p,j} = 0 \tag{2.71}$$

$$\frac{\partial}{\partial t}\rho_p\breve{\alpha}_p + \frac{\partial}{\partial x_j}\rho_p\breve{\alpha}_p\breve{u}_{p,j} = -\Gamma \tag{2.72}$$

$$\frac{\partial}{\partial t}\rho_p\breve{\alpha}_p\breve{u}_{p,i} + \frac{\partial}{\partial x_j}\rho_p\breve{\alpha}_p\breve{u}_{p,i}\breve{u}_{p,j} = -\frac{\partial}{\partial x_j}\rho_p\breve{\alpha}_p\,\delta\breve{R}_{p,ij} - \Gamma\,\breve{u}_{p,i} + F_{D,i} \tag{2.73}$$

$$\frac{\partial}{\partial t}\rho_p\breve{\alpha}_p\breve{h}_p + \frac{\partial}{\partial x_j}\rho_p\breve{\alpha}_p\breve{u}_{p,j}\breve{h}_p = -\Gamma\breve{h}_p + \Phi_p \tag{2.74}$$

$$\text{❶} + \text{❷} = \text{❸} + \text{❹} + \text{❺} + \text{❻}$$

where the terms noted ❶ correspond to the temporal variations, ❷ to the advection terms due to the mesoscopic motion, ❸ to the advection terms due to the uncorrelated motion, ❹ to the terms linked to the evaporation process, ❺ to the terms linked to drag force and ❻ to the terms linked to thermal conduction.

Closure models for the drag force in Eq. (2.73), have been proposed in Section 2.2.1. Closure for the terms linked to mass and heat transfer due to evaporation are worked on in Part III. In order to define closure models, some assumptions are needed:

H1 -The particles are considered as rigid spheres.

H2 -$\rho_p >> \rho_g$ so the only force exerted by the carrier phase on the dispersed phase is drag force.

H3 -Gravity is neglected.

H4 -Only diluted sprays are considered: $\breve{\alpha}_p < 0.0001$ and $1 - \breve{\alpha}_p \equiv 1$.

H5 -Considering H4, the effects of coalescence and collisions are neglected.

H6 -The spray is locally monodispersed.

Closure model for $\delta\breve{R}_{p,ij}$

The transport equation for $\delta\breve{R}_{p,ij}$ reads:

$$\begin{aligned}\frac{\partial}{\partial t}\rho_p\breve{\alpha}_p\delta\breve{R}_{p,ij} + \frac{\partial}{\partial x_j}\rho_p\breve{\alpha}_p\delta\breve{R}_{p,ij}\breve{u}_{p,j} = &- 2\frac{\rho_p\breve{\alpha}_p}{\breve{\tau}_p}\delta\breve{R}_{p,ij} - \rho_p\breve{\alpha}_p\delta\breve{R}_{p,im}\frac{\partial\breve{u}_{p,j}}{\partial x_m} \\ &- \rho_p\breve{\alpha}_p\delta\breve{R}_{p,mj}\frac{\partial\breve{u}_{p,i}}{\partial x_m} - \frac{\partial}{\partial x_m}\delta\breve{Q}_{p,ijm}.\end{aligned} \tag{2.75}$$

In Eq. (2.75), the term representing the 3^{rd} order particle uncorrelated velocity correlation tensor $\delta\breve{Q}_{p,ijm} = \langle\breve{u}_{p,i}\breve{u}_{p,j}\breve{u}_{p,m}\rangle$ needs closure as well.

Several approaches have been proposed for the closure of $\delta\breve{R}_{p,ij}$. Simonin *et al.* (2002) proposed a method consisting in directly solving Eq. (2.75) i.e. the six components of the tensor. However, this

shifts the difficulty to the modeling of $\delta\breve{Q}_{p,ijm}$. Based on the transport equation for this term:

$$\begin{aligned}\frac{\partial}{\partial t}\rho_p\breve{\alpha}_p\delta\breve{Q}_{p,ijm}+\frac{\partial}{\partial x_j}\rho_p\breve{\alpha}_p\delta\breve{Q}_{p,ijm} = &-3\frac{\rho_p\breve{\alpha}_p}{\breve{\tau}_p}\delta\breve{Q}_{p,ijm}+\rho_p\breve{\alpha}_p\delta\breve{Q}_{p,njm}\frac{\partial}{\partial x_n}\breve{u}_{p,i}\\ &+\rho_p\breve{\alpha}_p\delta\breve{Q}_{p,inm}\frac{\partial}{\partial x_n}\breve{u}_{p,j}-\rho_p\breve{\alpha}_p\delta\breve{Q}_{p,ijn}\frac{\partial}{\partial x_n}\breve{u}_{p,m}\\ &+\delta\breve{R}_{p,ij}\frac{\partial}{\partial x_n}\rho_p\breve{\alpha}_p\delta\breve{R}_{p,mn}+\delta\breve{R}_{p,jm}\frac{\partial}{\partial x_n}\rho_p\breve{\alpha}_p\delta\breve{R}_{p,in}\\ &+\delta\breve{R}_{p,im}\frac{\partial}{\partial x_n}\rho_p\breve{\alpha}_p\delta\breve{R}_{p,jn}-\frac{\partial}{\partial x_n}\rho_p\breve{\alpha}_p\delta\breve{M}_{p,ijmn},\end{aligned}\tag{2.76}$$

where $\delta\breve{M}_{p,ijmn}=\langle\breve{u}_{p,i}\breve{u}_{p,j}\breve{u}_{pm}\breve{u}_{p,n}\rangle$ is the 4^{rd}-order particle uncorrelated velocity correlation tensor. Assuming equilibrium of $\delta\breve{Q}_{p,ijm}$ and neglecting any deformation terms (2^{nd}, 3^{rd} and 4^{th} terms on the RHS of Eq. (2.76)), the transport equation reduces to (Moreau (2006)):

$$\begin{aligned}3\frac{\rho_p\breve{\alpha}_p}{\breve{\tau}_p}\delta\breve{Q}_{p,ijm} &= \delta\breve{R}_{p,jm}\frac{\partial}{\partial x_n}\rho_p\breve{\alpha}_p\delta\breve{R}_{p,in}+\delta\breve{R}_{p,im}\frac{\partial}{\partial x_n}\rho_p\breve{\alpha}_p\delta\breve{R}_{p,jn}\\ &+\delta\breve{R}_{p,ij}\frac{\partial}{\partial x_n}\rho_p\breve{\alpha}_p\delta\breve{R}_{p,mn}-\frac{\partial}{\partial x_n}\rho_p\breve{\alpha}_p\delta\breve{M}_{p,ijmn}.\end{aligned}\tag{2.77}$$

It is now necessary to model the 4^{th} order term $\delta\breve{M}_{p,ijmn}$. Simonin (1996) proposed to consider the Gaussian value of $\delta\breve{M}_{p,ijmn}$ in order to obtain a closure model:

$$\delta\breve{M}_{p,ijmn}=\delta\breve{R}_{p,ij}\delta\breve{R}_{p,mn}+\delta\breve{R}_{p,im}\delta\breve{R}_{p,jn}+\delta\breve{R}_{p,in}\delta\breve{R}_{p,jm}.\tag{2.78}$$

Finally combining Eqs. (2.77) and (2.78) leads to (Kaufmann (2004)):

$$\delta\breve{Q}_{p,ijm}=\frac{\breve{\tau}_p}{3}\left(\delta\breve{R}_{p,ml}\frac{\partial}{\partial x_l}\delta\breve{R}_{p,ij}+\delta\breve{R}_{p,jl}\frac{\partial}{\partial x_l}\delta\breve{R}_{p,im}+\delta\breve{R}_{p,il}\frac{\partial}{\partial x_l}\delta\breve{R}_{p,jm}\right),\tag{2.79}$$

which can be directly introduced in Eq. (2.75). However, this method is computationally very expensive and modeling the $\delta\breve{R}_{p,ij}$ tensor can follow simpler paths:

Simonin *et al.* (2002) introduced the particle RUE as half the trace of $\delta\breve{R}_{p,ij}$:

$$\delta\breve{\theta}_p=\frac{1}{2}\delta\breve{R}_{p,ll}.\tag{2.80}$$

Then Eq. (2.73) can be rewritten as follows:

$$\frac{\partial}{\partial t}\rho_p\breve{\alpha}_p\breve{u}_{p,i}+\frac{\partial}{\partial x_j}\rho_p\breve{\alpha}_p\breve{u}_{p,i}\breve{u}_{p,j}=-\frac{\partial}{\partial x_j}\frac{2}{3}\rho_p\breve{\alpha}_p\delta\breve{\theta}_p-\frac{\partial}{\partial x_j}\rho_p\breve{\alpha}_p\,\delta\breve{R}^*_{p,ij}-\Gamma\,\breve{u}_{p,i}+F_{D,i},\tag{2.81}$$

where $\delta\breve{R}^*_{p,ij}$ is the deviatoric part of $\delta\breve{R}_{p,ij}$, similar to the viscosity contribution in the theory of diluted gases. $\delta\breve{\theta}_p$ is the spherical part, similar to a pressure term:

$$\delta\breve{R}^*_{p,ij}=\delta\breve{R}_{p,ij}-\frac{2}{3}\delta\breve{\theta}_p\delta_{ij}\ .\tag{2.82}$$

A transport equation for the particle RUE is derived from and substitutes the set of 2^{nd} order particle correlations conservation equations for the dispersed phase:

$$\frac{\partial}{\partial t}\rho_p\breve{\alpha}_p\delta\breve{\theta}_p+\frac{\partial}{\partial x_j}\rho_p\breve{\alpha}_p\breve{u}_{p,j}\delta\breve{\theta}_p=-\frac{\partial}{\partial x_j}\rho_p\breve{\alpha}_p\delta\breve{Q}_{p,iij}-\rho_p\breve{\alpha}_p\left[\delta\breve{R}^*_{p,ij}+\frac{2}{3}\delta\breve{\theta}_p\delta_{ij}\right]\frac{\partial}{\partial x_j}\breve{u}_{p,i}-\Gamma\delta\breve{\theta}_p+W_\theta,\tag{2.83}$$

where $\Gamma\delta\breve{\theta}_p$ is the source term of particle RUE linked to evaporation. W_θ is a source term linked to drag force and its expression is deduced from Eq. (2.34):

$$W_\theta = \frac{2\rho_p\breve{\alpha}_p}{\breve{\tau}_p}\delta\breve{\theta}_p \ . \tag{2.84}$$

A closure model for $\delta\breve{Q}_{p,iim}$ is proposed hereinafter and there is only one more unclosed term left in Eq. (2.83), $\delta\breve{R}^*_{p,ij}$. Different closure models for this term are studied in Part II.

Closure model for $\delta\breve{Q}_{p,iim}$

Eq. (2.83) for particle RUE is very similar to the transport equation for fluid temperature (with the exception of the last two terms on the RHS, that are linked to evaporation and drag force source terms). Kaufmann *et al.* (2005) proposed a simpler model consisting in modeling $\delta\breve{Q}_{p,iim}$ in analogy with the Fick's law for the fluid temperature:

$$\frac{1}{2}\delta\breve{Q}_{p,iim} = -\kappa_{RUM}\frac{\partial\delta\breve{\theta}_p}{\partial x_m}, \tag{2.85}$$

where κ_{RUM} stands for the uncorrelated diffusion coefficient and is modeled in analogy with the RANS two-fluid approach (Simonin (1996)):

$$\kappa_{RUM} = \frac{10}{27}\breve{\tau}_p\delta\breve{\theta}_p. \tag{2.86}$$

2.3 Final set of conservation equations for the dispersed phase in the EE approach

In the remaining of the manuscript, the Mesoscopic Eulerian Approach is worked on (hereinafter it will be referred indistinctly as MEF or EE). Part II is dedicated to the *a posteriori* analysis of the closure models developped by Masi (2010) in the particle-laden slab HIT flow configuration. Part III presents a study on the evaporation of fuel droplets. Different evaporation models are compared and a new approach for the computation of the evaporation process of isolated droplets in AVBP is proposed. Finally, Part IV presents an example of joint application of the model for the closure of the RUM terms retained in Part II and the new approach for the evaporation presented in Part III. The configuration chosen is the MERCATO bench, whose experimental data were acquired at ONERA (Toulouse, France) (García-Rosa (2008)), and computed using EE (Sanjosé (2009)) and EL approaches (Senoner (2010)) in AVBP.

The final set of conservation equations for the dispersed phase that are transported in AVBP and

considered in the rest of this work is:

$$\frac{\partial}{\partial t}\breve{n}_p + \frac{\partial}{\partial x_j}\breve{n}_p\breve{u}_{p,j} = 0 \tag{2.87}$$

$$\frac{\partial}{\partial t}\rho_p\breve{\alpha}_p + \frac{\partial}{\partial x_j}\rho_p\breve{\alpha}_p\breve{u}_{p,j} = -\Gamma \tag{2.88}$$

$$\begin{aligned}\frac{\partial}{\partial t}\rho_p\breve{\alpha}_p\breve{u}_{p,i} + \frac{\partial}{\partial x_j}\rho_p\breve{\alpha}_p\breve{u}_{p,i}\breve{u}_{p,j} = &- \Gamma\,\breve{u}_{p,i} + F_{D,i} \\ &- \frac{\partial}{\partial x_j}\rho_p\breve{\alpha}_p\left[\delta\breve{R}^*_{p,ij} + \frac{2}{3}\delta\breve{\theta}_p\delta_{ij}\right]\end{aligned} \tag{2.89}$$

$$\frac{\partial}{\partial t}\rho_p\breve{\alpha}_p\breve{h}_p + \frac{\partial}{\partial x_j}\rho_p\breve{\alpha}_p\breve{u}_{p,j}\breve{h}_p = -\Gamma\breve{h}_p + \Phi_p \tag{2.90}$$

$$\begin{aligned}\frac{\partial}{\partial t}\rho_p\breve{\alpha}_p\delta\breve{\theta}_p + \frac{\partial}{\partial x_j}\rho_p\breve{\alpha}_p\breve{u}_{p,j}\delta\breve{\theta}_p = &- \Gamma\delta\breve{\theta}_p + W_\theta - \frac{\partial}{\partial x_j}\rho_p\breve{\alpha}_p\delta\breve{Q}_{p,iij} \\ &- \rho_p\breve{\alpha}_p\left[\delta\breve{R}^*_{p,ij} + \frac{2}{3}\delta\breve{\theta}_p\delta_{ij}\right]\frac{\partial}{\partial x_j}\breve{u}_{p,i}.\end{aligned} \tag{2.91}$$

2.3.1 Transport equations for the dipersed phase in compressed form

Similarly to Section 2.1, the conservation equations for the dispersed phase can be written in a compressed form. For the particle phase, one has:

$$\frac{\partial}{\partial t}\mathbf{w_p} + \nabla\cdot\mathcal{F}_p = \mathbf{s}_p, \tag{2.92}$$

where $\mathbf{w}_p = (\breve{n}_p, \rho_p\breve{\alpha}_p, \rho_p\breve{\alpha}_p u_{p,i}, \rho_p\breve{\alpha}_p\breve{h}_p, \rho_p\breve{\alpha}_p\delta\breve{\theta}_p)^T$ is the vector of conservative variables for the dispersed phase, $\mathcal{F}_p$ is the flux tensor composed by two parts, one due to convection by the mesoscopic motion ($\mathcal{F}_p^M$) and one due to the uncorrelated motion ($\mathcal{F}_p^U$). $\mathbf{s}_p$ is the vector of source terms.

Convective fluxes due to the mesoscopic motion, $\mathcal{F}_p^M$ and to the uncorrelated motion $\mathcal{F}_p^U$

The tensor of fluxes read:

$$\mathcal{F}_p^M = \begin{pmatrix} \breve{n}_p\breve{u}_{p,j} \\ \rho_p\breve{\alpha}_p\breve{u}_{p,j} \\ \rho_p\breve{\alpha}_p\breve{u}_{p,i}\breve{u}_{p,j} \\ \rho_p\breve{\alpha}_p\breve{u}_{p,j}\breve{h}_p \\ \rho_p\breve{\alpha}_p\breve{u}_{p,j}\delta\breve{\theta}_p \end{pmatrix}, \qquad \mathcal{F}_p^U = \begin{pmatrix} 0 \\ 0 \\ \rho_p\breve{\alpha}_p\left[\delta\breve{R}^*_{p,ij} + \frac{2}{3}\delta\breve{\theta}_p\delta_{ij}\right] \\ 0 \\ \rho_p\breve{\alpha}_p\delta\breve{Q}_{p,iij} \end{pmatrix}. \tag{2.93}$$

Vector of source terms, s_p

There are two contributions to the source terms: the first one is linked to the exchanges with the gas phase ($\mathbf{s}_{g-p}$) and the second one is linked to the uncorrelated motion ($\mathbf{s}_\theta$). $\mathbf{s}_{g-p}$ groups the source terms of mass, momentum and energy with the gas phase whereas $\mathbf{s}_\theta$ contains only one term due to the exchanges between the uncorrelated and the correlated motions. This term applies to the particle RUE transport equation. The vectors of source terms read:

$$\mathbf{s}_p = \mathbf{s}_{g-p} + \mathbf{s}_\theta \tag{2.94}$$

$$\mathbf{s}_{g-p} = \begin{pmatrix} 0 \\ -\Gamma \\ -\Gamma \breve{u}_{p,i} + F_{D,i} \\ -\Gamma \breve{h}_p + \Phi_p \\ -\Gamma \delta \breve{\theta}_p + W_\theta \end{pmatrix}, \qquad \mathbf{s}_\theta = \begin{pmatrix} 0 \\ 0 \\ 0 \\ 0 \\ -\rho_p \breve{\alpha}_p \left[\delta \breve{R}^*_{p,ij} + \frac{2}{3} \delta \breve{\theta}_p \delta_{ij} \right] \frac{\partial}{\partial x_j} \breve{u}_{p,i} \end{pmatrix}. \tag{2.95}$$

Inverse coupling between the dispersed and the gaseous phases

The source terms vector in Eq. (2.4) $\mathbf{s}_{p-g}$ has not been defined yet. It represents the coupling terms that include the influence of the particle phase on the gaseous phase. It reads:

$$\mathbf{s}_{p-g} = \begin{pmatrix} \Gamma \delta_{k,F} \\ -\Gamma \breve{u}_{p,i} - F_{D,i} \\ \Pi_g + \Gamma \frac{1}{2} \breve{u}^2_{p,i} - \breve{u}_{p,i} F_{D,i} \end{pmatrix} \tag{2.96}$$

where $\Gamma \frac{1}{2} \breve{u}^2_{p,i}$ and $\breve{u}_{p,i} F_{D,i}$ represent the gaseous kinetic energy transfer due to evaporation and drag force respectively. Π_g is the sensible energy transfer rate due to evaporation and thermal conduction. Γ and Π_g will be defined in Part III.

Chapter 3

Transport equations for LES of dispersed two-phase flows

Nowadays, the available computational power limits the use of DNS to academic configurations. When a second phase is taken into account, the complexity of the problem increases. The use of DNS becomes then prohibitive, especially in complex comfigurations. In LES, the equations are filtered, the large scales of the motion are resolved and only the high frequency scales, smaller than the filter width, are modeled.

In turbulent flows the largest scales strongly depend on the geometry of the system while the smallest ones present an universal behavior which is determined almost entirely by the rate at which they receive energy from the large scales (flow Reynolds number Re (Eq. (3.1))), and by the fluid viscosity. In such flows, LES has therefore a clear advantage compared to RANS since it is easier to develop models for the smallest structures than models for the whole range of scales.

The application of LES to two-phase flows is more recent than for purely gaseous flows. Fox (2012) provides a review of the different approaches for Large Eddy simulation of two-phase flows, pointing out the main fields of application of each approach, as well as their advantages, drawbacks and a summary of the closures and models for the sub-grid scale terms.

3.1 LES equations for the gaseous phase

The transition from laminar to turbulent flow is characterized by the Reynolds number Re, a dimensionless number representing the ratio of inertial to viscous forces:

$$Re = \frac{\mathcal{L}\mathcal{U}}{\nu}, \tag{3.1}$$

where $\mathcal{L}$ the characteristic size of the flow, $\mathcal{U}$ the characteristic velocity and ν the fluid kinematic viscosity. The higher the Reynolds number, the more turbulent the flow.

The velocity in a turbulent flow suffers significant variations in time and space. It is characterized by the pressence of vortices or eddies of different sizes. These eddies are in fact vortical structures that interact. The energy cascade (Richardson (1922)) suggests that the kinetic energy is essentially fed by the turbulence at the largest scales and is then transferred to smaller and smaller scales until its dissipation by the viscous forces at the smallest scales (Pope (2000)).

When the Reynolds number large enough, the smallest eddies of the flow can be characterized (Kolmogorov (1941)) being ϵ the dissipation rate of the flow, Kolmogorov (1941) stated that a unique set of length, velocity and time scales can be expressed for the smallest scales:

$$\eta \equiv (\nu^3/\epsilon)^{1/4}, \tag{3.2}$$
$$u_\eta \equiv (\epsilon\nu)^{1/4}, \tag{3.3}$$
$$\tau_\eta \equiv (\nu/\epsilon)^{1/2}. \tag{3.4}$$

where η refers to the smallest scales of the flow.

It is then possible to link the length, velocity and time scales of the smallest eddies to those of the largest eddies depending only on the Reynolds number:

$$\eta/l_0 \sim Re^{-3/4}, \tag{3.5}$$
$$u_\eta/u_0 \sim Re^{-1/4}, \tag{3.6}$$
$$\tau_\eta/\tau_0 \sim Re^{-1/2}, \tag{3.7}$$

where the subscript 0 refers to the largest scales of turbulence.

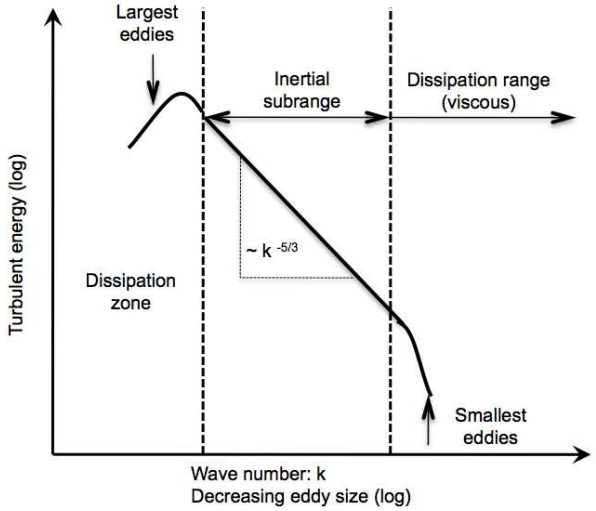

Figure 3.1: *Example of energy spectrum showing the distinction between integral, inertial and dissipation zones. Source Pope (2000).*

The energy spectrum $E(\kappa)$ represents the turbulent contribution os all scales to the turbulent kinetic energy. Figure 3.1 shows an example of energy spectrum. Three main zones can be distinguished (Pope (2000)):

- The integral or energy containing zone: the largest eddies belong to this part. They are characterized by the lowest frequencies and their size is comparable to the largest scales of the flow.
- The inertial zone represents the large eddies breaking into smaller ones and transferring their energy to smallest eddies.
- The dissipation range contains the high frequency structures, i.e. the smallest eddies. The viscous forces act in this zone converting the turbulent energy of the eddies into heat.

3.1.1 Filtering procedure

The separation of the small and large scales is achieved through the application of a low-pass filter G_Δ to the exact equations (Leonard (1974)). The filtered quantity $\overline{\Phi}$ is defined as the convolution of the

non-filtered quantity Φ with the spatial filter G_Δ, whose characteristic lenght is Δ:

$$\overline{\Phi}(x) = \int \Phi(x) G_\Delta(x' - x)\, dx'. \tag{3.8}$$

The filtered quantity or resolved large scale field, $\bar{\Phi}$, is calculated solving its transport equation. The unsolved residual field Φ' contains all the flow scales smaller than the filter size 2Δ:

$$\Phi' = \Phi - \overline{\Phi}. \tag{3.9}$$

For variable density flows, it is useful to use a mass weighted filtering or Favre averaging (Favre (1969)) in order to avoid unclosed terms due to density fluctuations:

$$\hat{\phi} = \frac{1}{\overline{\rho}}\,\overline{\rho\phi}. \tag{3.10}$$

In the context of this work, both phases are compressible, so Favre averaging is applied to both the gaseous and the dispersed phases.

3.1.2 Filtered Navier-Stokes equations

The final set of filtered Navier-Stokes equations for the gas phase are directly obtained by filtering Eqs. (2.1)-(2.3):

$$\frac{\partial}{\partial t}\overline{\rho_g} + \frac{\partial}{\partial x_j}\overline{\rho_g}\hat{u}_{g,j} = 0 \tag{3.11}$$

$$\frac{\partial}{\partial t}\overline{\rho_g}\hat{u}_{g,i} + \frac{\partial}{\partial x_j}\overline{\rho_g}\hat{u}_{g,i}\hat{u}_{g,j} = -\frac{\partial}{\partial x_j}\left[\overline{P_g}\delta_{ij} - \overline{\tau_{g,ij}} + \overline{\rho_g} T_{g,ij}\right] \tag{3.12}$$

$$\frac{\partial}{\partial t}\overline{\rho_g}\hat{E}_g + \frac{\partial}{\partial x_j}\overline{\rho_g}\hat{E}_g\hat{u}_{g,j} = -\frac{\partial}{\partial x_j}\left[\hat{u}_{g,i}(\overline{P_g}\delta_{ij} - \overline{\tau_{g,ij}}) + \overline{q_{g,j}} + \overline{\rho_g} Q_{g,j})\right]. \tag{3.13}$$

where the subgrid terms read:

$$T_{g,ij} = \widehat{u_{g,i}u_{g,j}} - \hat{u}_{g,i}\hat{u}_{g,j} \tag{3.14}$$

$$Q_{g,j} = \widehat{u_{g,j}E_g} - \hat{u}_{g,j}\hat{E}_g. \tag{3.15}$$

The subgrid-scale terms are modeled by their dissipative effects on the computed scales following the idea of energy transfer from the largest to the smallest scales (Kolmogorov (1941)). The Boussinesq hypothesis (Boussinesq (1877)) assumes that the energy transfer mechanism from the resolved to the subgrid scales is analogous to the molecular diffusion mechanism. Replacing the molecular viscosity by a turbulent kinematic viscosity ν_t, the fluid subgrid model is written:

$$T_{g,ij} - \frac{1}{3}T_{g,ll} \approx 2\nu_t\left(\hat{S}_{g,ij} - \frac{1}{3}\delta_{ij}\hat{S}_{g,ll}\right), \tag{3.16}$$

where

$$\hat{S}_{g,ij} = \frac{1}{2}\left(\frac{\partial \hat{u}_{g,i}}{\partial x_j} + \frac{\partial \hat{u}_{g,j}}{\partial x_i}\right). \tag{3.17}$$

In Eq. (3.16) only the turbulent viscosity ν_t needs to be modeled. Various models for the turbulent viscosity are available in AVBP (Smagorinsky (Smagorinsky (1963)), WALE (Ducros *et al.* (1998)), Filtered Smagorinsky (Ducros *et al.* (1996)), Dynamic Smagorisnsky model (Germano *et al.* (1991), Lilly (1992)) and the k-equation model). As it is not the scope of this work, the model used here is briefly presented in Section 3.1.3.

The subgrid-scale heat flux $Q_{g,j}$ model needs the determination of the turbulent thermal conductivity λ_t, that is, the thermal conductivity due to the residual turbulent motion. $Q_{g,j}$ is written as:

$$Q_{g,j} = -\frac{\lambda_t}{\overline{\rho_g}} \frac{\partial \hat{T}_g}{\partial x_j}, \tag{3.18}$$

with

$$\lambda_t = \frac{\overline{\rho_g} \nu_t \overline{Cp_g}}{Pr_t}. \tag{3.19}$$

In the LES presented in this work, the turbulent Prandtl number Pr_t has been set to 0.6.

Finally, the remaining filtered terms are approximated as follows:

$$\overline{\tau_{g,ij}} = 2\mu_g \left(\hat{S}_{g,ij} - \frac{1}{3}\delta_{ij}\hat{S}_{g,ll} \right), \tag{3.20}$$

$$\overline{q_{g,j}} = \lambda_g \frac{\partial \hat{T}_g}{\partial x_j}, \tag{3.21}$$

$$\overline{P} = \overline{\rho_g r} \hat{T}_g. \tag{3.22}$$

3.1.3 WALE model for the gaseous turbulent viscosity

Multiple models for the evaluation of the dissipative effects of the subgrid-scales (Lesieur (1997), Pope (2000)) exist. There are also several options to model the turbulent viscosity in AVBP. However, all the LES presented in this work have been performed with the WALE (Wall-Adapting Local Eddy-viscosity) model (Ducros *et al.* (1998)). This model automatically adapts the subgrid viscosity on boundary layer flows while preserving the dissipative effects of turbulence in HIT flows.

The WALE turbulent viscosity reads:

$$\nu_t = (C_w \Delta)^2 \frac{(s^d_{ij} s^d_{ij})^{3/2}}{(\hat{S}_{g,ij}\hat{S}_{g,ij})^{5/2} + (s^d_{ij} s^d_{ij})^{5/4}}. \tag{3.23}$$

where C_w is the same constant as in the Smagorinsky model, fixed to $C_w = 0.4929$. s^d_{ij} is the residual part in the resolved rate-of-deformation tensor:

$$s^d_{ij} = \hat{S}_{g,im}\hat{S}_{g,mj} + \hat{\Omega}_{g,im}\hat{\Omega}_{g,mj} - \frac{1}{3}\delta_{ij}\left[\hat{S}_{g,nl}\hat{S}_{g,nl} + \hat{\Omega}_{g,nl}\hat{\Omega}_{g,nl} \right], \tag{3.24}$$

where $\hat{\mathbf{\Omega}}_g$ is the filtered rotation rate tensor:

$$\hat{\mathbf{\Omega}}_{g,ij} = \frac{1}{2}\left(\frac{\partial \hat{u}_{g,i}}{\partial x_j} - \frac{\partial \hat{u}_{g,j}}{\partial x_i} \right). \tag{3.25}$$

3.2 LES equations for the dispersed phase

Filtering the mesoscopic Eulerian equations is done in analogy with the filtering of the gaseous phase equations presented in Section 3.1.1. Favre averaging is performed replacing the gaseous density ρ_g in Eq. (3.26) by the mesoscopic particle volume fraction $\breve{\alpha}_p$:

$$\overline{\alpha_p}\hat{\phi} = \overline{\breve{\alpha}_p \breve{\phi}}. \tag{3.26}$$

An equivalence between the Favre average based on $\breve{\alpha}_p$ and the particle number density $\breve{n}_p$ can be obtained assuming that the dispersed phase is locally monodisperse, i.e. within the filter size. Thus, the Favre average also reads:

$$\overline{\breve{n}_p\breve{\phi}} = \overline{\frac{6\breve{\alpha}_p}{\pi d^3}\breve{\phi}} = \overline{n_p}\hat{\phi}. \tag{3.27}$$

In the remaining of this chapter, the notation $\breve{.}$ will be abandoned for the sake of simplicity.

3.2.1 Filtered Mesoscopic Eulerian equations

The final set of LES equations for the dispersed phase reads:

$$\frac{\partial}{\partial t}\overline{n_p} + \frac{\partial}{\partial x_j}\overline{n_p}\hat{u}_{p,j} = 0 \tag{3.28}$$

$$\frac{\partial}{\partial t}\rho_p\overline{\alpha_p} + \frac{\partial}{\partial x_j}\rho_p\overline{\alpha_p}\hat{u}_{p,j} = -\overline{\Gamma} \tag{3.29}$$

$$\begin{aligned}\frac{\partial}{\partial t}\rho_p\overline{\alpha_p}\hat{u}_{p,i} + \frac{\partial}{\partial x_j}\rho_p\overline{\alpha_p}\hat{u}_{p,i}\hat{u}_{p,j} = &-\overline{\Gamma}\,\hat{u}_{p,i} + \overline{F_{D,i}} \\ &- \frac{\partial}{\partial x_j}\rho_p\overline{\alpha_p}\left[\widehat{\delta R^*_{p,ij}} + \frac{2}{3}\widehat{\delta\theta_p}\delta_{ij} + T_{p,ij}\right]\end{aligned} \tag{3.30}$$

$$\frac{\partial}{\partial t}\rho_p\overline{\alpha_p}\widehat{h_p} + \frac{\partial}{\partial x_j}\rho_p\overline{\alpha_p}\hat{u}_{p,j}\widehat{h_p} = -\overline{\Gamma}\widehat{h_p} + \overline{\Phi_p} \tag{3.31}$$

$$\begin{aligned}\frac{\partial}{\partial t}\rho_p\overline{\alpha_p}\widehat{\delta\theta_p} + \frac{\partial}{\partial x_j}\rho_p\overline{\alpha_p}\hat{u}_{p,j}\widehat{\delta\theta_p} = &-\overline{\Gamma}\widehat{\delta\theta_p} + \overline{W_\theta} - \frac{\partial}{\partial x_j}\rho_p\overline{\alpha_p}\widehat{\delta Q_{p,iij}} \\ &- \overline{\rho_p\breve{\alpha}_p\left[\delta\breve{R}^*_{p,ij} + \frac{2}{3}\delta\breve{\theta}_p\delta_{ij}\right]\frac{\partial}{\partial x_j}\breve{u}_{p,i}}.\end{aligned} \tag{3.32}$$

In the set of equations Eq. (3.28) - (3.32) several terms need closure. In this section, the closure approximations for the source terms due to drag force and evaporation are recalled. The filtered evaporation source terms here presented correspond to the classical model implemented in AVBP. The filtered terms corresponding to the models presented in Part III are computed similarly.

- Filtered source terms linked to evaporation:
  - Mass evaporation rate:

$$\overline{\Gamma} \approx \pi\overline{n}_p d\overline{Sh}\frac{\overline{\mu}}{Sc_F}ln(1+\overline{B}_M), \tag{3.33}$$

$$\overline{Sh} \approx 2 + 0.55\overline{Re}_p^{1/2}Sc_F^{1/3}, \tag{3.34}$$

$$\overline{B}_M \approx \frac{Y_{F,\zeta}(\hat{T}_p) - \hat{Y}_F}{1 - Y_{F,\zeta}(\hat{T}_p)}. \tag{3.35}$$

  - Sensible energy variation rate du to thermal conduction:

$$\overline{\Phi}_p \approx \overline{\Gamma}(\hat{h}_p - h_{s,F}(\hat{T}_p)) - \pi\overline{n}_p d\overline{Nu}(\hat{T}_p - \hat{T}), \tag{3.36}$$

$$\overline{Nu} \approx 2 + 0.55\overline{Re}_p^{1/2}Pr^{1/3}. \tag{3.37}$$

- Filtered source terms linked to drag force:
  - Momentum variation rate due to drag:

$$\overline{F}_{D,i} \approx \frac{\rho_p\overline{\alpha}_p}{\overline{\tau}_p}(\hat{u}_i - \hat{u}_{l,i}). \tag{3.38}$$

- Filtered source term linked to the RUM:
  - Rate of RUE variation due to drag force:

$$\overline{W_\theta} \approx -\frac{2\rho_p \overline{\alpha}_p}{\overline{\tau_p}} \hat{\delta\theta}_p, \tag{3.39}$$

where the filtered particle relaxation time is approximated as follows:

$$\overline{\tau}_p \approx (1 + 0.15\overline{Re}_p^{0.687}) \frac{\rho_p d^2}{18\overline{\mu}}, \tag{3.40}$$

and the filtered particle Reynolds number:

$$\overline{Re}_p \approx \frac{|\hat{u} - \hat{u}_p| d}{\overline{\nu}}. \tag{3.41}$$

Special attention is needed for the terms related to the Random Uncorrelated Motion:

- $T_{p,ij}$ is due to the subgrid correlated motion and is analogous to the fluid Reynolds tensor (Eq. (3.16)):

$$T_{p,ij} = \widehat{u_{p,i} u_{p,j}} - \hat{u}_{p,i} \hat{u}_{p,j}. \tag{3.42}$$

- $\widehat{\delta Q_{p,iij}}$ is modeled similarly to in Eq. (2.85):

$$\widehat{\delta Q_{p,iij}} = -\hat{\kappa}_{RUM} \frac{\partial \widehat{\delta\theta_p}}{\partial x_j}, \tag{3.43}$$

where $\hat{\kappa}_{RUM} = \frac{10}{27} \overline{\tau}_p \hat{\delta\theta}_p$.

- The filtered RUE production term is written as:

$$\overline{\rho_p \breve{\alpha}_p \underbrace{\left[\delta\breve{R}^*_{p,ij} + \frac{2}{3}\delta\breve{\theta}_p \delta_{ij}\right]}_{\delta\breve{R}_{p,ij}} \frac{\partial}{\partial x_j} \breve{u}_{p,i}} = \rho_p \overline{\alpha_p} \widehat{\delta R_{p,ij}} \frac{\partial \hat{u}_{p,i}}{\partial x_j} - \underbrace{\left[\overline{\rho_p \breve{\alpha}_p \delta\breve{R}_{p,ij} \frac{\partial \breve{u}_{p,i}}{\partial x_j}} - \rho_p \overline{\alpha_p} \widehat{\delta R_{p,ij}} \frac{\partial \hat{u}_{p,i}}{\partial x_j}\right]}_{\overline{U}^t_\theta}, \tag{3.44}$$

where $\widehat{\delta R_{p,ij}} = \widehat{\delta R^*_{p,ij}} + \frac{2}{3}\widehat{\delta\theta_p}\delta_{ij}$. $\delta\hat{\theta}_p$ is captured through its transport equation (Eq. 3.32). $\delta\hat{R}^*_{p,ij}$ is evaluated through the models described in Part II using filtered quantities.

$\overline{U}^t_\theta$ is a RUE production term due to the subgrid scale motion and is assumed to have a dissipative effect on the subgrid correalted energy. Assuming equilibrium in the subgrid correlated energy, Moreau (2006) modeled $\overline{U}^t_\theta$ as:

$$\overline{U}^t_\theta = T_{p,ij} \frac{\partial \hat{u}_{p,i}}{\partial x_j}. \tag{3.45}$$

For more details the reader is encouraged to see Moreau (2006) and Riber (2007).

Part II

Modeling the Random Uncorrelated Stress Tensor

Chapter 4

Modeling the RUM stress tensor

This Chapter, inspired in the work of Masi (2010), is dedicated to the closure models for the deviatoric part of the Random Uncorrelated Motion (RUM) stress tensor ($\delta\breve{R}^*_{p,ij}$) appearing for the MEF approach in the momentum (Eq. (2.89)) and Random Uncorrelated Energy equations (Eq. (2.91)). Such tensor may be compared to the fluid stress tensor due to thermal agitation in the Navier-Stokes equations for the gaseous phase. As stated in Chapter 2, the second order uncorrelated velocity correlation tensor, or RUM tensor $\delta\breve{R}_{p,ij}$, is splitted into an spherical part, the so-called RUE ($\delta\breve{\theta}_p$) and a deviatoric part $\delta\breve{R}^*_{p,ij}$. Section 2.2.4 presented the development of a transport equation for the RUE, while the deviatoric part remained unclosed.

Simonin *et al.* (2002) proposed to close the deviatoric RUM stress tensor using a viscosity assumption, the so-called VISCO model (Section 4.2). This model has proven to give satisfactory results in *a posteriori* inertial particle-laden HIT flows simulations (Kaufmann (2004), Riber (2007), Kaufmann *et al.* (2008), Vié (2010)). However, Riber (2007) showed that it failed when performing *a posteriori* tests in mean-sheared flows (Hishida *et al.* (1987)). Recently, Masi (2010) proposed new models for the closure of $\delta\breve{R}^*_{p,ij}$, that are briefly recalled in this Chapter. She performed an *a priori* analysis of a particle-laden turbulent planar jet (Fig. 4.1) proposed and validated models on this configuration with mean shear. The corresponding *a posteriori* study of the same configuration is presented in Chapter 5.

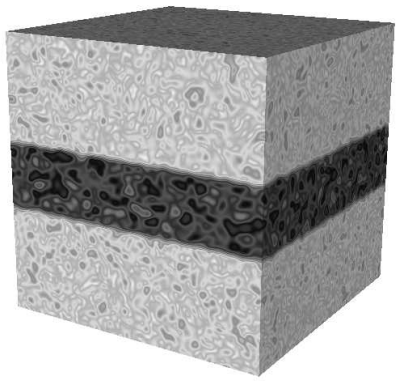

Figure 4.1: *Particle-laden turbulent planar jet configuration (Particle-laden HIT slab). Initial carrier phase velocity magnitude field.*

4.1 Preliminary considerations

In this Part of the manuscript, and in order to respect the notation used by Masi (2010), the equations are written using $\breve{n}_p$ instead of $\rho_p \breve{\alpha}_p$. In a monodisperse context, both quantities are proportional:

$$\breve{\alpha}_p = \frac{d_p^3 \cdot \pi \cdot \breve{n}_p}{6}. \tag{4.1}$$

Several quantites that are used throughout this Chapter are here defined. The RUM anisotropy stress tensor reads:

$$b^*_{p,ij} = \frac{\delta \breve{R}_{p,ij}}{2\delta \breve{\theta}_p} - \frac{1}{3}\delta_{ij} = \frac{\delta \breve{R}^*_{p,ij}}{2\delta \breve{\theta}_p}. \tag{4.2}$$

The particle rate-of-strain is the symmetric part of the mesoscopic particle velocity gradient:

$$S_{p,ij} = \frac{1}{2}\left(\frac{\partial \breve{u}_{p,i}}{\partial x_j} + \frac{\partial \breve{u}_{p,j}}{\partial x_i}\right). \tag{4.3}$$

The mesoscopic vorticity or rotation tensor $\mathbf{\Omega}$ reads:

$$\Omega_{p,ij} = \frac{1}{2}\left(\frac{\partial \breve{u}_{p,i}}{\partial x_j} - \frac{\partial \breve{u}_{p,j}}{\partial x_i}\right). \tag{4.4}$$

The mesoscopic velocity-gradient tensor is thus defined as:

$$\frac{\partial \breve{u}_{p,i}}{\partial x_j} = \mathbf{S}^* + \frac{1}{3}\{\mathbf{S}\}\mathbf{I} + \mathbf{\Omega}, \tag{4.5}$$

where $\mathbf{I}$ is the identity matrix, bold notation denotes three-dimensional (3D) second order tensors and $\{.\}$ represents the tensor trace. Asterisk is used to denote traceless tensors when associated with bold notation, otherwise means "deviatoric". The deviatoric particle rate-of-strain accounts for shearing and the spherical part for contraction or expansion.

The alignment between the particle rate-of-strain tensor and the rotation tensor provides information about the configuration of the flow. For information on the local behavior of the tensors the reader is referred to the works of Lund & Rogers (1994), Simonin (1991), George & Hussein (1991) and Masi (2010)).

4.2 A local equilibrium assumption

In order to be coherent with the notation used by Masi (2010), the equations for the RUM model proposed by Simonin *et al.* (2001) are here rewritten.

The transport equation for the 2^{nd} order particle velocity stress tensor $\delta \breve{R}_{p,ij}$ reads:

$$\frac{\partial}{\partial t}\breve{n}_p \delta \breve{R}_{p,ij} + \frac{\partial}{\partial x_j}\breve{n}_p \delta \breve{R}_{p,ij}\breve{u}_{p,j} = -2\frac{\breve{n}_p}{\breve{\tau}_p}\delta \breve{R}_{p,ij} - \breve{n}_p \delta \breve{R}_{p,ik}\frac{\partial \breve{u}_{p,j}}{\partial x_k} - \breve{n}_p \delta \breve{R}_{p,kj}\frac{\partial \breve{u}_{p,i}}{\partial x_k} - \frac{\partial}{\partial x_k}\delta \breve{Q}_{p,ijk}. \tag{4.6}$$

Neglecting all transport terms, Eq. (4.6) reduces to:

$$\delta \breve{R}_{p,ij} = -\frac{\breve{\tau}_p}{2}\left[\delta \breve{R}_{p,ik}\frac{\partial \breve{u}_{p,j}}{\partial x_k} + \delta \breve{R}_{p,kj}\frac{\partial \breve{u}_{p,i}}{\partial x_k}\right]. \tag{4.7}$$

The RUM stress tensor is then splitted into an spherical and a deviatoric part (Eq. (2.82)). Substracting the trace leads:

$$\begin{aligned}\delta\breve{R}^*_{p,ij} = & - \frac{\breve{\tau}_p}{2}\left[\frac{2}{3}\delta\breve{\theta}_p\left(\frac{\partial\breve{u}_{p,i}}{\partial x_j}+\frac{\partial\breve{u}_{p,j}}{\partial x_i}-\frac{2}{3}\frac{\partial\breve{u}_{p,m}}{\partial x_m}\delta_{ij}\right)\right] \\ & - \frac{\breve{\tau}_p}{2}\left[\delta\breve{R}^*_{p,kj}\frac{\partial\breve{u}_{p,i}}{\partial x_k}+\delta\breve{R}^*_{p,ik}\frac{\partial\breve{u}_{p,j}}{\partial x_k}-\frac{2}{3}\delta\breve{R}^*_{p,mn}\frac{\partial\breve{u}_{p,m}}{\partial x_n}\delta_{ij}\right].\end{aligned} \tag{4.8}$$

In order to close the deviatoric RUM stress tensor $\delta\breve{R}^*_{p,ij}$, a condition of equilibrium may be assumed. Assuming light anisotropy leads to neglect the 2^{nd} term in the RHS of Eq. (4.8) giving the known viscosity-like model (Simonin *et al.* (2001)):

$$\delta\breve{R}^*_{p,ij} = -\frac{\breve{\tau}_p}{2}\left[\frac{2}{3}\delta\breve{\theta}_p\left(\frac{\partial\breve{u}_{p,i}}{\partial x_j}+\frac{\partial\breve{u}_{p,j}}{\partial x_i}-\frac{2}{3}\frac{\partial\breve{u}_{p,m}}{\partial x_m}\delta_{ij}\right)\right] = -2\nu_{RUM}S^*_{p,ij}, \tag{4.9}$$

where $\nu_{RUM} = \breve{\tau}_p\delta\breve{\theta}_p/3$ is the so-called RUM viscosity.

This model has been extensively used to perform Eulerian-Eulerian simulations (Kaufmann *et al.* (2008), Riber (2007), Riber *et al.* (2009), Sanjosé (2009), Vié *et al.* (2009), Dombard (2011)). Riber (2007) showed that this model conducts to a re-laminarization of the dispersed phase flow when in the presence of mean shear (configuration of Hishida *et al.* (1987)). Hereinafter, Eq. (4.9) will be referred to as "VISCO" model.

Note that the viscosity model assumes that the deviatoric RUM and the particle rate-of-strain are related by a linear equation through an eddy-viscosity which uses the particle relaxation time as timescale. This assumption may be related to the kinetic theory of diluted gases. It implies that molecular motion adjust rapidly to the changes imposed by the local strain. This basic assumption at the basis of the VISCO model is violated when the Knudsen number (Kn, a dimensionless number relating the particle relaxation time and the mesoscopic shear timescale) is large.

4.3 A viscosity-type model for axisymmetric tensors

Masi (2010) adapted an idea of Jovanović & Otić (2000) suggested for turbulent flows to the dispersed phase behaving in one-component limit state. According to numerical onservations of turbulent flows, the tensors are assumed axisymmetric with respect to a preferential direction. That is, fluctuations are developed in a privileged direction of the flow. They can be written in bilinear form using eigenvalues (Batchelor (1946), Chandrasekhar (1950)). By using the second invariants of the rate-of-strain ($\mathbf{S}$, Eq. (4.3)), the anisotropy ($\mathbf{b}$) tensors, and the signs of their third invariants, one may write the following equation for $\delta\breve{R}^*_{p,ij}$:

$$\delta\breve{R}^*_{p,ij} = sign(III_S)sign(III_b)II_b^{1/2}2\delta\breve{\theta}_p\frac{S^*_{p,ij}}{S}. \tag{4.10}$$

The magnitude of the rate-of-strain tensor reads:

$$S = II_S^{1/2} = \{\mathbf{S}^{*2}\}^{1/2}, \tag{4.11}$$

S is the second invariant of the rate-of-strain tensor. The third dimensional invariant reads:

$$III_S = \{\mathbf{S}^{*3}\}, \tag{4.12}$$

The same invariants can be defined for the anisotropy tensor $\mathbf{b}$ respectively noted: II_b and III_b.

In Eq. (4.10), the product of the invariants' signs accounts for the possibility of both tensors being in the same configuration of contraction or expansion if positive, or in the opposite configuration if negative. Numerical simulations (Masi (2010)) showed that III_b is locally positive and only the sign

of III_S changes, and that $\mathbf{b}$ behaves in one-component limit state, which gives $II_b = \frac{2}{3}$. Taking into account these considerations, the Eq. (4.10) leads to:

$$\delta\breve{R}^*_{p,ij} = sign(III_S)\left(\frac{2}{3}\right)^{1/2} 2\delta\breve{\theta}_p \frac{S^*_{p,ij}}{S}. \tag{4.13}$$

Equation (4.13) still accounts for the possibility of reverse exchanges of energy through $sign(III_S)$. Under these assumptions, the sign of III_S reproduces both positive and negative viscosities, and thus energy exchanges from the RUM to the mesoscopic motion are accounted for. Equation (4.13) may be rewritten without including the sign of the third invariant of $\mathbf{S}$:

$$\delta\breve{R}^*_{p,ij} = -\left(\frac{2}{3}\right)^{1/2} 2\delta\breve{\theta}_p \frac{S^*_{p,ij}}{S}. \tag{4.14}$$

Hereinafter, Eq. (4.14) will be referred as "AXISY" model and Eq. (4.13) as "AXISY-C", "-C" standing for *corrected*, since the model includes a correction in the form of $sign(III_S)$.

4.3.1 Two different timescales

Section 4.2 presented a model for the deviatoric RUM stress tensor using the particle relaxation time $\breve{\tau}_p$ as timescale for the relationship between $\delta\breve{R}^*_{p,ij}$ and $S^*_{p,ij}$ (Eq. (4.9)). The so called AXISY model presented in Section 4.3 uses instead the mesoscopic-shear timescale to relate both tensors (Eq. (4.14)):

$$\underbrace{\frac{\breve{\tau}_p}{3}}_{VISCO} \longrightarrow \underbrace{\frac{II_b^{1/2}}{S}}_{AXISY}. \tag{4.15}$$

Hence, VISCO and AXISY are both eddy-viscosity models differing in their timescale: $\mathcal{F}(\breve{\tau}_p)$ for VISCO and $\mathcal{F}(S^{-1})$ for AXISY.

4.4 Quadratic algebraic approximation

Assuming equilibrium of stress components (i.e. neglecting all transport terms) in Eq. (4.8) and applying an iterative procedure invoking the isotropic approximation ($\delta\breve{R}^*_{p,ij} = 0$) at the zeroth-order approximation, Zaichik developped a non-linear model that, at the first approximation, is equivalent to VISCO model. The second approximation gives:

$$\delta\breve{R}^*_{p,ij} = -\frac{2\breve{\tau}_p\delta\breve{\theta}_p}{3}S^*_{p,ij} + \frac{2\breve{\tau}_p^2\delta\breve{\theta}_p}{6}\left(S^*_{p,ik}\frac{\partial\breve{u}_{p,j}}{\partial x_k} + S^*_{p,jk}\frac{\partial\breve{u}_{p,i}}{\partial x_k} - \frac{2}{3}S^*_{p,mn}\frac{\partial\breve{u}_{p,m}}{\partial x_n}\delta_{ij}\right). \tag{4.16}$$

Equation (4.16) is referred as "QUAD" model in Masi (2010). It has not been implemented in AVBP and analysis nor results concerning this model are presented in this work. However, it is a necessary step for the understanding of the model presented in Section 4.4.1.

4.4.1 A "rescaled" quadratic algebraic approximation.

Masi (2010) used Eq. (4.15) to construct a new non-linear model from Eq. (4.16). Replacing $\breve{\tau}_p$ with the timescale S^{-1} (cf Section 4.3.1) and applying the same iterative procedure to Eq. (4.8) that has been applied to obtain Eq. (4.16) leads to:

$$\delta\breve{R}^*_{p,ij} = -2\left(\frac{2}{3}\right)^{1/2}\delta\breve{\theta}_p\frac{S^*_{p,ij}}{S} + \frac{2\delta\breve{\theta}_p}{S^2}\left(S^*_{p,ik}\frac{\partial\breve{u}_{p,j}}{\partial x_k} + S^*_{p,jk}\frac{\partial\breve{u}_{p,i}}{\partial x_k} - \frac{2}{3}S^*_{p,mn}\frac{\partial\breve{u}_{p,m}}{\partial x_n}\delta_{ij}\right). \tag{4.17}$$

Equation (4.17) at the first order leads to "AXISY" model (Eq. (4.14)), if one-component limit state is assumed and a positive viscosity is used. It can be rewritten for the anisotropy tensor $\mathbf{b}^*$:

$$\mathbf{b}^* = -\left[\left(\frac{2}{3}\right)^{1/2} - \frac{2}{3}\{\mathbf{S}^+\}\right]\mathbf{S}^{*+} - (\mathbf{S}^{*+}\mathbf{\Omega}^+ - \mathbf{\Omega}^+\mathbf{S}^{*+}) + 2\left(\mathbf{S}^{*+2} - \frac{1}{3}\{\mathbf{S}^{*+2}\}\mathbf{I}\right), \tag{4.18}$$

where the superscript $^+$ stands for dimensionless tensors (normalization by $II_S^{1/2}$). The assessment of the model on the mean components of the stress tensor showed that including a coefficient of 0.5 in Eq. (4.18) produces better agreement in the particle-laden turbulent planar jet configuration (Fig. 4.1) of (Masi (2010)). Hereinafter, Eq. (4.18) will be referred as "QUAD-MOD" model. It has been implemented in AVBP with a coefficient of 0.5 for the study of Chapter 5 for the configuration shown in Fig. 4.1.

4.5 A local weak-equilibrium assumption

In the context of gaseous turbulence, Rodi (1972) introduced a "weak-equilibrium" assumption which does not need to neglect the transport terms in the stress equations. Instead, it supposes that the spatial and temporal variations of the stresses are related to the variations of the kinetic energy. The equilibrium hypothesis is thus transposed onto the anisotropy tensor. From this idea, Pope (1975) suggested an effective-viscosity approach. Several authors (Gatski & Speziale (1993), Girimaji (1996), Wallin & Johansson (2000)) contributed to the development of the so-called Algebraic Stress Models (ASM) where an "E", for explicit, is often added (EASM).

From this idea, Masi (2010) proposed an implicit equation for the modelisation of the RUM (Eq. (4.22)) and used the methods of Gatski & Speziale (1993), Girimaji (1996) and Wallin & Johansson (2000) to develop explicit solutions for it. Here, the main steps leading to Eq. (4.22) are recalled and the explicit solutions obtained presented.

Introducing the same "weak-equilibrium" assumption to the RUM anisotropy stress tensor leads:

$$\frac{D}{Dt}b^*_{p,ij} = 0, \tag{4.19}$$

or using Eq. (4.2) gives:

$$\frac{D}{Dt}\delta\breve{R}_{p,ij} = \frac{\delta\breve{R}_{p,ij}}{\delta\breve{\theta}_p}\frac{D}{Dt}\delta\breve{\theta}_p. \tag{4.20}$$

Injecting Eq. (2.75) and (2.91) into Eq. (4.20) and assuming equality between third-order correlations yields:

$$\delta\breve{R}_{p,ij}\left(-\frac{\delta\breve{R}_{p,nm}}{2\delta\breve{\theta}_p}\frac{\partial\breve{u}_{p,n}}{\partial x_m}\right) = -\frac{1}{2}\delta\breve{R}_{p,kj}\frac{\partial\breve{u}_{p,i}}{\partial x_k} - \frac{1}{2}\delta\breve{R}_{p,ik}\frac{\partial\breve{u}_{p,j}}{\partial x_k}. \tag{4.21}$$

The term inside the parenthesis represents the production of the local RUM kinetic energy by shear and compression (normalized by $2\delta\breve{\theta}_p$). Equation (4.21) may be written for the anisotropy tensor:

$$\mathbf{b}^*\left(-2\{\mathbf{b}^*\mathbf{S}^*\}\right) = -\frac{2}{3}\mathbf{S}^* - \left(\mathbf{b}^*\mathbf{S}^* + \mathbf{S}^*\mathbf{b}^* - \frac{2}{3}\{\mathbf{b}^*\mathbf{S}^*\}\mathbf{I}\right) + (\mathbf{b}^*\mathbf{\Omega} - \mathbf{\Omega}\mathbf{b}^*), \tag{4.22}$$

which is a non-linear implicit system. Masi (2010), developped explicit solutions for Eq. (4.22) following the ideas of Gatski & Speziale (1993), Girimaji (1996) and Wallin & Johansson (2000). They are briefly recalled in Sections 4.5.1 - 4.5.3. The family of models arising from the explicit solutions of Eq. (4.22) will be referred as "$2\Phi EASM$" models.

Equation (4.22) is a more generalized form of equilibrium "production-dissipation" that contains the models presented in previous sections.

$T^{(1)} = \mathbf{S}^{+}$	$T^{(6)} = \mathbf{\Omega}^{+2}\mathbf{S}^{+} + \mathbf{S}^{+}\mathbf{\Omega}^{+2} - \frac{2}{3}\{\mathbf{S}^{+}\mathbf{\Omega}^{+2}\}\mathbf{I}$
$T^{(2)} = \mathbf{S}^{+}\mathbf{\Omega}^{+} - \mathbf{\Omega}^{+}\mathbf{S}^{+}$	$T^{(7)} = \mathbf{\Omega}^{+}\mathbf{S}^{+}\mathbf{\Omega}^{+2} - \mathbf{\Omega}^{+2}\mathbf{S}^{+}\mathbf{\Omega}^{+}$
$T^{(3)} = \mathbf{S}^{+2} - \frac{1}{3}\{\mathbf{S}^{+2}\}\mathbf{I}$	$T^{(8)} = \mathbf{S}^{+}\mathbf{\Omega}^{+}\mathbf{S}^{+2} - \mathbf{S}^{+2}\mathbf{\Omega}^{+}\mathbf{S}^{+}$
$T^{(4)} = \mathbf{\Omega}^{+2} - \frac{1}{3}\{\mathbf{\Omega}^{+2}\}\mathbf{I}$	$T^{(9)} = \mathbf{\Omega}^{+2}\mathbf{S}^{+2} + \mathbf{S}^{+2}\mathbf{\Omega}^{+2} - \frac{2}{3}\{\mathbf{S}^{+2}\mathbf{\Omega}^{+2}\}\mathbf{I}$
$T^{(5)} = \mathbf{\Omega}^{+}\mathbf{S}^{+2} - \mathbf{S}^{+2}\mathbf{\Omega}^{+}$	$T^{(10)} = \mathbf{\Omega}^{+}\mathbf{S}^{+2}\mathbf{\Omega}^{+2} - \mathbf{\Omega}^{+2}\mathbf{S}^{+2}\mathbf{\Omega}^{+}$

Table 4.1: *The integrity basis for fully three-dimensional flows. Reproduced from Masi (2010).*

$G^{(1)} = -\frac{1}{2}(6 - 3\eta_1 - 21\eta_2 - 2\eta_3 + 30\eta_4)/D$	$G^{(6)} = -9/D$
$G^{(2)} = -(3 + 3\eta_1 - 6\eta_2 + 2\eta_3 + 6\eta_4)/D$	$G^{(7)} = 9/D$
$G^{(3)} = (6 - 3\eta_1 - 12\eta_2 - 2\eta_3 - 6\eta_4)/D$	$G^{(8)} = 9/D$
$G^{(4)} = -3(3\eta_1 + 2\eta_3 + 6\eta_4)/D$	$G^{(9)} = 18/D$
$G^{(5)} = -9/D$	$G^{(10)} = 0$

Table 4.2: *Coefficients associated to the integrity basis. Reproduced from Masi (2010).*

In order to provide an explicit solution, Eq. (4.22) is rearranged as follows:

$$\mathbf{b}^{+} = -\mathbf{S}^{+} - \left(\mathbf{b}^{+}\mathbf{S}^{+} + \mathbf{S}^{+}\mathbf{b}^{+} - \frac{2}{3}\{\mathbf{b}^{+}\mathbf{S}^{+}\}\mathbf{I}\right) + \left(\mathbf{b}^{+}\mathbf{\Omega}^{+} - \mathbf{\Omega}^{+}\mathbf{b}^{+}\right), \tag{4.23}$$

where $\mathbf{b}^{+} = \frac{3}{2}\mathbf{b}^{*}$, $\mathbf{S}^{+} = \mathbf{S}^{*}/(-2\{\mathbf{b}^{*}\mathbf{S}^{*}\})$ and $\mathbf{\Omega}^{+} = \mathbf{\Omega}/(-2\{\mathbf{b}^{*}\mathbf{S}^{*}\})$. According to Pope (1975), the anisotropy can be expressed in a general form:

$$\mathbf{b}^{+} = \sum_{\varsigma} G^{(\varsigma)} T^{(\varsigma)}, \tag{4.24}$$

where a set of ten tensors $T^{(\varsigma)}$ and coefficients $G^{(\varsigma)}$ is needed to form the integrity basis shown in Table 4.1. The coefficients are presented in Table 4.2. They are functions of the five dimensionless invariants:

$$\eta_1 = \{\mathbf{S}^{+2}\},\ \eta_2 = \{\mathbf{\Omega}^{+2}\},\ \eta_3 = \{\mathbf{S}^{+3}\},\ \eta_4 = \{\mathbf{S}^{+}\mathbf{\Omega}^{+2}\},\ \eta_5 = \{\mathbf{S}^{+2}\mathbf{\Omega}^{+2}\}, \tag{4.25}$$

the denominator D reading:

$$D = 3 - \frac{7}{2}\eta_1 + \eta_1^2 - \frac{15}{2}\eta_2 - 8\eta_1\eta_2 + 3\eta_2^2 - \eta_3 + \frac{2}{3}\eta_1\eta_3 - 2\eta_2\eta_3 + 21\eta_4 + 24\eta_5 + 2\eta_1\eta_4 - 6\eta_2\eta_4. \tag{4.26}$$

Singularities may appear when the denominator D vanishes. For this reason Gatski & Speziale (1993) proposed a regularization procedure applied to the two-dimensional formulation to ensure stability. In practice the 2D formulation is also used for three-dimensional flows. Two-dimensional flows are mean-free in one of the three directions. According to Gatski & Speziale (1993) in that case only three tensors from the integrity basis (Table 4.1) are needed: $T^{(1)}$, $T^{(2)}$ and $T^{(3)}$. Moreover, in 2D: $\eta_3 = \eta_4 = 0$ and $\eta_5 = \frac{1}{2}\eta_1\eta_2$. The expression for 2D flows reads:

$$\mathbf{b}^{+} = -\frac{3}{3 - 2\eta_1 - 6\eta_2}\left[\mathbf{S}^{+} + \left(\mathbf{S}^{+}\mathbf{\Omega}^{+} - \mathbf{\Omega}^{+}\mathbf{S}^{+}\right) - 2\left(\mathbf{S}^{+2} - \frac{1}{3}\{\mathbf{S}^{+2}\}\mathbf{I}\right)\right]. \tag{4.27}$$

4.5.1 Modeling the non-linearity

Equation (4.27) is implicit. In order to provide an explicit expression, an equation for $-2\{\mathbf{b}^{*}\mathbf{S}^{*}\}$ has to be provided. $\mathbf{b}^{*}$ and $\mathbf{S}^{*}$ are both axisymmetric tensors, $\mathbf{b}^{*}$ behaving in one-component limit state and $\mathbf{S}^{*}$

in axisymmetric expansion (Masi (2010)). Assuming alignment between the tensors and axisymmetric directions leads to:

$$-2\{\mathbf{b}^*\mathbf{S}^*\} = 2\left(\frac{2}{3}\right)^{1/2} II_s^{1/2}. \tag{4.28}$$

Equation (4.28) is invariant by definition. Using Eq. (4.28) to normalize the tensors in Eq. (4.27) guarantees that the 2D form is always non-singular. Re-writting the denominator for two-dimensional flows using the variable change $\eta^2 = \eta_1$, $\zeta^2 = -\eta_2$ leads to:

$$D = 3 - 2\eta^2 + 6\zeta^2, \tag{4.29}$$

which in the limit case where $\zeta^2 = 0$, η^2 must be greater than $\frac{3}{2}$ in order to avoid D becoming zero. This condition is always fulfilled. Combination of Eq. (4.27) and Eq. (4.28) will be referred to as "2ΦEASM1" model.

4.5.2 An explicit solution accounting for non-linearity I

Girimaji (1996) suggested a fully-explicit and consistent solution for 2D flows in the context of gaseous turbulence. Masi (2010) adapted the same approach to provide an explicit solution to Eq. (4.22). Equation (4.22) is rewritten in Girimaji's notation as follows:

$$\mathbf{b}^*\left(L_1^0 - L_1^1\{\mathbf{b}^*\mathbf{S}^+\}\right) = L_2\mathbf{S}^+ + L_3\left(\mathbf{b}^*\mathbf{S}^+ + \mathbf{S}^+\mathbf{b}^* - \frac{2}{3}\{\mathbf{b}^*\mathbf{S}^+\}\mathbf{I}\right) - L_4\left(\mathbf{b}^*\mathbf{\Omega}^+ - \mathbf{\Omega}^+\mathbf{b}^*\right) \tag{4.30}$$

where $L_1^0 = 0$, $L_1^1 = 2$, $L_2 = -\frac{2}{3}$, $L_3 = -1$ and $L_4 = -1$ and where the normalization is done dividing by $II_S^{1/2}$. The general representation of the anisotropy tensor in 2D reads:

$$\mathbf{b}^* = G_1\mathbf{S}^+ + G_2\left(\mathbf{S}^+\mathbf{\Omega}^+ - \mathbf{\Omega}^+\mathbf{S}^+\right) + G_3\left(\mathbf{S}^{+2} - \frac{1}{3}\{\mathbf{S}^{+2}\}\mathbf{I}\right) \tag{4.31}$$

where the coefficients G are:

$$G_2 = \frac{L_4}{\eta_1 L_1^1},\ G_3 = -\frac{2L_3}{\eta_1 L_1^1}, \tag{4.32}$$

and

$$G_1^2 = -\frac{1}{\eta_1 L_1^1}\left[L_2 + \frac{1}{3}\eta_1 L_3 G_3 - 2\eta_2 L_4 G_2\right]. \tag{4.33}$$

Here $\eta_1 = \{\mathbf{S}^{+2}\}$ and $\eta_2 = \{\mathbf{\Omega}^{+2}\}$. Unfortunately, as η_2 is always negative, Eq. (4.33) admits real solutions only for $\eta_1 \geq -\eta_2$. In the implementation of this model, local negative values will be set to zero. Concerning the sign of G_1, in the simplest case it is taken as negative. Combination of Eq. (4.31) and the coefficients in Eq. (4.32) and (4.33) (with negative sign) will be referred to as "2ΦEASM2" model.

4.5.3 An explicit solution accounting for non-linearity II

Another technique to provide explicit solutions was suggested by Wallin & Johansson (2000) in the context of turbulent gaseous flows and used in the context of the RUM by Masi (2010) to provide new explicit solution to Eq. (4.22). Using the integrity basis of Table 4.1, Eq. (4.23) is written for the dispersed phase, using the notation of Wallin & Johansson (2000), as follows:

$$N\mathbf{b}^* = -A_1\mathbf{S}^+ - A_2\left(\mathbf{b}^*\mathbf{S}^+ + \mathbf{S}^+\mathbf{b}^* - \frac{2}{3}\{\mathbf{b}^*\mathbf{S}^+\}\mathbf{I}\right) + \left(\mathbf{b}^*\mathbf{\Omega}^* - \mathbf{\Omega}^*\mathbf{b}^*\right), \tag{4.34}$$

where

$$N = A_3 + A_4(-2\{\mathbf{b}^*\mathbf{S}^+\}), \tag{4.35}$$

$A_1 = \frac{2}{3}$, $A_2 = 1$, $A_3 = 0$, $A_4 = 2$ and the normalization is done as in Section 4.5.2. In very diluted flows, as $A_3 = 0$, the polynomial of N is depressed to the second order and reads:

$$N = 2\eta_1 + 2\eta_2. \tag{4.36}$$

N admits real solutions only for $\eta_1 \geq -\eta_2$. As it has been done for 2ΦEASM2 model, local negative values are set to zero. Concerning the sign of N it must lead to a positive sign of the production and hence it will be chosen as positive in the simplest case. Masi (2010) developped the limit solutions for three and two-dimensional flows. Here, only the 2D form is presented. The final equation for the anisotropy tensor reads:

$$\mathbf{b}^* = G_1 T^{(1)} + G_2 T^{(2)} + G_3 T^{(3)}, \tag{4.37}$$

where the coefficients of the model depend on N as follows:

$$G_1 = -\frac{A_1 N}{Q},\ G_2 = -\frac{A_1}{Q},\ G_3 = 2\frac{A_1 A_2}{Q}, \tag{4.38}$$

with

$$Q = N^2 - 2\eta_2 - \frac{2}{3} A A_2^2 \eta_1. \tag{4.39}$$

Hereinafter this model will be referred to as "2ΦEASM3". 2ΦEASM2 and 2ΦEASM3 models lead to the same solution under the two-dimensional flows assumption. Since only the 2D form has been implemented in AVBP, only results using the 2D formulation will be shown in this work. The reader is encouraged to see Masi (2010) for more details about the development of the models briefly presented in this section.

4.5.4 Model correction

Section 4.3 showed that it is possible to acoount for a reverse exchange in the energy by introducing a correction by means of $sign(III_S)$. In the so-called "2ΦEASM" models, the reverse sign in the energy exchange is related to the sign of the coefficient G_1, which is the same than that of the scalar quantity $\{\mathbf{b}^*\mathbf{S}^*\}$. This coefficient is negative in single-phase turbulent flows ("weak-equilibrium", Girimaji (1996)). However, in dispersed phase interacting with turbulent flows, it is usual to have a reverse exchange of energy from the RUM to the mesoscopic motion, which would correspond to a reverse sign of G_1. Masi (2010) proposed to model this reverse exchange of energy in the 2ΦEASM models in the same way than in AXISY-C, giving the so-called "2ΦEASM-C" models.

2ΦEASM1-C model is constructed by including in Eq. (4.28) the sign of the third invariant of $\mathbf{S}$, $sign(III_S)$, as follows:

$$-2\{\mathbf{b}^*\mathbf{S}^*\} = -2sign(III_S)\left(\frac{2}{3}\right)^{1/2} II_S^{1/2}\ . \tag{4.40}$$

The coefficient G_1 of the model 2ΦEASM2 obtained by Eq. (4.33) is rewritten as

$$G_1 = sign(III_S)\frac{\sqrt{2\eta_1 + 2\eta_2}}{2\eta_1} \tag{4.41}$$

giving the so-called 2ΦEASM2-C model.

Finally, 2ΦEASM3-C model is obtained through a modification of the quantity N (Eq. (4.36)) as follows:

$$N = -sign(III_S)\sqrt{2\eta_1 + 2\eta_2}\ . \tag{4.42}$$

4.6 A hierarchy of models: Classification

Figure 4.2 shows a classification of the models presented in this Chapter taking into account wether they are linear or not and depending on the timescale they use (cf Section 4.3.1). There are two linear models: VISCO and AXISY that differ on their timescale ($\mathcal{F}(\breve{\tau}_p)$ for VISCO and $\mathcal{F}(S^{-1})$ for AXISY). QUAD is a non-linear model using the timescale of VISCO. However, since QUAD-MOD (a non-linear model using $\mathcal{F}(S^{-1})$ as timescale) showed better *a priori* results in the particle-laden turbulent planar jet configuration (Masi (2010)) than QUAD only QUAD-MOD has been implemented in AVBP and no results using QUAD model will be shown here. Finally, all 2ΦEASM models are non-linear models using $\mathcal{F}(S^{-1})$ as characteristic timescale.

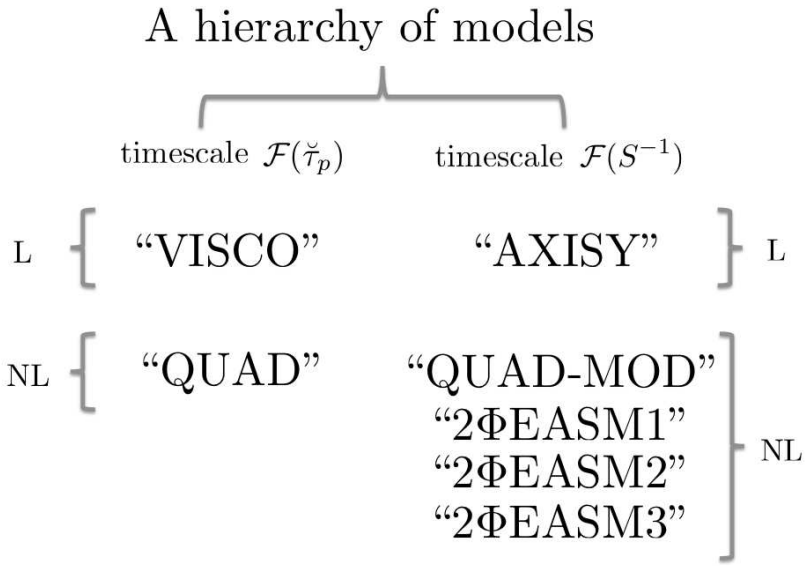

Figure 4.2: *Schematic representation of models. L=Linear, NL=Non-Linear constitutive relations. Modified from Masi (2010).*

4.7 Verification of the realizability conditions of the model

It is well known in gaseous turbulence, that certain models for the Reynolds stress tensor, containing closure assumptions relating algebraically unknown correlations to the known quantities, may not have a solution for a given set of initial and boundary conditions in the sense that the realizability conditions (Vachat (1977), Schumann (1977)) may be violated. The problem of non-realizable solutions has already been found in complicated analytical models for the turbulence. In particular, negative energies may develop (André *et al.* (1976)) and some properties of the turbulence can be violated (Orszag (1970)). Such realizability conditions for single-flow are written (Schumann (1977), Ortega (1987)):

$$R_{\alpha\beta} \geq 0 \qquad \text{for} \qquad \alpha = \beta, \tag{4.43}$$

$$R_{\alpha\beta}^2 \leq R_{\alpha\alpha} R_{\beta\beta} \qquad \text{for} \qquad \alpha \neq \beta. \tag{4.44}$$

Here, $R_{\alpha\beta}$ is any velocity based stress tensor. Summation is adopted for latin indices but not for greek indices. These conditions are the consequence of real velocities and Schwarz's inequality. Equation (4.43) implies non-negative energies and Eq. (4.44) states that the cross-correlations between different components of the fluctuating velocity are bounded by the magitude of the autocorrelations. Another condition

must be added to the set of Eqs. (4.43)-(4.44):

$$det(R_{\alpha\beta}) \geq 0. \tag{4.45}$$

Equation (4.45) can be rearranged as follows:

$$\frac{R_{12}R_{23}R_{31}}{R_{11}R_{22}R_{33}} \geq \frac{1}{2}\left[\frac{R_{12}^2}{R_{11}R_{22}} + \frac{R_{23}^2}{R_{22}R_{33}} + \frac{R_{31}^2}{R_{11}R_{33}} - 1\right]. \tag{4.46}$$

Equation (4.46) implies that the cross-correlations can not take arbitrary values (i.e. if two are well correlated with the same signs, the third one must be positive). Equation (4.43) to (4.46) produce five independent inequalities. However, Schumann (1977) showed that only three are independent.

Regarding the applicability of these conditions to numerical simulations, Deardorff (1973) and André *et al.* (1976) proposed to clip the non-realizable solutions at each time step and at every node of the grid. That is, for all points where the inequalities (4.43) - (4.46) do not hold, the stress tensor components take a new value corresponding to the equal sign of the condition. However, as Schumann (1977) showed, these changes may depend upon the orientation of the system and lead to nonsteady and noninvariant models. However, situations where the stress tensor is close to the extreme state of equality in the realizability conditions are rare and models which do not guarantee the realizability conditions at every location and instant might still be valid in most applications.

The models presented in this Chapter for the RUM stress tensor may lead to non-physical solutions in centain conditions. Since the realizability of the models is not always verified and in order to avoid imaginary solutions, the approach of Deardorff (1973) and André *et al.* (1976) has been retained to guarantee that the solutions produced by the models verify the realizability conditions. Since only three inequalities are independent, only Eqs. (4.43) and (4.44) have been implemented in AVBP. However, a number of tests including Eq. (4.45), and checking that the order on which the conditions are verified has no impact on the instantaneous fields, have been performed. The final set of equations retained for the conditioning of the models is:

$$\delta\breve{R}_{p,\alpha\beta} \geq 0 \quad \text{for} \quad \alpha = \beta, \tag{4.47}$$

$$\delta\breve{R}^2_{p,\alpha\beta} \leq \delta\breve{R}_{p,\alpha\alpha}\delta\breve{R}_{p,\beta\beta} \quad \text{for} \quad \alpha \neq \beta. \tag{4.48}$$

In the cases where conditioning is required, a third equation is to guarantee that $\delta\breve{R}^*_{p,ij}$ remains a traceless tensor so:

$$\delta\breve{R}^*_{p,ij} = 0 \quad \text{for} \quad i = j\ . \tag{4.49}$$

This conditioning has been applied to all the simulations presented in this work.

Chapter 5

Modeling the RUM: an a posteriori analysis.

In this Chapter, the different models for the deviatoric part of the RUM stress tensor presented in Chapter 4 are validated *a posteriori* against projected fields (cf Appendix A) issued from Euler-Lagrange calculations performed with the code NTMIX-2Φ (cf Appendix A). The test case chosen is presented in Section 5.1. It consists in a Direct Numerical Simulation (DNS) of a temporal particle-laden turbulent planar jet subject to a homogeneous isotropic decaying turbulence (Fig. 4.1). This test case aims at being representative of a control volume in the periphery of a hollow-cone spray (Fig. 5.1), where the flow is subjected to a strong mean shear. It is indeed a model of the local behavior of the dispersed phase in mean-sheared unsteady, inhomogeneous turbulent flows.

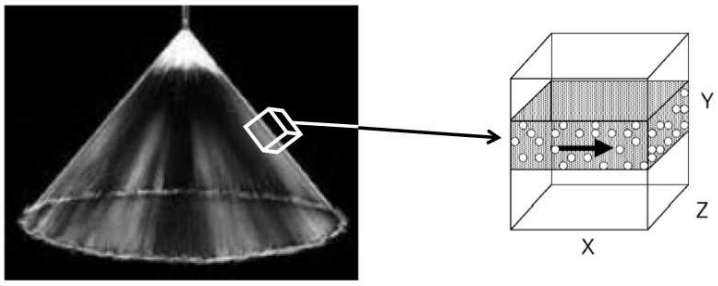

Figure 5.1: *Generic representation of the flow in a hollow-cone spray. Modified from Vermorel (2003).*

Masi (2010) performed an *a priori* analysis of the performances of the RUM models in this configuration (a simplified sketch is shown in Fig. 5.3). She performed Euler-Lagrange simulations for different particle inertia (i.e. Stokes numbers) and different levels of initial gaseous turbulence in the HIT field (i.e. acoustic Reynolds numbers, Re^{ac}) with the code NTMIX-2Φ. The *a priori* analysis uses particle Eulerian fields extracted from Euler-Lagrange DNS by means of a projection algorithm (Kaufmann *et al.* (2008)). Then, the models are tested against "exact" Eulerian fields. Statistics are computed over all the planes (YZ) of the slab. Since these planes may be considered as planes of homogeneity, the average gives an estimation of the theoretical ensemble average computed over a large number of particle and fluid realizations. Instantaneous fields are shown in the (XY) plane at the coordinate $Z = 0$ (Fig. 5.2).

The results obtained from the *a priori* analysis of the RUM models using the Eulerian projection of the Lagrangian fields computed with NTMIX-2Φ (Masi (2010)) are compared with *a posteriori* Euler-Euler simulations of the same configuration performed with the code AVBP. The *a priori* study of the

exact Lagrangian computations of this configuration was used for the validation of the models presented in Chapter 4. The results of Masi (2010) are not influenced by the choice of the RUM model. Indeed, the *a priori* analysis consists in the calculation of the RUM quantities ($\delta\breve{\theta}_p$, the RUM production terms and the components of the deviatoric RUM stress tensor) from the fields issued from an exact Lagrangian simulation. That is, from the fields of particle number density and velocity, the values of RUE and the other RUM quantities are calculated for every physical time at which the analysis is performed. Indeed, in the Lagrangian equations, there are no unclosed terms related to RUM, so no RUM modeling is needed. On the other hand, in the *a posteriori* simulations performed with AVBP, the choice of the model has an influence since the discrete phase flow field is affected by the field at the previous timestep, while the *a priori* results are obtained postprocessing exact Lagrangian simulations. There is then an effet of history in the *a posteriori* simulation. The magnitude of this effect is very difficult to quantify and this task is out of the scope of this work.

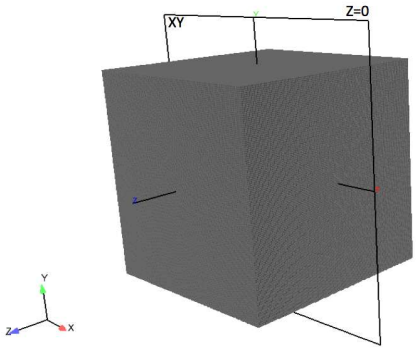

Figure 5.2: *Sketch of the (XY) cutting plane located at $Z = 0$ used to show instantaneous fields.*

This Chapter is organized as follows. In Section 5.1 the configuration, along with the initial and boundary conditions, and the numerical setup used for the simulations with AVBP, are presented. Section 5.2 presents a validation of the carrier phase flow. In Sections 5.3, a first validation for a low turbulent case ($Re^{ac} = 5500$) with a mean inertia ($St \sim 1$) is presented: statistics of low and high order moments along with instantaneous fields of the main moments are shown. Section 5.4 shows the results obtained for both a higher and a lower inertia ($St \sim 3$ and $St \sim 0.33$) flow. Section 5.5 shows the application to a higher turbulent case ($Re^{ac} = 20000$, $St \sim 1$). For all test cases, comparisons with the "exact" Eulerian fields obtained by Masi (2010) are provided. For the sake of simplicity, the term "Lagrangian" is used here to denote the *a priori* Eulerian fields coming from the projection of the Euler-Lagrange computations with NTMIX-2Φ (with the sense "from-Lagrangian") in order to distinguish them from the *a posteriori* Euler-Euler results obtained with AVBP, which will be referred to as "Eulerian".

5.1 Description of the test case

Figure 5.3 shows a simplified sketch of the configuration chosen to assess the *a posteriori* performances of the RUM models presented in Chapter 4. It consists in a temporal particle-laden turbulent planar jet embedded in a homogeneous decaying isotropic turbulence first studied by Vermorel (2003). The simulation domain is a cubic box with periodic boundary conditions in all directions. A slab with a mean gaseous velocity whose shape is a double hyperbolic tangent is added in the centrer of the box. Solid particles are added to the slab. Diluted conditions are assumed, and one-way coupling between the gas and the dispersed phase is taken into account. In fact, since the configuration is in diluted regime, it can be assumed that the dispersed phase has no impact on the carrier phase. A definition of the quantities used for the normalization and the equivalent in NTMIX-2Φ is briefly presented in Section 5.1.3, more details can be found in Dombard (2011).

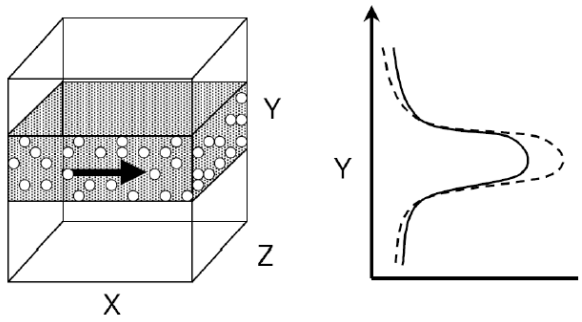

Figure 5.3: *Simplified sketch of the particle-laden turbulent planar jet configuration. (Extracted from Vermorel (2003)).*

5.1.1 Initial and boundary conditions

The initial condition for the carrier phase is the same for NTMIX-2Φ and AVBP in all cases. A slab with a gaseous mean velocity (U) is added to a homogeneous decaying isotropic turbulence. In this way, the jet is already turbulent at the initial time. The slab width L_{slab} is $0.25L_{box}$, where L_{box} is the length of the cube. The HIT is initialized with a Passot-Pouquet spectrum (Passot & Pouquet (1987)), setting the most energetic lengthscale to $L_e = 0.4L_{ref}$, where L_{ref} is a reference length. The choice of L_e yields initial turbulent eddies with a size approximately equal to one quarter of the slab width. This allows the jet to develop additional velocity fluctuations from the mean velocity gradient (Masi (2010)). The initial velocity profile in the slab is imposed as a hyperbolic-tangent profile:

$$\phi(y) = \phi^o + f(y)\left(\phi^i - \phi^o\right), \tag{5.1}$$

$$f(y) = \frac{1}{2}\left(1 + tanh\frac{\frac{1}{2}L_{slab} - |y|}{2\delta_\theta}\right), \tag{5.2}$$

where ϕ^i and ϕ^o denote the velocity in and outside the jet, y is the vertical coordinate and δ_θ refers to the initial momentum thickness of the slab.

For the low turbulence case, the initial turbulent Reynolds number based on Le is $Re \approx 73$. For the high turbulence case, it is approximately $Re \approx 264$.

In NTMIX-2Φ, particles are randomly embedded at the initial time at the same velocity than the gas phase. For the low turbulence cases, 80 millions particles are introduced in the domain, 210 millions for the high turbulence case. The corresponding particle velocities compared to the initial fluid velocities for both cases are listed in Table 5.1. Note that the initial particle volume fraction profile from NTMIX-2Φ has a very steep gradient at the periphery of the slab. he 3^{rd} order schemes implemented in AVBP are however not capable of handling such a steep gradient. For this reason, the initial particle volume fraction in AVBP has been initialized with a hyperbolic-tangent profile (Eq. (5.1)). A very low particle volume fraction field (six orders of magnitude lower than the value in the slab) is added to the whole domain to simulate the zones where no particles are present. Regarding the initial RUE profile, in NTMIX-2Φ it is initially equal to zero. However, due to the transport equation for RUE solved in AVBP, the RUM would never develop. A RUE profile is thus imposed at the initial time for the simulations with AVBP since all the terms on the RHS of the RUE transport equation directly depend on RUE. This initial RUE profile has been initialised in AVBP with two narrow hyperbolic-tangent profiles on each side of the slab, in order to mimic two "relaxed" Dirac's delta functions. This profile is assumed equivalent to the RUE profile of the NTMIX-2Φ calculation close to the initial time.

Boundary conditions are periodic in all directions for both codes.

The mesh used for the simulations is a 128^3 grid for NTMIX-2Φ and the low turbulence case. It is a 256^3 grid for the high turbulence simulations. Dombard (2011) analyzed the impact of the mesh resolution on the dispersed phase in this configuration using AVBP. He deduced that although the carrier phase is converged for a given mesh, it might not be the case for the dispersed phase. Increasing the mesh resolution in the Euler-Euler simulations leads to better agreement for the dispersed phase RMS quantities statistics. For this reason in AVBP, a 256^3 grid is used for both the low and the high turbulence cases. Some cases have also been performed on a 512^3 grid to assess the mesh resolution and for result comparison purposes. All meshes are composed by hexahedric cells.

Velocity	**Low turbulence**	**High turbulence**
MEAN-X	$U_p^0 = U_f^0$	$U_p^0 = U_f^0$
MEAN-Y	$V_p^0 = V_f^0 = 0$	$V_p^0 = V_f^0 = 0$
MEAN-Z	$W_p^0 = W_f^0 = 0$	$W_p^0 = W_f^0 = 0$
FLUCTUATION-X	$u_p^{0'} = 0$	$u_p^{0'} = 0$
FLUCTUATION-Y	$v_p^{0'} = v_f^{0'}$	$v_p^{0'} = 0$
FLUCTUATION-Z	$w_p^{0'} = w_f^{0'}$	$w_p^{0'} = 0$

Table 5.1: *Initial particle velocity conditions.*

5.1.2 Summary of test cases

The configuration is unsteady and depends only on initial conditions and parameters of the carrier and the dispersed phases. These parameters and initial conditions differ depending on the inertia and turbulence level simulated. Different levels of turbulence have been simulated. For the low Reynolds case (LR), three different values of particle inertia have been simulated. For the higher Reynolds (HR) case, one Stokes number has been simulated. Table 5.2 summarizes the test cases presented in this work. The symbol # represents the different RUM models tested for each case. Not all the RUM models have been evaluated for each case. Indeed, the results obtained in cases LR_St1_# and LR_St3_# allowed to distinguish the models that produced the best results. Those models were afterwards tested on both a lower inertia (LR_St033_#) and a higher turbulence cofigurations (HR_St1_#) along with the classical model VISCO and noRUM when possible. Table 5.3 shows the different models tested and in which configuration.

keyword	**Re^{ac}**	**St**
LR_St_#	5500	1
LR_St3_#	5500	3
LR_St033_#	5500	0.333
HR_St1_#	20000	1

Table 5.2: *Matrix of the tests presented in this chapter.*

Note that some simulations performed with the VISCO model or without taking into account the contribution of the RUM in the dispersed phase equations (noRUM model) were not numerically stable with the numerical setup chosen (cf Section 5.1.4). In all cases, the VISCO and noRUM models were tested as they may be taken as a reference for the comparison, since they were the only two models for the Random Uncorrelated Motion available until now in AVBP.

5.1.3 Normalization

This Section provides a summary of the quantities used for normalization that are needed to compare the results issued from AVBP and NTMIX-2Φ. Indeed, NTMIX-2Φ uses non-dimensional variables, while

	Case			
RUM model	**LR_St1_#**	**LR_St3_#**	**LR_St033_#**	**HR_St1_#**
noRUM	X	X(unstable)	X(unstable)	X(unstable)
VISCO	X(unstable)	X(unstable)	X	X(unstable)
AXISY	X	X	-	-
AXISY-C	X	X	-	-
QUAD-MOD	X	X	X	X
2ΦEASM1	X	X	-	-
2ΦEASM1-C	X	X	-	-
2ΦEASM3	X	X	X	X
2ΦEASM3-C	X	X	-	-

Table 5.3: *Matrix of the RUM models tested on each case.*

AVBP does not. In this Section, asterisk will denote non-dimensional quantities to make the difference with dimensional ones. This notation will be abandoned afterwards.

The reference length is chosen as $L_{ref} = 10^{-3}m$, it is an arbitrary value. The simulation domain is a cubic box of size $L^*_{box} = 2\pi$. The carrier phase is composed of pure air (density $\rho_f = 1.138\ kg/m^3$, dynamic viscosity μ_f) at constant pressure $P_{ref} = 101325\ Pa$ and temperature $T_{ref} = 300\ K$ ($\gamma = 1.4$). Particles have the same temperature as the carrier fluid. Under these conditions, the speed of sound in the flow is:

$$c = \sqrt{\gamma \frac{P_{ref}}{\rho_{ref}}}\ , \tag{5.3}$$

the reference time reads:

$$t_{ref} = \frac{L_{ref}}{c}\ . \tag{5.4}$$

The non-dimensional numbers characterizing the carrier phase are:

- The acoustic Reynolds number, Re^{ac}:

$$Re^{ac} = \frac{cL_{ref}}{\nu_f}\ , \tag{5.5}$$

  where $\nu_f = \mu_f/\rho_f$ is the kinematic viscosity of the carrier fluid.

- The Mach number, M:

$$M = \frac{U}{c}\ , \tag{5.6}$$

  where U is the mean velocity of the carrier phase.

- The turbulence intensity:

$$I = \frac{u'}{U}\ , \tag{5.7}$$

  where u' is the fluctuating velocity of the carrier phase

For the characterization of the dispersed phase the Stokes number is used:

- Dynamic Stokes number, St:

$$St = \frac{\tau^F_{fp}}{\tau_f}\ , \tag{5.8}$$

  where τ^F_{fp} is the characteristic particle relaxation time and τ_f is a characteristic timescale of the carrier flow.

In fact, in the *a posteriori* simulations the Stokes number used corresponds to the one of the *a priori* analysis. The Stokes number in the *a priori* analysis is computed over a characteristic timescale of the turbulence seen by the particles (Deutsch & Simonin (1991)). Such a timescale is estimated using the Tchen equilibrium in the z-direction (which is mean-flow free) (Simonin (1991)). The Stokes number is defined as done in Masi (2010). She estimates the Stokes number and τ_{fp}^F at the end of a simulation of reference, referred as "$St = 1$". The Stokes number of all other simulations is evaluated comparing the particle density (ρ_p), which is the only parameter modified. For example, the simulation called "$St = 3$" is initialized with a particle density which is three times larger than the particle density in the simulation $St = 1$, all other parameters remaining unchanged.

In order to calculate the dimensional values of the parameters for the calculation with AVBP, the following procedure is used (Dombard (2011)):

From the chosen values for the reference lenght $L_{ref} = 10^{-3}\ m$, mean pressure $P_f = 101325\ Pa$ and temperature $T_f = 300\ K$, the speed of sound is calculated ($c = 352.9\ m/s$, Eq. (5.3)). The acoustic Reynolds number Re^{ac} and the Mach number M are conserved since they are, by definition, dimensionless quantities. They allow to evaluate the convective Reynolds number, Re^c:

$$Re^c = \frac{U L_{box}}{\nu_f} = \frac{U}{c}\frac{L_{box}}{L_{ref}}\frac{c \cdot L_{ref}}{\nu_f} = M \cdot L_{box} \cdot Re^{ac} \ . \tag{5.9}$$

The mean velocity of the jet, is calculated from the Mach number and the sound speed:

$$U = M \cdot c \ . \tag{5.10}$$

The kinematic viscosity is:

$$\nu_f = \frac{c L_{ref}}{Re^{ac}} \ , \tag{5.11}$$

which allows to evaluate the dynamic viscosity needed for AVBP:

$$\mu_f = \nu_f \cdot \rho_f . \tag{5.12}$$

Specifying the convective Reynolds number, the initial mean velocity of the jet along with the charateristics of the carrier fluid (pressure, temperature, density and viscosity), the gaseous fluid is defined. The characteristics of the initial carrier flow field are described in Section 5.1.1.

Regarding the dispersed phase, the characteristics of the solid particles need to be defined:

The Stokes number must be the same in the Lagrangian and the Eulerian calculations:

$$St^{NTMIX-2\Phi} = St^{AVBP} \ . \tag{5.13}$$

The characteristic fluid timescales between NTMIX-2Φ and AVBP are linked:

$$\tau_f = \tau_f^* \cdot t_{ref} = \tau_f^* \frac{L_{ref}}{c} \ , \tag{5.14}$$

where the superscript $*$ denotes a non-dimensional time. Throughout this Chapter, the reference time t_{ref} will be used to characterize the physical time of the Eulerian simulation for which results are compared. In the Lagrangian simulation, since NTMIX-2Φ uses non-dimensional quantities, $t_{ref}^* = 1$. The particle relaxation time is calculated assuming a Stokes regime, so no Schiller-Naumann correction (Schiller & Nauman (1935), Eq. (2.39)) is taken into account. Note that, the Schiller-Naumann correction is accounted for in the Euler-Euler simulations. However, since the relative velocity between particles and fluid is small, the Schiller-Naumann correction has a very limited influence on the results in this configuration. Simulations performed on all the cases studied in this Chapter with 2ΦEASM3 model (not presented here for the sake of conciseness) and without taking into account the Schiller-Naumann correction did not show any noteworthy difference.

$$\tau_p = \frac{4}{3}\frac{\rho_p d_p}{\rho_f \frac{24}{Re_p}||u_{rel}||} = \frac{1}{18}\frac{\rho_p d_p^2}{\rho_f \nu_f} \ , \tag{5.15}$$

where $||u_{ref}||$ is the relative velocity between the particles and the carrier fluid.

Equation (5.15) the allows to calculate the particle density ρ_p:

$$\rho_p = \frac{18\rho_f\nu_f}{d_p^2}\tau_p = \frac{18\rho_f\nu_f}{d_p^2}\tau_p^{F*} \cdot t_{ref} \ . \tag{5.16}$$

The particle diameter can be chosen arbitrarly, however, the Stokes regime must be conserved, and the particle's relaxation times must be as similar as possible between the Lagrangian and the Eulerian simulations. In this case, the particle diameter used for the Lagrangian calculations with NTMIX-2Φ is too small, leading to dimensional values of the diameter for AVBP lower than $1\mu m$. This may lead to numerical stability problems when performing calculations with AVBP: in AVBP, variables $\breve{\alpha}_p$ and $\breve{n}_p$ are transported whereas the particle diameter is reconstructed. Small values of d_p may lead to very small values of $\breve{\alpha}_p$, close to the zero machine, which may produce numerical errors affecting the results or the stability of the code when reconstructing the diameter. A higher value of the particle diameter is therefore chosen for the Euler-Euler computations: $d_p = 2\mu m$ for all cases.

Table 5.4 shows the values of the parameters used for the different simulations performed at low turbulence ($Re^{ac} = 5500$, $St \sim 1$). For case LR_St3_# only the particle density is modified :$\rho_p = 3.633 \cdot 10^4 kg/m^3$. For case LR_St033_#, $\rho_p = 0.4037 \cdot 10^4 kg/m^3$. Table 5.5 shows the parameters of the high turbulence simulation (case HR_St1_#).

Parameter	**AVBP**
L_{box}	$2\pi \cdot 10^{-3}$ $[m]$
Re^{ac}	5500 $[-]$
M	0.15 $[-]$
I	0.1 $[-]$
Re^{c}	5183.63 $[-]$
P_f	101325 $[Pa]$
T_f	300 $[K]$
ρ_f	1.138 $[kg/m^3]$
ν_f	$6.42 \cdot 10^{-5}$ $[m^2/s]$
μ_f	$7.31 \cdot 10^{-5}$ $[kg/m \cdot s]$
c	352.9 $[m/s]$
U	52.935 $[m/s]$
u'	5.2935 $[m/s]$
t_{ref}	$2.834 \cdot 10^{-6}$ $[s]$
St	1
d_p	$2 \cdot 10^{-6}$ $[m]$
$\frac{\mathcal{W}_p}{\mathcal{W}_f}$	3.69 $[-]$
ρ_p	$1.2111 \cdot 10^4$ $[kg/m^3]$

Table 5.4: *Summary of AVBP initial parameters for the low turbulence mean inertia case (LR_St1_#).*

5.1.4 Numerical setup

Details about NTMIX-2Φ and the numerical setup used for the Euler-Lagrange reference simulations can be found in Appendix A. AVBP simulations have been performed using 3^{rd} order numerical scheme TTGC (Colin *et al.* (2000)) coupled with artificial viscosity (AV) for the dispersed phase. No AV is applied on the gaseous phase. The particle AV sensor used is CMS-Lite (Sanjosé (2009)). The values for the 2^{nd}-order (ϵ^2) and 4^{th}-order (ϵ^4) parameters are shown in Table 5.6. These values have been minimized for the LR_St1_2ΦEASM1 test case. All other simulations have been performed with exactly the same numerical setup. In order to avoid numerical problems in the regions of void numerical dissipation is applied for

Parameter	AVBP
Re^{ac}	20000 $[-]$
Re^{c}	18850 $[-]$
ν_f	$1.7645 \cdot 10^{-5}$ $[m^2/s]$
μ_f	$2.008001 \cdot 10^{-5}$ $[kg/m \cdot s]$
St	1
d_p	$2 \cdot 10^{-6}$ $[m]$
ρ_p	$2.417 \cdot 10^{3}$ $[kg/m^3]$

Table 5.5: *Summary of AVBP initial parameters for the high turbulence case (HR_St1_#). Only the parameters which differ from those of the LR_St1_# case are shown.*

particle number densities lower than $2 \cdot 10^7 m^{-3}$, which corresponds to a minimal particle volume fraction of $8.37 \cdot 10^{-11}$. Moreover, only positive values of RUE are kept to avoid unphysical phenomena.

Note that in the Euler-Euler approach, there is no lower limit in terms of numerical resolution. Compared with the gaseous flow, where the Kolmogorov length scale represents the lower limit for the energy transfer, there is no length scale at which it may be considered that the energy is completely dissipated. For solid, non-deformable particles, the particle diameter may be considered as the smallest length scale. On the contrary, for deformable particles or liquid droplets, compressibility and deformation effects make this assumption not valid. This characteristic of the dispersed flow treated with an Euler-Euler approach derives from the equations of conservation themselves. For this reason, the numerical scheme and the resolution of the mesh grid may have an enlarged importance compared to single-phase flows.

– Gaseous phase –

AV sensor	ϵ^2	ϵ^4
no AV	0.00	0.00

– Dispersed phase –

AV sensor	ϵ^2	ϵ^4
CMS-Lite	0.55	0.00

Table 5.6: *Artificial Dissipation parameters for all the simulation performed with AVBP.*

5.2 Gas phase validation

This Section presents a validation of the carrier phase flow. Comparisons between the Euler-Euler (AVBP) and Euler-Lagrange (NTMIX-2Φ) simulations at low and high Reynolds numbers are proposed in terms of mean and root mean squared fluctuations (RMS) fluid velocities as well as turbulent kinetic energy (q_f^2).

Since the simulations are performed taking into account the effect of the carrier flow on the dispersed phase, but not the effect of the particles on the carrier fluid (i.e. one-way coupling) it is not needed to verify the carrier phase flow for every simulation. Moreover, the carrier fluid flow is the same for all inertia (i.e. same Stokes number) if the level of turbulence (i.e. the Reynolds number) is the same. This means that all the simulations of a given case have the same carrier fluid flow whatever the RUM model used. Also, all simulations at low turbulence (LR_St1_#, LR_St3_# and LR_St033_#) share the same carrier fluid flow at the same instant.

Section 5.2.1 presents a validation of the carrier phase flow for the low turbulence cases (LR_St1_#,

LR_St3_#, LR_St033_#). Section 5.2.2 presents the results for the high turbulence case (HR_St1_#).

5.2.1 Low turbulence case

This section presents the validation of the carrier fluid flow for cases LR_St1_#, LR_St3_# and LR_St033_#. Mean and RMS velocities in the three directions, along with the turbulent kinetic energy profiles at times corresponding to 5, 40 and $80t_{ref}$ are shown. Instantaneous fields of fluid velocity magnitude are also shown.

Figures 5.4, 5.5 and 5.6 show the profiles of the mean velocity and the product of the fluid density ρ_f and the RMS fluid velocity in the X-, Y- and Z-directions respectively. Note that X-direction is the main direction of the flow. The agreement between AVBP and NTMIX-2Φ is very good for both the mean and the RMS values in all directions. Some discrepancies appear in the profiles of V_g which are due to small differences in the fluid density between AVBP and NTMIX-2Φ. Both codes solve the compressible NS equations, however, they differ in the numerical schemes they use, which may lead to small discrepancies. Nevertheless, the differences remain small and appear only in the Y- and Z- directions, where the order of magnitude of the velocity is much smaller than in the X-direction. This is also the reason why the RMS profiles are shown multiplied by the fluid density. Since the quantity transported in AVBP is the product of the density and the velocity, it has been chosen as the quantity to be shown. However, the mean velocities are shown without taking into account the density in order to show the order of magnitude of this difference. Finally in order to assess the quality of the carrier phase flow, Fig. 5.7 shows the profiles of turbulent kinetic energy at the three times chosen for the analysis. Since the profiles are very similar, it is guaranteed that the fluid flow is almost the same in the simulations performed with AVBP and with NTMIX-2Φ. Thus, the discrepancies that may appear between the simulations performed with the different RUM models are due to the models themselves and not to potential differences in the fluid phase flow.

In order to provide a qualitative comparison, the instantaneous fields of the fluid velocity magnitude are shown in Fig. 5.8 at 5, 40 and $80t_{ref}$. The results of both approaches are very close for the three times.

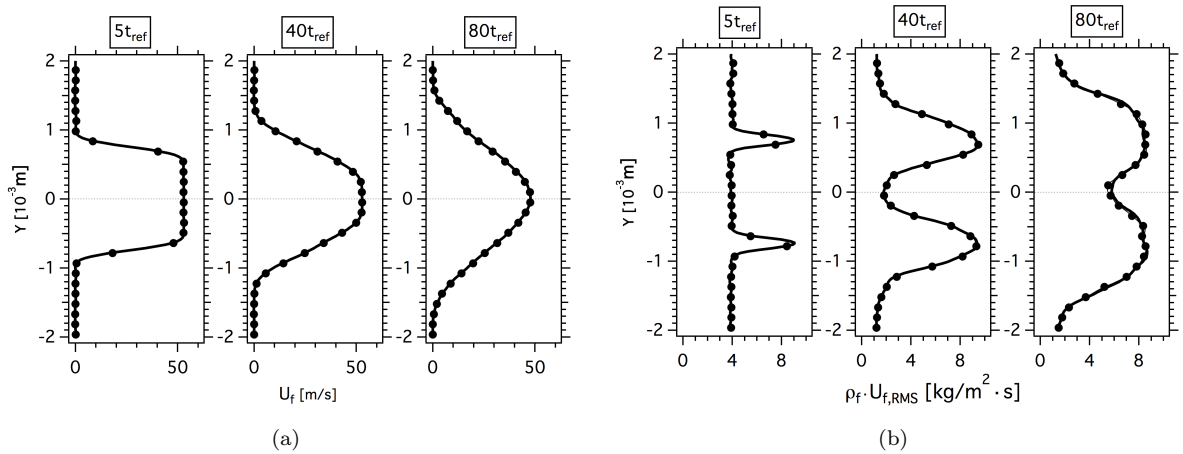

Figure 5.4: *Comparison of AVBP (—) and NTMIX-2Φ (-●-) carrier phase velocities in X-direction. LR_St1_# case. (a) Mean velocity (U_f) and (b) RMS velocity times the fluid density ($\rho_f U_{f,RMS}$).*

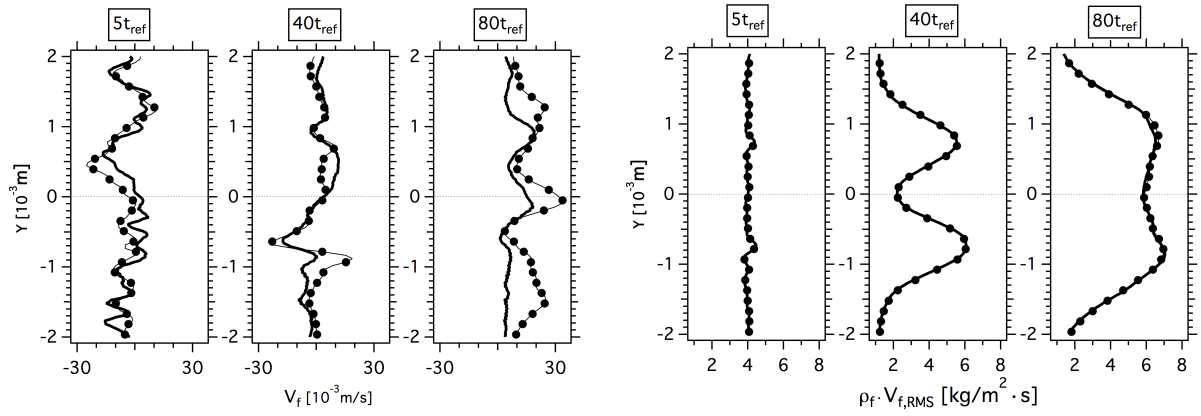

(a) (b)

Figure 5.5: *Comparison of AVBP (—) and NTMIX-2Φ (–●–) carrier phase velocities in Y-direction. LR_St1_# case. (a) Mean velocity (V_f) and (b) RMS velocity times the fluid density ($\rho_f V_{f,RMS}$).*

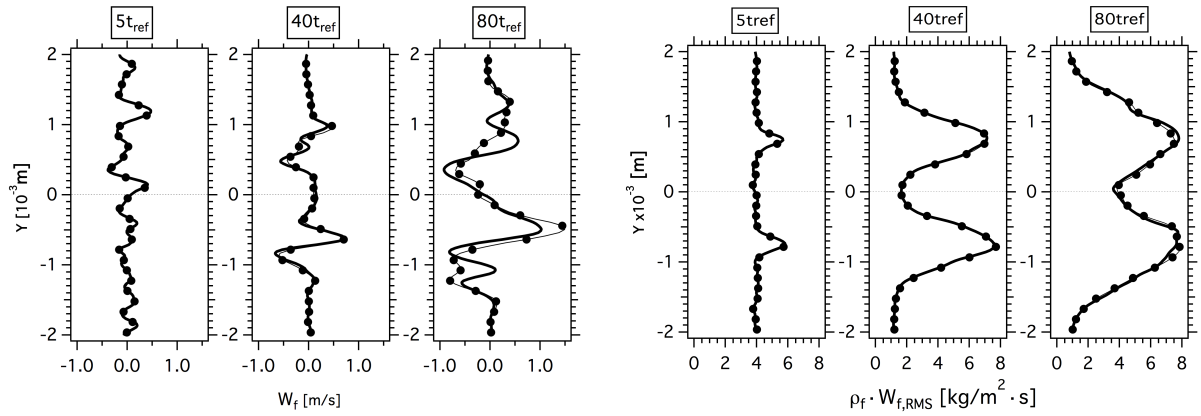

(a) (b)

Figure 5.6: *Comparison of AVBP (—) and NTMIX-2Φ (–●–) carrier phase velocities in Z-direction. LR_St1_# case. (a) Mean velocity (W_f) and (b) RMS velocity times the fluid density ($\rho_f W_{f,RMS}$).*

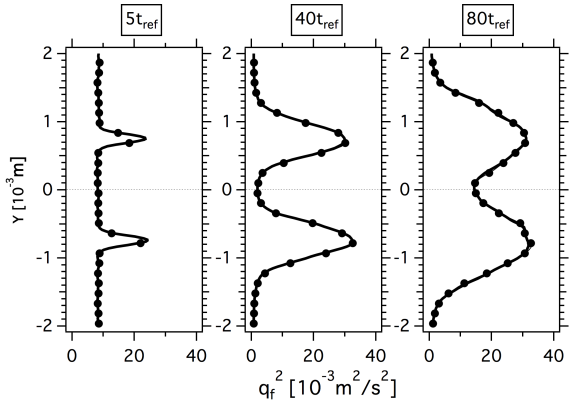

Figure 5.7: *Comparison of AVBP (—) and NTMIX-2Φ (–•–) carrier phase turbulent kinetic energies (q_f^2). LR_St1_# case.*

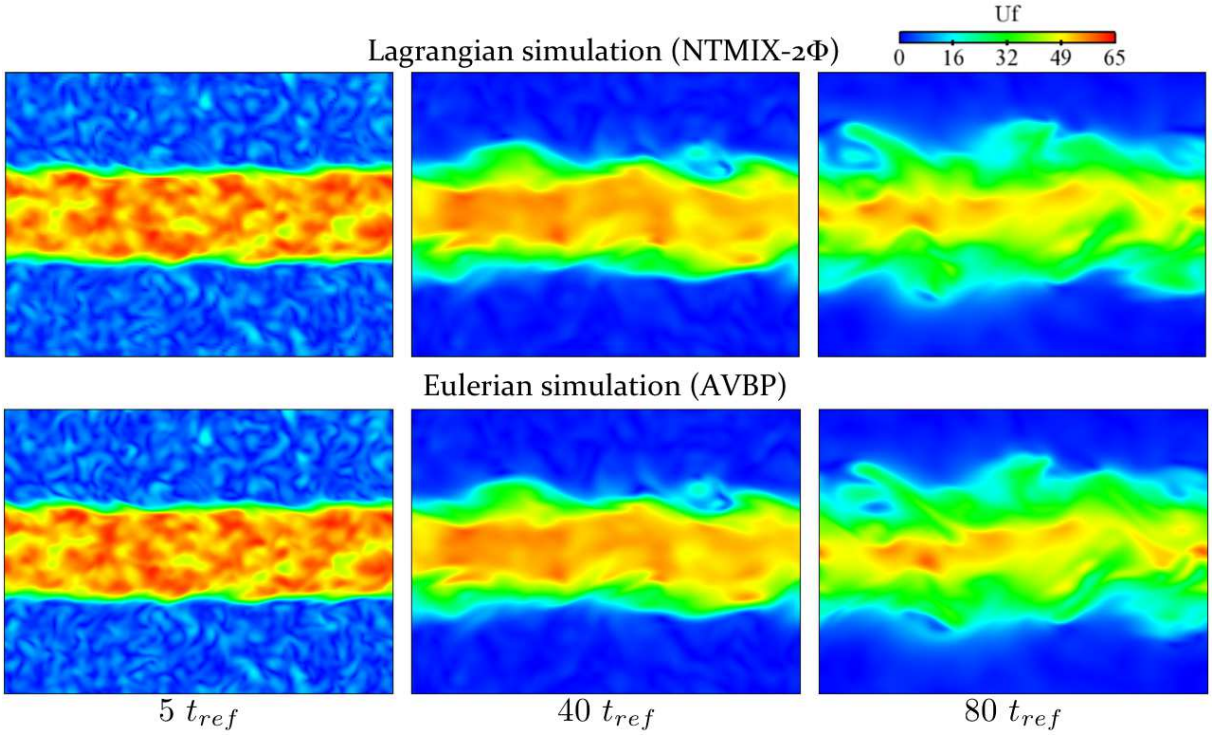

Figure 5.8: *Comparison of instantaneous NTMIX-2Φ and AVBP carrier phase fields ($[m/s]$) at* 5, 40 *and* $80t_{ref}$. *LR_St1_# case.*

5.2.2 High turbulence case

The carrier phase flow is modified with the Reynolds number changes. For this reason, it is necessary to verify that the carrier fluid flow keeps the same for the Lagrangian and the Eulerian simulations also for the HR_St1_# case. Since for the low turbulence cases, the agreement for the carrier phase profiles was very good, a good agreement is also expected in this case. The high turbulence Euler-Lagrnage simulations have been carried out only up to $70t_{ref}$ due to limited computational resources. Comparisons between Euler-Euler and Euler-Lagrange results are therefore shown at that time. Figure 5.9 shows the instantaneous carrier phase velocity magnitude fields for the Euler-Lagrange and the Euler-Euler simulations at $70t_{ref}$. It provides a qualitative assessment of the gaseous phase simulations of both codes. The results are very similar although the differences between the two simulations are more visible than in the low turbulence case (Fig. 5.8). In order to provide quantitative results, the profiles of mean and RMS velocities in the three spatial directions are compared at $70t_{ref}$. The profile of turbulent kinetic energy is also displayed on Fig. B.4. The same profiles corresponding to 5 and $40t_{ref}$ can be found in Appendix B. The agreement, as expected, is very good. The same discrepancies in the mean Y- and Z-velocity are present in this case due to differences in the fluid density profiles. The agreement for the RMS velocity and the turbulent kinetic energy profiles is again very good.

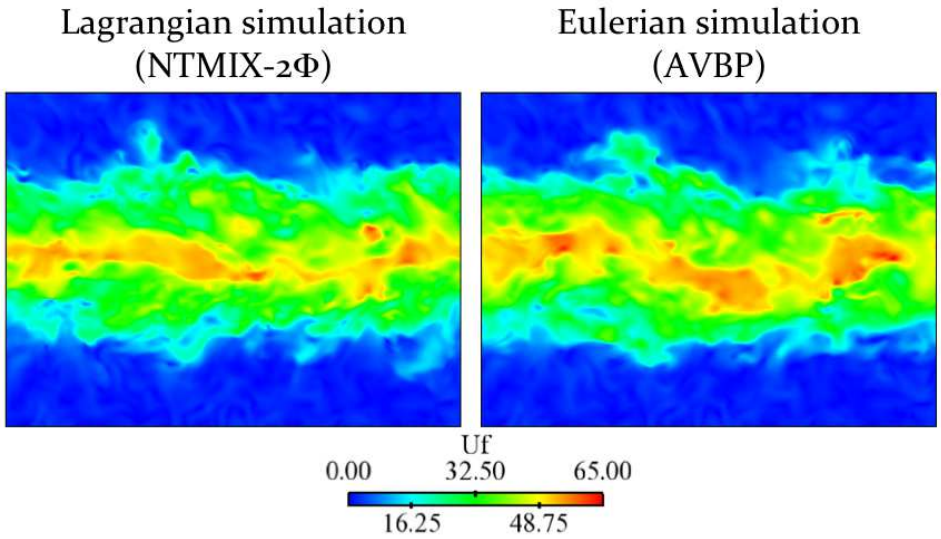

Figure 5.9: *Comparison of instantaneous NTMIX-2Φ and AVBP carrier phase fields ($[m/s]$) at $70t_{ref}$. HR_St1_# case.*

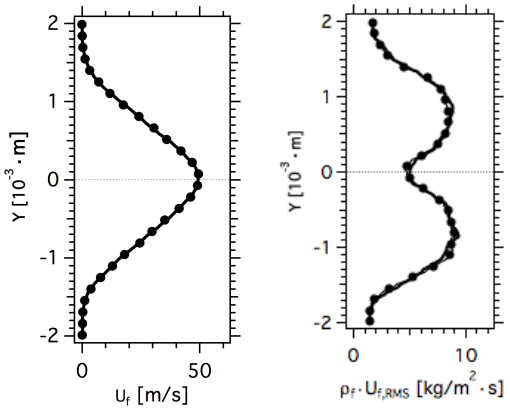

(a) (b)

Figure 5.10: *Comparison of AVBP (—) and NTMIX-2Φ (–●–) carrier phase velocities in X-direction. HR_St1_# case. (a) Mean velocity (U_f) and (b) RMS velocity times the fluid density ($\rho_f U_{f,RMS}$) at* $70t_{ref}$.

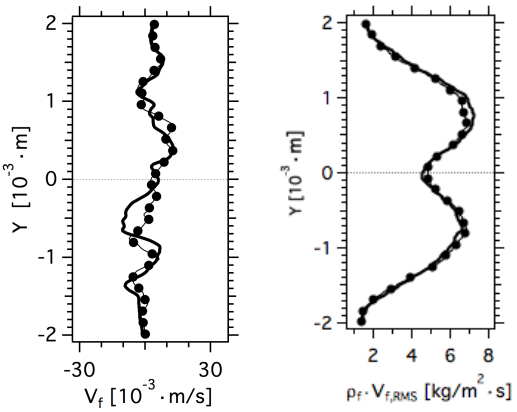

(a) (b)

Figure 5.11: *Comparison of AVBP (—) and NTMIX-2Φ (–●–) carrier phase velocities in Y-direction. HR_St1_# case. (a) Mean velocity (U_f) and (b) RMS velocity times the fluid density ($\rho_f U_{f,RMS}$) at* $70t_{ref}$.

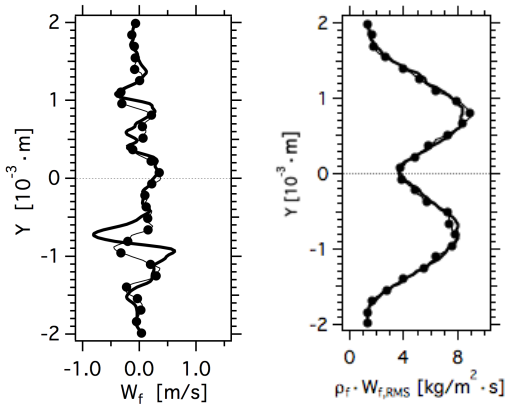

(a) (b)

Figure 5.12: *Comparison of AVBP (—) and NTMIX-2Φ (–●–) carrier phase velocities in Z-direction. HR_St1_# case. (a) Mean velocity (U_f) and (b) RMS velocity times the fluid density ($\rho_f U_{f,RMS}$) at $70t_{ref}$.*

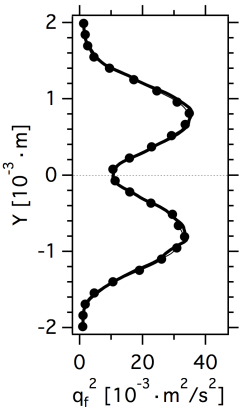

Figure 5.13: *Comparison of AVBP (—) and NTMIX-2Φ (–●–) carrier phase turbulent kinetic energy (q_f^2) at $70t_{ref}$. HR_St1_# case.*

5.3 Dispersed phase validation. Case LR_St1_#

The simulations of case LR_St1_# with the six models proposed in Chapter 4 and their corrected versions have been performed with AVBP. This case corresponds to a low turbulence, mean inertia simulation. The characteristic particle relaxation time is $\tau_{fp}^F \sim 13 t_{ref}$.

The VISCO model crashed after few iterations. Indeed, the particle RUE is considerably overestimated using VISCO for this range of particle inertia. Particle RUE has a diffusion effect in the fields of mesoscopic particle number density and particle volume fraction, as well as in the particle velocity fields. VISCO producing too much RUE from the beginning of the calculation, it leads to an excessive diffusion of the particles towards the periphery of the jet, creating empty zones which can not be handled numerically by the code. This behavior was somehow already pointed out by the *a priori* analysis of Masi (2010): VISCO overpredicted the shear-component of the deviatoric RUM stress tensor ($\delta\breve{R}^*_{p,12}$) and underpredicted the diagonal components ($\delta\breve{R}^*_{p,11}$, $\delta\breve{R}^*_{p,22}$ and $\delta\breve{R}^*_{p,33}$). In fact, the two models using $\breve{\tau}_p$, the characteristic particle relaxation time, as timescale (VISCO and QUAD) showed the same behavior, QUAD even overpredicting all the components of the tensor. Confirming the *a priori* analysis, the simulations with AVBP and QUAD model have not been possible either, since this model crashed even before VISCO does. In both cases a huge overproduction of particle RUE, makes the simulation unstable. For this reason, no results are displayed concerning these two models for LR_St1_# case.

Section 5.3.1 presents the statistics of the main low-order moments and RMS mean particle number density and particle velocity for three times: at the beginning of the simulation ($5t_{ref}$, after approx. $0.38\tau_{fp}^F$), at the middle ($40t_{ref}$, after $3.07\tau_{fp}^F$) and at the end of the simulation ($80t_{ref}$, after $6.15\tau_{fp}^F$). Results obtained in a particle-laden stationary HIT configuration (Février *et al.* (2005)) showed that at least three particle relaxation times are required to obtain statistics not influenced by the initial condition. This means that results at $5t_{ref}$ are not discriminatory to evaluate the performance of the models, and that results after $40t_{ref}$ must be taken into account to assess the validity of the models in this case. The results at $80t_{ref}$ allow to confirm the conclusions drawn at $40t_{ref}$. Instantaneous fields of particle number density and particle velocity at the end of the simulation are also displayed. Section 5.3.2 presents the statistics of the main high-order moments, including the particle RUE and the total particle agitation as well as the mean profiles of the tensor components and RUM production rates. Instantaneous fields of RUE at the end of the simulation are also shown. Complementary data can be found in Appendix C.

5.3.1 Low order moments

Low order moments such as the particle number density or the particle velocity are important since they define the main characteristics of a given dispersed phase flow field. In the presence of turbulence, the root-mean-square (RMS) values are of importance too, since they measure the fluctuations in the flow. These are in fact the variables of interest in most industrial applications. However, in this configuration, the particle preferential concentration (Squires & Eaton (1991*a*)) is an important parameter too. Indeed, in turbulent flows, the particles tend to accumulate in low-vorticity and high-shear regions, creating both high concentration and empty zones close to each other. This produces very steep particle number density gradients in the flow field similarly to a highly compressible gaseous flow. This behavior is strongly related to the particle number density and the particle velocity divergency fields. The preferential concentration is measured by the so-called "segregation" parameter, noted seg:

$$\text{seg} = \frac{\langle \breve{n}_p^2 \rangle}{\langle \breve{n}_p \rangle^2} \ . \tag{5.17}$$

Figure 5.14 shows the statistics of the particle number density for three different times along the simulation. The values are normalized by the initial particle number density at the center of the slab. The results at $5t_{ref}$ are presented to show that when the simulation is close to the begining, the results are very influenced by the initial condition. Indeed, Figs. 5.14(a), 5.15(a), 5.16(a), 5.17(a) and 5.18(a) show that all models give the same results. All models perform equally in the prediction of the particle number density and the particle velocity at 5, 40 and $80t_{ref}$, except AXISY and its corrected version AXISY-C. Figure 5.14(b) shows that both models predict peaks at the borders of the plateau located at the center of the slab. Note that the peaks are stronger for AXISY than for AXISY-C. At $80t_{ref}$ (Fig. 5.14(c)), the two peaks have disappeared, but both models overestimate the maximum of $\langle \check{n}_p \rangle$ at the center of the slab. Regarding the mean particle velocity (Fig. 5.15), all models give very close results. Figure 5.15(a) underlines a slight inaccuracy of the projection algorithm. Indeed, the profiles obtained by projection from NTMIX-2Φ deviate from the hyperbolic tangent profile at the borders of the jet. This is due to the steepness of the velocity gradient or to a lack of particles in this region in the Lagrangian sumulations, which introduces errors when projected onto the Eulerian grid.

The profiles of particle RMS number density (Fig. 5.16) and particle RMS velocity (Fig. 5.17) produced by the models are also very similar. However, AXISY predicts a steeper gradient at the periphery of the slab. AXISY-C and QUAD-MOD give the same maximum level of RMS number density but both models predict lower levels towards the periphery producing a thinner slab. QUAD-MOD underestimates the maximum RMS particle velocity and AXISY behaves even worse. This behavior is already visible at $40t_{ref}$ and remains at $80t_{ref}$.

Figure 5.18 shows the profiles of particle segregation at 5, 40 and $80t_{ref}$. AVBP is not able to capture the initial shock. This is due to the influence of numerics which are not capable of handling such highly compressible dispersed phase flows.

A qualitative analysis of the instantaneous fields of the particle number density and particle velocity (Figs. 5.19 and 5.20) is not sufficiently discriminatory. Indeed, from the instantaneous fields of these variables, the noRUM model arises as the model who performs the best, but Section 5.3.2 will explain the reasons for this behavior. Indeed, the noRUM model does not take into account the Random Unocrrelated Motion and thus, the balance between the mesoscopic energy, the RUE and the total particle energie is not correct. Taking this into account, only AXISY shows a clear weakness if compared to the rest of the models.

In conclusion, the results concerning the low order moments do not allow to differenciate between the models, and are definitely not sufficient to discard a model in front of the others. Analysing the statistics of the higher order moments is therefore necessary.

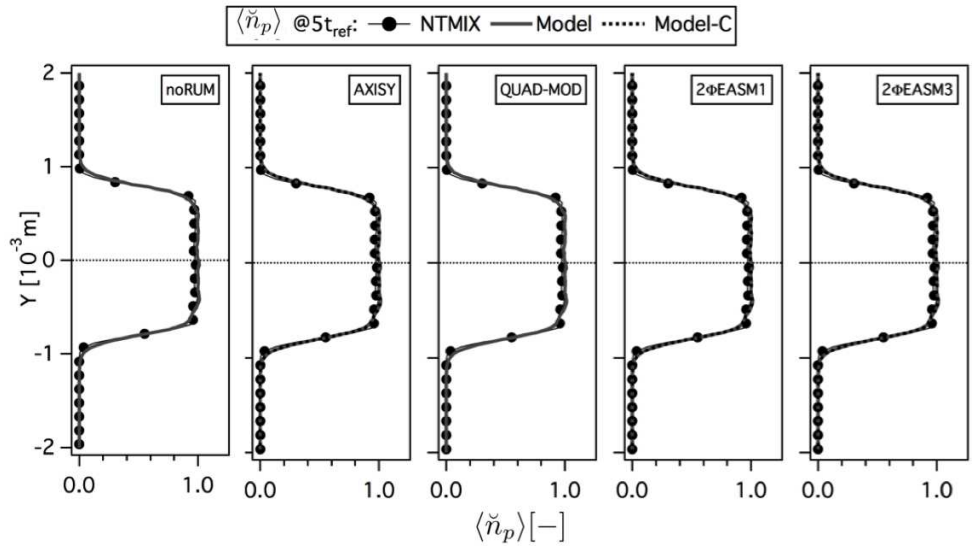

(a)

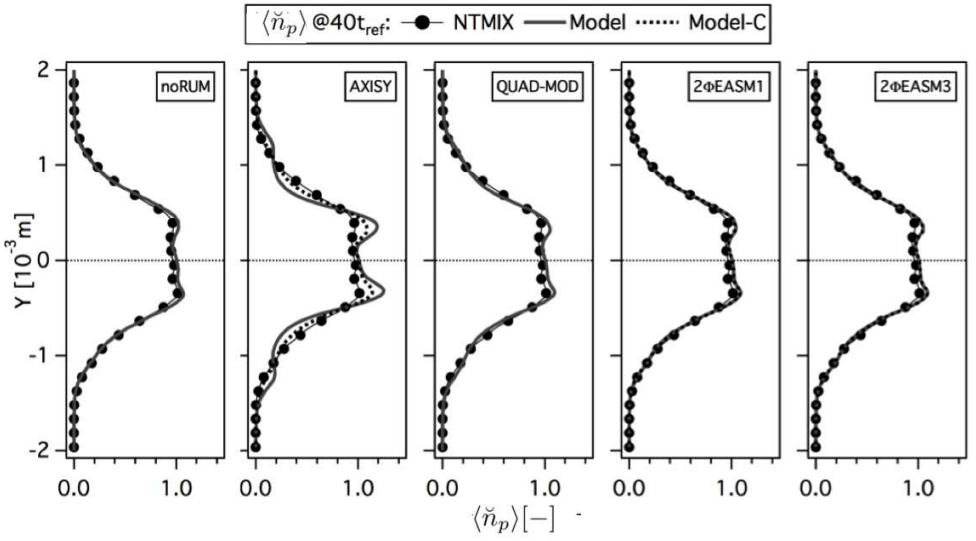

(b)

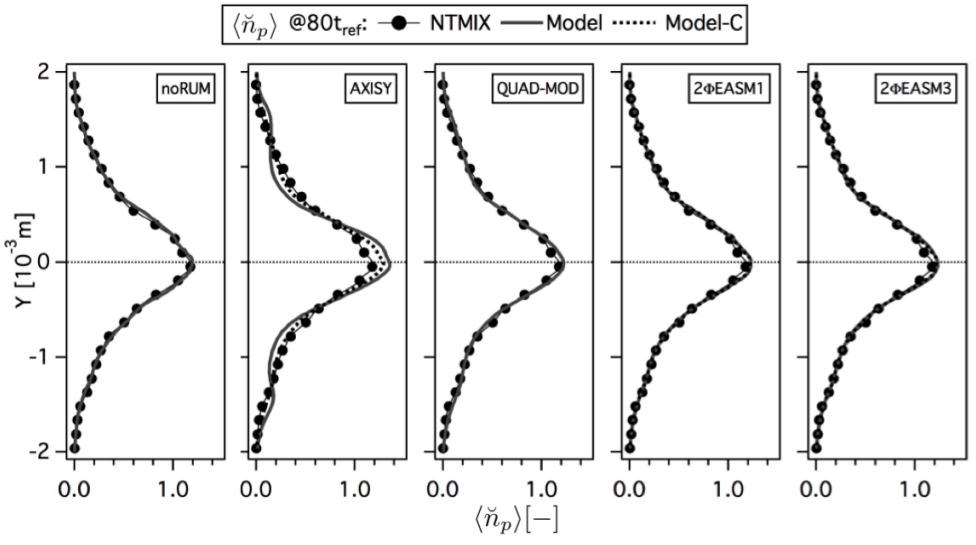

(c)

Figure 5.14: *Comparison of Eulerian and Lagrangian mean particle number density (< $\breve{n}_p$ >) at 5, 40 and 80t_{ref}. Normalized by the initial particle number density at the center of the slab. LR_St1_# case.*

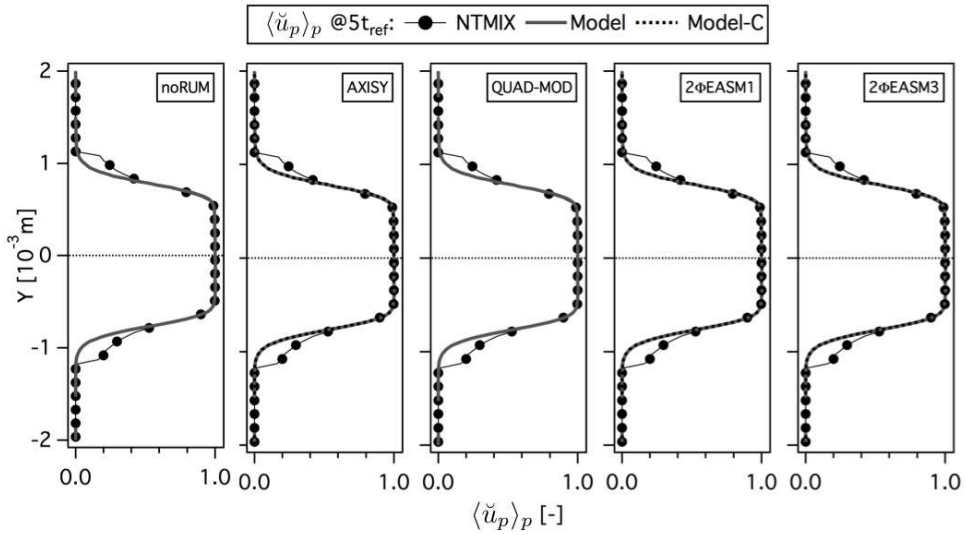

(a)

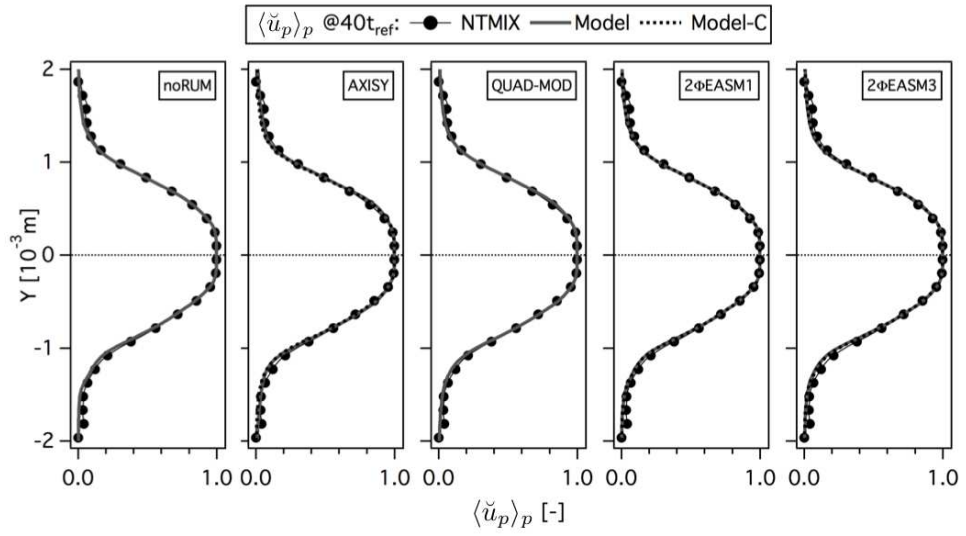

(b)

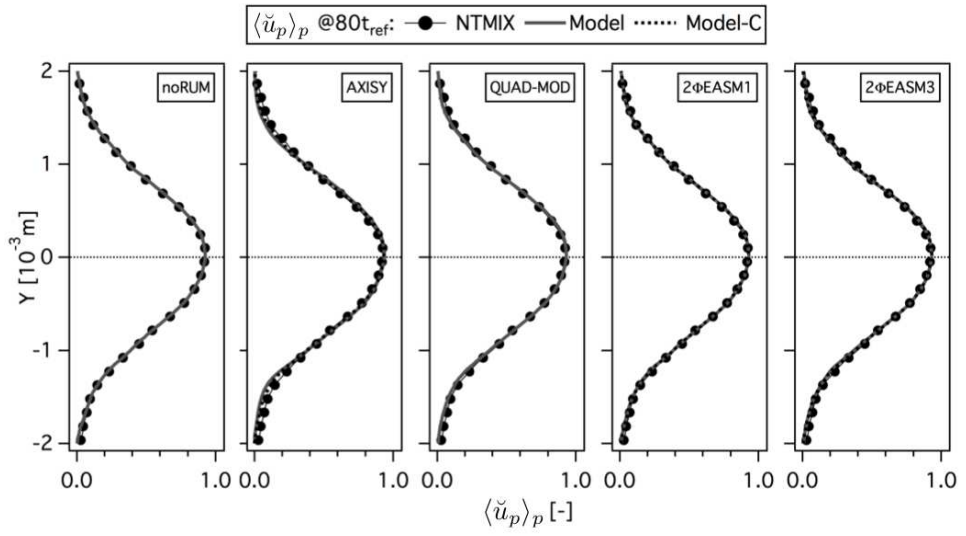

(c)

Figure 5.15: *Comparison of Eulerian and Lagrangian mean particle velocity in X-direction (< $\breve{u}_p$ >$_p$) at 5, 40 and 80t_{ref}. Normalized by the initial particle velocity in X-direction at the center of the slab. LR_St1_# case.*

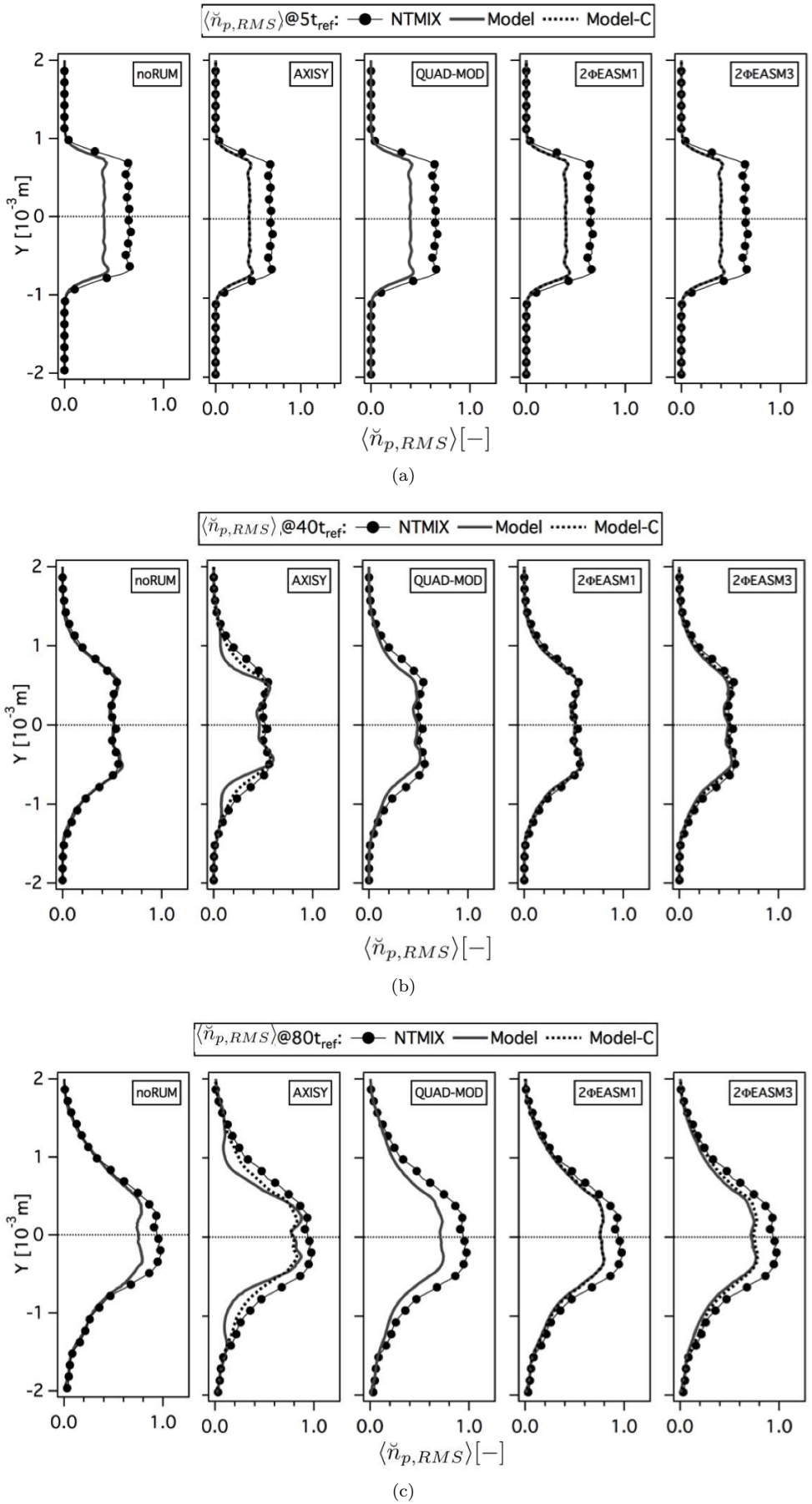

Figure 5.16: *Comparison of Eulerian and Lagrangian RMS particle number density (*$< \check{n}_{p,RMS} >$*) at 5, 40 and* $80t_{ref}$*. Normalized by the initial particle number density at the center of the slab. LR_St1_# case.*

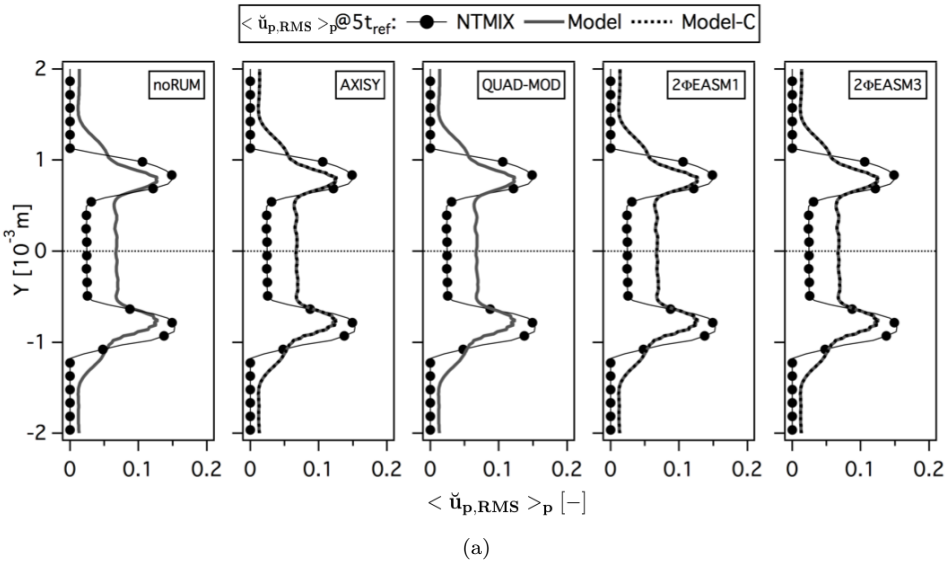

(a)

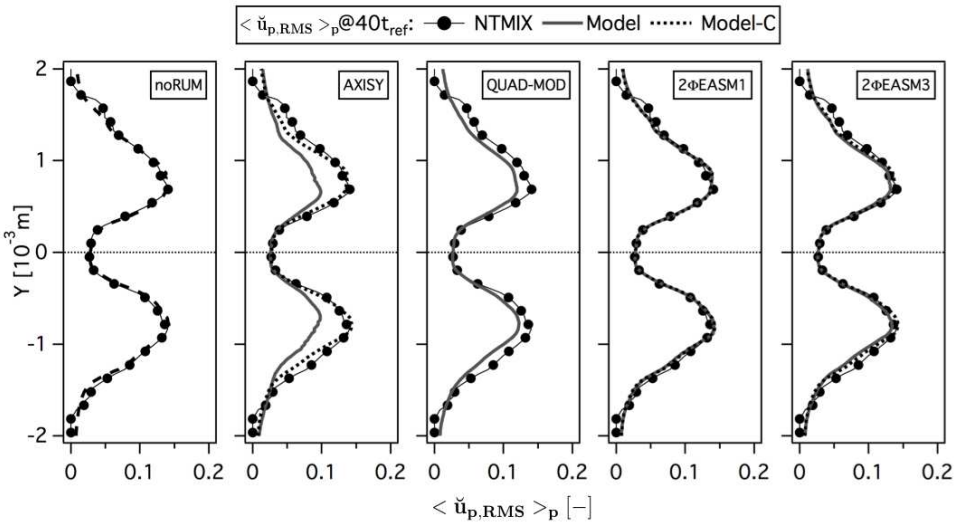

(b)

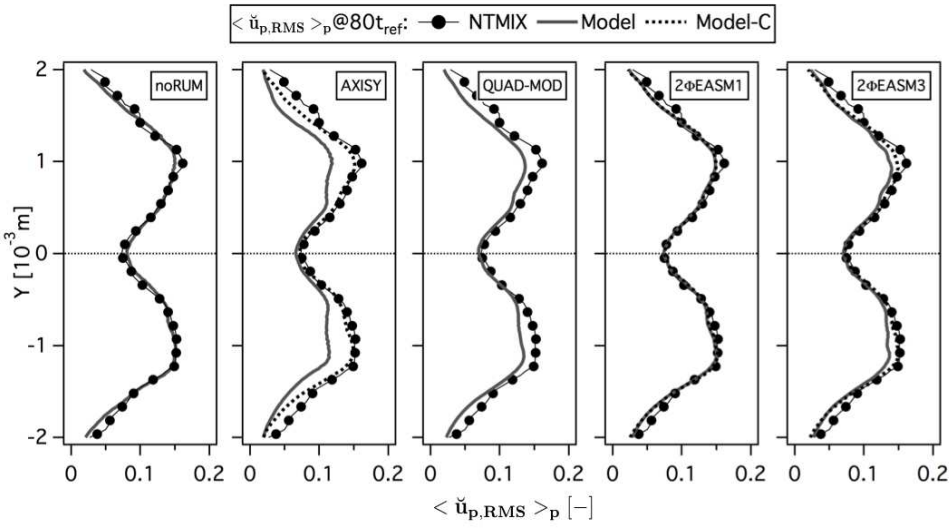

(c)

Figure 5.17: *Comparison of Eulerian and Lagrangian RMS particle velocity in X-direction ($< \breve{u}_{p,RMS} >_p$) at 5, 40 and 80t_{ref}. Normalized by the initial particle velocity in X-direction at the center of the slab. LR_St1_# case.*

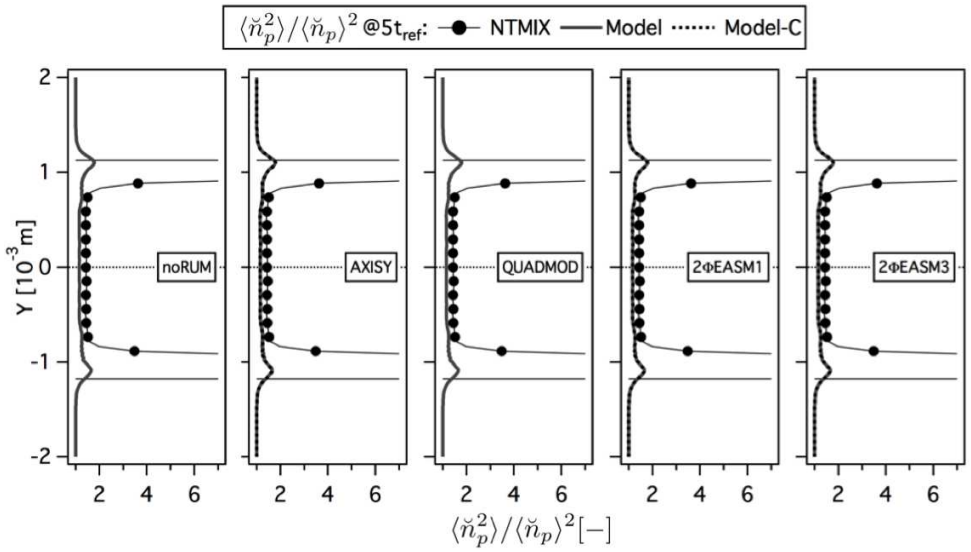

(a)

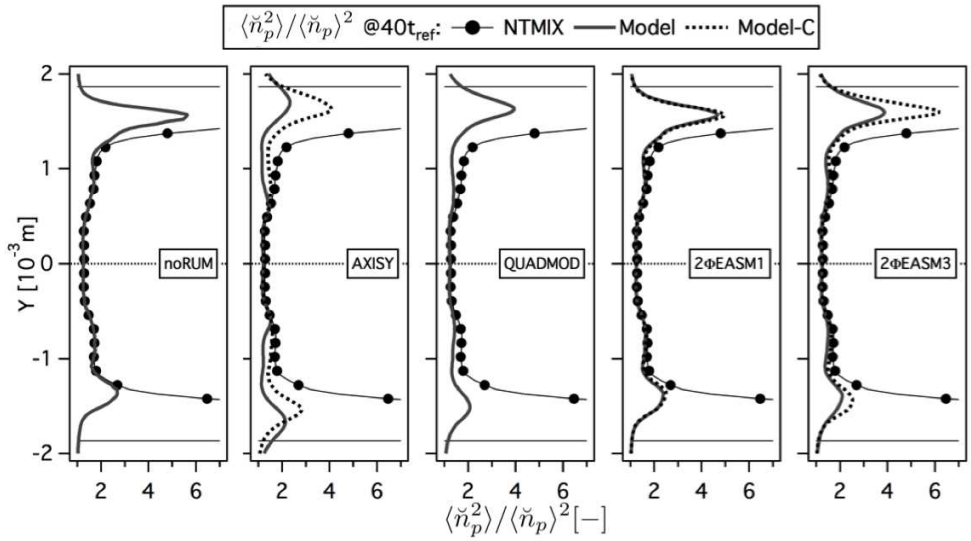

(b)

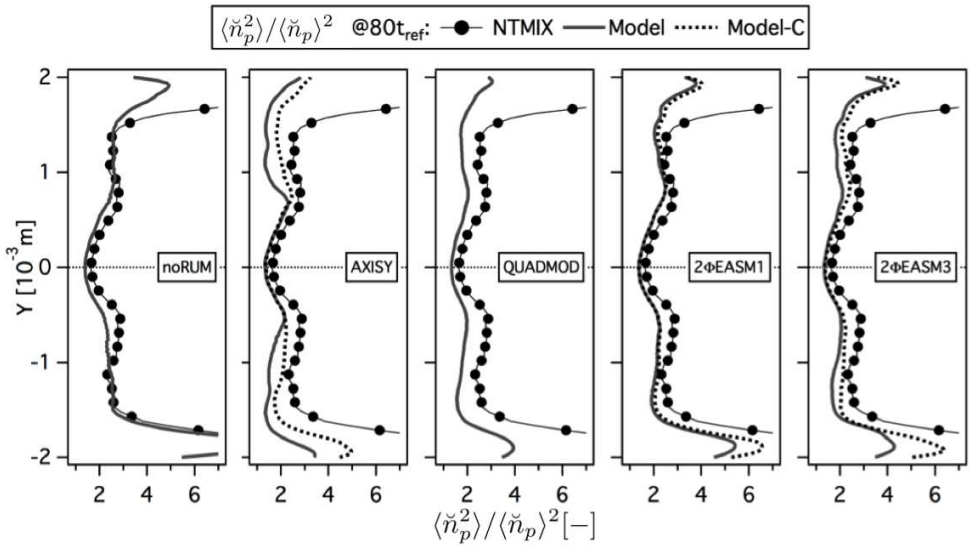

(c)

Figure 5.18: *Comparison of Eulerian and Lagrangian RMS particle segregation ($< \breve{n}_p^2 > / < \breve{n}_p >^2$) at 5, 40 and $80t_{ref}$. LR_St1_# case.*

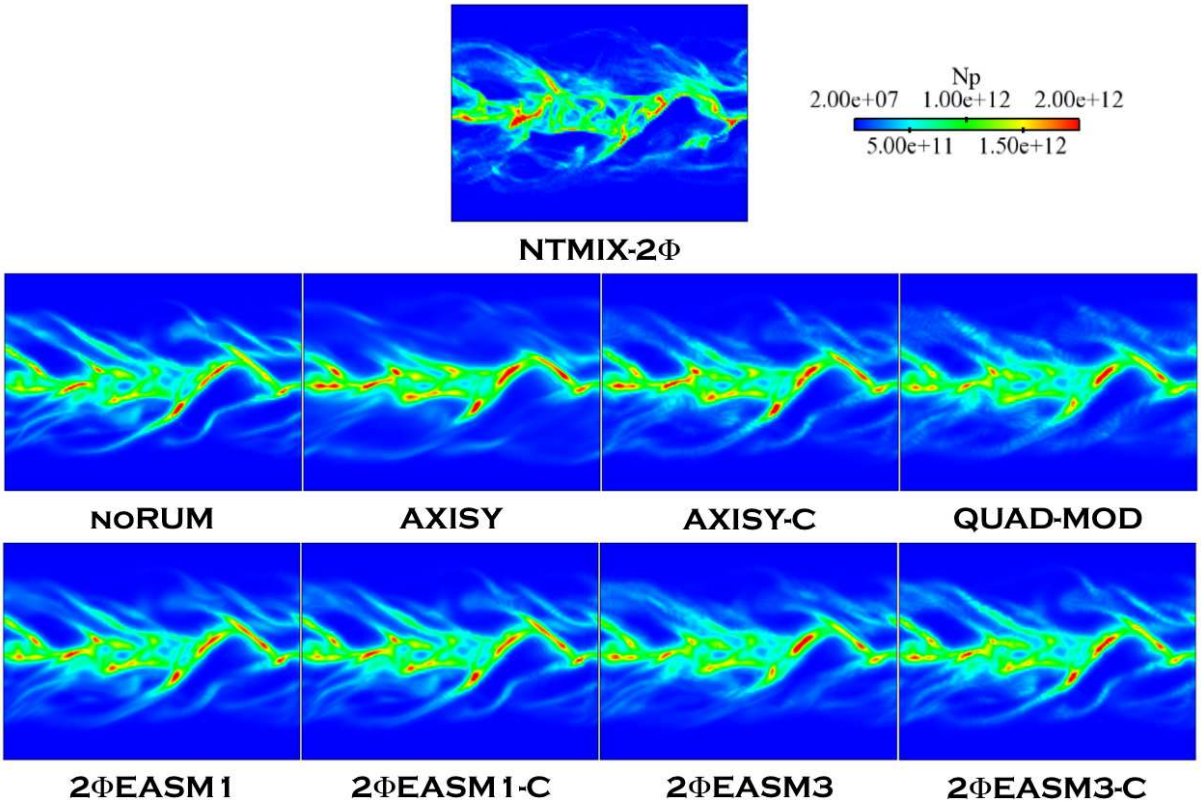

Figure 5.19: *Comparison of Lagrangian (NTMIX-2Φ) and Eulerian particle number density (N_p) at $80t_{ref}$. LR_St1_# case.*

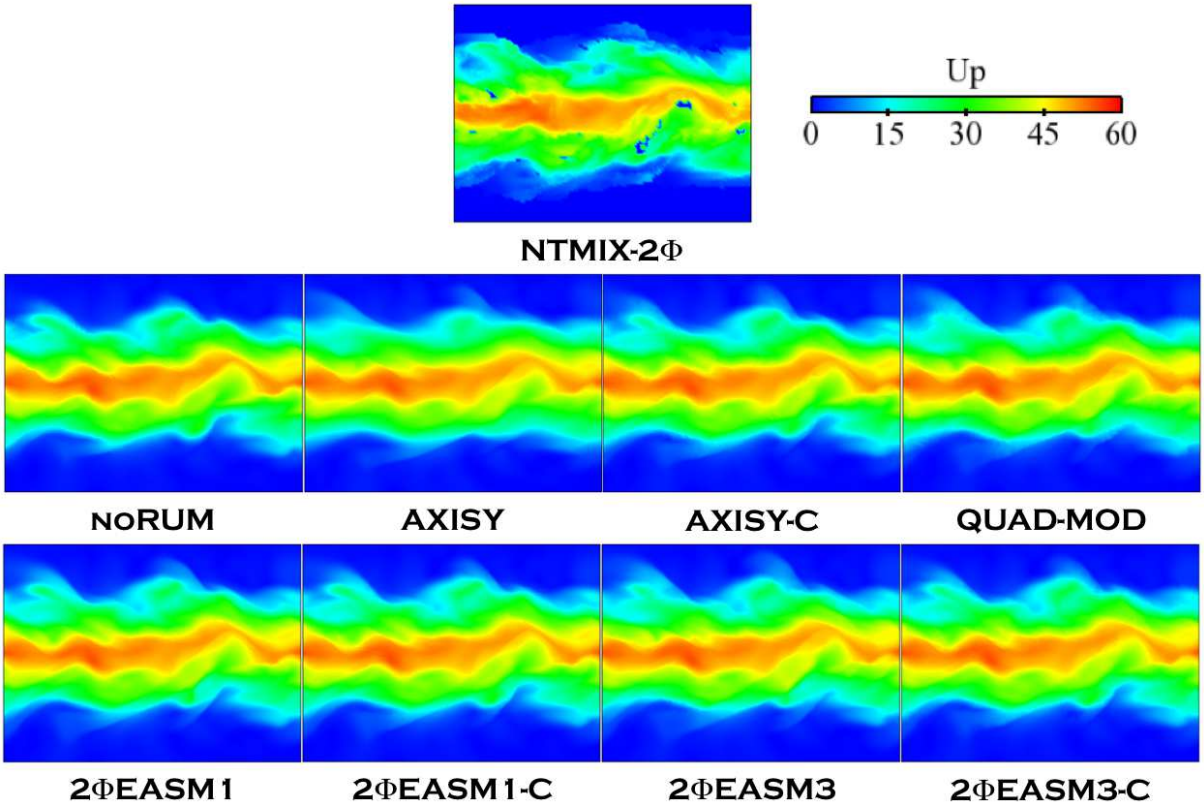

Figure 5.20: *Comparison of Lagrangian (NTMIX-2Φ) and Eulerian particle velocity magnitude (U_p) at $80t_{ref}$. LR_St1_# case.*

5.3.2 High order moments

The analysis of the higher order moments such as the RUE ($\delta\breve{\theta}_p$) and mesoscopic energy ($\breve{q}_p^2$) energies, is expected to enable to discriminate which models produce better *a posteriori* results in mean-sheared configuration. In industrial applications, the only high-order moment really taken into account is the total energy or total particle agitation ($q_p^2 = \breve{q}_p^2 + \delta\breve{q}_p$). The importance of the Random Uncorrelated Motion is due to the particle trajectory crossing (PTC, Falkovich *et al.* (2002)). Indeed, the prediction of the RUE is crucial in applications (industrial or not) where particle collision and/or coalescence are taken into account (such as fluidized beds or non-diluted regimes, i.e. injector-close zones in sprays). If the RUE is not well predicted, the dispersed phase will not have enough energy for collisions or coalescence. For example, if $\delta\breve{\theta}_p$ is overestimated, it may lead to a relaminarization of the dispersed phase flow (Riber (2007)). Masi (2010) performed an *a priori* analysis of the particle-laden temporal turbulent planar-jet studied here taking into account the particle collisions. Masi rewrote the models presented in Chapter 4 to the case of a colliding dispersed phase in diluted regime (one-way coupling with the gas phase). However, as in AVBP the possibility of taking into account collisions or coalescence is not available yet, these phenomena have not been studied here. Nevertheless, collisions may be taken into account in AVBP with minor modifications along with the implementation of the corresponding RUM models.

Figure 5.21 shows the predicted RUE profiles at 5, 40 and $80t_{ref}$. While AXISY overestimates the particle RUE, 2ΦEASM1 underestimates it. QUAD-MOD, 2ΦEASM3 and AXISY-C provide correct levels of RUE. However, QUAD-MOD and 2ΦEASM3 are able to recover the good profile at $40t_{ref}$ while AXISY-C underestimates the RUE level at $40t_{ref}$ and predicts a correct value at $80t_{ref}$. Figure 5.22 shows the mesoscopic energy $\breve{q}_p^2$ and the total energy $q_p^2 = \breve{q}_p^2 + \delta\breve{q}_p$ for the three simulation times. The main conclusions obtained comparing the statistics of $\delta\breve{q}_p$, $\breve{q}_p^2$ and q_p^2 are:

1. The main contribution to the total agitation q_p^2 comes from the mesoscopic motion (i.e. from $\breve{q}_p^2$), while the RUM has a limited impact for such particle inertia.

2. The models that overestimate the particle RUE (e.g. AXISY), predict a lower value of the mesoscopic energy. In the same way, the models that underestimate the RUM energy (e.g. 2ΦEASM1) produce higher values of $\breve{q}_p^2$ than the Lagrangian reference. In all cases, the final energy budget gives the correct amount of total agitation (q_p^2).

The analysis of the high-order models is completed with the statistics of the productions of RUE by shear and by compression. The production (Fig. 5.23) is defined as:

$$P_{RUM}^{Shear} = -\delta\breve{R}_{p,ij}^{*}\frac{\partial u_i}{\partial x_j}. \tag{5.18}$$

The production by compression (Fig. 5.24) depends on the divergence of the particle velocity and reads:

$$P_{RUM}^{Compression} = -\frac{2}{3}\delta\breve{\theta}_p\left[\frac{\partial u_i}{\partial x_i}\right] . \tag{5.19}$$

QUAD-MOD and 2ΦEASM3 give the best predictions of P_{RUM}^{Shear}. However, the profile of $P_{RUM}^{Compression}$ produced by 2ΦEASM3 is closer to the reference than that of QUAD-MOD. AXISY greatly overestimates the production by shear. As well, the production by compression is no longer a production term but a dissipation term when using this model. A test performed without taking into account the production by compression term (Eq. (5.19)) in the RUE transport equation using the AXISY model has shown that the overestimation of RUE was much larger neglecting this term, confirming the dissipative nature of $.P_{RUM}^{Compression}$ in AXISY model. Finally for all models, the shear term is one order of magnitude larger than the compression term.

The main components of the deviatoric RUM stress tensor are also shown (Figs. 5.25 - 5.28). The diagonal components ($\delta\breve{R}^*_{p,11}$, $\delta\breve{R}^*_{p,22}$ and $\delta\breve{R}^*_{p,33}$) are well predicted by QUAD-MOD and 2ΦEASM3 models, greatly underpredicted by AXISY-C, 2ΦEASM1 and 2ΦEASM1-C models and slightly underpredicted by AXISY and 2ΦEASM3-C models. In fact, the *a priori* analysis showed that the diagonal components have a limited impact in the prediction of the mean RUE compared to the components out of the diagonal. $\delta\breve{R}^*_{p,12}$ is shown in Fig. 5.28 for all the models. QUAD-MOD and 2ΦEASM3 profiles agree well with the Lagrangian reference, AXISY-C produces as well good results, which is coherent with the RUE predictions of this three models. The good agreement in the shear component for AXISY-C helps to overcome the small underestimation of the diagonal components. On the contrary, AXISY greatly overestimates this component, which has a direct impact on P^{Shear}_{RUM} terms and creates large amounts of RUE (Fig. 5.21). Regarding 2ΦEASM1 models (with and without correction), both models underestimate all components of the deviatoric RUM stress tensor, and thus underestimate the RUE as well. In fact, the correction seems to have a more limited impact on this model than predicted by *a priori* analysis. In the case of the 2ΦEASM3-C model, the *a priori* analysis showed that the correction improved the predictions of the deviatoric tensor components (and thus the productions and the RUE). In the *a posteriori* simulations, the correction has the opposite effect: it gives worse agreement.

A qualitative comparison of the model predictions for RUE is shown in Fig. 5.29. It shows the instantaneous fields of RUE at $80t_{ref}$ (5 and $40t_{ref}$ fields can be found in Appendix C). All models capture the zones where the RUE must be located referencing to the Lagrangian simulations. However, AXISY gives too high levels and the structures overlap giving two continuous bands located at the limits of the slab. The rest of the models are able to correctly reproduce the structures. 2ΦEASM1 and 2ΦEASM1-C show again very similar results but the predicted level of RUE is smaller than the Lagrangian reference, as for 2ΦEASM3-C and AXISY models. QUAD-MOD and 2ΦEASM3 give the best predictions for both the location of the structures and the level of RUE.

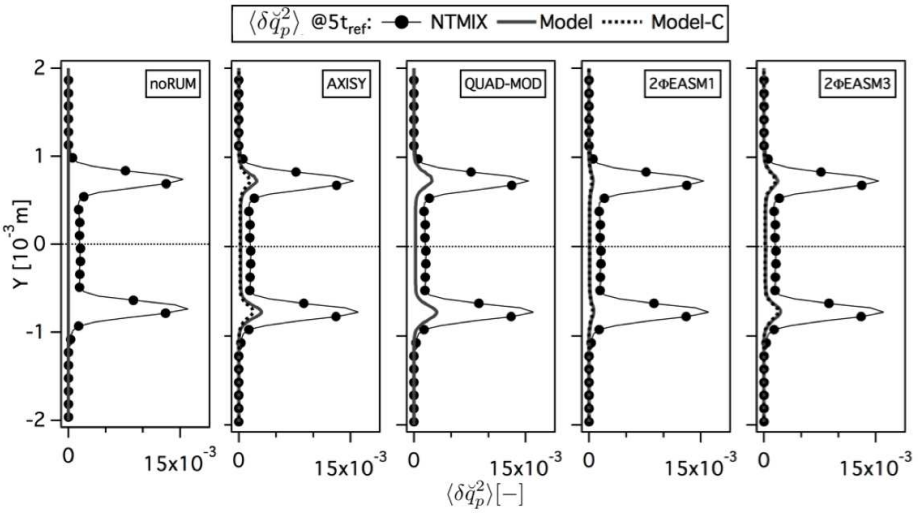

(a)

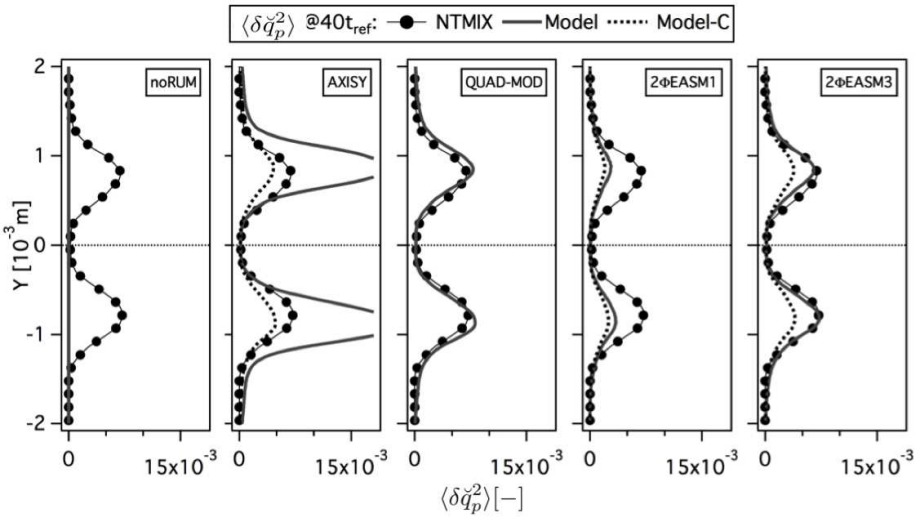

(b)

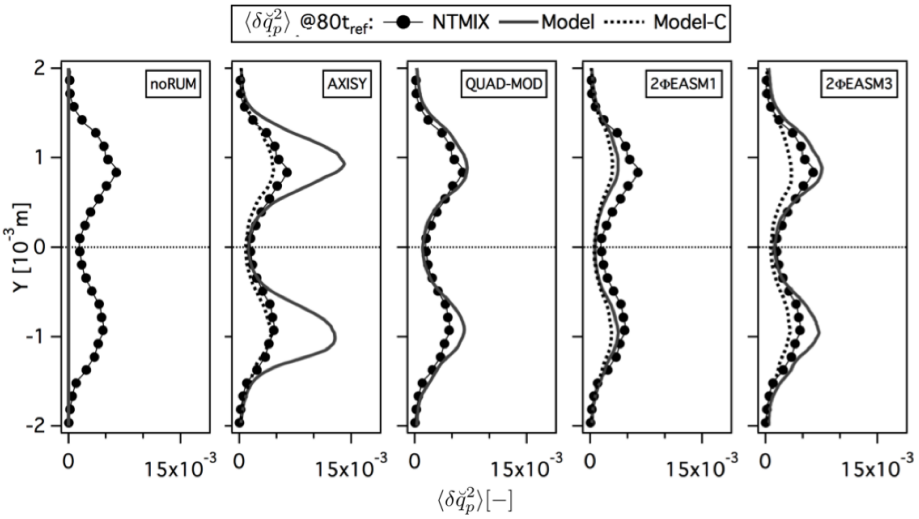

(c)

Figure 5.21: *Comparison of Eulerian and Lagrangian mean Random Uncorrelated Energy (*$< \delta\breve{\theta}_p >_p$*) at 5, 40 and 80*$t_{ref}$*. Normalized by the square of the initial particle velocity in X-direction at the center of the slab. LR_St1_# case.*

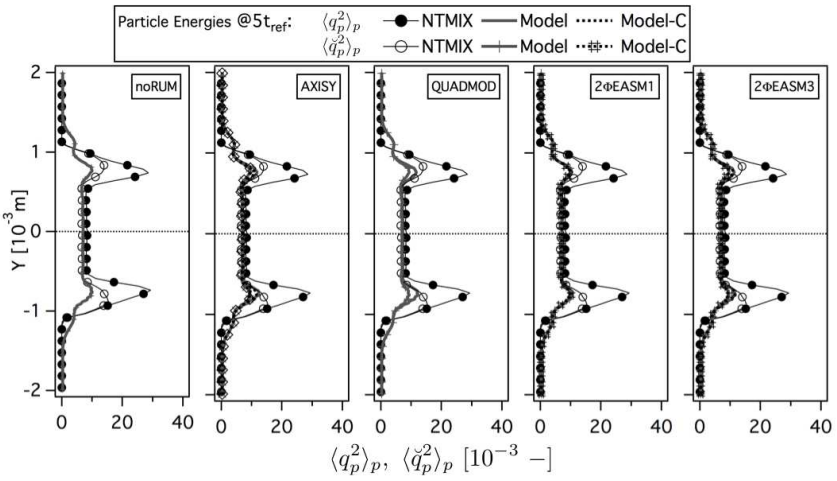

(a)

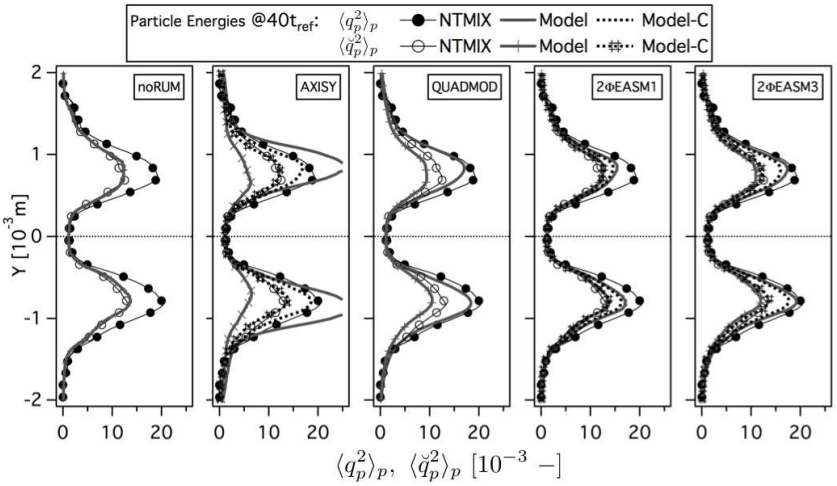

(b)

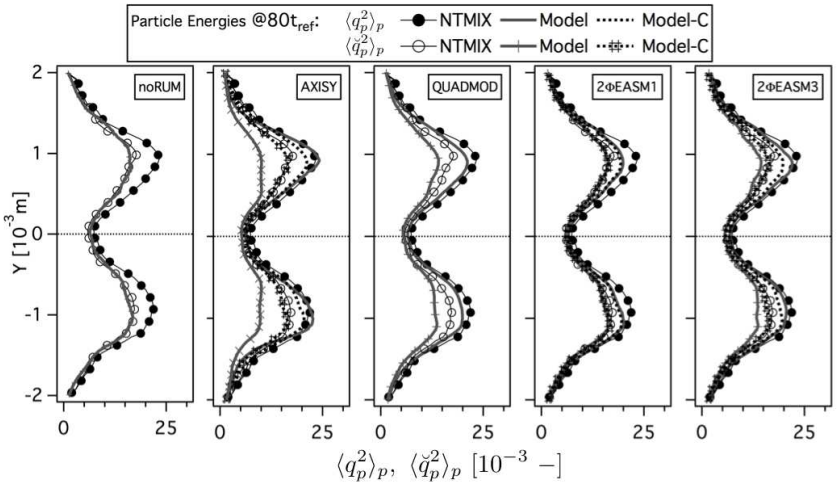

(c)

Figure 5.22: *Comparison of Eulerian and Lagrangian mean total energy ($< q_p^2 >_p$) and mean mesoscopic energy ($\langle \breve{q}_p^2 \rangle_p$) at 5, 40 and 80$t_{ref}$. Normalized by the square of the initial particle velocity in X-direction at the center of the slab. LR_St1_# case.*

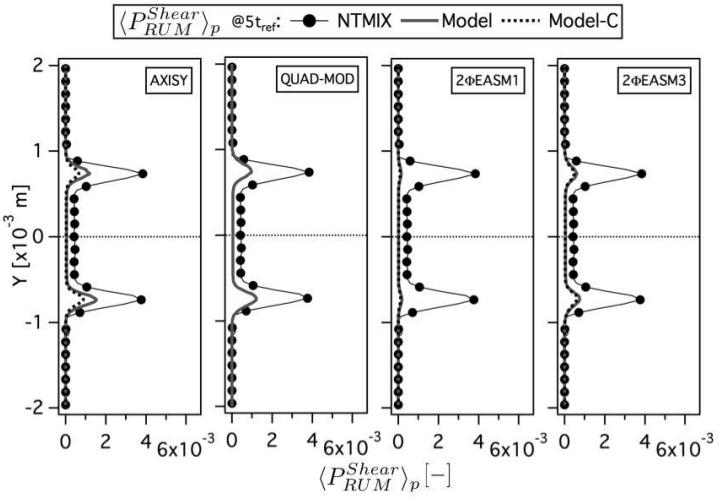

(a)

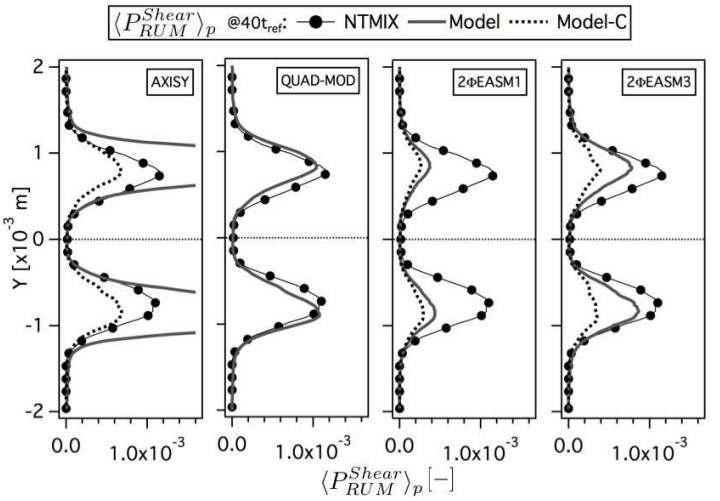

(b)

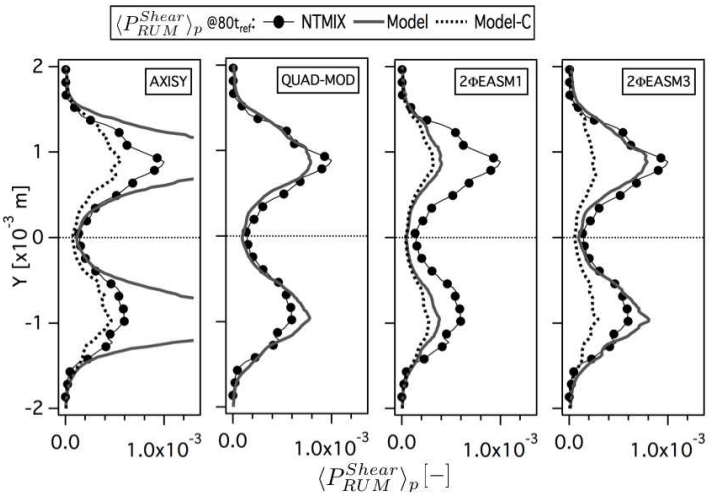

(c)

Figure 5.23: *Comparison of Eulerian and Lagrangian mean productions of RUM energy by shear ($< P_{RUM}^{Shear} >_p$) at 5, 40 and 80t_{ref}. Normalized by the square of the initial particle velocity in X-direction at the center of the slab and the reference time (t_{ref}). LR_St1_# case.*

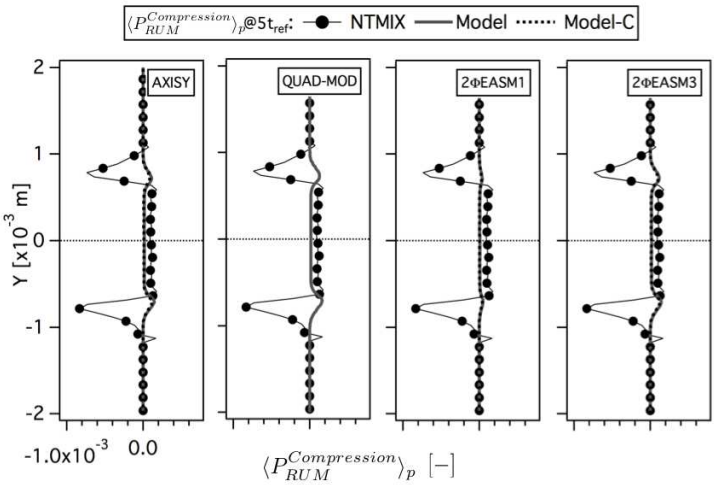

(a)

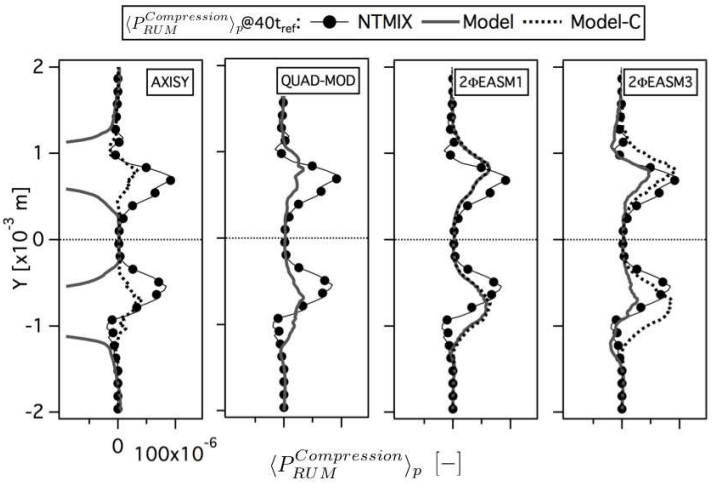

(b)

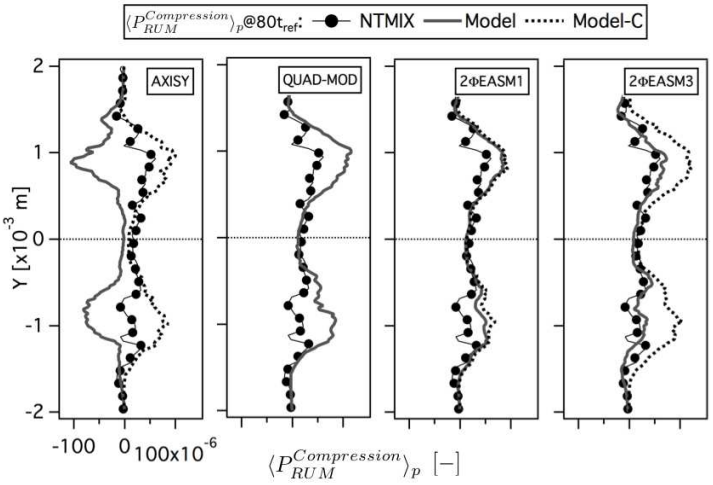

(c)

Figure 5.24: *Comparison of Eulerian and Lagrangian mean productions of RUM energy by compression* ($< P_{RUM}^{Compression} >_p$) *at 5, 40 and 80$t_{ref}$. Normalized by the square of the initial particle velocity in X-direction at the center of the slab and the reference time (t_{ref}). LR_St1_# case.*

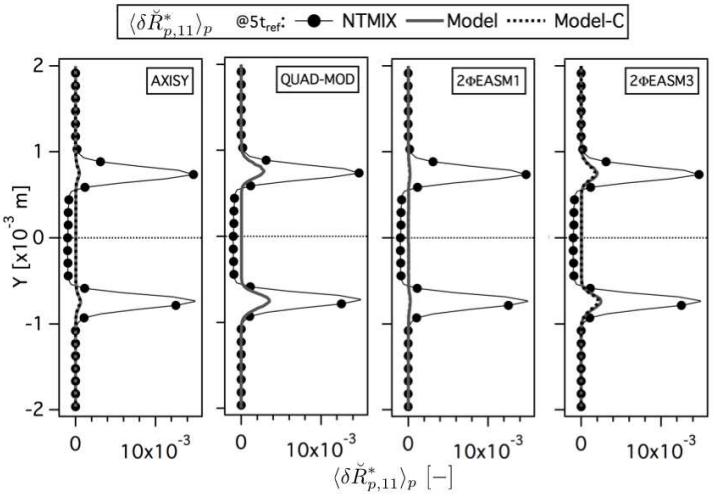

(a)

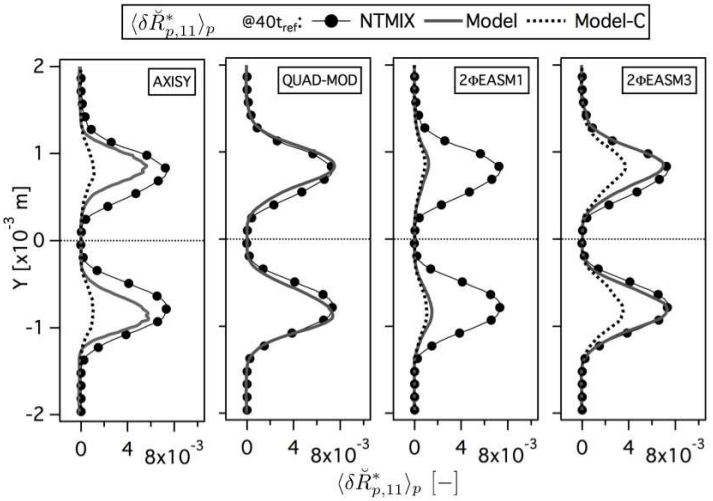

(b)

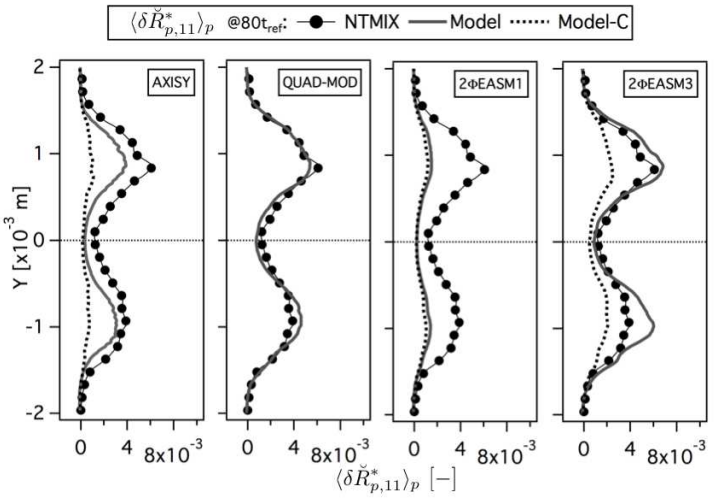

(c)

Figure 5.25: *Comparison of Eulerian and Lagrangian mean deviatoric RUM stress tensor XX component* ($< \delta \check{R}^*_{p,11} >_p$) *at 5, 40 and 80*$t_{ref}$. *Normalized by the square of the initial particle velocity in X-direction at the center of the slab. LR_St1_# case.*

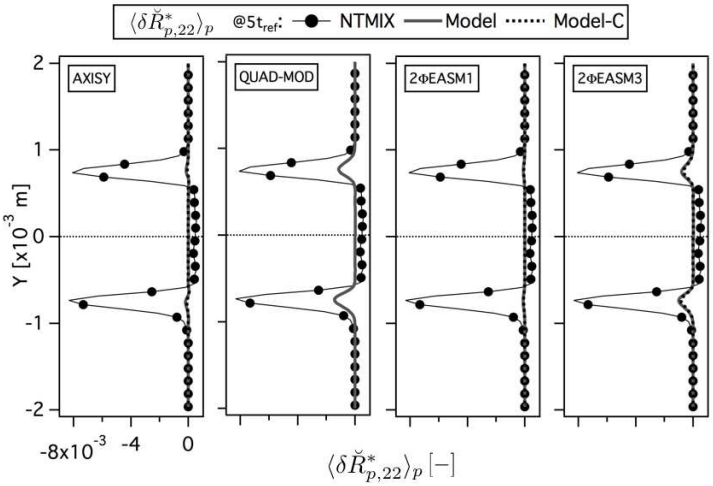

(a)

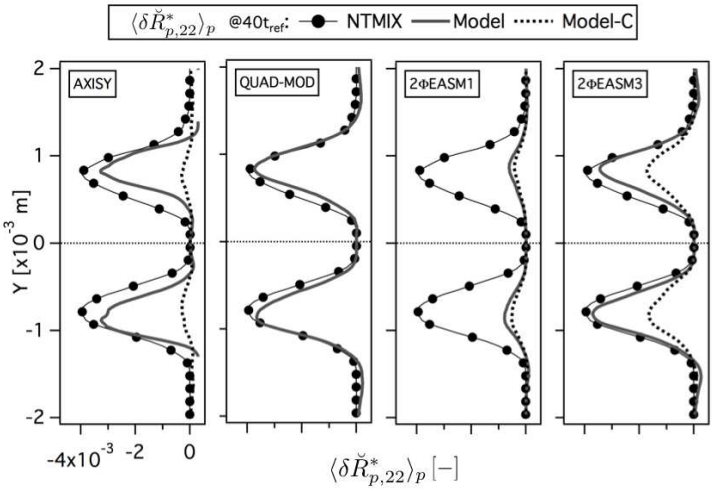

(b)

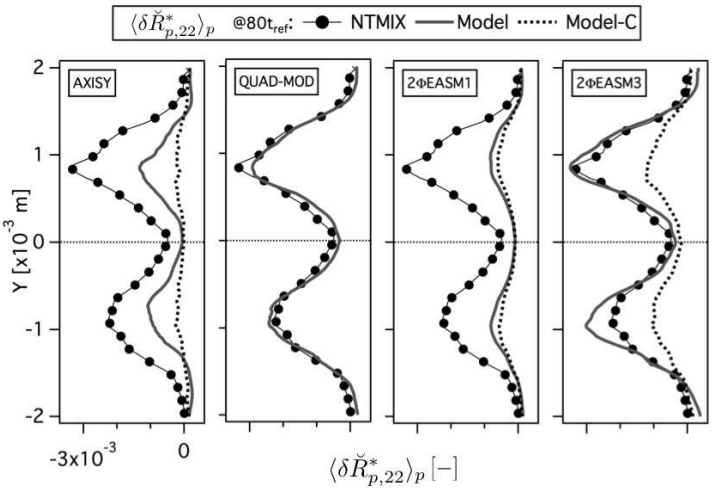

(c)

Figure 5.26: *Comparison of Eulerian and Lagrangian mean deviatoric RUM stress tensor YY component* ($< \delta \breve{R}^*_{p,22} >_p$) *at 5, 40 and 80*$t_{ref}$. *Normalized by the square of the initial particle velocity in X-direction at the center of the slab. LR_St1_# case.*

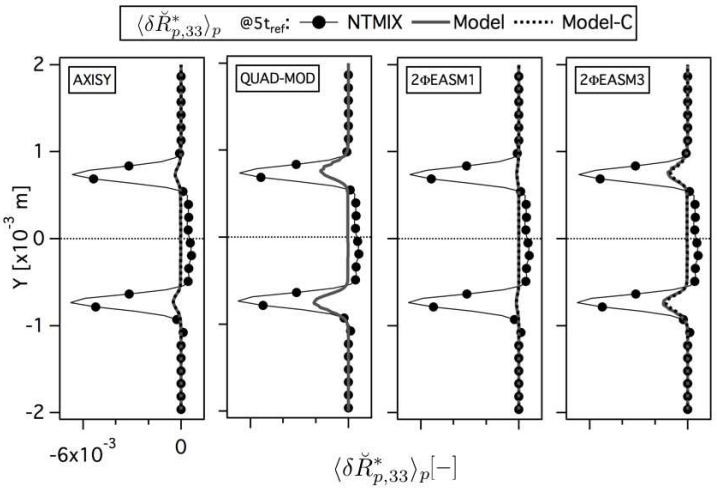

(a)

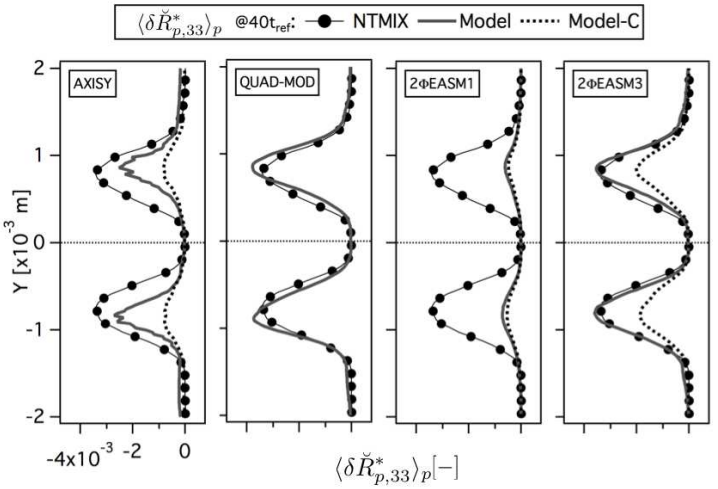

(b)

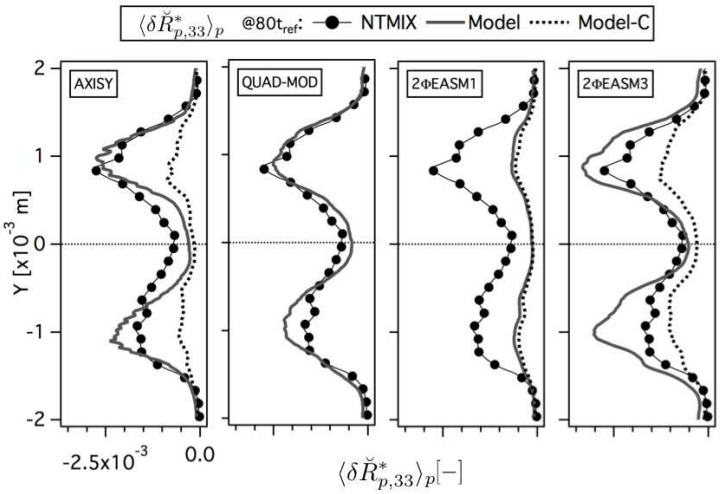

(c)

Figure 5.27: *Comparison of Eulerian and Lagrangian mean deviatoric RUM stress tensor ZZ component* ($< \delta \breve{R}^*_{p,33} >_p$) *at 5, 40 and 80*$t_{ref}$. *Normalized by the square of the initial particle velocity in X-direction at the center of the slab. LR_St1_# case.*

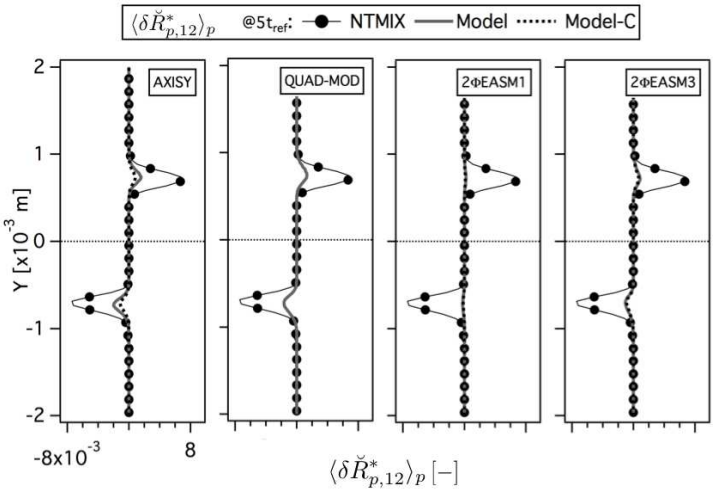

(a)

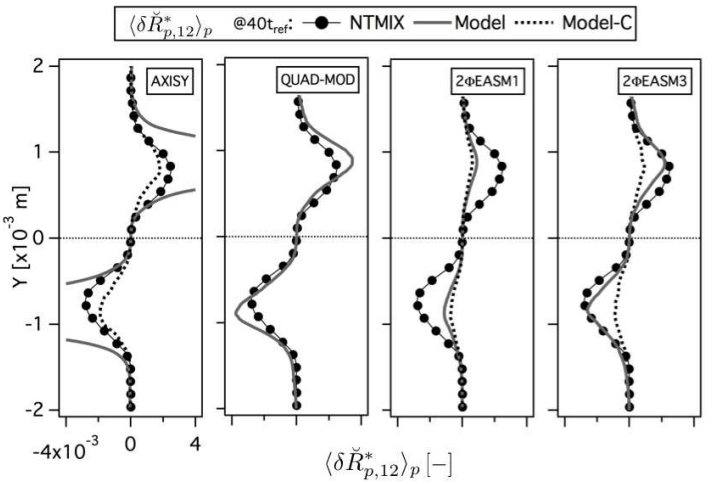

(b)

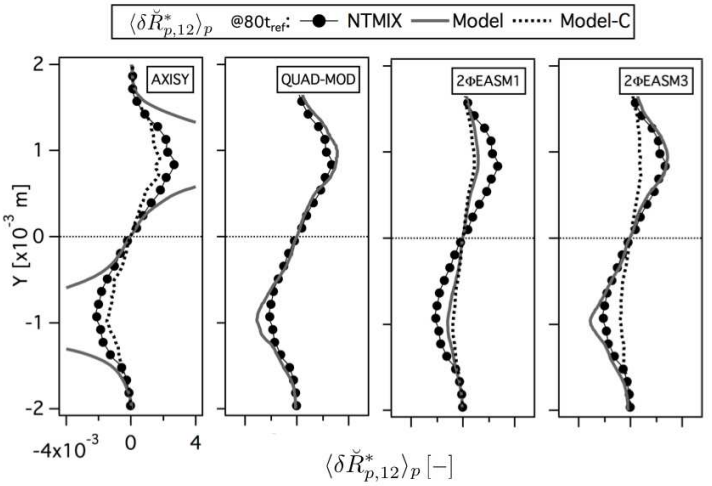

(c)

Figure 5.28: *Comparison of Eulerian and Lagrangian mean deviatoric RUM stress tensor XY component* ($< \delta \breve{R}^*_{p,12} >_p$) *at 5, 40 and 80*$t_{ref}$. *Normalized by the square of the initial particle velocity in X-direction at the center of the slab. LR_St1_# case.*

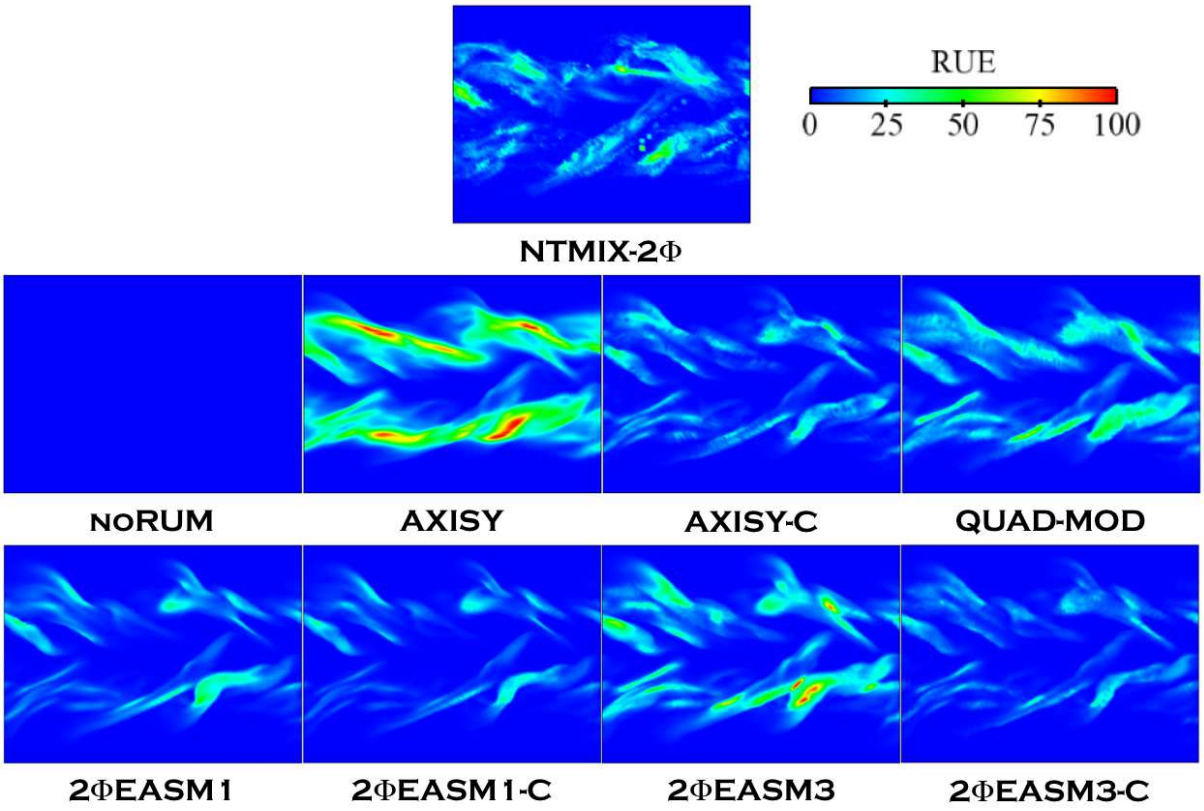

Figure 5.29: *Comparison of Lagrangian (NTMIX-2Φ) and Eulerian Random Uncorrelated Energy at* $80t_{ref}$*. LR_St1_# case.*

5.3.3 Effect of the user-defined artificial dissipation

Artificial dissipation (AD) is required in AVBP to guarantee the stability of the simulation using a centered numerical scheme (TTGC). It plays an important role in the development of the two-phase flow simulation itself. Artificial dissipation is applied in two steps. First, a sensor detecting too steep gradients to be resolved on the current grid is computed. There are several expressions for this sensor in AVBP which can take values from 0 to 1, 0 being no AD applied and 1 denotes where the maximum value of AD is applied in the domain. Second, a certain amount of 2^{nd} (shock capturing) and 4^{th} (background dissipation) AD is applied depending on the sensor value and user-defined coefficients. As a matter of fact, the AV sensor (CMS-Lite) used during this work seems to act similarly to the RUM, i.e. it has an effect of diffusion in the fields of the particle number density and velocity. Actually, there seems to exist an inverse correlation between the activation of the AV sensor and the RUE.

The models which are not able to predict the correct amount of RUE (e.g. noRUM) compensate the lack of diffusion naturally produced by the model by a higher amount of AD, which artificially smoothes the gradients and allows the code to complete the simulation. On the contrary, the AV sensor activates much less when models which overestimate the RUE are used (e.g. AXISY). The noRUM model for example, is able to correctly predict the low order moments such as the particle number density, the particle velocity and their RMS values. AD helps to stabilize the code producing an effect that mimics the one of the RUM. However, it is not able to produce RUE and thus it predicts a wrong repartition between the energies (the only contribution to the total energy is the mesoscopic energy, which leads to an underestimation of q_p^2). On the one hand, a correct balance between the RUM and the mesoscopic energy is a key point to reproduce complex effects such as PTC or collisions/coalescence. On the other hand, the effect of RUM becomes more important as the particle inertia increases. This means that while at $St = 1$ the simulations with models which underpredict the RUE are stable enough (due to the AD) to complete the calculation, it is not guaranteed that these models will keep valid at larger Stokes (Section 5.4.1).

Recently, another numerical scheme called PSI (Lamarque (2007), Roux *et al.* (2010)) has been implemented in AVBP. This residual distribution scheme is lower order than TTGC, but positive and linear preserving, which are interesting properties to capture shocks or very steep gradients. No AD is required when using PSI. Some tests performed during this work have shown that this scheme diffused too much at the limits of the slab due to the initial condition gradients. Thus, the slab spreads in the Y-direction, giving worse predictions of the low order and high order moments than the combination of TTGC scheme with a higher amount of AD. This effect was already visible after $5t_{ref}$ only. For this reason, the use of PSI scheme was quickly discarded in this configuration.

Figure 5.30 shows profiles of AV sensor for all models (included the calculation without RUM (noRUM)) at 5, 40 and $80t_{ref}$. It should be pointed out that due to the steep gradients at the limits of the slab in the initial solution, the AV sensor initially activates whatever the RUM model, and always at the same locations and with the same strength. This helps the code to overcome that extreme initial condition. Afterwards, the differences between the models are clear: AXISY, which greatly overestimates the RUE, needs less AD than 2ΦEASM1, which underestimates the RUE. Since Euler-Euler simulations need the application of a certain amount of AD in order to numerically stabilize the computations, the goal is then to find a model which presents good compromise between RUM and AD. That is, a model able to capture the physical phenomena related to RUM and that limits the action of AD to the dissipation of numerical instabilities. QUAD-MOD and 2ΦEASM3 seem good candidates.

Figure 5.31 shows an instantaneous field AV sensor at $80t_{ref}$. When neglecting the RUM contribution (noRUM model), the AV sensor is activated in a wider way and with a higher level than when using a RUM model. The sensor is very little activated with AXISY model. 2ΦEASM3 model seems again to be the best compromise.

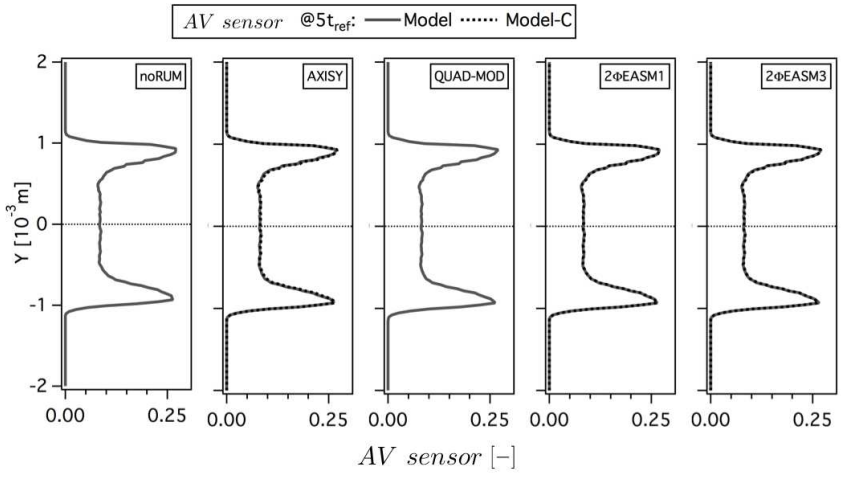

(a)

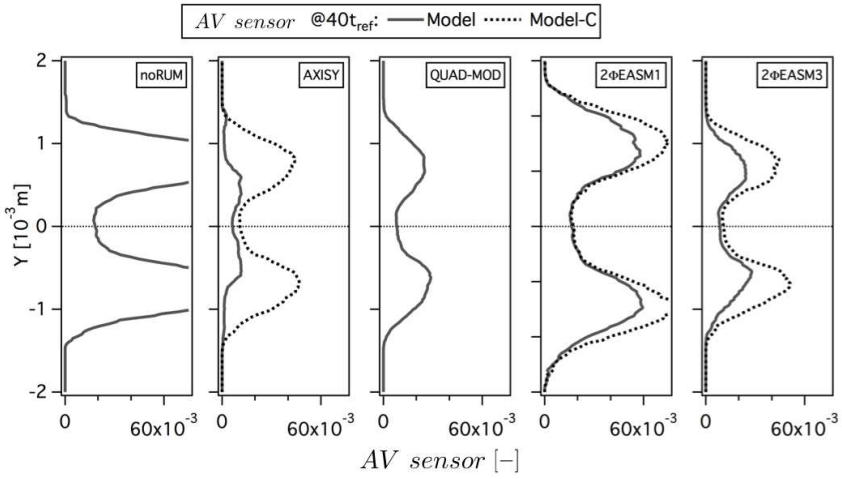

(b)

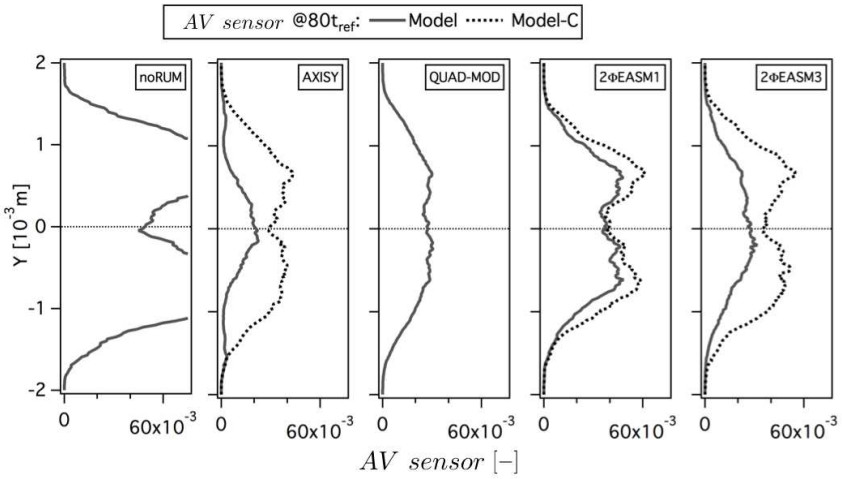

(c)

Figure 5.30: *Mean Artificial Viscosity sensor activation at 5, 40 and 80t_{ref}. LR_St1_# case.*

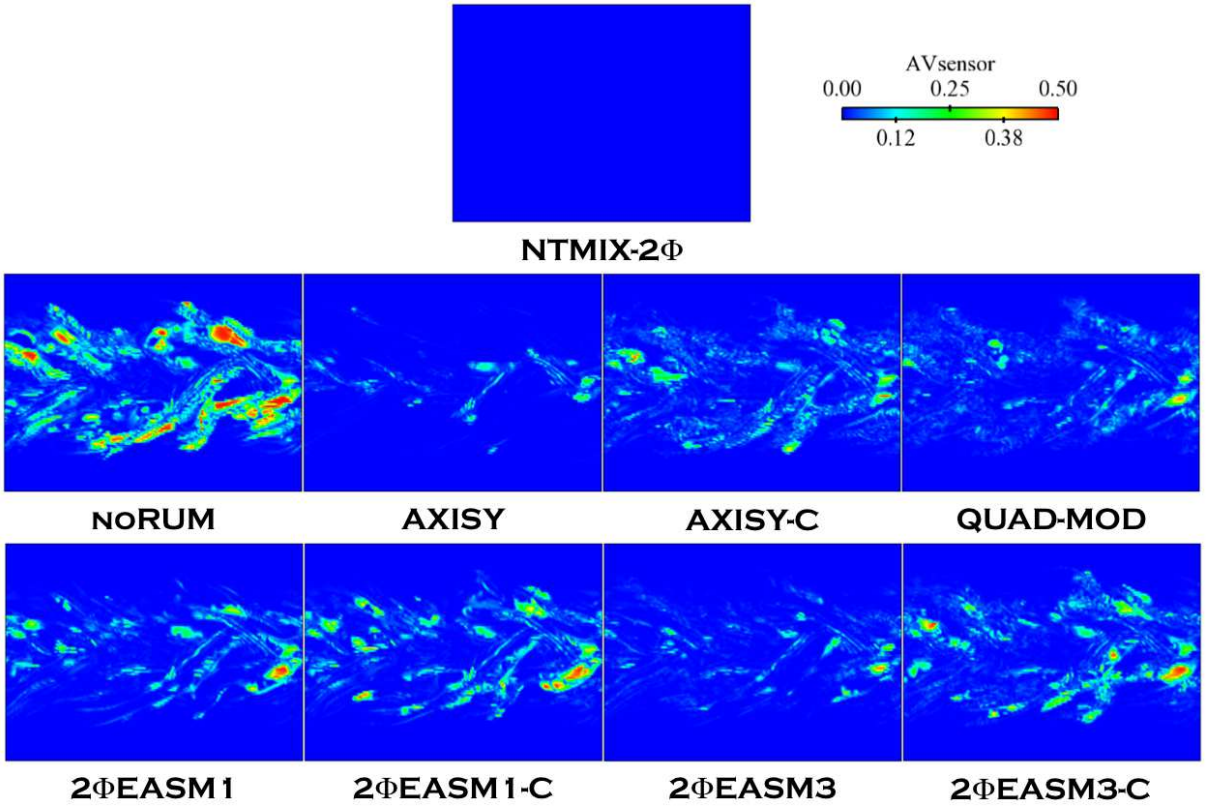

Figure 5.31: *Comparison of AV sensor levels at* $80t_{ref}$*. LR_St1_# case.*

5.3.4 Effect of mesh resolution

The effect of mesh resolution is studied in this Section. Case LR_St1_# has been computed on a 512^3 hexahedrical grid with the 2ΦEASM3 model. That is, the resolution has been doubled compared to the 256^3 mesh used in the computations presented in the previous sections. It is conjectured that the mesh resolution has an important impact on high order moments statistics of the dispersed phase. This effect has already been studied by Dombard (2011) on the Euler-Euler simulations. However, the mesh resolution may impact the Euler-Lagrange simulations too. Due to limited computational resources, the simulation has been carried out until $40t_{ref}$ and with one model only. 2ΦEASM3 has been chosen to perform the high resolution simulation following the results obtained in Sections 5.3.1-5.3.3. Furthermore, only the low order moments and the RUE have been computed.

Figure 5.32(a) shows the statistics of the non-dimensional particle number density obtained from the Euler-Lagrange computation performed with NTMIX-2Φ and the Euler-Euler computations performed with AVBP using 2ΦEASM3 model and two different grids. Mesh_256 corresponds to the simulation on a 256^3 grid and Mesh_512 to the 512^3 grid simulation. The numerical setups are the same for the two Euler-Euler calculations, including the Artificial Dissipation parameters. The scales of the graphs have been stretched to highlight the differences between the two meshes, otherwise they are not visible and the profiles given by the two meshes superpose and there is no noticeable difference. Figure 5.32(b) shows the profiles of the non-dimensional particle velocity. At the center of the slab, Mesh_256 matches the reference NTMIX-2Φ, the same happens with Mesh_512. However, at the periphery of the jet, only the simulation performed with the high resolution mesh (Mesh_512) reproduces the opening of the jet. Indeed, Mesh_512 sticks to the profile of NTMIX-2Φ except at some points where the differences are attributed to the projection algorithm used to recontruct the Eulerian fields from the Euler-Lagrange computation with NTMIX-2Φ.

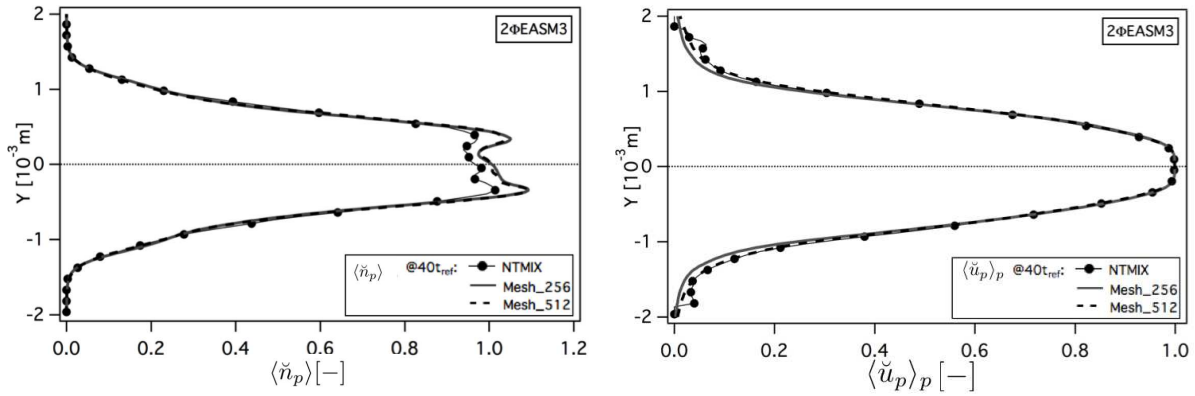

(a) Non-dimensional mean particle number density.

(b) Non-dimensional mean particle velocity.

Figure 5.32: *Comparison between Lagrangian and Eulerian results. The Lagrangian computation has been performed on a* 128^3 *mesh grid. Mesh_256 corresponds to the Eulerian simulation on a* 256^3 *mesh and Mesh_512 to the Eulerian simulation on a* 512^3 *mesh.*

The increase in mesh resolution improves the predictions of RMS particle number density profiles (Fig. 5.33(a)) as well. The profile corresponding to Mesh_512 captures the maximum level predicted by NTMIX-2Φ at the peaks located at the periphery. However, the opening of the jet is the same as for Mesh_256, narrower than the corresponding to NTMIX-2Φ. On the contrary, Fig. 5.33(b) shows the RMS particle velocity statistics. The increase in mesh resolution leads to a decrease in the maximum value of the profile. Otherwise, the opening of the jet is wider in Mesh_512 case. Note that the projection algorithm produces inaccurate results at the periphery of the slab for NTMIX-2Φ computations. The accuracy of the reference values at the periphery and thus the jet opening can not be assessed in this case.

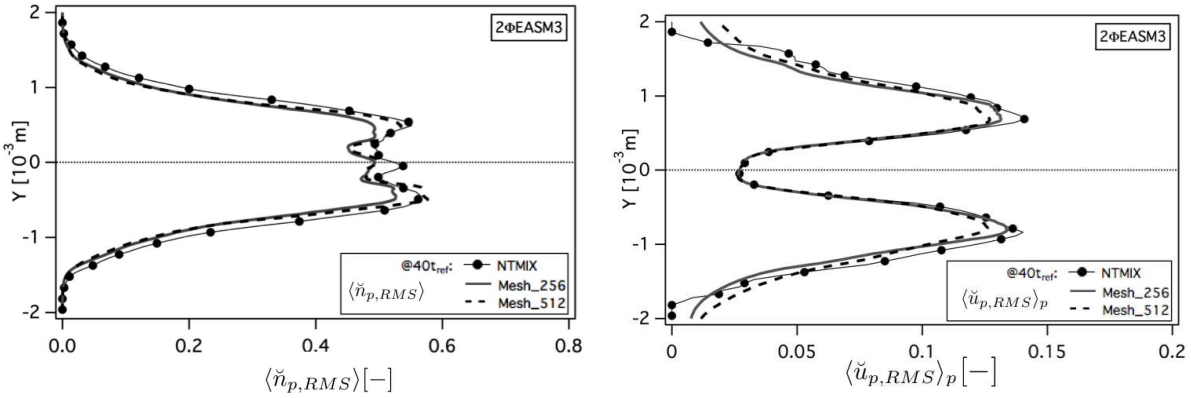

(a) Non-dimensional RMS particle number density.

(b) Non-dimensional RMS particle velocity.

Figure 5.33: *Comparison between Lagrangian and Eulerian results. The Lagrangian computation has been performed on a* 128^3 *mesh grid. Mesh_256 corresponds to the Eulerian simulation on a* 256^3 *mesh and Mesh_512 to the Eulerian simulation on a* 512^3 *mesh.*

Figure 5.34 shows the segregation profiles for both mesh resolutions. Mesh_512 simulation predicts a higher segregation peak than Mesh_256 at one of the borders of the slab. However, the position of the second peak has moved outwards the slab and its level has decreased. On both meshes, the level is too low compared to NTMIX-2Φ, except at the center of the slab, where both simulations give a good approximation of preferential concentration. Note that, the projection errors due to the presence of too few particles in the computational cells at the periphery of the slab on the Lagrangian simulation, provide very high segregation levels in that zone. However, the stretching on the graphs scale allows a better comparison between the simulations. Indeed, the accuracy with NTMIX-2Φ decreases when reaching the periphery.

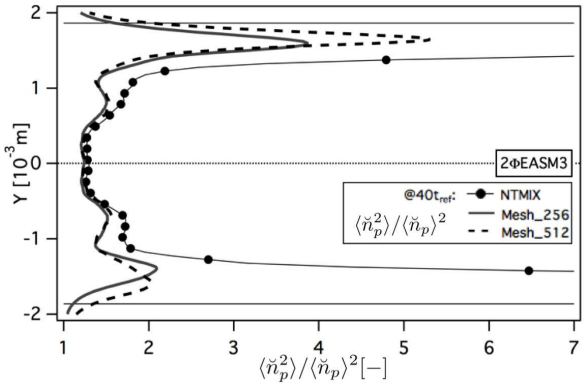

Figure 5.34: *Comparison between Lagrangian and Eulerian results. The Lagrangian computation has been performed on a* 128^3 *mesh grid. Mesh_256 corresponds to the Eulerian simulation on a* 256^3 *mesh and Mesh_512 to the Eulerian simulation on a* 512^3 *mesh.*

The high order moments statistics analyzed for Mesh_512 simulation reduce to the energy profiles. The finer the mesh resolution the higher the RUE level, which leads to a slight overprediction of RUE (Fig. 5.35(a)). The total agitation profiles are very similar, excepted at the slab borders where the total particle agitation predicted by Mesh_512 case is higher (Fig. 5.35(c)). The overprediction of RUE leads to a slight underprediction of the mesoscopic energy compared to Mesh_256 case (Fig. 5.35(b)). In general, increasing the mesh resolution has only a limited impact on the statistics of the dispersed phase.

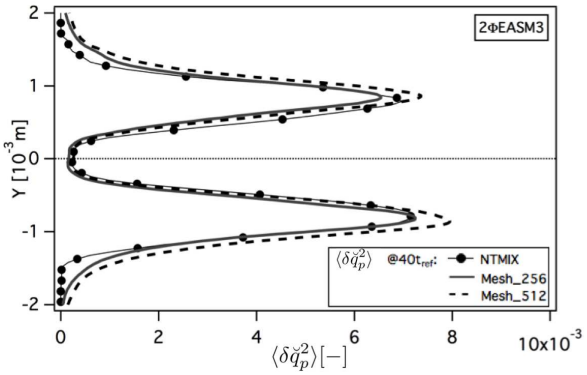

(a) Non-dimensional RUE.

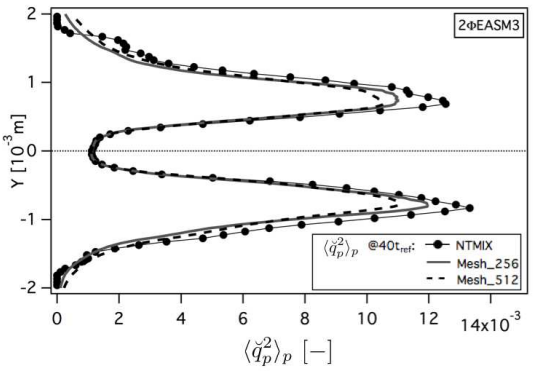

(b) Non-dimensional particle mesoscopic energy.

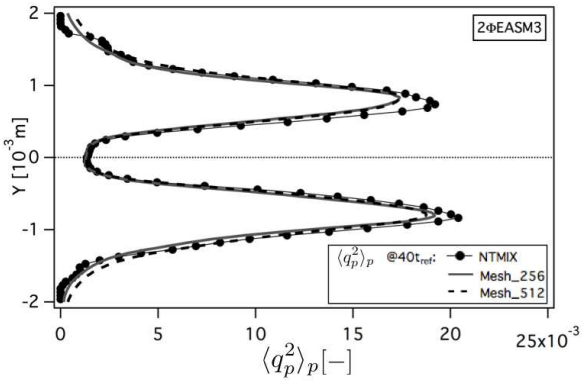

(c) Non-dimensional total particle energy.

Figure 5.35: *Comparison between Lagrangian and Eulerian results. The Lagrangian computation has been performed on a* 128^3 *mesh grid. Mesh_256 corresponds to the Eulerian simulation on a* 256^3 *mesh and Mesh_512 to the Eulerian simulation on a* 512^3 *mesh.*

That is not the case for the instantaneous fields. Fig. 5.36 shows the instantaneous fields of particle number density at $40t_{ref}$. The regions where the differences between 2ΦEASM3_256 and 2ΦEASM3_512 cases are the most visible have been highlighted using circles and arrows. Increasing the mesh resolution has an important impact on the particle number density fields. Indeed, the small structures are better captured as well as the diffusion at the periphery of the jet. The empty zones, as well as the zones of high concentration are also more precisely reproduced when the mesh resolution is increased. In Fig. 5.37 the only visible effect on the particle velocity fields is an increased diffusion at the borders (Fig. 5.37). Compared to NTMIX-2Φ, Mesh_256 gives the best qualitative results. Nevertheless, the statistics of Mesh_512 case are in better agreement with the Lagrangian reference at the periphery. The inaccuracy of the projection algorithm hinders any conclusion at this respect. Regarding the RUE fields (Fig. 5.38), 2ΦEASM3_512 predicts, in general, higher RUE levels (Fig. 5.38). Confirming the statistics (Fig. 5.35(a)), the RUE is slightly overpredicted when the mesh resolution is increased. Euler-Lagrange results on a higher resolution grid are nevertheless needed in order to compare Eulerian and Lagrangian results on the same conditions.

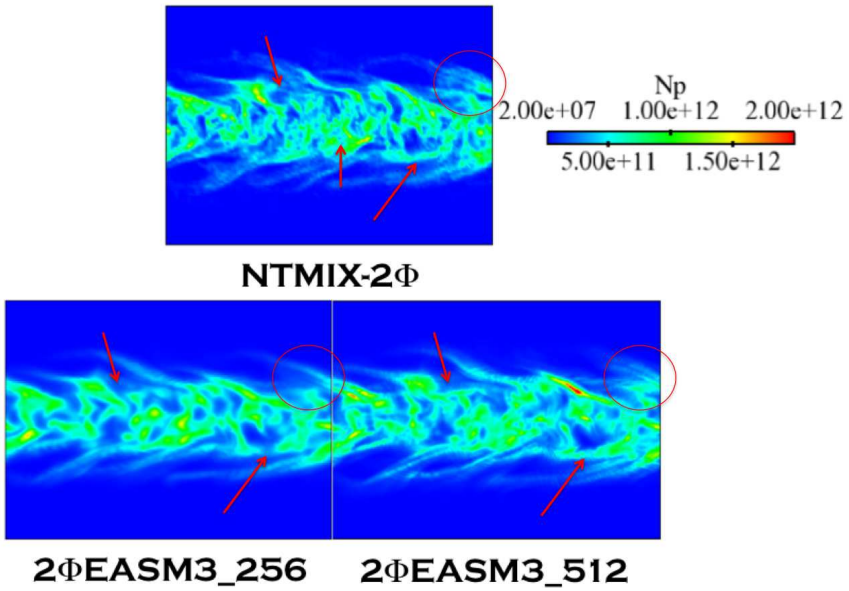

Figure 5.36: *Comparison betwenn Lagrangian and Eulerian particle number density instantaneous fields at* $40t_{ref}$*. The Lagrangian computation has been performed in a* 128^3 *grid. 2ΦEASM3_256 corresponds to the Eulerian simulation on a* 256^3 *mesh and 2ΦEASM3_512 to an Eulerian simulation on a* 512^3 *mesh.*

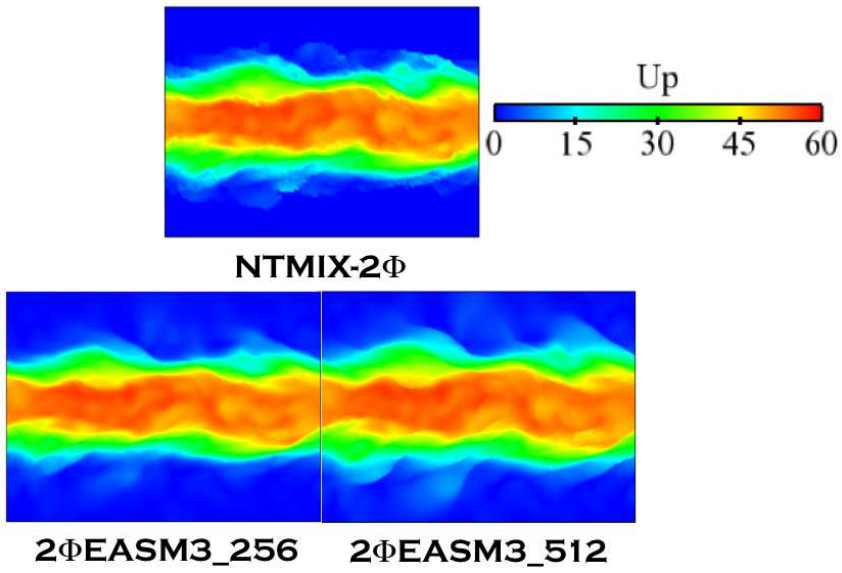

Figure 5.37: *Comparison between Lagrangian and Eulerian particle velocity instantaneous fields at* $40t_{ref}$*. The Lagrangian computation has been performed in a* 128^3 *grid. 2ΦEASM3_256 corresponds to the Eulerian simulation on a* 256^3 *mesh and 2ΦEASM3_512 to an Eulerian simulation on a* 512^3 *mesh.*

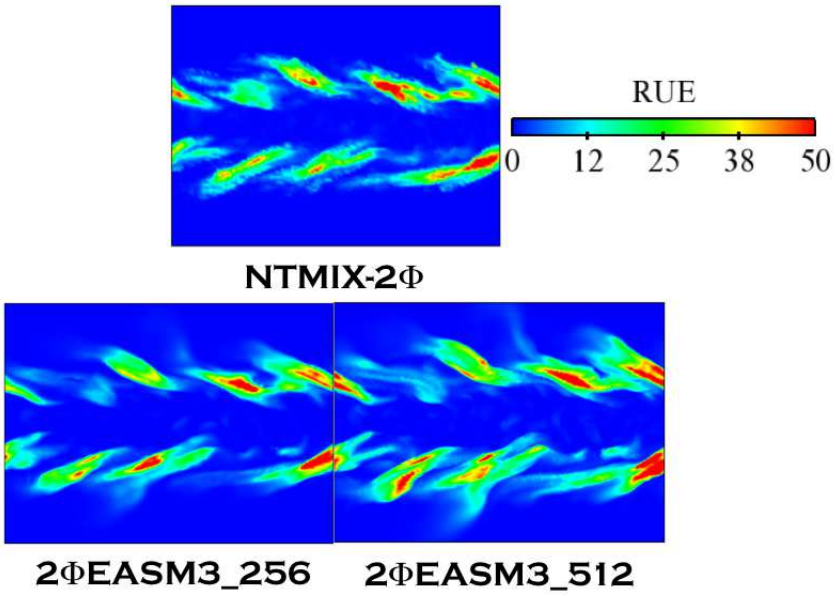

Figure 5.38: *Comparison between Lagrangian and Eulerian RUE instantaneous fields at* $40t_{ref}$*. The Lagrangian computation has been performed in a* 128^3 *grid. 2ΦEASM3_256 corresponds to the Eulerian simulation on a* 256^3 *mesh and 2ΦEASM3_512 to an Eulerian simulation on a* 512^3 *mesh.*

5.4 Performances of the RUM models at different inertia

In real applications the particle or droplet size can range from less than $1\mu m$ (once they have evaporated) up to millimeters (at injection). The range of particle Stokes numbers encountered is thus very large. This implies that the performances of the different models presented in Chapter 4 must be analyzed on a wide range of Stokes numbers too. Masi (2010) performed an *a priori* analysis for many Stokes numbers. This work only presents three, the more significative ones.

The results presented in Section 5.3 distinguished 2ΦEASM3 and QUAD-MOD as the models giving the best predictions for the low and the high-order moments for a $Re^{ac} = 5500$ and $St \sim 1$ particle-laden turbulent sheared flow. The particles in case LR_St3_# are very inertial. The phenomena of particles being pushed towards the upper and lower outer regions observed on LR_St1_# case is expected to increase. This Section aims at analyzing if the two models still behave correctly at $St \sim 3$ (Section 5.4.1) confirming the potential of the 2ΦEASM3 and QUAD-MOD models.

Then in Section 5.4.2, the ability of the two models to correctly predict the dispersed phase in a low inertia case is tested. Indeed, the Stokes number in LR_St033_# case ($St \sim 0.33$) is very close to the value of the Stokes number for which the preferential concentration phenomenon is maximal in this configuration, creating empty spaces close to regions of very high particle concentration. The particle density gradients are thus very steep and difficult to handle numerically potentially leading to simulation crashes.

5.4.1 High inertia case: Stokes=3

All RUM models are tested here in a low turbulence high inertia case. The Stokes number is $St \sim 3$. The particle relaxation time is $\tau_{fp}^F \sim 39$. The simulation has been performed up to $120t_{ref}$ ($3.07\tau_{fp}^F$). Note that results at $120t_{ref}$ will not be equivalent to those of LR_St1_# case at $40t_{ref}$ (equally $3.07\tau_{fp}^F$) since the corresponding physical time is not the same from the fluid flow point of view. All results are then shown at $120t_{ref}$. Additional results at 40 and $80t_{ref}$ can be found in Appendix D.

In this case, the AD model is not sufficient to allow the simulation without any RUM (noRUM model) to finish since numerical instabilities appear. This fact clearly reveals the importance of the RUM in this type of two-phase flow configurations.

Low order moments

At high inertia, the particle laden slab, subjected to strong flow shear at its limits, diffuses towards the periphery of the box as a result of the entrainment of particles by the fluid turbulence eddies. For this reason, the particle number density profiles (Fig. 5.39(a)) are much flatter than in the LR_St1_# case. As already pointed out, the AD is not able to sufficiently diffuse the profile for those models that underpredict the RUE (2ΦEASM1 and 2ΦEASM1-C) showing a higher level of $\breve{n}_p$ at the center of the jet. AXISY and its corrected version AXISY-C present the same behavior as for the mean inertia case. The maximum of $\breve{n}_p$ is highly overpredicted and consequently, the global shape of the profile is not well captured: the slope of the predicted profile is too high in the center and too low in the periphery. This effect is more visible for AXISY. On the contrary, QUAD-MOD and both 2ΦEASM3 or 2ΦEASM3-C models give very accurate results at the periphery and slightly overestimate the maximum level at the center line.

The initial guess of QUAD-MOD and 2ΦEASM3 as the best models seems to be confirmed by the predictions of the RMS values of $\breve{n}_p$ and $\breve{u}_p$. Indeed, the agreement with the Lagrangian results is very good for these two models (Fig. 5.40(a)). 2ΦEASM3 captures not only the good trend but also the correct level of $\breve{n}_{p,RMS}$. The agreement is slightly worse with QUAD-MOD. The effect of the correction

is more pronounced at high inertia when compared to LR_St1_# case. The results obtained when using the correction in 2ΦEASM3 are worse than when not using it. The same happens with 2ΦEASM1. However, it seems that when applied to the linear model (AXISY) the correction greatly improves the predictions. Figure 5.40(a) shows that AXISY-C and 2ΦEASM1-C reproduce the shape of the $\breve{n}_{p,RMS}$ profile although they overestimate the level of the peak at the center of the jet. On the contrary, AXISY and 2ΦEASM1 show a flatter profile at the periphery of the slab followed by a steeper slope near the center of the slab.

Regarding the particle velocity statistics, all models perfectly reproduce the mean particle velocity (Fig. 5.39(b)) and all models except AXISY produce acceptable RMS velocity profiles (Fig. 5.40(b)). Again, QUAD-MOD and 2ΦEASM3 give the best results together with 2ΦEASM1 (but 2ΦEASM1 fails to reproduce mean and RMS particle number density).

The instantaneous fields of particle number density (Fig. 5.42) and particle velocity (Fig. 5.43) produce a qualitative comparison of the performances of the models . The particle velocity is well predicted by all models (except AXISY that diffuses too much at the border of the jet) but there are important differences in the particle number density fields. AXISY produces a very concentrated jet at the center of the box and all the corrected models (AXISY-C, 2ΦEASM1-C and 2ΦEASM3-C) predict well defined filaments towards the periphery of the jet, which are not predicted by the Lagrangian reference simulations. 2ΦEASM is unable to recover the separated spots of high particle concentration at the center of the slab. QUAD-MOD shows a lot of wiggles (node-to-node or high-frequency oscillations). This can be avoided by adding some 4th-order artificial dissipation to the simulation. However, as the idea is to keep the same numerical setup for all the simulations performed, it has been decided to keep the results as they are shown. Indeed, the results for RUE could be biased by this additional dissipation term.

Figure 5.41 displays the segregation profiles. QUAD-MOD and 2ΦEASM3 agree very well with the Lagrangian results. As a matter of fact, the agreement is better in this case than in LR_St1_# case. There is less preferential concentration effect at this inertia, the slab being flattened, the segregation peaks at the limits of the jet present in LR_St1_# case (cf Fig 5.18(c)) have disappeared. The segregation then shows a more uniform profile. The model correction increases the segregation for all models, that is largely overestimated. All the corrected profiles are very similar. Similarly, AXISY, which produces a very flat profile at the periphery, produces very small values of segregation in this region.

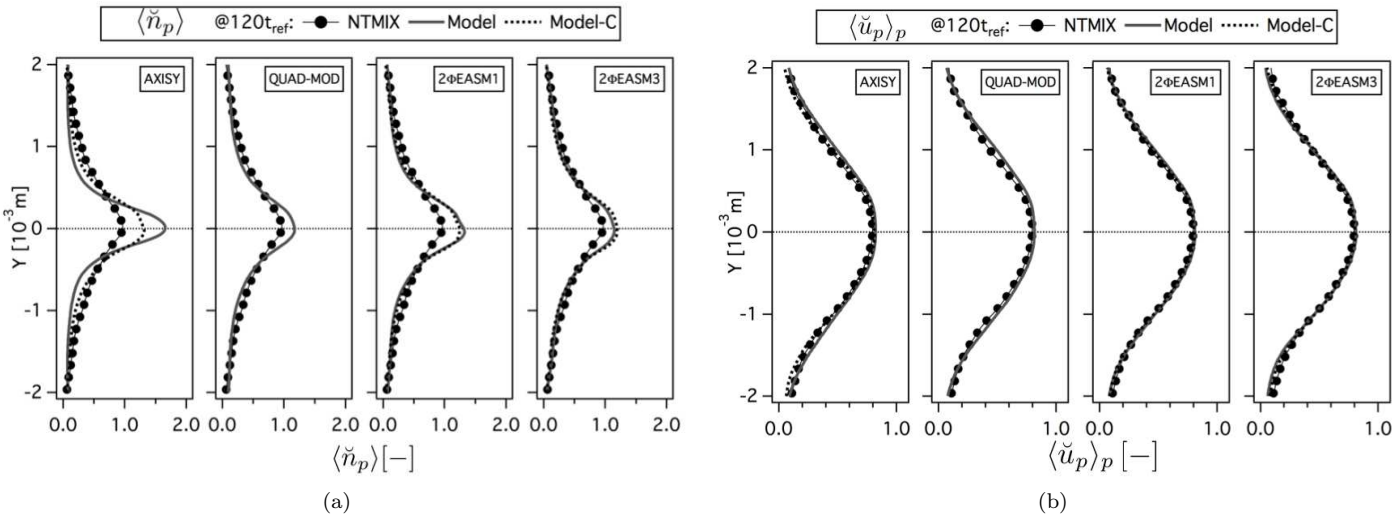

Figure 5.39: *Comparison of Eulerian and Lagrangian (a) mean particle number density (< $\breve{n}_p$ >, normalized by the initial particle number density at the center of the slab) and (b) mean particle velocity in X-direction (< $\breve{u}_p$ >$_p$, normalized by the initial particle velocity in X-direction at the center of the slab) at 120t_{ref}. LR_St3_# case.*

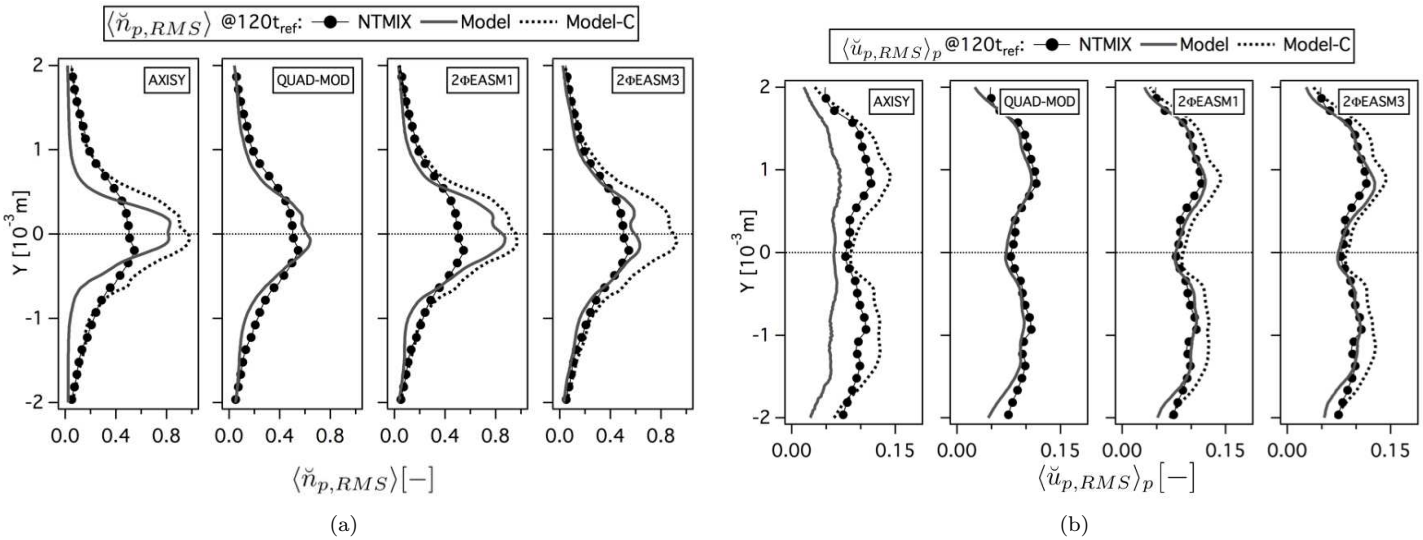

(a) (b)

Figure 5.40: *Comparison of Eulerian and Lagrangian (a) RMS particle number density (*$< \breve{n}_{p,RMS} >$*, normalized by the initial particle number density at the center of the slab) and (b) RMS particle velocity in X-direction (*$< \breve{u}_{p,RMS} >_p$*, normalized by the initial particle number density at the center of the slab)at* $120t_{ref}$*. LR_St3_# case.*

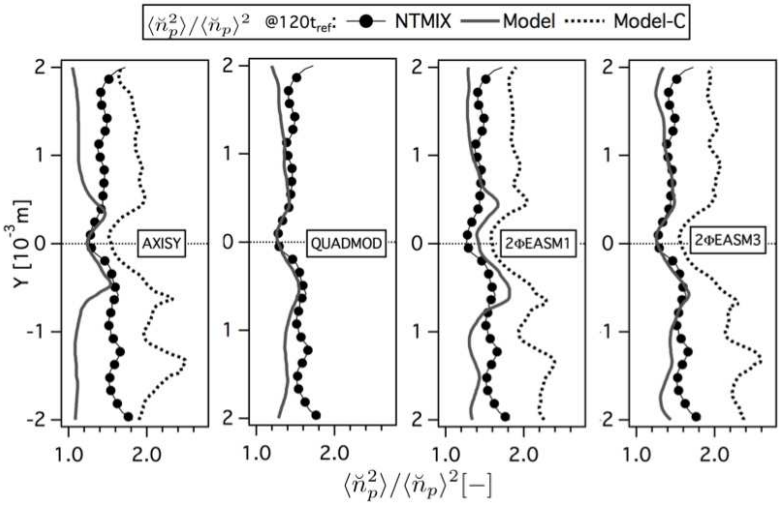

Figure 5.41: *Comparison of Eulerian and Lagrangian RMS particle segregation (*$< \breve{n}_p^2 > / < \breve{n}_p >^2$*) at* $120t_{ref}$*. LR_St3_# case.*

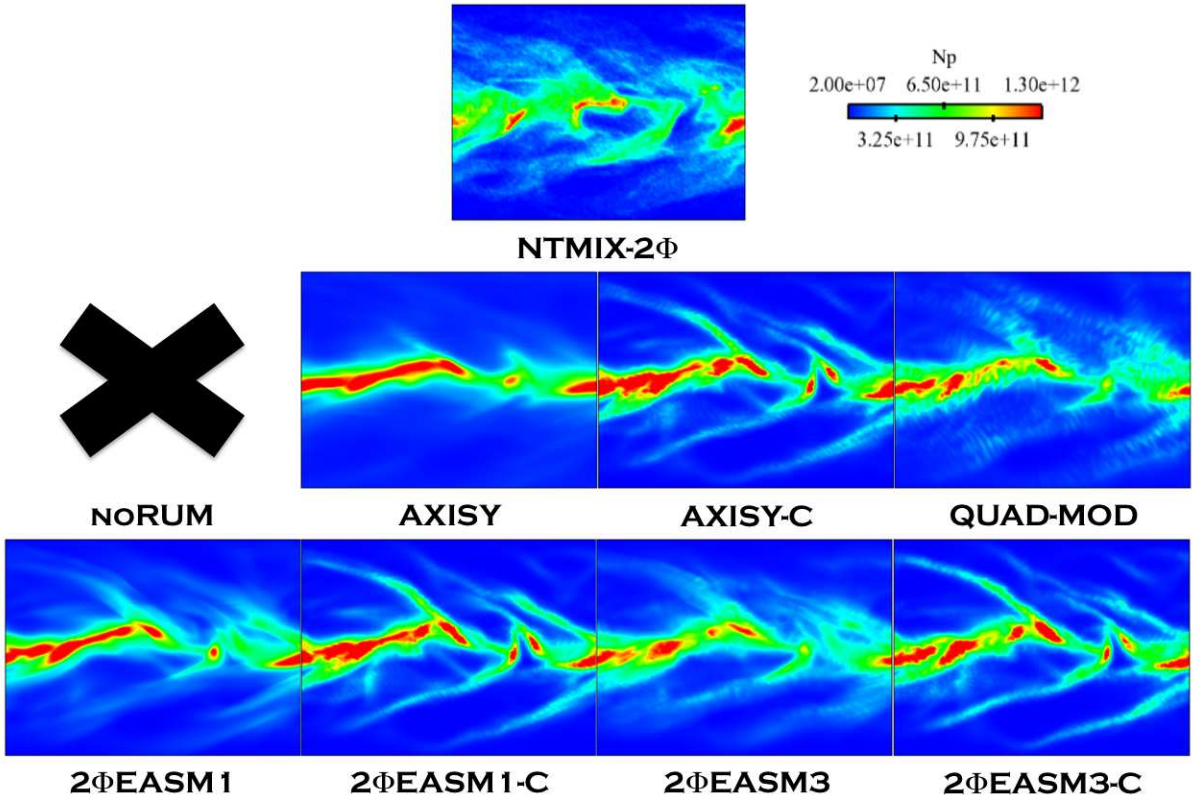

Figure 5.42: *Comparison of Lagrangian (NTMIX-2Φ) and Eulerian particle number density fields (N_p) at $120t_{ref}$. LR_St3_# case.*

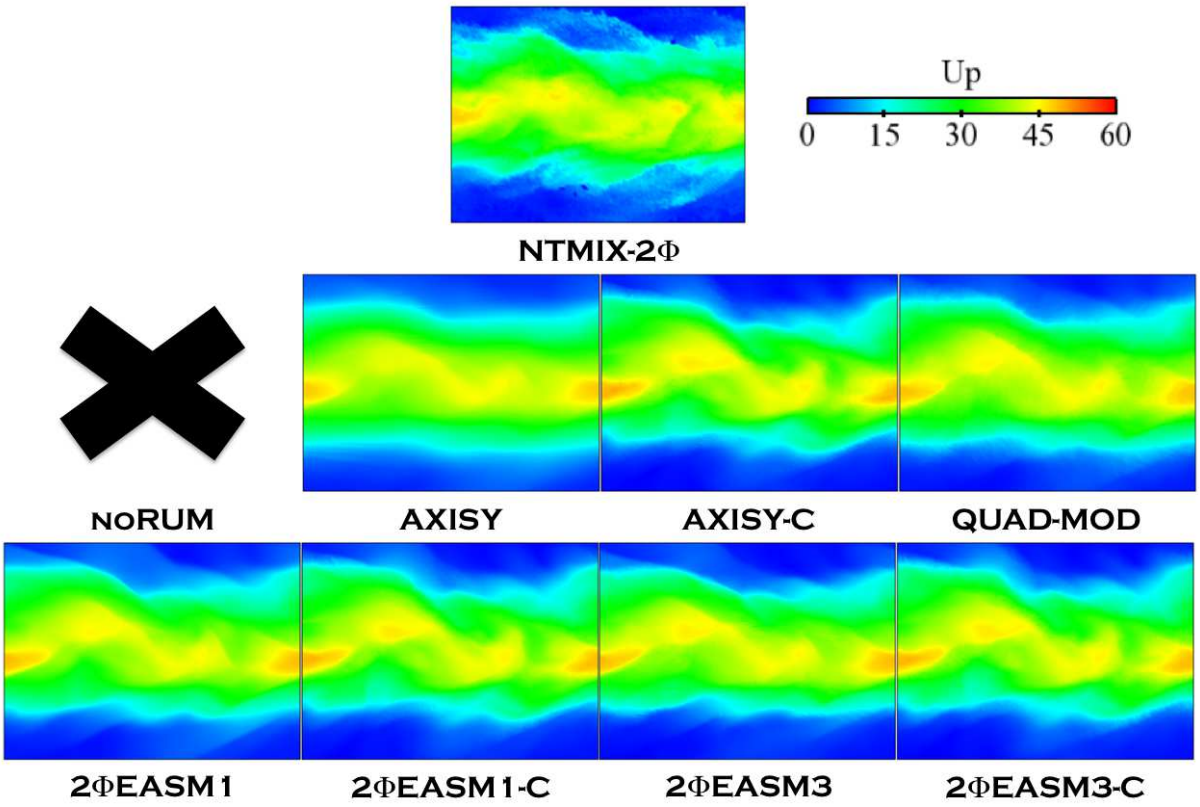

Figure 5.43: *Comparison of Lagrangian (NTMIX-2Φ) and Eulerian particle velocity magnitude fields (U_p) at $120t_{ref}$. LR_St3_# case.*

High order moments

The analysis of the high-order moments reveals that, globally, the models have the same behavior for the high inertia case ($St = 3$) as observed in the mean inertia case ($St = 1$, cf Section 5.3). Indeed, 2ΦEASM3 and QUAD-MOD give the best agreement with the Lagrangian results. Figure 5.44(a) shows the mean RUE profiles. QUAD-MOD performs very well at the periphery of the slab but it is not able to recover the good level of the peaks and at the center of the jet. 2ΦEASM1 gives very similar predictions. The correction degrades the performances of the model, giving highly underestimated RUE levels. The same happens with 2ΦEASM3-C, while 2ΦEASM3 predicts the good shape and level of the profile, 2ΦEASM3-C underestimates the level over the whole width of the slab. The correction has the same impact on AXISY, AXISY-C underestimating the results. At the same time, AXISY predicts (as it did for LR_St1_# case) too high RUE values, especially for the peaks location. Figure 5.44(b) shows the mesoscopic energy ($\breve{q}_p^2$) profile and the total energy. The agreement of the non-linear models is very good when the correction is not taken into account. Indeed, the corrected models give good predictions of total agitation but overestimate the mesoscopic energy compensating the underestimation of the RUM energy. The linear model AXISY does not capture well the levels with or without correction. The performances on the RUE can be linked to the predictions of the RUM productions. As stated in Section 5.3.2, RUM production by shear is more important than RUM production by compression. For this reason, models that underestimate P_{RUM}^{Shear} (all the corrected models) underestimate as well the RUE. AXISY shows at high inertia the same behavior as observed in Fig. 5.23(c) for a mean inertial case. Even when the production by compression, $P_{RUM}^{Compression}$, Fig. 5.45(b), acts as a dissipation, P_{RUM}^{Shear} is so overestimated that it cannot be overcome by the dissipative effects and thus, the RUE level is too high. In this case, it is 2ΦEASM3 which gives the best predictions both for the shear and the compression productions. For comparisons, QUAD-MOD produces a level of P_{RUM}^{Shear} too low and overestimates $P_{RUM}^{Compression}$.

The results for the components of the deviatoric RUM stress tensor are in agreement with those of LR_St1_# case. Indeed, AXISY slightly underestimates the diagonal components, but due to the huge overestimation of the shear component, it shows too high values of P_{RUM}^{Shear} and thus of $\delta\breve{q}_p$. When applying the correction to this model, the levels of all components are damped resulting in productions and RUE levels that are too low (Figs. 5.46 and 5.47). QUAD-MOD slightly underestimates the diagonal components but gives very good agreement for the shear component (the most important) and thus predicts acceptable values of RUE. 2ΦEASM1 model has an intermediate behavior between AXISY and AXISY-C. In any case, it is 2ΦEASM3 that gives the best predictions for the components of the tensor, the productions as well as for the energies. The instantaneous RUE fields shown in Fig. 5.48 confirm this statement. 2ΦEASM1 and 2ΦEASM3 produce fields in very good agreement with NTMIX-2Φ. 2ΦEASM3, however, reproduces better local RUE values. QUAD-MOD is also able to reproduce the shape of the RUE field, however, wiggles are clearly present.

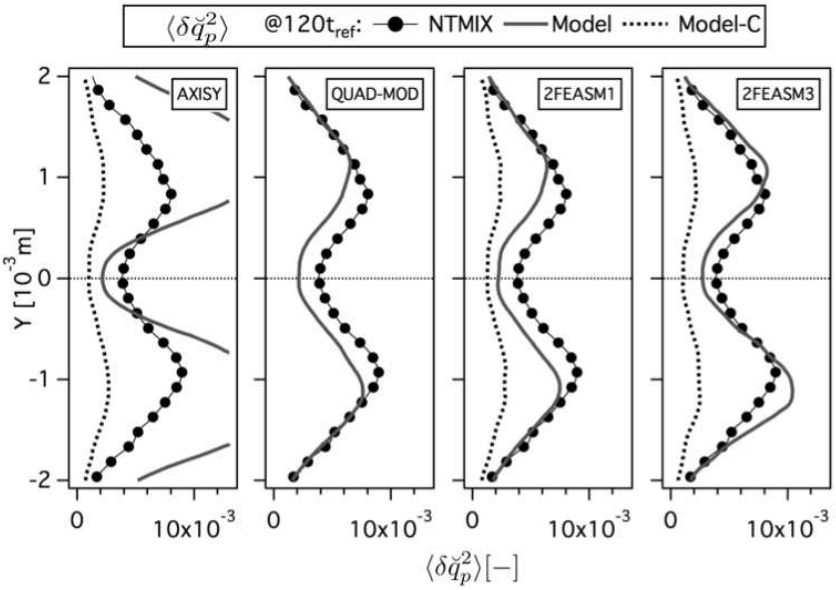

(a)

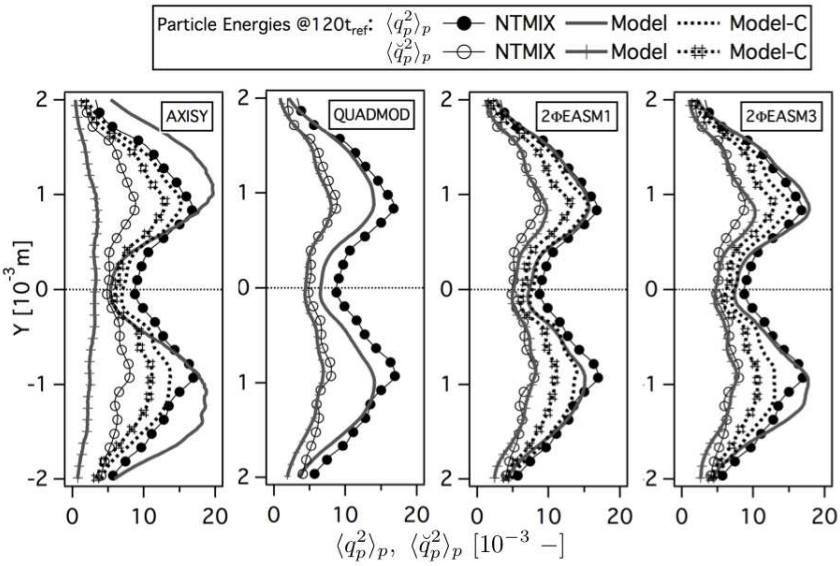

(b)

Figure 5.44: *Comparison of Eulerian and Lagrangian (a) mean Random Uncorrelated Energy ($< \delta \breve{q}_p >_p$) and (b) mean total ($\langle q_p^2 \rangle_p$) and mesoscopic ($\langle \breve{q}_p^2 \rangle_p$) particle energies at $120t_{ref}$. Normalized by the square of the initial particle velocity in X-direction at the center of the slab. LR_St3_# case.*

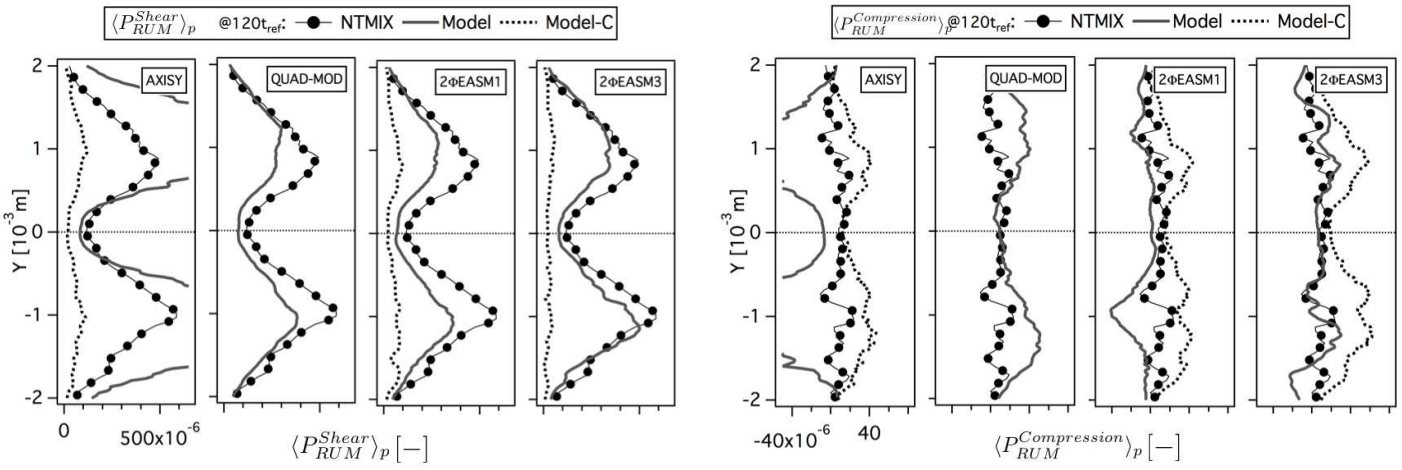

(a) (b)

Figure 5.45: *Comparison of Eulerian and Lagrangian (a) mean production of RUM energy by shear ($< P_{RUM}^{Shear} >_p$) and (b) mean productions of RUM energy by compression ($< P_{RUM}^{Compression} >_p$) at $120t_{ref}$. Normalized by the square of the initial particle velocity in X-direction at the center of the slab and the reference time (t_{ref}). LR_St3_# case.*

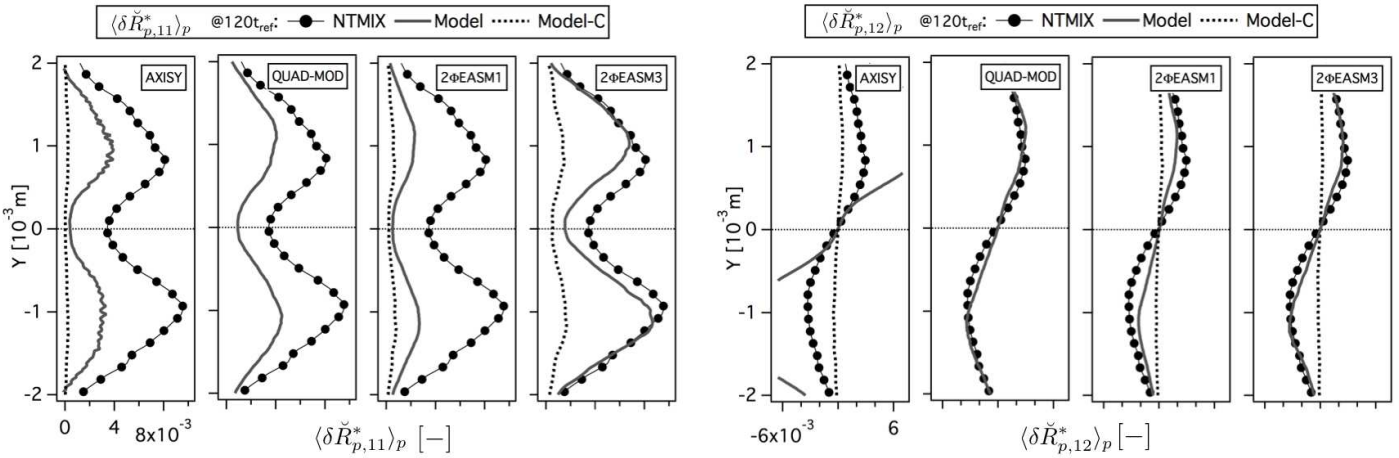

(a) (b)

Figure 5.46: *Comparison of Eulerian and Lagrangian (a) mean deviatoric RUM stress tensor XX component ($< \delta \breve{R}_{p,11}^{*} >_p$) and (b) mean deviatoric RUM stress tensor XY component ($< \delta \breve{R}_{p,12}^{*} >_p$) at $120t_{ref}$. Normalized by the square of the initial particle velocity in X-direction at the center of the slab. LR_St3_# case.*

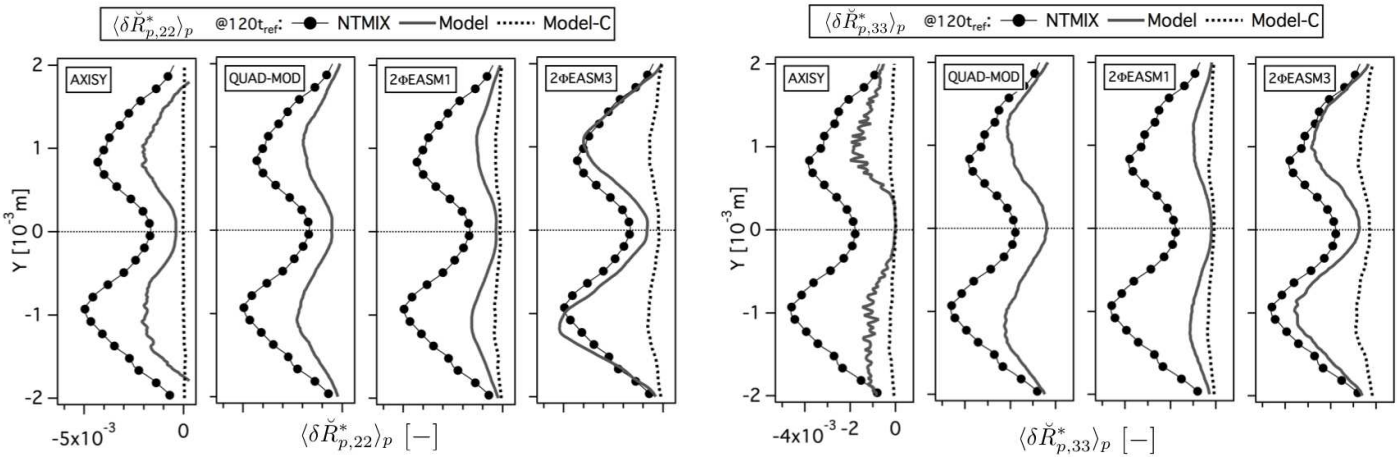

(a) (b)

Figure 5.47: *Comparison of Eulerian and Lagrangian (a) mean deviatoric RUM stress tensor YY component ($< \delta \breve{R}^*_{p,22} >_p$) and (b) mean deviatoric RUM stress tensor ZZ component ($< \delta \breve{R}^*_{p,33} >_p$) at $120t_{ref}$. Normalized by the square of the initial particle velocity in X-direction at the center of the slab. LR_St3_# case.*

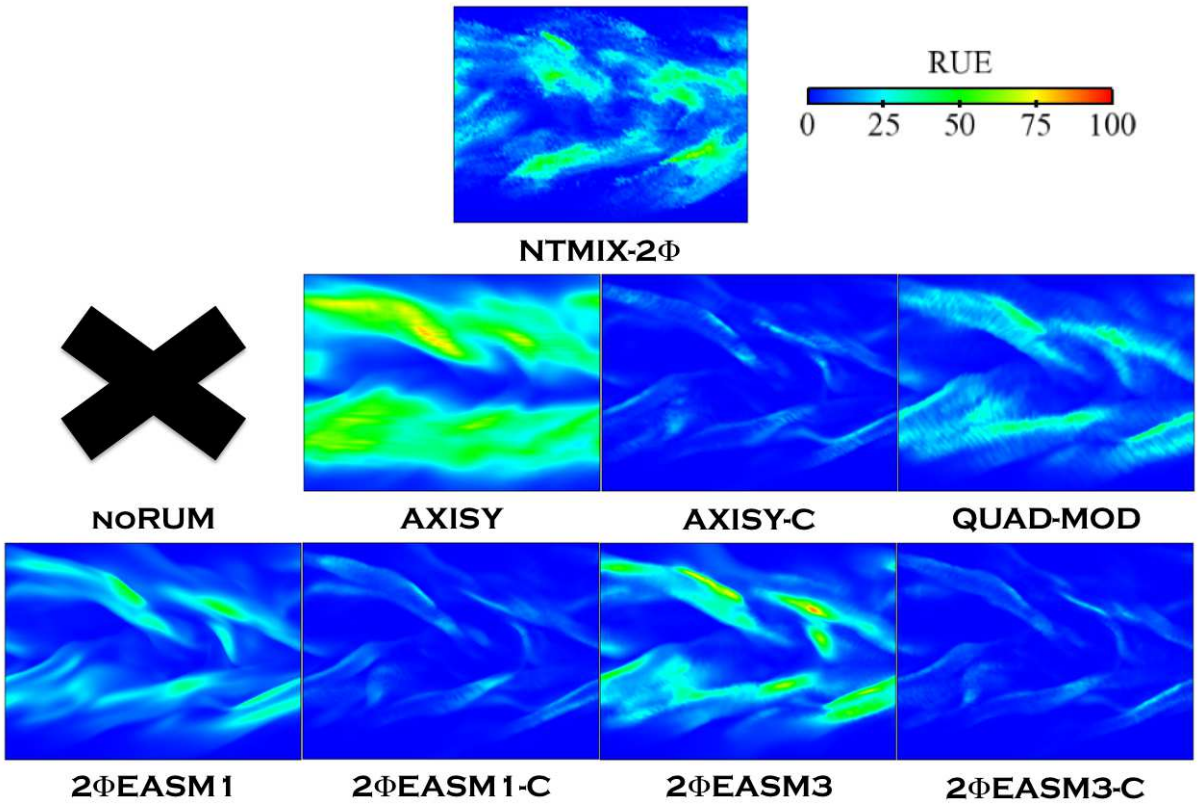

Figure 5.48: *Comparison of Lagrangian (NTMIX-2Φ) and Eulerian Random Uncorrelated Energy ($\delta \breve{q}_p$) at $120t_{ref}$. LR_St3_# case.*

Effect of Artificial Dissipation

For this case (LR_St3_#), where AD is not powerful enough to allow the whole calculation without RUM (noRUM) to finish, the activation of the AV sensor is very reduced when the models giving the best predictions (2ΦEASM3 and QUAD-MOD) are used. This effect can be observed in Fig. 5.49 where the profiles of the AV sensor are shown. Again, as it happened with LR_St1_# case, the AD activates when the RUM models do not predict the correct level of RUE. This fact is confirmed by Fig 5.50 where the instantaneous fields of AV sensor at $120t_{ref}$ are shown. Indeed, non-corrected 2ΦEASM# models do not need much artificial viscosity. QUAD-MOD however, needs much more artificial viscosity to overcome the problems due to the high-frequency oscillations.

In fact, it seems that, unexpectedly, the AV sensor CMS-Lite activates at the same locations where the RUE is maximal. This may be due to a need to diffuse the steep concentration and velocity gradients. When the RUM model correctly predicts the RUE field, the RUE diffuses those gradients, but in those cases where the RUE is not active or its value is too low to diffuse the gradients, the sensor activates to stabilize the simulation. The AV sensor has not been developped to this purpose and the effects observed are more a matter of coincidence.

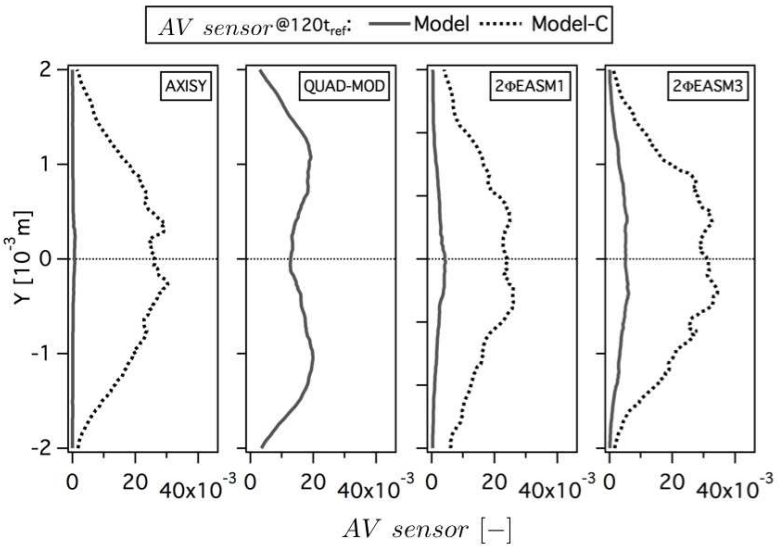

Figure 5.49: *Mean Artificial Viscosity sensor activation at $120t_{ref}$. LR_St3_# case.*

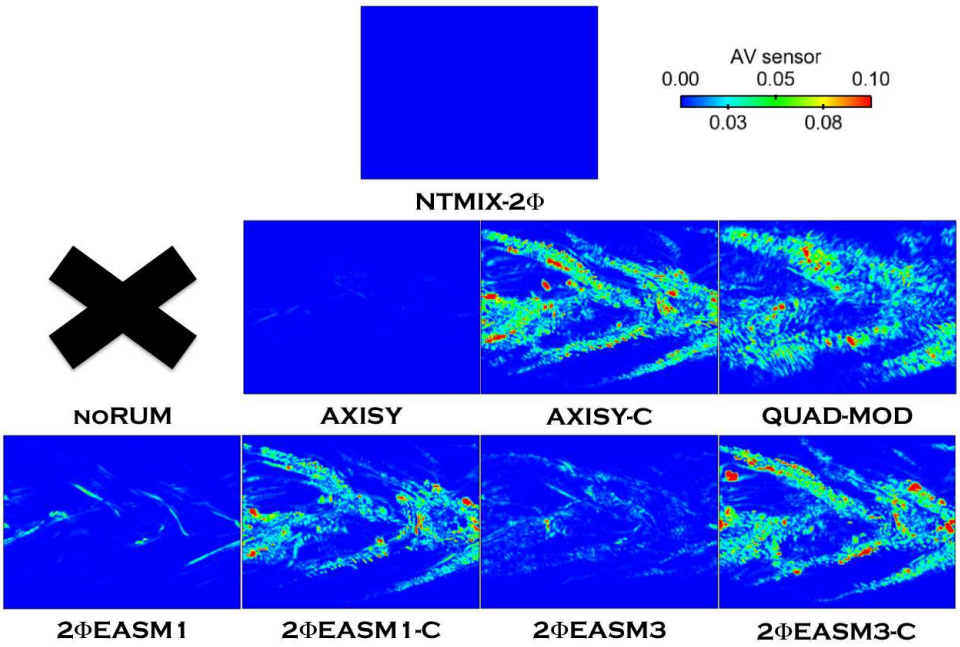

Figure 5.50: *Fields of Artificial Viscosity sensor activation at* $120t_{ref}$*. LR_St3_# case.*

5.4.2 Low inertia case: Stokes=0.33

Sections 5.3 and 5.4.1 have shown the results of the RUM models proposed in Chapter 4 in a low turbulence case for mean ($St \sim 1$) and high ($St \sim 3$) inertia respectively. From the assessment of the models, both qualitatively and quantitatively, two models (QUAD-MOD and 2ΦEASM3) have been identified as the ones giving the best performances when compared with the Lagrangian reference.

In this Section, the capability of QUAD-MOD and 2ΦEASM3 to correctly predict the low and high order moments in a case of low turbulence and low inertia is analyzed. The Reynolds number keeps the same ($Re^{ac} = 5500$) but the Stokes number is now $St \sim 0.33$. The particle relaxation time is $\tau_{fp}^{F} \sim 4.33$. This case is in fact an extreme case. Indeed, as already pointed out, the preferential concentration effect is maximal at $St = 0.3$, which creates empty spaces close to very high concentration spots. The steep concentration gradients between both zones are very difficult to handle numerically and the Artificial Diffusion is expected not to be powerful enough to diffuse them.

Only noRUM, VISCO, QUAD-MOD and 2ΦEASM3 models have been tested in this case. noRUM crashed shortly after $5t_{ref}$. In contrast to LR_St1_# and LR_St3_# cases, VISCO model was able to complete the whole simulation. This is due to the dependency of the model to $\breve{\tau}_p$ (Eq. 4.9). Since $\delta\breve{R}^{*}_{p,ij}$ is directly proportional to $\breve{\tau}_p$ in the VISCO model, the RUE production at small inertia (small particle response time) is reduced when decreasing the Stokes number. In this case, the overestimation of RUE observed in cases St=1 and St=3 is no longer present.

Results are shown at $80t_{ref}$. Complementary data at 5, 20 and $40t_{ref}$ can be found in Appendix E.

Figures 5.51(a) and 5.51(b) show the mean particle number density and the mean particle velocity profiles. Figure 5.52 shows the RMS particle number density and particle velocity profiles, included here for the sake of simplicity. Figure 5.53 shows the mean segregation profiles. The three models (VISCO, QUAD-MOD and 2ΦEASM3) give the same results for the low order moments, the mean and the RMS quantities and the segregation. The RMS particle number density and segregation profiles are underestimated by all models. There are no differences on the instantaneous fields either (Figs. 5.54 and 5.55). None of the models captures the empty spaces inside the slab as predicted by the Lagrangian reference. This is due to the reduced contribution of RUE in this configuration (as conjectured).

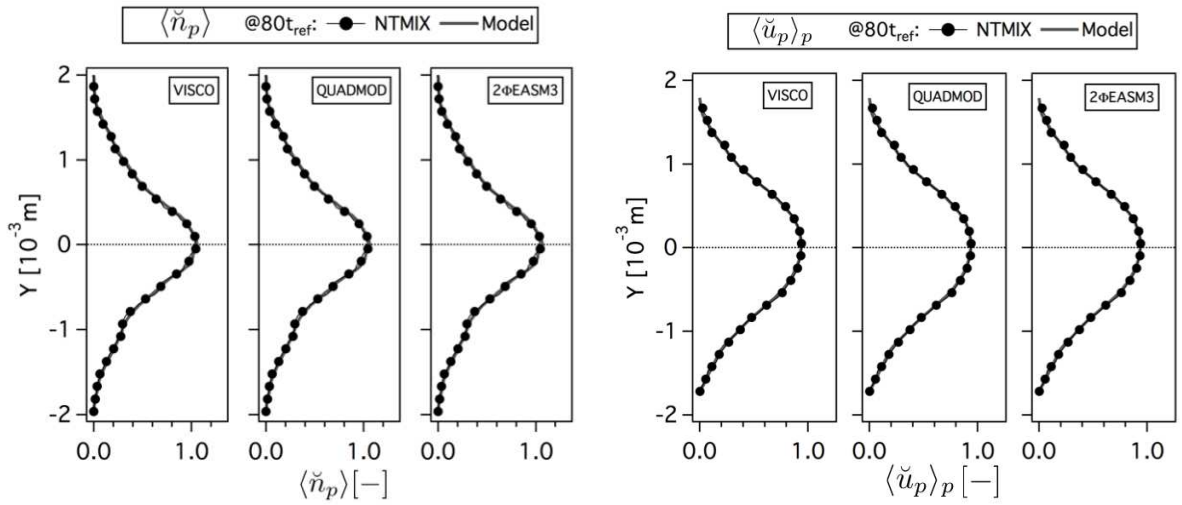

(a) (b)

Figure 5.51: *Comparison of Eulerian and Lagrangian (a) mean particle number density (< $\breve{n}_p$ >, normalized by the initial particle number density at the center of the slab) and (b) mean particle velocity in X-direction (< $\breve{u}_p$ >$_p$, normalized by the initial particle velocity in X-direction at the center of the slab) at 80t_{ref}. LR_St033_# case.*

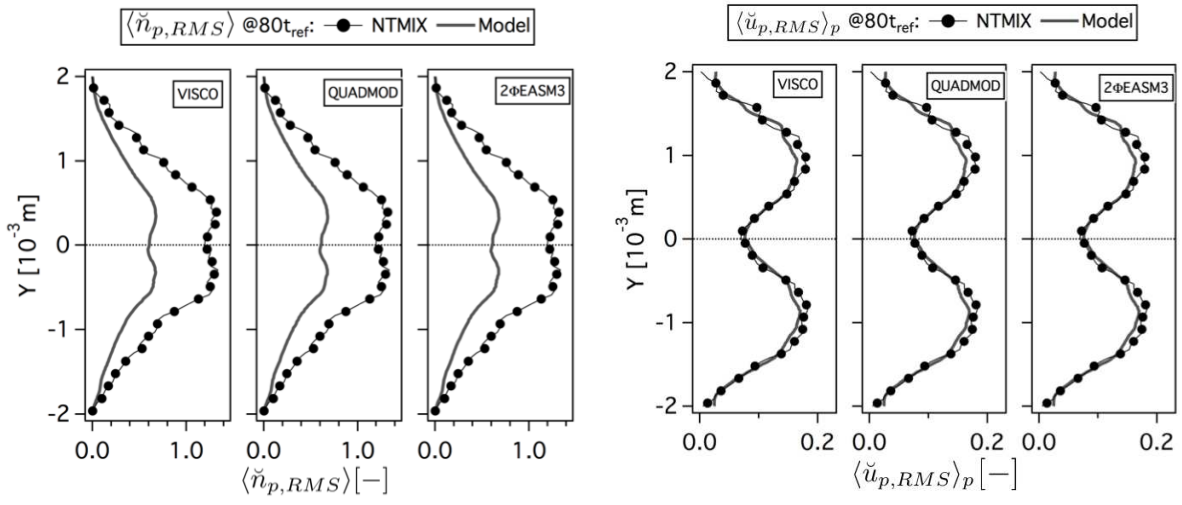

(a) (b)

Figure 5.52: *Comparison of Eulerian and Lagrangian (a) RMS particle number density (< $\breve{n}_{p,RMS}$ >, normalized by the initial particle number density at the center of the slab) and (b) RMS particle velocity in X-direction (< $\breve{u}_{p,RMS}$ >$_p$, normalized by the initial particle number density at the center of the slab) at 80t_{ref}. LR_St033_# case.*

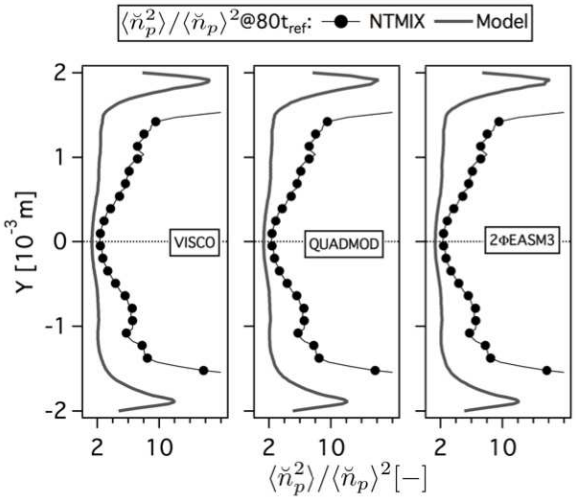

Figure 5.53: *Comparison of Eulerian and Lagrangian RMS particle segregation ($< \check{n}_p^2 > / < \check{n}_p >^2$) at $80t_{ref}$. LR_St033_# case.*

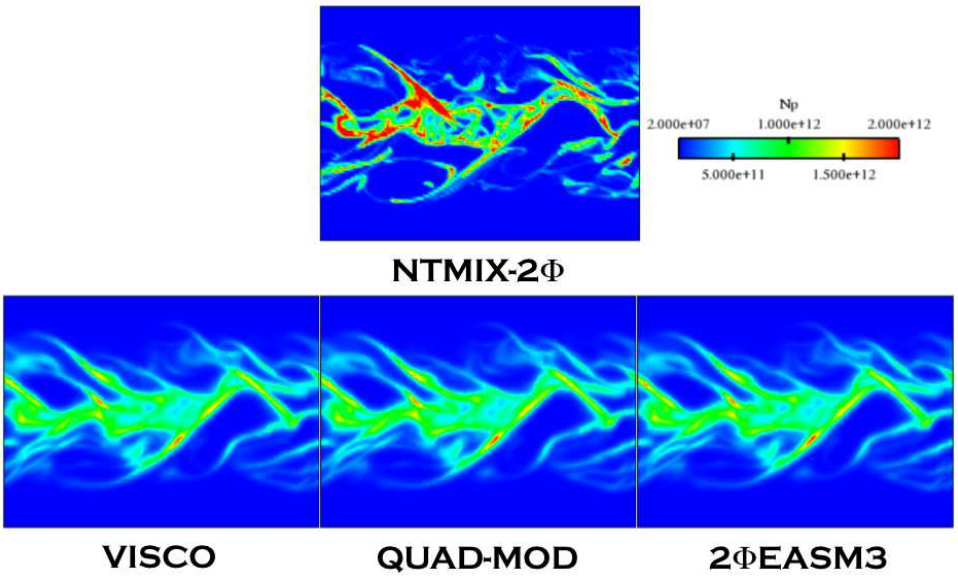

Figure 5.54: *Comparison of Lagrangian (NTMIX-2Φ) and Eulerian particle number density (N_p) at $80t_{ref}$. LR_St033_# case.*

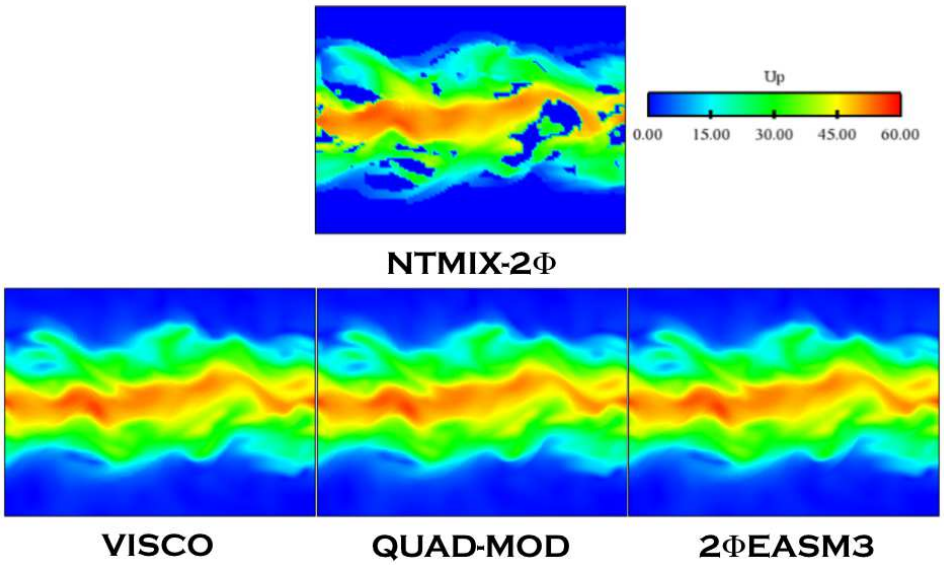

Figure 5.55: *Comparison of Lagrangian (NTMIX-2Φ) and Eulerian particle velocity magnitude (U_p) at $80t_{ref}$. LR_St033_# case.*

Indeed, compared to $\breve{q}_p^2$, $\delta\breve{q}_p$ is much smaller (Figs. 5.56(a) and 5.56(b)). The main contribution to the total particle agitation comes from the mesoscopic energy ($\breve{q}_p^2$) and thus the RUM has a very limited effect. However, Fig. 5.56(a) shows that VISCO is not able to produce the correct level of RUE. Even when the low order moments are well predicted, this model will not work in configurations with collisions or coalescence without being modified (besides the fact that it crashes for mean and high inertia). On the other hand, QUAD-MOD and 2ΦEASM3 provide very good agreement with the Lagrangian reference. They give very good results for the low order moments providing the correct repartition between the mesoscopic and the RUE at the same time. Indeed, the RUM productions (Fig. 5.57) as well as the deviatoric RUM tensor components (Figs. 5.58 and 5.59) are very accurately predicted by both models, whose results are in fact very similar.

The qualitative analysis of the instantaneous fields of RUE shows that, while VISCO underestimates the RUE, QUAD-MOD and 2ΦEASM3 correctly predict the locations where the RUE is predicted by NTMIX-2Φ. However, only the largest structures are reproduced. This is probably due to a lack of resolution of the Eulerian calculation (Dombard (2011)) which prevents from capturing the small structures caused by the high segregation.

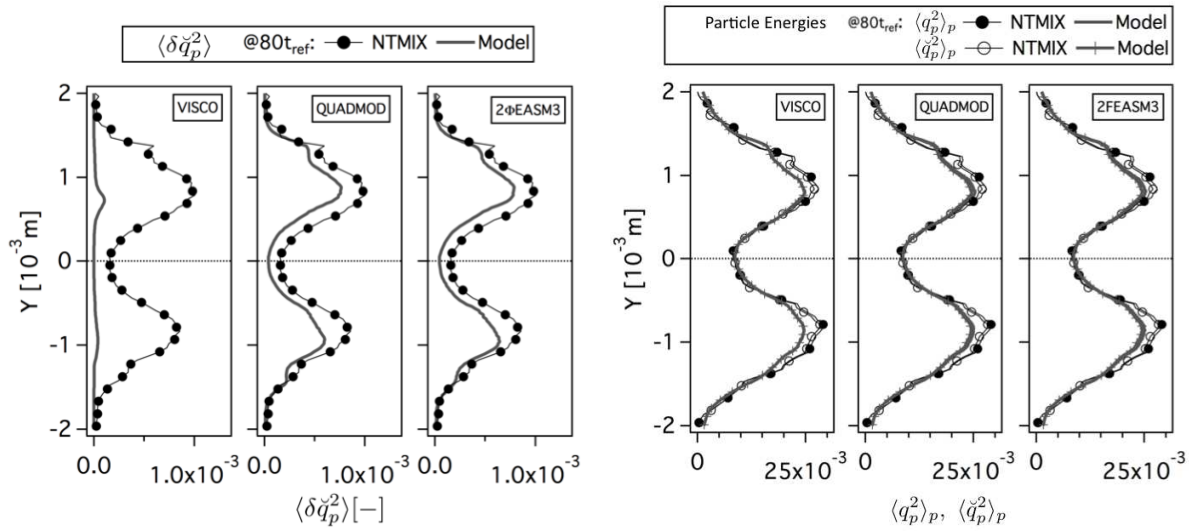

(a) (b)

Figure 5.56: *Comparison of Eulerian and Lagrangian (a) mean Random Uncorrelated Energy (*$< \delta\breve{q}_p >_p$*) and (b) mean total (*$\langle q_p^2\rangle_p$*) and mesoscopic (*$\langle\breve{q}_p^2\rangle_p$*) particle energies at* $80t_{ref}$*. Normalized by the square of the initial particle velocity in X-direction at the center of the slab. LR_St033_# case.*

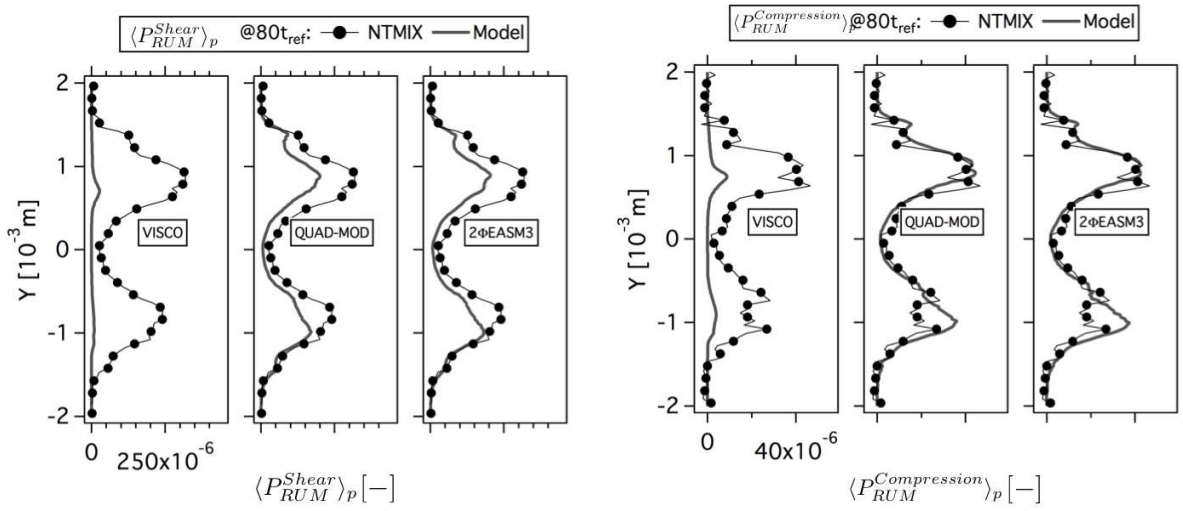

(a) (b)

Figure 5.57: *Comparison of Eulerian and Lagrangian (a) mean production of RUM energy by shear ($< P^{Shear}_{RUM} >_p$) and (b) mean productions of RUM energy by compression ($< P^{Compression}_{RUM} >_p$) at $80t_{ref}$. Normalized by the square of the initial particle velocity in X-direction at the center of the slab and the reference time (t_{ref}). LR_St033_# case.*

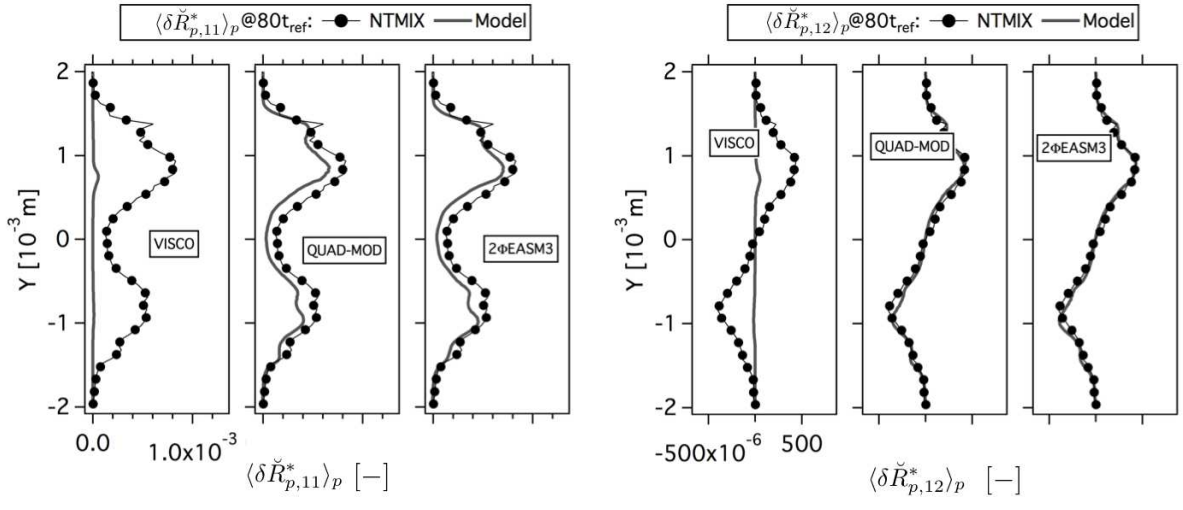

(a) (b)

Figure 5.58: *Comparison of Eulerian and Lagrangian (a) mean deviatoric RUM stress tensor XX component ($< \delta\breve{R}^*_{p,11} >_p$) and (b) mean deviatoric RUM stress tensor XY component ($< \delta\breve{R}^*_{p,12} >_p$) at $80t_{ref}$. Normalized by the square of the initial particle velocity in X-direction at the center of the slab. LR_St033_# case.*

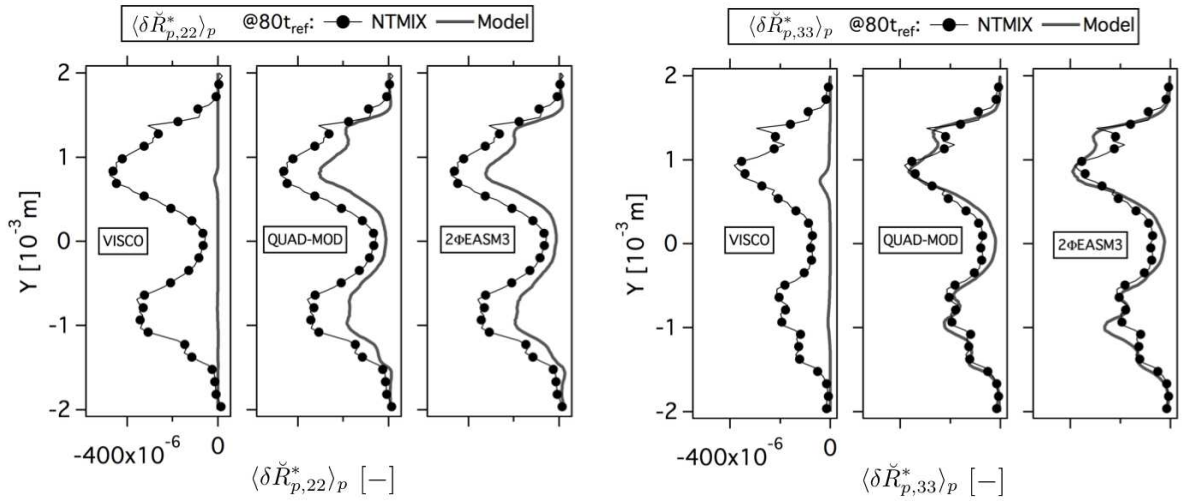

(a) (b)

Figure 5.59: *Comparison of Eulerian and Lagrangian (a) mean deviatoric RUM stress tensor YY component ($< \delta \check{R}^*_{p,22} >_p$) and (b) mean deviatoric RUM stress tensor ZZ component ($< \delta \check{R}^*_{p,33} >_p$) at $80t_{ref}$. Normalized by the square of the initial particle velocity in X-direction at the center of the slab. LR_St033_# case.*

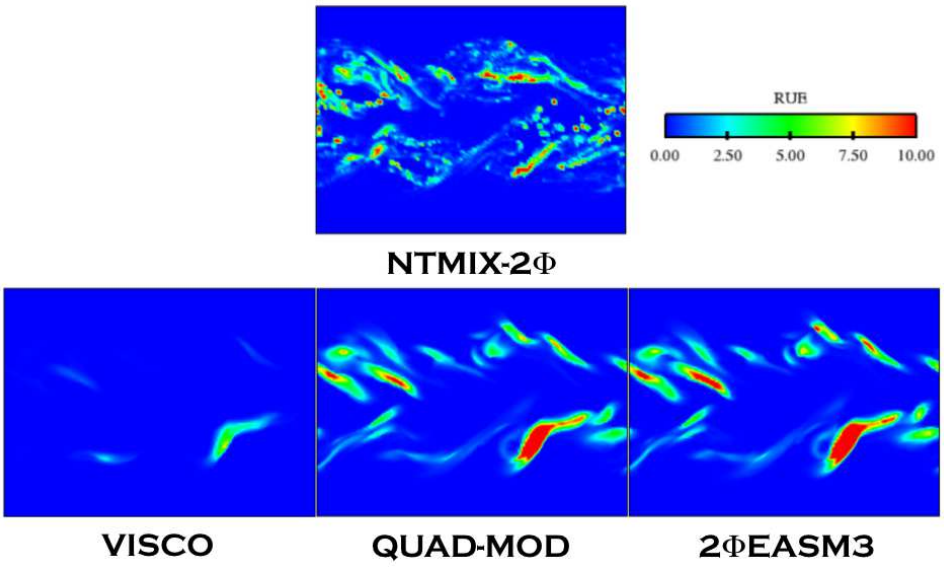

Figure 5.60: *Comparison of Lagrangian (NTMIX-2Φ) and Eulerian Random Uncorrelated Energy ($\delta \check{q}_p$) at $80t_{ref}$. LR_St033_# case.*

5.5 High turbulent conditions

The performances of QUAD-MOD and 2ΦEASM3 models have been until now validated in a low turbulence case for three different inertia. However, the Reynolds numbers encountered in industrial configurations are very high and flows are, in general, much more turbulent. In this Section, both models are evaluated in a higher turbulence case ($Re^{ac} = 20000$, $St \sim 1$, $\tau_{fp}^F \sim 9.44$). This study aims at assessing the validity of these models and their application in more complex cases such as the MERCATO test rig presented in Part IV.

From the *a priori* results, it is expected that the interaction of the particle phase with the vortical structures of the carrier phase (stronger that in case LR_St1_#) will create much more smaller structures in the dispersed phase fields that in the low turbulence case. The entrainment of the particles by the eddies will create very thin filaments that will afterwards detach from the jet. The capability of QUAD-MOD and 2ΦEASM3 to capture this kind of small structures is analyzed in this Section.

The Euler-Lagrange simulation of this case has been performed in a 256^3 mesh (i.e. the resolution has been doubled compared to the low turbulence computations). This means that in order to achieve the same level of comparison as for the previous sections, it may be necessary to double the resolution of the grid used in the Eulerian simulations of this case.

Figure 5.61 shows the statistics for the particle number density and particle velocity at $70t_{ref}$ ($7.41\tau_{fp}^F$). The agreement with the Lagrangian reference is again very good for both models. They also give very good results in the RMS particle velocity (Fig. 5.62(b)). However, the levels obtained for the RMS particle number density (Fig. 5.62(a)) are too low. Figure 5.63 shows the segregation profiles. Both models give the same results. The segregation levels are too low compared to the reference. This behavior has already been observed in the low turbulence cases. It is again probably due to a lack of resolution.

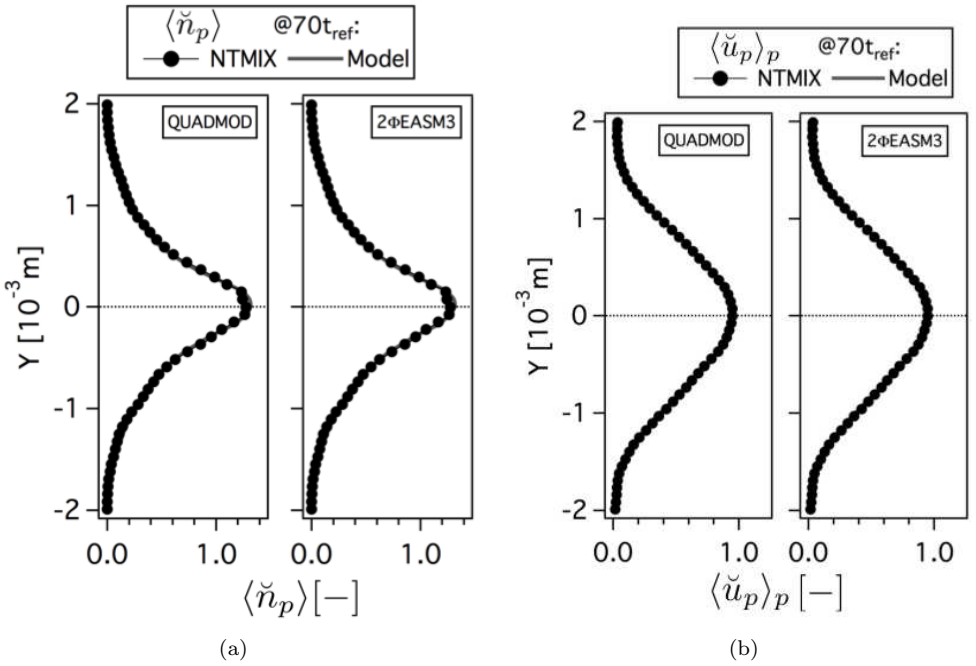

(a) (b)

Figure 5.61: *Comparison of Eulerian and Lagrangian (a) mean particle number density (< $\breve{n}_p$ >, normalized by the initial particle number density at the center of the slab) and (b) mean particle velocity in X-direction (< $\breve{u}_p$ >$_p$, normalized by the initial particle velocity in X-direction at the center of the slab) at $70t_{ref}$. HR_St1_# case.*

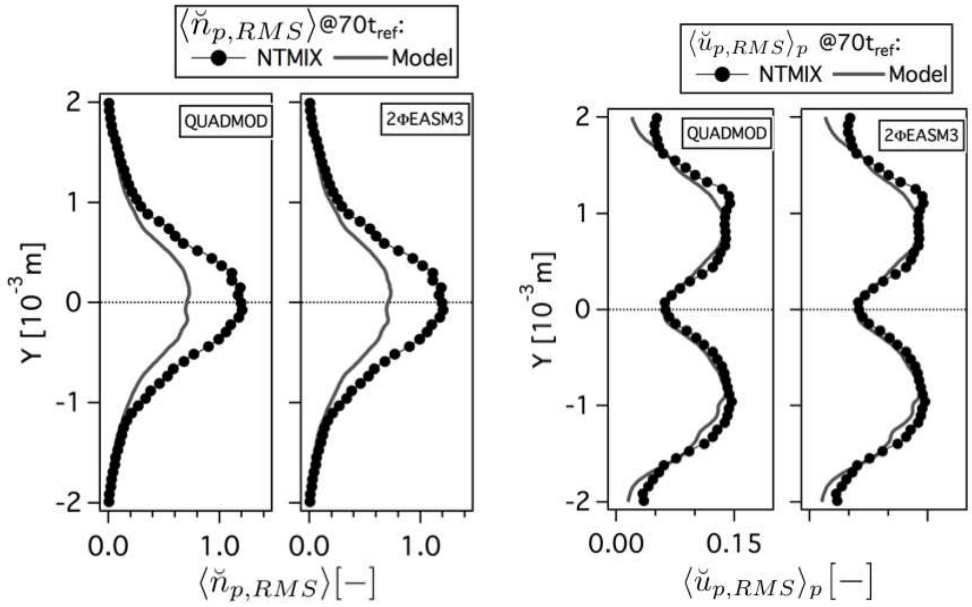

(a) (b)

Figure 5.62: *Comparison of Eulerian and Lagrangian (a) RMS particle number density (*$< \breve{n}_{p,RMS} >$*, normalized by the initial particle number density at the center of the slab) and (b) RMS particle velocity in X-direction (*$< \breve{u}_{p,RMS} >_p$*, normalized by the initial particle number density at the center of the slab)at* $70t_{ref}$*. HR_St1_# case.*

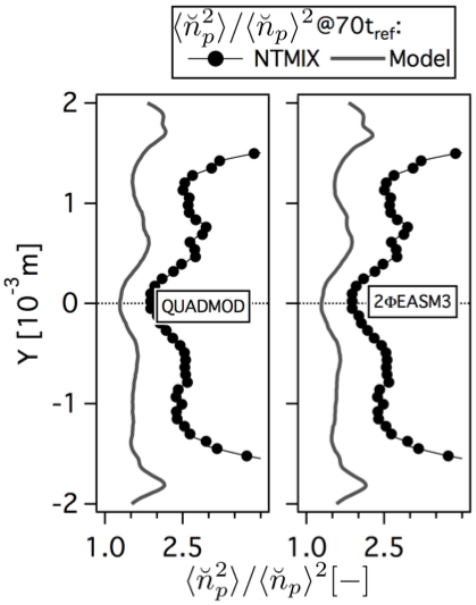

Figure 5.63: *Comparison of Eulerian and Lagrangian RMS particle segregation (*$< \breve{n}_p^2 > / < \breve{n}_p >^2$*) at* $70t_{ref}$*. HR_St1_# case.*

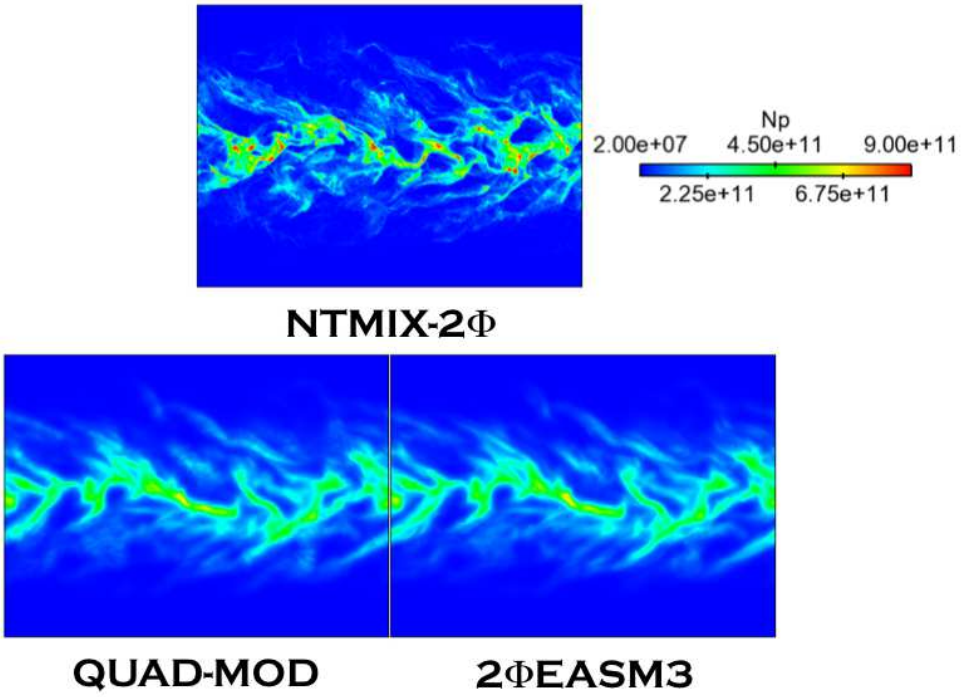

Figure 5.64: *Comparison of Lagrangian (NTMIX-2Φ) and Eulerian particle number density (N_p) at $70t_{ref}$. HR_St1_# case.*

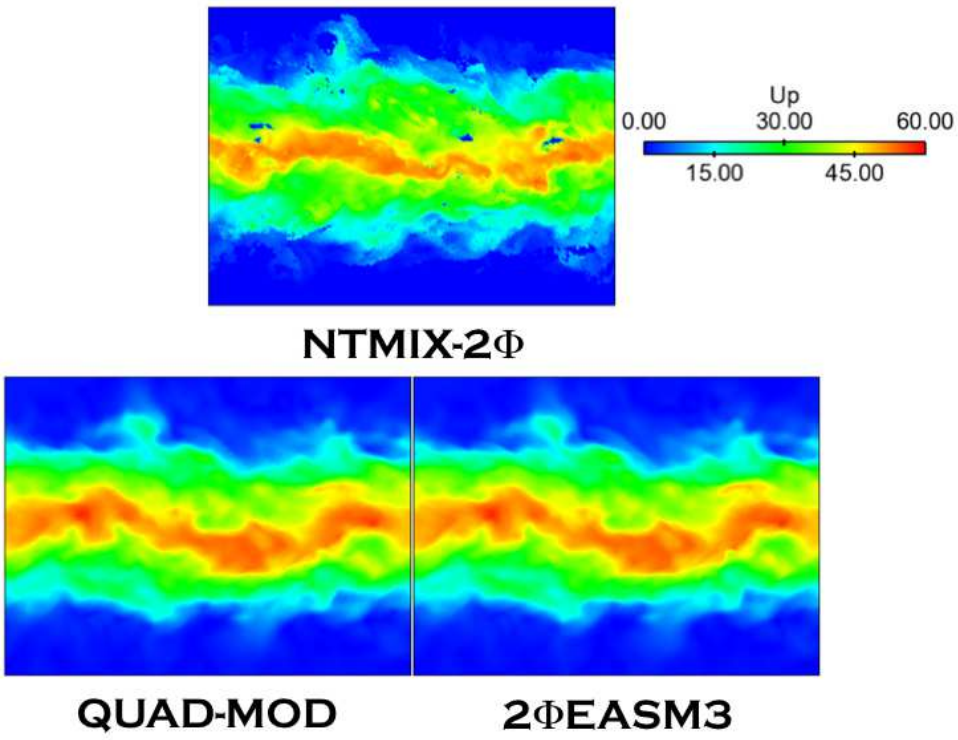

Figure 5.65: *Comparison of Lagrangian (NTMIX-2Φ) and Eulerian particle velocity magnitude (U_p) at $70t_{ref}$. HR_St1_# case.*

Although the resolution of the Eulerian grid may not be enough, both models show good agreement for the profiles of RUE (Fig. 5.66(a)). However, none of them captures the level reached at the upper border of the jet. Nevertheless, both closures are able to reproduce the non-symmetric profile. The production by shear (Fig. 5.67(a)) is well predicted by both models. $\delta\breve{R}^*_{p,12}$ is equally well reproduced (Fig. 5.68(b)). 2ΦEASM3 provides better agreement for the production by compression (Fig. 5.67(b)), which may come from a better balance between the components belonging to the diagonal of the deviatoric RUM tensor. Even when at first sight QUAD-MOD seems to provide better agreement, its level is good for $\delta\breve{R}^*_{p,11}$ and $\delta\breve{R}^*_{p,22}$ components and too low for $\delta\breve{R}^*_{p,33}$. On the other hand, 2ΦEASM3 gives very good $\delta\breve{R}^*_{p,22}$ results and an overestimation of the $\delta\breve{R}^*_{p,11}$ and $\delta\breve{R}^*_{p,33}$ components. But the total balance between both terms is better than for QUAD-MOD.

Finally, the analysis of the instantaneous fields confirms that both models give very similar results.

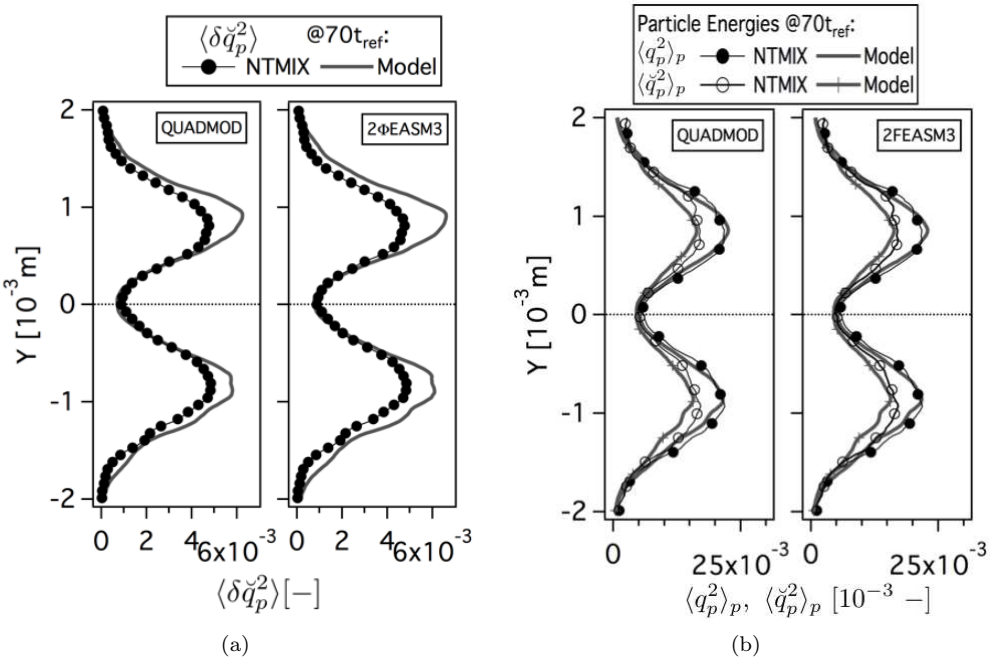

(a) (b)

Figure 5.66: *Comparison of Eulerian and Lagrangian (a) mean Random Uncorrelated Energy (*$< \delta\breve{q}_p >_p$*) and (b) mean total (*$\langle q_p^2\rangle_p$*) and mesoscopic (*$\langle\breve{q}_p^2\rangle_p$*) particle energies at 70*t_{ref}*. Normalized by the square of the initial particle velocity in X-direction at the center of the slab. HR_St1_# case.*

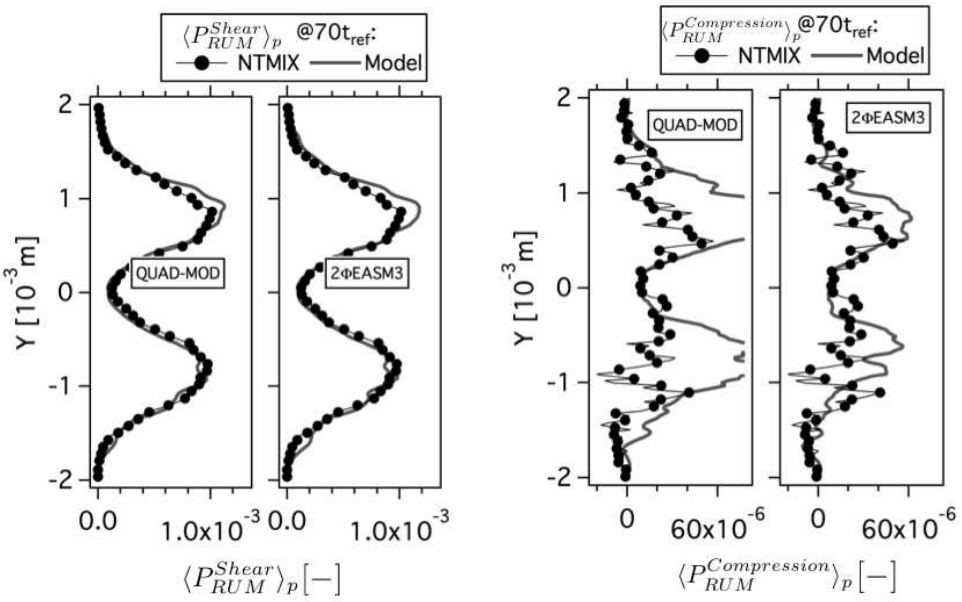

(a) (b)

Figure 5.67: *Comparison of Eulerian and Lagrangian (a) mean production of RUM energy by shear ($< P_{RUM}^{Shear} >_p$) and (b) mean productions of RUM energy by compression ($< P_{RUM}^{Compression} >_p$) at $70t_{ref}$. Normalized by the square of the initial particle velocity in X-direction at the center of the slab and the reference time (t_{ref}). HR_St1_# case.*

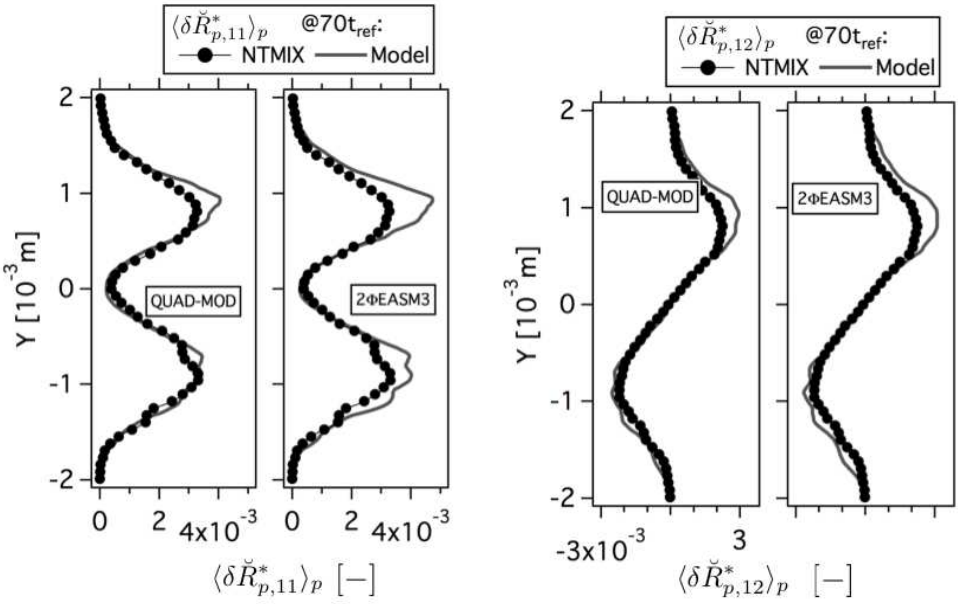

(a) (b)

Figure 5.68: *Comparison of Eulerian and Lagrangian (a) mean deviatoric RUM stress tensor XX component ($< \delta \breve{R}_{p,11}^* >_p$) and (b) mean deviatoric RUM stress tensor XY component ($< \delta \breve{R}_{p,12}^* >_p$) at $70t_{ref}$. Normalized by the square of the initial particle velocity in X-direction at the center of the slab. HR_St1_# case.*

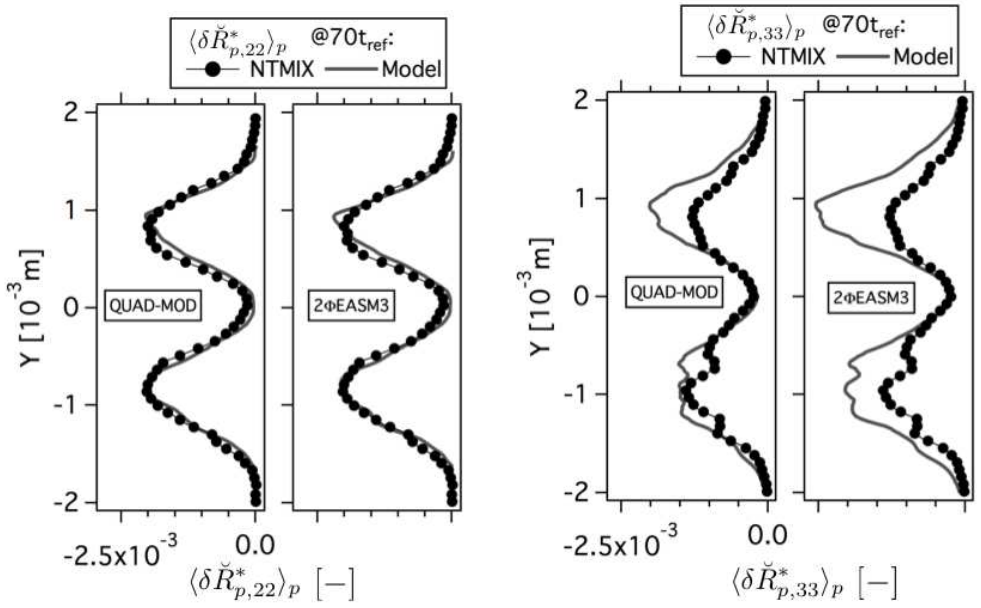

(a) (b)

Figure 5.69: *Comparison of Eulerian and Lagrangian (a) mean deviatoric RUM stress tensor YY component ($< \delta \breve{R}^*_{p,22} >_p$) and (b) mean deviatoric RUM stress tensor ZZ component ($< \delta \breve{R}^*_{p,33} >_p$) at $70t_{ref}$. Normalized by the square of the initial particle velocity in X-direction at the center of the slab. HR_St1_# case.*

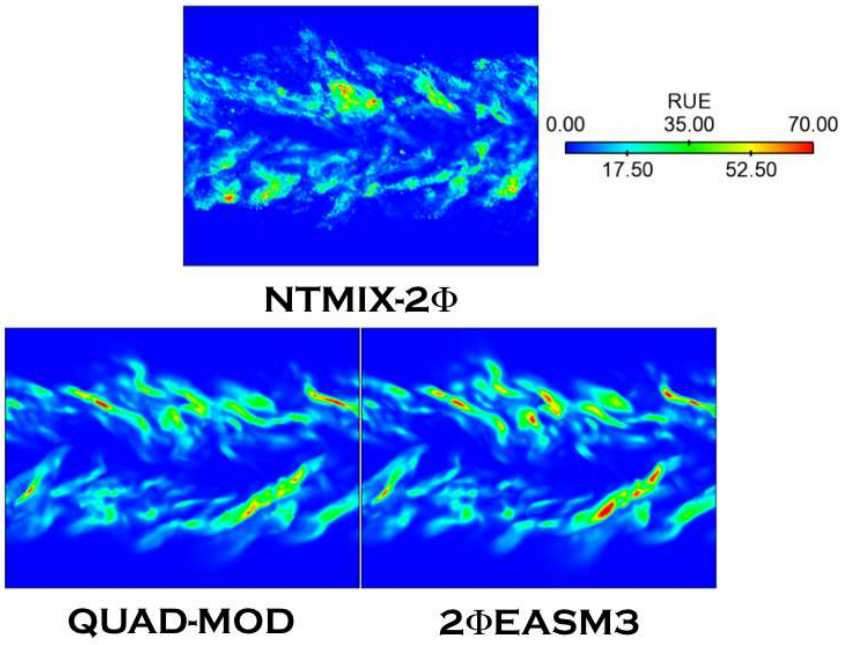

Figure 5.70: *Comparison of Lagrangian (NTMIX-2Φ) and Eulerian Random Uncorrelated Energy ($\delta \breve{q}_p$) at $70t_{ref}$. HR_St1_# case.*

5.5.1 Effect of mesh resolution

Case HR_St1 has been computed on a higher resolution mesh grid (512^3 computational cells) with AVBP for 2ΦEASM3 model. Results are compared with the lower resolution mesh (256^3) and with the reference (Eulerian fields obtained by projection from Euler-Lagrange simulation performed on a 256^3 grid). Due to computational limitations in time and memory, the simulation has only been performed up to $40t_{ref}$ and only the fields of particle number density, particle velocity and RUE stored. The fields corresponding to the RUM stress tensor components and the productions are not accesible for this simulation.

Figures 5.71(a) and 5.71(b) shows the plane averages of the mesoscopic particle number density and particle velocity respectively. Increasing the mesh resolution does not have an impact on the statistics of these two quantities. Indeed, no noticeable difference exists on the profiles of the mean quantities. On the contrary, the profiles of the RMS quantities (Figs. 5.72(a) and 5.72(b)) are improved when using a higher resolution mesh for the computations. The RMS particle number density is improved of 25% approximately. The improvement on the RMS particle velocity is much more reduced. This improvement is transposed to the segregation profiles too (Fig. 5.73). The segregation level is highly increased at the center of the slab and the level of the maximal peaks at the periphery is greatly increased too. Thus, the agreement with the reference is improved.

Increasing the resolution of the mesh has a negative impact on the RUE profile (Fig. 5.74(a)). Indeed, the level of uncorrelated energy increases, which produces an overestimation of the RUE already overestimated with the lower resolution mesh. Nevertheless, the level increase is not very high and at the same time the mesoscopic energy statistics are improved (Fig. 5.74(b)). This leads to a slight overestimation of the total particle agitation, which is very accurately captured with the lower-resolution mesh (Fig. 5.74(c)).

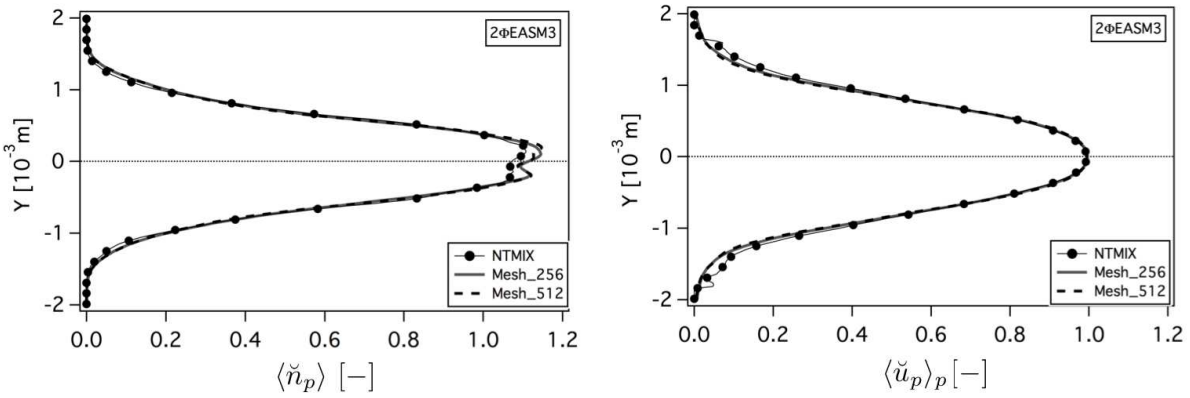

(a) Non-dimensional mean particle number density.

(b) Non-dimensional mean particle velocity.

Figure 5.71: *Comparison Lagrangian and Eulerian results. The Lagrangian computation has been performed in a* 128^3 *mesh grid. Mesh_256 corresponds to the Eulerian simulation on a* 256^3 *mesh and Mesh_512 to an Eulerian simulation on a* 512^3 *mesh.*

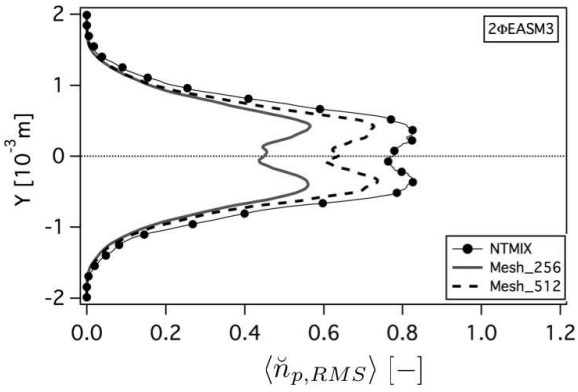

(a) Non-dimensional RMS particle number density.

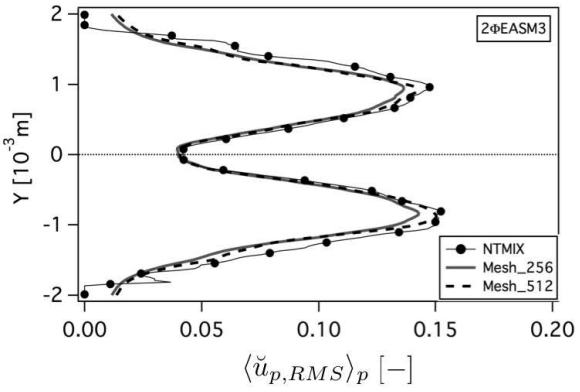

(b) Non-dimensional RMS particle velocity.

Figure 5.72: *Comparison Lagrangian and Eulerian results. The Lagrangian computation has been performed in a* 128^3 *mesh grid. Mesh_256 corresponds to the Eulerian simulation on a* 256^3 *mesh and Mesh_512 to an Eulerian simulation on a* 512^3 *mesh.*

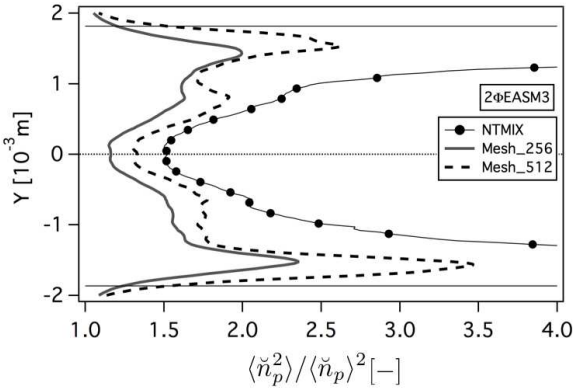

Figure 5.73: *Comparison Lagrangian and Eulerian particle segregation. The Lagrangian computation has been performed in a* 128^3 *mesh grid. Mesh_256 corresponds to the Eulerian simulation on a* 256^3 *mesh and Mesh_512 to an Eulerian simulation on a* 512^3 *mesh.*

Regarding the qualitative comparison of the instantaneous fields, the structures of particle number density (Fig. 5.75) are more defined when increasing the resolution, the diffusion seems to be reduced and thus the empty spaces and high concentration spots are better captured. However, the overall appearence of the fields has not changed much. Changes are even less obvious in the case of the particle velocity fields (Fig. 5.76), the fields corresponding to the Eulerian simulations with the two computational meshes are very similar and changes appear but may be due to small differences on the physical times of the simulations. The RUE field corresponding to the high resolution mesh (Fig. 5.77) is more defined than the one corresponding to the lower resolution grid. More small structures are present and the size of the spots of very high RUE has been reduced. This seems to be in disagreement with the increased level of the RUE average profiles (cf Fig. 5.74(a)), however, the number of small structures in the field has considerably increased which increases the global RUE level.

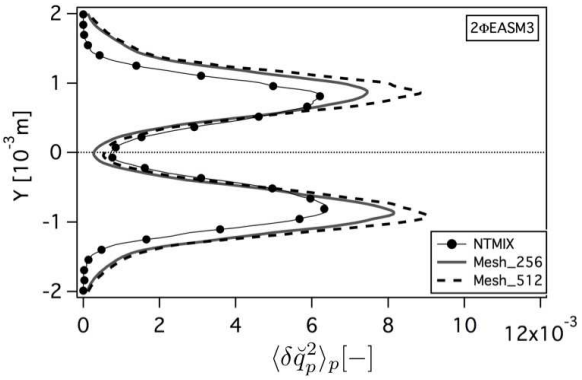

(a) Non-dimensional RUE.

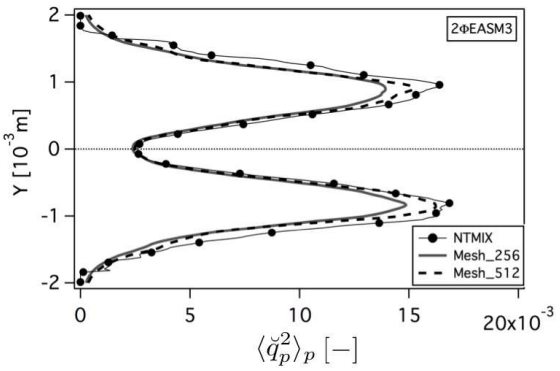

(b) Non-dimensional particle mesoscopic energy.

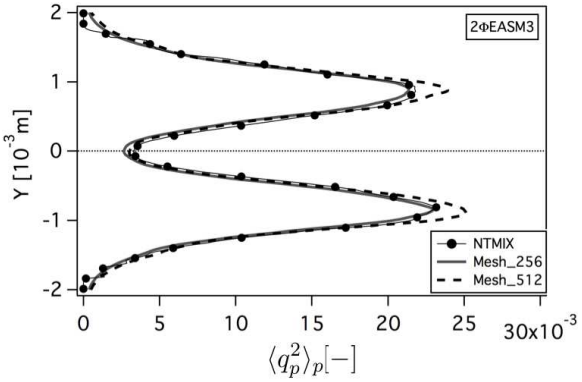

(c) Non-dimensional total particle energy.

Figure 5.74: *Comparison Lagrangian and Eulerian results. The Lagrangian computation has been performed in a* 128^3 *mesh grid. Mesh_256 corresponds to the Eulerian simulation on a* 256^3 *mesh and Mesh_512 to an Eulerian simulation on a* 512^3 *mesh.*

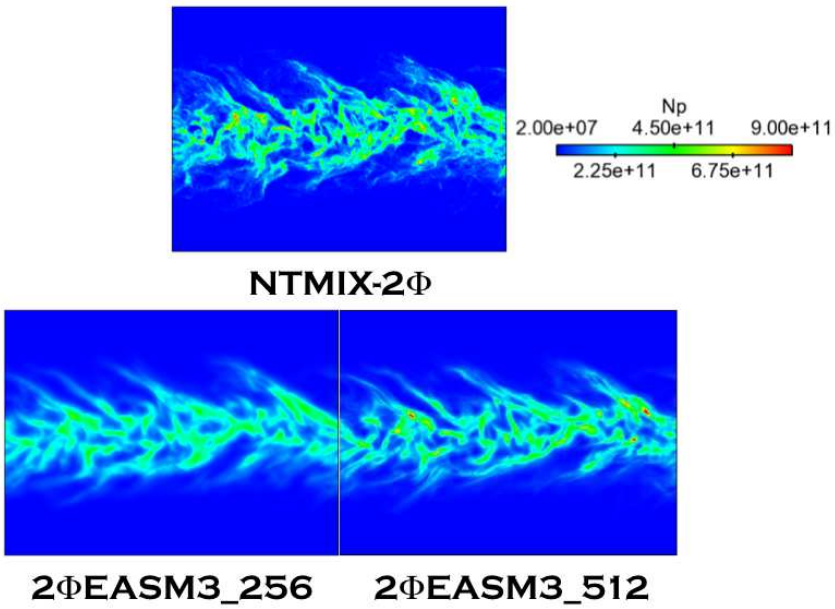

Figure 5.75: *Comparison Lagrangian and Eulerian particle number density instantaneous fields at* $40t_{ref}$*. The Lagrangian computation has been performed in a* 128^3 *mesh grid. 2ΦEASM3_256 corresponds to the Eulerian simulation on a* 256^3 *mesh and 2ΦEASM3_512 to an Eulerian simulation on a* 512^3 *mesh.*

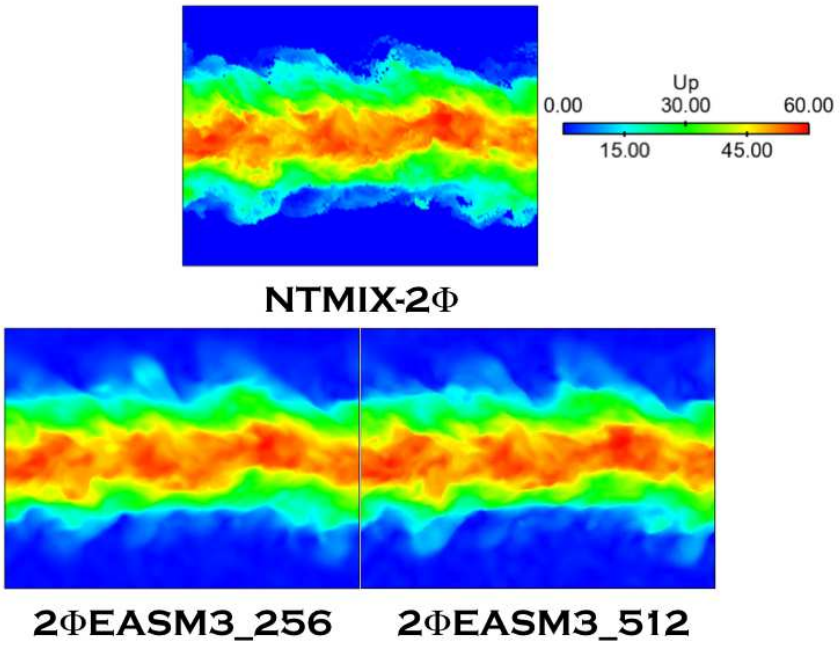

Figure 5.76: *Comparison Lagrangian and Eulerian particle velocity instantaneous fields at* $40t_{ref}$*. The Lagrangian computation has been performed in a* 128^3 *mesh grid. 2ΦEASM3_256 corresponds to the Eulerian simulation on a* 256^3 *mesh and 2ΦEASM3_512 to an Eulerian simulation on a* 512^3 *mesh.*

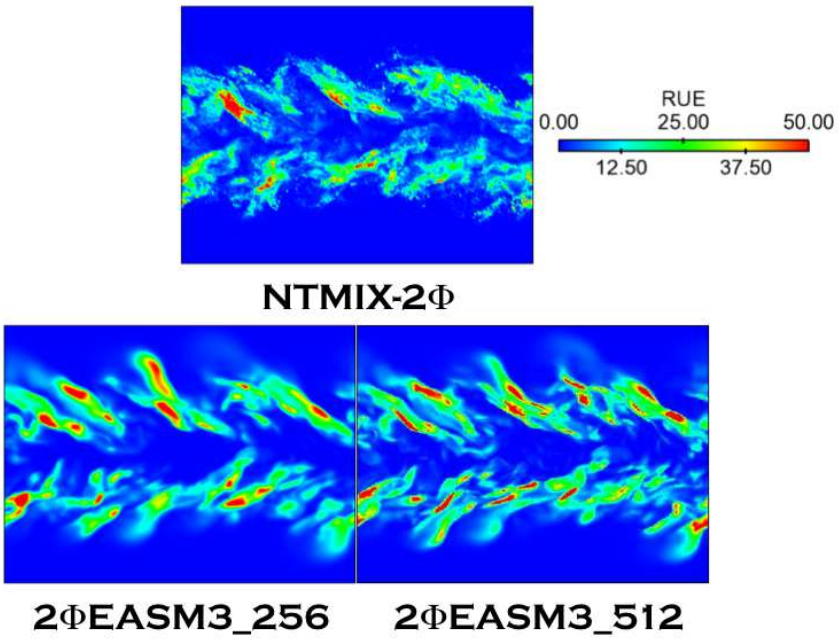

Figure 5.77: *Comparison Lagrangian and Eulerian RUE instantaneous fields at* $40t_{ref}$*. The Lagrangian computation has been performed in a* 128^3 *mesh grid. 2ΦEASM3_256 corresponds to the Eulerian simulation on a* 256^3 *mesh and 2ΦEASM3_512 to an Eulerian simulation on a* 512^3 *mesh.*

5.6 Conclusions

The different approaches for the modelisation of the deviatoric RUM tensor presented in Chapter 4 have been *a posteriori* validated in a configuration with mean shear. Comparisons with *a priori* results issued from exact Lagrangian calculations projected onto an Eulerian grid have been carried out for two levels of turbulence ($Re^{ac} = 5000,\ 20000$) and three levels of inertia ($St \sim 0.33,\ 1,\ 3$). The observations resulting from these tests are:

- The model based on a viscosity assumption and $\breve{\tau}_p$ as timescale, VISCO, crashes after a few iterations in all cases except for the low inertia case (LR_St0.33_#). When performing simulations without taking into account the contribution of the RUM (noRUM), only the low turbulence unity Stokes number case (LR_St1_#) is able to complete the simulation. If the turbulence is increased or the Stokes number changed, the simulation crashes before reaching the end. The rest of the models presented have been tested in low Reynolds, mean and high Stokes numbers with success (LR_St0.33_# and LR_St3_#).
- The results obtained in LR_St1_# and LR_St3_# cases show that AXISY model is too diffusive due to an overestimation of the RUE level. The correction (AXISY-C) improves the results by reducing the RUE levels and thus the diffusion of the particle number density and particle velocity fields. The overestimation of RUE seems to be characteristic of the linear models (VISCO and AXISY). Increasing the order of the model (QUAD-MOD) clearly improves the results. Indeed, from the comparisons performed in Sections 5.3 and 5.4.1, QUAD-MOD has been identified as one of the models to be retained.
- 2ΦEASM1 underestimates the RUE level at low turbulence and mean inertia. It gives better results when increasing the inertia. The correction (2ΦEASM1-C) has a very limited effect for this model. 2ΦEASM3 gives very good results at low turbulence for mean and high inertia and for higher turbulence and mean inertia. This model is to be retained for future simulations. In this case, the correction (2ΦEASM3-C) reduces the RUE level yielding a degradation of the results.
- For low turbulence and low inertia limit case (LR_St0.33_#) both QUAD-MOD and 2ΦEASM3 correctly downgrade: the RUM is reduced, giving accurate results. The two models have also been tested in a mean inertia and high turbulence case (HR_St1_#), also providing good agreement with the Lagrangian reference.

Special attention must be paid to artificial dissipation:

- AD is needed for all models at the beginning to numerically stabilize the simulation due to the presence of too steep gradients on the borders of the slab that the centered scheme TTGC is unable to handle.
- A link between the AD and the RUM has been observed: AD activates in the zones where RUE should be produced but is not because RUM has not been accounted for or because the RUM model behaves uncorrectly. The models that overestimate the RUE show very low levels of AD and *vice versa*.
- Although the models that underestimate RUE produce good results of the low order moments, AD is not able to substitute the RUM contribution in terms of high order moments and numerical stability.

The effect of the resolution needed to perform two-phase Eulerian calculations has also been adressed. Cases LR_St1_2ΦEASM3 and HR_St1_2ΦEASM3 have been simulated on a 512^3 grid. Due to limited computational resources, the simulations have been carried out until $40t_{ref}$ only. The profiles of mean and RMS particle number density and particle velocity, segregation and mean RUE have been compared with

the simulations performed on the lower resolution (256^3) grid and the Lagrangian reference. Dombard (2011) studied the effect of the mesh resolution on this configuration showing that it has an important impact on the statistics of the high order moments. This statement has been confirmed by the results presented here. The mean particle number density and particle velocity statistics are not affected by the increase in mesh resolution. However, the instantaneous fields of particle number density are highly improved. The presence of small structures is better captured whit the 512^3 grid. The location of the spots of high and low particle concentration are better reproduced and the diffusion is reduced. The simulations in the higher resolution mesh provide a better prediction of the RMS particle number density and particle velocity, especially on the higher turbulence simulation where the particle number density fluctuation level (very underestimated by the lower grid resolution simulation) is highly improved. The impact on the RMS particle velocity is much more limited. The RUE instantaneous fields are also improved when the grid resolution is increased. The shape of the Lagrangian field is better reproduce and the presence and location of the small structures are better captured. However, the mean RUE profiles are slightly overestimated by the higher resolution simulations, while the total particle agitation is less affected.

The presence of wiggles in the instantaneous fields for the QUAD-MOD model provided a reason to choose between 2ΦEASM3 and QUAD-MOD to perform the simulations of the configuration presented in Part IV. Those wiggles are due to high frequency oscillations coming from numerical errors and potential low grid resolution, which makes the simulation susceptible to numerical instabilities or to the need of additional AD. The reason why they only appear in QUAD-MOD has not been identified yet. It may mean that this particular model needs a higher resolution than the rest of the models. The simulations on a 512^3 mesh with QUAD-MOD have not been performed during this work due to a lack of time and computational resources.

Finally, the 2ΦEASM3 model provides very good agreement with the Lagrangian reference for all the cases tested. This model represents a good compromise in terms of reproduction of physical phenomena and AD. The model has been implemented in the code AVBP. On the short term, deeper analysis of the link between the RUM and the AD is however necessary for future studies. Recently, new AV sensors have been implemented in AVBP (Vié (2010)) which have proven to provide good results on particle-laden HIT and two-dimensional particle-laden spatial jet configurations (Dombard (2011)). On the mean and long term, the implementation of high-order upwind numerical schemes (de Chaisemartin (2009), Kah (2010)) in AVBP may solve the issues related to AD, providing simpler analysis of the performances of the RUM models.

Masi (2010) studied the impact of LES in the configuration studied here. The performances of the models were assessed and the coefficients of the dispersed phase turbulent viscosity model developed by Moreau (2006) adjusted. The model proposed by Moreau (2006) was implemented in AVBP by Riber (2007). The same study presented here in the case of a DNS approach needs to be conducted in the LES context in order to further validate the RUM models with the perspective of their application to LES simulations of industrial configurations.

2ΦEASM3 model correctly reproduces the level of RUE in this configuration, which allows the consideration of collisions in two-phase flows simulations, which was not the case of the model available until now (VISCO). The modification of the dispersed transport equations in not extremely difficult and Masi (2010) provided an extense Lagrangian data base on a colliding particle-laden turbulent planar jet which may be used for validation purposes as has been done here.

The effect of the grid resolution needs further analysis. First, it is desirable to perform simulations on the higher resolution mesh grid both with the Euler-Lagrange and the Euler-Euler approaches with the condition of being able to obtain detailed information on the deviatoric RUM stress tensor components and RUM production terms. Indeed, comparisons between Euler-Euler and Euler-Lagrange simulations performed with the same mesh resolution eliminates a possible source of differences between the simulations. Having access to the tensor components and production terms allows a deeper comparison.

Masi (2010) performed an analysis of the performances of the RUM models in the context of the LES of the particle-laden temporal planar jet configuration studied here. The results showed that 2ΦEASM3 behaves correctly when applied along with the model of Moreau (2006) for the dispersed phase turbulent viscosity (with minor modifications). This justifies the application of the 2ΦEASM3 model to the LES of the MERCATO configuration presented in Part IV. However, an *a posteriori* validation of the RUM models in the configuration presented her using LES is of great importance. Due to a lack of time, it has not been done during this work, but it is planned for the future.

Finally, the application of 2ΦEASM3 model to a complex semi-academic configuration is on sight. The configurations of Hishida *et al.* (1987) or Sommerfeld & Qiu (1993) are good candidates for this task. For both configurations, experimental data are available. For the configuration of Sommerfeld & Qiu (1993), numerical data obtained from Euler-Lagrange simulations (Apte *et al.* (2003*b*)) are available too. The Euler-Euler LES of both simulations with 2ΦEASM3 model is in prospect at CERFACS.

Part III

Evaporation of single isolated droplets

Chapter 6

Modeling the evaporation of fuel droplets

The process of droplet vaporization is of great importance in many energy systems involving spray combustion such as diesel engines, gas turbines, liquid rocket engines, industrial furnaces, etc. In a general way, without accounting for droplet burning at injection, the liquid fuel atomizes into multiple droplets of different sizes, creating a polydispersed spray, the fuel droplets vaporize, the gaseous fuel mixes with the oxydant and then burns. In this type of studies the prediction of the gaseous fuel concentration is of primary importance for the correct evaluation of critical parameters, such as flame position and heat release (Lefebvre (1999)).

The vaporization of droplets has been widely studied during the past century, experimentally and theoretically. Many studies were performed on complex spray flows in similar conditions to those encountered in real applications (theoretically by Faeth (1996) and Borghi (1996*b*) and experimentally by Sommerfeld & Qiu (1998) and Li *et al.* (2011) amongst others). The phenomena taking place in this type of configurations are very complex. Multiple interactions between the atomization, the dispersion and the evaporation of droplets take place at the same time. For this reason, developping models from studies of complex configurations is almost an impossible task.

Another approach is to study the evaporation of single droplets, under different conditions, as a first step towards the understanding of the process in a spray. An isolated droplet represents an ideal model of the physical phenomena involved in the diluted regions of the spray. The vaporization of a single droplet is a process involving heat, mass and momentum transfers in both gas and liquid phases, with coupling at the droplet interface. Its study provides the basis for the development of complex spray flow modeling, which may be found in many textbooks: Williams (1985), Kuo (2005), Sirignano (1999) and reviews: Sirignano (1983), Faeth (1977), Law (1982) and more recently Birouk & Gokalp (2006). Heating, evaporation and combustion models of isolated droplets are widely available in the literature (Sirignano (1983); Abramzon & Sirignano (1989), Sazhin (2006); Sazhin *et al.* (2006); Harstad & Bellan (2001)).

Many experimental studies have been performed on suspended evaporating droplet. Studies on droplet evaporation in convective streams have also been reported by several authors (Ranz & Marshall (1952), Yang & Wong (2002), Maqua *et al.* (2008), Kristyadi *et al.* (2010)). Most non-convective droplet evaporation studies have been conducted at normal gravity. However, under microgravity conditions (Nomura *et al.* (1996), Yang & Wong (2001), Chauveau *et al.* (2008)), the spherical symmetry of the droplet is guaranteed and the models simplified. For this reason experiments performed under microgravity conditions are better suited for the validation of theoretical and numerical models which usually suppose droplet symmetry.

Numerical studies of isolated droplets in the literature are devoted to the study of theoretical models

in comparison with experimental results. Zhang *et al.* (2008) studied the evaporation of single droplets in stagnant and convective stream. Yang & Chang (2001) and Yang & Wong (2002) analyzed the effects of heat conduction through the support fiber and furnace radiation in the evaporation of suspended droplets. Hubbard *et al.* (1975) studied the effects of different properties on the evaporation of single droplets of different types of fuels into a stagnant atmosphere. Hohmann & Renz (2003) studied the influence of real gas effects and gas solubility.

The Chapter is organized as follows. Section 6.1 provides a classification of the evaporation models existing in the literature and summarizes the main assumptions of the classical model implemented in AVBP. Section 6.2 gives the context of the work presented in this Part of the manuscript. Finally, Section 6.3 present the evaporation models studied in this work and the formulation of the transport and themodynamic governing laws.

6.1 Review of the existing evaporation models

Following Sirignano (1999) the models of droplet-vaporization can be classified into the following six groups with increasing complexity:

1. *constant droplet-temperature model*: the droplet surface temperature is uniform and does not change with time; it yields the famous d^2 law.
2. *infinite liquid-conductivity model*: the droplet surface temperature is uniform, time-varying and equal to the temperature inside the droplet.
3. *spherically symmetric transient droplet heating model*: it takes into account finite liquid thermal conductivity, but not the recirculation inside the droplets (conduction limit).
4. *effective-conductivity model*: it takes into account both finite liquid thermal conductivity and recirculation.
5. *vortex model for droplet heating*: it describes the recirculation inside the droplet in terms of vortex dynamics.
6. *Navier-Stokes solution*: full exact solution of the Navier-Stokes equations inside the droplet and in the gaseous flow.

The evaporation models can be more precisely classified by independently describing the models used on each of the process taking place in the vaporization of a droplet. Four main phenomena take place in the evaporation of an isolated droplet:

1. the heat in the gas phase diffuses to the droplet surface.
2. the heat arriving to the droplet surface is diffused inside the droplet.
3. the molecules of fuel detach fron the droplet surface due to their increased internal energy (vaporization process).
4. the gaseous fuel is diffused from the droplet surface to the surrounding gas.

Most models assume the diffusion in the gas phase (from and to the droplet surface) to be spherically symmetric. This assumption is at the root of the Spalding model (Spalding (1953)) used in AVBP. However, some effects due to convection may modify the flow around the droplet. The spherically symmetric model takes into account the convection effects through the Frössling correlations (Frössling (1938)) for the Sherwood and Nusselt numbers. Other models include the effect of convection taking

into account the presence of a film around the droplet, introducing correction factors in the spherically symmetric model (Abramzon & Sirignano (1989), Yao *et al.* (2003)) or completely solving the flow around the droplet (Sirignano (1999)). This last option is computationally very expensive.

By addition, transport properties are often considered constant between the droplet surface and the infinity. Miller *et al.* (1998) showed that the heat and mass fluxes to the droplet strongly depend on the evaluation of the transport and thermodynamic properties of both the gas and the liquid phases. This will be specifically studied in Section 6.3.1.

To model the temperature distribution inside the droplet (and thus the diffusion in the liquid phase), multiple options exist: the simplest models neglect the heat diffusion inside the droplet and suppose constant droplet temperature, assuming that all the heat arriving to the surface is employed for the vaporization process. The model implemented in AVBP takes a step further in the modelisation of the diffusion in the liquid phase by assuming an infinitely rapid heat diffusion inside the droplet. The droplet temperature is considered uniform but may vary with time. Sazhin *et al.* (2005) and Laurent (2008) supposed the droplet temperature to follow a polynomial profile. More complex models solve the heat equation inside the droplet, suppose a Hill's vortex flow type inside the droplet (Abramzon & Sirignano (1989)) or even solve the complete set of equations inside the droplet (Rangel & Sirignano (1989)). A comparison of the effects of each of these models may be found in Abramzon & Sirignano (1989).

6.2 A new experimental approach for the characterization of evaporating droplets.

Chauveau *et al.* (2008) recently presented new experimental measurements for the evaporation of n-heptane droplets in the configuration previously studied by Nomura *et al.* (1996). In these experiments, a unique n-heptane droplet of initial diameter $d_0 = 500\ \mu m$, suspended by quartz fibers, evaporates in a N_2 quiescent atmosphere at different temperatures and pressures under microgravity conditions. Chauveau used a new method to suspend the droplets during the evaporation process: while Nomura used horizontal quartz fibers of 0.15 mm of diameter (Fig 6.1(a)), Chauveau suspended the droplets by the center using a "cross-fiber" system of 14 μm (Fig 6.1(b)). He claimed that this new method was more accurate, since it reduces the heat conduction through the fiber and keeps the droplet spherical until the last stages of evaporation.

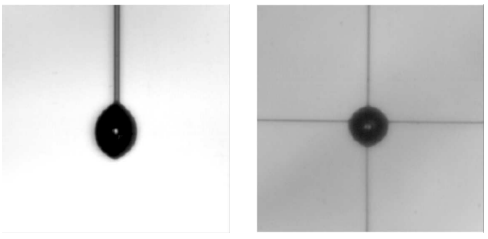

(a) (b)

Figure 6.1: *Droplet suspending technique: classical fiber (a), cross-fiber (b). Extracted from Chauveau* et al. *(2008).*

The evaporation times measured by Chauveau *et al.* (2008) were much larger than those measured by Nomura *et al.* (1996) or Ghassemi *et al.* (2006). To explain this difference he adduced that in Ghassemi and Nomura's experiments, the measurements were conditioned by the heat conduction through the support fiber. Yang & Wong (2002) performed a numerical study of the experience carried out by Nomura to investigate the effects of radiation and fiber heat conduction. They simulated the evaporation of a single n-heptane droplet under the same conditions for a wide range of gaseous temperatures and pressures.

They used three numerical models:

- the first model computes the evaporation process without any source term other than the exchanges between the gas and the liquid phases (case 1).
- the second model takes into account an extra contribution due to the heat conduction through the fiber (case 2)
- the third model takes into account the radiation emitted by the internal walls of the furnace where the experiments were performed and the fiber heat conduction (case 3).

They showed that when radiation and fiber conduction effects are not included, the evaporation rate is slower. They also showed that the results of Nomura are very sensitive to the contributions of the fiber and radiative source terms. Results including radiation and the effect of the fiber matched the results of Nomura for a wide range of pressures and temperatures. In AVBP, fiber heat conduction and radiation are often ignored. For this reason, only case 1 in Yang & Wong (2001) will be used for comparison means in this work. Nevertheless, these terms may be accounted for coupling AVBP with the codes AVTP (Duchaine *et al.* (2009)) to account for the heat conduction through the support fiber, and PRISSMA (Joseph *et al.* (2005), Amaya *et al.* (2010)) to take into account the radiation effects.

6.3 Evaporation models for single isolated droplet

Section 6.3 recalls the equations used in the evaporation model of Spalding (Spalding (1953)) and introduces the modifications proposed by Abramzon and Sirignano (Abramzon & Sirignano (1989)) into this evaporation model. Section 6.3.1 compares two procedures to evaluate the transport and thermodynamic properties and proposes a new method for the calculation of the transport properties in the gas phase around the droplet with the code AVBP. Following the classification proposed by Sazhin (2006), infinite conduction in the liquid and spherical symmetry are assumed. In other words, inside the droplet, the thermal conductivity is considered infinitely fast and the temperature is uniform (Fig 6.2). The gas is considered quasi-stationary, so the thermal and mass transferts in the gaseous phase depend only on the distance to the surface of the droplet. Furthermore, the particle density being larger than the fluid density ($\rho_p >> \rho_g$), the velocity of regression of the droplet surface is much smaller than that of the gaseous fuel leaving the surface, so that the position of the liquid surface may be considered constant.

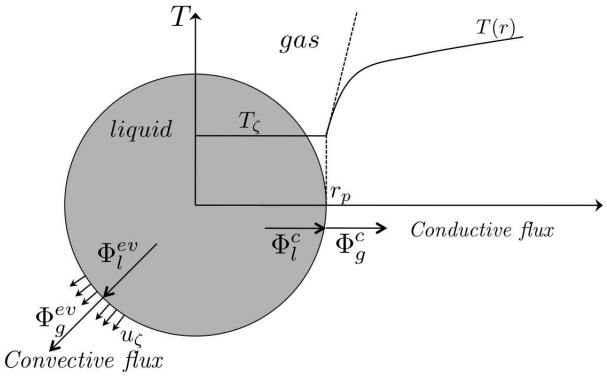

Figure 6.2: *Sketch of the heat fluxes and temperature profile in the evaporation of an isolated droplet following the infinite liquid-conductivity model. Source AVBP Handbook.*

The Spalding evaporation model (Spalding (1953))

The mass exchange through the droplet surface may be represented by the fuel mass flux leaving the surface (ζ represents the surface of the droplet and u the droplet surface regression velocity):

$$\dot{m}_F = (4\pi\rho_g u r_p^2)_\zeta. \tag{6.1}$$

where r_p is the droplet radius.

Another description of this mass exchange is obtained using the temporal evolution of the total mass of the droplet m_p:

$$\dot{m}_p = \frac{dm_p}{dt}. \tag{6.2}$$

As the mass loss of the droplet due to evaporation is totally converted into gaseous fuel, a simple relationship between $\dot{m}_p$ and $\dot{m}_F$ can be obtained:

$$\dot{m}_F = -\dot{m}_p. \tag{6.3}$$

Spalding (1953) proposed the following expression for the calculation of the droplet mass loss:

$$\dot{m}_p = -\pi d_p Sh \rho_g D_F ln(1 + B_M), \tag{6.4}$$

where $\rho_g D_F$ includes the diffusion coefficient (D_F) of the fuel species in the mixture and the density (ρ_g) of the gaseous mixture. Sh is the Sherwood number, a dimensionless number that represents the ratio of convective to diffusive mass transport and B_M is the so-called mass Spalding number given by:

$$B_M = \frac{Y_{F,\zeta} - Y_{F,\infty}}{1 - Y_{F,\zeta}}, \tag{6.5}$$

where $Y_{F,\zeta}$ and $Y_{F,\infty}$ are the mass fractions of evaporated fuel in the film surrounding the droplet surface and at the far field respectively. The vapor mass fraction at the droplet surface is deduced from the Clausius-Clapeyron law:

$$p_{F,\zeta} = p_{cc} exp\left(\frac{\mathcal{W}_p L_{evap}}{\mathcal{R}}\left(\frac{1}{T_{cc}} - \frac{1}{T_\zeta}\right)\right), \tag{6.6}$$

where the subscript cc designates an arbitrary reference point on the saturation curve of the fuel. $\mathcal{W}_p$ is the molecular weight of the liquid fuel, $\mathcal{R}$ is the universal gas constant and L_{evap} is the latent heat of vaporization of the liquid fuel. The vapor partial pressure $p_{F,\zeta}$ yields the molar fraction $X_{F,\zeta}$ which allows to obtain $Y_{F,\zeta}$. Tabulating the saturation pressure versus the temperature from $0K$ to the critical temperature of the fuel species, Eq. (6.6) is not needed and the values of $p_{F,\zeta}$ are directly looked up in the table.

The Sherwood number is equal to 2 in the case of evaporation in quiescent atmosphere. When convection effects are taken into account, different correlations are available: Ranz & Marshall (1952) proposed a modification of the one originally derived by Frössling (Frössling (1938)), based on the particle Reynolds number Re_p and the Schmidt number of the fuel species Sc_F:

$$Sh = 2 + 0.55 Re_p^{1/2} Sc_F^{1/3}. \tag{6.7}$$

The mass evaporation rate is evaluated with Eq. (6.4). In order to completely characterize the evaporation process, an equation for the evolution of the droplet temperature needs to be provided. The energy conservation equation on the gas side of the droplet surface leads to:

$$\rho_g u r_p^2 \frac{\mathrm{d}h_{s,g}}{\mathrm{d}r} = \frac{\mathrm{d}}{\mathrm{d}r}\left(r_p^2 \frac{\lambda}{C_p} \frac{\mathrm{d}h_{s,g}}{\mathrm{d}r}\right). \tag{6.8}$$

Furthermore evaluating the conductive Φ^c and convective Φ^{ev} heat fluxes in the gaseous and the liquid phases (with subscripts g and p respectively, Fig 6.2) yields:

$$\Phi_p^c + \Phi_p^{ev} + \Phi_g^c + \Phi_g^{ev} = 0 \ . \tag{6.9}$$

The fluxes leaving the liquid are due to the vaporization process itself and depend directly on the latent heat of vaporization:

$$\Phi_p^c + \Phi_p^{ev} = -\dot{m}_F h_{s,p}(T_\zeta) + \dot{m}_p h_{s,F}(T_\zeta) = -\dot{m}_p L_{evap}(T_\zeta) \ . \tag{6.10}$$

The total heat flux out of the liquid phase $\Phi_p = \Phi_p^c + \Phi_p^{ev}$ is directly linked to the temporal evolution of the liquid enthalpy:

$$\Phi_p = \frac{d}{dt}(m_p h_{s,p}(T_p)) \ . \tag{6.11}$$

The liquid conductive flux is opposite to the conductive flux in the gas phase ($\Phi_p^c = -\Phi_g^c$). Using Eq. (6.10) and the relation $\mathrm{d}h_{s,p}(T_p) = C_{p,p}\,\mathrm{d}T_p$ one may write:

$$\frac{d}{dt}T_p = \frac{1}{m_p C_{p,p}}\left(-\Phi_g^c - \dot{m}_p L_{evap}(T_\zeta)\right) \ . \tag{6.12}$$

Similarly to the saturation pressure, the latent heat of vaporization L_{evap} may be tabulated versus temperature. The equation for the conductive heat flux in the gas phase is obtained integrating Eq. (6.8) twice. Assuming constant thermal conductivity, λ, yields:

$$\Phi_g^c = \pi d_p \lambda Nu\,(T_\zeta - T_\infty)\,\frac{ln(B_T+1)}{B_T}, \tag{6.13}$$

where B_T is the Spalding thermal number, analogous to the mass Splading number (Eq.(6.5)):

$$B_T = (1+B_M)^\beta - 1 \ , \tag{6.14}$$

with

$$\beta = \frac{Sh \cdot Pr}{Nu \cdot Sc_F}. \tag{6.15}$$

Pr is the Prandtl number of the gaseous mixture and Nu is the Nusselt number, representing the ratio of convective to conductive heat transfer normal to the droplet boundary. It is equal to 2 for evaporation in quiescent atmosphere. When convection is taken into account, the Ranz-Marshall correlation (Ranz & Marshall (1952)) is used:

$$Nu = 2 + 0.55 Re_p^{1/2} Pr^{1/3}. \tag{6.16}$$

When the mass fraction of evaporated fuel at the surface of the droplet, $Y_{F,\zeta}$, approaches 1, the evaporation reaches saturation conditions. Accordingly, the Spalding mass number (Eq. (6.5)) becomes singular. When saturation is reached, the droplet is assumed to be at its saturation point, that is, the evaporation takes place without heating in the liquid and the droplet temperature stays constant. All the heat arriving to the droplet is invested on the evaporation of the liquid fuel. In this case, the mass transfer can be evaluated directly from the conductive heat transfer:

$$\dot{m_p} = \frac{\phi_g^c}{h_{s,F}(T_\zeta) - h_{s,p}(T_\zeta)}, \tag{6.17}$$

where $h_{s,F}(T_\zeta)$ is the enthalpy of the gaseous fuel at the temperature of the droplet surface (T_ζ) and $h_{s,p}(T_\zeta)$ is the enthalpy of the liquid fuel at the same temperature. It is calculated from the tables of latent heat of evaporation L_{evap} and gaseous sensible enthalpy, $h_{s,F}$:

$$h_{s,p}(T) = h_{s,F}(T) - L_{evap}(T) \ . \tag{6.18}$$

The Abramzon-Sirignano evaporation model (Abramzon & Sirignano (1989))

The Spalding model for evaporation does not take into account the existence of a vapour film around the droplet. That is, it does not consider the finite thickness of the thermal and mass boundary layers around the droplet. Taking into account these layers leads to the following modified expressions for the Sherwood and Nusselt numbers appearing in the equations for the mass and heat fluxes respectively:

$$Sh = 2 + 0.55 \frac{Re_p^{1/2} Sc_F^{1/3}}{F(B_M)} \tag{6.19}$$

$$Nu = 2 + 0.55 \frac{Re_p^{1/2} Pr^{1/3}}{F(B_T)} \ , \tag{6.20}$$

where

$$F(B) = (1+B)^{0.7} \frac{ln(1+B)}{B} \tag{6.21}$$

where B refers to B_M for the Sherwood number and B_T for the Nusselt number.

The parameter β in the relation between B_M and B_T (Eq.(6.15)) is also modified to take into account the thickness of the thermal boundary layer as follows:

$$\beta = \frac{C_{p_{F,ref}}}{C_{p_{g,ref}}} \frac{Sh \cdot Pr}{Nu \cdot Sc_F} \ . \tag{6.22}$$

$C_{p_{F,ref}}$ and $C_{p_{g,ref}}$ are the heat capacity at constant pressure of the gaseous fuel and the gaseous mixture in the film around the droplet (or reference state) respectively.

The composition and temperature of the mixture in the film (or reference state) are evaluated by interpolation between their values at the droplet surface and the conditions in the far field (denoted by the subscript ∞) using the third law (Hubbard *et al.* (1975), Miller *et al.* (1998)). This law assumes that the properties of the gaseous mixture in the film around the droplet, follow a quasi-stationary evolution. Afterwards, the different thermodynamic properties are calculated at this temperature and composition (cf Section 6.3.1).

$$T_{ref} = T_\zeta + \frac{1}{3}(T_\infty - T_\zeta) \tag{6.23}$$

$$Y_{k,ref} = Y_{k,\zeta} + \frac{1}{3}(Y_{k,\infty} - Y_{k,\zeta}) \tag{6.24}$$

Due to the inter-dependency of B_T and Nu through β (Eq.(6.22)), this model requires an iterative method to find the converged value of B_T. A convergence study in a real test case (the MERCATO test rig studied in Part IV), including evaporation and combustion, shows that few iterations (approximately five) allow to converge.

This model will be called from now on Abramzon-Sirignano or AS model. As shown by Sazhin (2006), the AS model predicts larger evaporation times compared to the Spalding model in the same conditions, i.e. the evaporation rate decreases when considering a finite thickness of the thermal and mass boundary layers around the droplet (instead of an infinitely thin film).

6.3.1 Governing laws for the thermodynamic and transport properties

Sanjosé (2009) performed a numerical study of the effects of the thermodynamic and transport properties in the evaporation of single droplets, using the results of the experiments of Nomura *et al.* (1996) and Chauveau *et al.* (2008) as reference. Using the Spalding evaporation model, Sanjosé showed that the models used for the transport properties of the gaseous mixture have a considerable impact on the evaporation process. Two different approaches for the calculation of the thermodynamics and transport properties were studied:

- the simplified calculation implemented in AVBP (called thermo_AVBP),
- a more complex evaluation based on collision potentials and CHEMKIN coefficients implemented in the code CANTERA[1] (Goodwin (2009)) (referred to as thermo_CANTERA)).

The use of detailed thermodynamics and transport properties implies the calculation of binary species collision potentials, which considerably increases the complexity of the code as well as the computational cost.

In the following, the model for the transport and thermodynamic properties for the gaseous mixture implemented in AVBP (thermo_AVBP) as well as the complex formulation implemented in CANTERA (thermo_CANTERA, used as reference) are first described. Then, the results of a parametric study are described to show the impact of the Prandtl and Schmidt numbers of the gaseous fuel species in the evaporation process. Finally, a method is proposed to account for the mixture composition when computing the transport and thermodynamic properties without explicitly evaluating the collision integrals which would be too expensive in AVBP (thermo_AVBPmix).

Simplified transport and thermodynamic properties

To evaluate the mixture dynamic viscosity, the thermal conductivity and the heat capacity at the droplet surface the third law is used (Eqs. (6.23) and (6.24)).

The product $\rho_g D_F$ is considered constant in the film, evaluated with a constant Schmidt number for the fuel (Sc_F):

$$\rho_g D_F = \frac{\mu(T_{ref})}{Sc_F} = const \ . \tag{6.25}$$

Similarly, the thermal conductivity and the heat capacity of the mixture are evaluated at the reference state and considered constant between the droplet surface and the far field. The heat capacity depends on the reference state composition and on the species heat capacity evaluated at the reference temperature. A constant Prandtl number is used to evaluate the thermal conductivity:

$$Cp = \sum_{k=1}^{N} Y_{k,ref} \cdot Cp_k(T_{ref}) \ , \tag{6.26}$$

$$\lambda = \frac{Cp \cdot \mu(T_{ref})}{Pr} \ . \tag{6.27}$$

The viscosity of the mixture is computed using a Power law (Eq. (2.19)) that depends only on the temperature of the reference state. Both the Prandtl and the Schmidt numbers are fixed by the chemical scheme used in reactive conditions.

Complex transport and thermodynamic properties

The kinetic theory for gases (Hirschfelder *et al.* (1964), Chapman & Cowling (1939 (digital reprint 1999)) is used to compute the transport and thermodynamic properties of the mixture. The Lennard-Jones potentials (Hirschfelder *et al.* (1964), Bird *et al.* (1960)) are used to calculate the inter-molecular forces (Kee *et al.* (1986)). The expressions for diffusivity, conductivity and viscosity are summarized in this section, more details can be found in Kuo (2005).

[1] CANTERA is an open-source code that computes reactive flows for zero and one-dimensional problems using detailed chemistry, thermodynamic and transport properties based on CHEMKIN potentials.

First, the diffussion coefficient of a species k into a gaseous mixture reads:

$$D_k = \frac{1 - Y_k}{\sum_{j \neq k} X_j / D_{jk}} \ , \tag{6.28}$$

where Y_k and X_k are the mass and molar fractions of species k and D_{jk} is the binary mass diffusion coefficient of species k into species j, which reads:

$$D_{jk} = \frac{3}{16} \frac{\sqrt{2\pi\kappa_B^3 T^3 / m_{jk}}}{\pi P \sigma_{jk}^2 \Omega_{D,jk}} \ . \tag{6.29}$$

m_{jk} is the reduced atomic mass of the pair $j - k$, σ_{jk} is the reduced collision diameter and $\Omega_{D,jk}$ is the collision integral for the diffusion coefficient.

Second, the thermal conductivity of the mixture is calculated using the Mathur's equation (Kee *et al.* (1986)):

$$\lambda = \frac{1}{2} \left(\sum_k X_k \lambda_k + \frac{1}{\sum_k X_k / \lambda_k} \right) \ , \tag{6.30}$$

where the thermal conductivity of each species λ_k is calculated using a complex function of the parameters describing the geometry of the molecule (here denoted F_G, Kee *et al.* (1986)) and the dynamic viscosity of species k:

$$\lambda_k = \frac{\mu_k}{W_k} F_G \ . \tag{6.31}$$

The dynamic viscosity of species k is evaluated as:

$$\mu_k = \frac{5}{16} \frac{\sqrt{\pi m_k \kappa_B T}}{\pi \sigma_k^2 \Omega_{\mu,k}} \tag{6.32}$$

with σ_k being the collision diameter, m_k the mass of the molecule, κ_B the Boltzmann's constant and $\Omega_{\mu,k}$ the collision integral for the dynamic viscosity. The viscosity of the mixture is calculated following Wilke's equation (Bird *et al.* (1960)):

$$\mu = \sum_i \frac{X_i \mu_i}{\sum_j X_j \Phi_{ij}} \tag{6.33}$$

$$\Phi_{ij} = \frac{1}{\sqrt{8}} \left(1 + \frac{W_i}{W_j} \right)^{-1/2} \left[1 + \left(\frac{\mu_i}{\mu_j} \right)^{1/2} \left(\frac{W_j}{W_i} \right)^{1/4} \right] . \tag{6.34}$$

This formulation, is evaluated at the reference state (Eqs. (6.23) and (6.24)) when used for the calculation of the evaporation processes presented in this work.

To evaluate the impact of the complex transport and thermodynamic properties on the evaporation process, Sanjosé (2009) computed the evaporation of single monocomponent droplets in a quiescent atmosphere using the Spalding model with simple and detailed thermodynamic and transport properties:

Results sowed a great impact of the thermodynamic and transport properties on the evaporation process, demonstrating the necessity to take into account accurate transport properties in evaporation calculations. This however is very expensive in terms of CPU time, and a methodology proposed here provides accurate results for transport and thermodynamic properties without increasing drastically the CPU cost of the evaporation calculation in a CFD code.

A new methodology for the evaluation of the transport and thermodynamic properties in CFD codes

The Prandtl and Schmidt numbers used in simplified models are usually fixed by adjusting the reduced chemical schemes in the context of reacting flows. However, there is no reason why the values required

to adjust reduced chemistry would be suitable to describe the evaporation process. Therefore, in this work, it is proposed to use different values for the Prandtl and fuel Schmidt numbers (Pr^{evap} and Sc_F^{evap}) than those used for the gaseous phase for evaporation. These values are adjusted from an evaporation calculation using detailed properties. This new methodology will be referred to as thermo_AVBPmix.

Concerning viscosity, the Wilke's formula (Eq.(6.33)) is used when each species viscosity μ_k is modeled by a Power law, fitted on thermodynamic tables:

$$\mu_k = \mu_{k,0} \left(\frac{T}{T_0} \right)_k^b . \tag{6.35}$$

where $\mu_{k,0}$ is a reference viscosity and b_k is the exponent for the Power law, both depending on the species k, $T_0 = 300\ K$ is the reference temperature used for all the species.

This new methodology allows to take into account complex transport properties art a reduced cost in a CFD calculation. It requires only one simple *a priori* evaporation calculation to fit the Prandtl and Schmidt evaporation numbers (Pr^{evap} and Sc_F^{evap}). The delicate point is here to determine the reference state for this evaporation calculation, which should be representative for the whole CFD simulation. This will be discussed in Section 7.4.

Chapter 7

Application to the evaporation of a single droplet in stagnant atmosphere

7.1 Implementation

The CFD codes chosen to perform the study presented in this chapter are AVBP for thermo_AVBP and thermo_AVBPmix methods and CANTERA to account for complex thermodynamic and transport properties (thermo_CANTERA). This Section briefly describes the implementation of the new methodology in AVBP and the methodology allowing to perform evaporation calculations with CANTERA.

The evaporation of liquid fuel in AVBP follows a model developped for single isolated droplet, where the interactions between droplets are neglected. The Spalding evaporation model is the classical model used by AVBP which was implemented in the code by Jaegle (2009). Here, it is referred to as ievap_1. During this work, the AS model has been included in AVBP. It is referred to as ievap_11. Sanjosé (2009) developed a fortran tool coupling an evaporation module from AVBP with the code CANTERA. This tool allowed to perform evaporation calculations using complex thermodynamical and transport properties as in CANTERA. During this work, the tool has been modified to include the Abramzon-Sirignano evaporation model. The methodology thermo_AVBPmix has also been implemented. This tool is actually included in AVBP under the name "CANTEVOL_EVAP0D". It is used to perform the preliminary evaporation calculation that allows to obtain the values of Pr^{evap} and Sc_F^{evap} needed to simulate evaporation processes with thermo_AVBPmix method. Finally, thermo_AVBPmix model has been implemented in AVBP for both the Spalding and the Abramzon-Sirignano evaporation models (denoted ievap_2 and ievap_21 respectively).

Note that, in AVBP, the latent heat of evaporation and the saturation pressure are tabulated. The tables have been provided by IPF-EN. They are issued from the code IFP-C3D, based on experimental results. However, the number of fuels for which the tables are available is limited. For those fuels for which tabulated values are not available, tables of saturation pressure and latent heat of evaporation have been calculated using the Clasius-Clapeyron law (Eq. (6.6)) and assuming constant liquid heat capacity respectively.

The models presented in Chapter 6 are validated hereafter in the configuration of Nomura *et al.* (1996) where, a n-heptane droplet of initial diameter $d_p = 500\ \mu m$, evaporates in a quiescent N_2 atmosphere. The initial droplet temperature is 300 K. The pressure is 1 bar and the initial gas temperature ranges from 473 K to 973 K. The experimental results of Chauveau *et al.* (2008) and the results of the simulations

of Yang & Wong (2001) are also included for comparison. Table 7.1 describes the six calculations used in the following:

Evaporation model:	Thermo and transport formulation	Referred as:
Spalding	thermo_CANTERA	ievap_0
AS	thermo_CANTERA	ievap_01
Spalding	thermo_AVBP	ievap_1
AS	thermo_AVBP	ievap_11
Spalding	thermo_AVBPmix	ievap_2
AS	thermo_AVBPmix	ievap_21

Table 7.1: *Classification of the different models studied in this work.*

Section 7.2 shows the performances of the three models for the thermodynamic and transport properties using the AS evaporation model. Section 7.3 shows the effect of the evaporation model (either Spalding or AS). In real industrial applications, the fuel droplets are subject to different conditions of gaseous temperature and composition, depending on their position in the combustion chamber. Therefore, Section 7.4 discusses the choice of the temperature at which Pr^{evap} and Sc_F^{evap} are evaluated to be afterwards applied to a wide rage of initial gas temperatures. Section 7.5 shows the limits of the methodology thermo_AVBPmix presented in Section 6.3.1 when used over a range of pressures, which is the case of piston engines for instance. Finally, Section 7.6 shows the results for a kerosene droplet in similar conditions to those of the MERCATO configuration.

7.2 Effect of the thermodynamic and transport properties on the evaporation

This Section presents the numerical results for the configuration of Nomura *et al.* (1996) at ambient pressure and a temperature of 623 K using the AS evaporation model. The effect of the methodology used for the computation of the thermodynamic and transport properties (ievap_01 (thermo_CANTERA), ievap_11 (thermo_AVBP) and ievap_21 (thermo_AVBPmix)) on both the gaseous and liquid phases is analyzed.

Table 7.2 summarizes the values of the Prandtl and Schmidt numbers chosen for thermo_AVBP and thermo_AVBPmix models. The values of the Prandtl and Schmidt numbers for thermo_AVBPmix model have been obtained from a first calculation with thermo_CANTERA model. They correspond to the values at equilibrium obtained with thermo_CANTERA model. Note that in the calculations performed with thermo_CANTERA, the Prandlt and Schmidt numbers are not constant. Figure 7.1 shows the evolution of the Prandtl and Schmidt numbers during the evaporation process for the three calculations.

Name	Properties	Prandtl	Schmidt
ievap_11	thermo_AVBP	0.71	2.10
ievap_21	thermo_AVBPmix	0.82536	1.4807
ievap_01	thermo_CANTERA	variable	variable

Table 7.2: *Prandtl and Schmidt numbers used in the calculations presented in Section 7.2.*

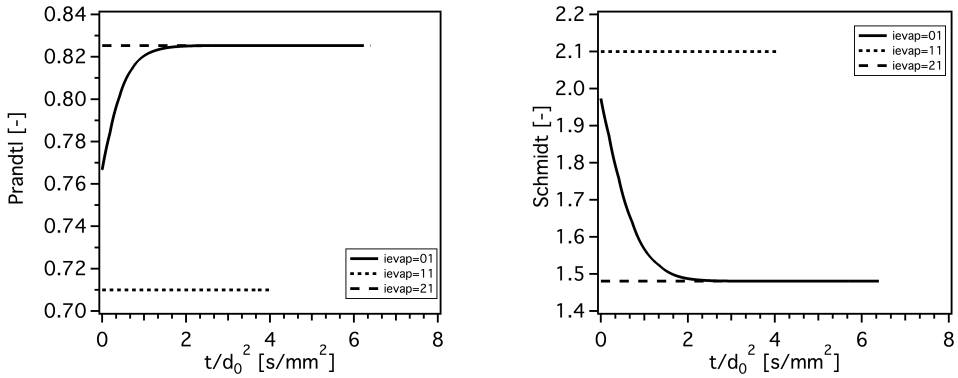

(a) (b)

Figure 7.1: *Prandtl and Schmidt numbers used in the calculations. n-heptane, $T_g = 623K$, $P_g = 1bar$. Numerical simulations performed using the AS evaporation model.*

Figure 7.2 shows that the diffferent methods produce important differences on the evolution and equilibrium values of the main transport properties: the implementation of Wilke's formula (Eq.(6.33)) in ievap_21 predicts an evolution of the gaseous mixture viscosity at the reference state close to that of ievap_01. The main differences are due to the fitting of the individual viscosities by a Power law instead of using the collision potentials as it is done in CANTERA. Moreover, it demonstrates that the use of individual fittings of the dynamic viscosity using Power laws along with Wilke's formula (Eq.(6.33)), is a good compromise for the calculation of the viscosity of the mixture in the film.

However, a study performed during this work revealed that the change in the computation of the viscosity alone, was not a sufficient condition to obtain a correct prediciton of the thermal conductivity (λ_g, Fig. 7.2(b)) or the diffusion coefficient (D_F, Fig. 7.2(c)). However, including the use of the pre-calculated equilibrium values for the Prandtl and Schmidt numbers, as shown in Fig. 7.1, allows a better agreement on the estimation of these properties.

Figure 7.3 shows the temporal evolution of the droplet diameter normalized by its initial value.

- The characteristic evaporation time ranges, for n-heptane in the conditions of the experiment, from 1 s for Nomura to 2 s for the results of Chauveau, i.e. the evaporation time predicted by Chauveau *et al.* (2008) is approximately two times longer than that predicted by Nomura *et al.* (1996). Chauveau *et al.* (2008) and Yang & Wong (2001) experimentally and numerically respectively, showed that the results of Nomura are, in general, notably influenced by the heat conduction through the support fiber and by radiation of the internal walls of the furnace. For this reason, the experimental results of Nomura *et al.* (1996) must be carefully considered when performing comparisons with numerical results, especially when the computational code used does not take into account those effects.

- The numerical results obtained using ievap_11 predict an evaporation process one third shorter than the evaporation time predicted by ievap_01. The evaporation time obtained with ievap_21 is slightly longer than that of ievap_01. However, ievap_01 and ievap_21 are very similar in terms of droplet diameter temporal evolution.

- Compared with the experimental results, ievap_01 and ievap_21 agree well with the results of Chauveau *et al.* (2008). ievap_11 produces results very close to the experimental measurements of Nomura *et al.* (1996).

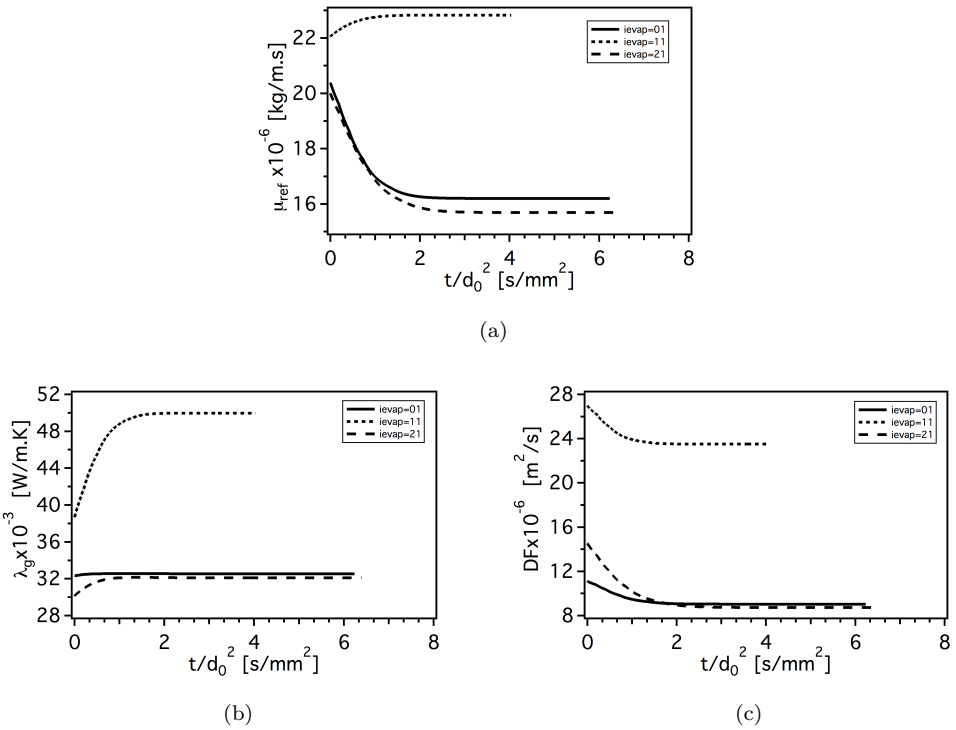

Figure 7.2: *Temporal evolution of the main transport properties: (a) gaseous mixture viscosity, (b) thermal conductivity, (c) diffusion coefficient. n-heptane, $T_g = 623K$, $P_g = 1bar$. Numerical simulations performed using the AS evaporation model.*

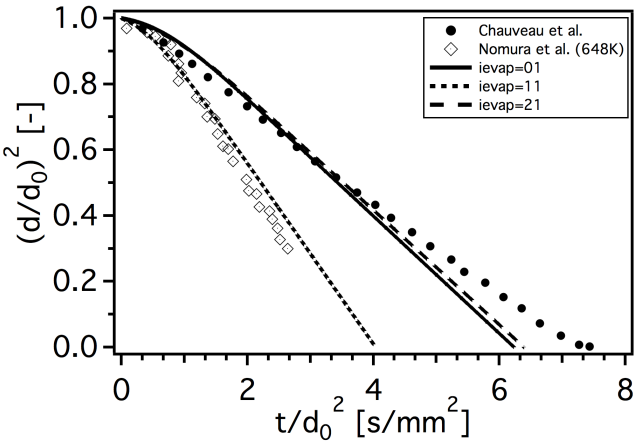

Figure 7.3: *Temporal evolution of the non-dimensional droplet surface. n-heptane, $T_g = 623K$, $P_g = 1bar$. Numerical simulations performed using the AS evaporation model. Experimental results of Chauveau et al. (2008) and Nomura et al. (1996).*

The choice of the Prandtl and Schmidt numbers has a great impact on the calculation of the equilibrium or wetbulb temperature. The wetbulb temperature T_{wb} corresponds to the temperature of a droplet surrounded by hot gases once the equilibrium state is reached:

$$T_{wb} = T_g - \frac{L_{evap}(T_{ref})}{Cp} B_T \ , \tag{7.1}$$

where T_g is the gaseous temperature in the far field, L_{evap} is the latent heat of evaporation of the liquid fuel evaluated at the reference temperature T_{ref} (Eq. (6.23)), C_p is the heat capacity of the gaseous mixture in the film around the droplet (Eq. (6.26)) and B_T is the Spalding thermal number (Eq. (6.14)). The Prandtl and Schmidt numbers have a direct impact on the parameter β (Eq. (6.22)) and thus on B_T. As the choice of Pr^{evap} and Sc_F^{evap} for ievap_21 depends on the conditions, the effect on the liquid temperature will also vary with the conditions. In this particular case, Pr^{evap} for ievap_21 is higher than the Pr used for ievap_11. On the contrary Sc_F^{evap} is smaller than the Schmidt number used for ievap_11. This choice produces an increase in β and a smaller value for B_T, resulting in an increase of the wetbulb temperature. Yuen & Chen (1976) measured the wetbulb temperature of n-heptane droplets evaporating in N_2 at atmospheric pressure for a wide range of initial gaseous temperatures. An interpolation of the results of Yuen & Chen (1976) gives a wetbulb temperature of 344 K in the conditions of the experiment of Nomura *et al.* (1996).

Figure 7.4 shows the influence of each model on the droplet temperature T_l. The liquid temperature has a non-negligible impact on the evaporation process, but also on other phenomena in the combustion chamber such as liquid films on the inner walls due to droplet impinging and heat losses at walls. The droplet temperature at equilibrium obtained with ievap_11 is approximately 15 K lower than the temperature predicted with ievap_01. ievap_21 gives a droplet temperature evolution very similar to ievap_01. The wetbulb temperature predicted by ievap_01 and ievap_21 is in very good agreement with the wetbulb temperature experimentally measured by Yuen & Chen (1976).

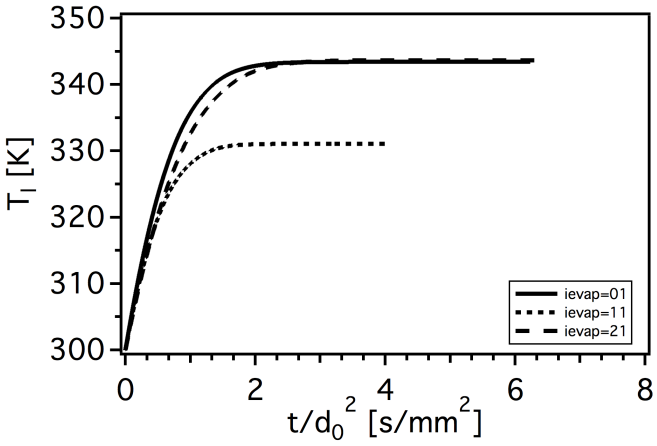

Figure 7.4: *Temporal evolution of the droplet temperature. n-heptane, $T_g = 623K$, $P_g = 1bar$. Numerical simulations performed using the AS evaporation model.*

The new calculation methodology implemented in AVBP (ievap_21) have also a strong impact on the value of mass transfer rate Γ (Fig. 7.5(a)), even when its impact in the heat transfer rate Φ_g is limited (Fig. 7.5(b)). ievap_21 shows a behavior very close to the one predicted by ievap_01: the slope of the mass transfer rate during the early stage of the vaporization process is less stiff than the corresponding to ievap_11, which predicts a more rapid evaporation at the beginning of the process, while the evaporation rate decays very quickly. The evaporation rates calculated with ievap_01 and ievap_21 are slower at the beginning but more sustained along the whole period needed for the complete evaporation.

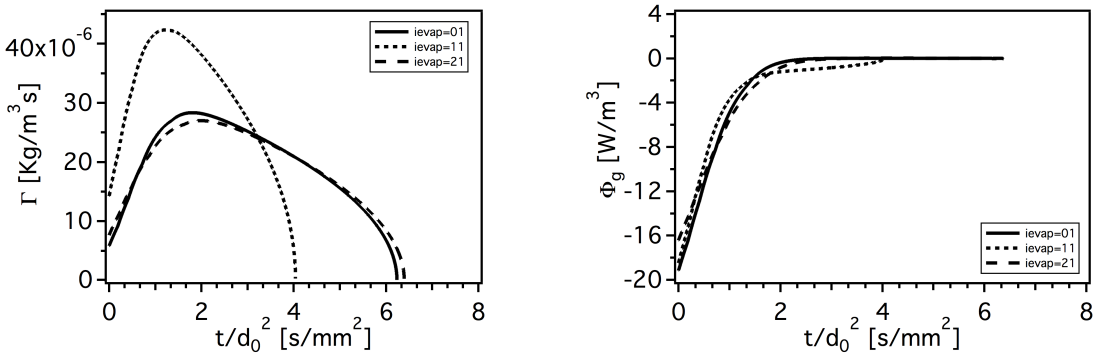

(a) (b)

Figure 7.5: *Evolution of the mass (a) and heat transfer rates (b). n-heptane, $T_g = 623K$, $P_g = 1bar$. Numerical simulations performed using the AS evaporation model.*

The differences in diameter and equilibrium droplet temperature temporal evolution have an important influence on the variables involved in the vaporization process. Figure 7.6 shows the temporal evolution of the gaseous mixture temperature, pressure and density, as well as the mass fraction of gaseous fuel.

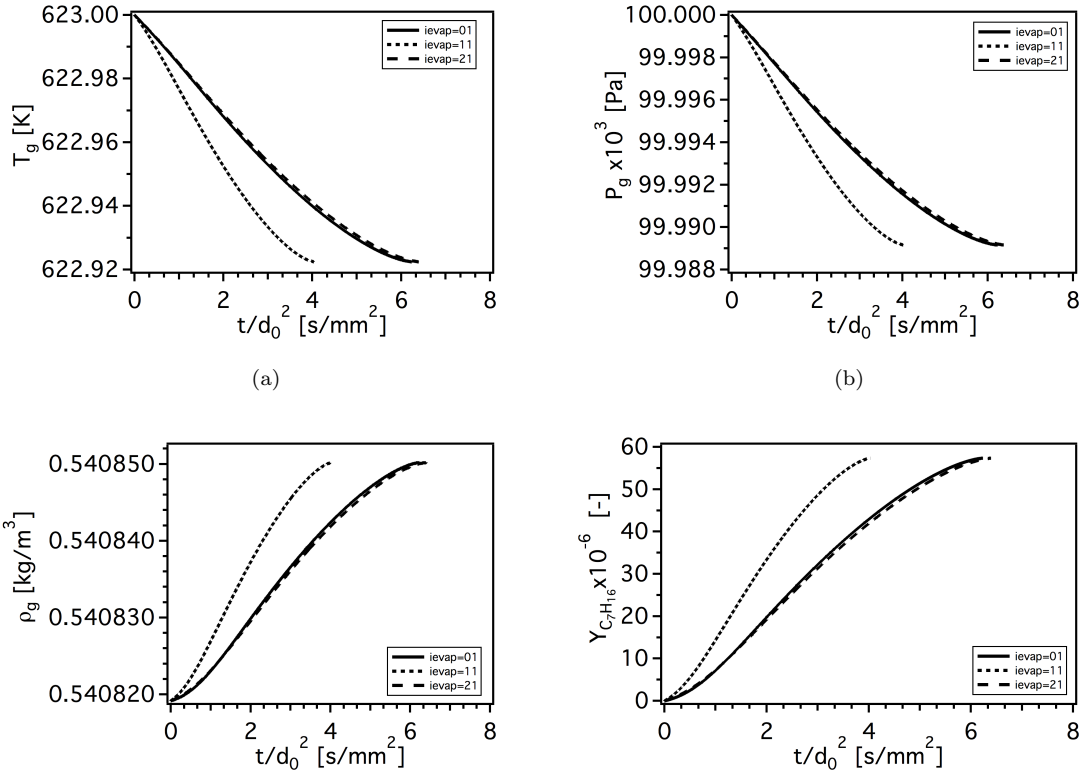

(a) (b)

(c) (d)

Figure 7.6: *Temporal evolution of the main gaseous mixture properties: (a) gaseous temperature, (b) pressure, (c) gaseous density and (d) mass fraction of gaseous fuel. n-heptane, $T_g = 623K$, $P_g = 1bar$. Numerical simulations performed using the AS evaporation model.*

The results of ievap_21 are very close to those of ievap_01, predicting a slower decrease in gaseous temperature and pressure and a slower increase in gaseous fuel mass fraction and gaseous density. As expected, once the evaporation is finished, the values at equilibrium are the same for the three models, as they depend only on the final compostion of the mixture, driven by the initial quantity of liquid fuel.

7.3 Comparison of the Spalding and the Abramzon-Sirignano evaporation models

Section 7.2 showed that the thermodynamic and transport properties strongly impact the evaporation process. This Section proposes to evaluate the impact of the evaporation model itself once the thermodynamic and transport properties are fixed, comparing the Spalding and AS models. The same configuration as in Section 7.2 is computed, varying the evaporation model for the three methodologies for the calculation of the thermodynamic and transport properties (thermo_AVBP, thermo_CANTERA, thermo_AVBPmix). Figure 7.7 displays the droplet diameter and the droplet temperature temporal evolutions.

Whatever the thermodynamic and transport properties used, the AS model predicts a longer evaporation time and a smaller liquid temperature at equilibrium. Comparing with the experimental results of Chauveau *et al.* (2008), the AS model using complex thermodynamic and transport properties shows the best agreement in terms of droplet diameter temporal evolution.

These comparisons show that the transport and thermodynamic properties have a stronger impact than the evaporation model itself on the evaporation process.

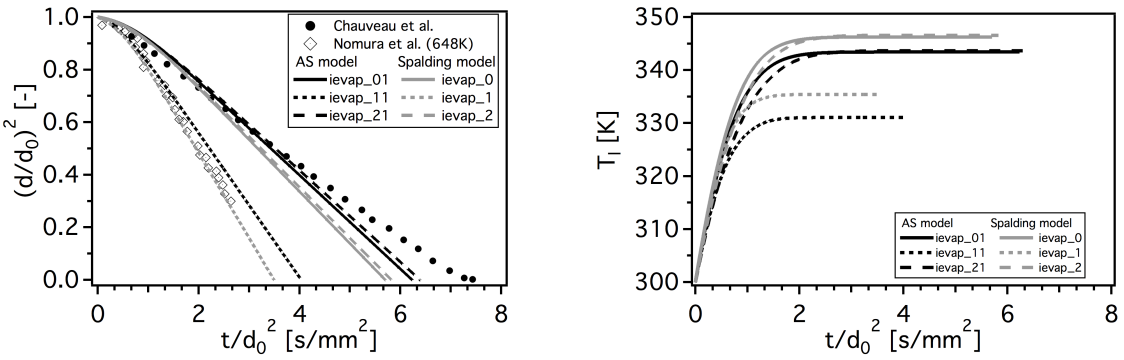

(a) (b)

Figure 7.7: *Comparison of the evolution of the non-dimensional droplet surface (a) and temperature (b) for the different evaporation models. n-heptane droplet, $T_g = 623K$, $P_g = 1bar$. Simulations performed with the Spalding and the AS evaporation models. Experimental results of Chauveau* et al. *(2008) and Nomura* et al. *(1996).*

7.4 Application of a determined fitting to different ambient temperatures

Sections 7.2 and 7.3 showed that the new methodology proposed in Chapter 6, namely thermo_AVBPmix, correctly predicts the evaporation process as measured by Chauveau *et al.* (2008) and as computed with

a complex thermodynamic and transport properties calculation (thermo_CANTERA).

In real applications, such as aeronautical combustion chambers, the conditions (in the evaporation zone) are not homogeneous. The droplets issued from the atomization process may reach very different regions in terms of gaseous temperature and mixture composition. For example, the biggest droplets (with high inertia) may penetrate further inside the chamber than the smallest ones, therefore encountering much higher gaseous temperatures. The effect of gaseous temperature used to evaluate Pr^{evap} and Sc_F^{evap} at equilibrium for ievap_21 must therefore be evaluated.

In this Section, the configuration of Nomura *et al.* (1996) is simulated using the AS evaporation model, for a wide range of initial gaseous temperatures ($T_g = 473\ K$, $548\ K$ and $748\ K$). The values of Pr^{evap} and Sc_F^{evap} numbers are kept from the case at an initial gaseous temperature of $623K$ (Table 7.2). These values have been used for all the other gaseous temperatures. The fitting has been performed at $623K$ because it approximately corresponds to the middle of the temperature range and because experimental measurements are available at this temperature.

Figure 7.8 shows the results for the three initial gaseous temperatures using the three methodologies for the computation of the transport and thermodynamic properties. The experimental results of Nomura *et al.* (1996) show evaporation times much shorter than the results of Chauveau *et al.* (2008). The numerical results of Yang & Wong (2001) are very close to the experimental results of Chauveau *et al.* (2008) in all cases.

The agreement between ievap_21 and ievap_01 is good for $548K$ and $748K$, however, the differences between both methods increase at $473K$. For the three temperatures, ievap_11 is in good agreement with Nomura, while ievap_21 is closer to Chauveau and agrees very well with the results of Yang.

Figure 7.9 shows the evaporation rates corresponding to the linear part of the squared diameter evolution curve for a wide range of initial gaseous temperatures and at ambient pressure. The experimental results show that the evaporation rate increases linearly with the gaseous temperature. The results of Nomura *et al.* (1996) and Morin *et al.* (2000) are very similar. Ghassemi *et al.* (2006) predicts much higher evaporation rates for the whole range of gaseous temperatures. Chauveau *et al.* (2008), however, obtains evaporation rates 50% lower than Nomura *et al.* (1996). The numerical results of Yang & Wong (2001), obtained without taking into account the radiation and fiber conduction effects, are very close to the experimental measurements of Chauveau *et al.* (2008).

The numerical results obtained with thermo_AVBP method (ievap_1 and ievap_11) are close to the experiments of Nomura and Ghassemi, and that for the whole range of temperatures. themo_CANTERA (ievap_0 and ievap_01) and thermo_AVBPmix (ievap_2 and ievap_21) produce very similar results. In both cases, the evaporation rates predicted are in very good agreement with the results of Chauveau *et al.* (2008) and Yang & Wong (2001).

The results showed that the fitting of the Prandtl and Schmidt numbers for thermo_AVBPmix method at a determined gaseous temperature can be used for the calculation of the evaporation over a wide range of gas temperatures and produces good agreement with experimental results (Chauveau *et al.* (2008)) and numerical results obtained with complex thermodynamic and transport calculation (Yang and thermo_CANTERA). This validates the application of the new method (thermo_AVBPmix) for industrial configurations where the gaseous temperature is not constant or homogenous.

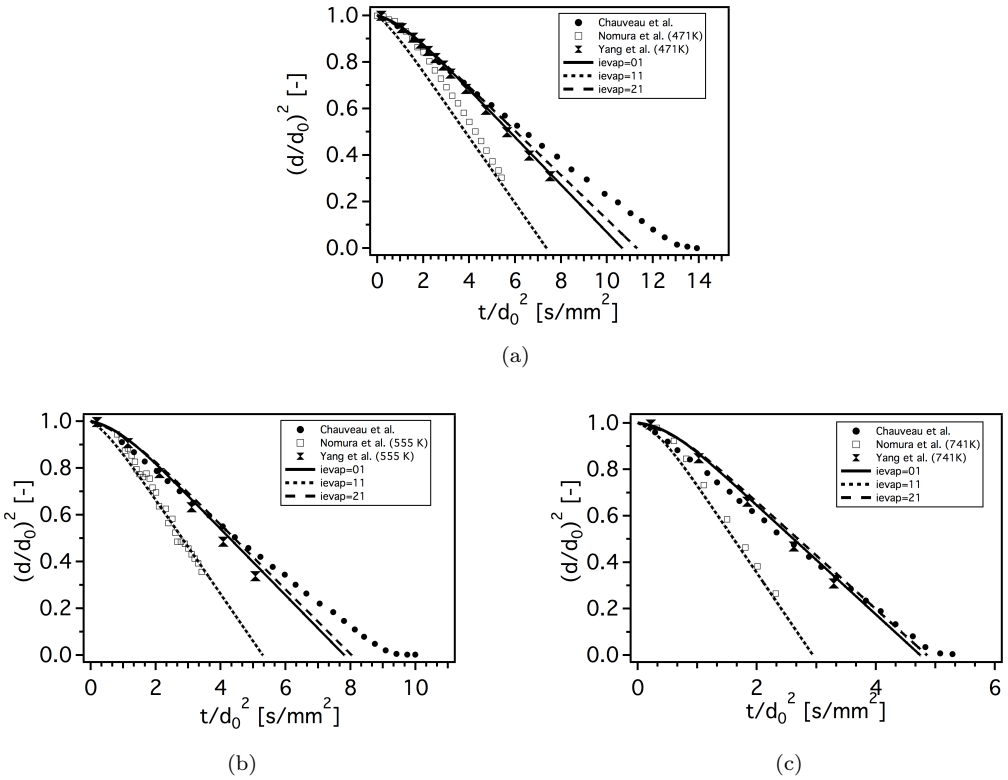

Figure 7.8: *Temporal evolution of the non-dimensional droplet surface. n-heptane, $P = 1bar$: (a) $T = 473K$, (b) $T = 548K$, (c) $T = 748K$. Numerical simulations performed using the AS evaporation model. Experimental results of Chauveau et al. (2008) and Nomura et al. (1996); numerical results of case 1 in Yang & Wong (2001).*

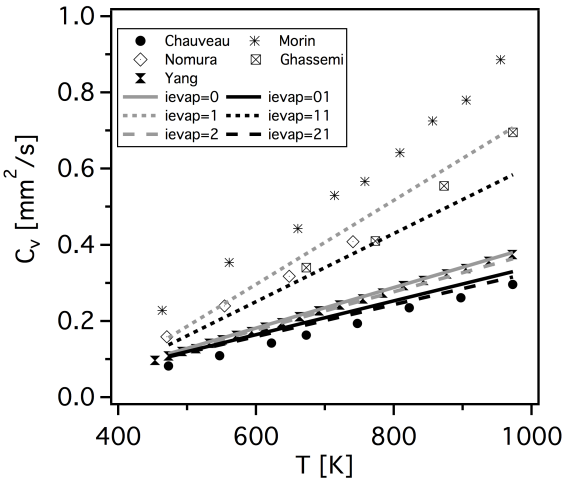

Figure 7.9: *Comparison of the vaporization rate of n-heptane isolated droplets, versus temperature. Experimental results of Chauveau et al. (2008), Nomura et al. (1996), Yang & Wong (2001), Morin et al. (2000) and Ghassemi et al. (2006)*

7.5 Evaluation of the fitting procedure for different pressures

The variations of pressure are not very significative in aeronautical combustion chambers. However, that is not the case in piston engines. Indeed, in spark ignition piston engine, the evaporation process takes place at a narrow interval of moderately high pressures (4 to 5 bars). The mixture is ignited shortly after ignition. On Diesel engines, however, the pressure is much higher and the range larger. Indeed, the pressure in one cycle may vary from 20 bar to 150 bar. The evaporation process takes place of pressures around 45 bar.

Several reviews are available on high pressure droplet vaporization (Givler & Abraham (1996), Bellan (2000)), but only a few studies have been conducted on convective flows (Lee *et al.* (1990), Delplanque & Sirignano (1993), Lee *et al.* (1990)). Nomura *et al.* (1996) and Matlosz *et al.* (1972) performed experiments on n-heptane and n-hexadecane evaporation under normal and microgravity conditions at high pressures. Yang & Wong (2001) and Gogos *et al.* (2003) studied the same test cases numerically. Both found that the numerical models for the calculation of the thermodynamic properties and the assumptions made on the evaporation models used, are not suitable for their application at high pressures.

The purpose being to assess the performances of the different approaches for the calculation of the thermodynamic and transport properties and evaporation models at different initial conditions, four different gaseous pressures have been tested: 1, 5, 10 and 20 *bar*. The gaseous temperature varies from one pressure to the other depending on the availability of experimental measurements, but it is close to 500 K for the four pressures tested.

The results for the AS evaporation model along with the three different approaches for the calculation of the thermodynamic and transport properties (ievap_01, ievap_11 and ievap_21) are compared with the experimental results of Nomura *et al.* (1996) (and Chauveau *et al.* (2008) only for the case at 1 *bar*) as well as the numerical simulations Yang & Wong (2001) for different pressures: 1 *bar* (Fig. 7.10(a)), 5 *bar* (Fig. 7.10(b)), 10 *bar* (Fig. 7.10(c)) and 20 *bar* (Fig. 7.10(d)).

Contrary to Section 7.4, the Pr^{evap} and Sc_F^{evap} values for the computations performed with thermo_AVBPmix (ievap_21) have been fitted with a pre-calculation with thermo_CANTERA for each pressure. Table 7.3 summarizes the values of Pr^{Evap} and Sc_F^{evap} obtained from the pre-calculations with thermo_CANTERA.

Pressure	Pr^{evap}	Sc_F^{evap}
1 bar	0.804	1.5382
5 bar	0.829	1.566
10 bar	0.819	1.667
20 bar	0.826	1.7055

Table 7.3: *Prandtl and Schmidt numbers used in the calculations presented in Section 7.5.*

Figure 7.10 first shows that the agreement between ievap_21 and ievap_01 is very good for all pressures. Second, the differences between ievap_11 and ievap_21 or ievap_01 keep constant when the pressure increases. Using complex thermodynamic and transport properties leads to an evaporation time 1.5 times slower than using simplified thermodynamic and transport properties.

Finally, whereas at low pressure (1 *bar*) the results of the models ievap_01 and ievap_21 are also close to those of Yang & Wong (2001), the discrepancies increase when the pressure increases. Yang & Wong (2001) and Gogos *et al.* (2003) already explained the sources of the differences between the numerical results and the experiments. First, high pressure effects, such as the solubility of the gas into the droplet and the real-gas effects on vapor-liquid equilibrium at the gaseous film surrounding the droplet, are not taken into account. Moreover, at high pressure, the droplet may also deform, thus the spherical symmetry assumption is no longer valid, due to a decrease in the surface tension. Natural convection effects also increase with the pressure. Note that to account for natural convection, gravity must be considered, which

is not the case in this work, nor in the work of Yang & Wong (2001). Gogos *et al.* (2003) showed that taking into account the gravity effects through the inclusion of the Grashof number in the correlations for the Sherwood and Nusselt numbers (Ranz & Marshall (1952)) leads to shorter evaporation times, which would modify the results.

Figure 7.11 shows the evolution of the evaporation rate for n-heptane droplets as a function of the surrounding pressure at different gaseous temperatures ($T_g = [673\ K, 973\ K]$). Ghassemi *et al.* (2006) found that the evaporation rate increases with temperature and pressure, whereas Nomura *et al.* (1996) obtained almost constant evaporation rates for a pressure range between 1 and 25 bar, except for the high temperature case. The numerical results obtained with ievap_21 show very small variations with the gaseous temperature. The evaporation rates predicted are constant for the whole range of pressures.

Note that on the one hand, Chauveau *et al.* (2008) and Yang & Wong (2001) showed that the experimental results of Nomura and Ghassemi are questionable since they are biased by the setup used for the measurements in terms of heat conduction through the support fiber and radiation. On the other hand, Yang discarded the data of Nomura at 20 bar and high temperature considering that it was inconsistent with the rest of results.

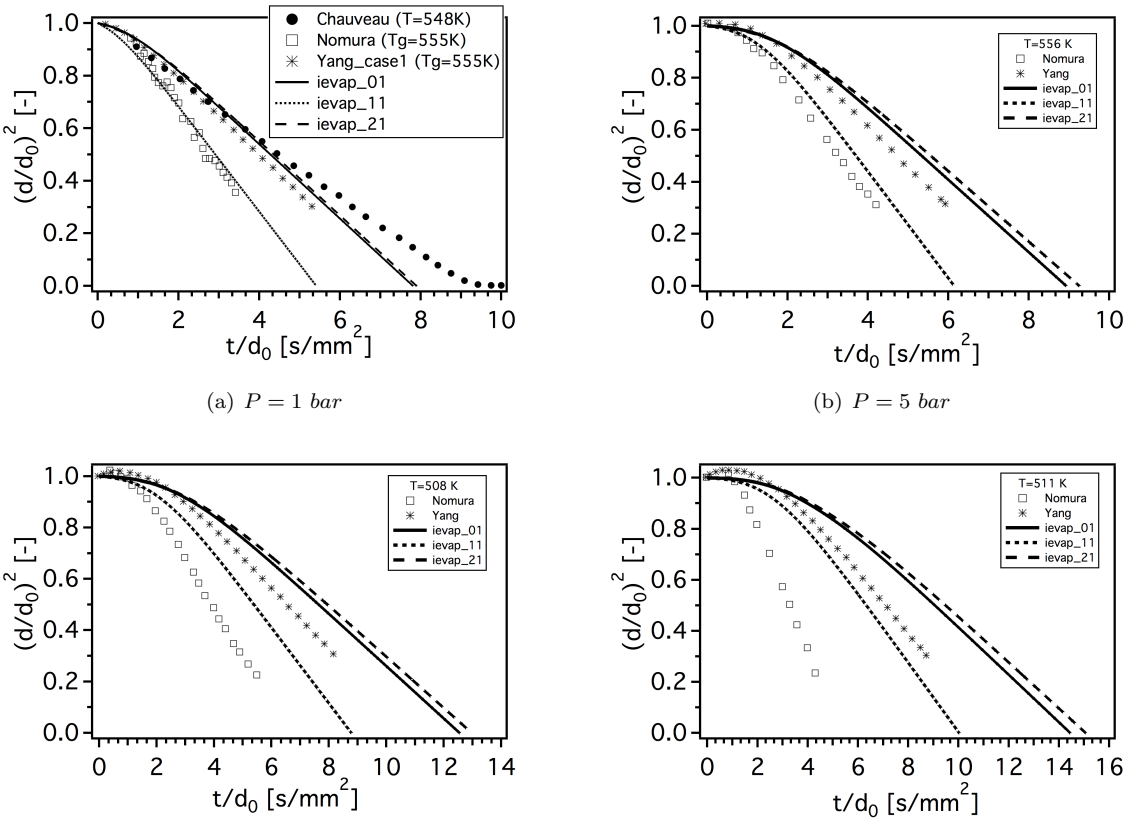

(a) $P = 1\ bar$ (b) $P = 5\ bar$

(c) $P = 10\ bar$ (d) $P = 20\ bar$

Figure 7.10: *Temporal evolution of the non-dimensional droplet surface. Evaporation of n-heptane droplet.* $T = 548K$. $P = 1bar$ *(a),* $P = 5bar$ *(b),* $P = 10bar$ *(c) and* $P = 20bar$ *(d). Comparison of numerical results performed using AS evaporation model, case 1 in Yang & Wong (2001) and eperimental results of Nomura* et al. *(1996).*

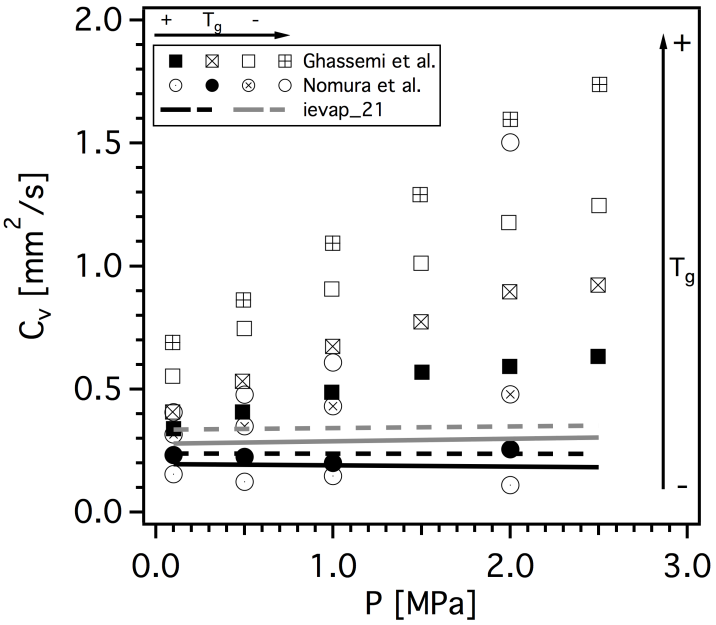

Figure 7.11: *Comparison of the vaporization rate of n-heptane isolated droplets, according to the pressure. Experimental results of Ghassemi et al. (2006) and Nomura et al. (1996).*

7.6 Application to the evaporation of kerosene droplets

In the prospect of aeronautical combustion chamber simulations, this Section proposes to test the evaporation models for isolated kerosene droplets on conditions that are representative of those of the MERCATO test rig. Droplets are injected at an initial temperature of $400K$ approximately with an initial diameter of $55\mu m$. The pressure is 1 *bar* and the average gaseous temperature $440K$. These conditions correspond to the outer part of the hollow cone injection of the MERCATO configuration as simulated by Sanjosé (2009). Sanjosé (2009) proposed a modelisation of the properties for the kerosene surrogate relying on the work of Luche (2003). This surrogate is chosen because it is very similar to the kerosene models used by SNECMA and TURBOMECA. It is composed of three main components: $nC_{10}H_{22}$, C_9H_{12}, C_9H_{18} (Table 7.4). The properties of the so-called surrogate KERO_LUCHE are calculated as averages of the properties of the three main components. The values of the main thermodynamic and transport properties can be found in Franzelli *et al.* (2010) and in Sanjosé (2009) for the liquid phase. The lack of data for liquid heat capacity and latent heat of vaporization for this surrogate as a function of the temperature requires to tabulate the properties from a constant value of heat capacity at constant pressure.

	Composition	Mass fraction [-]	Molar weight [g/mol]	Molar fraction [-]
Linear	$nC_{10}H_{22}$	0.767	142.284	0.7396
Aromatic	C_9H_{12}	0.132	120.1916	0.1507
Naphthenic	C_9H_{18}	0.101	126.241	0.1097
KERO_LUCHE	$C_{9.73957}H_{20.0542}$	1.000	137.195	1.0000

Table 7.4: *Definition of the composition of the kerosene surrogate by Luche (2003) (KERO_LUCHE). Reproduced from Franzelli et al. (2010).*

Figure 7.12(a) shows the temporal evolution of the non-dimensional droplet diameter using the AS model and the three approaches for the thermodynamic and transport properties. The computations with ievap_01 and ievap_21 shows very similar results and an evaporation time larger than ievap_11 (25%). Figure 7.12(b) shows the evolution of the droplet temperature normalized by the initial droplet temperature: the evolution is similar for all the calculations, the equilibrum values being 5 K lower with ievap_01 and ievap_21 than with ievap_11.

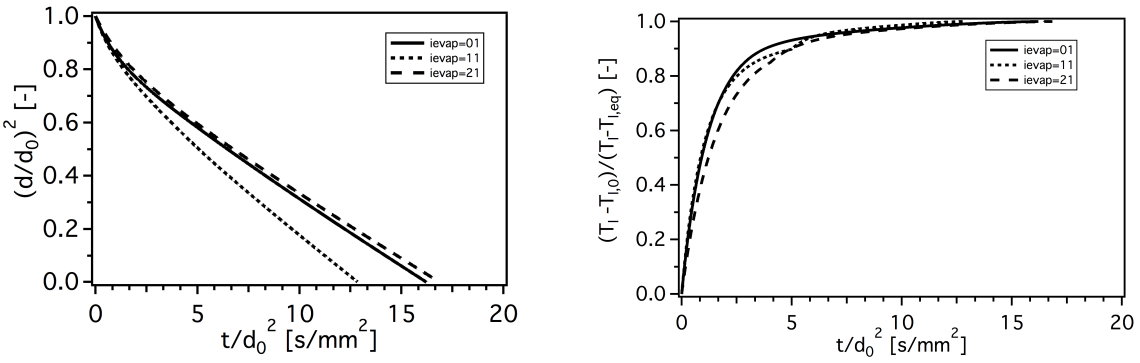

(a) (b)

Figure 7.12: *Temporal evolution of the non-dimensional droplet surface (a) and droplet temperature (b). Evaporation of KERO_LUCHE droplet.* $T = 440K$, $P = 1bar$ *and* $Tl_0 = 426K$.

Ghassemi *et al.* (2006) performed experiments on evaporation of kerosene droplets, obtaining the rates of evaporation of the fuel in a N_2 atmosphere. The results correspond to the evaporation of a kerosene droplet of $1mm$ of diameter at $0.1MPa$ and different gaseous temperatures. The experiment of Ghassemi *et al.* (2006) have been reproduced in this work using the Spalding and the AS evaporation models and the three approaches for the calculation of the properties implemented in AVBP. The results obtained using the thermo_CANTERA approach are very close to those of the thermo_AVBPmix approach and are not presented. The evaporation rates are extracted once the pre-heating period is finished (in the straight part of the curve in Fig. 7.12(a)).

The results of ievap_11 show good agreement with Ghassemi for low temperatures. As the temperature increases, ievap_11 deviates and ievap_1 agrees better with the experimental results. As it happened with the test for n-heptane, the AS model reduces the evaporation rate. This is also the case of the results obtained with thermo_AVBPmix.

The calculations performed with complex transport and thermodynamic properties laws show worst agreement with the experimental results of Ghassemi *et al.* (2006), except for $500°C$. None of the numerical models predict the exponential behaviour of the curve. All of them predict a linear increase in the evaporation rate with the temperature.

The ievap_21 model will be retained to be used when performing the simulation of the MERCATO configuration in Part IV. Taking into account that the same experiments performed by Ghassemi *et al.* (2006) with n-heptane overestimated the evaporation rate at high temperature (Fig. 7.9), the same results for kerosene are expected. The conditions in the MERCATO configuration studied in Part IV correspond to a cold operating point close to $400K$. The good agreement between ievap_21 and the experiments at low temperature justifies the choice of ievap_21 as the evaporation model for the simulations of this configuration.

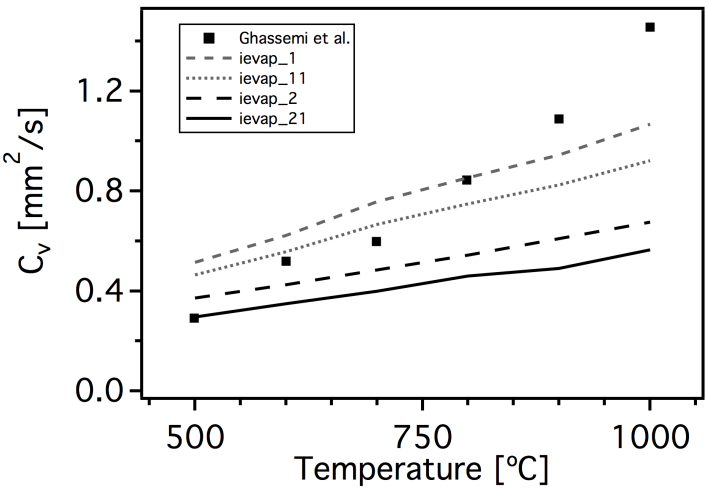

Figure 7.13: *Evaporation rates of kerosene as a function of the gaseous temperature. Comparison with experimental results of Ghassemi* et al. *(2006)*

7.7 Conclusions

This Chapter presents a study on the evaporation of single isolated droplets. This work is motivated by the publication of new experimental results (Chauveau *et al.* (2008)) that question the widely accepted results of Nomura *et al.* (1996). Chauveau *et al.* (2008) proposed a new experimental setup able to reduce the heat conduction through the support fiber during the experiment keeping the spherical shape of the droplet at the same. This new technique leads to much slower evaporation processes. The importance of the heat conduction though the fiber was already pointed out by Yang & Chang (2001), who demonstrated, using numerical calculations, that the experimental data obtained by Nomura *et al.* (1996) were biased by the contribution of a radiative source term coming from the inner walls of the furnace were the experiments were conducted and by an extra heat contribution through the support fiber.

Sanjosé (2009) showed that the thermodynamic and transport properties have a great impact on the evaporation process and that taking into account complex laws for them is crucial to perform evaporation calculations. However, the complex thermodynamics and transport laws are not adapted to perform industrial-type simulations due to their increased computational cost. The evaporation model available in AVBP (ievap_1) uses the Spalding evaporation model and simplified thermodynamic and transport properties (thermp_AVBP) and shows very good agreement with the results of Nomura *et al.* (1996). The Abramzon-Sirignano evaporation model has been implemented in AVBP, showing small di?erences with the former model, which confirms the importance of the thermodynamical and transport properties. A new methodology consisting in using adapted Prandtl and Schmidt numbers for the evaporation, di?erent from those optimized for the reduced chemical schemes implemented in AVBP, along with a laminar viscosity law depending not only on the temperature but also on the mixture composition (thermo_AVBPmix) has been proposed. The new methodology produces results close to the experimental results of Chauveau *et al.* (2008) and to the simulation using a complex evaluation of the thermodynamic and transport properties, without increasing the computational cost of the simulation.

Table 7.5 shows a summary of the performances of the different approaches studied when comparing with the reference (results obtained with thermo_CANTERA). All the approaches show the same evolution when applied to a different range of temperatures or pressures and to different fuels too. Test have been performed on evaporation of n-heptane droplets for temperatures in the range [473 K, 748 K] and pressures in the rage [1 bar, 20 bar]. When the ambient pressure increases, the saturation state is reached sooner and the evaporation time further increases. Evaporation of kerosene droplets in the conditions of

the MERCATO combustion chamber configuration.

Evaporation model:	Agreement with reference:	
	thermo_AVBP	thermo_AVBPmix
Spalding	-	++
AS	+	+++

Table 7.5: *Summary of the performances of the different approaches studied in this Part, for the comparison with the reference under the same conditions.*

In real applications, the initial diameter of the droplets is usually smaller than 100 μm, the spray is injected in most cases at ambient temperature. In non-reactive cases, the gas temperature is usually lower than 700 K, resulting in relatively long evaporation times. In reactive cases, droplets may encounter the flame close to the injection. Depending on the characteristics of the liquid fuel and the spray (diameter, initial droplet temperature) they may then evaporate before reaching the flame or cross the flame front and enter a droplet burning regime. In this case the effect of the evaporation model in the global statistics of the gaseous and the dispersed phases is reduced.

during this work, the impact of the evaporation has been studied in a complex configuration: the MERCATO test rig (Part IV). In the MERCATO configuration, the characteristic droplet evaporation time ranges from about 45 to 60 ms, while the droplet response time ranges from $1.5 \cdot 10^{-2}$ to 5.3 ms and convective time is 20 ms. The life-time of the droplets is larger than the flow convective time. The droplets are expected to occupy a large portion of the chamber and to interact with the largest scales of the gas flow, being trapped in the reciculation zones where they finish their evaporation. The evaporation model should therefore have a major effect on the gaseous fuel distribution in the recirculation zones.

The application of the new methodology to a wider variety of fuel species and conditions would confirm the validity of the new method. To do so, a detailed experimental data based on liquid fuel evaporation is needed. As it has been demonstrated by Chauveau *et al.* (2008), the improvement of the experimental measurement techniques is key for the development and validation of numerical models. Accounting for natural and forced convection on single isolated configuration for which experimental data is already available is straightforward with AVBP. This step, however, has been skipped here but it would provide deeper insight in the behavior and performances of the model. Moreover, convection effects may increase considerably the differences between the AS and the Spalding models, although the general tendency is expected to remain unchanged. As it has been done in the methodology proposed here for the mixture viscosity, an improvement of the evaluation of the diffusion coefficient and/or the thermal conductivity by means of the implementation of more accurate expressions but without including collision potentials may further improve the results. A step further in the validation of the methodology proposed here is to perform simulations in more complex configurations and to compare with experiments which would provide both the droplet and the gaseous fuel distributions.

Part IV

Application to MERCATO configuration

Chapter 8

MERCATO configuration: Experimental and Numerical setups

This Part of the manuscript discusses the application of the developpements of RUM modeling presented in Part II and the evaporation modeling presented in Part III on a semi-industrial configuration: the MERCATO test rig. This configuration has been experimentally investigated by ONERA in a timely collaboration with CERFACS and TURBOMECA. The goal being to obtain a better comprehension of the ignition sequences in a real aeronautical combustion chamber in high altitude conditions, prior to the experiments in ignition conditions, the experimental campaign has extensively measured both the single-phase and the two-phase flows for this setup. For this reason, it is a very good candidate for the evaluation of two-phase flow LES: the experimental data on both phases is very comprehensive and provides detailed comparisons.

The experimental investigations of this combustor were performed by García-Rosa (2008) under the supervision of R. Lecourt. Numerically, this configuration has been extensively investigated in the past. Lamarque (2007) and Sanjosé (2009) performed simulations of the non-reacting two-phase flow using an Euler-Euler approach for the liquid phase. Sanjosé (2009) performed comparisons using different numerical schemes, mesh resolutions and numerical parameters, Roux (2009) also studied the influence of a more adapted numerical scheme (PSI) for the LES of the dispersed phase. Senoner (2010) performed non-reacting simulations using a Lagrangian approach for the dispersed phase and studied the effect of polydispersity and secondary-breakup modeling. Extensive comparisons between the results of Sanjosé and Senoner can be found in Sanjosé (2009) and Senoner (2010). Vié (2010) performed simulations using a sectional approach (Laurent *et al.* (2004)) to account for polydispersity. Sanjosé *et al.* (2011) developed a new model for spray injection adapted to the Euler-Euler approach and tested it in this configuration. Finally, Eyssartier (2012) simulated a confined variation of the configuration to study ignition phenomena.

In the present work, the non-confined evaporating configuration studied by García-Rosa (2008), Lamarque (2007), Roux (2009), Sanjosé (2009) and Senoner (2010) is investigated.The aim is to analyze the performances of the models retained in Parts II and III. This work benefits from past experiences and conclusions obtained in previous works in terms of geometry description, boundary conditions, numerical scheme and parameters.

This Chapter is organized as follows: the experimental configuration and setup are described in Section 8.1, a brief description of the mesurement techniques used is also provided. The numerical setup is then deeply described in Section 8.2. The simulation domain, mesh, boundary conditions and numerical parameters used are specified. In Section 8.2.3 a test matrix summarizing the different cases simulated is presented. Finally, the results are shown in Chapter 9.

8.1 Description of the experimental setup

Figure 8.1 shows two pictures of the MERCATO test rig experimentally investigated by ONERA at the Fauga-Mauzac center located near Toulouse (France). It contains all elements of a standard aeronautical combustor: plenum, swirler, liquid fuel injector and a combustion chamber. It is a relatively complex configuration. The air is injected through an inlet channel into a plenum of square section (100×100 mm) and 200 mm in length. At the end of the plenum a radial swirler system composed by 12 channels imposes a very strong rotating motion to the flow entering the combustion chamber. Afterwards, but prior to the flow entry into the chamber, a cylindrical diffusor of 30 mm in diameter leads the flow into the combustion chamber (13 cm^2 square section and 285 mm in length). The combustion chamber has plane walls in order to have optical access to the flow. If the combustion chamber is rather simple it is not the same for the rest of components. The liquid fuel injection system is located at the center of the diffusor and corresponds to a modified pilot injector of the Malika helicopter chamber (Turbomeca). The atomizing system uses a pressure swirl type Delavan atomizer for the liquid kerosene. To finish, the flow leaves the combustion chamber directly into the atmosphere.

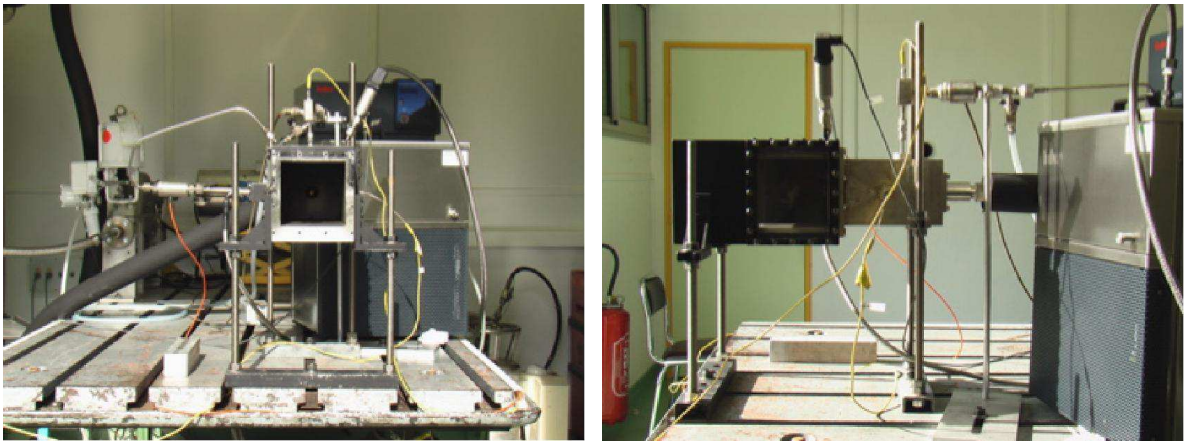

(a) (b)

Figure 8.1: *Views of the MERCATO experimental setup at Fauga (García-Rosa (2008)).*

8.1.1 Experimental conditions

Many operating points have been experimentally investigated in this configuration (García-Rosa (2008)). Only one operating point, defined by the reduced flow rate (W_R, Eq. (8.1)) is investigated here (Table 8.1). The conditions presented correspond to $W_R = 0.32\ kg\sqrt{K}/(s \cdot bar)$ and a liquid fuel flow rate of 1 g/s.

$$W_R = \frac{\dot{m}_{air}\sqrt{T_{air}}}{P} \ . \tag{8.1}$$

Air flow rate [g/s]	T_{Air} [K]	$T_{Kerosene}$ [K]	Kerosene flow rate [g/s]	Injection equiv. ratio
463	15	300	1	0.97

Table 8.1: *Parameters of the operating point presented in this Part.*

8.1.2 Experimental data measurement

Laser Doppler Anemometry (LDA) was used to characterize the gaseous flow. This technique analyses the frequency signal emmited by a particle when crossing a laser volume at the point where two distinct laser sheets interfere. The measurements were performed in purely gaseous flow seeded with fine oil droplets ($d_p < 2\ \mu m$) in order to obtain the gaseous velocity fields. Measurements were performed in five different axial planes at 6, 26, 56, 86 and 116 mm away from the injector outlet located at an axial coordinate $z = 0\ mm$. The data was collected along the vertical and horizontal orientations (Fig. 8.2). The measurements of the gaseous flow include mean and root mean square (RMS) velocity values in the axial, radial and tangential directions.

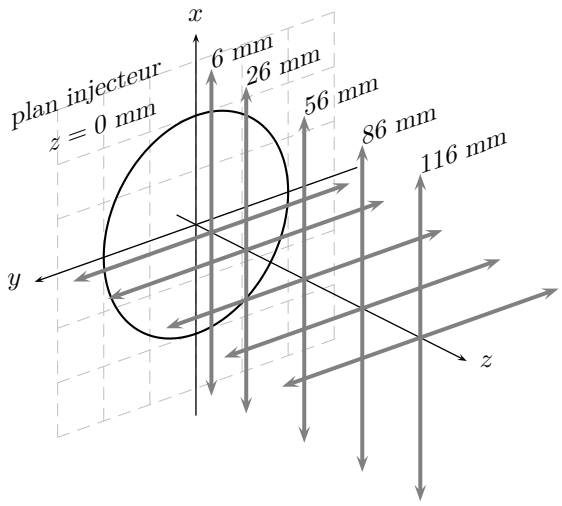

Figure 8.2: *Sketch of the experimental measurement planes (Extracted from Sanjosé (2009)).*

Phase Doppler Anemometry (PDA) technique was used for the liquid phase flow. It gives information about the droplet diameters. The combination of LDA and PDA techniques provides a complete characterization of the two-phase flow. However, the formation of a liquid film on the visualization windows limited the measurement planes at which experimental data was collected. Indeed, droplet diameter and velocities are available only at $z = 6$, 26 and 56 mm. Moreover, for the measurements at $z = 56\ mm$, the air mass flow rate was increased to 18 g/s in order to reduce the liquid film formation on the visualization windows. For this reason, comparisons between numerical and experimental results at this axial location must be taken with care due to this difference in air mass flow rates.

The operating point detailed in Table 8.1 was used to adjust the optical diagnostics for the experimental measurements. For this reason, redundant data was collected, which allows the calculation of an estimation of the error in the experimental results (Table 8.2). Since the gaseous phase data was collected in single-phase conditions, an extra contribution in the gaseous data due to two-way coupling, must be added to these values.

Measured Variable Mean value	Standard Deviation between measurement sets	Measured Variable RMS value	Standard Deviation between measurement sets
$u_{g,z}$	9%	$u_{g,z}\|_{RMS}$	12%
$u_{g,y}$	13%	$u_{g,y}\|_{RMS}$	6%
$u_{l,z}$	18%	$u_{l,z}\|_{RMS}$	10%
$u_{l,y}$	30%	$u_{l,y}\|_{RMS}$	20%
d_{10}	25%		

Table 8.2: *Estimation of the measurement errors of the LDA system. Calculated over the measurements obtained at $z = 26mm$. Reproduced from Sanjosé (2009).*

8.2 Description of the numerical setup

This section is devoted to the description of the numerical setup used for the Euler-Euler simulations performed with AVBP in the MERCATO configuration. The computational domain includes all the elements relevant to the characterization of the flow field inside the chamber (Fig. 8.3).

The experiments were performed in a configuration where the flow exited directly into the atmosphere. For this reason, apart from the air inlet tube and all the other elements until the chamber exit, part of the atmosphere at the chamber outlet is included in the computational domain. Indeed, the central toroidal recirculation zone appearing at the center of the chamber is longer than the chamber itself. The combination of inflow and outflow in the same boundary condition is very difficult to handle numerically, in particular due to the present formulation of the NSCBC formalism (Poinsot & Lele (1992)) which is one-dimensional at boundaries. The atmosphere is taken into account by means of a cubic box with a slight coflow of air. A simplified sketch of the simulation domain is shown in Fig. 8.4.

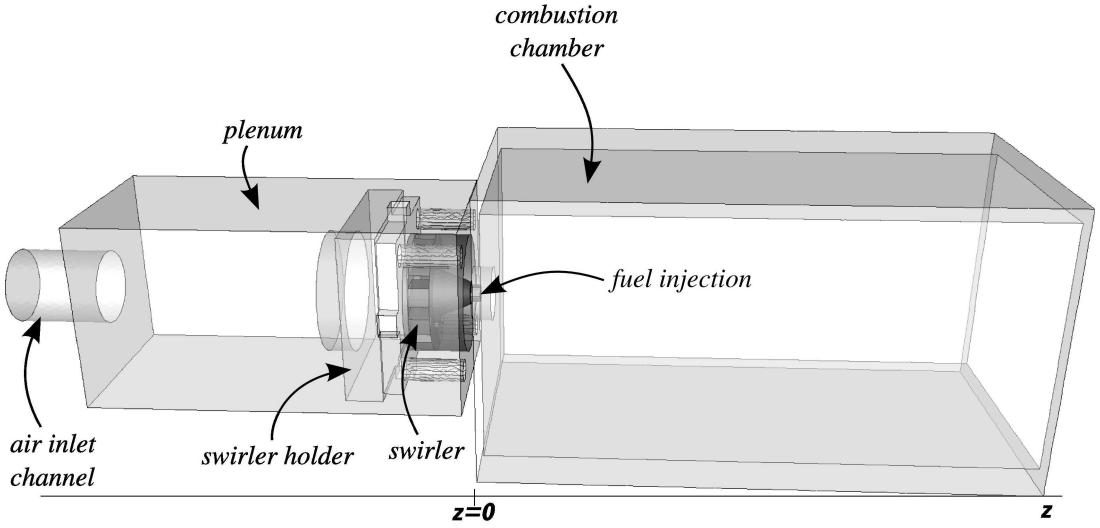

Figure 8.3: *Sketch of the MERCATO geometry (z is the axial coordinate). Extracted from Senoner (2010).*

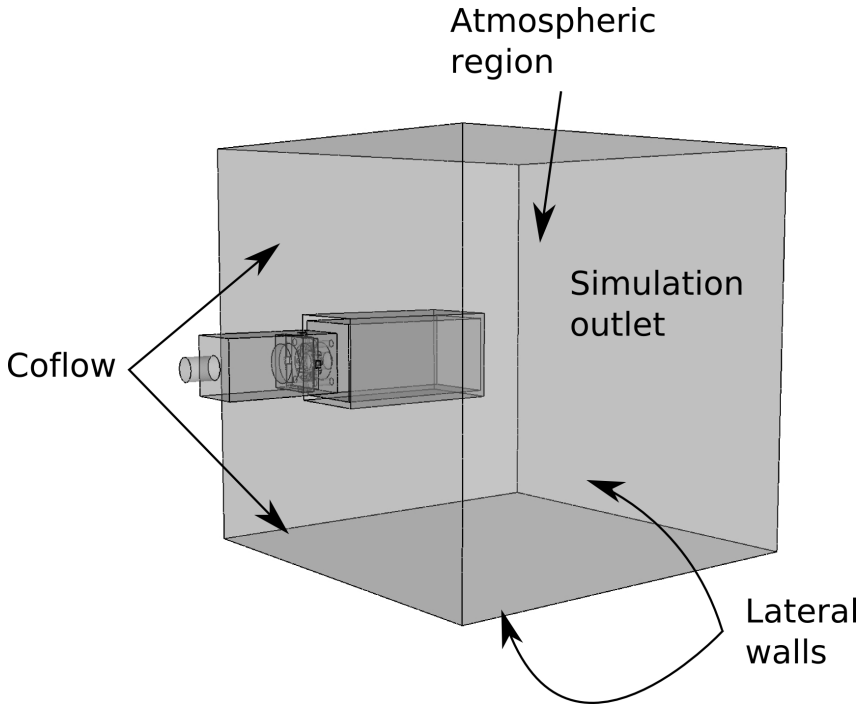

Figure 8.4: *Sketch of the domain retained for the numerical simulations. Extracted from Senoner (2010).*

8.2.1 Computational mesh

The mesh grid used is totally composed by tetrahedra, which allows fine refinements in the zones of interest. Indeed, the zones close to the swirler and the injector have been strongly refined. The grid is progressively coarsened up to the chamber exit. Finally the atmosphere has been coarsely meshed in order to reduce the computational cost since the flow field in this region is of no interest. Figure 8.5 shows total and partial views of the mesh grid in 3D and 2D. Table 8.3 summarizes the main parameters describing the mesh grid used.

Parameter	Value
Number of cells	14047346
Number of nodes	2486230
Smallest cell volume	$1.54719 \cdot 10^{-12}\ m^3$
Time step (CFL=0.7)	$1.498 \cdot 10^{-7}\ s$

Table 8.3: *Parameters describing the mesh grid.*

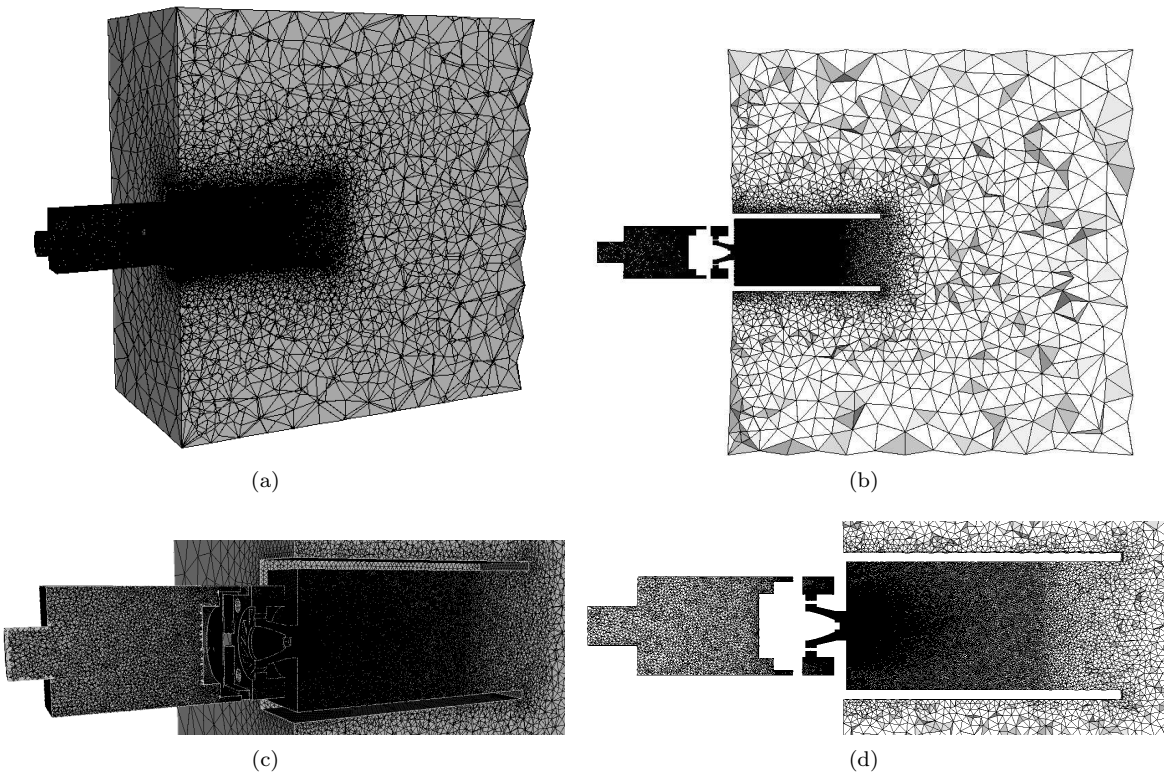

Figure 8.5: *Different views of the mesh grid used. Total views including the atmosphere: (a) and (b). Partial views, zoom on plenum and chamber: (c) and (d).*

8.2.2 Boundary conditions

Table 8.4 shows the Boundary Conditions (BCs) for the gaseous phase. Table 8.5 shows the BCs for the liquid phase. The liquid fuel used is kerosene, modeled by the species KERO_LUCHE already defined in Section 7.6. The FIM_UR methodology (Sanjosé *et al.* (2011)) is used to mimic the liquid injection without simulating the liquid jet itself, i.e. neglecting the primary and secondary atomizations. The parameters used are presented in Table 8.6. Due to the Euler-Euler formulation, a small liquid volume fraction must be specified in the regions where there are no droplets in practice. For this reason, a minimal value of liquid volume fraction and droplet number density at a very small droplet diameter is injected along with the carrier fluid at the air injection and the coflow injection with the same gas velocity to avoid drag force effects. At the beginning of the simulation, considered at the moment when the liquid injection starts after several gaseous convection times, a uniform field of droplets of diameter 3 μm of diameter and droplet number density $7 \cdot 10^6$ m^{-3} is added at the initial time with the same velocity of the gas phase.

The injection parameters mimic the values measured in the experiments. Since the MEF implemented in AVBP treats only monodispersed flows, the droplet diameter at the liquid injection has been chosen equal to the mean droplet diameter experimentally measured at $z = 6$ mm.

BC name	Type	Imposed value
Inlet channel	Inlet NSCBC	$T_g = 463K$ $\dot{m}_g = 15.0g/s$ $Y_{N_2} = 0.767$; $Y_{O_2} = 0.232$
Coflow	Inlet NSCBC	$T_g = 463K$ $u = 0.15m/s$ $Y_{N_2} = 0.767$; $Y_{O_2} = 0.232$
Injector	Inlet NSCBC	$T_g = 463K$ $u = 1.3 \cdot 10^{-3}m/s$ $Y_{N_2} = 0.767$; $Y_{O_2} = 0.232$
Plenum	Wall	No-slip adiabatic
Swirler	Wall	No-slip adiabatic
Chamber	Wall	No-slip adiabatic
Atmosphere lateral walls	Wall	Slip adiabatic
Outlet	Outlet NSCBC	$P = 1atm$

Table 8.4: *Boundary conditions for the gaseous phase.*

BC name	Type	Imposed value
Inlet channel	Dirichlet	$T_l = 300K$ $\alpha_l = 7.7 \cdot 10^{-9}$ $n_l = 5 \cdot 10^8 m^{-3}$ $u_l = 22m/s$
Coflow	Dirichlet	$T_l = 300K$ $\alpha_l = 7.7 \cdot 10^{-9}$ $n_l = 5 \cdot 10^8 m^{-3}$ $u_l = 0.15m/s$
Injector	Dirichlet	$T_l = 300K$ $\dot{m}_l = 1g/s$ $d_l = 55\mu m$
Plenum	Wall	Slip
Swirler	Wall	Slip
Chamber	Wall	No-slip
Atmosphere lateral walls	Wall	Slip
Outlet	Convective	

Table 8.5: *Boundary conditions for the liquid phase.*

Parameter	Imposed value
Mass flow rate	$\dot{m}_l = 1g/s$
Atomizer orifice diameter	$D_0 = 0.5mm$
Half-spray angle	$\theta_S = 40°$
Swirl rotation direction	clockwise

Table 8.6: *Characteristics of the liquid injection.*

8.2.3 Numerical parameters

This section describes the numerical parameters used for the simulations of the MERCATO configuration. As it has been done with the configuration presented in Part III, the numerical parameters have been kept equal for all the cases simulated in order to reduce the possible sources of variability and ease the comparisons. Table 8.7 summarizes the main parameters for both the gaseous and liquid phases. TTGC numerical scheme (3^{rd} order in time and space) is chosen for the convection of both phases because of its low numerical dissipation. Roux (2009) performed Eulerian simulations using two different combinations of numerical schemes: TTGC and FCT PSI-LW. However, the results showed for the second case were not sufficiently converged, so no clear conclusions could be drawn. Since the FCT PSI-LW scheme was not available in AVBP at the moment when the simulations presented here were performed, it was not possible to use it. Sanjosé (2009) performed comparisons using TTGC for both phases and PSI for the liquid phase along with LW for the gaseous phase. The results were better when using TTGC.

Subgrid scale modeling relies on the WALE model (Ducros *et al.* (1998)) for the gas phase since its behavior is expected to be more physical in zones of pure shear compared to the Smagorinsky model. The Moreau (Moreau (2006)) model is used for the liquid phase. The walls are non-slip and no model is used to take into account either the boundary-layer effects or any liquid film at the walls. Indeed, near-wall phenomena are out of the scope of this work. Colin sensor (Colin *et al.* (2000)) is used for artificial viscosity in the gaseous phase. The values of the coefficients are limited to the lowest levels guaranteeing numerical stability. The CMS AD model (Sanjosé (2009)) is used for the liquid phase. The parameters of the model are the lowest values that ensure numerical stability.

Parameter	Value
Numerical scheme	TTGC
Diffusion operator	2Δ
Sub-grid scale model	WALE
AV model (gas phase): Colin	$\epsilon_2 = 0.10$
	$\epsilon_4 = 0.01$
AV model (liquid phase): CMS	$\epsilon_2 = 0.50$
	$\epsilon_4 = 0.01$

Table 8.7: *Summary of the numerical parameters.*

8.2.4 Test cases

The purpose being to assess the performances of the RUM model retained in Part II (2ΦEASM3) and the new evaporation procedure proposed in Part III (ievap_21) four different combinations are tested.

Regarding the RUM modeling, a case that does not take into account the RUM at all (the RUE is zero during the whole calculation) is opposed to a case for which the RUM is modeled with the 2ΦEASM3 model. Note that, the classic RUM model implemented in AVBP, namely VISCO does not work for this configuration. Indeed, the simulation is numerically unstable and the problem can not be overcome with the use of AD. Previous works showed results using VISCO model (Sanjosé (2009)). However, in these studies, the maximum value of the RUE was artificially limited to a percentage of the mesoscopic energy (around 20%) to ensure stability. Indeed, as shown in Part II, VISCO model overpredicted the RUE and the simulations became unstable. Limiting the maximum value of RUE was the only way to stabilize the simulations performed taking into account the RUM. However, the results presented in Chapter 5 showed that, depending on the Stokes number, the RUE can be larger than the mesosocopic energy (e.g. Figs. 5.44(a) and 5.44(b)). For these cases, limiting the RUE to a percentage of the mesoscopic energy means ignoring a part of the flow physics. In this work, when a model needs to be limited in order to be numerically stable, it is considered that the model does not work and it is discarded.

The new methodology for the evaporation of liquid droplets proposed in Part III (ievap_21) is compared to the classical evaporation model (Spalding along with a gaseous viscosity depending only in the temperature and the gaseous Prandtl and Schmidt numbers) (ievap_1). At the time the results of Sanjosé (2009) were obtained, only the ievap_1 model existed in AVBP. When studying the evaporation of kerosene isolated droplets and performing comparisons with the results obtained with CANTERA, Sanjosé (2009) showed that the evaporation rate was largely overestimated using ievap_1. The problem was overcome applying a correction factor to the evaporation source terms. New models have been developed and implemented during this work which solve this problem.

Table 8.8 shows the matrix of test cases presented in this Part of the manuscript.

Case name	RUM model	Evaporation model
noRUM_Ev1	noRUM	evap_1
noRUM_Ev21	noRUM	evap_21
RUM_Ev1	2ΦEASM3	evap_1
RUM_Ev21	2ΦEASM3	evap_21

Table 8.8: *Matrix of test cases.*

Chapter 9

MERCATO configuration: Numerical Results

This Chapter presents the results obtained from the LES of the MERCATO configuration presented in Chapter 8. The main purpose is to assess the impact of the evaporation model developed in Part III and the RUM model retained in Part II in a complex geometry. Four cases have therefore been simulated (Table 8.8) that combine two evaporation models and two RUM models. Since the objective is to validate the models ievap_21 for the evaporation and 2ΦEASM3 for RUM, results will be compared with the classical evaporation model implemented in AVBP (ievap_1) and without any RUM model (noRUM). The classical RUM model used until now in AVBP (VISCO) is not well suited for this configuration. It leads to the crash of the simulation.

Previous works (Sanjosé (2009), Senoner (2010)) have studied the MERCATO configuration performing an extensive analysis of the carrier fluid flow. The operating point is the same as studied by Sanjosé (2009). For this reason, only the topology of the carrier flow will be presented here. No frequency analysis has been performed because and interested readers are redirected to Sanjosé (2009) since it is considered that the results of Sanjosé are applicable to this case.

The Chapter is organized as follows: Section 9.1 evaluates the main timescales of the flow field, for the gas and liquid phases, which can be useful to understand the phenomena taking place. Section 9.2 presents the main features of the carrie flow topology. Qualitative comparisons in the form of instantaneous and time-averaged fields are shown. Quantitative analysis is performed by comparing the numerical results with the experimental data of García-Rosa (2008) assessing the quality of the LES. Section 9.3 presents an analysis of the liquid phase. In this Section, the effect of the evaporation model (cf Section 9.3.2) is first analyzed in a case where the RUM effects are ignored (Cases noRUM_Ev1 and noRUM_Ev21 in Table 8.8). Finally, in Section 9.3.3, the effect of the RUM model is analyzed by comparing the simulations performed with 2ΦEASM3 model and without RUM for the same evaporation model (ievap_21) (Cases noRUM_Ev21 and RUM_Ev21). Qualitative as well as quantitative comparisons are performed. Appendix G shows additional quantitative comparisons (i.e. time-averaged profiles compared to the experimental data) of the four cases for the liquid phase.

9.1 Characteristic timescales of the flow

The Reynolds number of the flow at the entrance of the chamber is evaluated using the bulk velocity, the gaseous density, the gaseous dynamic viscosity and the diameter of the diffusor:

$$Re = \frac{\rho_g u_{bulk} D}{\mu_g} \approx 25000. \tag{9.1}$$

One way to characterize the flow inside the MERCATO configuration is to compare the characteristic timescales of the phenomena taking place:

- The convective timescale τ_{conv} is the time that the flow takes for a complete passage through the chamber. It can be linked to the axial velocity if the rotational motion due to the swirl is ignored. Since the axial velocity is not constant in the whole domain, an approximation can be made using the bulk velocity calculated from the mass flow rate at the entrance of the chamber, $u_{bulk} \approx 28\ m/s$.

$$\tau_{conv} = \frac{L_{chamber}}{u_{bulk}}. \tag{9.2}$$

- The swirl timescale τ_{swirl} is linked to the tangential velocity. It is the time for a complete rotation of the flow. If the radial expansion of the flow is ignored, it can be calculated using the rotation velocity of the flow at the exit of the diffusor, $u_{g,x}$ and the radius of the diffusor:

$$\tau_{swirl} = \frac{R_d \pi}{u_{g,x}}\ . \tag{9.3}$$

The dispersed or liquid phase may also be characterized by its own timescales:

- The droplet relaxation timescale τ_p represents the response time of a droplet to changes in the carrier fluid flow. It depends on the droplet diameter. In this case where evaporation is accounted for, the diameter of the droplets is not constant in the whole domain. Each droplet has its own response time, creating differences in the drag force terms and thus, different behaviors depending on their diameter. In this work, the injection model assumes a monodisperse distributions at the nozzle. Afterwards and depending on the topology of both the gaseous and liquid phases, each droplet will encounter different conditions and the evaporation process will be different for each one. A range of characteristic relaxation timescale is then evaluated: $1.52 \cdot 10^{-5}\ s$ for the smallest droplets ($d_p = 3\ \mu m$) and 5.3 ms for the biggest ones ($d_p = 55\ /mum$).

  This range of particle relation time leads to a range of Stokes numbers depending on the location inside the chamber, which directly impacts the evolution of the dispersed phase flow fields and also the gaseous flow since two-way coupling is accounted for. A Stokes number range can be calculated using a fluid timescale based on the bulk velocity and the width of the chamber:

$$St = \frac{\tau_p}{\tau_f} = \frac{\frac{\rho_p d^2}{18\mu_g}}{\frac{L_{side}}{u_{bulk}}}\ , \tag{9.4}$$

  The Stokes number obtained ranges from 0.15 for the smallest droplets to 1.14 for the biggest ones. It is desirable to compare this value to the Stokes numbers of the temporal particle-laden planar jet studied in Chapter 5. However, since the fluid timescale used for the calculation of the Stokes number in the slab is obtained from the Tchen's equilibrium, a new evaluation of the Stokes number based on a fluid timescale comparable to that used in the MERCATO configuration, must be computed. For the case LR_St1_# in Chapter 5, a new timescale for the carrier phase can be calculated using the initial gaseous velocity in the slab ($u = 52.935\ m/s$) and the length of the box ($L_{box} = 2\pi$ mm). This leads to $St \approx 0.31$.

HIT SLAB			MERCATO
Case	St (Tchen's equilibrium)	St (Initial slab velocity)	Stokes
LR_St0.33	0.33	0.10	$St_{min} = 0.15$
LR_St1	1	0.31	
LR_St3	3	0.93	$St_{max} = 1.14$

Table 9.1: *Equivalence of Stokes numbers based on Tchen's equilibrium and on initial slab velocity for the temporal particle-laden planar jet configuration of Chapter 5.*

Table 9.1 summarizes the equivalence between Stokes numbers based on Tchen's equilibrium and based on the initial slab velocity for the configuration presented in Chapter 5, as well as the Stokes numbers in the MERCATO configuration.

The Stokes numbers in MERCATO range from 0.5 to 3.5 times the value on the temporal particle-laden planar jet. This means that in the MERCATO configuration the behaviors of the cases LR_St1, LR_St3 and LR_St0.33, are present at the same time. The level of turbulence is however much higher.

- The evaporation timescale τ_{evap}: is the time needed for the complete evaporation of a droplet. Here, two different evaporation models are used. The first one (ievap_1) is the classic model implemented in AVBP. It uses simple transport laws and the Spalding evaporation model along with the gaseous Prandtl and Schmidt numbers. The second one, ievap_21, uses more adapted Prandtl and Schmidt numbers along with a more complex calculation of the viscosity in the gaseous film around the droplet and the Abramzon-Sirignano evaporation model. As stated in Chapter 7, these two models give different results in single isolated droplet evaporation. The associated evaporation timescales are thus different. They can be obtained from a 0D calculation of the evaporation of a droplet exiting the injection system of MERCATO ($d_p = 55\mu m$) assuming the mean conditions for the gaseous pressure ($P = 1\ atm$), gaseous and liquid temperatures ($T_g = 440\ K$ and $T_l = 340\ K$).

  The evaporation timescale, corresponding to the droplet lifetime, is longer for ievap_21. This means that the droplets will evaporate slower than with ievap_1. This may have an impact on the dispersed phase topology, since bigger droplets could be convected further downstream, increasing gaseous kerosene concentration further from the injection than in the ievap_1 case.

In all cases, the evaporation timescale is larger than any other timescale of the flow as shown in Table 9.2. In a case without swirl motion, the droplets would exit the chamber before finishing their evaporation. Here the swirl motion creates recirculation zones in the center and in the corners of the chamber where the droplets get trapped and have enough time to completely evaporate. This is a very important feature regarding the possibility of combustion in this configuration, since the presence of recirculation zones also has a stabilizing effect on the flame position.

Timescale	Value
τ_{conv}	$\approx$ 19.6 ms
τ_{swirl}	$\approx$ 2.65 ms
τ_p	$[1.52 \cdot 10^{-5},\ 5.3]$ ms
τ_{evap} (ievap_1)	$\approx$ 44.1 ms
τ_{evap} (ievap_21)	$\approx$ 57.6 ms

Table 9.2: *Summary of the characteristic timescales of the flow.*

9.2 Analysis of the carrier phase flow

The gaseous phase in the MERCATO configuration is characterized by the turbulent nature of the flow field. The analysis performed by Sanjosé (2009) and Senoner (2010) revealed that the flow increases its turbulence while passing through the swirler. Indeed, the gaseous phase is only weakly turbulent at the entrance of the swirler but the rotating motion imposed by the swirler to the flow greatly modifies its nature. Furthermore, the rotational motion combined with the increase in section at the entrance of the combustion chamber leads to a sudden opening of the gaseous jet. At the border of the jet, the shear is strong due to the velocity difference with the quiescent flow inside the chamber, which creates additional turbulence. The turbulence is then gradually dissipated while the flow is convected downstream. Figure 9.1 shows an isosurface of Q-criterion at the entrance of the chamber. This quantity gives an idea of the presence of vortical structures in the flow which have a longitudinal direction and acquire a spiral shape due to the rotating motion imposed by the swirler. The results presented in this Section correspond to Case RUM_Ev21 in Table 8.8.

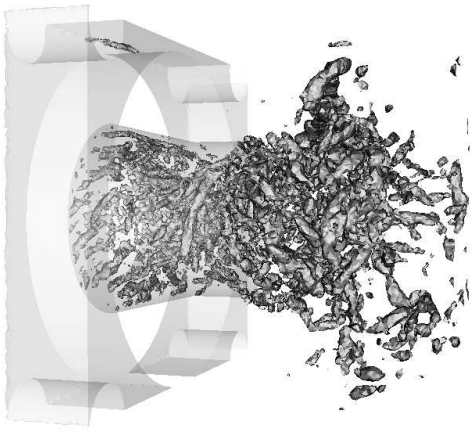

Figure 9.1: *Instantaneous isosurface of Q-criterion ($Q = 2 \cdot 10^8$) at the entrance of the chamber. Case RUM_Ev21.*

Figure 9.2 shows a mean axial velocity field with zero axial velocity isolines in a longitudinal plane at the center of the chamber. Figure 9.3 shows a transverse cut at $z = 20$ mm and $z = 40$ mm. These two figures show the structure of the recirculation zones. A first recirculation zone, the CTRZ (Central Toroidal Recirculation Zone), appears at the center of the chamber. Other recirculation zones appear in the corners of the configuration (CRZ or Corner Recirculation Zones). They are clearly visible in Fig. 9.3(a) where the cross-shaped structure of the CRZ delimited by zero velocity contours is observed. These CRZ are no longer present in the cut plane located at $z = 40$ *mm* as shown by Fig. 9.3(b). These recirculation zones will be useful for the stabilization of a flames in this configuration. Indeed, the negative axial velocities at the center of the domain anchor the flame in front of the injection zone and avoid its convection downstream. The rotation motion creates a negative pressure gradient at the center of the CRZ just in front of the injection nozzle. The gaseous jet opens due to the sudden change in cross-section, however, the negative pressure gradient leads the flow at the center to invert its direction. Figure 9.4 recapitulates the main characteristics of the flow topology: the two types of recirculation zones along with the opening of the gaseous jet at the exit of the nozzle and the mean zones of gaseous shear. Note that the fluid is strongly accelerated at the exit of the diffusor, the axial velocity is very high in this zone and allows the observation of the gaseous jet opening direction.

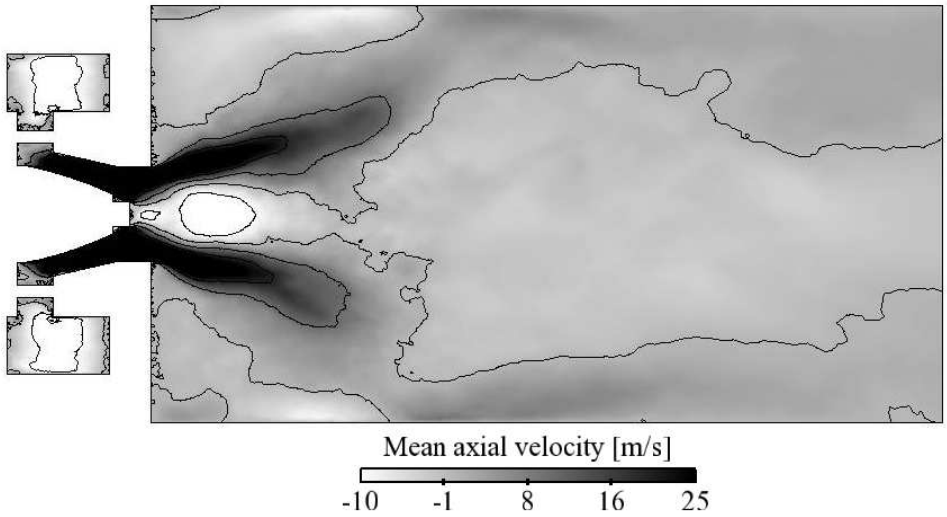

Figure 9.2: *Mean gaseous axial velocity field with isolines of axial velocity in the range -20 m/s and 20 m/s in the longitudinal cut $x = 0$ mm. Case RUM_Ev21.*

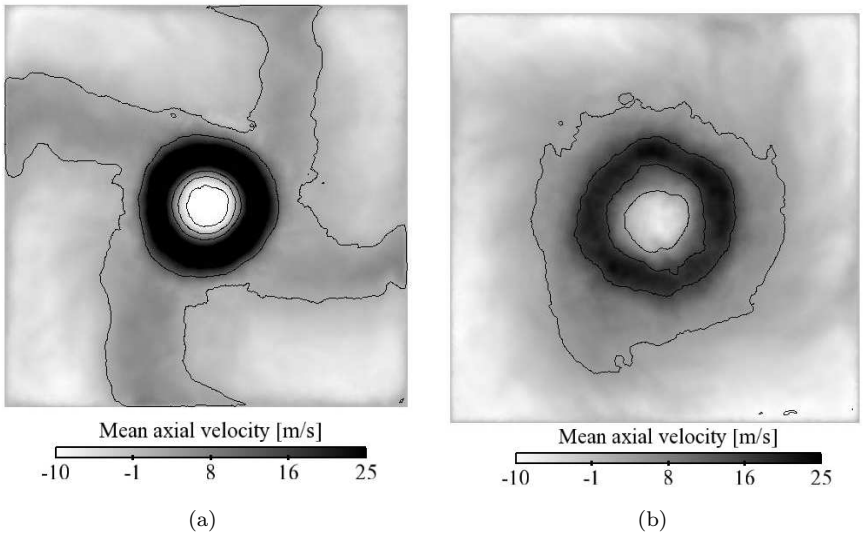

Figure 9.3: *Mean gaseous axial velocity in transverse cuts at (a) $z = 20$ mm and (b) $z = 40$ mm. Isolines of axial velocity in the range -10 m/s and 25 m/s. Case RUM_Ev21.*

Figure 9.5 shows the mean swirl (or tangential) velocity field. The same behavior as found on the axial velocity field is retrieved here. Indeed, the tangential velocity suddenly decreases at the entrance of the chamber since the flow is no more confined by the diffusor and the rotation is no longer imposed by the geometry. However, the swirl endures in the chamber although weakening away from the swirler. Sanjosé (2009) performed a frequency analysis of the gaseous flow. She showed that the gaseous jet is characterized by a precessing vortex core (PVC) located on a highly sheared zone close to the exit of the diffusor. The PVC is an oscillating structure typical of swirling flows with Swirl number higher than 0.6 (Lucca-Negro & O'Doherty (2001)). In this case the Swirl number is equal to 0.75. The PVC rotates around the CTRZ with a frequency close to 830 Hz (Sanjosé (2009)).

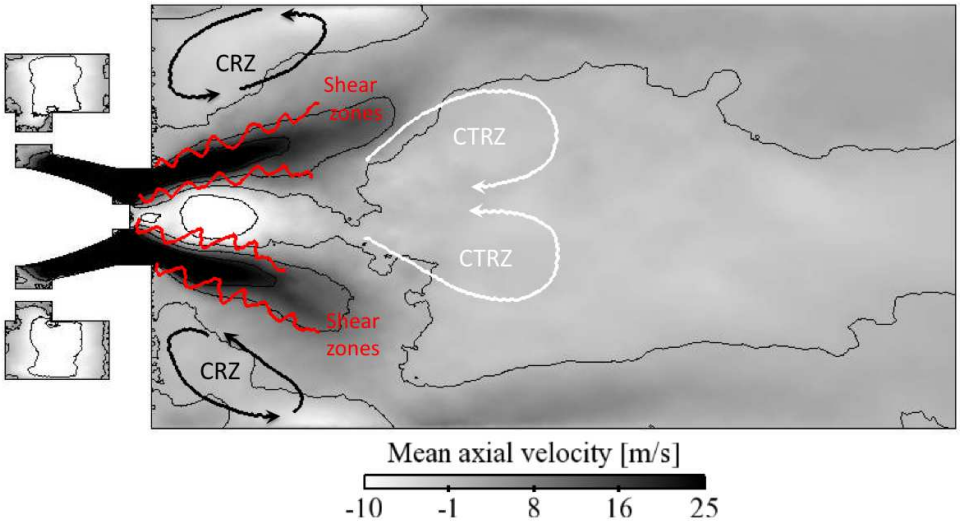

Figure 9.4: *Main features of the gaseous flow topology in the longitudinal cut $x = 0$ mm. Case RUM_Ev21.*

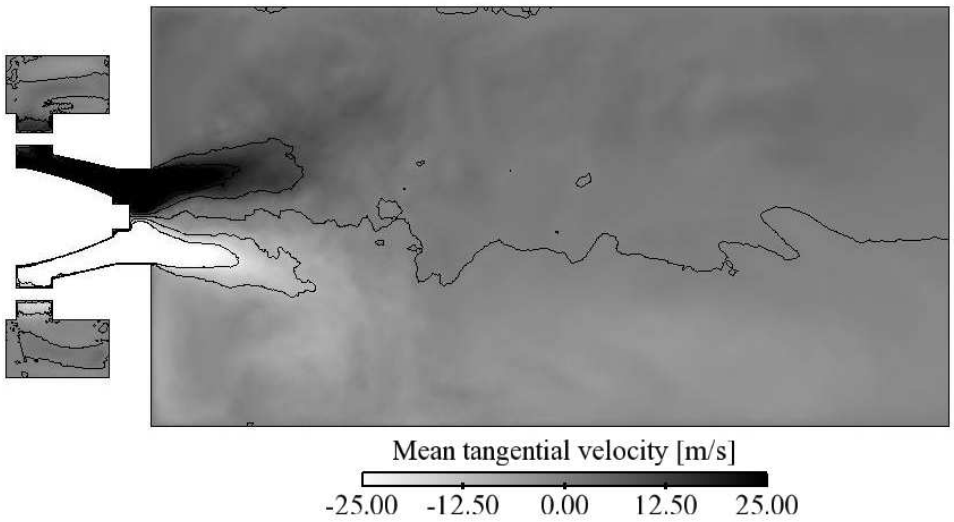

Figure 9.5: *Mean gaseous tangential velocity field in the longitudinal cut $x = 0$ mm. Isolines of tangential velocity in the range -25 m/s and 25 m/s. Case RUM_Ev21.*

9.2.1 Comparison between the gaseous phase results and experiments

The previous Section describes the flow topology. This Section presents the statistics of the gaseous field only for the our cases in Table 8.8. The mean and RMS profiles of the axial, radial and tangential gaseous velocities are compared with the experimental results. Profiles are shown at five different axial coordinates (6, 26, 56, 86 and 116 mm) for the four cases simulated (Fig. 9.6).

LES provides space-filtered values, while the experimental data are generally obtained with a different type of filter. However, for constant density flows, time-averages of scalar quantities are left unchanged by the filtering operation if the filter size is sufficiently small compared to the spatial evolution of the time-averaged scalar (Veynante & Knikker (2006)). Since the gaseous flow in this configuration is weakly compressible and the filter width is assumed small enough, numerical and experimental spatially filtered

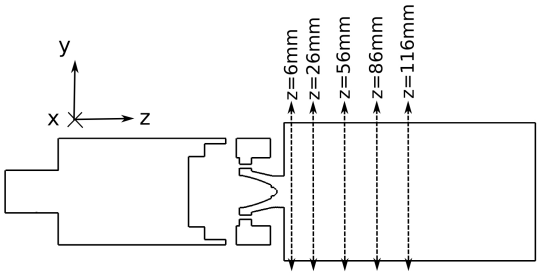

Figure 9.6: *Location of the five sections used for comparisons. Extracted from Senoner (2010).*

data can be directly compared. Time-averaging has been performed during approximately 50 ms for all the cases simulated. This corresponds to two and a half convective times, which may be insufficient to obtain fully converged statistics.

Mean velocities

Figure 9.7 shows the mean axial velocity profiles for the four cases in the five sections. Figure 9.8 shows the mean profiles of the radial velocity and Fig. 9.9 the mean tangential velocity profiles. The results of the four cases are very similar, and that, for the three components of the velocity vector. The profiles match quite well the experimental results, except at the axial coordinates located the further downstream where issues about grid resolution are possible.

Regarding the axial velocity, results at $z = 56\ mm$ show a small deviation from the experimental results. Note that the experimental profiles are not symmetric at this location. Taking this into account, both the shape and the level of the axial velocity is well captured by all cases. Nevertheless, at $z = 86\ mm$ the deviation is more visible. Indeed, the peaks of maximum velocity are located more towards the walls of the chamber. The gaseous jet almost impacts the lateral walls, while in the experiment the peaks are located closer to the center line. A good agreement is however recovered at $z = 116\ mm$. The same behavior has already been observed by Sanjosé (2009), who studied the source of discrepancies at this position. She noticed that around that axial location, the gaseous jet suffered a sudden expansion which makes the flow approach the walls. She stated that the attachment of the jet to the walls and the difficulties to capture this type of phenomena would be at the origin of the disagreements between the numerical and the experimental results.

The experimental radial velocity profiles show important asymmetry downstream of $z = 26\ mm$ (Fig. 9.8). On the contrary, the numerical results are perfectly symmetric for the four cases, noRUM_Ev1 showing slightly higher levels, especially at the peaks. Nevertheless, the overall agreement is good. In all sections, the shape of the profile is well reproduced and the maximum of at least one peak is captured. The agreement is even better for the tangential component of the velocity (Fig. 9.9). Indeed, in this case the experimental results are almost perfectly symmetric and the numerical results are in very good agreement with measurements. The exception is the profile at $z = 26\ mm$ where, again, the experimental profile is not symmetric.

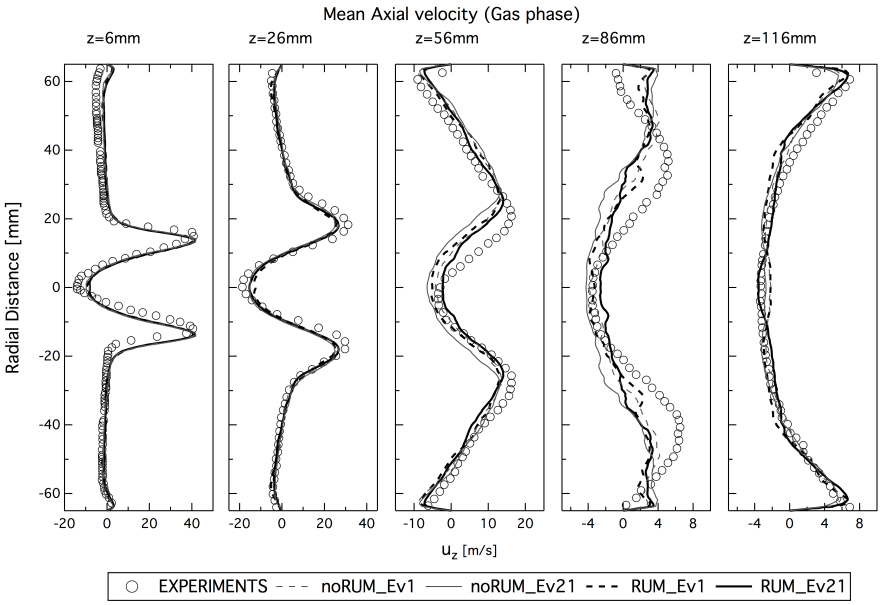

Figure 9.7: *Mean axial velocity profiles. Gaseous phase.*

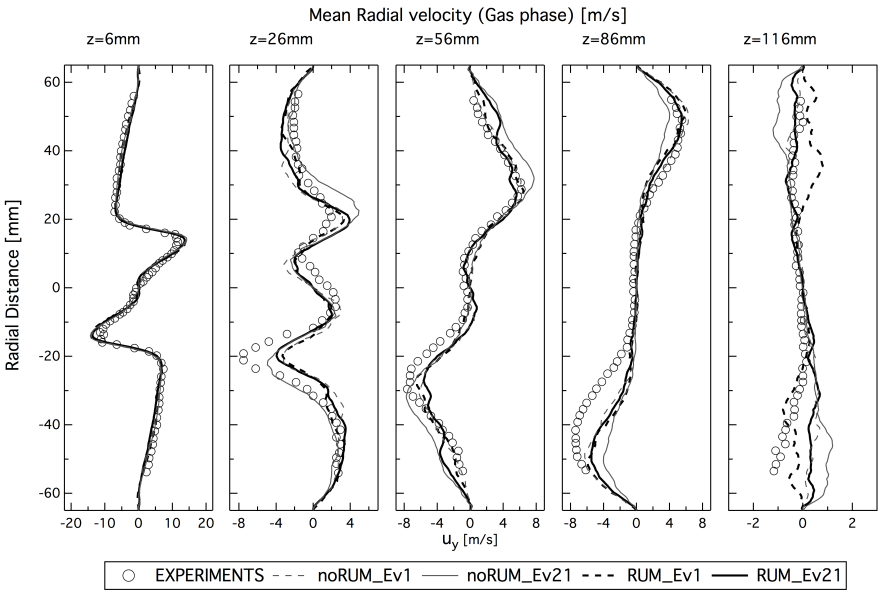

Figure 9.8: *Mean radial velocity profiles. Gaseous phase.*

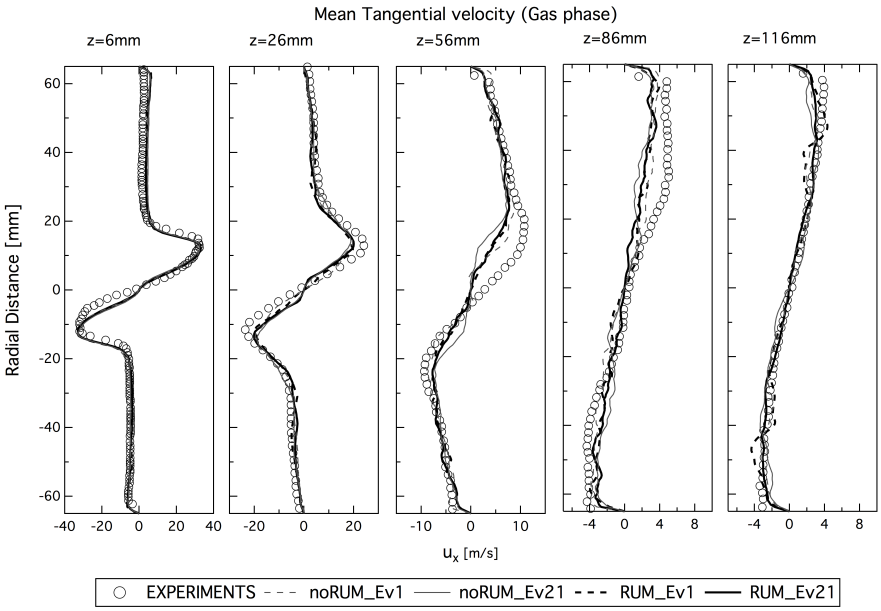

Figure 9.9: *Mean tangential velocity profiles. Gaseous phase.*

RMS velocities

The RMS profiles shown in Fig. 9.10, 9.11 and 9.12 (for the axial, radial and tangential components of the velocity respectively) show relatively good agreement with the experiment. The main features of the profiles are captured by the LES but the level of the fluctuations progressively decreases downstream the chamber and the levels given by the simulations seem too low compared to the experimental results. It is conjectured that this is caused by the progressive de-refinement of the computational mesh, which increases the influence of the subgrid-scale fluctuation terms not taken into account. Note also that a longer averaging time would in general lead to higher RMS values. The profiles are not sufficiently converged. However, some differences between the models are already visible. Case RUM_Ev21 predicts higher RMS values at the center of the chamber. noRUM_Ev21 predicts RMS levels lower than the other three models at the center of the chamber. The section located at $z = 86\ mm$ presents the worst agreement between the LES and the experiments.

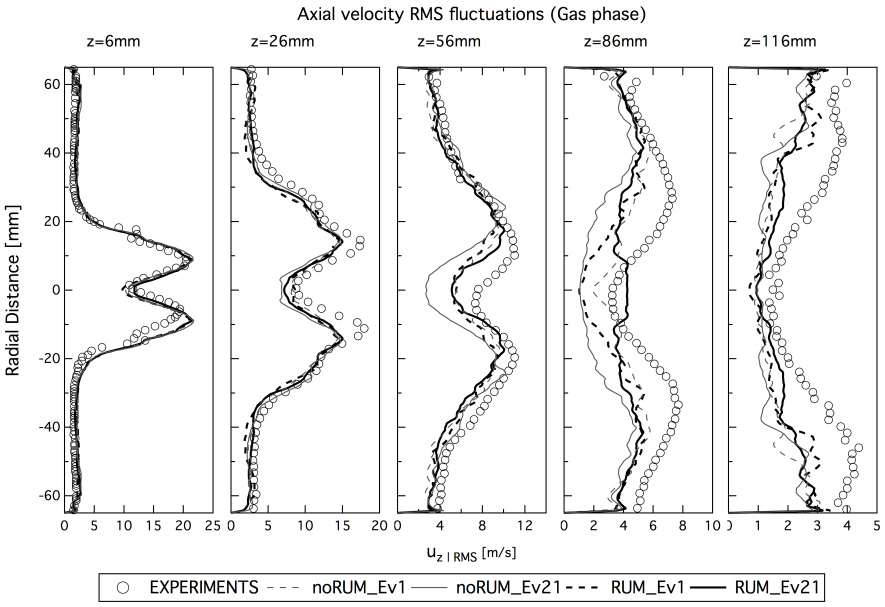

Figure 9.10: *RMS axial velocity profiles. Gaseous phase.*

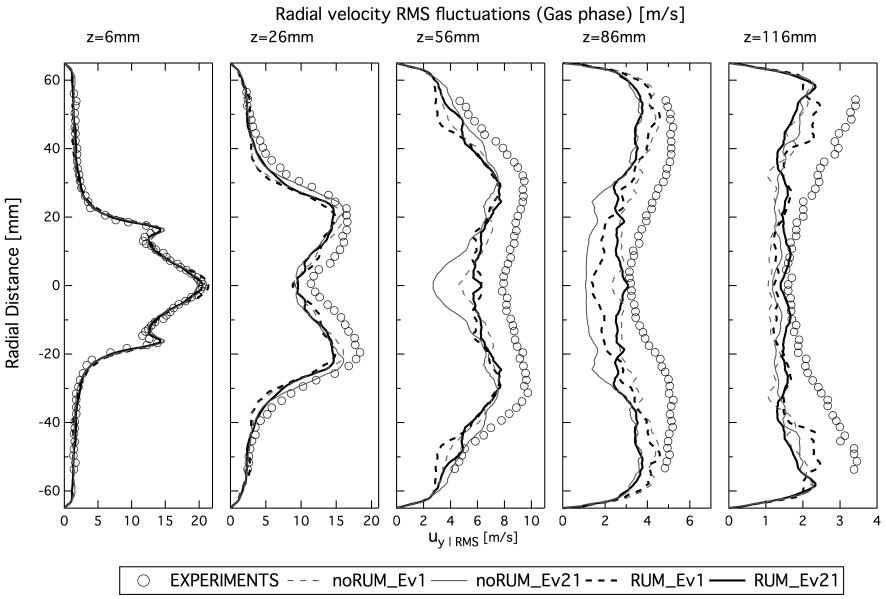

Figure 9.11: *RMS radial velocity profiles. Gaseous phase.*

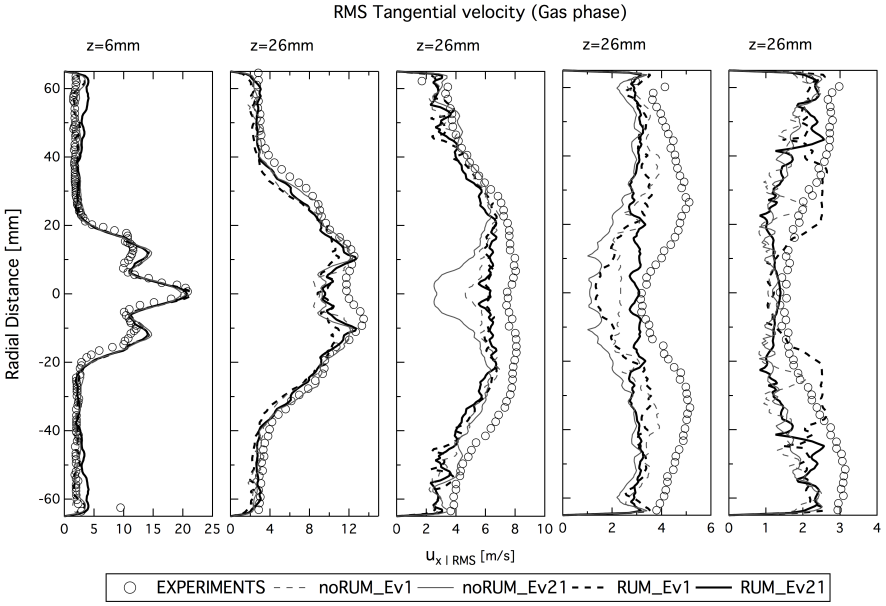

Figure 9.12: *RMS tangential velocity profiles. Gaseous phase.*

9.2.2 Quality of the gaseous LES

This Section aims at providing an analysis of the quality of the LES in terms of turbulent and artificial gaseous viscosities. Figure 9.13 displays the ratio of subgrid scale to dynamic laminar viscosities corresponding to an instantaneous field at $t = 56.76\ ms$ of the simulation of Case RUM_Ev21. The maxima are saturated for better visibility and isolines in the range $0 - 20$ are included to hightlight the zones where the ratio is higher. The contribution of the subgrid scale model is very local and follows the opening of the gaseous jet. Close to the exit of the chamber the subgrid scale model contribution is increased due to the progressive mesh derefinement.

Figure 9.14 shows the ratio of artificial to laminar viscosities corresponding to the same instantaneous solution shown in Fig. 9.13.

The artificial viscosity is calculated with the formula proposed by Lamarque (2007) and provides an estimation of the 2^{nd} order artificial dissipation applied in the LES:

$$\nu_{AV,j} = \frac{\epsilon^2 \zeta_j V_j^{\frac{2}{3}}}{4\Delta t} \ , \tag{9.5}$$

where ϵ^2 is a user defined parameter, ζ_j is the artificial viscosity sensor, V_j represents the nodal volume and Δt is the local timestep. The artificial viscosity levels are one order of magnitude lower than the laminar viscosity. Its application is localized at the borders and follows the shape of the gaseous jet. Globally, the quality of the LES is ensured.

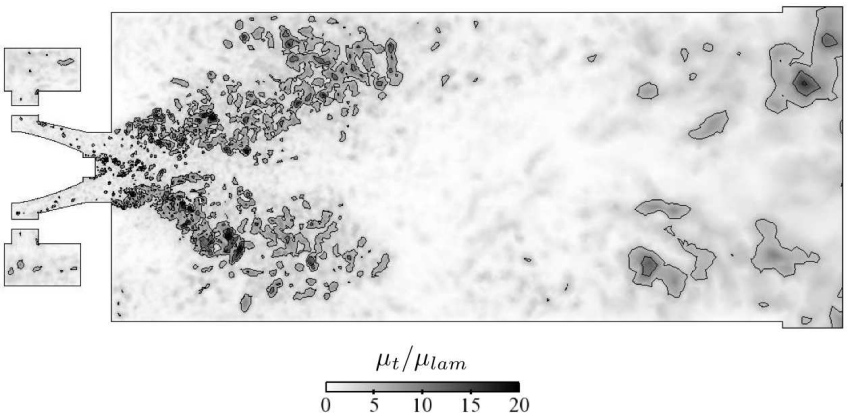

Figure 9.13: *Ratio of turbulent to laminar viscosity corresponding to an instantaneous solution of Case RUM_Ev21.*

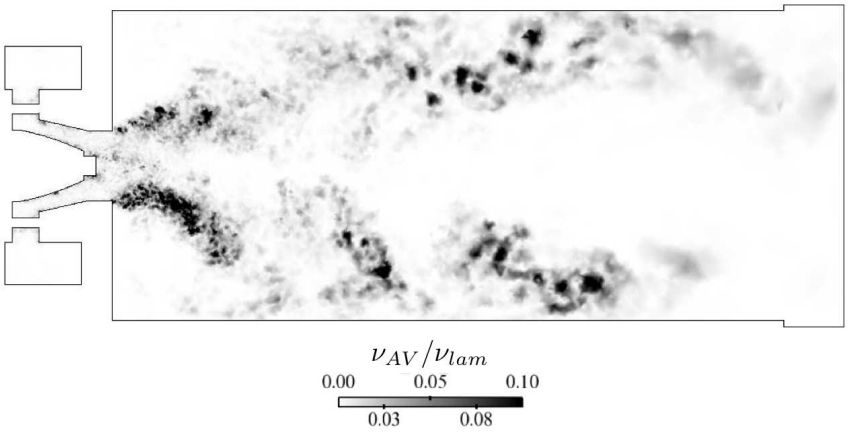

Figure 9.14: *Ratio of artificial to laminar viscosity corresponding to an instantaneous solution of Case RUM_Ev21.*

Conclusions

This Section has shown that LES is able to reproduce the behavior of the gaseous phase flow. The main features of the flow are well captured. The profiles of the mean and the RMS velocities over the three spatial directions agree well with the experimental results. However, the simulations are not able to reproduce the level of fluctuations for the profiles located further from the chamber entrance and room for improvement is clear here.

The four cases simulated (noRUM_Ev1, noRUM_Ev21, RUM_Ev1 and RUM_Ev21) show very similar results. It is expected that the gaseous flow field will have a limited impact on the discrepancies between the four cases concerning the liquid phase flow. The level of convergence of the simulation is yet not sufficient and time-averaging should be performed longer.

9.3 Analysis of the dispersed phase flow

This Section provides an analysis of the dispersed phase fields in the MERCATO configuration. First, an analysis of the global topology of the dispersed phase is presented in Section 9.3.1. Then, Section 9.3.2 focuses on the impact of the evaporation model comparing the cases noRUM_Ev1 and noRUM_Ev21. In these two LES, the RUM is neglected to avoid any impact of the RUM model on the evaporation process.

Section 9.3.3 provides an analysis of the effect of the RUM model. Comparisons between cases noRUM_Ev21 and RUM_Ev21 are presented. The evaporation model is ievap_21, which gives the best agreement with the reference (the code CANTERA) on single isolated droplet evaporation. The performances of 2ΦEASM3 RUM model are assessed through comparison with a simulation without RUM. Comparisons are shown in terms of mean and RMS profiles as well as time-averaged and instantaneous profiles.

The numerical setup is the same in terms of numerical scheme and artificial dissipation for both the gaseous and the dispersed phases for all cases. A simulation with 2ΦEASM3 model for the RUM and ievap_1 model for the evaporation has also been performed. For the sake of conciseness, the corresponding results are not included here. However, they can be found in Appendix G.

9.3.1 Topology of the dispersed phase flow

This Section provides a general overview of the topology of the liquid phase flow field. Liquid droplets of $55\mu m$ of diameter are injected at a temperature of 300 K in the chamber. The temperature of the gas field is initially higher than that of the liquid spray. The injection nozzle is located on the swirler axis at one end of the chamber. The spray is injected following a hollow cone pattern. Droplets are entrained by the gaseous flow and the liquid jet pattern follows the gaseous jet opening. The general features of the liquid phase flow field are similar for the four simulations performed. For the sake of simplicity, only the results corresponding to case RUM_Ev21 are included in this Section. Figure 9.15(a) shows a time-averaged field of liquid mean axial velocity. The liquid spray opening follows the shape of the gas jet. Similarly to the gaseous phase, two recirculation zones, a CRZ and a CTRZ are present. The CTRZ is located close to the injector nozzle and extends downstream towards the exit of the chamber, as happened with the gaseous CTRZ. However, the liquid phase shows a particular behavior close to the injector. The CTRZ is divided in two parts. A small zone characterized by negative axial velocities is located near the injector nozzle. This zone is separated from the main CTRZ located further downstream. The CRZ are disposed on the same way than in the gaseous phase.

Figure 9.15(b) displays the mean tangential velocity field. The spray is entrained by the rotating movement of the gaseous swirl. The frequency analysis performed by Sanjosé (2009) showed that the liquid spray interacts with the gaseous PVC, following the rotating motion of the gas phase at the exit of the diffusor. However, the intensity of the liquid phase rotation movement is lower than that of the gaseous phase. The opening of the liquid phase swirl is not the same either.

Figure 9.16(a) shows an instantaneous field of gaseous velocity magnitude taken at $t = 48\ ms$. Figure 9.16(b) shows the magnitude of the liquid velocity. The liquid velocity field presents the same features as the gaseous velocity field. It is maximal at the same locations of the gaseous velocity. This is due to the entrainment of the droplets by the gaseous flow. The droplets are accelerated at the exit of the diffusor due to the opening of the gaseous jet. Note that the structures present on the gaseous field are much smaller than those of the liquid field. Indeed, the liquid phase is denser than the gaseous phase and the level of turbulence is much lower in the dispersed phase.

Figure 9.17 shows binarized thresholded snapshots extracted from experimental tomographic visualization of the fuel spray (Linassier *et al.* (2011)). It provides a visual description of the spray structure. Note that the flow is oriented on the direction contrary to the flow in the LES. Figure 9.18 shows an instantaneous field of liquid volume fraction corresponding to case RUM_Ev21 ($t = 48\ ms$). Both images

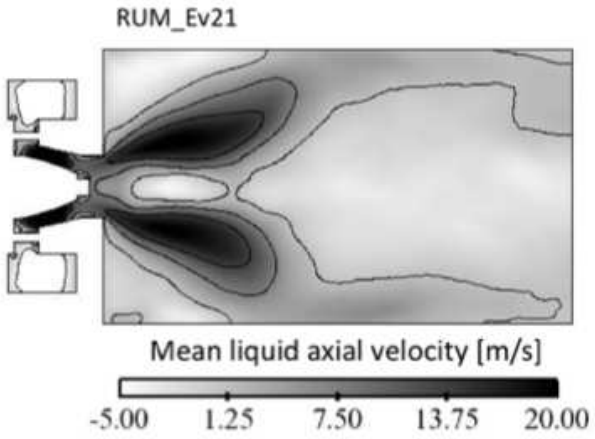

(a) Liquid axial velocity

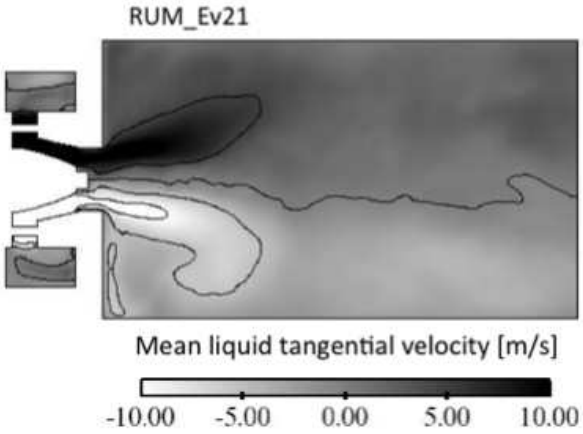

(b) Liquid tangential velocity

Figure 9.15: *Average fields of liquid phase axial (a) and tangential (b) velocities. Case RUM_Ev21.*

show similar features. There is a high concentration of liquid close to the injector nozzle as well as on the lips of the diffusor. The liquid spray impacts the lips of the diffusor and impinges the inner walls at this location. Semi-circular clusters of droplets detach from the main jet and are convected downstream by the gaseous flow. As shown by Fig. 9.18, LES is able to capture this phenomena. Nevertheless, due to the continuous nature of the liquid phase in the Euler-Euler approach and the LES filtering, the field appears more diffused than the experimental images.

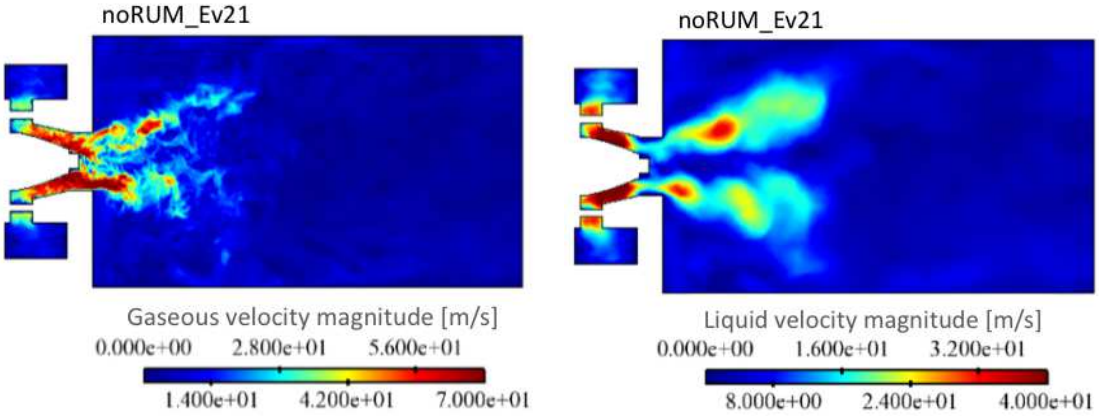

(a) Gaseous velocity magnitude (b) Liquid velocity magnitude

Figure 9.16: *Instantaneous fields of gaseous (a) and Liquid (b) velocity magnitude at $t = 48$ ms. Case RUM_Ev21.*

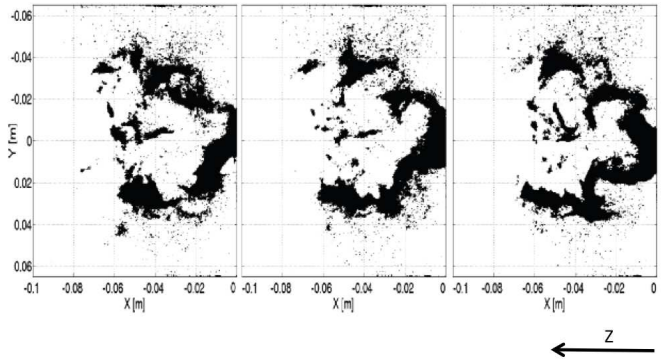

Figure 9.17: *Tomographic visualization of the fuel spray. Binarized thresholded snapshots. Source Linassier et al. (2011).*

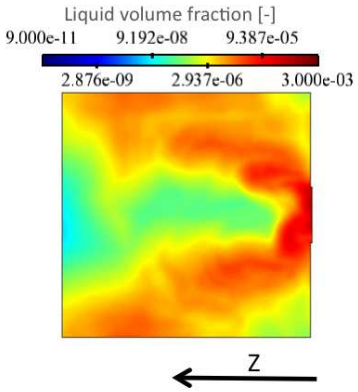

Figure 9.18: *Instantaneous field of liquid volume fraction at $t = 48$ ms. Case RUM_Ev21*

9.3.2 Effect of the evaporation model

The goal of this Section is to compare the performances of two different evaporation models in the MERCATO configuration. Cases noRUM_Ev1 and noRUM_Ev21 are compared. Case noRUM_Ev1 uses the classical approach for the evaporation implemented in AVBP which corresponds to the Spalding model where the viscosity at the droplet surface is calculated with a simple Power law depending only on the temperature of the mixture and the Prandtl and Schmidt numbers fixed by chemistry ($Pr = Sc_F = 0.739$). Case noRUM_Ev21 uses the new approach presented in Part III. The Abramzon-Sirignano model is used for the droplet evaporation, the viscosity in the film around the droplet is calculated by means of the Bird's formula (i.e. the viscosity is function of the mixture temperature and composition) and adapted Prandtl and Schmidt numbers fitted with a pre-calculation performed with CANTERA are used ($Pr^{evap} = 0.782043$, $Sc_F^{evap} = 2.0495$). The test on isolated droplets presented in Part III showed that ievap_21 (case noRUM_Ev21 in this Section) predicts slower evaporation process than ievap_1 (case noRUM_Ev1).

Mean and RMS profiles of the components of the velocity vector are compared as well as mean fields of the quantities of interest regarding evaporation.

Velocity profiles

Figure 9.19 shows a comparison of the mean and RMS liquid axial velocity profiles between cases noRUM_Ev1, noRUM_Ev21 and the experiments. The mean velocity profiles are very similar between both cases simulated and they agree very well with the experiments. Small differences are however visible at the axial coordinate $z = 56\ mm$. The axial velocity corresponding to noRUM_Ev1 case is higher at the center of the jet for this axial position. This improves slightly the agreement with the experimental results. At this location, the droplets corresponding to case noRUM_Ev1 are larger (Fig. 9.20). The gaseous velocities at this location are very similar in both cases, and of the order of $-10\ m/s$. The liquid phase axial velocity is smaller at this point. Larger droplets have a larger response time and thus (for equal fluid characteristic time) a higher Stokes number. Droplets are more inertial and less affected by the gaseous flow. This is why the negative axial velocity at this location produces negative axial velocities on the smaller droplets of case noRUM_Ev21 but not on the big droplets of case noRUM_Ev1, whose axial velocity is close to zero. Close to the chamber walls, noRUM_Ev21 produces slightly better agreement with the experiment. Note that in the experiments the droplet spray is polydisperse, which is not the case here. Polydispersity effects are very important when studying the droplet diameter fields. For this reason, results regarding the diameter profiles must very carefully treated.

Figures 9.21(a) and 9.22(a) show the mean profiles of radial and tangential liquid velocities for cases noRUM_Ev1 and noRUM_Ev21. The overall agreement with the experiments is good. In both cases, there is no noticeable difference between the two LES.

Figures 9.19(b), 9.21(b) and 9.22(b) shows the profiles of axial, radial and tangential velocity RMs fluctuations respectively. The profiles of noRUM_Ev1 and noRUM_Ev21 are very similar. Case noRUM_Ev1 shows slightly higher level of fluctuations at the center of the chamber. However, the RMS levels are too low compared to the experiments.

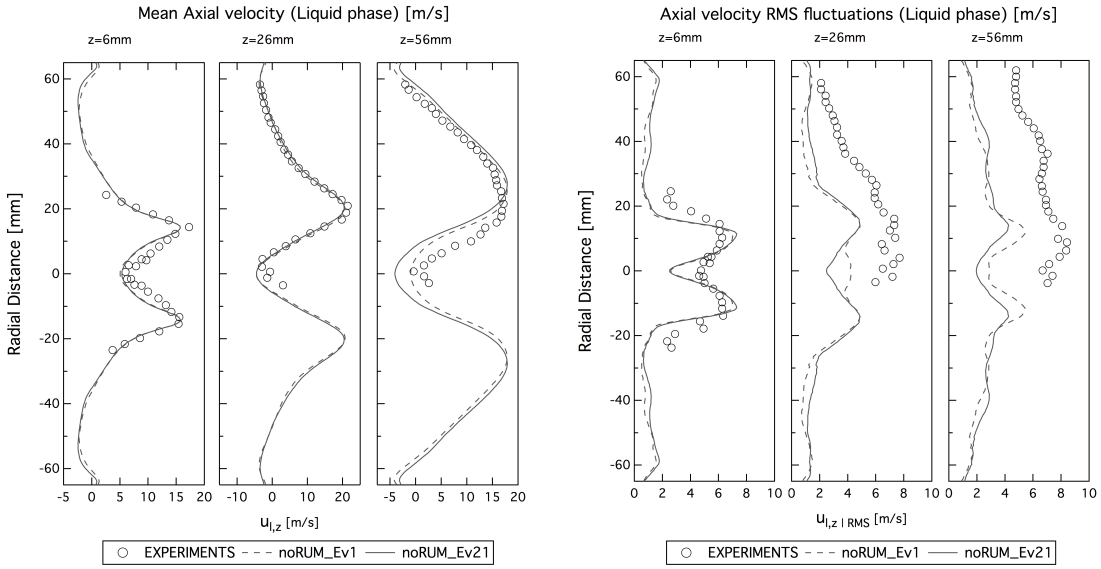

(a) Mean axial velocity.

(b) RMS axial velocity.

Figure 9.19: *Mean and RMS axial velocity profiles. Liquid phase. Cases noRUM_Ev1 and noRUM_Ev21. Comparison with the experiments.*

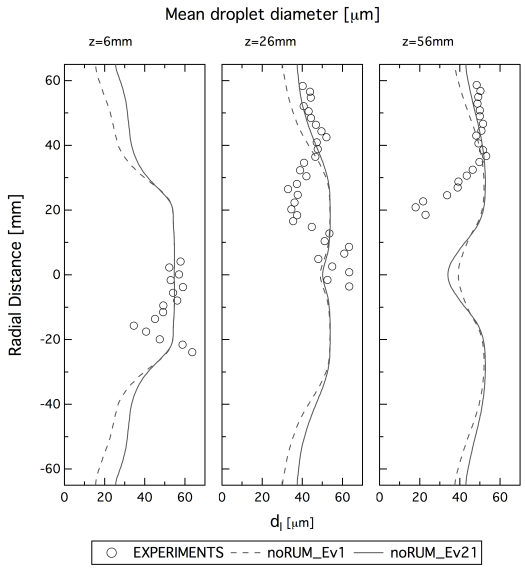

Figure 9.20: *Profiles of mean droplet diameter. Cases noRUM_Ev1 and noRUM_Ev21. Comparison with the experiments.*

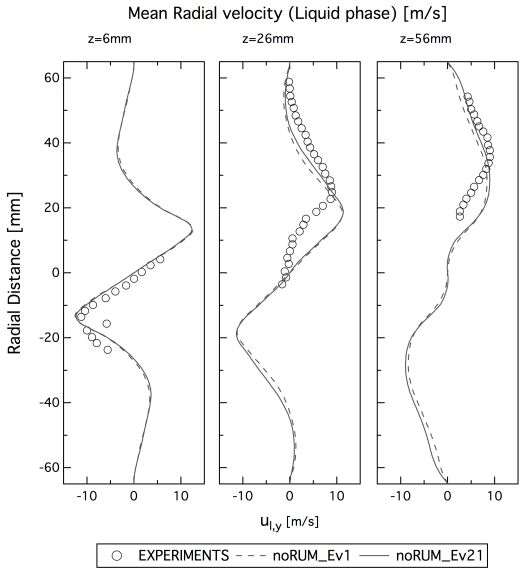

(a) Mean radial velocity.

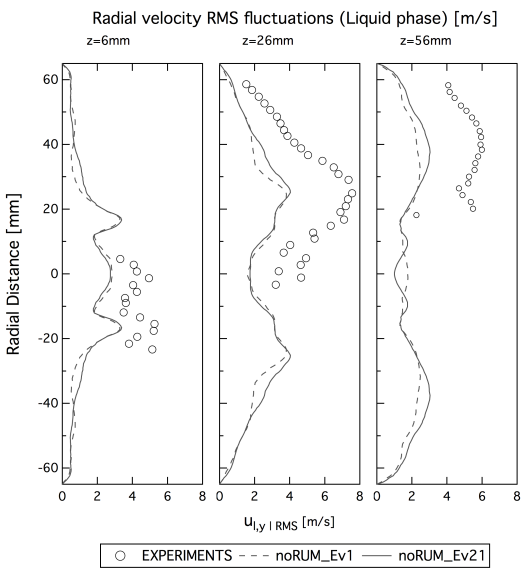

(b) RMS radial velocity.

Figure 9.21: *Mean and RMS radial velocity profiles. Liquid phase. Cases noRUM_Ev1 and noRUM_Ev21. Comparison with the experiments.*

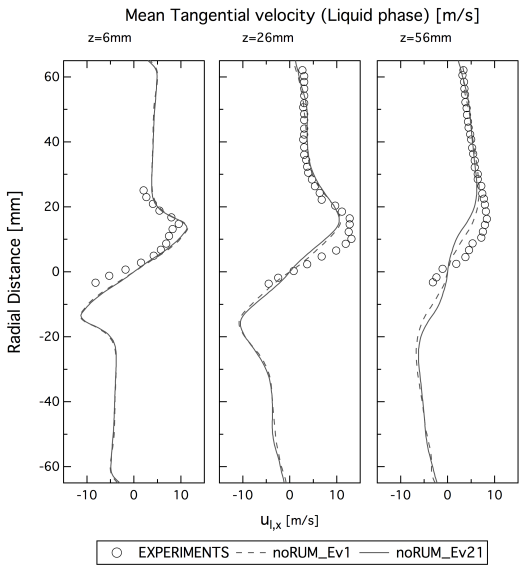

(a) Mean tangential velocity.

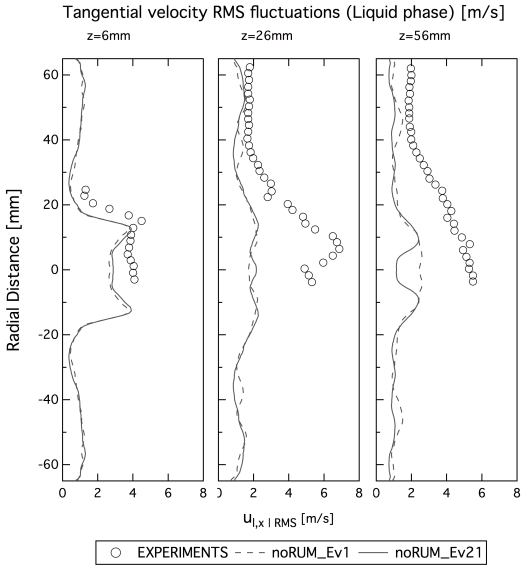

(b) RMS tangential velocity.

Figure 9.22: *Mean and RMS tangential velocity profiles. Liquid phase. Cases noRUM_Ev1 and noRUM_Ev21. Comparison with the experiments.*

Impact of the evaporation model on the topology of the dispersed phase flow

The evaporation model has almost no impact on the liquid velocity profiles and impacts slightly the diameter profiles close to the chamber walls. The evaporation models affects, however, in a stronger manner:

- the concentration of droplets close to the walls,
- the heat and mass transfer fields due to evaporation,
- and the gaseous kerosene distribution.

Figures 9.23 and 9.24 show the time-averaged fields of the liquid volume fraction and the droplet diameter for both cases. The spray penetrates further downstream in case noRUM_Ev21. The liquid spray impinges more the chamber wall and the spray angle is smaller. Indeed, at the corners of the chamber, case noRUM_Ev21 shows higher values of liquid volume fraction. Figure 9.25 shows the profiles of liquid volume fraction extracted from the averaged solutions of both cases. The profiles are very similar close to the longitudinal axis of the chamber and differ close to the walls. From the axial location $z = 6\ mm$, the level of liquid volume fraction predicted by case noRUM_Ev21 is higher than that of case noRUM_Ev1. In case noRUM_Ev21 bigger droplets are present inside the CRZ and close to the walls. This is due to the evaporation model ievap_21, which predicts lower evaporation rates than ievap_1, as shown by the instantaneous fields of mass evaporation rate (Fig. 9.26). Both fields have globally the same shape, however, the levels predicted by noRUM_Ev1 are higher.

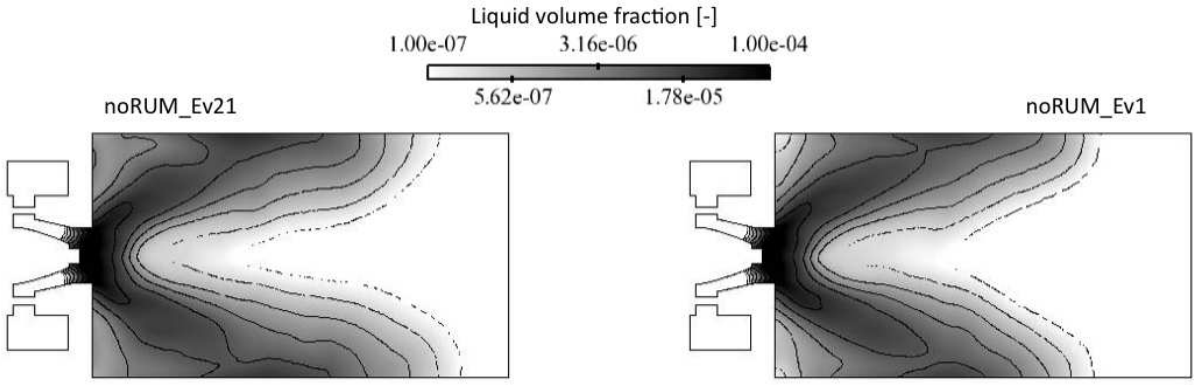

Figure 9.23: *Liquid volume fraction time-averaged fields. Cases noRUM_Ev1 (right) and noRUM_Ev21 (left).*

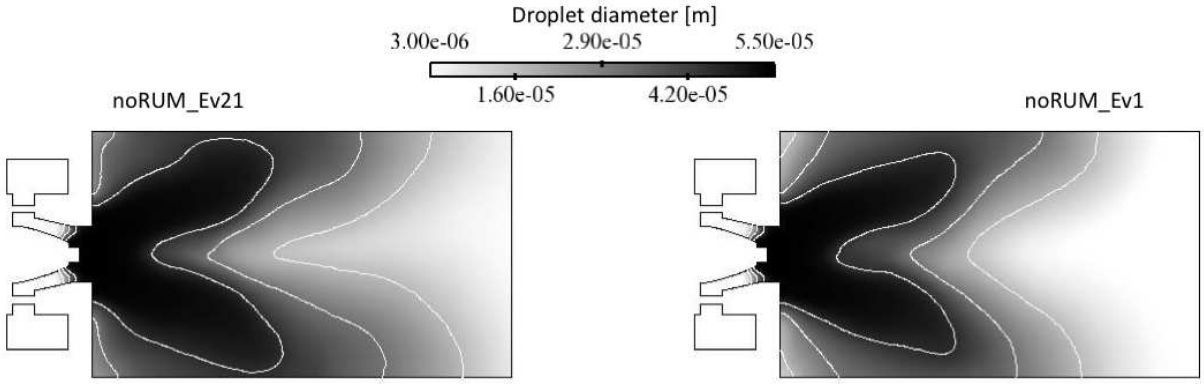

Figure 9.24: *Droplet diameter time-averaged fields. Cases noRUM_Ev1 (right) and noRUM_Ev21 (left).*

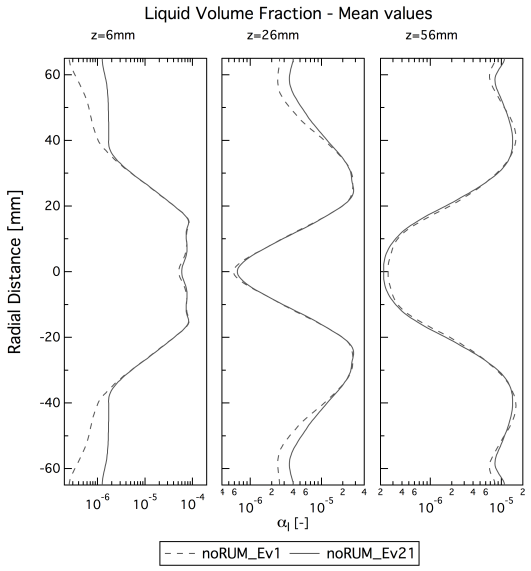

Figure 9.25: *Profiles of mean liquid volume fraction. Cases noRUM_Ev1 and noRUM_Ev21. Comparison with the experiments.*

The heat transfer rate is not the same either. Figure 9.27 shows the time-averaged fields of the gaseous and liquid temperatures. Hot gases from the plenum reach the combustion chamber through the swirler. Liquid kerosene is injected at the center of the diffusor at a lower temperature. When both mix, there is a heat transfer from the gaseous phase to the liquid phase which evaporates. Figure 9.27(a) shows that the gaseous temperature averaged fields are very similar in both cases. However, the liquid temperature fields show several differences. Cold droplets penetrate the chamber further downstream in case noRUM_Ev21 than in case noRUM_Ev1. Moreover, the liquid temperature is globally higher in case noRUM_Ev1. The tests performed on single isolated droplets (cf Part III) showed that the heat transfer rate is higher and quicker when using ievap_1 model. Indeed, the pre-heating time of the droplets is shorter and the droplet temperature higher than when ievap_21 is used.

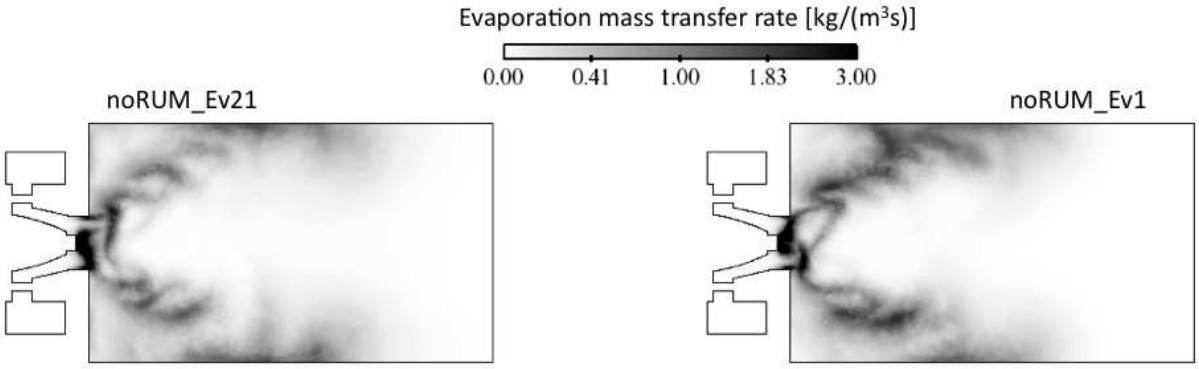

Figure 9.26: *Evaporation mass transfer rate instantaneous fields. Cases noRUM_Ev1 (right) and noRUM_Ev21 (left).*

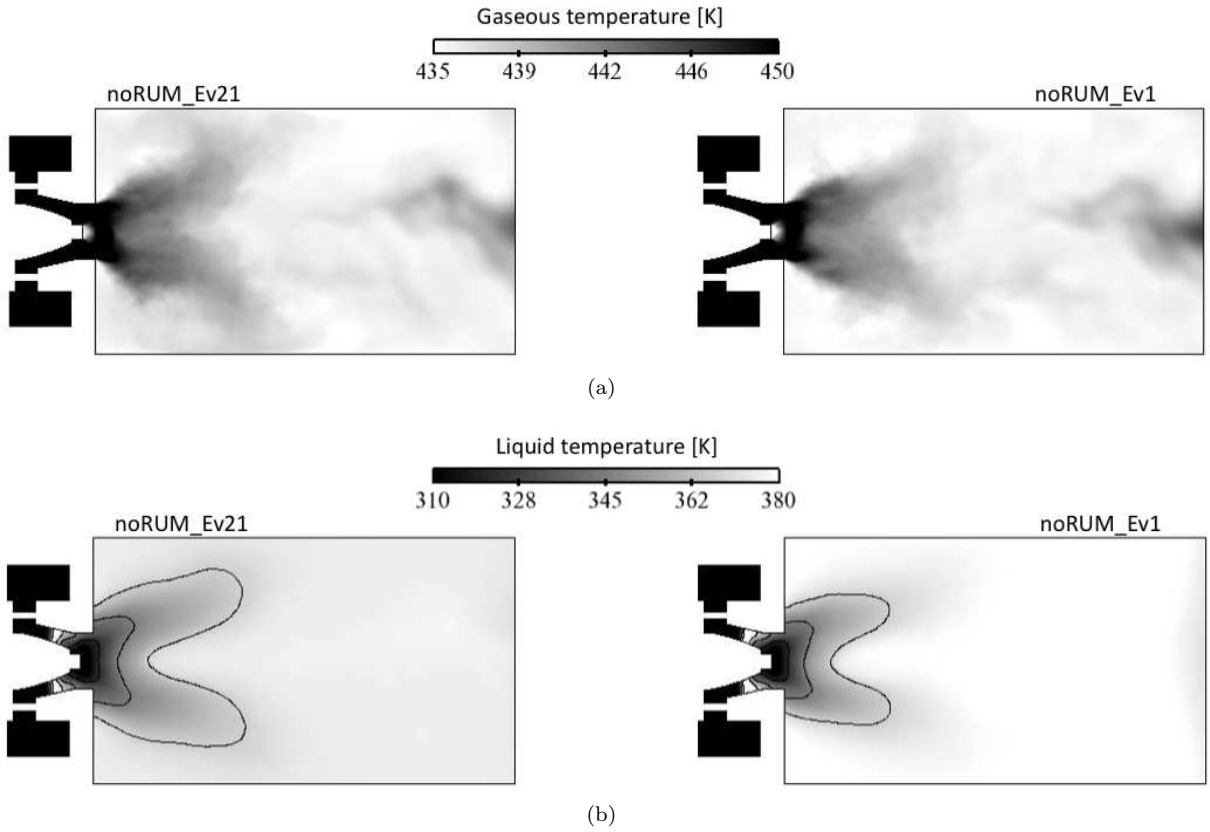

Figure 9.27: *Gaseous (a) and liquid (b) temperatures. Time-averaged fields. Cases noRUM_Ev1 (right) and noRUM_Ev21 (left).*

This is the behavior found in this configuration as shown by Fig. 9.28, where the instantaneous fields of heat transfer rate for both cases are shown. Note that the heat transfer rate includes the transfers from the gaseous phase to the liquid phase and *vice versa*. For this reason this quantity has a very wide scale range. Here, the scale has been on purpose saturated on both extremes to show the locations where the higher heat transfer rates take place. The dark blue zone close to injection delimits the zone where the bigger droplets are present. In this zone, the liquid temperature is very cold and the gaseous

temperature very high. Heat is transferred from the gaseous to the liquid phase. The mass transfer rate in this zone is not very high. This is due to the high concentration of liquid at low temperature, which favors a saturation regime. This zone is smaller in case noRUM_Ev1 because the liquid temperature is higher in this case. Close to the inner walls of the chamber high heat transfer zones are present. In these zones, the liquid volume fraction is smaller than close to the injection. It is zone of high mass transfer rate where a large amount of heat needs to be provided to evaporate the already pre-heated droplets. According to the fields of mass transfer rate (fig. 9.26), case noRUM_Ev1 presents higher heat transfer rate in these zones, which in addition are bigger and extend further towards the center of the chamber.

The impact of the evaporation model is of high importance for the prediction of the gaseous fuel field, in views of a reactive case computation. Figure 9.29 displays the gaseous kerosene mass fraction time-averaged field. noRUM_Ev1, due to the higher evaporation and heat transfer rates predicted, shows higher concentration of gaseous fuel globally in the whole chamber but especially close to the walls. This feature may be of key importance for ignition studies in this configuration.

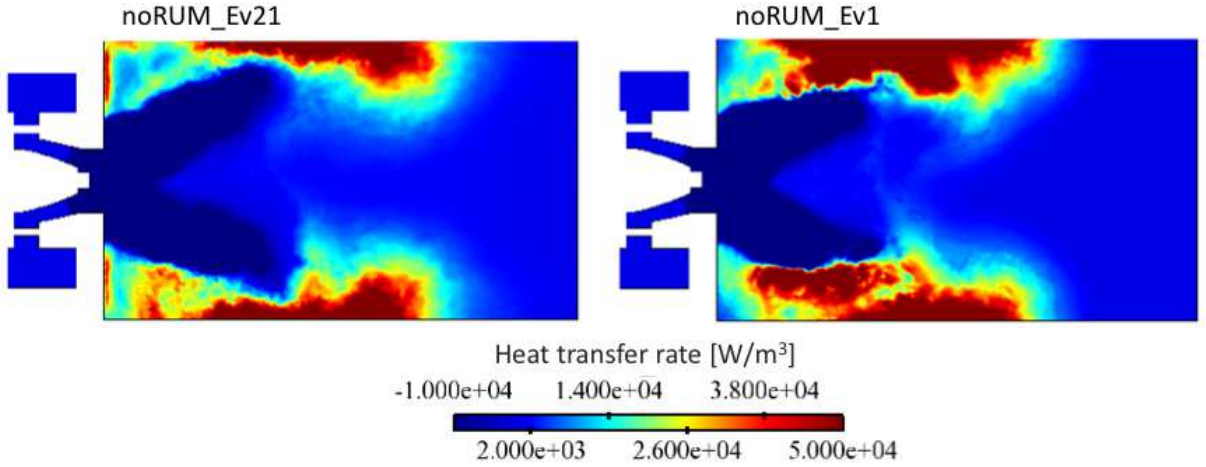

Figure 9.28: *Evaporation heat transfer rate instantaneous fields. Cases noRUM_Ev1 (right) and noRUM_Ev21 (left).*

spe

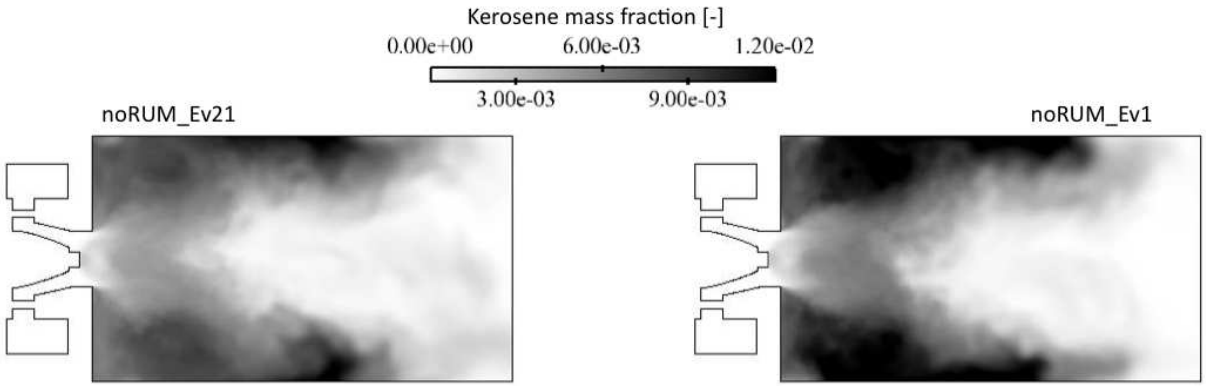

Figure 9.29: *Gaseous kerosene mass fraction averaged fields. Cases noRUM_Ev1 (right) and noRUM_Ev21 (left).*

9.3.3 Effect of the RUM model

This Section aims at analyzing the performances of 2ΦEASM3 RUM model in complex configurations by comparing the results of a simulation performed with this model (RUM_Ev21) with a simulation performed with the same evaporation model but without taking into account the RUM (noRUM_Ev21). 2ΦEASM3 model was chosen over the rest of the models presented in Chapter 4 because it gives the best results in a non-evaporating configuration with mean shear (cf Chapter 5) for different particle inertia (i.e. Stokes numbers) and fluid turbulence levels (i.e. Reynolds numbers). In the MERCATO configuration, however, evaporation is taken into account, which implies that droplets of different sizes are present leading to different levels of particle inertia (cf Table 9.1). Moreover, the Reynolds number is higher in the MERCATO configuration ($Re = 25000$) than in the configuration of Chapter 5 ($Re^c \approx 18850$). The VISCO model classically sued in AVBP does not work on this configuration.

Velocity profiles

First, the effect of the RUM on the configuration is analyzed through comparison of the mean and RMS velocity profiles of cases noRUM_Ev21 and RUM_Ev21. Figure 9.30(a) shows the mean axial velocity profiles of both cases compared to the experimental measurements. In the section $z = 6\ mm$ case noRUM_Ev21 shows higher axial velocities at the borders of the liquid jet. This behavior has an impact on the profiles downstream. At $z = 56\ mm$, the location of the peaks are different between case noRUM_Ev21 and case RUM_Ev21. Indeed, for noRUM_Ev21, the peaks of profile are located closer to the chamber walls. Moreover, the axial velocity at the center of the chamber is negative (it corresponds to a recirculation point), where in case RUM_Ev21 is zero, which corresponds to a stagnation point. The agreement with the experimental measurements is better for case RUM_Ev21. The difference in jet opening angles are confirmed by the profiles of the mean radial velocity shown in Fig. 9.31(a). Indeed, the maximal radial velocity is higher in the case noRUM_Ev21, and that for all the axial locations. Moreover, any of the simulations captures the position of the peaks of radial velocity observed on the experiments. In both cases, the peaks are located closer to the chamber axis than in the experimental results. No noticeable differences are visible on the profiles of mean tangential velocity (Fig. 9.32(a)), both cases show good agreement with the experiments.

Accounting for the RUM increases the RMS velocity values, improving the agreement with the experimental results (especially close to the chamber walls), for the three velocity components (Figs. 9.30(b), 9.31(b) and 9.32(b)). At the center of the profiles, both cases give similar results at the axial locations close to the injection. Further downstream, accounting for the RUM improves the results. Note that a reason for the underestimation of the RMS velocities downstream is the progressive derefinement of the computational mesh. As shown in Chapter 5, the mesh resolution needed for a correct reproduction of the dispersed phase phenomena is higher than the required for the gaseous phase. The high compressibility of the liquid phase needs a higher mesh resolution to capture certain features such as the particle segregation and the RMS values of droplet number density and velocity. Polydispersity effects, which are not considered here, must be taken into account too. A shown by Fig. 9.33, the RMS values of the droplet diameter are not captured by any of the cases simulated due to the monodispersed nature of the dispersed phase considered here.

Impact of the evaporation model on the topology of the dispersed phase flow

Figure 9.34(a) shows the mean liquid volume fraction profiles corresponding to cases noRUM_Ev21 and RUM_Ev21. Case RUM_Ev21 shows a flatter profile than noRUM_Ev21. The RUM acts on the liquid phase diffusing the droplets located on the borders of the jet. The droplets are ejected of the main jet both in the inner and outer directions. For this reason, the liquid volume fraction at the center of the chamber and close to the walls is higher in case RUM_Ev21, while the levels at the peaks are similar for both cases. The RUM contributes to keep the spray jet in a more confined region. Indeed, the mean axial

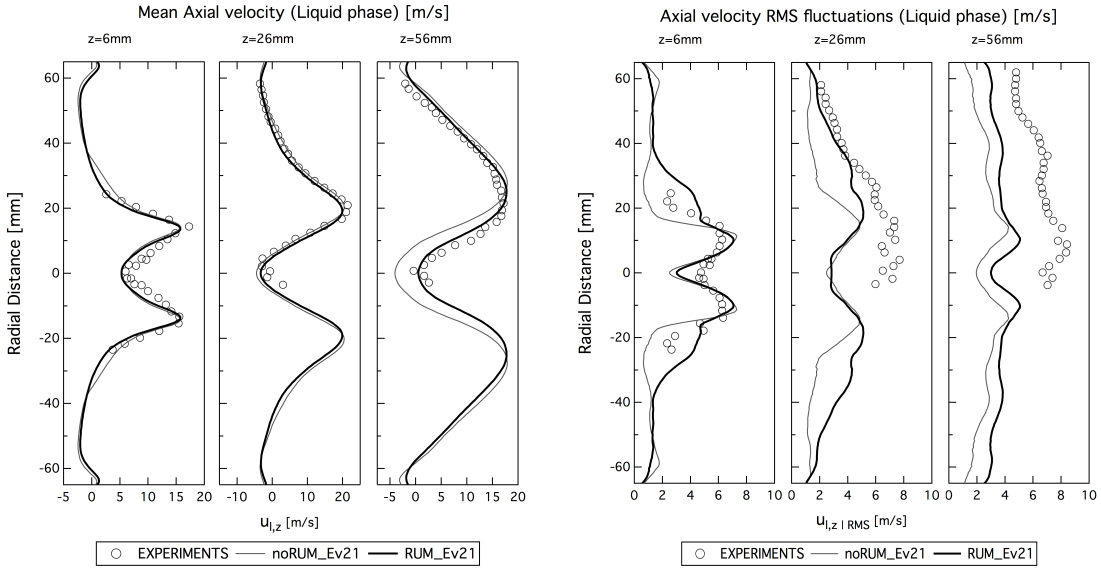

(a) Mean axial velocity.

(b) RMS axial velocity

Figure 9.30: *Mean and RMS axial velocity profiles. Liquid phase. Cases noRUM_Ev21 and RUM_Ev21. Comparison with the experiments.*

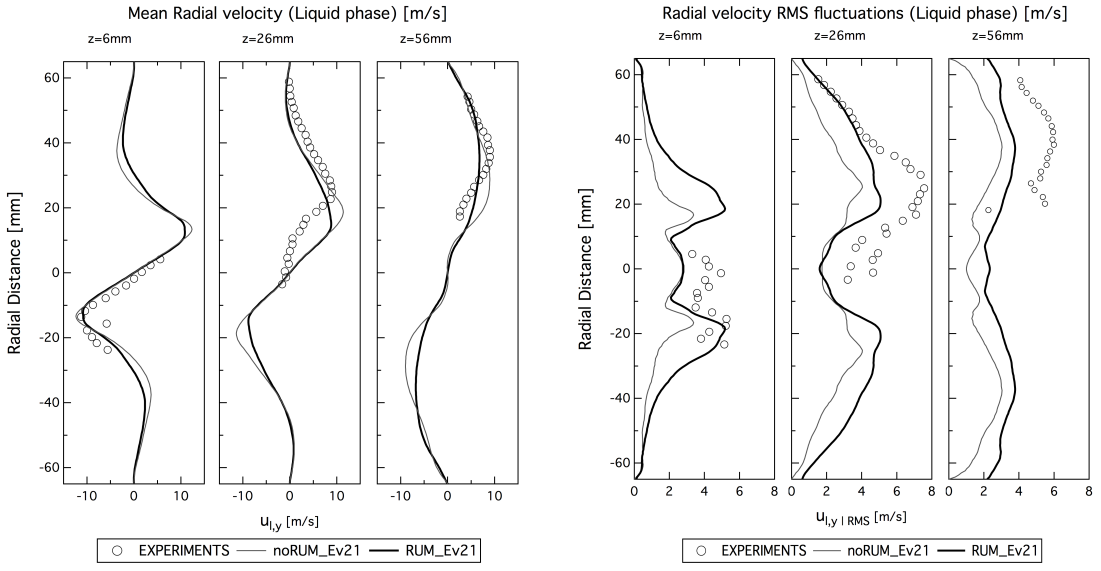

(a) Mean radial velocity.

(b) RMS radial velocity

Figure 9.31: *Mean and RMS radial velocity profiles. Liquid phase. Cases noRUM_Ev21 and RUM_Ev21. Comparison with the experiments.*

liquid volume flux profiles (Fig. 9.34(b)) show that the spray penetrates further downstream and with a wider angle on case noRUM_Ev21. This is also visible on the liquid volume fraction averaged fields displayed on Fig. 9.35.

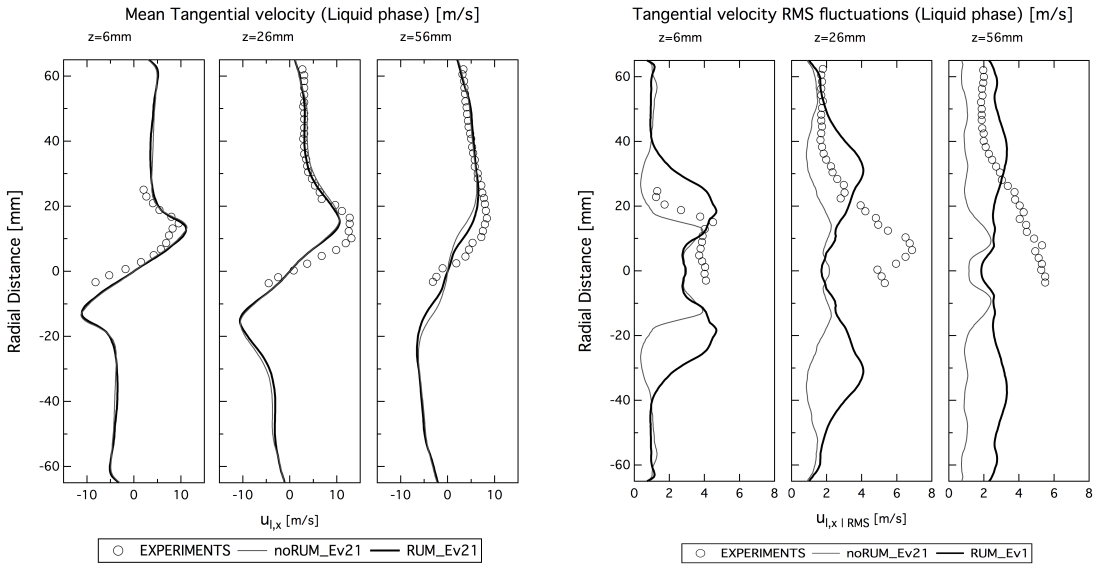

(a) Mean tangential velocity.

(b) RMS tangential velocity

Figure 9.32: *Mean and RMS tangential velocity profiles. Liquid phase. Cases noRUM_Ev21 and RUM_Ev21. Comparison with the experiments.*

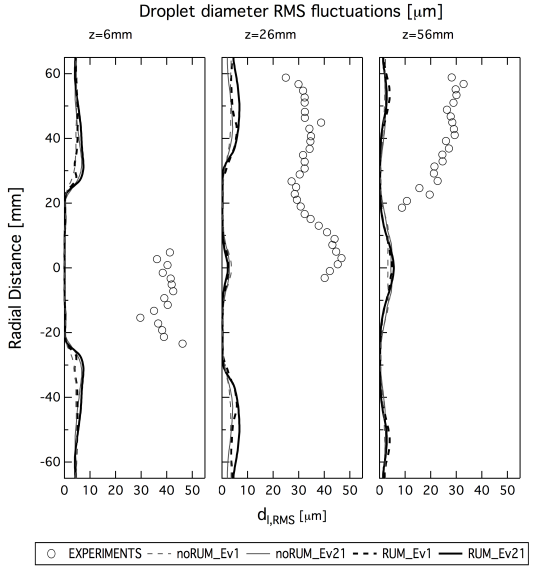

Figure 9.33: *RMS droplet diameter profiles. Cases noRUM_Ev1, noRUM_Ev21 RUM_Ev1 and RUM_Ev21. Comparison with the experiments.*

The field corresponding to case noRUM_Ev21 shows a spray on which a higher quantity of liquid impinges the chamber walls. On case RUM_Ev21, the spray is diffused towards the center creating a different repartition of the liquid phase on the chamber and modifying the liquid behavior on the inner walls. Figure 9.36 shows the time-averaged field of the mean droplet diameter. The simulation performed with RUM shows a field of diameter on which bigger droplets penetrate further downstream along the central axis, as also shown by the profiles of Fig. 9.37.

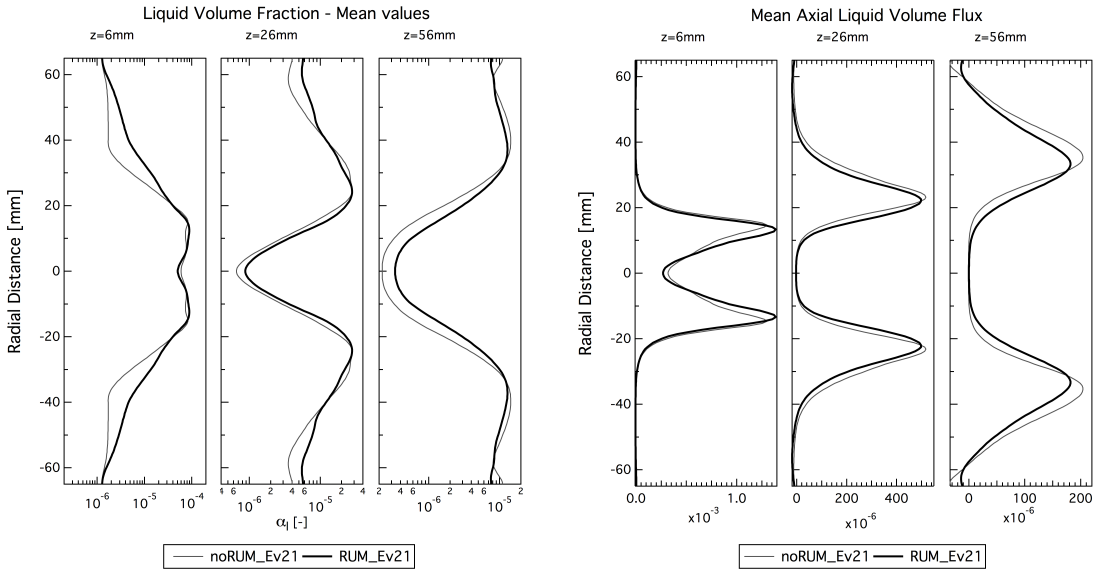

(a) Mean liquid volume fraction.

(b) Mean axial liquid volume flux.

Figure 9.34: *Mean liquid volume fraction (a) and axial liquid volume flux (b) profiles. Cases noRUM_Ev21 and RUM_Ev21.*

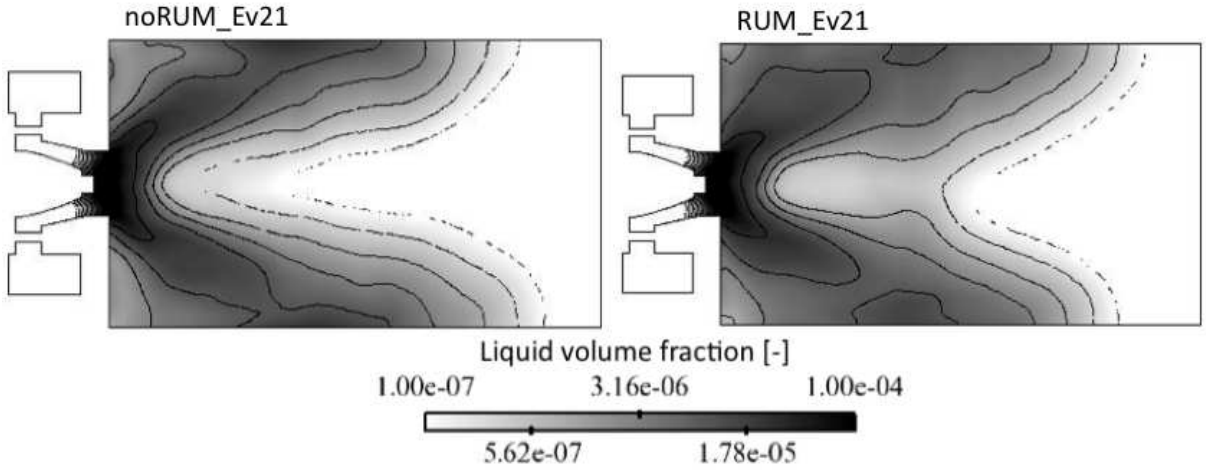

Figure 9.35: *Liquid volume fraction averaged fields. Cases noRUM_Ev21 (left) and RUM_Ev21 (right).*

Figure 9.38 shows an instantaneous profile of mass transfer rate due to evaporation for both cases. The snapshots have been taken 48 *ms* after injection started. The mass transfer rate at the center of the chamber is higher on noRUM_Ev21 case, which corresponds to the information shown by the mean profiles of droplet diameter. On the contrary, in the CRZ the evaporation rate is higher for case RUM_Ev21. This is also the case for heat transfer rate (Fig. 9.39). Inside the CRZ, heat transfer is much higher in case RUM_Ev21. Further downstream and close to the walls case noRUM_Ev21 shows a stranger heat transfer rate.

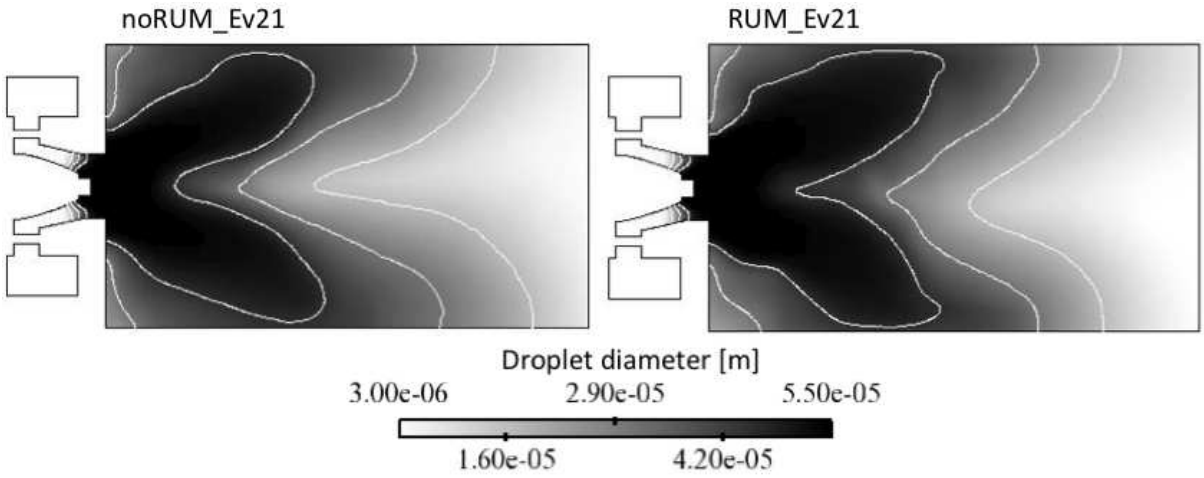

Figure 9.36: *Droplet diameter averaged fields. Cases noRUM_Ev21 (left) and RUM_Ev21 (right).*

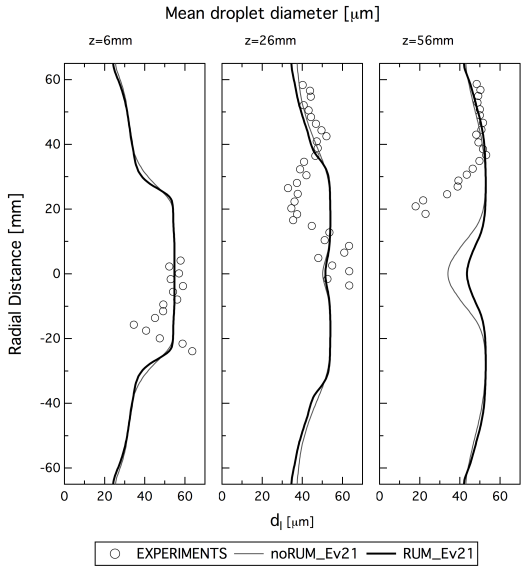

Figure 9.37: *Profiles of mean droplet diameter. Cases noRUM_Ev21and RUM_Ev21. Comparison with the experiments.*

The differences on heat and mass transfer rates have a direct impact on the gaseous kerosene repartition inside the chamber. Figure 9.40 shows instantaneous fields of gaseous kerosene mass fraction for both cases. The quantity of kerosene inside the CRZ is higher in case RUM_Ev21 and close to the walls downstream for noRUM_Ev21. This is very important in real applications, because the ignition system is usually located close to the walls and moreover in the CRZ, as it is the case of the ignition tests performed in this configuration (Linassier *et al.* (2011)).

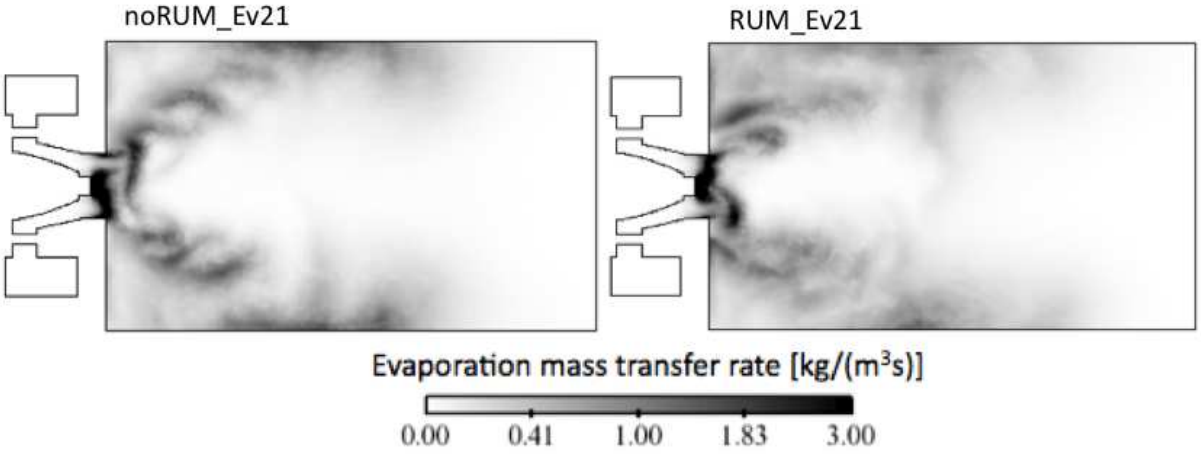

Figure 9.38: *Evaporation mass transfer rate instantaneous fields. Cases noRUM_Ev21 (left) and RUM_Ev21 (right).*

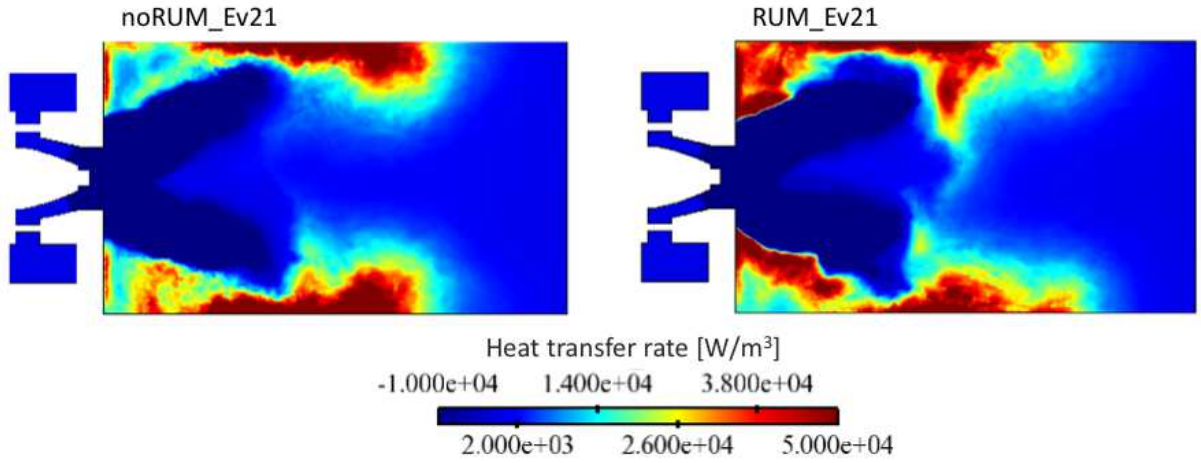

Figure 9.39: *Evaporation heat transfer rate instantaneous fields. Cases noRUM_Ev21 (left) and RUM_Ev21 (right).*

Finally, the RUE has an important effect on the spray. The zones where the RUE is higher are located (Fig. 9.41(b)):

1. on the diffusor lips, where the spray impinges the walls and where, as experimentally observed, the liquid film formed is atomized by the swirled flow (Linassier *et al.* (2011)),
2. in highly sheared zones,
3. close to the walls on the zones where the spray impinges the chamber inner walls.

Liquid velocity shear is an important mechanism of RUE production. A link between the RUE and the phenomenon of droplet cluster detachment and convection (cf Section 9.3.1) can be stated by comparing the instantaneous fields of RUE and liquid volume fraction (Fig. 9.41(a)). Indeed, similar structures are present on both fields. A correct prediction of the RUE in these zones is very important since it is crucial for the prediction of phenomena such as collisions and coalescence, which have a higher importance in these zones.

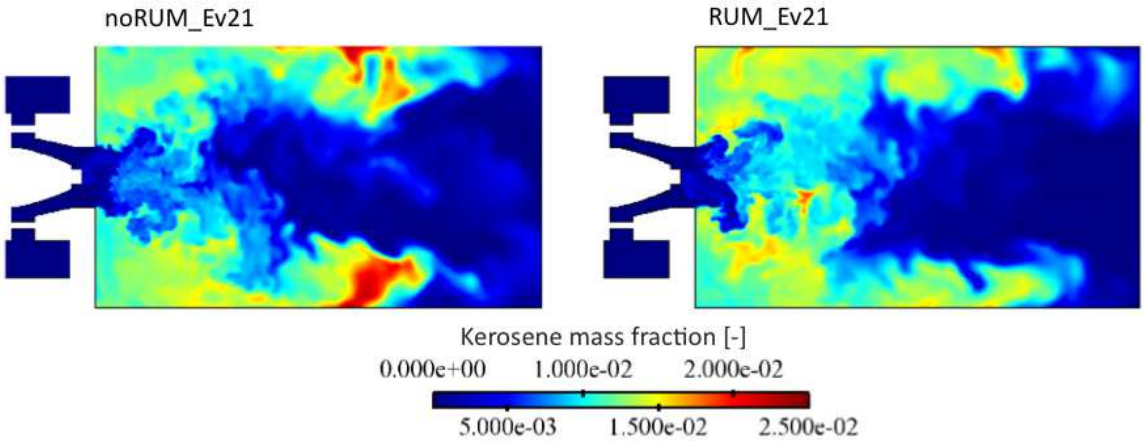

Figure 9.40: *Gaseous kerosene mass fraction instantaneous fields. Cases noRUM_Ev21 (left) and RUM_Ev21 (right).*

Figure 9.42 displays the mesoscopic kinetic energy averaged fields corresponding to noRUM_Ev21 and RUM_Ev21 cases. As already pointed out in the configuration studied on Chapter 5, when the RUM is not taken into account, the level of mesoscopic energy increases. This is also the case here. Case noRUM_Ev21 shows higher levels of mesoscopic energy located on the zones of high liquid velocity magnitude at the exit of the diffusor. The field corresponding to the case with RUM (RUM_Ev21) shows lower maxima and a more diffused mesoscopic energy field. Note that the level of mesoscopic energy is lower than the level of RUE. This is consistent with the presence of highly inertial droplets, which is the case here (Table 9.2), as shown in Chapter 5 for the high inertia case.

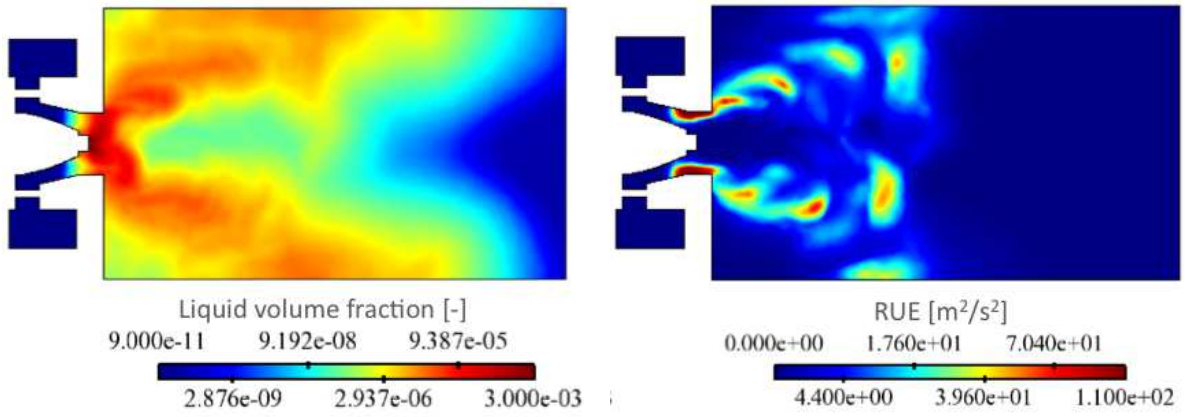

(a) Liquid volume fraction.

(b) Uncorrelated energy.

Figure 9.41: *Instantaneous fields of (a) liquid volume fraction and (b) RUE at* $t = 48$ *ms. Case RUM_Ev21.*

As observed in Chapter 5, the activation of the artificial viscosity sensor is reduced when the RUM is accounted for. Figure 9.43 shows the activation of the AV sensor at a given instant in the chamber. Close to the chamber exit, the artificial viscosity acts due to the low concentration of liquid in that zone in order to avoid numerical problems since AVBP cannot manage empty spaces. Nevertheless, on the zones where that is not a concern for the numerical stability of the code (i.e. closer to the injection), the AV sensor is less activated in case RUM_Ev21, especially on the zones where the RUE acts (cf Fig. 9.41(b)). Indeed, for this case and close to the injection, the sensor is activated in the zones where the liquid volume fraction is smaller.

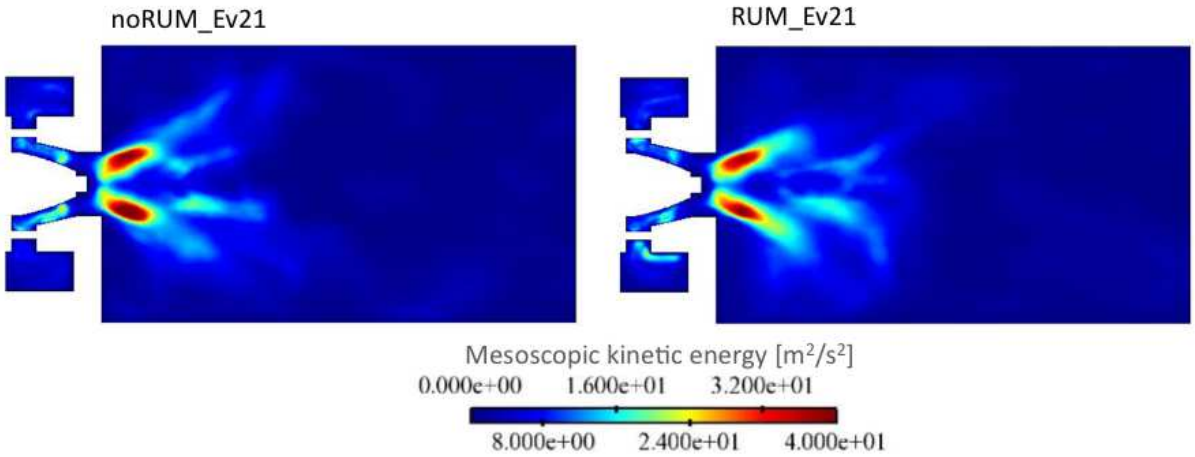

Figure 9.42: *Mesoscopic kinetic energy averaged fields. Cases noRUM_Ev21 (left) and RUM_Ev21 (right).*

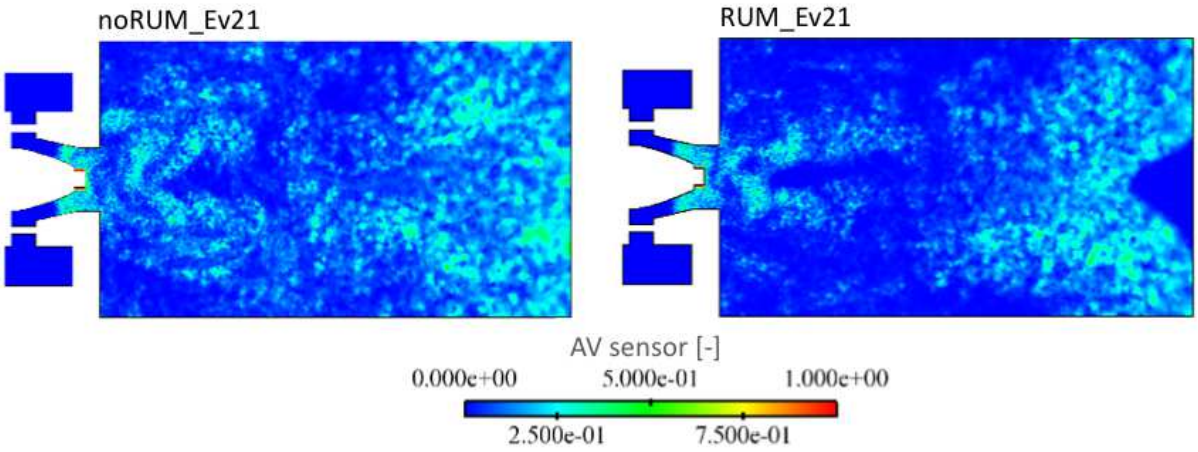

Figure 9.43: *Artificial viscosity sensor activation. Instantaneous field. Cases noRUM_Ev21 (left) and RUM_Ev21 (right).*

9.4 Conclusions

Four different cases combining two approaches for the RUM modeling and two evaporation models (Table 8.8) have been simulated using LES in the MERCATO configuration. The gaseous flow topology has been analyzed and compared with experimental results. Profiles of mean and RMS velocity in the three directions of space have been computed and the flow field topology analyzed by means of averaged fields of axial, radial and tangential velocities. Two recirculation zones, the CTRZ and the CRZ, have been identified. The same flow configuration was already reported by Sanjosé (2009) and Senoner (2010). The mean velocity profiles agree well with the experimental results, however, small differences between the LES and the experiments have been identified. The RMS velocities corresponding to the LES show lower levels of fluctuations on the profiles located more downstream of the chamber. This has been attributed to the progressive derefinement of the computational mesh. The results presented showed that either the RUM model nor the evaporation model produce great differences on the gaseous flow field, even when two-way coupling is taken into account. Indeed, the mean and RMS velocity profiles of the four simulations are very similar for all axial locations. However, the level of convergence of the gaseous field is not optimum, averaging during a longer period should be performed in order to obtain definitive conclusions. Finally an analysis of the quality of the LES simulation has been performed. Instantaneous fields of turbulent to laminar viscosity and artificial to laminar viscosity ratios have been presented. The fields show that the contribution of the subgrid scale model is very local and follows the gaseous jet opening. The artificial viscosity levels, calculated with the method proposed by Lamarque (2007) is lower than the laminar viscosity.

Then the liquid field topology has been analyzed. First, a general analysis of the topology of the liquid phase flow has been presented. The averaged fields of liquid velocity show the same features previously observed on the gaseous flow topology. Two recirculation zones are present, a CTRZ divided in two parts by a stagnation point downstream the liquid injection and a CRZ zone located on the chamber corners. The opening of the liquid jet follows that of the gaseous jet. The liquid spray is accelerated at the exit of the diffusor due to the sudden expansion of the gaseous jet. Instantaneous fields of gaseous and liquid velocity magnitude have been presented too. Both phases show similar fields, the liquid phase field being less turbulent, with fewer structures larger than those of the gaseous phase, due to the higher density of the liquid phase. The droplet cluster detachment phenomena observed experimentally (Linassier *et al.* (2011)) is also reproduced by the LES. However, the LES results are more diffused due to the description of the dispersed phase as a continuum in the Euler-Euler approach and to filtering of the smallest scales of the LES approach.

The effects of the evaporation model and the RUM model have been assessed:

- The impact of the evaporation model has been analyzed comparing the results of two simulations performed first with the Spalding evaporation model coupled with simple thermodynamic and transport properties (the only model existing in AVBP before this work), namely noRUM_Ev1, and secondly with the Abramzon-Sirignano evaporation model along with a more complex calculation of the properties (cf Part III) or case noRUM_Ev21. RUM has not been taken into account in these simulations in order to avoid the possibility of coupling effects between the RUM and the evaporation. The results showed that the evaporation is stronger in case noRUM_Ev1 than in case noRUM_Ev21. This is consistent with the results of the tests performed on the evaporation of single isolated droplets in Chapter 7. However, the evaporation models have a limited impact on the liquid velocity profiles. Indeed, few differences have been noticed on the mean and RMS profiles of the three components of the liquid velocity vector. The stronger effects due to the evaporation model are linked to the distribution of the biggest droplets inside the chamber and the production of gaseous fuel. Indeed, case noRUM_Ev1 showed gaseous kerosene concentration much higher than case noRUM_Ev21, especially close to the chamber walls. This may have a non-negligible impact on the study of the ignition process on this configuration.
- The impact of the RUM modeling has been analyzed through comparisons of the results obtained from cases noRUM_Ev21 and RUM_Ev21. The first case does not take into account the contribution

of the RUM, the second case uses the so-called 2ΦEASM3 model retained from the study of the configuration presented in Chapter 5. Both cases use the same approach for the modeling of the evaporation. The analysis of the mean and RMS velocity profiles shows that accounting for the RUM increases the level of RMS fluctuations, which produces better agreement with the experiments. In any case the RMS levels are still far from the experimental results, especially at downstream locations. This is mainly due to the progressive derefinement of the computational mesh on a first place, and to polydispersion effects not taken into account on a second place. Regarding the mean velocity profiles, the simulation performed with RUM is the only that captures the zero velocity point on the chamber axis at an axial location $z = 56\ mm$ as reported by the experimental results. Secondly, ignoring the RUM contribution leads to higher radial velocities, reducing the level of agreement with the experiments and leading to a larger angle of the spray jet. The analysis of the dispersed flow field in these cases confirmed the observations on the configuration studied in Chapter 5. The RUM has a diffusive effect on the fields of liquid volume fraction. Indeed, the results of case noRUM_Ev21 presented a more penetrating liquid jet with a smaller opening angle and a lower liquid concentration along the axis of the chamber. The RUM has also an impact on the evaporation process. Indeed, the fields of mass and heat transfer rates as well as the gaseous kerosene fields are affected by the RUM. Due to the diffusive effect of the RUE, the droplets located on the borders of the spray are captured inside the CRZ where they evaporate. The mass and heat transfer rates in this zone is higher for case RUM_Ev21. Case noRUM_Ev21 show higher evaporation rates further downstream and close to the chamber walls. The gaseous kerosene field is thus modified by the RUM modeling. Case RUM_Ev21 shows a higher kerosene concentration in the CRZ, which may have an important impact on the ignition process, since the ignition devices are often located close to the walls and near the injection plane.

Finally, the analysis of the instantaneous fields of liquid volume fraction and RUE showed that the RUE is activated in the regions of high shear where clusters of droplets are detached from the main jet and convected downstream by the gaseous flow. Zones of high RUE are also present on the diffusor lips, where the experiments show an impingement of the wall by the spray and the liquid film formed is atomized by the swirled flow. In agreement with the results on the configuration of Chapter 5, it has been observed that ignoring the RUM contribution leads to an increase in the predicted mesoscopic energy. Moreover, in this case, the RUE level is higher than the mesoscopic energy (due to the presence of highly inertial droplets). For this reason, the RUM contribution must be absolutely accounted for. Moreover, the simulation performed with RUM shows a more local and less strong activation of the artificial viscosity applied to the liquid phase than the simulation performed without RUM.

This work is part of a set of studies performed in the MERCATO configuration both with the Euler-Euler and the Euler-Lagrange approaches. In this sense, other works in the same configuration are in process at CERFACS. Eyssartier (2012) studied the ignition effects on the confined version of the MERCATO test rig. However, the effects of the RUM and the evaporation models stated here are expected to have a considerable impact on the reactive simulations of this configuration. Eyssartier (2012) used seven different ignition criteria. One on those criteria directly depends on the gaseous fuel field. The evaporation models studied here predict very different gaseous fuel distributions. Moreover, using the same evaporation model, the choice of the RUM model also have an impact on the gaseous fuel field. This statement is to be confirmed by future studies.

The application of the new RUM and evaporation models to the multi-fluid (Laurent *et al.* (2004)) Euler-Euler approach implemented by Vié (2010) in AVBP may considerably improve the results, especially regarding the droplet diameter fluctuations which are not well reproduced by the monodispersed simulations. Further comparisons with Euler-Lagrange LES of this configuration (Senoner *et al.* (2009), Hannebique (2012)) are of interest too. Indeed, the evaluation of the evaporation models on an Euler-Lagrange simulation will decouple the effects of the evaporation model from those of the RUM. Including the effect of collisions and coalescence may also change the results and may provide better agreement with the experiments. Finally, as it has been observed, the liquid spray impinges the diffusor lips and the inner walls of the chamber, for which liquid films models (actually not included in AVBP for the

Euler-Euler approach) are needed in order to completely represent the physics of the dispersed phase flow. The effect of these liquid films on the wall temperature can be assessed with a LES using AVBP coupled with the code AVTP (Duchaine *et al.* (2009)).

Conclusions

The main objective of this work is to develop and validate models for the two main phenomena occurring in a combustion chamber after primary and secondary atomization and before combustion, i.e. the dispersion and the evaporation of liquid droplets. Using the mesoscopic Euler-Euler approach (Février *et al.* (2005)), new RUM models are being tested to be used in mean sheared two-phase flows and the evaporation model used in AVBP is being improved. In both cases the models are first studied in academic configurations with the perspective of applying them to a semi-academic configuration to assess their validity for their future use in LES of two-phase flow industrial configurations. The results are validated against experimental data or Euler-Lagrange simulations depending on the available data. The conservation equations for the gaseous and the dispersed phase both in DNS and LES contexts are briefly described in Part I along with the models for the unclosed terms in the transport equations. Part II is dedicated to the study of the Random Uncorrelated Motion. Part III presents a study of the evaporation of single isolated droplets. Finally, Part IV presents the results obtained in LES of a complex configuration (MERCATO) comparing two RUM modeling approaches and two evaporation models.

Numerous algebraic models for the RUM deviatoric tensor developed and *a priori* validated by Masi (2010) have been *a posteriori* validated in a particle-laden temporal planar jet configuration in strong collaboration with Dr. E. Masi and Pr. O. Simonin. Linear and non-linear models using two different characteristic timescales (the particle relaxation timescale and the mesoscopic shear timescale) have been studied. Simulations at two levels of gaseous turbulence and different particle Stokes numbers have been performed and compared to a Lagrangian reference. The influence of the mesh resolution and the artificial dissipation has been assessed. The results show that using the particle relaxation timescale to model the RUM (which is the case of the viscosity-type model ("VISCO") proposed by Simonin *et al.* (2001)) leads to overestimated RUE fields and numerical instabilities when the level of gaseous turbulence increases or the particle inertia is not moderate. This confirms the results of Riber (2007) in LES of particle-laden turbulent jet (Hishida *et al.* (1987)). Linear models using the mesoscopic shear timescale ('AXISY" model) also lead to RUE overestimation but the application of a correction ("AXISY-C") in order to account for reverse energy exchanges (from the RUM to the mesoscopic motion) greatly improves the results. However, the performances of the corrected model strongly depend on the gaseous turbulence level and particle inertia. The so-called non-linear "QUAD-MOD" model gives satisfactory results but high-frequency oscillations are present on the instantaneous fields, which may eventually produce numerical instabilities and an indiscriminate application of artificial dissipation when used in complex configurations. Other high order models have been tested. The 2ΦEASM1 model underpredicts the particle RUE in all cases and needs high amounts of artificial dissipation to keep the numerical stability of the code. The 2ΦEASM3 model predicts very accurate statistics of the low and high order moments of the dispersed phase flow, at the same time giving good accuracy on the instantaneous fields. Applying the correction proposed by Masi (2010) to this family of models decreases the level of RUE which increases the necessity of artificial dissipation to numerically stabilize the simulation. The artificial dissipation model used in AVBP has been shown capable of artificially playing the role of the RUM. However, compared to the non-linear models, it does not degenerate correctly neither when the Stokes number changes nor when the gaseous turbulence is increased. The effect of the mesh resolution has been assessed in two cases with different levels of gaseous turbulence for a unity Stokes number using

the 2ΦEASM3 model. The dispersed phase needs higher grid resolution than the gaseous phase due to strong compressibility effects present on the dispersed phase. Increasing the mesh resolution leads to a better prediction of RMS fluctuations and segregation. Although, it has no noticeable effect on the low order moments statistics, it considerably improves both the high order statistics and the quality of the instantaneous fields. Finally, the 2ΦEASM3 model has been retained for implementation in AVBP and is used in the LES of the MERCATO combustion chamber configuration presented in Part IV of this work. A first conference paper showing the *a priori* results obtained with the AXISY model was presented to the *International Conference of Multiphase Flow, 2010.* A second publication presenting the models tested and the *a priori* results in the particle-laden temporal planar jet has been submitted to *Journal of Fluid Mechanics* both with Dr. E. Masi and Pr. Simonin. A second one showing the *a posteriori* analysis is being prepared to be submitted to *JFM* too.

Following another research line, a study on the evaporation of single isolated droplets motivated by the publication of new experimental results (Chauveau *et al.* (2008)) questioning the widely accepted results of Nomura *et al.* (1996) has been carried out in Part III. The new experimental technique proposed by Chauveau *et al.* (2008) is claimed to be less affected by heat conduction by the support fiber and by radiation from the furnace walls leading to much slower evaporation processes. The importance of these effects on the experimental results of Nomura *et al.* (1996) was already identified by Yang & Wong (2001) using numerical simulations including radiation and heat conduction through the support fiber. The model available in AVBP (ievap_1) uses the Spalding evaporation model and simplified thermodynamic and transport properties (thermo_AVBP) and shows very good agreement with the results of Nomura *et al.* (1996). The Abramzon-Sirignano evaporation model has been implemented in AVBP, showing small differences with the former model. The thermodynamic and transport properties are shown to have a much larger impact on the evaporation process. A new methodology consisting in using adapted Prandtl and Schmidt numbers for the evaporation different from those optimized for the reduced chemical schemes implemented in AVBP along with a laminar viscosity law depending not only on the temperature but also on the mixture composition (thermo_AVBPmix) has been proposed. The new methodology produces results close to the experimental results of Chauveau *et al.* (2008) and to the simulation using a complex evaluation of the thermodynamic and transport properties, which would considerably increase the computational cost in AVBP. The new methodology has been validated in a wide range of gaseous temperature and pressure conditions using the Spalding (ievap_2, Spalding (1953)) and the Abramzon-Sirignano evaporation models (ievap_21, Abramzon & Sirignano (1989)). A conference paper showing a LES of a complex aeronautical burner using the new methodology was presented at the *Mediterranean Combustion Symposium 2011* in collaboration with G. Hannebique.

Finally, Part IV presents the LES of the MERCATO configuration (García-Rosa (2008), Sanjosé (2009), Roux (2009), Senoner (2010), Vié (2010)) using two evaporation models (the classical approach using the Spalding evaporation model and a simplified evaluation of the thermodynamic and transport properties (ievap_1) and the Abramzon-Sirignano evaporation model along with thermo_AVBPmix approach (ievap_21)) and two approaches for the RUM (neglecting the RUM contribution (noRUM model in Part II) and using the 2ΦEASM3 model retained in Part II to model the RUM). Note that the VISCO RUM model previously implemented in AVBP cannot be used in this configuration since it considerably overpredicts the RUE in the shear regions and makes the simulation crash. First the gaseous flow is validated. Second, the general features of the liquid phase flow are presented. The effects of the evaporation and the RUM models are then analyzed separately. The new evaporation model leads to longer evaporation times. The spray distribution, as well as its temperature and the gaseous fuel field are considerably affected by the choice of the evaporation model, which may have an important impact on the ignition characteristics and the flame position in reactive conditions. The lack of experimental data and the use of a monodisperse approach (not able to reproduce the RMS fluctuations of droplet diameter) prevents further validation. The RUM model affects the results too. Accounting for RUM improves the predictions of RMS velocities and has an impact on the evaporation process too. The changes on the dispersed phase distribution due to the RUM lead to changes in the fields of mass and heat transfers due to evaporation and on the gaseous fuel field too. Phenomena such as spray impingement on the diffusor lips and detachment of clusters of droplets from the main jet observed in the experiments are also present on the LES. The 2ΦEASM3 model also enables to decrease and localize more the application

of the artificial dissipation.

There are still many working lines related to the evaporation and the RUM modeling and room for improvement too. The RUM models have been *a posteriori* validated in the DNS of an academic configuration and directly applied afterwards to the LES of a complex semi-industrial evaporating configuration. *A posteriori* validation in LES of a non-evaporating academic configuration by comparison with a Lagrangian reference is the main missing step. Note that this step was not studied in this work due to a lack of time. The *a priori* results shown by Masi (2010) however provided confidence in the capacity of the 2ΦEASM3 model to be valid in LES with only minor modifications. Including both dispersion and evaporation models increases the complexity of the analysis not allowing to obtain final conclusion on the effect of the RUM (and the evaporation) models due to the mutual interaction of the evaporation and the RUM processes. One solution would consist in comparing the evaporation models in Euler-Lagrange simulations where the uncorrelated motion of the particles is implicitly accounted for. There is however an obvious lack of experimental data providing at the same time the droplet distribution and the gaseous fuel distribution. New techniques have recently been developed (Duchaine (2010)) and should provide additional information to further validate the models.

Several options are foreseen in the way to real industrial two-phase flows simulations. In order to account for a large number of physical phenomena the following is on perspective:

1. To further improve the MEF in LES context:
   - Account for polydispersity, for which the multi-fluid method (Laurent *et al.* (2004)) implemented in AVBP by Vié (2010) is an option.
   - Account for collisions and coalescence. Since the RUE field is well reproduced with the 2ΦEASM3 model, the simulation of colliding two-phase flows can be accounted for with the MEF implemented in AVBP.
   - Implement higher order numerical schemes more adapted to the simulation of the dispersed phase (de Chaisemartin (2009), Kah (2010)) in order to reduce the application of artificial diffusion and provide better numerical accuracy and stability.
2. To test the impact of the models analyzed here in other phenomena taking place in the combustion chamber:
   - Study the impact of RUM and evaporation models on ignition phenomena which is affected by the gaseous fuel distribution.
3. Integration of new phenomena actually not taken into account:
   - Model the formation of liquid films both on the diffusor walls and on the inner walls of the chamber. Even further, LES in the combustion chamber could be coupled to conduction on the walls (Duchaine *et al.* (2009)) to predict mode accurately the wall temperature and thermal flux through the walls.
   - Account for droplet burning regime is key to correctly predict flame instabilities, especially in configurations where the flame is located close to the injector.
   - Account for primary atomization and secondary breakup to improve the description of the injection. The numerical methods used in AVBP are not adapted to solve these phenomena using the classical methods currently developed (VOF, level set, ghost fluid (Menard *et al.* (2007), Desjardins *et al.* (2008), Zuzio *et al.* (2011))). The idea would be to couple the primary and secondary atomization with a polydispersed Euler-Euer (or Euler-Lagrange) simulation. Preliminary tests have recently been shown by Zuzio *et al.* (2011). This is in fact a long term perspective.

Bibliography

Abramzon, B. & Sirignano, W. A. 1989 Droplet vaporisation model for spray combustion calculations. *Int. J. Heat and Mass Transfer* **9**, 1605–1618. 131, 133, 134, 137, 204

Albrecht, A., Bédat, B., Poinsot, T. & Simonin, O. 1999 Direct numerical simulation and modelling of evaporating droplets in homogeneous turbulence: application to turbulent flames. In *15th Annual Conference on Liquid Atomization and Spray System - ILASS Europe*. Toulouse, France. 9

Almgren, A.S., Bell, J.B., Colella, P. & Howell, L.H. 1993 An adaptive projection method for the incompressible Euler equations. *AIAA computational fluid dynamics conference, Orlando* . 5

Amaya, J., Cabrit, O., Poitou, D., Cuenot, B. & El Hafi, M. 2010 Unsteady coupling of Navier-Stokes and radiative heat transfer solvers applied to an anisothermal multicomponent turbulent channel flow. *J. Quant. Spec. Rad. Transf.* **111** (2), 295–301. 134

Anderson, J. D. 1990 *Modern Compressible Flow*. New York: McGraw-Hill. 19

André, J. C., Moor, G. De, Lacarrère, P., Thierry, G. & Vachat, R. Du 1976 Turbulence approximation for inhomogeneous flows. Part I: The clipping approximation. *J. Atmos. Sci.* **33**, 476–481. 53, 54

Apte, S. V., Mahesh, K. & Lundgren, T. 2003*a* A Eulerian-Lagrangian model to simulate two-phase/particulate flows. In *Annual Research Briefs*, pp. 161–171. Center for Turbulence Research, NASA Ames/Stanford Univ. 5, 8, 11

Apte, S. V., Mahesh, K., Moin, P. & Oefelein, J. C. 2003*b* Large-eddy simulation of swirling particle-laden flows in a coaxial-jet combustor. *Int. J. Multiphase Flow* **29** (8), 1311–1331. 128

Basset, A. B. 1888 *Treatise on Hydrodynamics*, , vol. 2. Deighton Bell, London. 23

Batchelor, G. K. 1946 The theory of axisymmetric turbulence. *Proceedings of the Royal Society of London. Series A: Mathematical, Physical and Engineering Sciences* **186** (1007), 480–502. 47

Bayvel, L. P. & Orzechowski, Z. 1993 *Liquid Atomization*. Washington, USA: Taylor & Francis. 4

Beau, P.A., Ménard, T., Lebas, R., Berlement, A., Tanguy, S. & Demoulin, F.-X. 2006, Paper 98166 Numerical jet atomization. Part II: modeling information and comparison with DNS. In *Proceedings of the Fluid Engineering Division Summer Meeting*. ASME. 5

Bellan, J. 2000 Supercritical (and subcritical) fluid behavior and modeling: drops, streams, shear and mixing layers, jets and sprays. *Prog. Energy Comb. Sci.* **26**, 329–366. 150

Berger, M. J. 1982 Adaptive mesh refinement for hyperbolic partial differential equations. *PhD thesis, Stanford university* . 5

Bird, R. B., Stewart, W. E. & Lighfoot, E. N. 1960 *Transport phenomena*. New York: John Wiley. 138, 139

Birouk, M. & Gokalp, I. 2006 Current status of droplet evaporation in turbulent flows. *Prog. Energy Comb. Sci.* **32**, 408–423. 131

Boileau, M. 2007 Simulation aux grandes échelles de l'allumage diphasique des foyers aéronautiques. Phd thesis, INP Toulouse. 1, 13

Boivin, M., Simonin, O. & Squires, K. D. 1998 Direct numerical simulation of turbulence modulation by particles in isotropic turbulence. *J. Fluid Mech.* **375**, 235–263. 8, 26

Boivin, M., Simonin, O. & Squires, K. D. 2000 On the prediction of gas-solid flows with two-way coupling using large eddy simulation. *Phys. Fluids* **12** (8), 2080–2090. 8, 26

Borée, J., Ishima, T. & Flour, I. 2001 The effect of mass loading and inter-particle collisions on the development of the polydispersed two-phase flow downstream of a confined bluff body. *J. Fluid Mech.* **443**, 129–165. 13

Borghi, R. 1996*a* Background on droplets and sprays. In *Combustion and turbulence in two phase flows, Lecture Series 1996-02*. Von Karman Institute for Fluid Dynamics. 9

Borghi, R. 1996*b* The links between turbulent combustion and spray combustion and their modelling. In *8th International Symposium on Transport Phenomena in Combustion*, pp. 1–18. 131

Borghi, R. & Champion, M. 2000 *Modélisation et théorie des flammes*, editions technip edn. TECHNIP. 10

Boussinesq, J. 1877 Théorie de l'écoulement tourbillant. *Mém. Présentés par Divers Savants. Acad. Sci. Inst. Fr.* **23**, 46–50. 39

Boussinesq, J. 1885 Sur la résistance qu'oppose un liquide indéfini au repos. *C. R. Acad. Sci.Inst. Fr.* . 23

Carvalho, I., Heitor, M. & Santos, D. 2002 Liquid film desintegration regimes and proposed correlations. *Int. J. Multiphase Flow* **28**, 773–789. 5

de Chaisemartin, S. 2009 Modèles Eulériens et simulation numérique de la dispersion turbulente de brouillards qui s'évaporent. PhD thesis, Ecole Centrale de Paris, Chatenay-Malabry, France. 28, 127, 205

de Chaisemartin, S., Fréret, L., Kah, D., Laurent, F., Fox, R. O., Réveillon, J. & Massot, M. 2008 Turbulent combustion of polydisperse evaporating sprays with droplets crossing: Eulerian modeling and validation in the infinite Knudsen limit. In *Proc. of the Summer Program*. Center for Turbulence Research, NASA Ames/Stanford Univ. 28

Chandrasekhar, S. 1950 The theory of axisymmetric turbulence. *Proceedings of the Royal Society of London. Series A: Mathematical, Physical and Engineering Sciences* **242** (855), 557–577. 47

Chapman, S. & Cowling, T. G. 1939 (digital reprint 1999) *The Mathematical Theory of Non-Uniform Gases*, Cambridge Mathematical Library edn. Cambridge University Press. 29, 138

Chasnov, J. R. 1991 Simulation of the Kolmogorov inertial subrange using an improved subgrid model. *Phys. FluidsA* **3**, 188–200. 3

Chassaing, P. 2000 *Turbulence en mécanique des fluides, analyse du phénomène en vue de sa modélisation à l'usage de l'ingénieur*. Toulouse, France: Cépaduès-éditions. 3

Chauveau, C., Halter, F, Lalonde, A. & Gokalp, I. 2008 An experimental study on the droplet vaporization : effects of heat conduction through the support fiber. In *ILASS*, *08* 4-1. Como Lake, Italy. 8, 15, 131, 133, 137, 141, 143, 144, 147, 148, 149, 150, 151, 154, 155, 204

Chesnel, J. 2010 Simulation aux grandes echelles de l'atomisation, application à l'injection automobile. Phd thesis, Université de Rouen. 5

Clift, R., Grace, J. R. & Weber, M. E. 1978 *Bubbles, Drops, and Particles*. Academic Press. 24

Colin, O., Ducros, F., Veynante, D. & Poinsot, T. 2000 A thickened flame model for large eddy simulations of turbulent premixed combustion. *Phys. Fluids* **12** (7), 1843–1863. 61, 166

Couderc, F. & J.-L., Estivalezes 2003 Numerical simulation of the air-blasted liquid sheet: development of a DNS solver based on the level-set method. *ILASS Europe Notthingham* . 5

Crowe, C., Sommerfeld, M. & Tsuji, Y. 1998 *Multiphase Flows with Droplets and Particles*. 25

Deardorff, J. 1970 A numerical study of three-dimensional turbulent channel flow at large Reynolds numbers. *J. Fluid Mech.* **41**, 453–480. 3

Deardorff, J. W. 1973 The use of subgrid transport equations in a three-dimensional model of atmospheric turbulence. *J. Fluids Eng.* **95**, 429–438. 54

Deardorff, J. W. 1974 Three-dimensional numerical study of the height and mean structure of a heated planetary boundary layer. *Boundary-Layer Meteorology* **7** (1), 81–106. 3

DeBar, R. 1974 A method in 2d Eulerian hydrodynamics. *Tech. Rep.*. 5

Delplanque, J. P. & Sirignano, W. A. 1993 Numerical study of the transient vaporization of an oxygen droplet at sub- and super-critical conditions. *Int. J. Heat and Mass Transfer* **36**, 303–314. 150

Desjardins, O., Fox, R. O. & Villedieu, P. 2006 A quadrature-based moment closure for the Williams spray equation. In *Proc. of the Summer Program*, pp. 223–234. Center for Turbulence Research, NASA Ames/Stanford Univ. 28

Desjardins, O., Moureau, V. & Pitsch, H. 2008 An accurate conservative level set/ghost fluid method for simulating turbulent atomization. *J. Comput. Phys.* **227**, 8395–8416. 5, 205

Desjonqueres, P., Gouesbet, G., Berlemont, A. & Picart, A. 1986 Dispersion of discrete particles by continuous turbulent motions: new results and discussions. *Phys. Fluids* **29**, 2147–2151. 25, 26

Deutsch, E. 1992 Dispersion de particules dans une turbulence homogène isotrope stationnaire calculée par simulation numérique directe des grandes échelles. Phd thesis, EDF-DRD. 8

Deutsch, E. & Simonin, O. 1991 Large eddy simulation applied to the motion of particles in stationnary homogeneous fluid turbulence. In *Turbulence Modification in Multiphase Flows*, , vol. 110, pp. 35–42. ASME FED. 26, 27, 60

Dombard, J. 2011 Direct numerical simulation of non-isothermal dilute sprays using the mesoscopic Eulerian approach. Phd thesis, INP Toulouse. 13, 47, 56, 58, 60, 92, 112, 127

Druzhinin, O. A. 1995 On the two-way interaction in two-dimensional particle-laden flows - the accumulation of particles and flow modification. *J. Fluid Mech.* **297**, 49–76. 26

Druzhinin, O. A. & Elghobashi, S. 1998 Direct numerical simulations of bubble-laden turbulent flows using the two-fluid formulation. *Phys. Fluids* **10** (3), 685–697. 28

Duchaine, F., Mendez, S., Nicoud, F., Corpron, A., Moureau, V. & Poinsot, T. 2009 Conjugate heat transfer with large eddy simulation application to gas turbine components. *C. R. Acad. Sci.Mécanique* **337** (6-7), 550–561. 134, 202, 205

Duchaine, P. 2010 Experimental analysis of the dynamics of gaseous and two-phase counterflow flames submitted to upstream modulations. PhD thesis, Ecole Centrale de Paris, Chatenay-Malabry, France. 205

Ducros, F., Comte, P. & Lesieur, M. 1996 Large-eddy simulation of transition to turbulence in a boundary layer developing spatially over a flat plate. *J. Fluid Mech.* **326**, 1–36. 39

Ducros, F., Nicoud, F. & Poinsot, T. 1998 Wall-adapating local eddy-viscosity models for simulations in complex geometries. In *ICFD*, pp. 293–300. Baines M. J. 39, 40, 166

Dukowicz, J. K. 1980 A particle-fluid numerical model for liquid sprays. *J. Comput. Phys.* **35**, 229–253. 11

Eaton, J. K. & Fessler, J. R. 1994 Preferential concentration of particles by turbulence. *Int. J. Multiphase Flow* **20**, 169–209. 8

Elghobashi, S. & Truesdell, G. C. 1992 Direct simulation of particle dispersion in a decaying isotropic turbulence. *J. Fluid Mech.* **242**, 655–700. 8

Elghobashi, S. & Truesdell, G. C. 1993 On the two-way interaction between homogeneous turbulence and dispersed solid particles. I: Turbulence modification. *Phys. Fluids* **5(7)**, 1790–1801. 8, 25

Eyssartier, A. 2012 Study and modelisation of stationnary and transient two-phase flow combustion. Phd thesis, INP Toulouse. 159, 201

Faeth, G. M. 1977 Current status of droplet and liquid combustion. *Prog. Energy Comb. Sci.* **3** (4), 191–224. 131

Faeth, G. M. 1983 Evaporation and combustion of sprays. *Prog. Energy Comb. Sci.* **9**, 1–76. 10

Faeth, G. M. 1987 Mixing, transport and combustion sprays. *Prog. Energy Comb. Sci.* **13** (4), 293–345. 10

Faeth, G. M. 1996 Spray combustion phenomena. *Prog. Energy Comb. Sci.* **26** (1), 1593–1612. 131

Falkovich, G., Fouxon, A. S. & Stepanov, M. G. 2002 Acceleration of rain initiation by cloud turbulence. *Nature* **419**, 151–154. 78

Favre, A. 1969 Statistical equations of turbulent gases. In *Problems of hydrodynamics and continuum mechanics*, pp. 231–266. Philadelphia: SIAM. 39

Fede, P., Simonin, O. & Patino, G. 2004 Multifluid modeling of the effect of inter-particle collisions in polydispersed gas-solid turbulent flows. In *Third International Symposium on Two-Phase Flow Modelling and Experimentation*. Pisa, Italy. 7, 8

Ferry, J. & Balachandar, E. 2002 Equilibrium expansion for the Eulerian velocity of small particles. *Powder Technology* **125**, 131–139. 11, 28

Février, P., Simonin, O. & Squires, K. 2005 Partitioning of particle velocities in gas-solid turbulent flows into a continuous field and a spatially uncorrelated random distribution: Theoretical formalism and numerical study. *J. Fluid Mech.* **533**, 1–46. 11, 13, 26, 28, 30, 31, 69, 203

Fox, R.O., Laurent, F. & Massot, M. 2008 Numerical simulation of spray coalescence in an Eulerian framework: Direct quadrature method of moments and multi-fluid method. *J. Comput. Phys.* **227**, 058–3088. 28

Fox, R. O . 2012 Large-eddy-simulation tools for multiphase flows. *Ann. Rev. Fluid Mech.* **44**, 47–76. 11, 22, 23, 37

Fox, R. O. 2008 A quadrature-based third-order moment method for dilute gas-particle flows. *J. Comput. Phys.* **227** (12), 6313–6350. 28

Fox, R. O. 2009 Higher-order quadrature-based moment methods for kinetic equations. *J. Comput. Phys.* **228** (20), 7771–7791. 28

Franzelli, B., Riber, E., Sanjosé, M. & Poinsot, T. 2010 A two-step chemical scheme for kerosene-air premixed flames. *Combust. Flame* **157**, 1364 – 1373. 152

Frössling, N. 1938 Über die Verdunstung fallender Tropfen (On the evaporation of falling drops). *Gerlands Beitr. Geophys.* **52**, 170–216. 132, 135

García, M. 2009 Développement et validation du formalisme Euler-Lagrange dans un solveur parallèle et non-structuré pour la simulation aux grandes échelles. Phd thesis, INP Toulouse. 11, 12, 26

García-Rosa, N. 2008 Phénomènes d'allumage d'un foyer de turbomachine en conditions de haute altitude. PhD thesis, Université de Toulouse - Ecole doctorale : Mécanique, Energétique, Génie civil, Procédés, Toulouse, France. 15, 34, 159, 160, 169, 204

Gatignol, R. 1983 The faxén formulae for a rigid particle in an unsteady non-uniform Stokes flow. *J. Méc. Théor. Appl.* **1** (2), 143–160. 23

Gatski, T. B. & Speziale, C. G. 1993 On explicit algebraic stress models for complex turbulent flows. *J. Fluid Mech.* **254**, 59–78. 49, 50

George, W. K. & Hussein, H. J. 1991 Locally axisymmetric turbulence. *J. Fluid Mech.* **233**, 1–23. 46

Germano, M., Piomelli, U., Moin, P. & Cabot, W. 1991 A dynamic subgrid-scale eddy viscosity model. *Phys. Fluids* **3** (7), 1760–1765. 39

Ghassemi, H., W., Baek S. & Khan, Q. S. 2006 Experimental study on evaporation of kerosene droplets at elevated pressures and temperatures. *Combust. Sci. Tech.* **178**, 1669–1684. 8, 133, 148, 149, 151, 152, 153, 154

Girimaji, S. S. 1996 Fully explicit and self-consistent algebraic Reynolds stress model. *Theoret. Comput. Fluid Dynamics* **8** (6), 387–402. 49, 51, 52

Givler, S. D. & Abraham, J. 1996 Supercritical droplet vaporization and combustion studies. *Prog. Energy Comb. Sci.* **22**, 1–28. 150

Godsave, G.A.E. 1953 Studies of the combustion of drops in a fuel spray: the burning of single drops of fuel. *Proc. Combust. Inst.* **4** (1), 818–830. 9

Gogos, G., Soh, S. & Pope, D. N. 2003 Effects of gravity and ambient pressure on liquid fuel droplet evaporation. *Int. J. Heat and Mass Transfer* **46**, 283–296. 150, 151

Goodwin, David G. 2009 Cantera C++ Users Guide, http://sourceforge.net/projects/cantera. 138

Gorokhovski, M. & Herrmann, M. 2008 Modelling primary atomization. *Ann. Rev. Fluid Mech.* **40**, 343–366. 5

Greenberg, J. B., Silverman, I. & Tambour, Y. 1993 On the origin of spray sectional conservation equations. *Combust. Flame* **93**, 90–96. 11, 28

Hannebique, G. 2012 LES des écoulements diphasiques réactifs, comparaison Euler-Euler, Euler-Lagrange. Application à l'allumage. Phd thesis, INP Toulouse. 201

Harstad, K. & Bellan, J. 2001 Evaluation of commonly used assumptions for isolated and cluster heptane drops in nitrogen at all pressures. *Combust. Flame* **127**, 1861–1879. 131

Haworth, D., Cuenot, B., Poinsot, T. & Blint, R. 2000 Numerical simulation of turbulent propane-air combustion with non homogeneous reactants. *Combust. Flame* **121**, 395–417. 3

Haworth, D. C. & Pope, S. B. 1986 A generalized Langevin model for turbulent flows. *Phys. Fluids* **2**, 738–744. 27

Hinze, J. O. 1975 *Turbulence*. New-York: McGraw-Hill. 25, 26, 27

Hirsch, C. 1990 *Numerical Computation of Internal and External Flows*, , vol. 2. New York: John Wiley & Sons. 22

Hirsch, C. 2007 Finite volume method and conservative discretization with an introduction to finite element method. In *Numerical Computation of internal & external flows: Fundamentals of Computational Fluid Dynamics, second edition*, chap. 5, pp. 203–248. New York: John Wiley & Sons. 19

Hirschfelder, J. O., Curtiss, F. & Bird, R. B. 1964 *Molecular theory of gases and liquids*. John Wiley & Sons. 138

Hishida, K., Takemoto, K. & Maeda., M. 1987 Turbulent characteristics of gas-solids two-phase confined jet. *Japanese Journal of Multiphase Flow* **1** (1), 56–69. 13, 45, 47, 128, 203

Hohmann, S. & Renz, U. 2003 Numerical simulaiton nof fuel sprays at high ambient pressure: the influence of real gas effects and gas solubility on droplet vaporisation. *Int. J. Heat and Mass Transfer* **46**, 3017–3028. 132

Hubbard, G. L., Denny, V. E. & Mills, A. F. 1975 Droplet evaporation: effects of transient and variable properties. *Int. J. Heat and Mass Transfer* **18**, 1003–1008. 8, 132, 137

Jaegle, F. 2009 LES of two-phase flow in aero-engines. PhD thesis, Université de Toulouse - Ecole doctorale MEGeP, CERFACS - CFD Team, Toulouse. 6, 141

Jameson, A. 1991 Time dependent calculations using multigrid, with applications to unsteady flows past airfoils and wings. *Tech. Rep.* AIAA-91-1596. AIAA 10th Computational Fluid Dynamics Conference. 3

Johnson, R. W. 1998 *The handbook of fluid dynamics*. CRC Press. 25

Jones, W. P. & Whitelaw, J. H. 1982 Calculation methods for reacting turbulent flows: a review. *Combust. Flame* **48**, 1–26. 4

Joseph, D., El Hafi, M., Fournier, R. & Cuenot, B. 2005 Comparison of three spatial differencing schemes in discrete ordinates method using three-dimensional unstructured meshes. *Int. J. of Therm. Sci.* **44** (9), 851–864. 134

Jovanović, J. & Otić, I. 2000 On the constitutive relation for the Reynolds stresses and the Prandtl-Kolmogorov hypothesis of effective viscosity in axisymmetric strained turbulence. *J. Fluids Eng.* **122** (1), 48–50. 47

Kadota, T. & Hiroyasu, H. 1976 Evaporation of a single droplet at elevated pressures and temperatures. *Bull. JSME* **19** (138), 1515–1521. 8

Kah, D. 2010 Prise en compte des aspects polydispersés pour la modélisation d'un jet de carburant dans les moteurs à combustion interne. Phd thesis, Ecole Centrale Paris. 28, 127, 205

Kah, D., Laurent, F., Massot, M. & Jay, S. 2011 A high order moment method simulating evaporation and advection of a polydisperse liquid spray. *J. Comput. Phys.* In Press, Corrected Proof. 28

Kaufmann, A. 2004 Vers la simulation des grandes échelles en formulation Euler/Euler des écoulements réactifs diphasiques. Phd thesis, INP Toulouse. 13, 29, 33, 45

Kaufmann, A., Hélie, J., Simonin, O. & Poinsot, T. 2005 Comparison between Lagrangian and eulerian particle simulations coupled with DNS of homogeneous isotropic decaying turbulence. In *Proceedings of the Estonian Academy of Sciences*, , vol. 11, pp. 91–105. 13, 34

Kaufmann, A. & Moreau, M. 2008 A spectral projection method for analysis of autocorrelation functions and projection errors in discrete particle simulation. *Int. J. Numer. Meth. Fluids* **58** (7), 709–725. 221

Kaufmann, A., Moreau, M., Simonin, O. & Hélie, J. 2008 Comparison between Lagrangian and mesoscopic Eulerian modelling approaches for inertial particles suspended in decaying isotropic turbulence. *J. Comput. Phys.* **227** (13), 6448–6472. 45, 47, 55

Kee, R. J., Dixon-Lewis, G., Warnatz, J., E., Coltrin M. & Miller, J. A. 1986 A Fortran computer code package for the evaluation of gas phase, multicomponent transport properties. *Tech. Rep.* SAND86-8246. Sandia National Laboratories. 138, 139

Kolmogorov, A. N. 1941 The local structure of turbulence in incompressible viscous fluid for very large Reynolds numbers. *C. R. Acad. Sci., USSR* **30**, 301. 37, 39

Kraichnan, R. H. 1976 Eddy viscosity in two and three dimensions. *J. Atmos. Sci.* **33**, 1521–1536. 3

Kristyadi, T., Deprédurand, V., Castanet, G., Lemoine, F., Sazhin, S. S., Elwardany, A., Sazhina, E.M. & Heikal, M.R. 2010 Monodisperse monocomponent fuel droplet heating and evaporation. *Fuel* **89**, 3995–4001. 131

Kuo, K. K. 2005 *Principles of combustion*, 2nd edn. Hoboken, New Jersey: John Wiley & Sons, Inc. 8, 131, 138

Lamarque, N. 2007 Schémas numériques et conditions limites pour la simulation aux grandes échelles de la combustion diphasique dans les foyers d'hélicoptère. Phd thesis, INP Toulouse. 13, 89, 159, 180, 200

Lathouwers, D. & Bellan, J. 2001 Modeling of dense gas-solid reactive mixtures applied to biomass pyrolysis in a fluidized bed. *Int. J. Multiphase Flow* **27** (12), 2155–2187. 3

Laurent, C. 2008 Développement et validation de modèles d'évaporation multi-composant. PhD thesis, Institut Supérieur de l'Aéronautique et de l'Espace - Ecole doctorale MEGeP, EDyF, ONERA-DMAE, Toulouse. 133

Laurent, F. & Massot, M. 2001 Multi-fluid modelling of laminar polydisperse sprayflames: origin, assumptions and comparison of sectional and sampling methods. *Combust. Theory and Modelling* **5**, 537–572. 28

Laurent, F., Massot, M. & Villedieu, P. 2004 Eulerian multi-fluid modeling for the numerical simulation of coalescence in polydisperse dense liquid sprays. *J. Comput. Phys.* **194** (2), 505–543. 11, 159, 201, 205

Laviéille, J. 1997 Simulations numériques et modélisation des interactions entre l'entrainement par la turbulence et les collisions interparticulaires en écoulement gaz-solide.. Phd thesis, Université de Rouen. 8

Law, C. K. 1982 Recent advances in droplet vaporisation and combustion. *Prog. Energy Comb. Sci.* **8**, 171–201. 10, 131

Lee, S., Moin, P. & Lele, S. 1990 Simulation of spatially evolving turbulence. *Bul. of Am. Phys. Soc.* **34** (10), 2252. 150

Lefebvre, A. H. 1989 *Atomization and Sprays*. Taylor & Francis. 4, 5

Lefebvre, A. H. 1999 *Gas Turbines Combustion*. Taylor & Francis. 131

Lele, S.K. 1992 Compact finite difference schemes with spectral like resolution. *J. Comput. Phys.* **103**, 16–42. 221

Leonard, A. 1974 Energy cascade in large eddy simulations of turbulent fluid flows. *Adv. Geophys.* **18** (A), 237–248. 38

Lesieur, M. 1997 Recent approaches in large-eddy simulations of turbulence. In *New tools in turbulence modelling* (ed. O. Métais & J. Ferziger), pp. 1 – 28. Les Editions de Physique - Springer Verlag. 40

Li, T., Nishida, K. & Hiroyasu, H. 2011 Droplet size distribution and evaporation characteristics of fuel spray by a swirl type atomizer. *Fuel* **90**, 2367–2376. 131

Lilly, D. K. 1967 The representation of small-scale turbulence in numerical simulation experiments. In *Proceedings of the IBM Scientific Computing Symposium on Environmental Sciences*. Yorktown Heights, USA. 3

Lilly, D. K. 1992 A proposed modification of the germano sub-grid closure method. *Phys. Fluids* **4** (3), 633–635. 39

Linassier, G., Lecourt, R., Villedieu, P., Lavergne, G. & Verdier, H. 2011 Experimental data base on high altitude turbojet ignition for numerical simulation validation. In *ILASS-Europe*. Estoril, Portugal. 182, 184, 196, 197, 200

Liu, H. 2000 *Science and engineering of droplets. Fundamentals and applications*. Noyes Publications (William Sndrew Publishing). 10

Lozano, A., Barreras, F., Hauke, G. & Dopazo, C. 2001 Longitudinal instabilities in a air-blasted liquid sheet. *J. Fluid Mech.* **437**, 143–173. 5

Lucca-Negro, O. & O'Doherty, T. 2001 Vortex breakdown: a review. *Prog. Energy Comb. Sci.* **27**, 431–481. 173

Luche, J. 2003 Elaboration of reduced kinetic models of combustion. application to a kerosene mechanism. PhD thesis, LCSR Orleans. 152

Lund, T. S. & Rogers, M. M. 1994 An improved measure of strain state probability in turbulent flows. *Phys. Fluids* **6** (5), 1838–1847. 46

Mahesh, K., Constantinescu, G., Apte, S., Iaccarino, G., Ham, F. & Moin, P. 2002 Progress toward large-eddy simulation of turbulent reacting and non-reacting flows in complex geometries. In *Annual Research Briefs*, pp. 115–142. Center for Turbulence Research, NASA Ames/Stanford Univ. 26

Maqua, C., Castanet, G., Grisch, F., Lemoine, F., Kristyadi, T. & Sazhin, S. S. 2008 Monodisperse droplet heating and evaporation: Experimental study and modelling. *Int. J. Heat and Mass Transfer* **51**, 3932–3945. 131

Marchisio, D. L. & Fox, R. O. 2005 Solution of population balance equations using the direct quadrature method of moments. *J. Aerosol Sci.* **36**, 43–73. 28

Marmottant, P. & Villermaux, E. 2004 On spray formation. *J. Fluid Mech.* **498**, 73–111. 5

Mashayek, F. & Pandya, R. 2003 Analytical description of particle/droplet-laden turbulent flows. *Prog. Energy Comb. Sci.* **29**, 329–378. 26

Masi, E. 2010 Theoretical and numerical study of the modeling of unsteady non-isothermal particle-laden turbulent flows by an Eulerian-Eulerian approach. Phd thesis, INP Toulouse. 13, 14, 26, 29, 34, 45, 46, 47, 48, 49, 50, 51, 52, 53, 55, 56, 57, 60, 69, 78, 97, 127, 203, 205, 221, 222

Matlosz, R. L., Leipziger, S. & Torda, T. P. 1972 Investigation of liquid drop evaporation in a high temperature and high pressure environment. *Int. J. Heat and Mass Transfer* **15**, 831–852. 8, 150

Maxey, M.R. & Patel, B.K. 2001 Localized force representations for particles sedimenting in Stokes flow. *Int. J. Multiphase Flow* **27** (9), 1603–1626. 11

Maxey, M. & Riley, J. 1983 Equation of motion for a small rigid sphere in a nonuniform flow. *Phys. Fluids* **26** (4). 23

Maxey, M. R. 1987 The gravitational settling of aerosol particles in homogeneous turbulence and random flow fields. *J. Fluid Mech.* **174**, 441–465. 8, 28

Mei, R., Adrian, R. J. & Hanratty, T. J. 1991 Particle dispersion in isotropic turbulence under Stokes drag and Basset force with gravitational settling. *J. Fluid Mech.* **225**, 481–495. 8

Menard, T., Tanguy, S. & Berlemont, A. 2007 Coupling level set/VOF/ghost fluid methods: Validation and application to 3d simulation of the primary break-up of a liquid jet. *Int. J. Multiphase Flow* **33**, 510–524. 5, 205

Miller, R. S., Harstad, K. & Bellan, J. 1998 Evaluation of equilibrium and non-equilibrium evaporation models for many-droplet gas-liquid flow simulations. *Int. J. Multiphase Flow* **24** (6), 1025–1055. 133, 137

Moin, P. & Kim, J. 1982 Numerical investigation of turbulent channel flow. *J. Fluid Mech.* **118**, 341–377. 3

Moreau, M. 2006 Modélisation numérique directe et des grandes échelles des écoulements turbulents gaz-particules dans le formalisme eulérien mésoscopique. Phd thesis, INP Toulouse. 13, 14, 26, 33, 42, 127, 128, 166

Moreau, V. & Desjardins, O. 2008 A second-order ghost-fluid method for the primary atomization of liquid fuel in air-blast type injectors. In *Proceedings of the Summer Program* (ed. CTR). 5, 221

Morin, C., Chauveau, C., Dagat, P., Gokalp, I. & Cathonnet, M. 2004 Vaporization and oxidation of liquid fuel droplets at high temperature and pressure. application to n-alkanes and vegetable oil methyl esters. *Combust. Sci. Tech.* **176**, 499–524. 8

Morin, C., Chauveau, C. & Gokalp, I. 2000 Droplet vaporisation characteristics of vegetable oil derived biofuels at high temperatures. *Exp. Thermal Fluid Sci.* **21** (1 - 3), 41 – 50. 148, 149

Mossa, J.-B. 2005 Extension polydisperse pour la description Euler-Euler des écoulements diphasiques réactifs - th/cfd/05/74. Phd thesis, INP Toulouse. 13, 28

Nomura, H., Ujiie, Y., Rath, H. J., Sato, J. & Kono, M. 1996 Experimental study on high-pressure droplet evaporation using microgravity conditions. *Proc. Combust. Inst.* **26**, 1267–1273. 8, 15, 131, 133, 137, 141, 142, 143, 144, 145, 147, 148, 149, 150, 151, 152, 154, 204

Orszag, S. A. 1970 Analytical theories of turbulence. *J. Fluid Mech.* **41** (02), 363–386. 53

Ortega, J. M. 1987 *Matrix theory*. Plenum. 53

Oseen, C. W. 1927 *Hydrodynamik*. Leipzig. 23, 24

Osher, S. & Fedwik, R. 2003 Level set method and dynamic implicit surfaces. *Springer applied mathematical sciences* **153**. 5

Pandya, R. & Mashayek, F. 2002 Two-fluid large-eddy simulation approach for particle-laden turbulent flows. *Int. J. Heat and Mass Transfer* **45**, 4753–4759. 26

Pascaud, S. 2006 Vers la simulation aux grandes échelles des écoulements turbulents diphasiques réactifs: application aux foyers aéronautiques. Phd thesis, INP Toulouse. 13

Passot, T. & Pouquet, A. 1987 Numerical simulation of compressible homogeneous flows in the turbulent regime. *J. Fluid Mech.* **181**, 441–466. 57

Poinsot, T., Echekki, T. & Mungal, M. G. 1992 A study of the laminar flame tip and implications for premixed turbulent combustion. *Combust. Sci. Tech.* **81** (1-3), 45–73. 221

Poinsot, T. & Lele, S. 1992 Boundary conditions for direct simulations of compressible viscous flows. *J. Comput. Phys.* **101** (1), 104–129. 13, 162

Poinsot, T. & Veynante, D. 2005 *Theoretical and Numerical Combustion*. R.T. Edwards, 2nd edition. 22

Pope, S. B. 1975 A more general effective-viscosity hypothesis. *J. Fluid Mech.* **72** (02), 331–340. 49, 50

Pope, S. B. 2000 *Turbulent flows*. Cambridge University Press. 3, 37, 38, 40

Rachner, M., Becker, J., Hassa, C. & Doerr, T. 2002 Modelling of the atomization of a plain liquid fuel jet in crossflow at gas turbine conditions. *Aerospace science and technology* **6**, 495–506. 5

Rangel, R. & Sirignano, W. 1991 The linear and nonlinear shear instability of a fluid sheet. *Phys. Fluids* **3**, 2392–2400. 5

Rangel, R. H. & Sirignano, W. A. 1989 An evaluation of point-source approximation in spray calculations. *Num. Heat TRansfer* **16** (A), 37–57. 133

Rani, S. & Balachandar, E. 2004 Preferential concentration of particles in isotropic turbulence: a comparison of the Lagrangian and the equilibrium Eulerian approaches. *Int. J. Multiphase Flow* **141** (1-2), 109–118. 28, 30

Ranz, W. E. & Marshall, W. R. 1952 Evaporation from drops. *Chem. Eng. Prog.* **48** (4), 173. 131, 135, 136, 151

Reeks, M. W. 1991 On a kinetic equation for the transport of particles in turbulent flows. *Phys. Fluids* **3** (3). 8, 29

Reeks, M. W. 1993 On the constitutive relations for dispersed particles in nonuniform flows. I. Dispersion in a simple shear flow. *Phys. Fluids* **5** (3), 750–761. 8

Reitz, R.D. 1978 Atomization and other breakup regimes of a liquid jet. PhD thesis, Princeton University. 5

Réveillon, J. & Vervisch, L. 2004 Analysis of weakly turbulent diluted-spray flames and spray combustion diagram. *Under consideration for publication in J. Fluid Mech.* . 9

Réveillon, J. & Vervisch, L. 2005 Analysis of weakly turbulent diluted-spray flames and spray combustion regimes. *J. Fluid Mech.* **537**, 317–347. 9, 10

Riber, E. 2007 Développement de la méthode de simulation aux grandes échelles pour les écoulements diphasiques turbulents. Phd thesis, INP Toulouse. 13, 30, 42, 45, 47, 78, 127, 203

Riber, E., García., M., Moureau, V., Pitsch, H., Simonin, O. & Poinsot, T. 2006 Evaluation of numerical strategies for LES of two-phase reacting flows. In *Proc. of the Summer Program*, pp. 197–211. Center for Turbulence Research, NASA Ames/Stanford Univ. 28

Riber, E., Moureau, V., García., M., Poinsot, T. & Simonin, O. 2009 Evaluation of numerical strategies for LES of two-phase reacting flows. *J. Comput. Phys.* **228**, 539–564. 47

Richardson, L. F. 1922 *Weather Prediction by Numerical Process*, Cambridge edn. Cambridge University Press. 37

Rodi, W. 1972 The prediction of free turbulent boundary layers by use of a two-equation model of turbulence. Phd thesis, University of London. 49

Rouson, D. W. I. & Eaton, J. K. 2001 On the preferential concentration of solid particles in turbulent channel flow. *J. Fluid Mech.* **428**, 149–169. 30

Roux, A. 2009 Simulation aux grandes échelles d'un statoréacteur. PhD thesis, Université de Toulouse - Ecole doctorale MEGeP, CERFACS - CFD Team, Toulouse. 159, 166, 204

Roux, A., Gicquel, L. Y. M., Reichstadt, S., Bertier, N., Staffelbach, G., Vuillot, F. & Poinsot, T. 2010 Analysis of unsteady reacting flows and impact of chemistry description in large eddy simulations of side-dump ramjet combustors. *Combust. Flame* **157**, 176–191. 89

Roux, A., Reichstadt, S., Bertier, N., Gicquel, L. Y. M., Vuillot, F. & Poinsot, T. 2009 Comparison of numerical methods and combustion models for LES of a ramjet. *C. R. Acad. Sci.Mécanique* **337** (6-7), 352–361. 13

Sanjosé, M. 2009 Evaluation de la méthode Euler-Euler pour la simulation numérique aux grandes échelles des chambres à carburant liquide. Phd thesis, INP Toulouse. 13, 15, 34, 47, 61, 137, 139, 141, 152, 154, 159, 161, 162, 166, 167, 169, 172, 173, 175, 182, 200, 204

Sanjosé, M., Senoner, J., Jaegle, F., Cuenot, B., Moreau, S. & Poinsot, T. 2011 Fuel injection model for Euler-Euler and Euler-Lagrange large-eddy simulations of an evaporating spray inside an aeronautical combustor. *Int. J. Multiphase Flow* **37**, 514–529. 159, 164

Sankaran, V. & Menon, S. 2002 LES of spray combustion in swirling flows. *J. Turb.* **3**, 011. 11

Sazhin, S. S. 2006 Advanced models of fuel droplet heating and evaporation. *Prog. Energy Comb. Sci.* **32**, 162–214. 8, 131, 134, 137

Sazhin, S. S., Abdelghaffar, W. A., Krutitskii, P. A., Sazhina, E. M. & Heikal, M. R. 2005 New approaches to numerical modelling of droplet transient heating and evaporation. *Int. J. Heat and Mass Transfer* **48**, 4215–4228. 133

Sazhin, S. S., Kristyadi, T., Abdelghaffar, W. A. & Heikal, M. R. 2006 Models for fuel droplet heating and evaporation: Comparative analysis. *Fuel* **85**, 1613–1630. 131

Schiller, L. & Nauman, A. 1935 A drag coefficient correlation. *VDI Zeitung* **77**, 318–320. 24, 60

Schønfeld, T. & Poinsot, T. 1999 Influence of boundary conditions in LES of premixed combustion instabilities. In *Annual Research Briefs*, pp. 73–84. Center for Turbulence Research, NASA Ames/Stanford Univ. 13

Schumann, U. 1975 Subgrid scale model for finite difference simulations of turbulent flows in plane channels and annuli. *J. Comput. Phys.* **18**, 376–404. 3

Schumann, U. 1977 Realizability of Reynolds-stress turbulence models. *Phys. Fluids* **20** (5). 53, 54

Senoner, J.M., Sanjosé, M., Lederlin, T., Jaegle, F., García, M., Riber, E., Cuenot, B., Gicquel, L., Pitsch, H. & Poinsot., T. 2009 Evaluation of numerical strategies for two-phase reacting flows. *C. R. Acad. Sci.Mécanique* **337** (6-7), 528–538. 201

Senoner, J. M. 2010 Simulation aux grandes échelles de l'écoulement diphasique dans un bruûleur aéronautique par une approche Euler-Lagrange. Phd thesis, INP Toulouse. 15, 26, 34, 159, 162, 163, 169, 172, 175, 200, 204

Simonin, O. 1991 Prediction of the dispersed phase turbulence in particle-laden jets. In *Proc. 1st Int. Symp. Gas-Solid Flows*, pp. 197–206. ASME. 8, 11, 46, 60

Simonin, O. 1996 Combustion and turbulence in two phase flows. Lecture Series 1996-02. Von Karman Institute fo Fluid Dynamics. 33, 34

Simonin, O. 2002 Gaz particules. Cours d'options. Ecole Nationale Superieure d'Electrotechnique, d'Electronique, d'Informatique, d'Hydraulique et des Télécommunications. 13

Simonin, O., Février, P. & Laviéville, J. 2001 On the spatial distribution of heavy particle velocities in turbulent flow: From continuous field to particulate chaos. In *2nd Int. Symp. On Turbulence and Shear Flow Phenomena*. Stockholm. 13, 14, 46, 47, 203

Simonin, O., Fevrier, P. & Lavieville, J. 2002 On the spatial distribution of heavy particle velocities in turbulent flow: from continuous field to particulate chaos. *J. Turb.* **3**. 32, 33, 45

Sirignano, W. A. 1983 Fuel droplet vaporisation and spray combustion theory. *Prog. Energy Comb. Sci.* **9**, 291–322. 10, 131

Sirignano, W. A. 1999 *Fluid dynamics and transport of droplets and sprays*. Cambridge University Press. 8, 131, 132, 133

Smagorinsky, J. 1963 General circulation experiments with the primitive equations: 1. the basic experiment. *Mon. Weather Rev.* **91**, 99–164. 3, 39

Snyder, W. H. & Lumley, J. L. 1971 Some measurements of particle velocity autocorrelation functions in a turbulent flow. *J. Fluid Mech.* **48** (1), 41–71. 8

Sommerfeld, M. & Qiu, H. H. 1993 Characterisation of particle-laden, confined swirling flows by phase-doppler anemometry ad numerical calculation. *Int. J. Multiphase Flow* **19** (6), 1093–1127. 128

Sommerfeld, M. & Qiu, H. H. 1998 Experimental studies of spray evaporation in turbulent flow. *Int. J. Heat Fluid Flow* **19**, 10–22. 131

Spalding, D. B. 1953 The combustion of liquid fuels. In *4th Symp. (Int.) on Combustion*, pp. 847–864. The Combustion Institute, Pittsburgh. 132, 134, 135, 204

Squire, H. 1953 Investigation of the instability of a moving film. *British Journal of applied physics* **4**, 167–169. 5

Squires, K. D. & Eaton, J. 1991*a* Measurements of particle dispersion obtained from direct numerical simulations of isotropic turbulence. *J. Fluid Mech.* **226**, 1–35. 8, 69

Squires, K. D. & Eaton, J. K. 1990 Particle response and turbulence modification in isotropic turbulence. *Phys. FluidsA* **2** (7), 1191–1203. 8, 26

Squires, K. D. & Eaton, J. K. 1991*b* Lagrangian and Eulerian statistics obtained from direct numerical simulations of homogeneous turbulence. *Phys. FluidsA* **3** (1), 130–143. 30

Stapper, B. & Samuelsen, G. 1990 An experimental study of the breakup of a two dimensional liquid sheet in the presence of co-flow air shear. *AIAA Paper 89-0461* . 5

Stokes, G. G. 1851 On the effect of the inertial friction of fluids on the motions of pendulums. *Trans. Cambridge Phil. Soc.* **9**, 8–23. 24

Stull, D. R. & Prophet, H. 1971 Janaf thermochemical tables, 2nd edition. *Tech. Rep.* NSRDS-NBS 37. US National Bureau of Standards. 20

Sundaram, S. & Collins, L. R. 1999 A numerical study of the modulation of isotropic turbulence by suspended particles. *J. Fluid Mech.* **379**, 105–143. 8

Sussman, M., Almgren, A.S., Bell, J.B., Colella, P., Howell, L.H. & Welcome, M.L. 1999 An adaptive level set approach for incompressible two-phase flows. *J. Comput. Phys.* **148**, 81–124. 5

Taylor, G.I. 1948 The mechanics of swirl atomizer. In *7th Int. Cong. Appl. Mech.*, , vol. 2, pp. 280–285. 4

Taylor, G. 1959 The dynamics of thin sheets of fluid. I. Water bells. *Proc. R. Soc. Lond.* **253**, 280–296. 5

Tchen, C.-M. 1947 Mean value and correlation problems connected with the motion of small particles supended in a turbulent fluid. Phd thesis, Technical University of Delft, Netherlands. 8, 23, 26, 27

Thomas, P. J. 1992 On the influence of the Basset history force on the motion of the particle through a fluid. *Phys. Fluids* **4(9)**, 2090–2093. 25

Trontin, P. 2009 Développement d'une approche de type les pour la simulation d'écoulements diphasiques avec interface. Application à l'atomisation primaire. Phd thesis, Institut SupŽrieur de l'Aéronautique et de l'Espace (ISAE). 5

Vachat, R. Du 1977 Realizability inequalities in turbulent flows. *Phys. Fluids* **20**, 551–556. 53

Vance, M. W., Squires, K. D. & Simonin, O. 2006 Properties of the particle velocity field in gas-solid turbulent channel flow. *Phys. Fluids* **18** (063302). 8, 31

Vermorel, O. 2003 Étude numérique et modélisation de la turbulence dans un écoulement de nappe chargée en particules. Phd thesis, INP Toulouse. 8, 13, 14, 55, 56, 57, 221

Vermorel, O., Bédat, B., Simonin, O. & Poinsot, T. 2003 Numerical study and modelling of turbulence modulation in a particle laden slab flow. *J. Turb.* **4, 025**. 8

Veynante, D. & Knikker, R. 2006 Comparison between LES results and experimental data in reacting flows. *J. Turb.* **7** (35), 1–20. 174

Vié, A. 2010 Simulation aux grandes échelles d'écoulements diphasiques turbulents à phase liquide dispersée. Phd thesis, INP Toulouse. 11, 13, 45, 127, 159, 201, 204, 205

Vié, A., Martinez, L., Jay, S., Benkenida, A. & Cuenot, B. 2009 Validation of the Eulerian mesoscopic approach in particle-charged homogeneous isotropic decaying turbulence in the scope of large eddy simulation of fuel spray. In *ICLASS Proceedings*. Colorado, USA. 47

Wallin, S. & Johansson, A. V. 2000 An explicit algebraic Reynolds stress model for incompresible and compresible turbulent flows. *J. Fluid Mech.* **403**, 89–132. 49, 51

Wang, W. & Pletcher, R. H. 1996 On the large eddy simulation of a turbulent channel flow with significant heat transfer. *Phys. Fluids* **8** (12), 3354–3366. 8

Wells, M. & Stock, D. 1983 The effects of crossing trajectories on the dispersion of particles in a turbuelent flow. *J. Fluid Mech.* **136**, 31–62. 8

Whitaker, S. 1999 *The method of volume averaging*. Kluwer Academic Publishers. 11

Williams, F. A. 1971 Theory of combustion in laminar flows. *Ann. Rev. Fluid Mech.* **3**, 171–188. 9

Williams, F. A. 1985 *Combustion Theory*. Menlo Park, CA: Benjamin Cummings. 8, 131

Wolf, P., Staffelbach, G., Balakrishnan, R., Roux, A. & Poinsot, T. 2010 Azimutal instabilitites in annular combustion chambers. In *Proc. of the Summer Program*, pp. 259–269. Center for Turbulence Research, NASA Ames/Stanford Univ. 1

Wong, S. C. & Lin, A. R. 1992 Internal temperature distributions of droplets vaporizing in high-temperature convective flows. *J. Fluid Mech.* **237**, 671–687. 8

Wright, D. L. 2007 Numerical advection of moments of the particle size distribution in Eulerian models. *J. Aerosol Sci.* **38**, 352–369. 28

Yamamoto, Y., Potthoff, M., Tanaka, T., Kajishima, T. & Tsuji, Y. 2001 Large-eddy simulation of turbulent gas-particle flow in a vertical channel: effect of considering inter-particle collisions. *J. Fluid Mech.* **442**, 303–334. 8

Yang, J.-C. & Chang, K.-C. 2001 Inflow conditions in stochastic Eulerian-Lagrangian calculations of two-phase turbulent flow. *AIAA Journal* **39** (11), 2100–2110. 8, 132, 154

Yang, J-R. & Wong, S-C. 2001 On the discrepancies between theoretical and experimental results for microgravity droplet evaporation. *Int. J. Heat and Mass Transfer* **44**, 4433–4443. 131, 134, 142, 143, 148, 149, 150, 151, 204

Yang, J-R. & Wong, S-C. 2002 An experimental and theoretical study of the effects of heat conduction through the support fiber on the evaporation of a droplet in a weakly convective flow. *Int. J. Heat and Mass Transfer* **45**, 4589–4598. 8, 131, 132, 133

Yao, G. F., Abdel-Khalil, S. I. & Ghiaasiaan, S. M. 2003 An investigation of simple evaporation models used in spray simulations. In *ASME J. Heat Trans.*, , vol. 82, pp. 125–179. 133

Yuen, M. C. & Chen, L. W. 1976 On drag evaporating liquid droplets. *Combust. Sci. Tech.* **14**, 147–154. 145

Zhang, D. & Prosperetti, A. 1994 Ensemble phase-averaged equations for bubbly flows. *Phys. Fluids* **6** (9), 2956–2970. 11

Zhang, H., Raghavan, V. & Gogos, G. 2008 Subcritical and supercritical droplet evaporation within a zero-gravity environment: Low Weber number relative motion. *Int. Commun. Heat and Mass Transfer* **35**, 385–394. 132

Zuzio, D. 2010 Direct numerical simulation of two phase flows with adaptive mesh refinement. Phd thesis, Institut Supérieur de l'Aéronautique et de l'Espace (ISAE). 5

Zuzio, D., Villedieu, P., Estivalezes, J. & Blanchard, G. 2011 Numerical simulation of primary and secondary atomization. In *3rd colloque INCA*. 205

Appendix A

Eulerian-Lagrangian simulations with the code NTMIX-2Φ

A.1 The code NTMIX-2Φ

NTMIX-2Φ is a parallel code. It solves the compressible Navier-Stokes equations in three-dimensions and non-dimensional form. The temporal advancement uses third-order Runge-Kutta scheme and it uses a sixth-order compact difference scheme on cartesians grids (Lele (1992)). Direct Particle Simulation by means of Lagrangian tracking is performed through the Newton's equations. The dispersed phase simulations use the same time advancement scheme that the gaseous phase. Two-way coupling between the gas and the dispersed phase is taken into account. The interpolation of the gaseous properties at the particle's position is done by means of a third-order Lagrangian polynomial algorithm.

In the configuration of Chapter 5 boundary conditions are periodic in all directions. However, NTMIX-2Φ can use non-reflecting boundary conditions (Poinsot *et al.* (1992)) if needed. The calculations performed by Masi (2010) in the particle-laden temporal turbulent planar jet used a domain decomposition method (Vermorel (2003)) with MPI message passing protocol. More details about the code and its characteristics can be found in Masi (2010).

A.2 Projection algorithm

Eulerian fields are obtained from Lagrangian quantities by means of a projection algorithm, that projects the Lagrangian quantities into an Eulerian grid. Kaufmann & Moreau (2008) performed comparisons of different projection algorithms. The retained projector is a Gaussian filter (Eq. (A.1), Kaufmann & Moreau (2008), Moreau & Desjardins (2008)):

$$w(\mathbf{x}_p^{(k)} - \mathbf{x}) = \frac{(2\Delta_p)^3}{\mathrm{erf}(6^{3/2})} \left(\frac{6}{\pi\Delta_p^2}\right) \exp\left(-\frac{6|\mathbf{x}_p^{(k)} - \mathbf{x}|^2}{\Delta_p^2}\right), \tag{A.1}$$

where $w(\mathbf{x}_p^{(k)}$ is the weight function, Δ_p is the filter width or the size of the projection, which is taken equal to the grid spacing. $\mathbf{x}_p^{(k)}$ is the particle position and $\mathbf{x}$ is the coordinates of each grid node in the mesh.

The projected Eulerian particle density and velocity read:

$$\breve{n}_p(\mathbf{x},t) = \frac{1}{(2\Delta_p)^3}\sum_k w(\mathbf{x}_p^{(k)}(t)-\mathbf{x}), \tag{A.2}$$

$$\breve{n}_p(\mathbf{x},t)\breve{\mathbf{u}}_p(\mathbf{x},t) = \frac{1}{(2\Delta_p)^3}\sum_k w(\mathbf{x}_p^{(k)}(t)-\mathbf{x})\breve{\mathbf{u}}_p^{(k)}(t). \tag{A.3}$$

Problems may appear in regions of the flow where the number of particles is not sufficient. This may lead to discontinuities in the Eulerian projected fields. This problem can be overcome with an interpolation procedure taking the values in the cells around the problematic point. In the simulations performed by Masi (2010), low-inertia cases presented a higher level of preferential concentration, leading to more empty zones in the flow and thus, the simulations of low Stokes numbers (between 0.1 and 0.5) were the most affected by this problem.

Appendix B

Gaseous phase validation for particle-laden slab. Additional graphs.

B.1 High turbulence case (HR_St1_#).

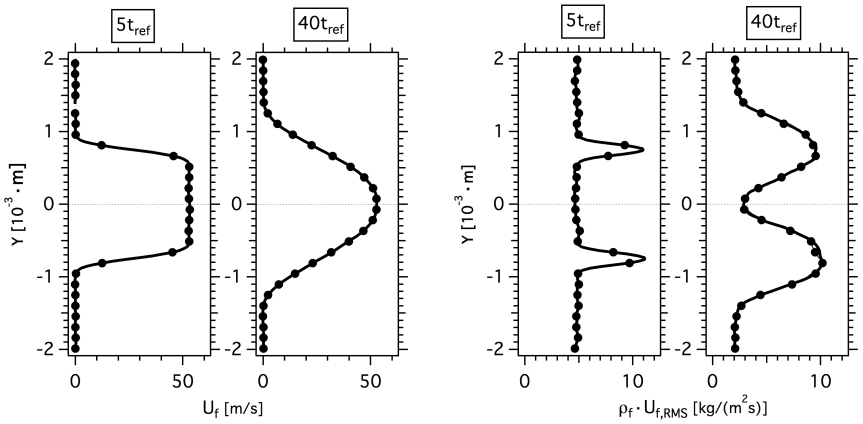

(a) (b)

Figure B.1: *Comparison of Eulerian and Lagrangian carrier phase velocities in X-direction. HR_St1_# case. (a) Mean velocity (U_f) and (b) RMS velocity times the fluid density ($\rho_f U_{f,RMS}$) at* 5 *and* $40t_{ref}$*. Simulations performed with AVBP (—) and NTMIX-2Φ (–●–).*

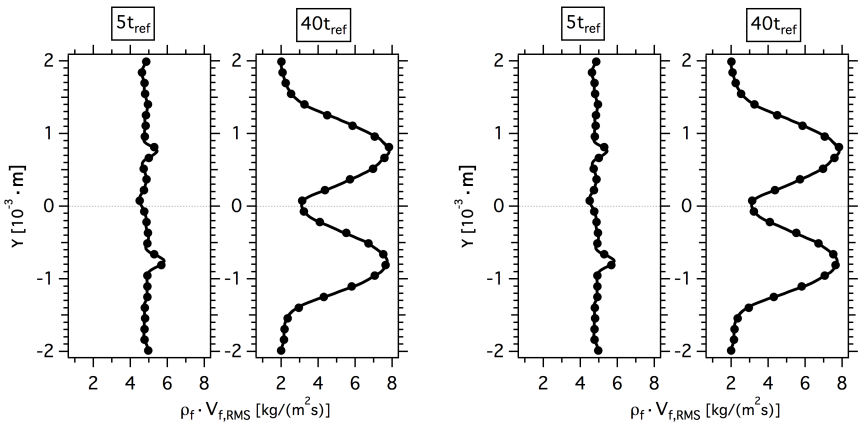

(a) (b)

Figure B.2: *Comparison of Eulerian and Lagrangian carrier phase velocities in Y-direction. HR_St1_# case. (a) Mean velocity (V_f) and (b) RMS velocity times the fluid density ($\rho_f V_{f,RMS}$) at 5 and 40t_{ref}. Simulations performed with AVBP (—) and NTMIX-2Φ (–●–).*

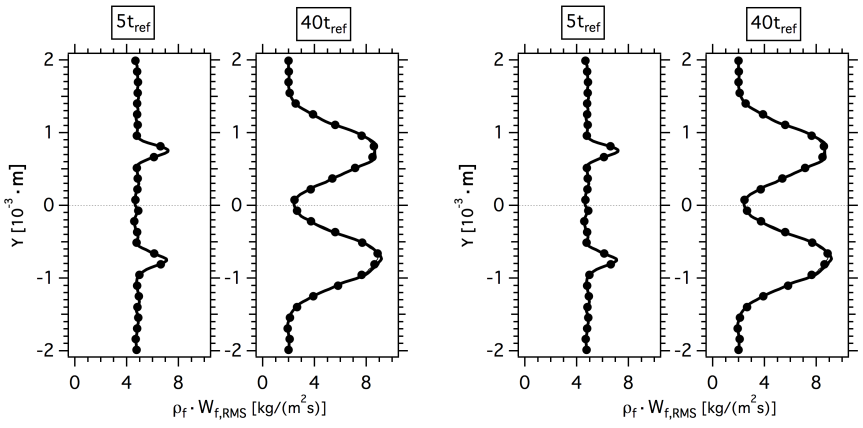

(a) (b)

Figure B.3: *Comparison of Eulerian and Lagrangian carrier phase velocities in Z-direction. HR_St1_# case. (a) Mean velocity (W_f) and (b) RMS velocity times the fluid density ($\rho_f W_{f,RMS}$) at 5 and 40t_{ref}. Simulations performed with AVBP (—) and NTMIX-2Φ (–●–).*

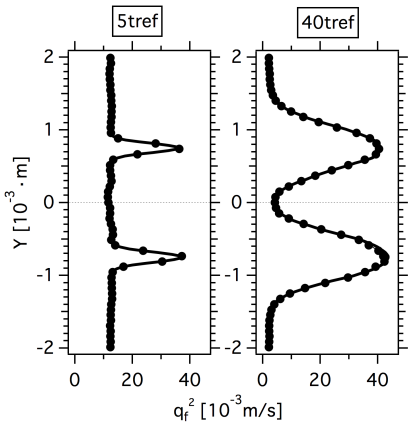

Figure B.4: *Comparison of Eulerian and Lagrangian carrier phase turbulent kinetic energy (q_f^2) at 5 and 40t_{ref}. HR_St1_# case. Simulations performed with AVBP (—) and NTMIX-2Φ (–●–).*

Appendix C

Particle-laden slab. Case LR_St1_#. Additional data.

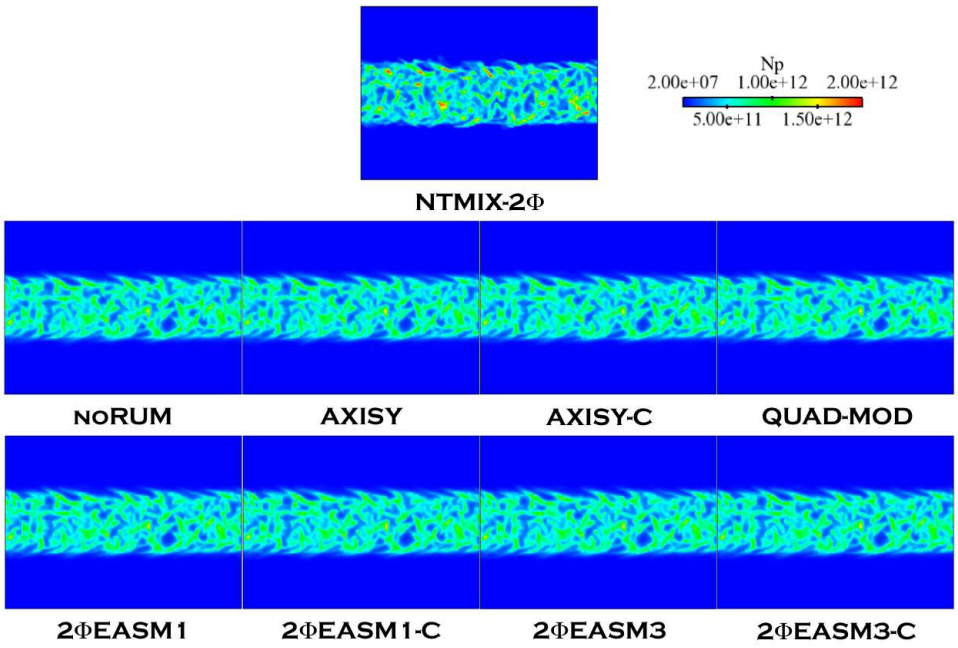

Figure C.1: *Comparison of Lagrangian (NTMIX-2Φ) and Eulerian particle number density (N_p) at $5t_{ref}$. LR_St1_# case.*

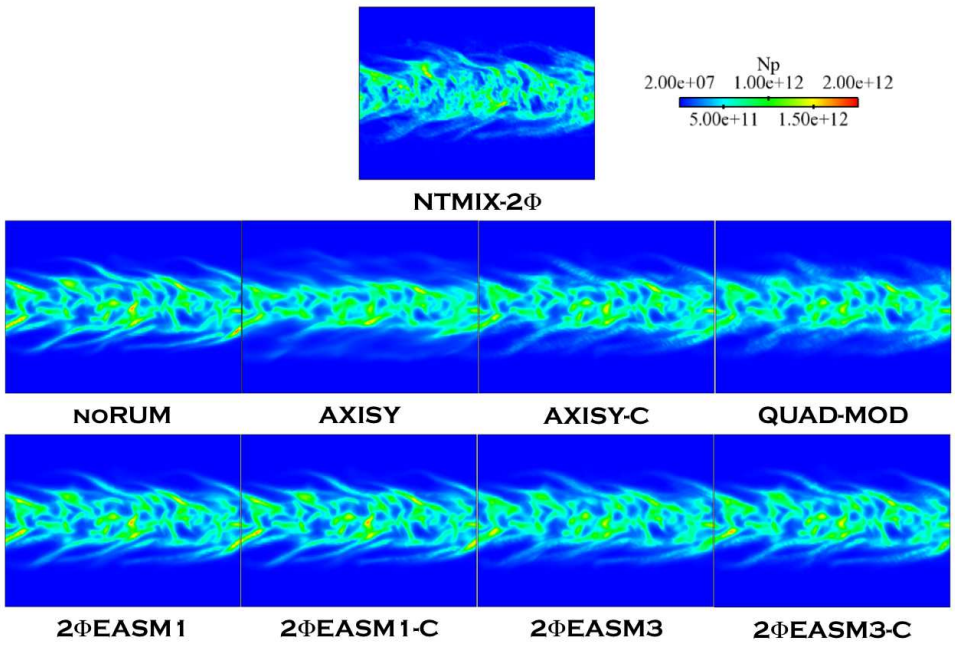

Figure C.2: *Comparison of Lagrangian (NTMIX-2Φ) and Eulerian particle number density (N_p) at $40t_{ref}$. LR_St1_# case.*

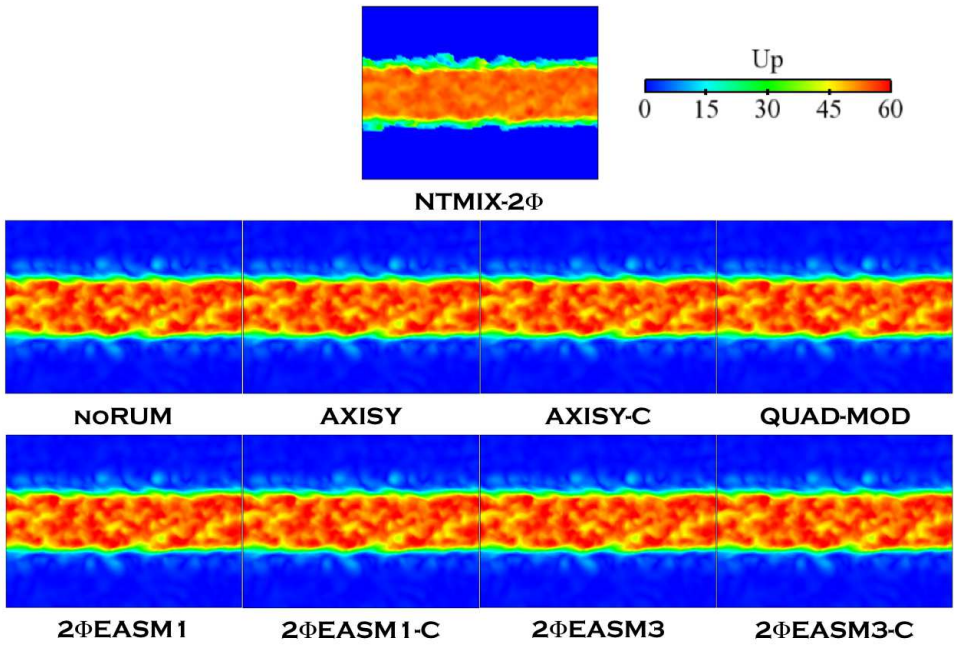

Figure C.3: *Comparison of Lagrangian (NTMIX-2Φ) and Eulerian particle velocity magnitude (U_p) at $5t_{ref}$. LR_St1_# case.*

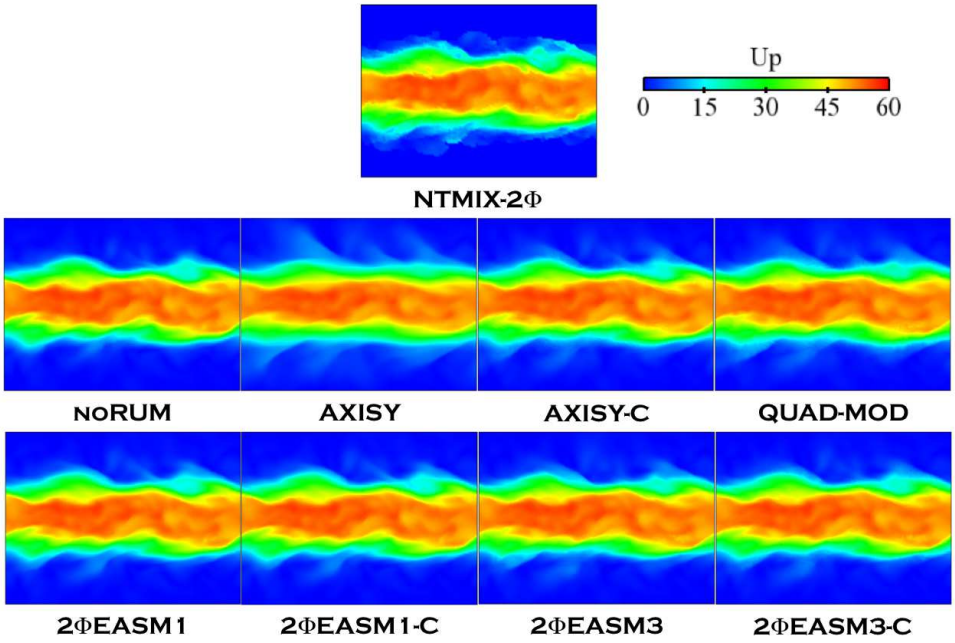

Figure C.4: *Comparison of Lagrangian (NTMIX-2Φ) and Eulerian particle velocity magnitude (U_p) at $40t_{ref}$. LR_St1_# case.*

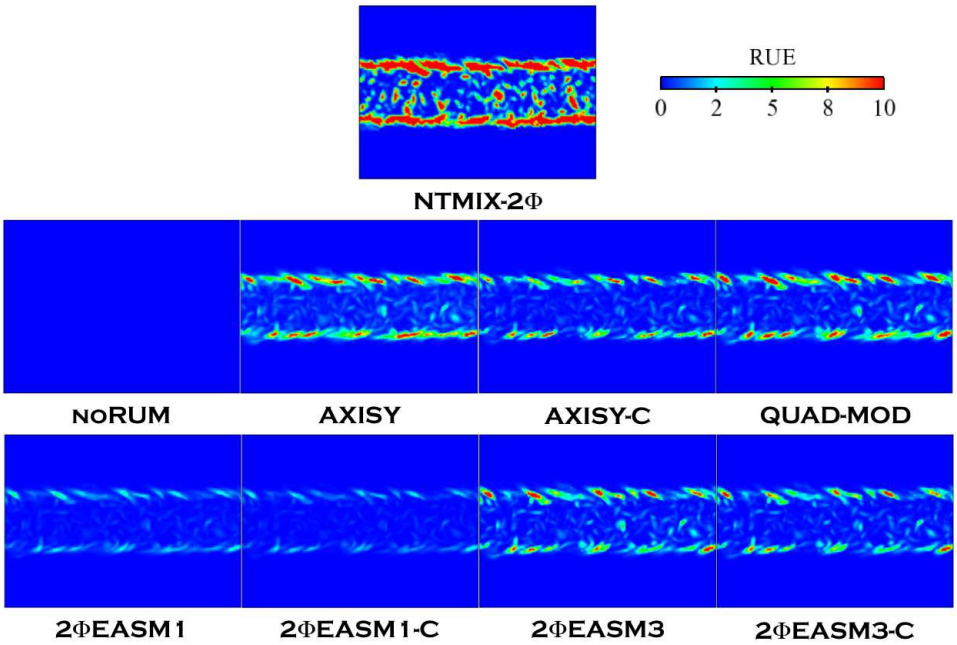

Figure C.5: *Comparison of Lagrangian (NTMIX-2Φ) and Eulerian Random Uncorrelated Energy at $5t_{ref}$. LR_St1_# case.*

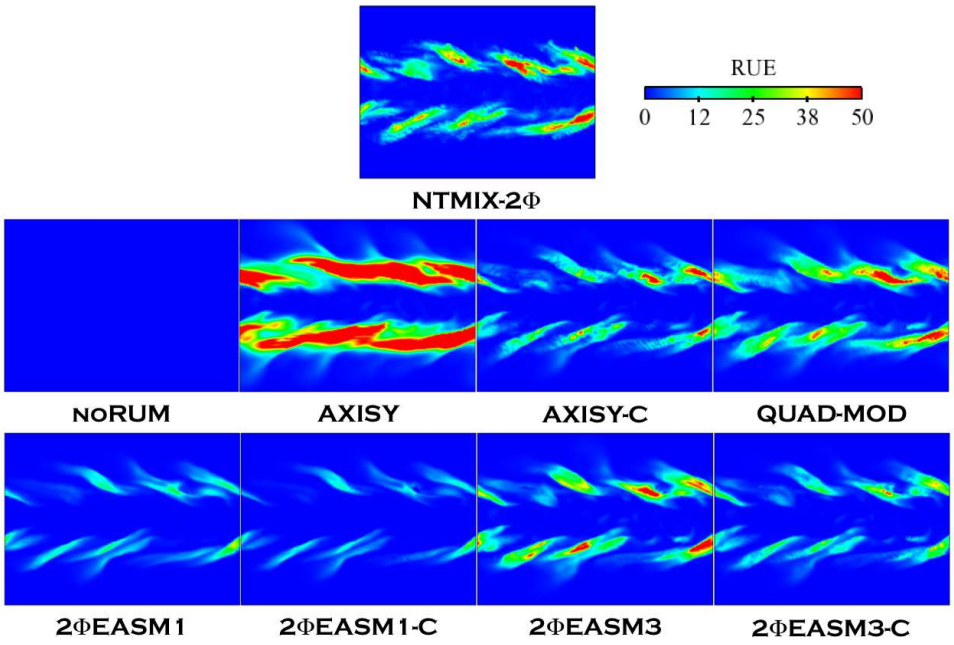

Figure C.6: *Comparison of Lagrangian (NTMIX-2Φ) and Eulerian Random Uncorrelated Energy at $40t_{ref}$. LR_St1_# case.*

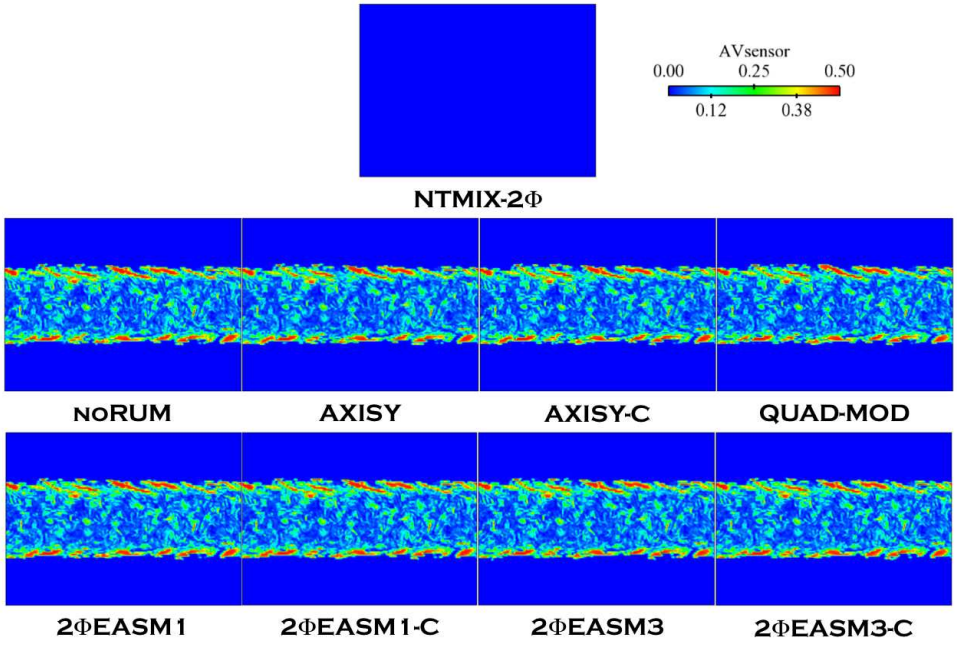

Figure C.7: *Comparison of AV sensor levels at $5t_{ref}$. LR_St1_# case.*

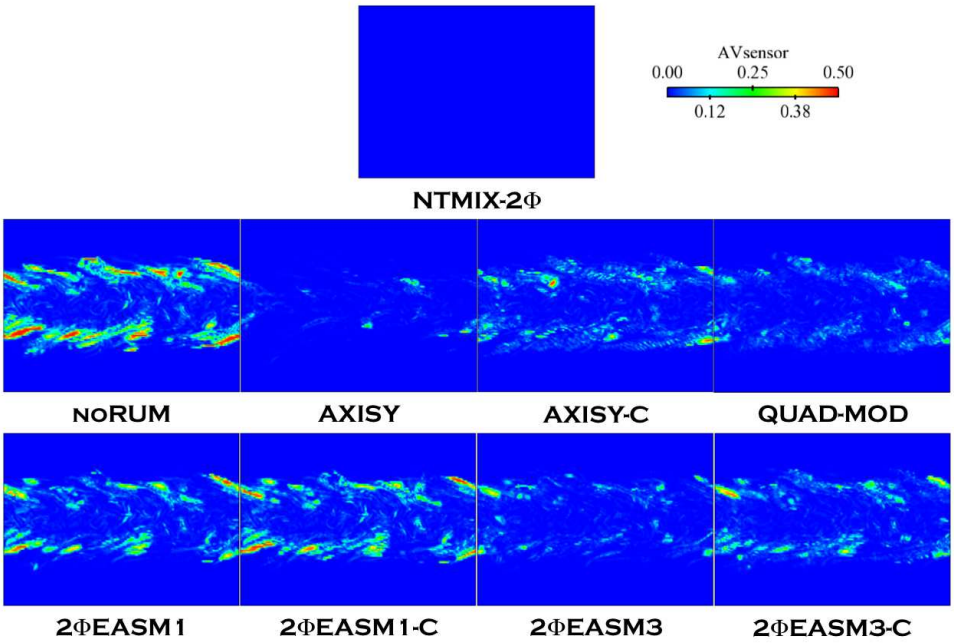

Figure C.8: *Comparison of AV sensor levels at* $40t_{ref}$*. LR_St1_# case.*

Appendix D

Particle-laden slab. Case LR_St3_#. Additional data.

D.1 Dispersed phase statistics at $40t_{ref}$

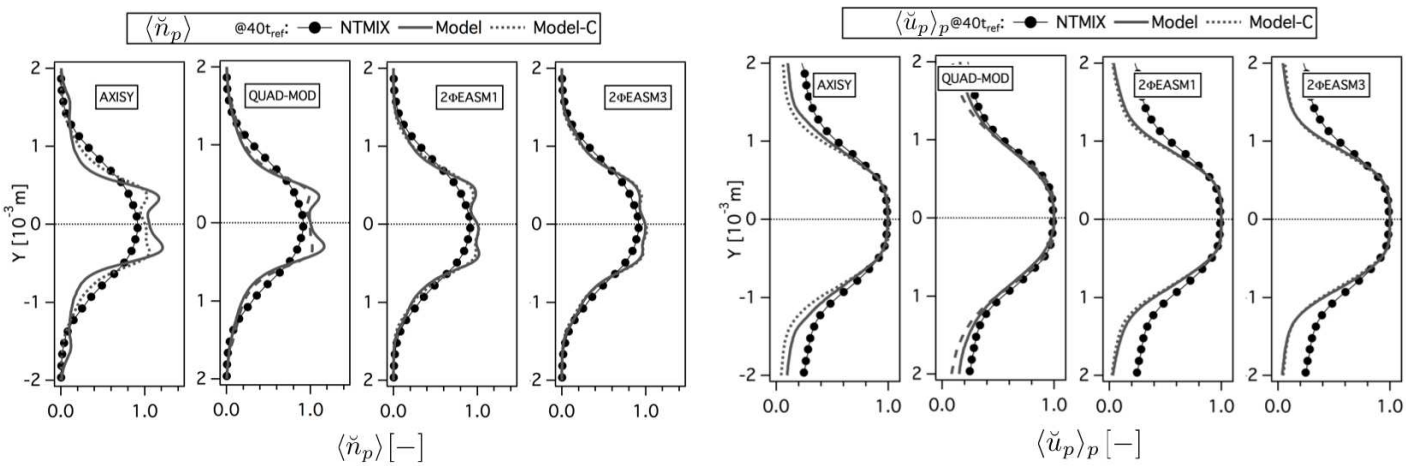

(a) (b)

Figure D.1: *Comparison of Eulerian and Lagrangian (a) mean particle number density (< $\breve{n}_p$ >, normalized by the initial particle number density at the center of the slab) and (b) mean particle velocity in X-direction (< $\breve{u}_p$ >$_p$, normalized by the initial particle velocity in X-direction at the center of the slab) at $40t_{ref}$. LR_St3_# case.*

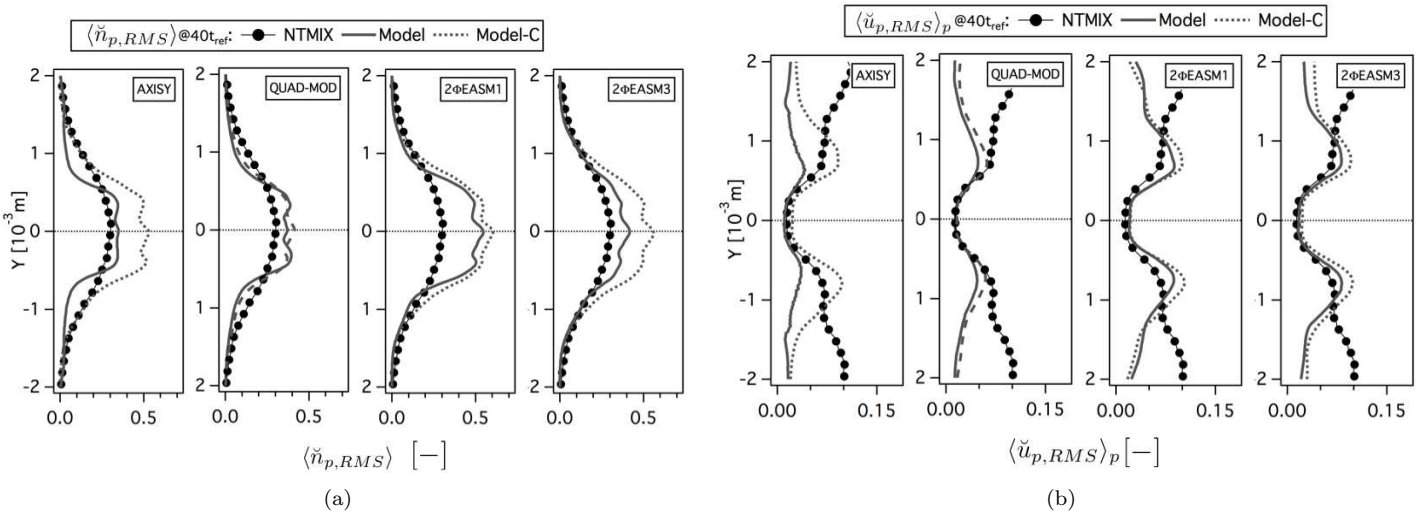

Figure D.2: *Comparison of Eulerian and Lagrangian (a) RMS particle number density (*$< \breve{n}_{p,RMS} >$*, normalized by the initial particle number density at the center of the slab) and (b) RMS particle velocity in X-direction (*$< \breve{u}_{p,RMS} >_p$*, normalized by the initial particle number density at the center of the slab)at* $40t_{ref}$*. LR_St3_# case.*

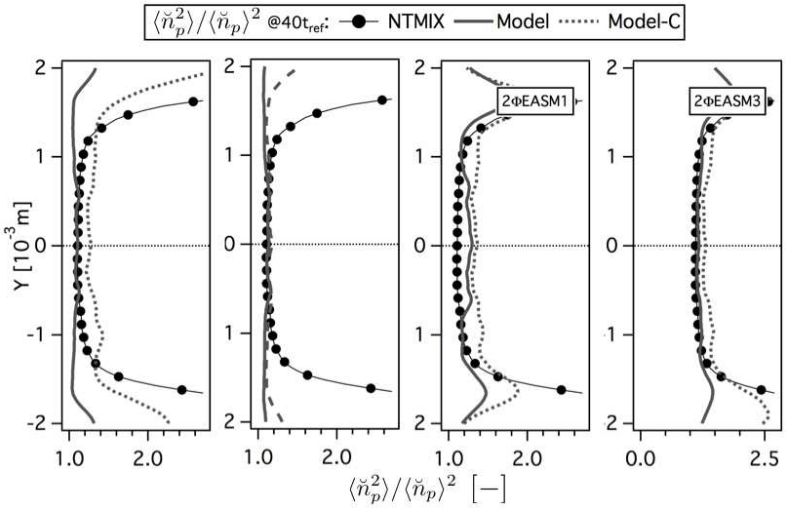

Figure D.3: *Comparison of Eulerian and Lagrangian RMS particle segregation (*$< \breve{n}_p^2 > / < \breve{n}_p >^2$*) at* $40t_{ref}$*. LR_St3_# case.*

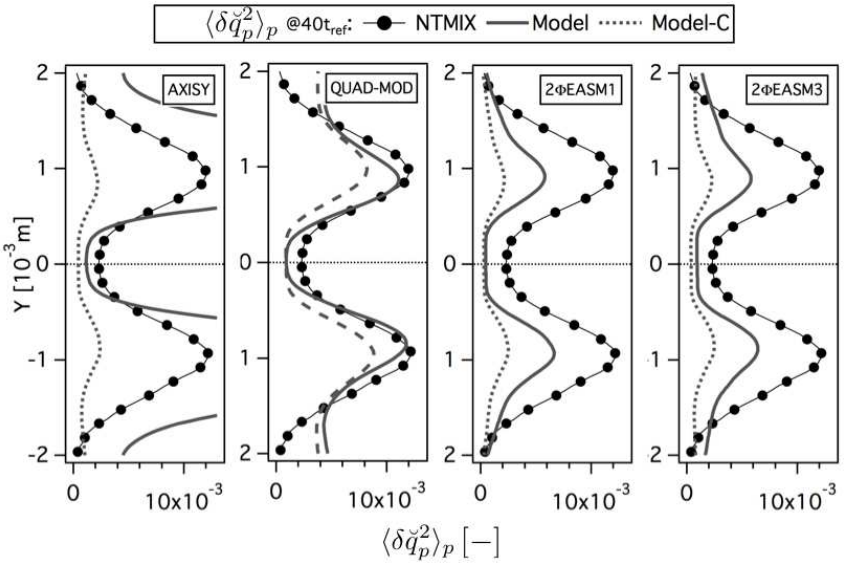

(a)

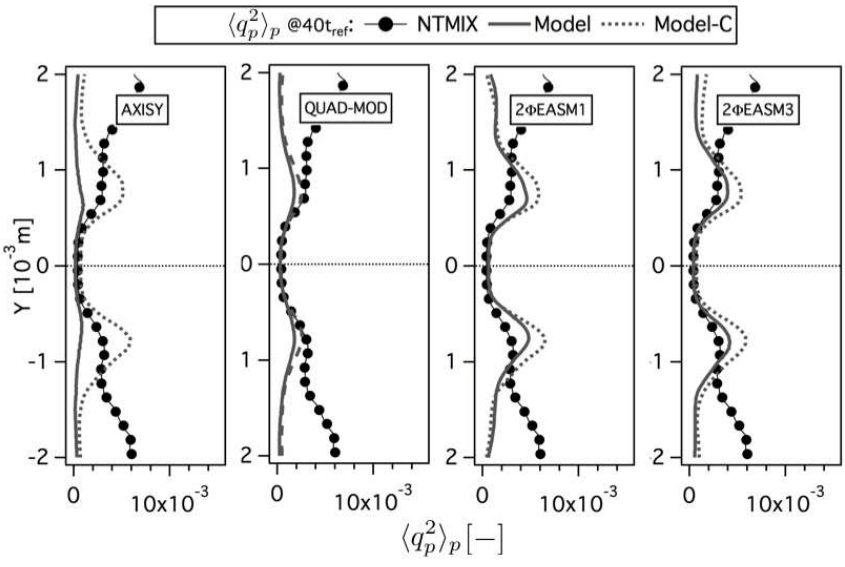

(b)

Figure D.4: *Comparison of Eulerian and Lagrangian (a) mean Random Uncorrelated Energy (*$< \delta\breve{q}_p >_p$*) and (b) mean mesoscopic (*$\langle /meso q_p^2 \rangle_p$*) and mesoscopic (*$\langle \breve{q}_p^2 \rangle_p$*) particle energies at* $40t_{ref}$*. Normalized by the square of the initial particle velocity in X-direction at the center of the slab. LR_St3_# case.*

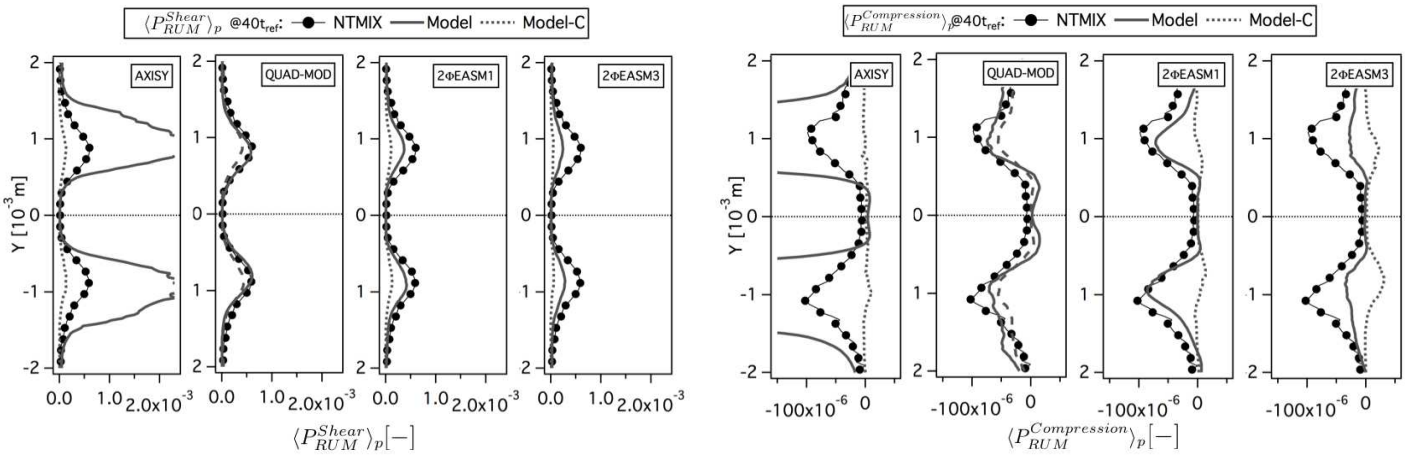

(a) (b)

Figure D.5: *Comparison of Eulerian and Lagrangian (a) mean production of RUM energy by shear components ($< P_{RUM}^{Shear} >_p$) and (b) mean productions of RUM energy by compression ($< P_{RUM}^{Compression} >_p$) at $40t_{ref}$. Normalized by the square of the initial particle velocity in X-direction at the center of the slab and the reference time (t_{ref}). LR_St3_# case.*

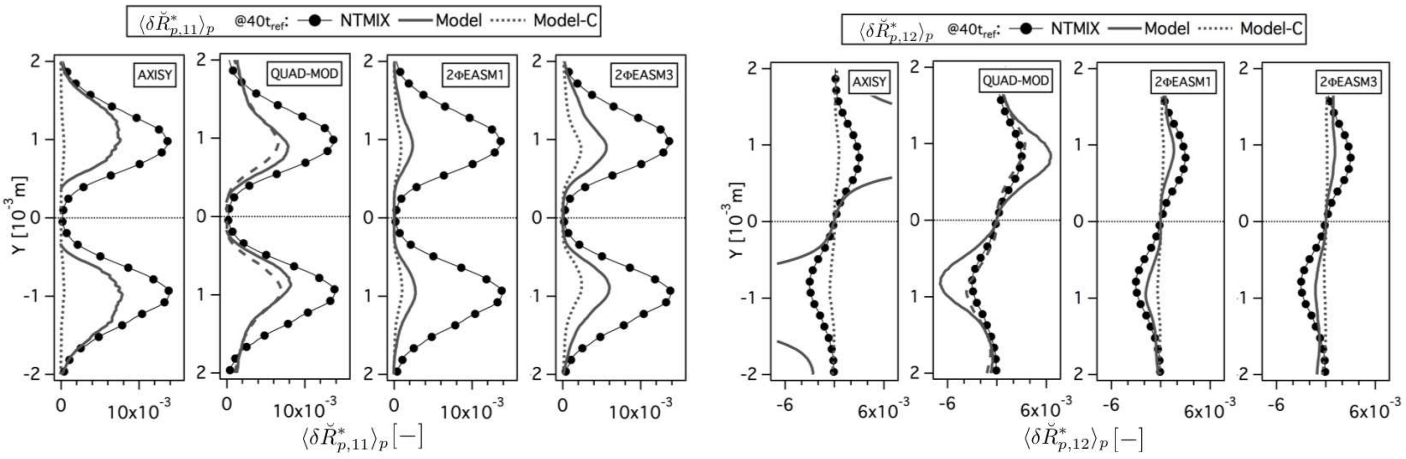

(a) (b)

Figure D.6: *Comparison of Eulerian and Lagrangian (a) mean deviatoric RUM stress tensor XX component ($< \delta \breve{R}_{p,11}^{*} >_p$) and (b) mean deviatoric RUM stress tensor XY component ($< \delta \breve{R}_{p,12}^{*} >_p$) at $40t_{ref}$. Normalized by the square of the initial particle velocity in X-direction at the center of the slab. LR_St3_# case.*

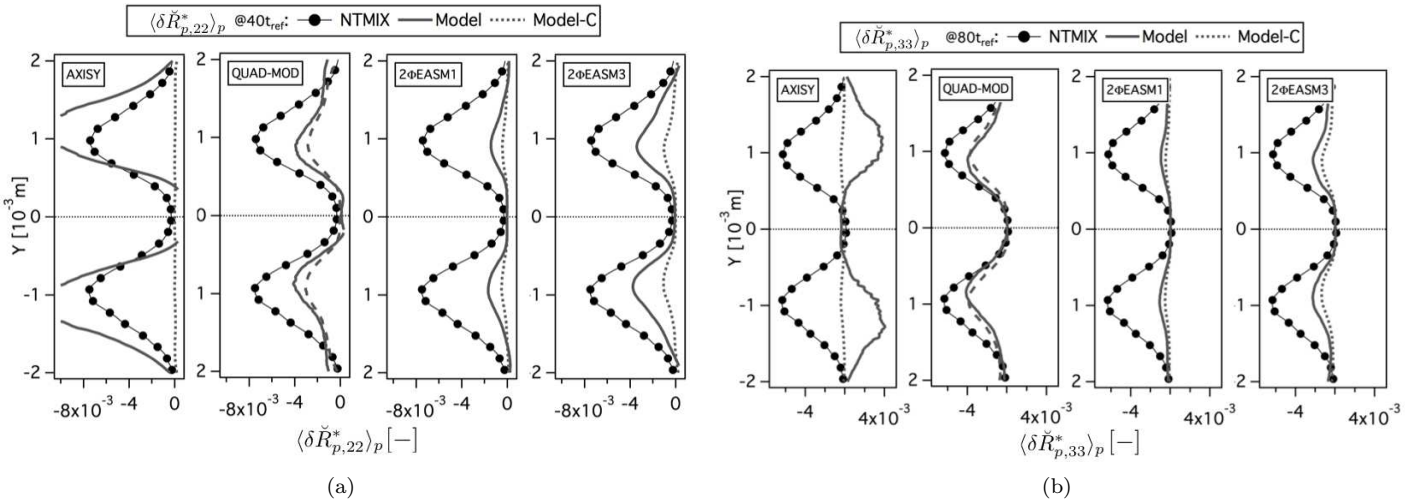

(a) (b)

Figure D.7: *Comparison of Eulerian and Lagrangian (a) mean deviatoric RUM stress tensor YY component ($< \delta \breve{R}^*_{p,22} >_p$) and (b) mean deviatoric RUM stress tensor ZZ component ($< \delta \breve{R}^*_{p,33} >_p$) at $40t_{ref}$. Normalized by the square of the initial particle velocity in X-direction at the center of the slab. LR_St3_# case.*

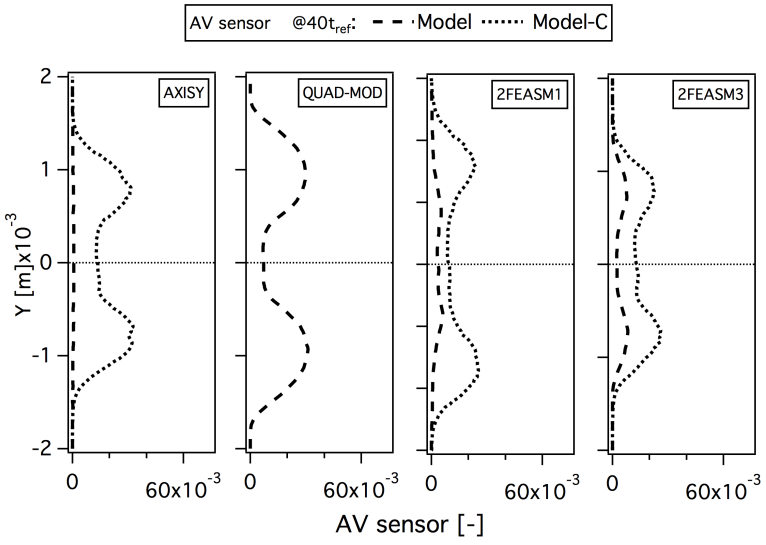

Figure D.8: *Mean Artificial Viscosity sensor activation at $40t_{ref}$. LR_St3_# case.*

D.2 Dispersed phase statistics at $80t_{ref}$

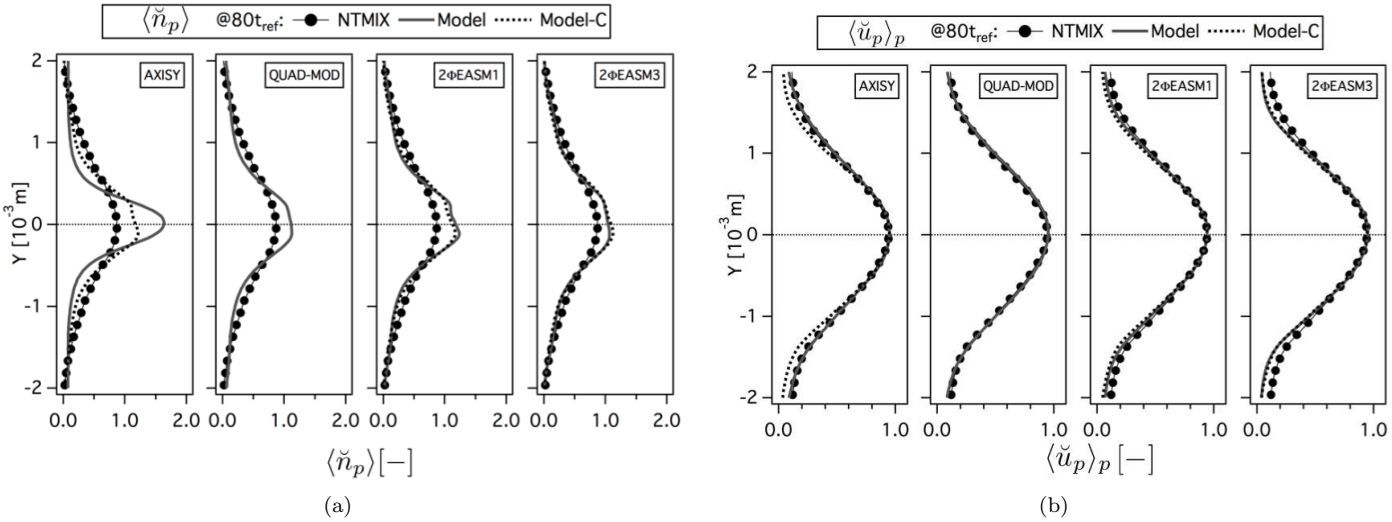

Figure D.9: *Comparison of Eulerian and Lagrangian (a) mean particle number density (< $\breve{n}_p$ >, normalized by the initial particle number density at the center of the slab) and (b) mean particle velocity in X-direction (< $\breve{u}_p$ >$_p$, normalized by the initial particle velocity in X-direction at the center of the slab) at $80t_{ref}$. LR_St3_# case.*

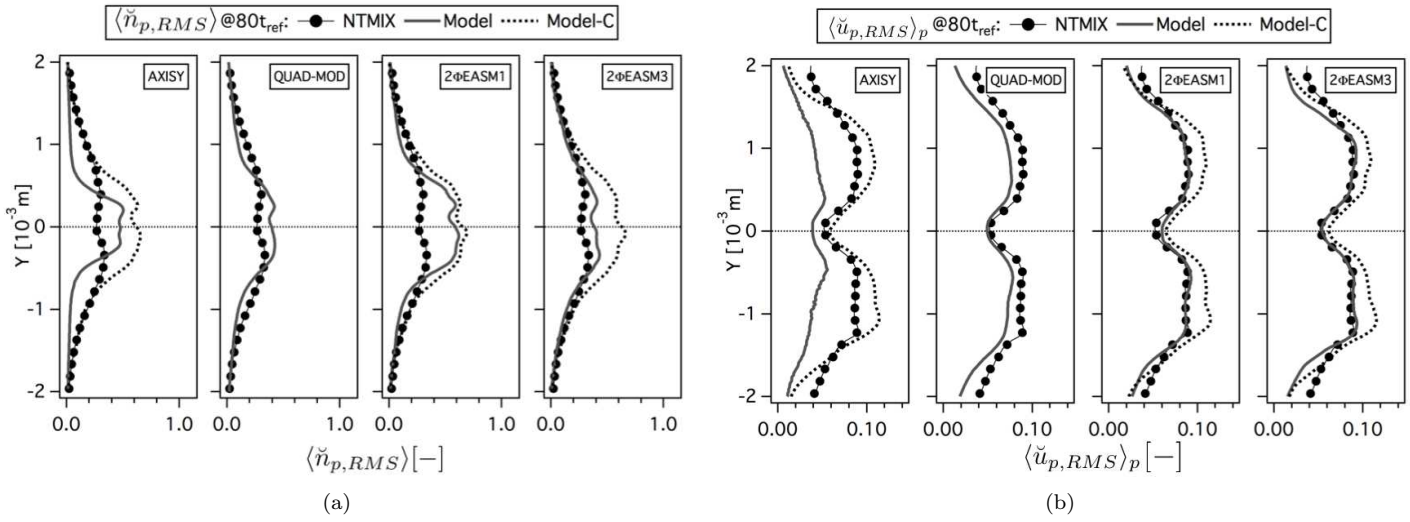

Figure D.10: *Comparison of Eulerian and Lagrangian (a) RMS particle number density (< $\breve{n}_{p,RMS}$ >, normalized by the initial particle number density at the center of the slab) and (b) RMS particle velocity in X-direction (< $\breve{u}_{p,RMS}$ >$_p$, normalized by the initial particle number density at the center of the slab)at $80t_{ref}$. LR_St3_# case.*

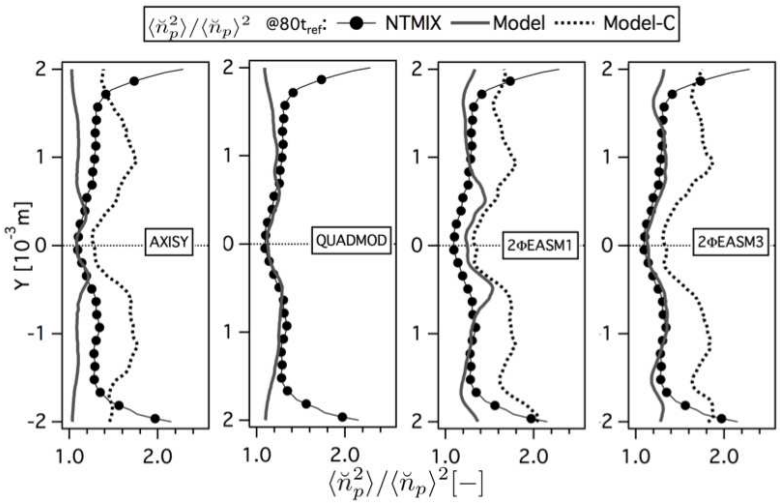

Figure D.11: *Comparison of Eulerian and Lagrangian RMS particle segregation ($< \breve{n}_p^2 > / < \breve{n}_p >^2$) at $80t_{ref}$. LR_St3_# case.*

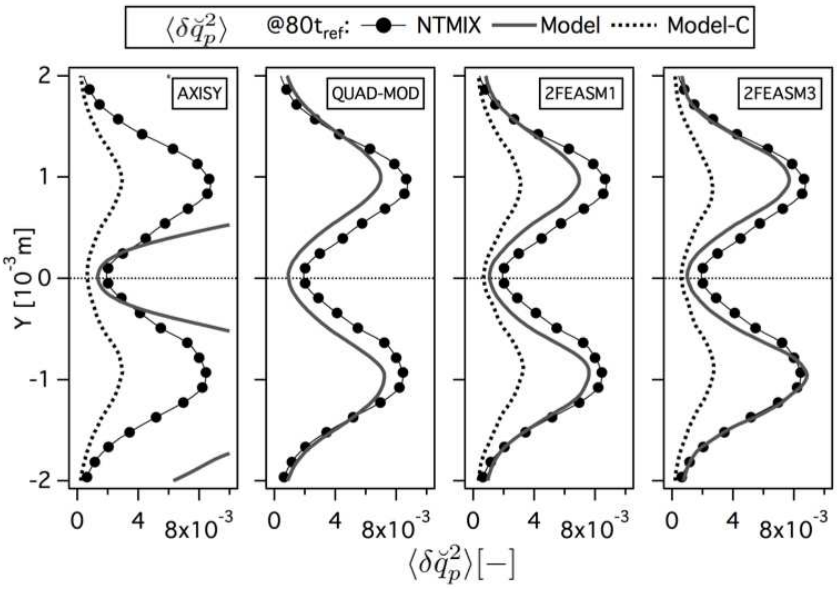

(a)

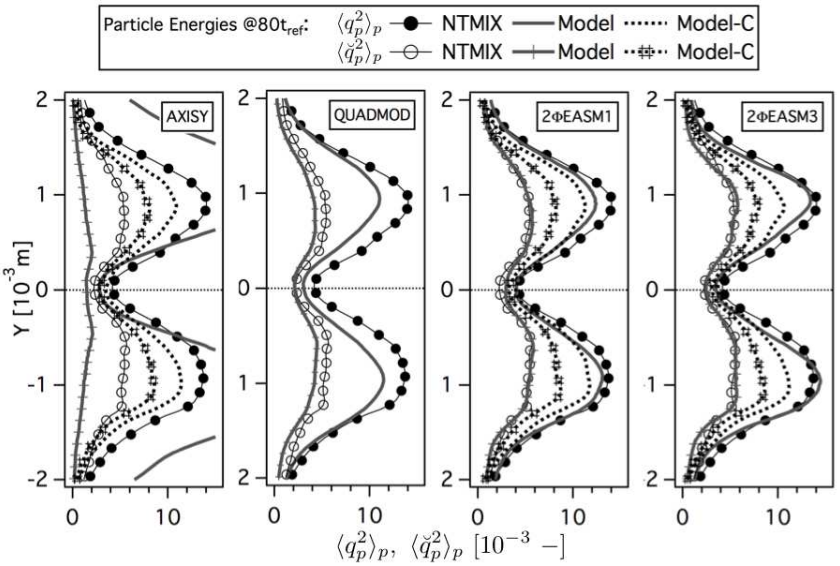

(b)

Figure D.12: *Comparison of Eulerian and Lagrangian (a) mean Random Uncorrelated Energy ($< \delta \breve{q}_p >_p$) and (b) mean total ($\langle q_p^2 \rangle_p$) and mesoscopic ($\langle \breve{q}_p^2 \rangle_p$) particle energies at $80t_{ref}$. Normalized by the square of the initial particle velocity in X-direction at the center of the slab. LR_St3_# case.*

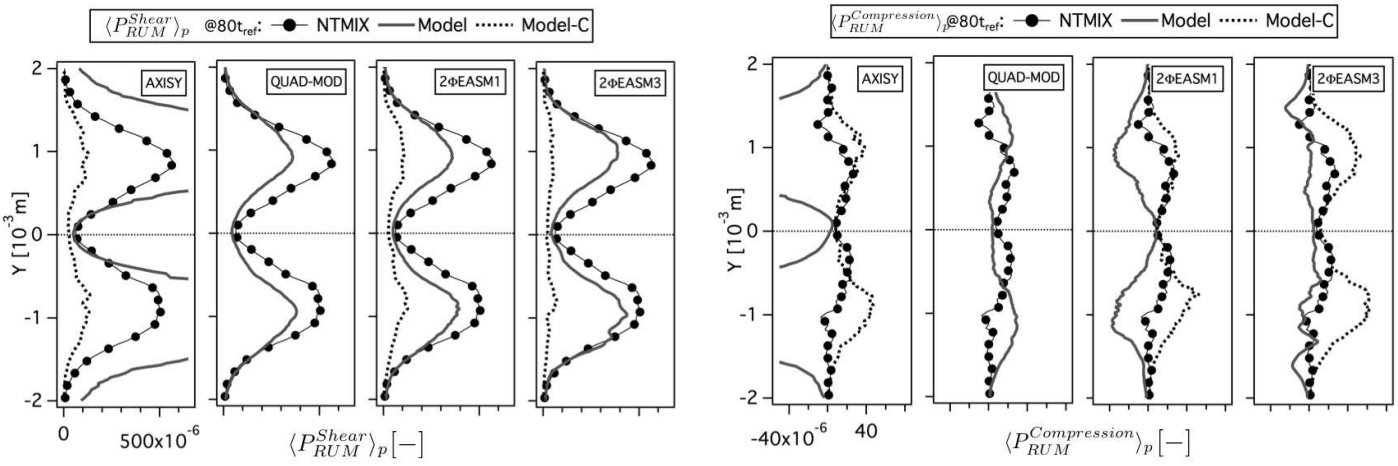

(a) (b)

Figure D.13: *Comparison of Eulerian and Lagrangian (a) mean production of RUM energy by shear components ($< P^{Shear}_{RUM} >_p$) and (b) mean productions of RUM energy by compression ($< P^{Compression}_{RUM} >_p$) at $80t_{ref}$. Normalized by the square of the initial particle velocity in X-direction at the center of the slab and the reference time (t_{ref}). LR_St3_# case.*

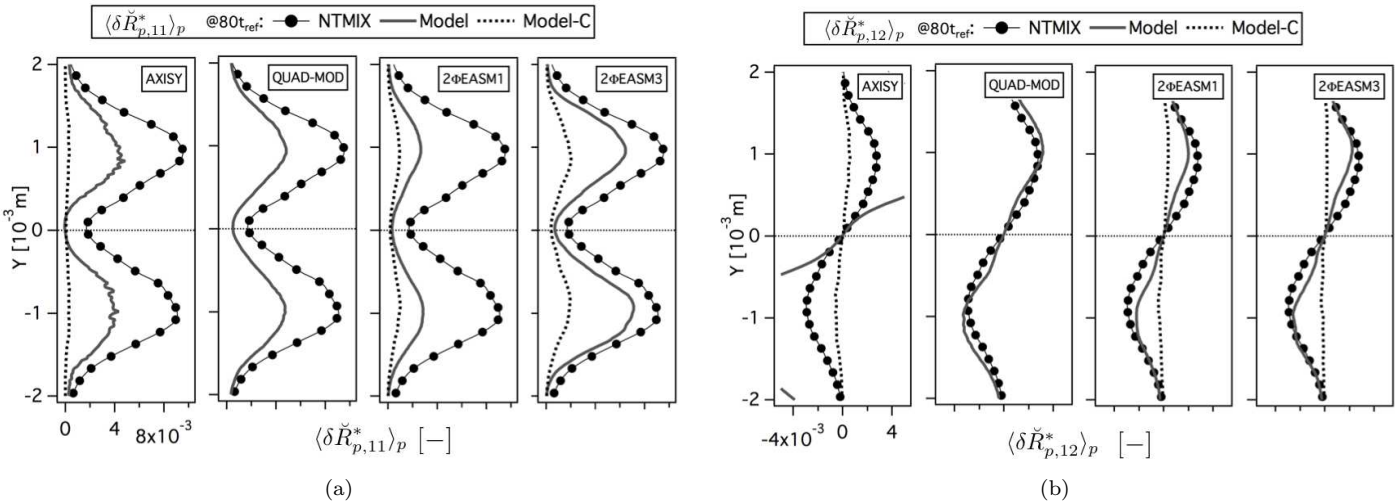

(a) (b)

Figure D.14: *Comparison of Eulerian and Lagrangian (a) mean deviatoric RUM stress tensor XX component ($< \delta \breve{R}^*_{p,11} >_p$) and (b) mean deviatoric RUM stress tensor XY component ($< \delta \breve{R}^*_{p,12} >_p$) at $80t_{ref}$. Normalized by the square of the initial particle velocity in X-direction at the center of the slab. LR_St3_# case.*

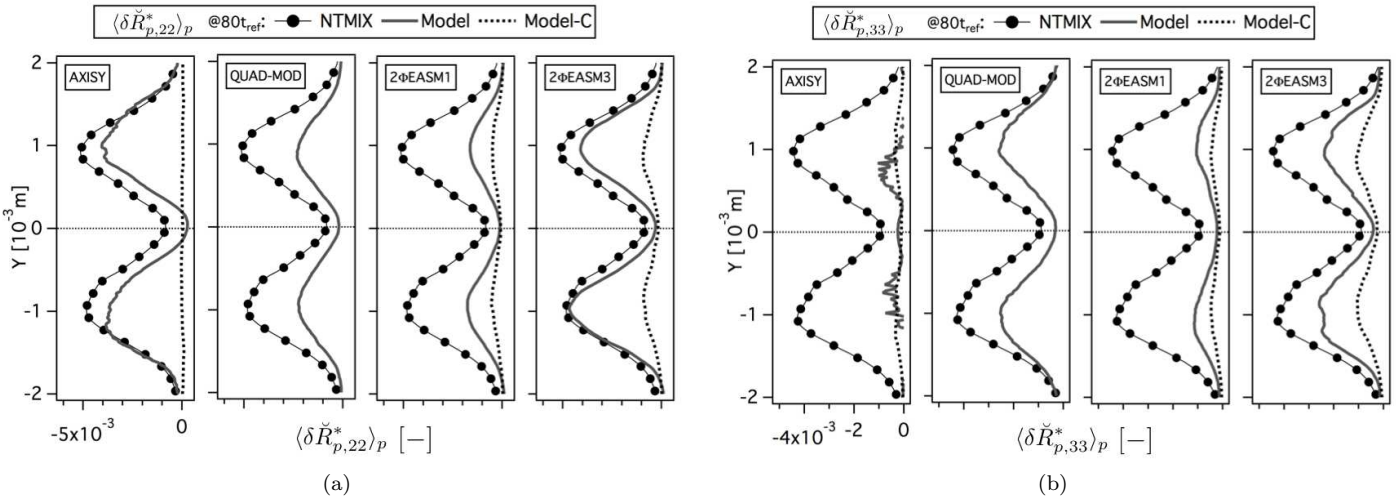

Figure D.15: *Comparison of Eulerian and Lagrangian (a) mean deviatoric RUM stress tensor YY component ($< \delta \breve{R}^*_{p,22} >_p$) and (b) mean deviatoric RUM stress tensor ZZ component ($< \delta \breve{R}^*_{p,33} >_p$) at $80t_{ref}$. Normalized by the square of the initial particle velocity in X-direction at the center of the slab. LR_St3_# case.*

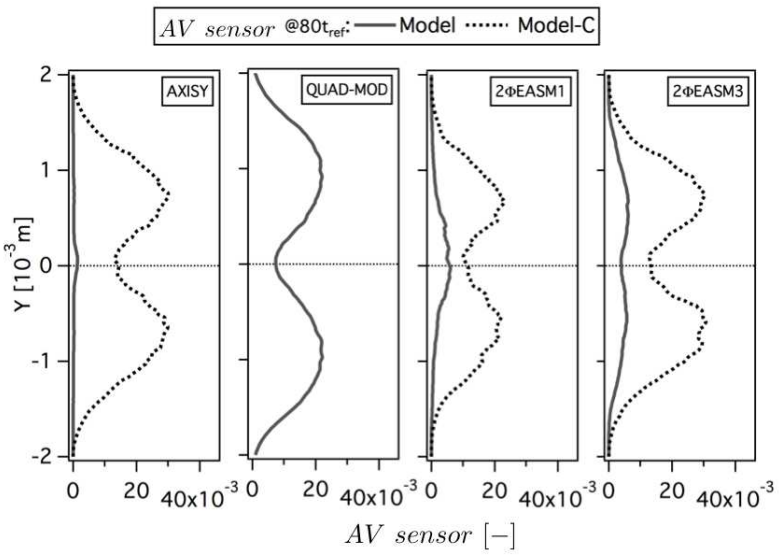

Figure D.16: *Mean Artificial Viscosity sensor activation at $80t_{ref}$. LR_St3_# case.*

D.3 Instantaneous fields at 40 and 80t_{ref}

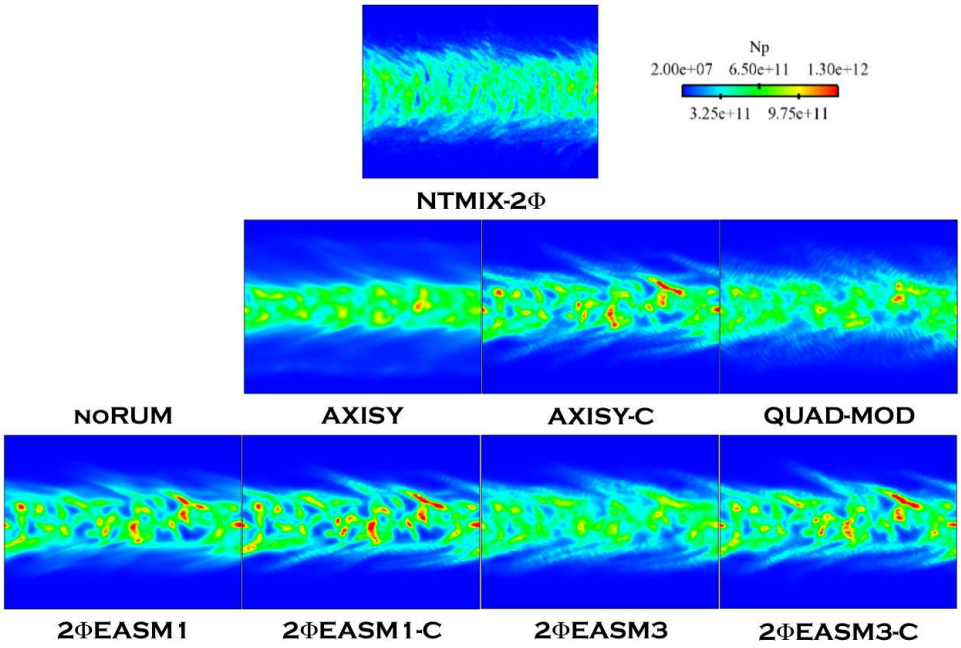

Figure D.17: *Comparison of Lagrangian (NTMIX-2Φ) and Eulerian particle number density (N_p) at 40t_{ref}. LR_St3_# case.*

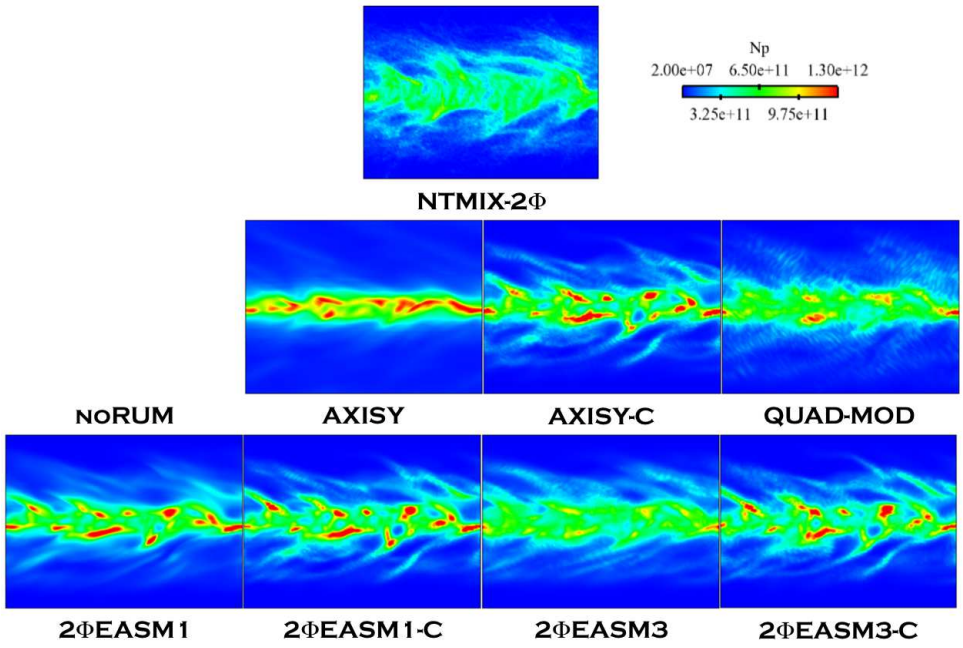

Figure D.18: *Comparison of Lagrangian (NTMIX-2Φ) and Eulerian particle number density (N_p) at 80t_{ref}. LR_St3_# case.*

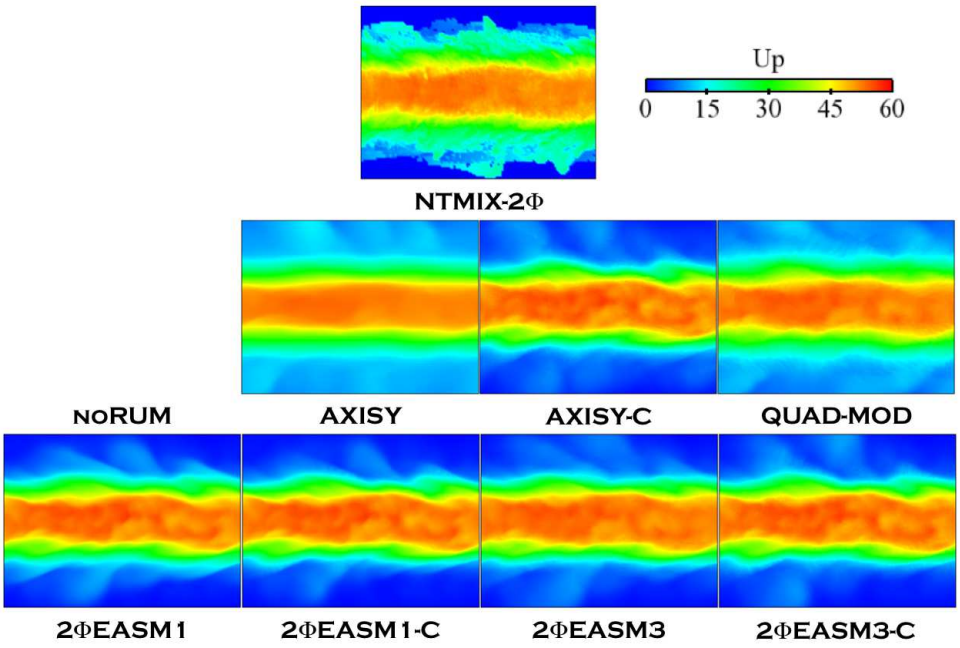

Figure D.19: *Comparison of Lagrangian (NTMIX-2Φ) and Eulerian particle velocity magnitude (U_p) at $40t_{ref}$. LR_St3_# case.*

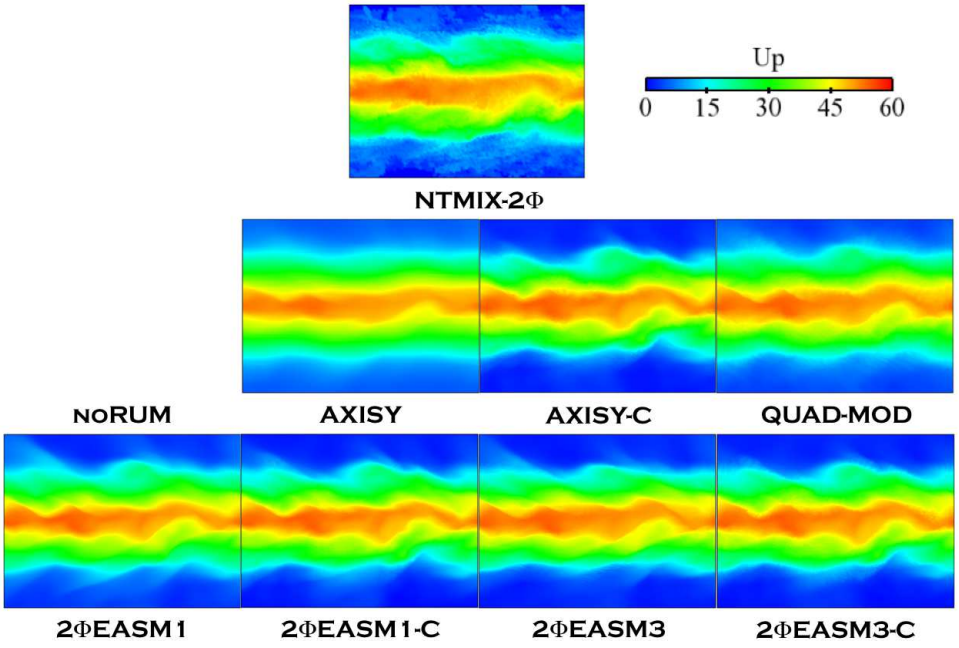

Figure D.20: *Comparison of Lagrangian (NTMIX-2Φ) and Eulerian particle velocity magnitude (U_p) at $80t_{ref}$. LR_St3_# case.*

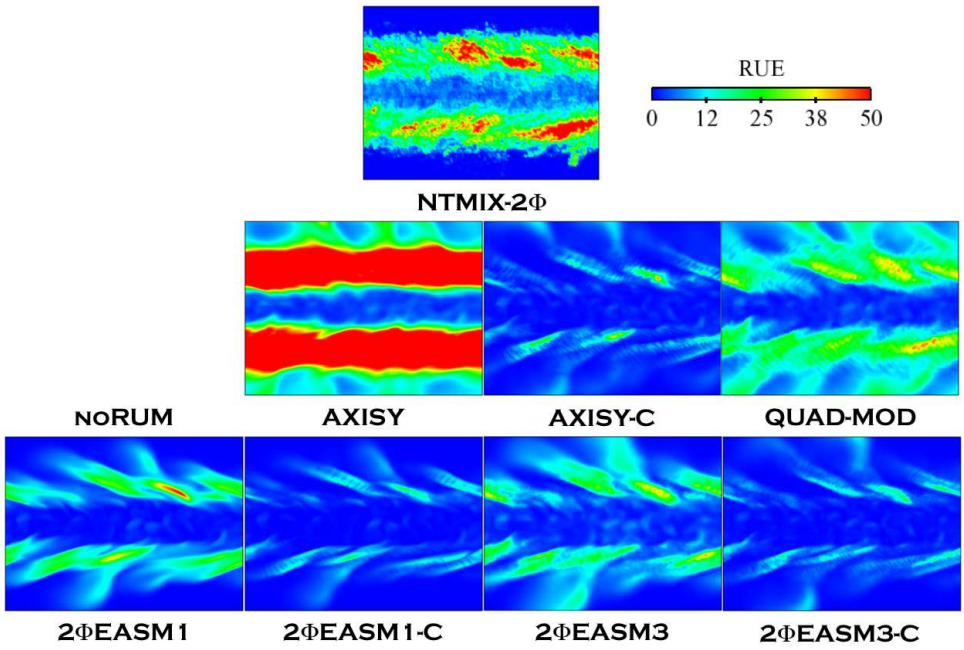

Figure D.21: *Comparison of Lagrangian (NTMIX-2Φ) and Eulerian Random Uncorrelated Energy at $40t_{ref}$. LR_St3_# case.*

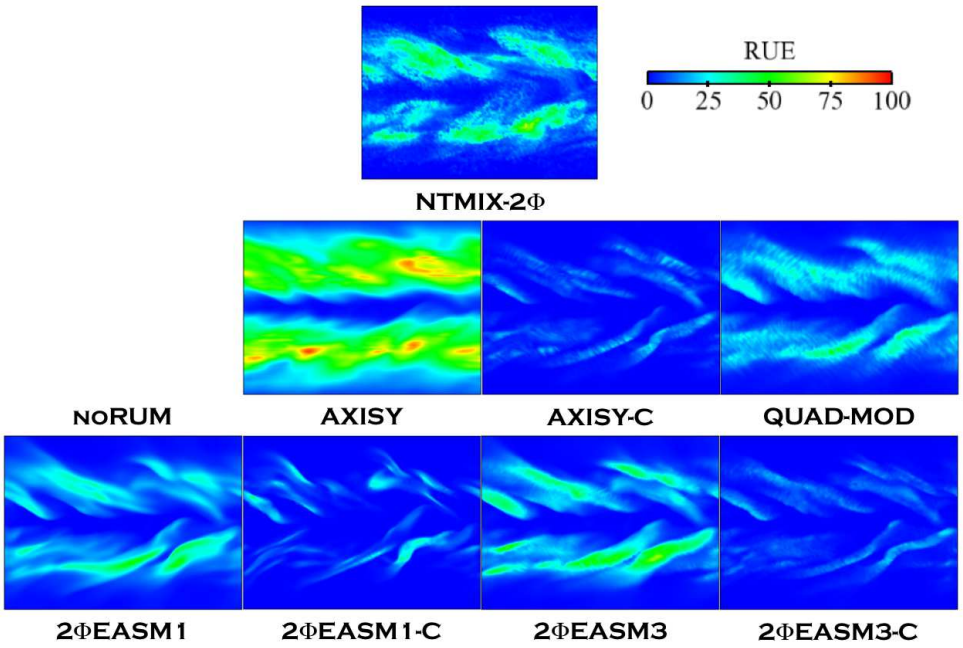

Figure D.22: *Comparison of Lagrangian (NTMIX-2Φ) and Eulerian Random Uncorrelated Energy at $80t_{ref}$. LR_St3_# case.*

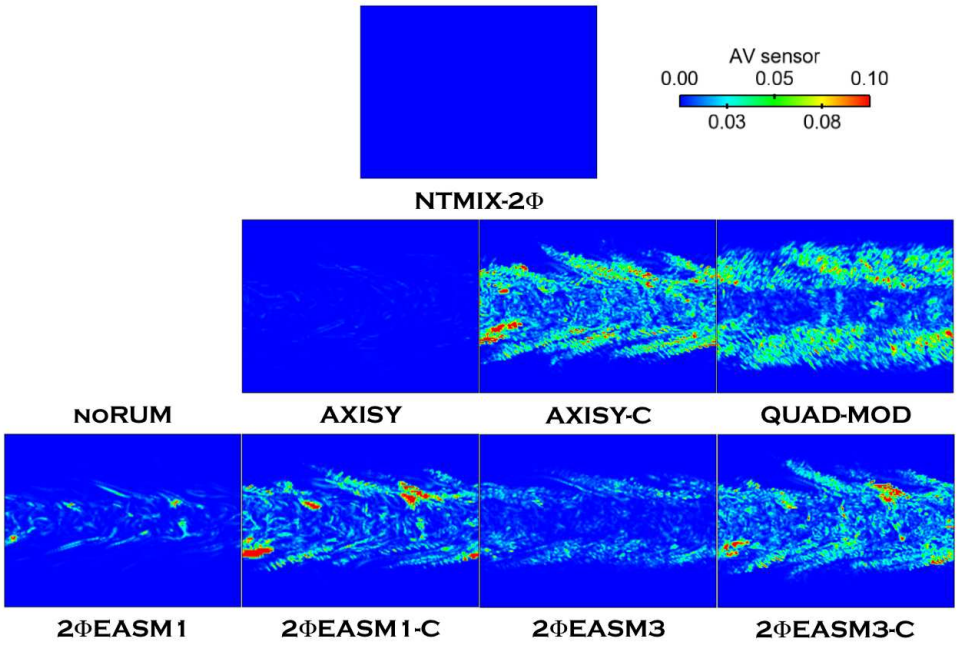

Figure D.23: *Comparison of AV sensor levels at $40t_{ref}$. LR_St3_# case.*

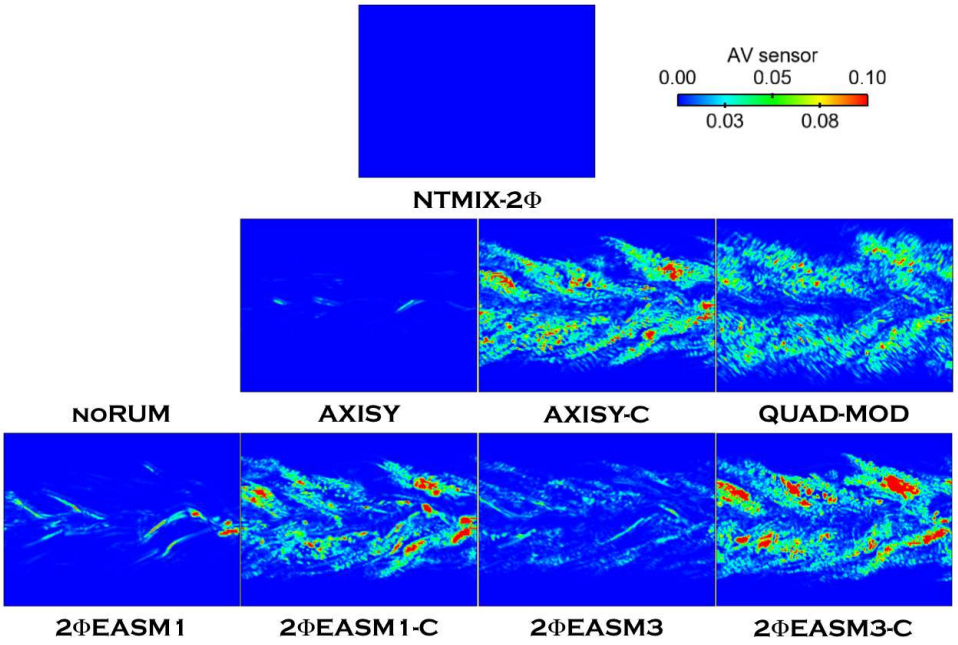

Figure D.24: *Comparison of AV sensor levels at $80t_{ref}$. LR_St3_# case.*

Appendix E

Particle-laden slab. Case LR_St0.33_#. Additional data.

E.1 Dispersed phase statistics at $20t_{ref}$

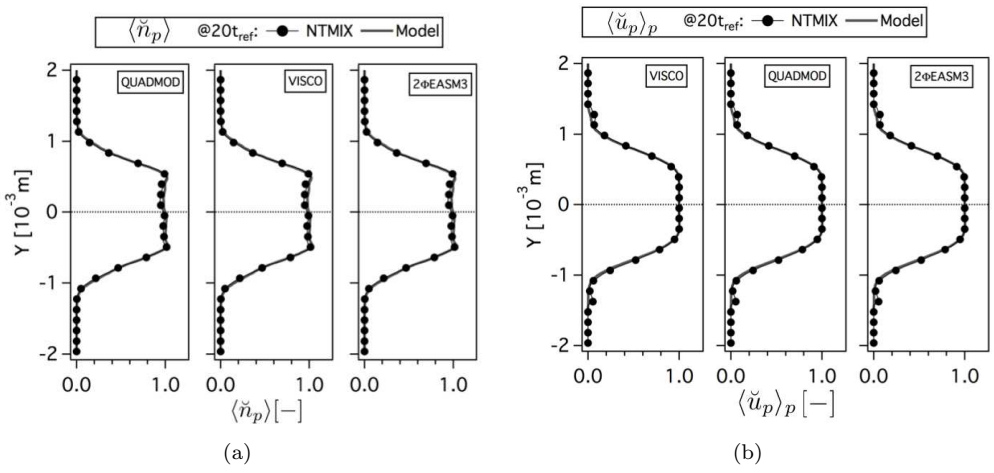

Figure E.1: *Comparison of Eulerian and Lagrangian (a) mean particle number density (< $\breve{n}_p$ >, normalized by the initial particle number density at the center of the slab) and (b) mean particle velocity in X-direction (< $\breve{u}_p$ >$_p$, normalized by the initial particle velocity in X-direction at the center of the slab) at 20t_{ref}. LR_St033_# case.*

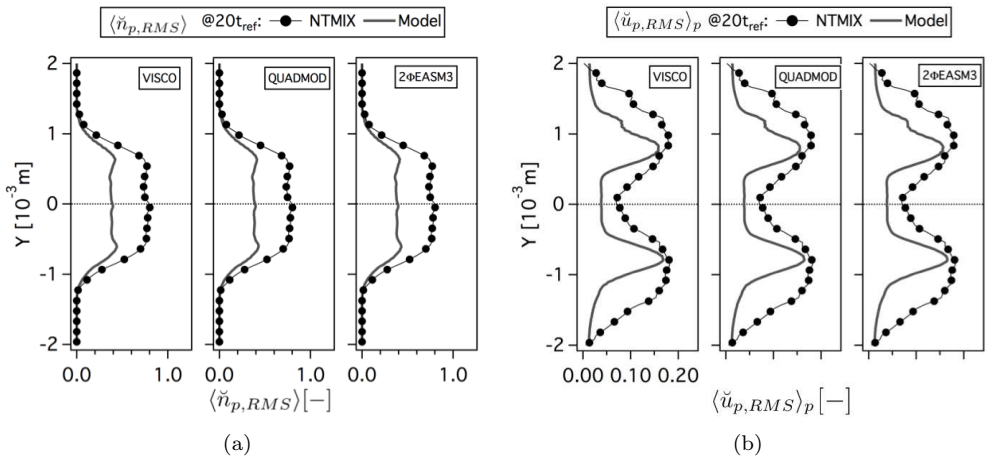

(a) (b)

Figure E.2: *Comparison of Eulerian and Lagrangian (a) RMS particle number density (*$< \breve{n}_{p,RMS} >$*, normalized by the initial particle number density at the center of the slab) and (b) RMS particle velocity in X-direction (*$< \breve{u}_{p,RMS} >_p$*, normalized by the initial particle number density at the center of the slab)at* $20t_{ref}$*. LR_St033_# case.*

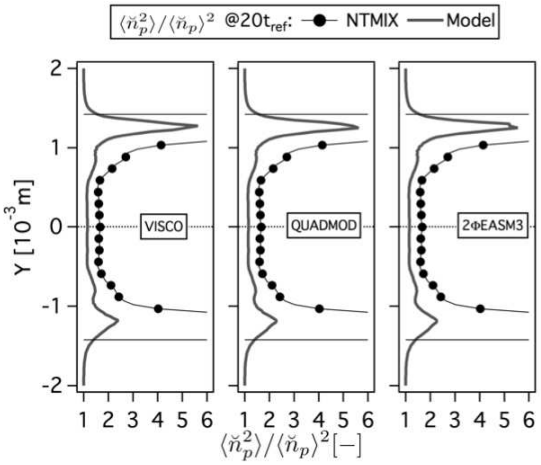

Figure E.3: *Comparison of Eulerian and Lagrangian RMS particle segregation (*$< \breve{n}_p^2 > / < \breve{n}_p >^2$*) at* $20t_{ref}$*. LR_St033_# case.*

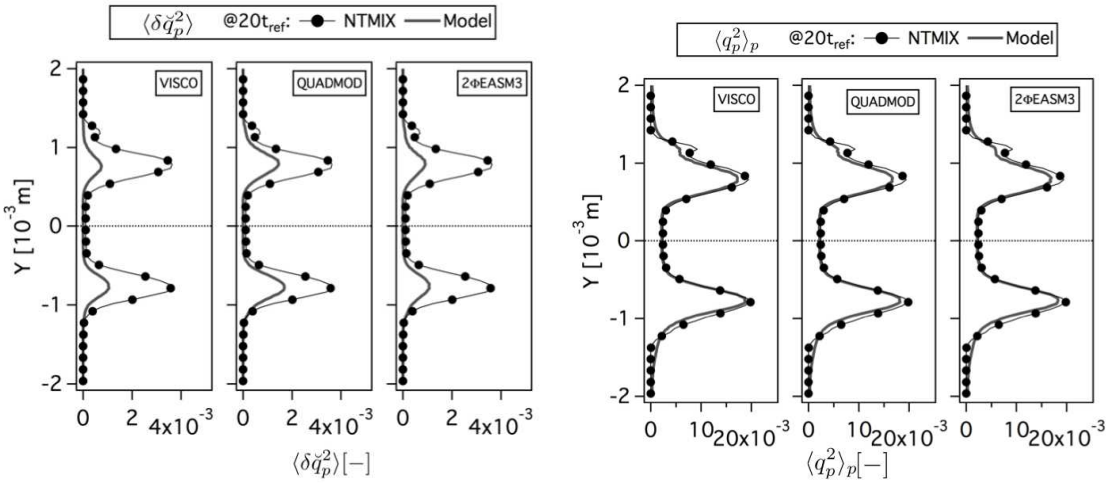

(a) (b)

Figure E.4: *Comparison of Eulerian and Lagrangian (a) mean Random Uncorrelated Energy (< $\delta\breve{q}_p$ >$_p$) and (b) mean mesoscopic ($\langle \breve{q}_p^2 \rangle_p$) particle energies at 20t_{ref}. Normalized by the square of the initial particle velocity in X-direction at the center of the slab. LR_St033_# case.*

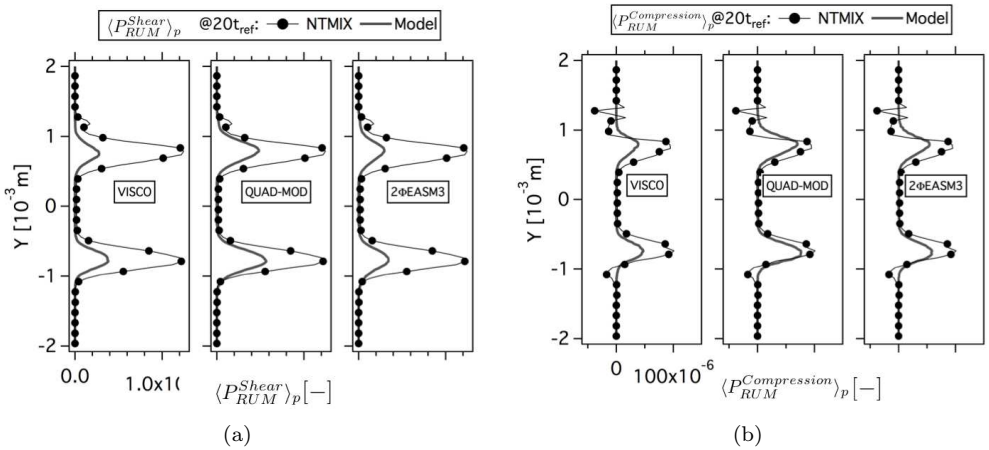

(a) (b)

Figure E.5: *Comparison of Eulerian and Lagrangian (a) mean production of RUM energy by shear components (< P_{RUM}^{Shear} >$_p$) and (b) mean productions of RUM energy by compression (< $P_{RUM}^{Compression}$ >$_p$) at 20t_{ref}. Normalized by the square of the initial particle velocity in X-direction at the center of the slab and the reference time (t_{ref}). LR_St033_# case.*

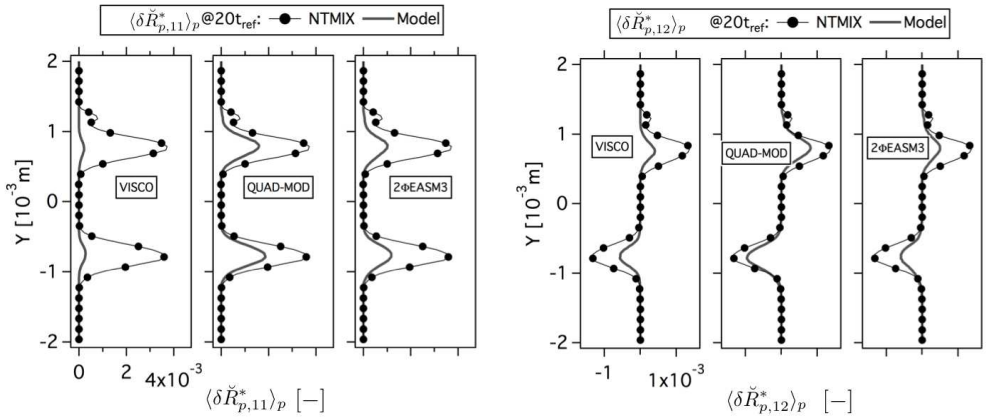

(a) (b)

Figure E.6: *Comparison of Eulerian and Lagrangian (a) mean deviatoric RUM stress tensor XX component ($< \delta \breve{R}^*_{p,11} >_p$) and (b) mean deviatoric RUM stress tensor XY component ($< \delta \breve{R}^*_{p,12} >_p$) at $20t_{ref}$. Normalized by the square of the initial particle velocity in X-direction at the center of the slab. LR_St033_# case.*

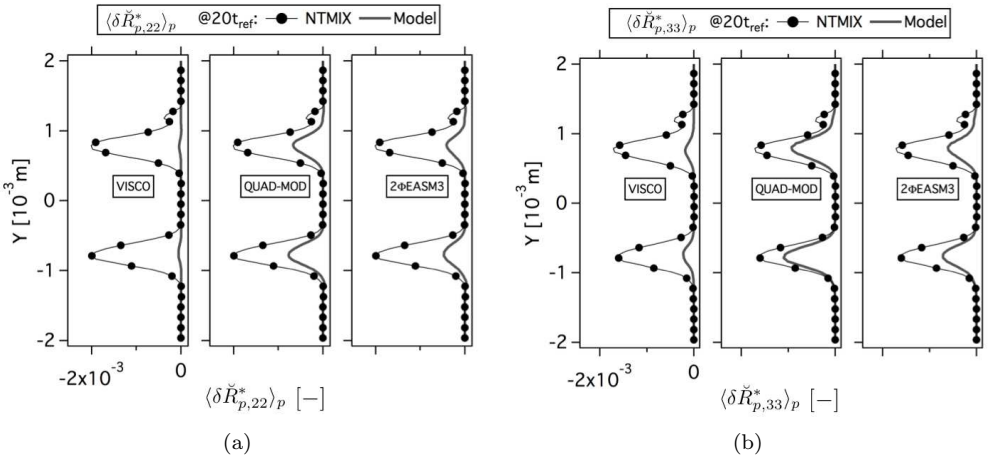

(a) (b)

Figure E.7: *Comparison of Eulerian and Lagrangian (a) mean deviatoric RUM stress tensor YY component ($< \delta \breve{R}^*_{p,22} >_p$) and (b) mean deviatoric RUM stress tensor ZZ component ($< \delta \breve{R}^*_{p,33} >_p$) at $20t_{ref}$. Normalized by the square of the initial particle velocity in X-direction at the center of the slab. LR_St033_# case.*

E.2 Dispersed phase statistics at $40t_{ref}$

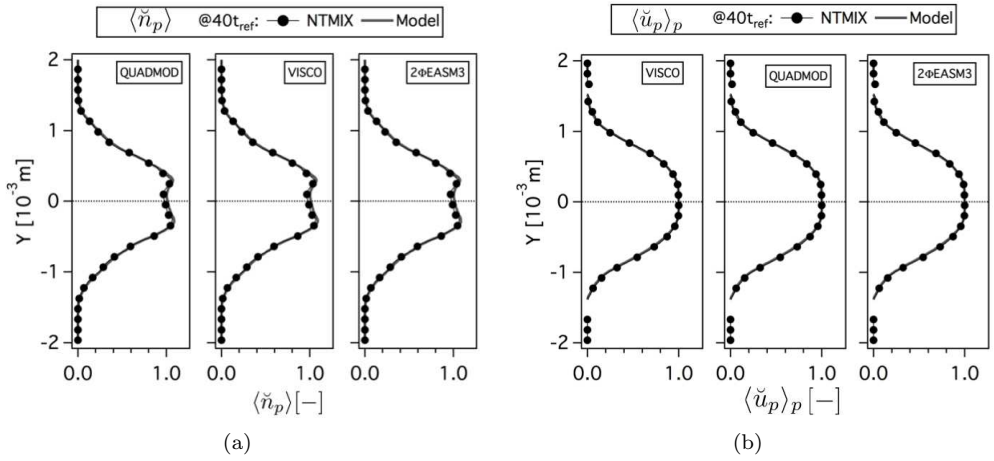

Figure E.8: *Comparison of Eulerian and Lagrangian (a) mean particle number density (< $\breve{n}_p$ >, normalized by the initial particle number density at the center of the slab) and (b) mean particle velocity in X-direction (< $\breve{u}_p$ >$_p$, normalized by the initial particle velocity in X-direction at the center of the slab) at $40t_{ref}$. LR_St033_# case.*

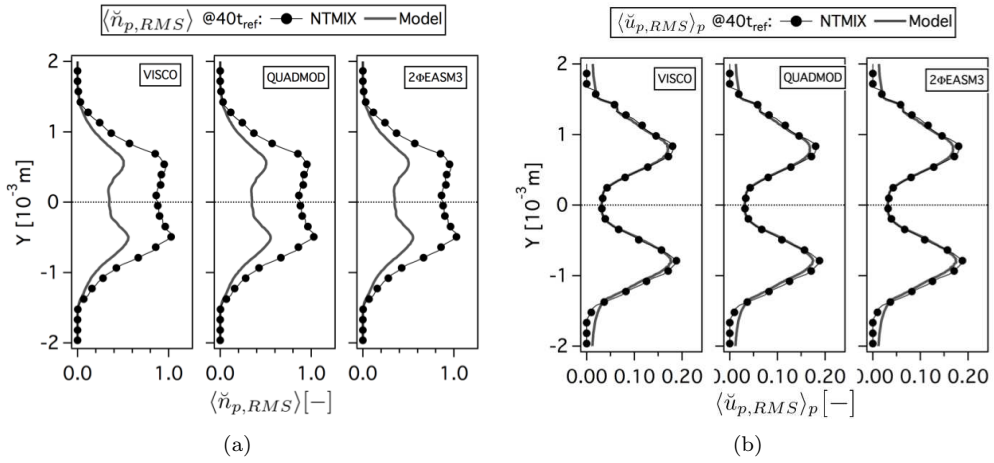

Figure E.9: *Comparison of Eulerian and Lagrangian (a) RMS particle number density (< $\breve{n}_{p,RMS}$ >, normalized by the initial particle number density at the center of the slab) and (b) RMS particle velocity in X-direction (< $\breve{u}_{p,RMS}$ >$_p$, normalized by the initial particle number density at the center of the slab)at $40t_{ref}$. LR_St033_# case.*

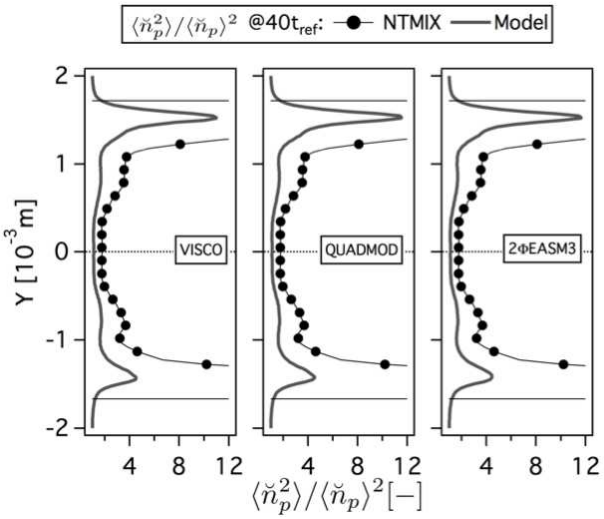

Figure E.10: *Comparison of Eulerian and Lagrangian RMS particle segregation ($< \breve{n}_p^2 > / < \breve{n}_p >^2$) at $40t_{ref}$. LR_St033_# case.*

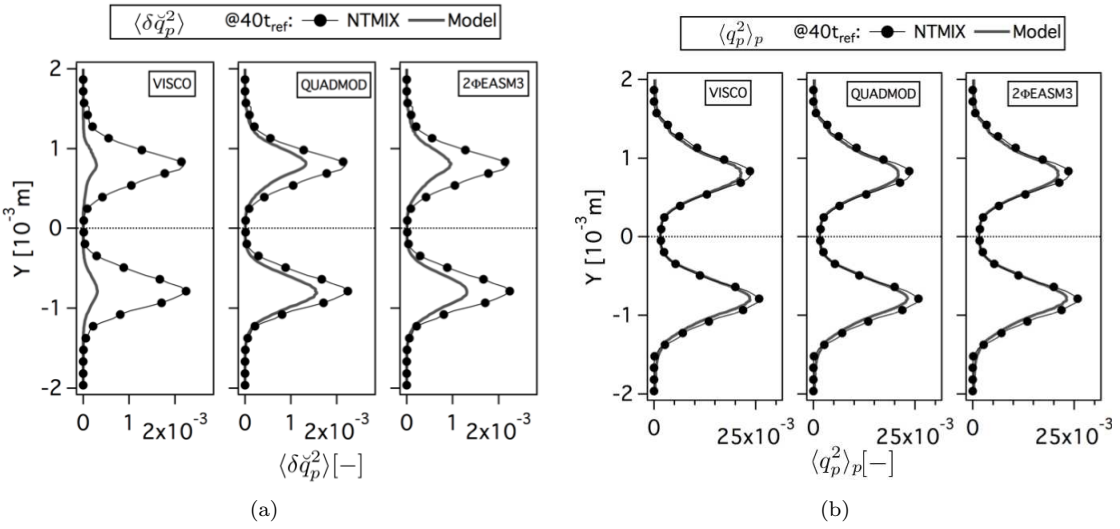

(a) (b)

Figure E.11: *Comparison of Eulerian and Lagrangian (a) mean Random Uncorrelated Energy ($< \delta \breve{q}_p >_p$) and (b) mean mesoscopic ($\langle \breve{q}_p^2 \rangle_p$) particle energies at $40t_{ref}$. Normalized by the square of the initial particle velocity in X-direction at the center of the slab. LR_St033_# case.*

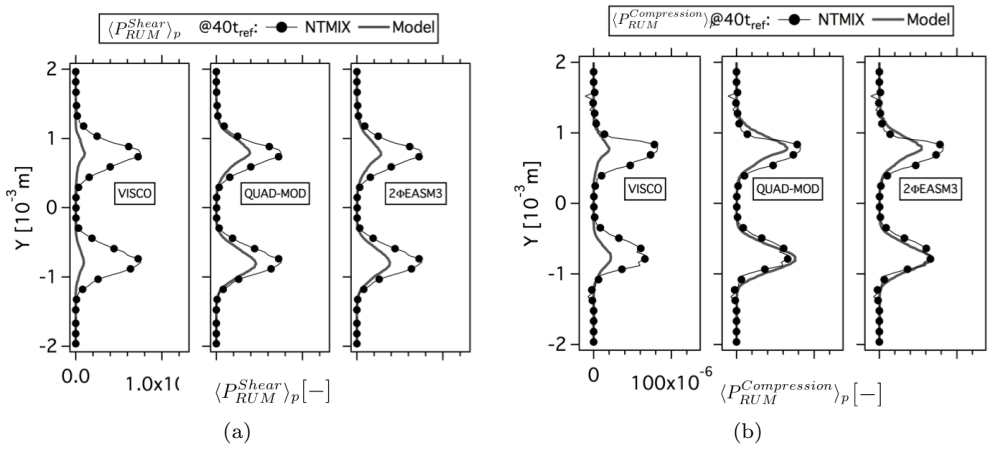

(a) (b)

Figure E.12: *Comparison of Eulerian and Lagrangian (a) mean production of RUM energy by shear components ($< P_{RUM}^{Shear} >_p$) and (b) mean productions of RUM energy by compression ($< P_{RUM}^{Compression} >_p$) at $40t_{ref}$. Normalized by the square of the initial particle velocity in X-direction at the center of the slab and the reference time (t_{ref}). LR_St033_# case.*

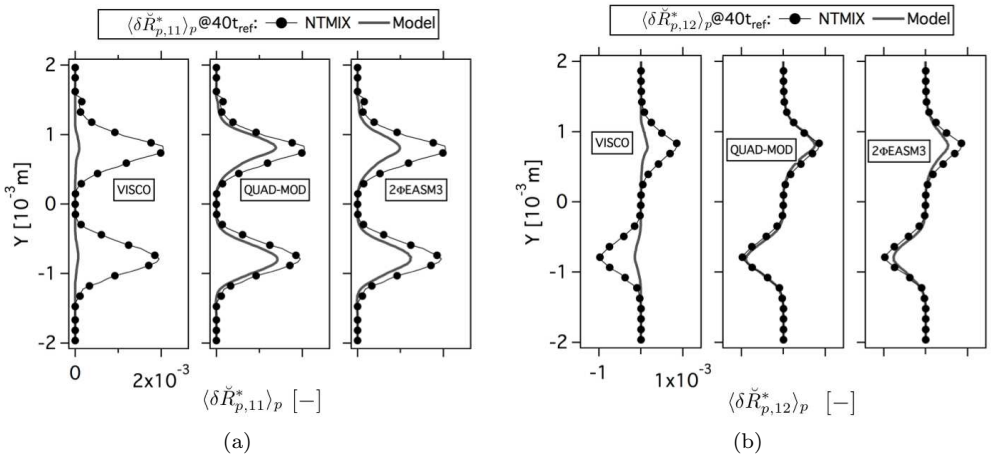

(a) (b)

Figure E.13: *Comparison of Eulerian and Lagrangian (a) mean deviatoric RUM stress tensor XX component ($< \delta \breve{R}_{p,11}^* >_p$) and (b) mean deviatoric RUM stress tensor XY component ($< \delta \breve{R}_{p,12}^* >_p$) at $40t_{ref}$. Normalized by the square of the initial particle velocity in X-direction at the center of the slab. LR_St033_# case.*

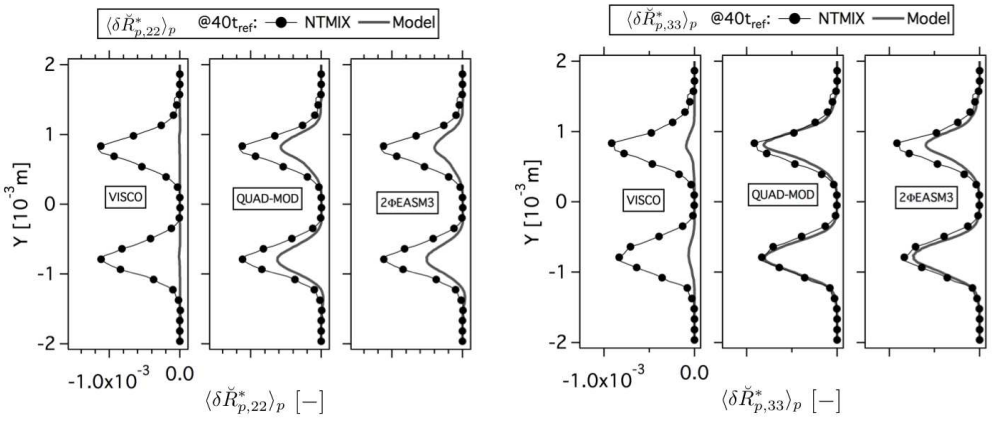

Figure E.14: *Comparison of Eulerian and Lagrangian (a) mean deviatoric RUM stress tensor YY component* ($< \delta \breve{R}^*_{p,22} >_p$) *and (b) mean deviatoric RUM stress tensor ZZ component* ($< \delta \breve{R}^*_{p,33} >_p$) *at* $40t_{ref}$. *Normalized by the square of the initial particle velocity in X-direction at the center of the slab. LR_St033_# case.*

E.3 Instantaneous fields at 40 and $20t_{ref}$

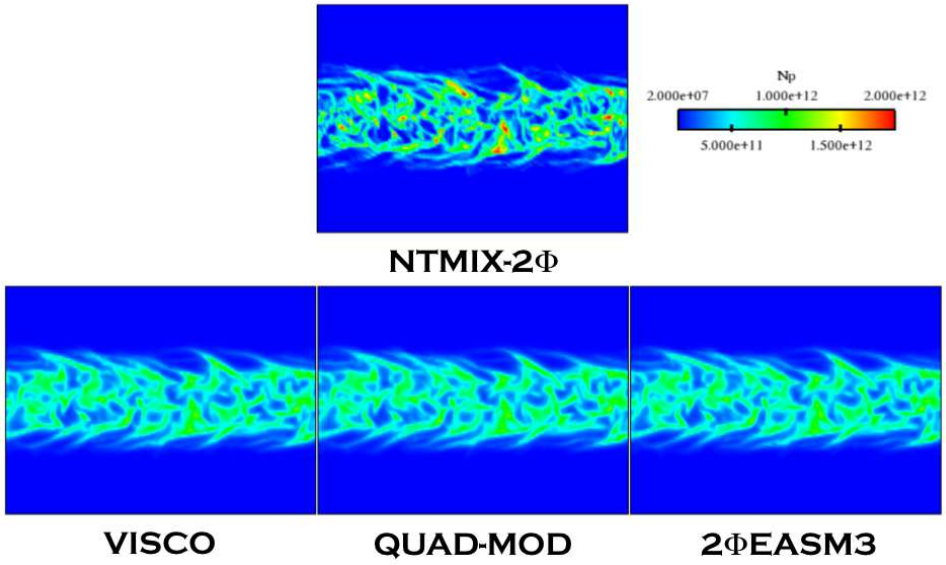

Figure E.15: *Comparison of Lagrangian (NTMIX-2Φ) and Eulerian particle number density (N_p) at $20t_{ref}$. LR_St033_# case.*

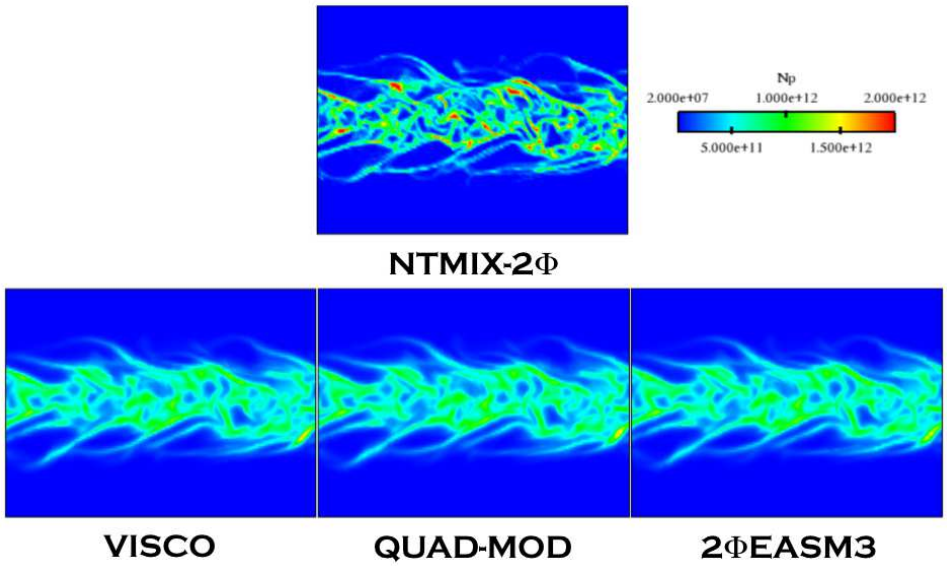

Figure E.16: *Comparison of Lagrangian (NTMIX-2Φ) and Eulerian particle number density (N_p) at $40t_{ref}$. LR_St033_# case.*

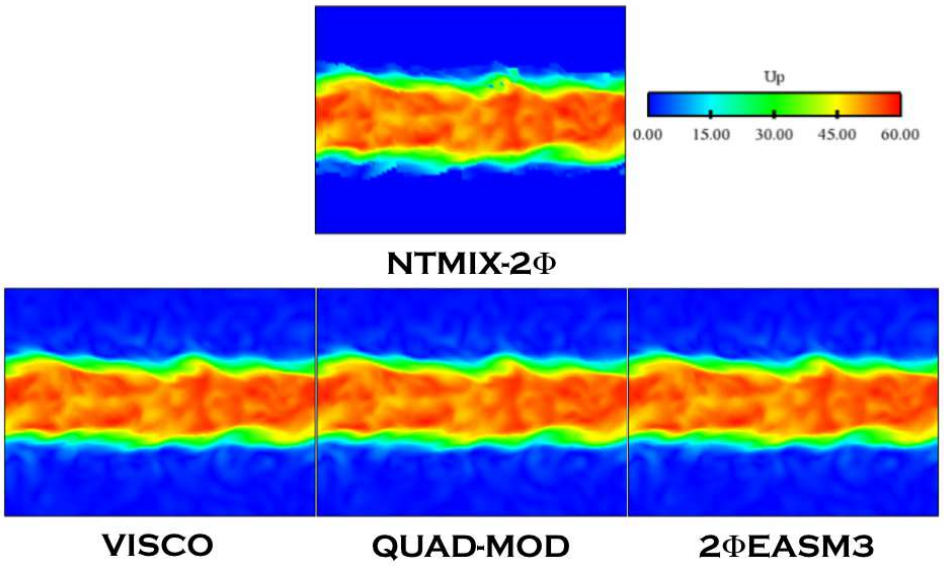

Figure E.17: *Comparison of Lagrangian (NTMIX-2Φ) and Eulerian particle velocity magnitude (U_p) at $20t_{ref}$. LR_St033_# case.*

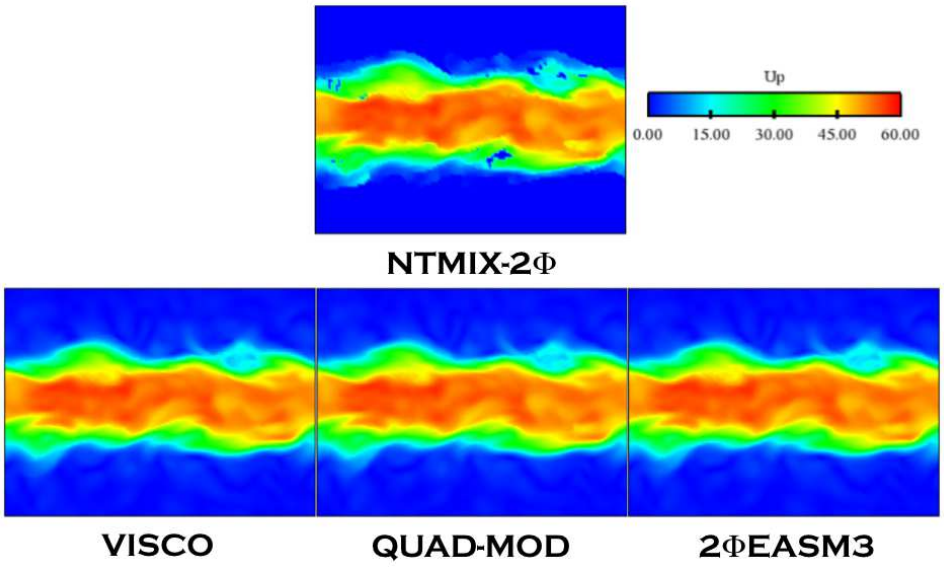

Figure E.18: *Comparison of Lagrangian (NTMIX-2Φ) and Eulerian particle velocity magnitude (U_p) at $40t_{ref}$. LR_St033_# case.*

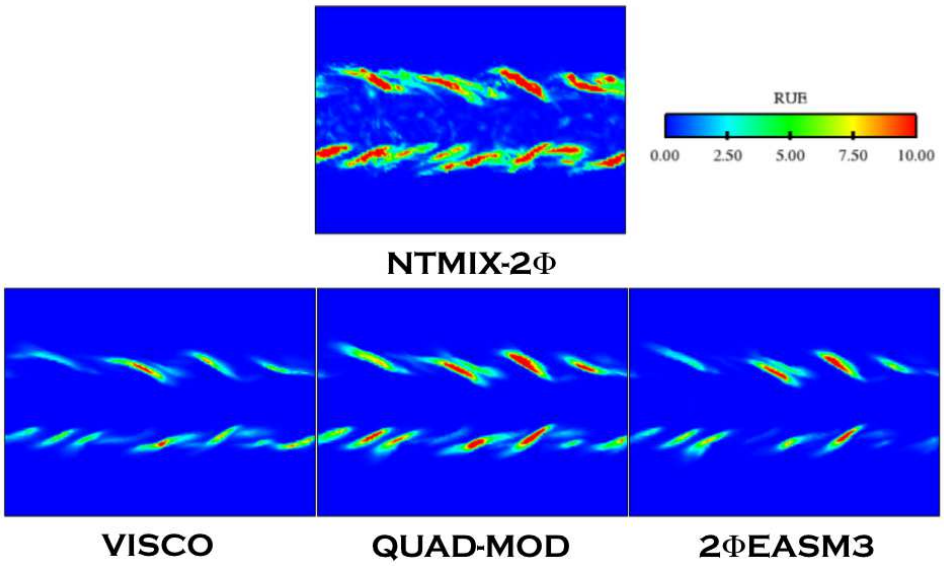

Figure E.19: *Comparison of Lagrangian (NTMIX-2Φ) and Eulerian Random Uncorrelated Energy at* $20t_{ref}$*. LR_St033_# case.*

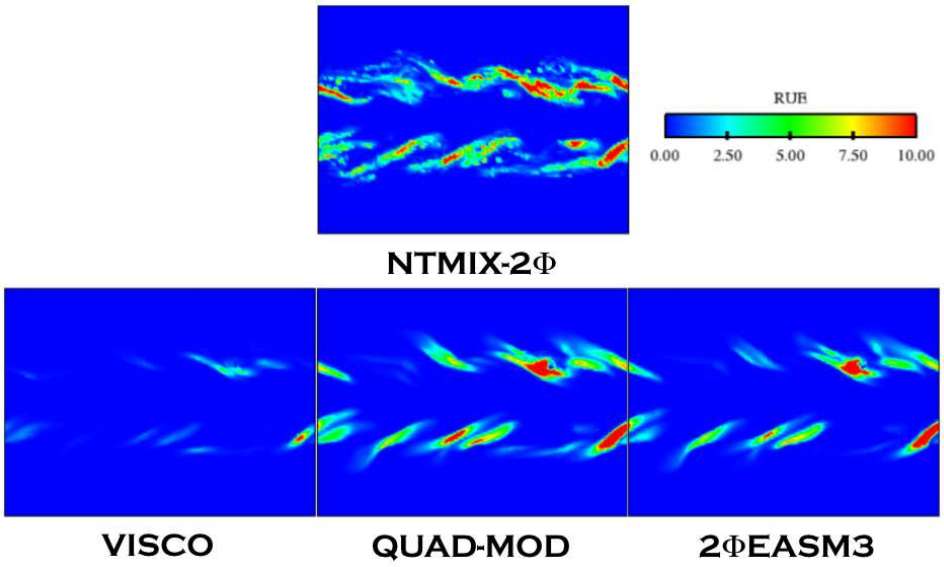

Figure E.20: *Comparison of Lagrangian (NTMIX-2Φ) and Eulerian Random Uncorrelated Energy at* $40t_{ref}$*. LR_St033_# case.*

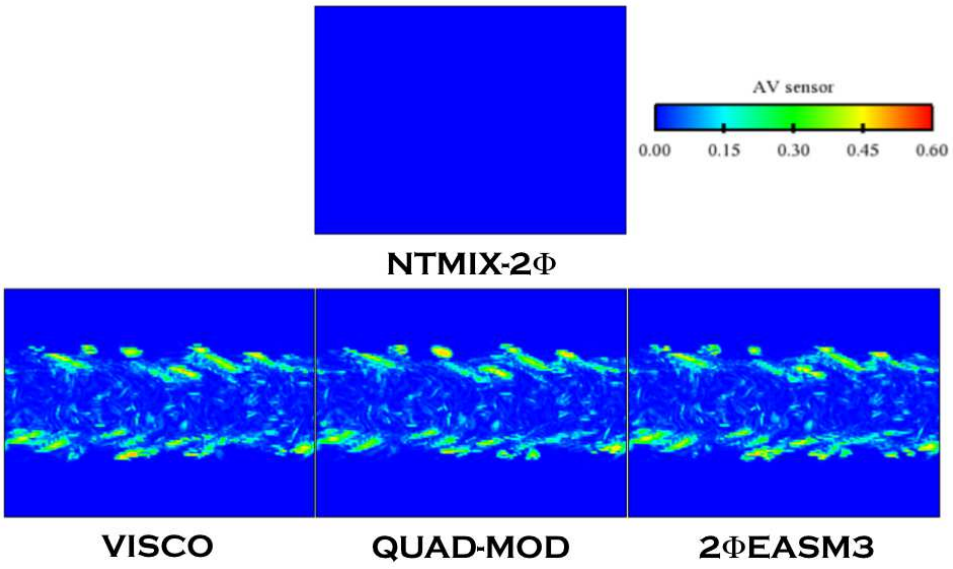

Figure E.21: *Comparison of AV sensor levels at $20t_{ref}$. LR_St033_# case.*

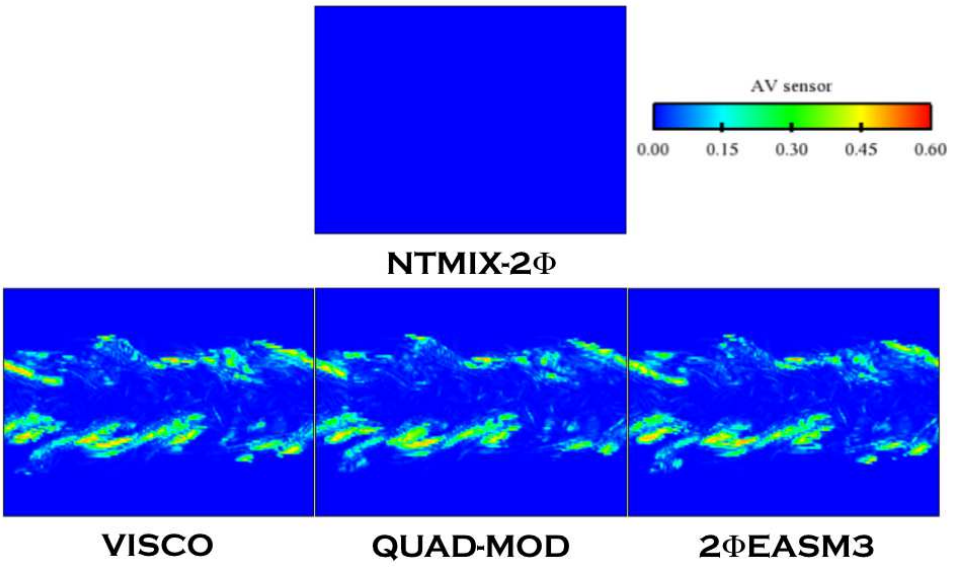

Figure E.22: *Comparison of AV sensor levels at $40t_{ref}$. LR_St033_# case.*

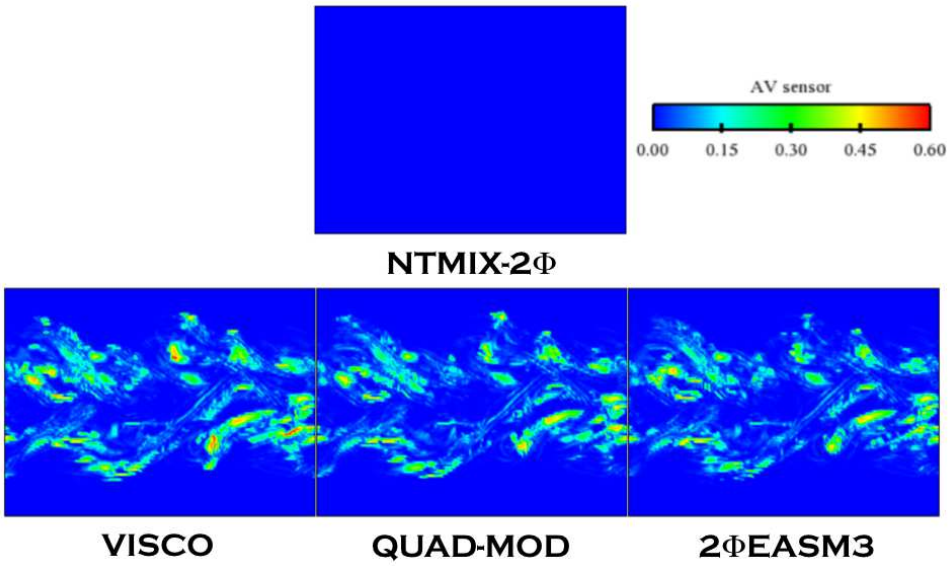

Figure E.23: *Comparison of AV sensor levels at* $80t_{ref}$*. LR_St033_# case.*

Appendix F

Particle-laden slab. Case HR_St1_#. Additional data.

F.1 Dispersed phase statistics at $5t_{ref}$

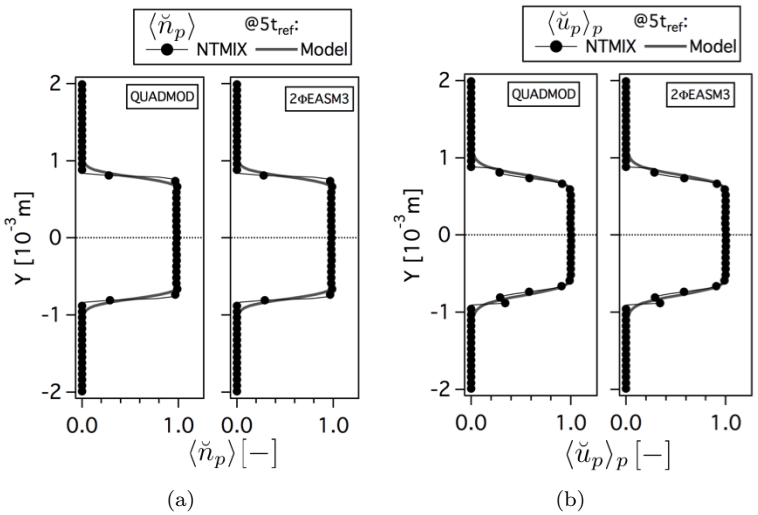

(a) (b)

Figure F.1: *Comparison of Eulerian and Lagrangian (a) mean particle number density (< $\breve{n}_p$ >, normalized by the initial particle number density at the center of the slab) and (b) mean particle velocity in X-direction (< $\breve{u}_p$ >$_p$, normalized by the initial particle velocity in X-direction at the center of the slab) at $5t_{ref}$. HR_St1_# case.*

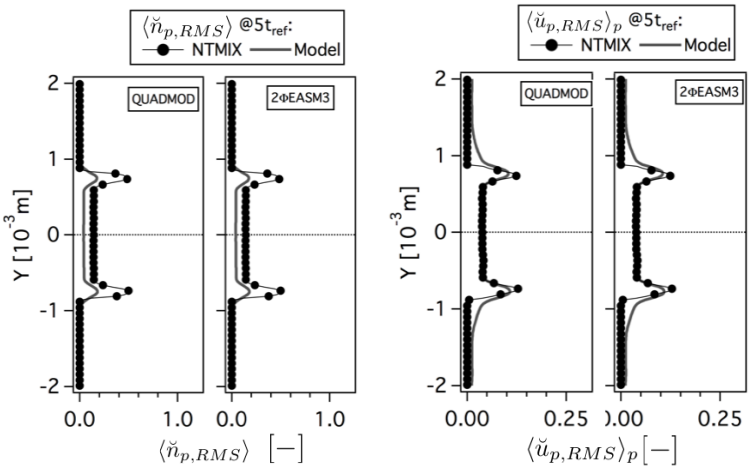

(a) (b)

Figure F.2: *Comparison of Eulerian and Lagrangian (a) RMS particle number density (*$< \breve{n}_{p,RMS} >$*, normalized by the initial particle number density at the center of the slab) and (b) RMS particle velocity in X-direction (*$< \breve{u}_{p,RMS} >_p$*, normalized by the initial particle number density at the center of the slab) at* $5t_{ref}$*. HR_St1_# case.*

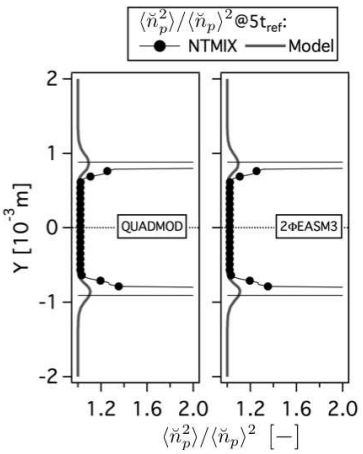

Figure F.3: *Comparison of Eulerian and Lagrangian RMS particle segregation (*$< \breve{n}_p^2 > / < \breve{n}_p >^2$*) at* $5t_{ref}$*. HR_St1_# case.*

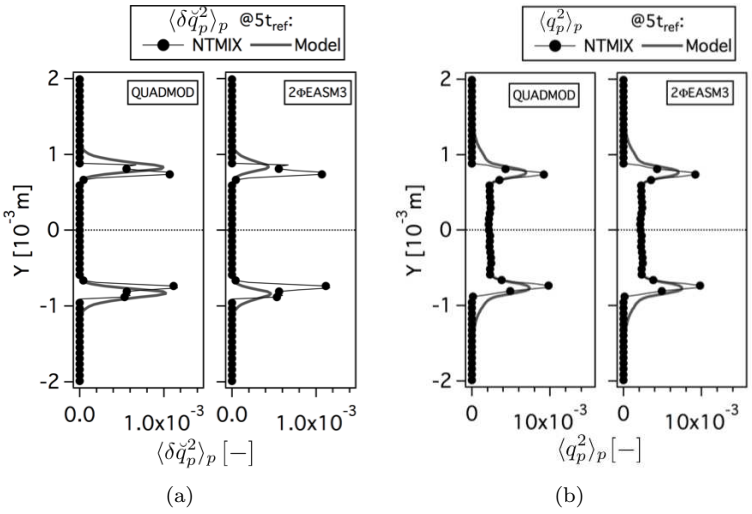

(a) (b)

Figure F.4: *Comparison of Eulerian and Lagrangian (a) mean Random Uncorrelated Energy (*$< \delta\breve{q}_p >_p$*) and (b) mean mesoscopic (*$\langle \breve{q}_p^2 \rangle_p$*) particle energies at* $5t_{ref}$*. Normalized by the square of the initial particle velocity in X-direction at the center of the slab. HR_St1_# case.*

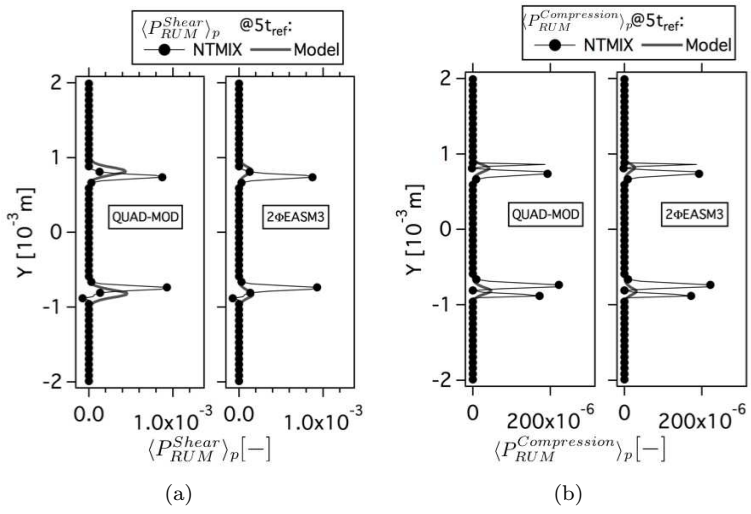

(a) (b)

Figure F.5: *Comparison of Eulerian and Lagrangian (a) mean production of RUM energy by shear components (*$< P_{RUM}^{Shear} >_p$*) and (b) mean productions of RUM energy by compression (*$< P_{RUM}^{Compression} >_p$*) at* $5t_{ref}$*. Normalized by the square of the initial particle velocity in X-direction at thecenter of the slab and t[h!]e reference time (*t_{ref}*). HR_St1_# case.*

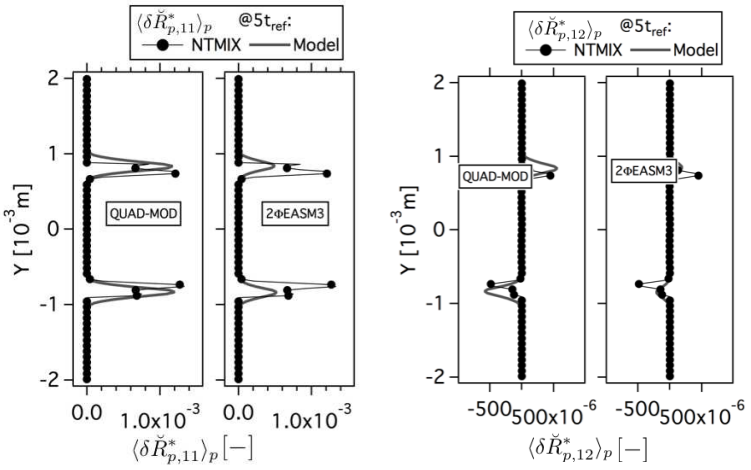

(a) (b)

Figure F.6: *Comparison of Eulerian and Lagrangian (a) mean deviatoric RUM stress tensor XX component ($< \delta \breve{R}^*_{p,11} >_p$) and (b) mean deviatoric RUM stress tensor XY component ($< \delta \breve{R}^*_{p,12} >_p$) at $5t_{ref}$. Normalized by the square of the initial particle velocity in X-direction at the center of the slab. HR_St1_# case.*

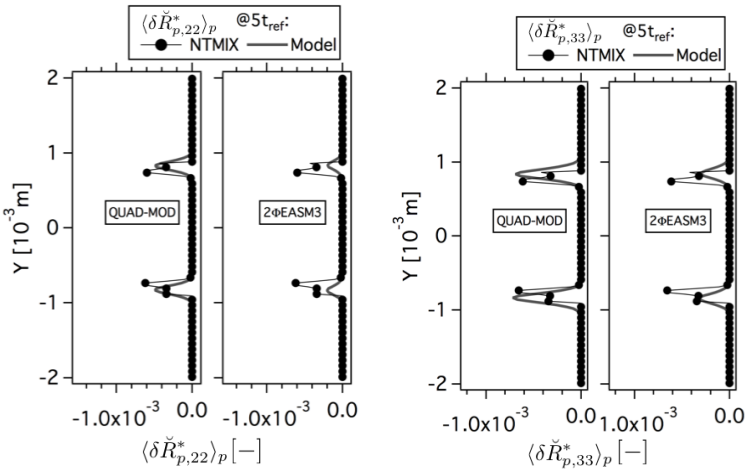

(a) (b)

Figure F.7: *Comparison of Eulerian and Lagrangian (a) mean deviatoric RUM stress tensor YY component ($< \delta \breve{R}^*_{p,22} >_p$) and (b) mean deviatoric RUM stress tensor ZZ component ($< \delta \breve{R}^*_{p,33} >_p$) at $5t_{ref}$. Normalized by the square of the initial particle velocity in X-direction at the center of the slab. HR_St1_# case.*

F.2 Dispersed phase statistics at $40t_{ref}$

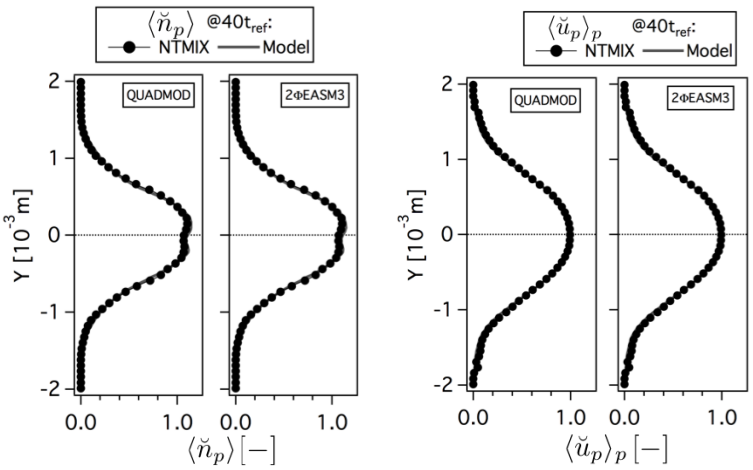

(a) (b)

Figure F.8: *Comparison of Eulerian and Lagrangian (a) mean particle number density (< $\breve{n}_p$ >, normalized by the initial particle number density at the center of the slab) and (b) mean particle velocity in X-direction (< $\breve{u}_p$ >$_p$, normalized by the initial particle velocity in X-direction at the center of the slab) at $40t_{ref}$. HR_St1_# case.*

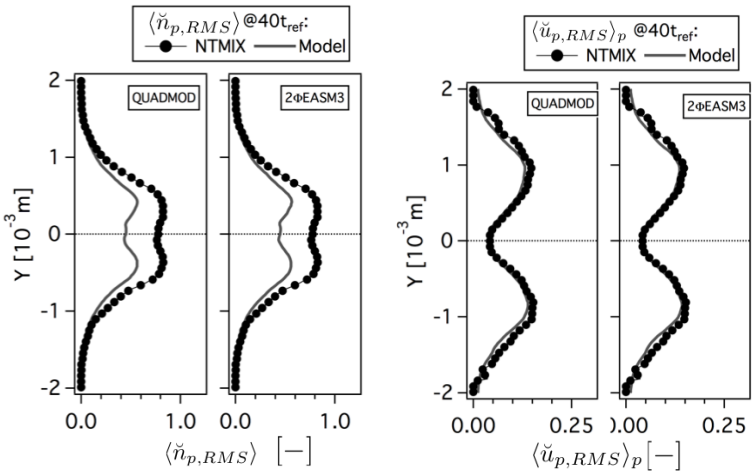

(a) (b)

Figure F.9: *Comparison of Eulerian and Lagrangian (a) RMS particle number density (< $\breve{n}_{p,RMS}$ >, normalized by the initial particle number density at the center of the slab) and (b) RMS particle velocity in X-direction (< $\breve{u}_{p,RMS}$ >$_p$, normalized by the initial particle number density at the center of the slab)at $40t_{ref}$. HR_St1_# case.*

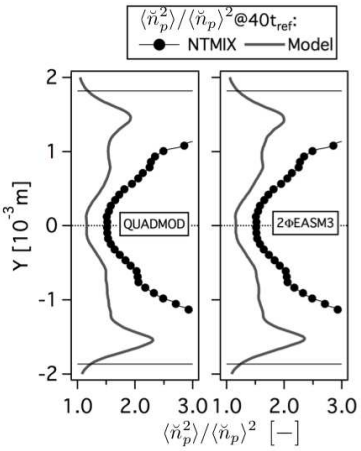

Figure F.10: *Comparison of Eulerian and Lagrangian RMS particle segregation ($< \breve{n}_p^2 > / < \breve{n}_p >^2$) at $40t_{ref}$. HR_St1_# case.*

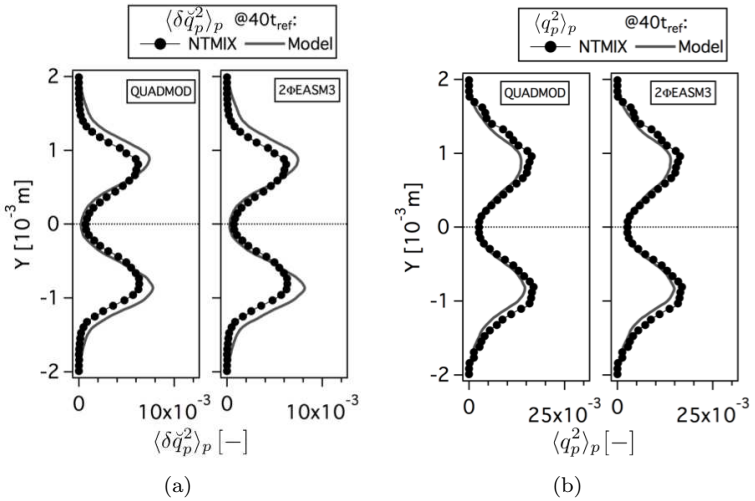

Figure F.11: *Comparison of Eulerian and Lagrangian (a) mean Random Uncorrelated Energy ($< \delta \breve{q}_p >_p$) and (b) mean mesoscopic ($\langle \breve{q}_p^2 \rangle_p$) particle energies at $40t_{ref}$. Normalized by the square of the initial particle velocity in X-direction at the center of the slab. HR_St1_# case.*

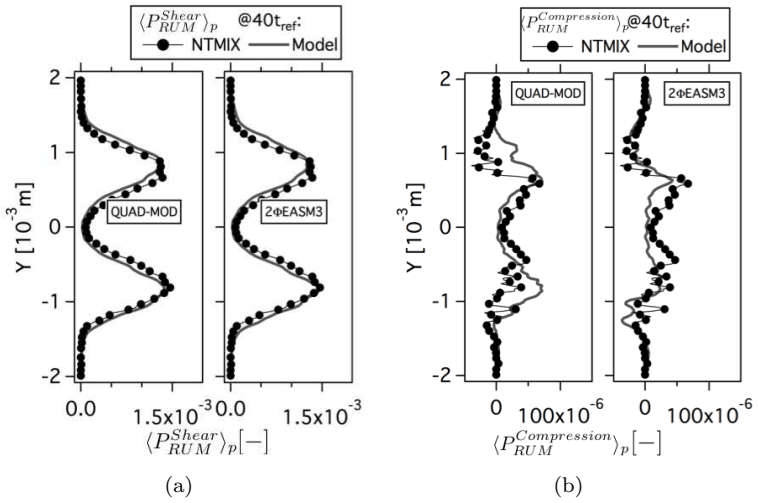

(a) (b)

Figure F.12: *Comparison of Eulerian and Lagrangian (a) mean production of RUM energy by shear components ($< P_{RUM}^{Shear} >_p$) and (b) mean productions of RUM energy by compression ($< P_{RUM}^{Compression} >_p$) at $40t_{ref}$. Normalized by the square of the initial particle velocity in X-direction at the center of the slab and the reference time (t_{ref}). HR_St1_# case.*

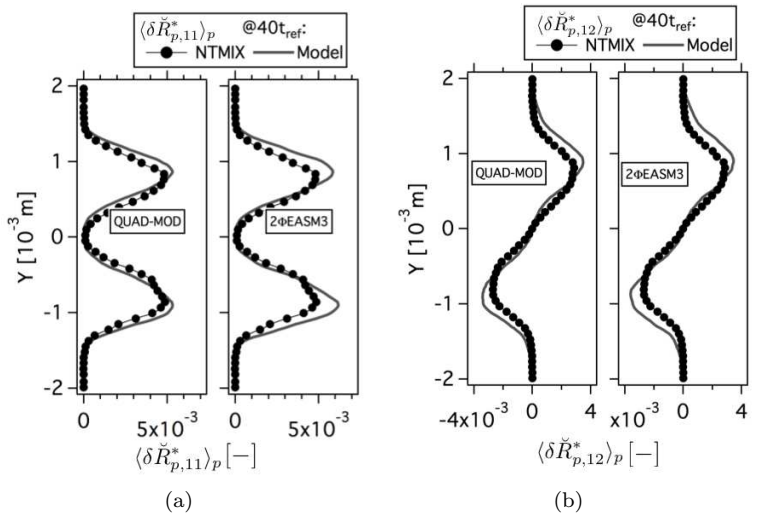

(a) (b)

Figure F.13: *Comparison of Eulerian and Lagrangian (a) mean deviatoric RUM stress tensor XX component ($< \delta \breve{R}_{p,11}^* >_p$) and (b) mean deviatoric RUM stress tensor XY component ($< \delta \breve{R}_{p,12}^* >_p$) at $40t_{ref}$. Normalized by the square of the initial particle velocity in X-direction at the center of the slab. HR_St1_# case.*

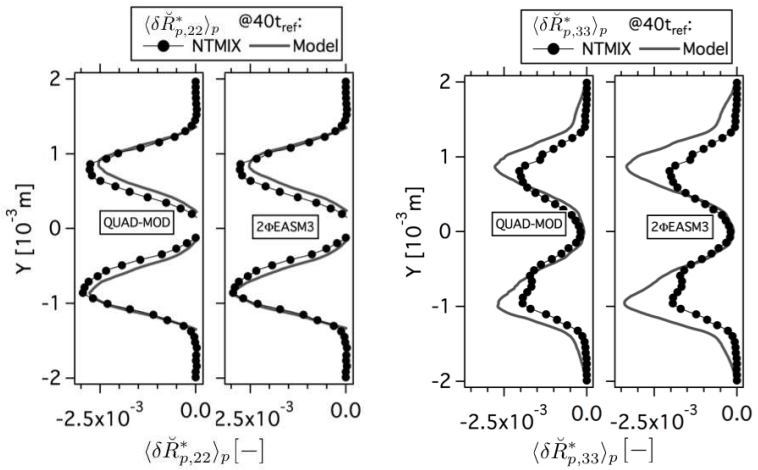

(a) (b)

Figure F.14: *Comparison of Eulerian and Lagrangian (a) mean deviatoric RUM stress tensor YY component ($< \delta \breve{R}^*_{p,22} >_p$) and (b) mean deviatoric RUM stress tensor ZZ component ($< \delta \breve{R}^*_{p,33} >_p$) at $40t_{ref}$. Normalized by the square of the initial particle velocity in X-direction at the center of the slab. HR_St1_# case.*

F.3 Instantaneous fields at 5 and $40t_{ref}$

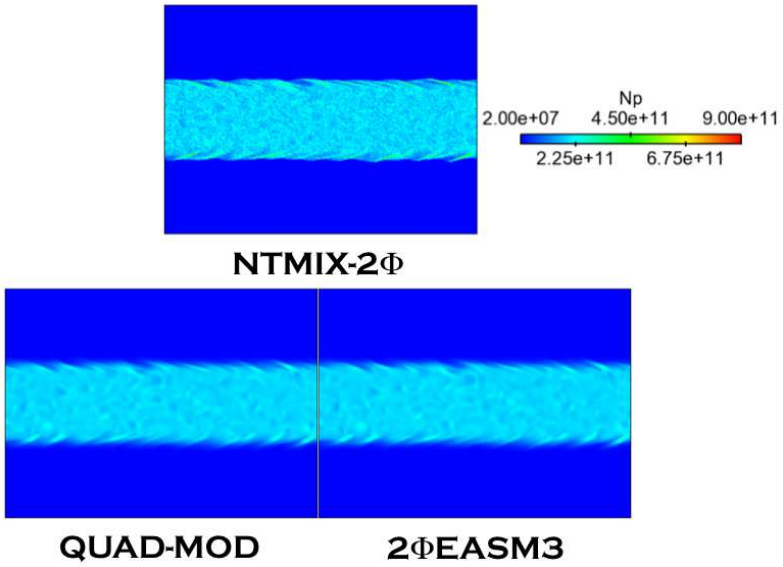

Figure F.15: *Comparison of Lagrangian (NTMIX-2Φ) and Eulerian particle number density (N_p) at $5t_{ref}$. HR_St1_# case.*

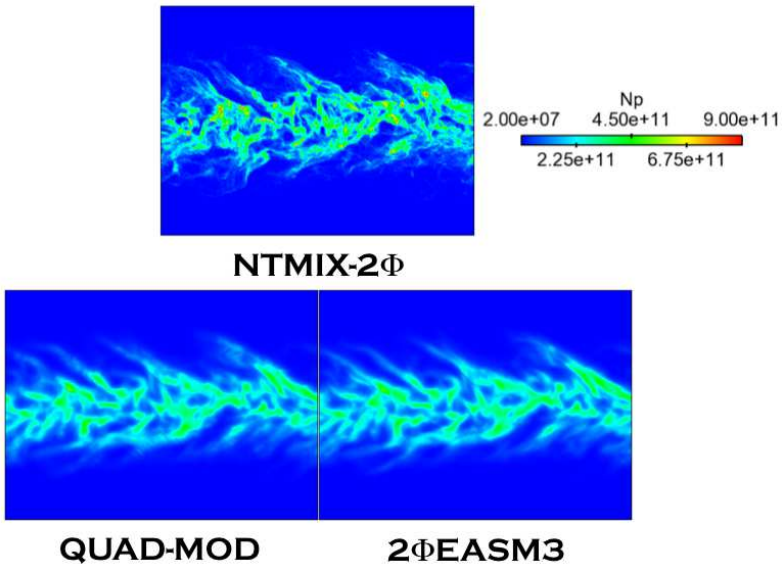

Figure F.16: *Comparison of Lagrangian (NTMIX-2Φ) and Eulerian particle number density (N_p) at $40t_{ref}$. HR_St1_# case.*

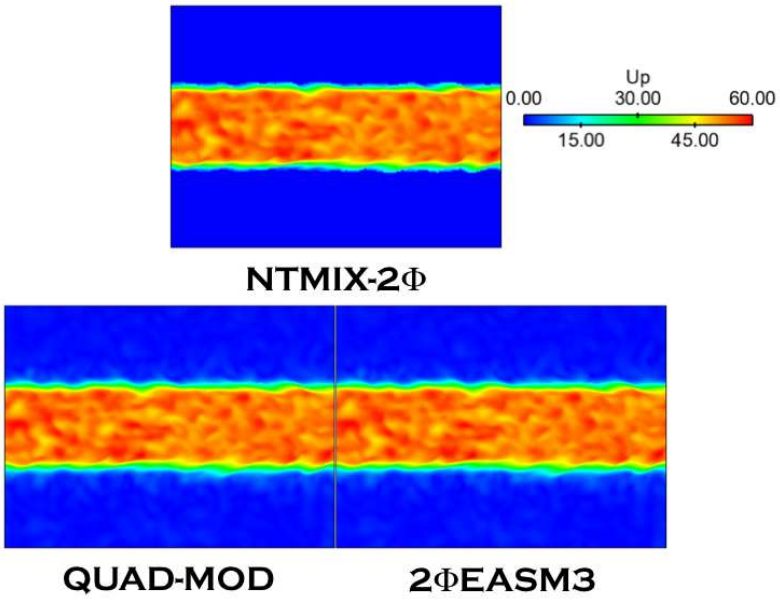

Figure F.17: *Comparison of Lagrangian (NTMIX-2Φ) and Eulerian particle velocity magnitude (U_p) at $5t_{ref}$. HR_St1_# case.*

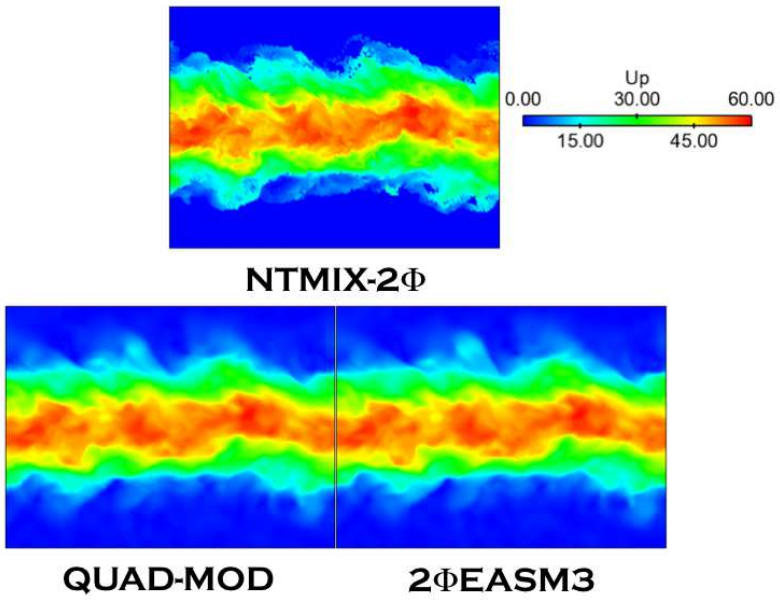

Figure F.18: *Comparison of Lagrangian (NTMIX-2Φ) and Eulerian particle velocity magnitude (U_p) at $40t_{ref}$. HR_St1_# case.*

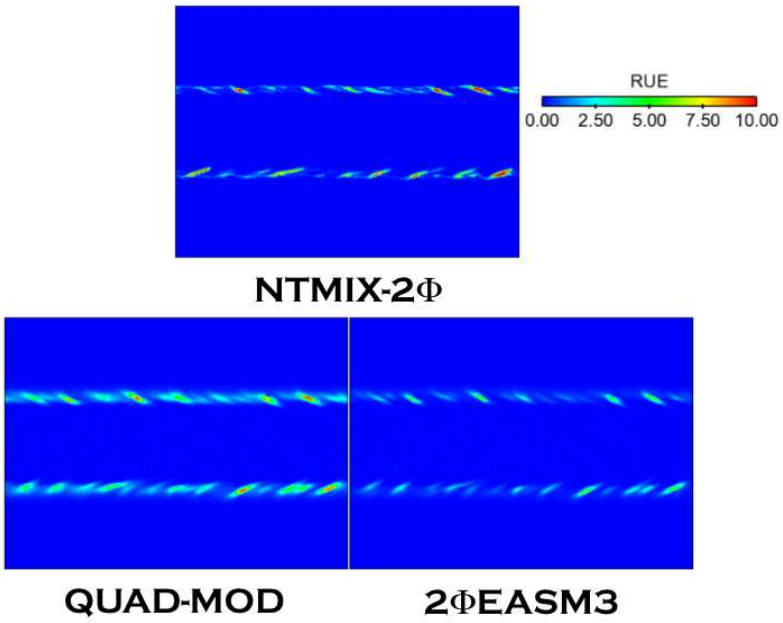

Figure F.19: *Comparison of Lagrangian (NTMIX-2Φ) and Eulerian Random Uncorrelated Energy at* $5t_{ref}$*. HR_St1_# case.*

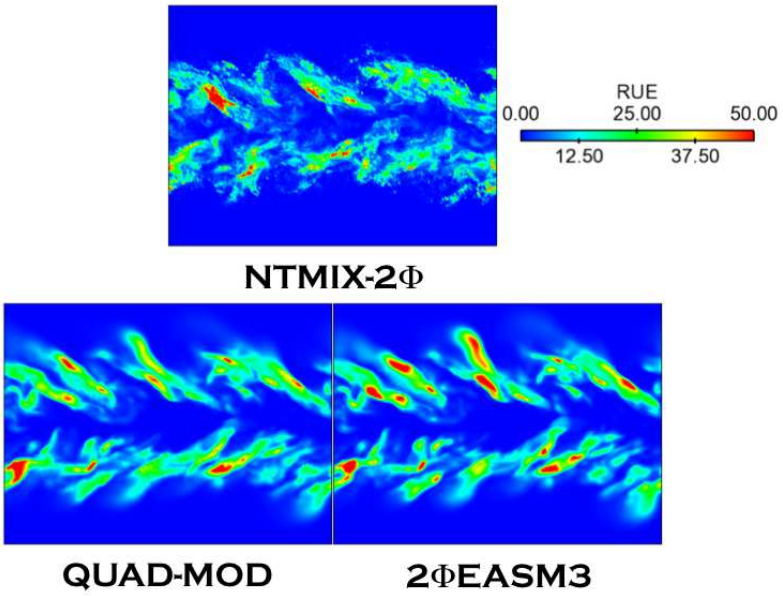

Figure F.20: *Comparison of Lagrangian (NTMIX-2Φ) and Eulerian Random Uncorrelated Energy at* $40t_{ref}$*. HR_St1_# case.*

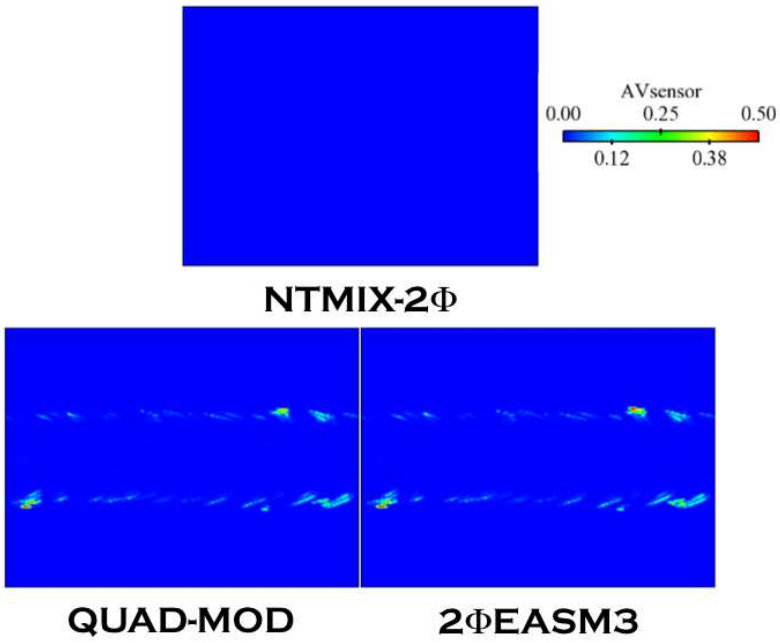

Figure F.21: *Comparison of AV sensor levels at* $5t_{ref}$*. HR_St1_# case.*

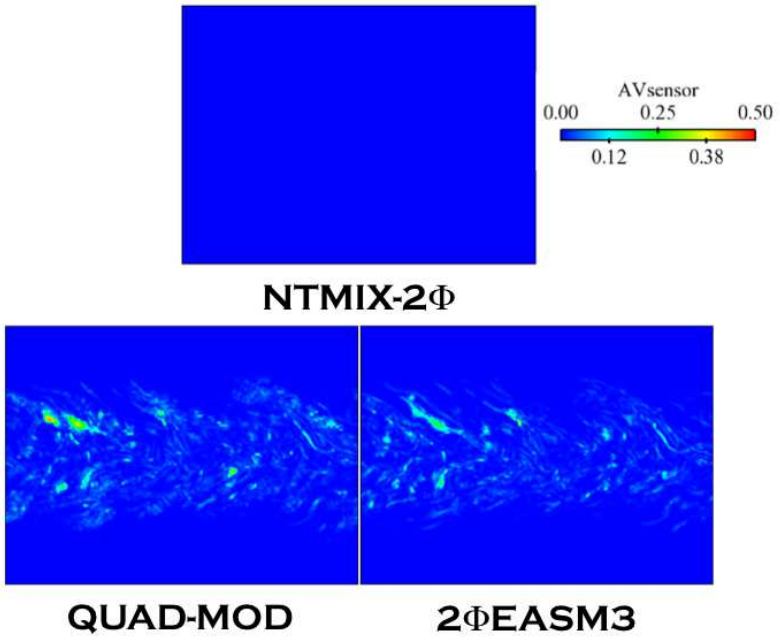

Figure F.22: *Comparison of AV sensor levels at* $40t_{ref}$*. HR_St1_# case.*

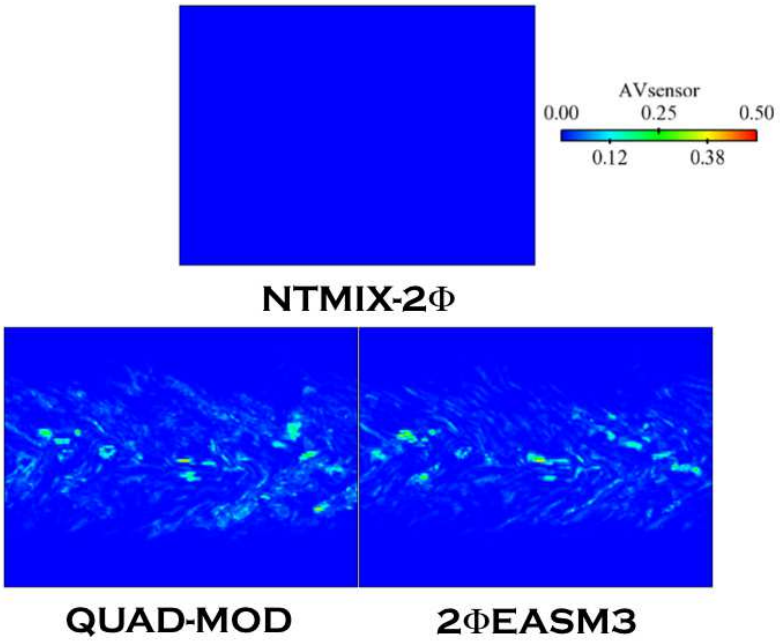

Figure F.23: *Comparison of AV sensor levels at* $70t_{ref}$*. HR_St1_# case.*

Appendix G

MERCATO configuration. Additional graphs.

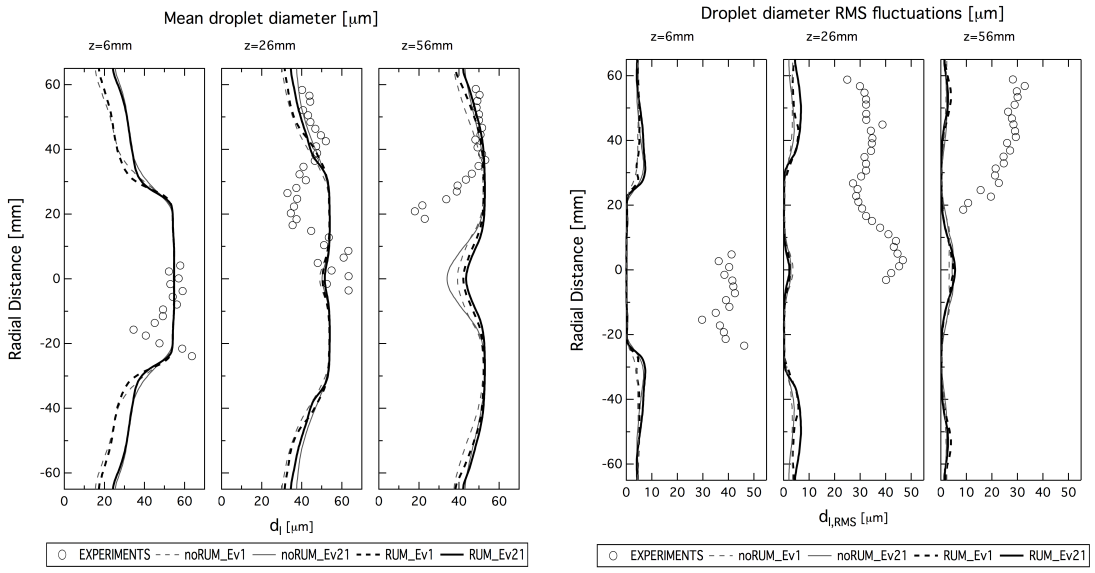

(a) (b)

Figure G.1: *Mean (a) and RMS (b) droplet diameter profiles.*

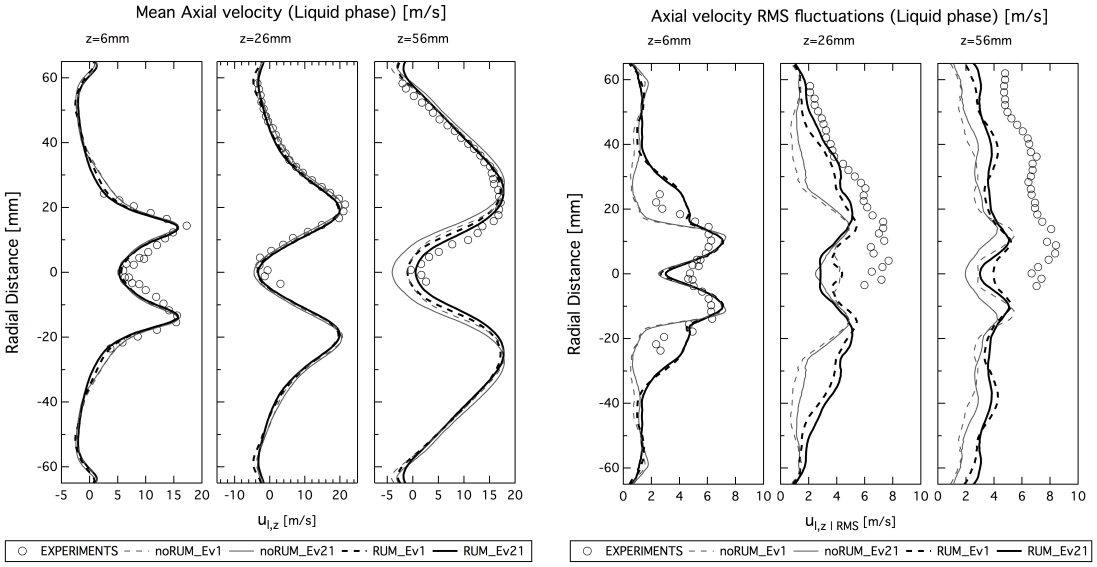

(a) (b)

Figure G.2: *Mean (a) and RMS (b) liquid axial velocity profiles.*

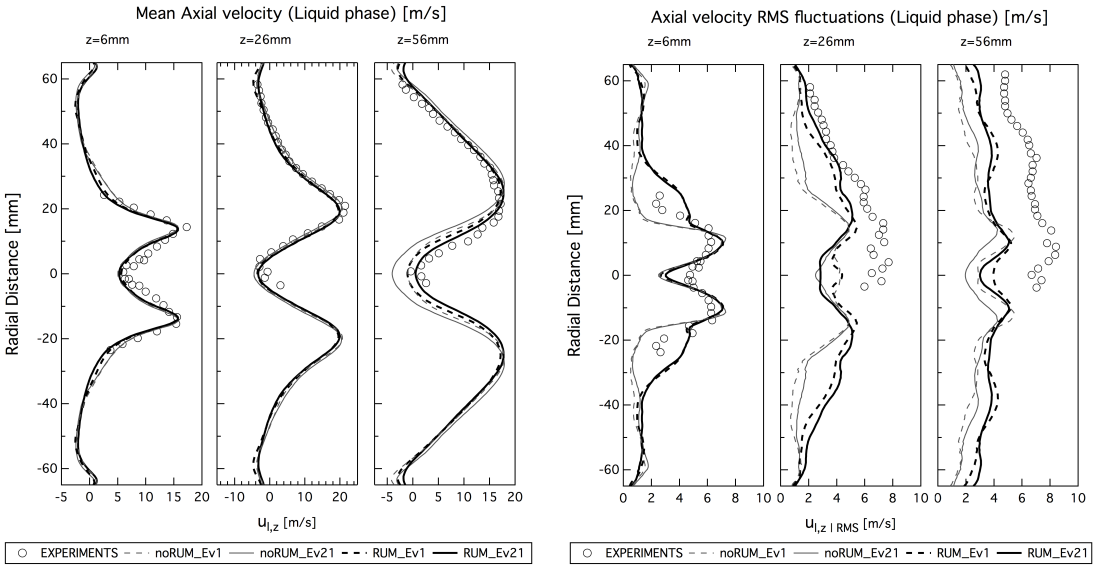

(a) (b)

Figure G.3: *Mean (a) and RMS (b) liquid radial velocity profiles.*

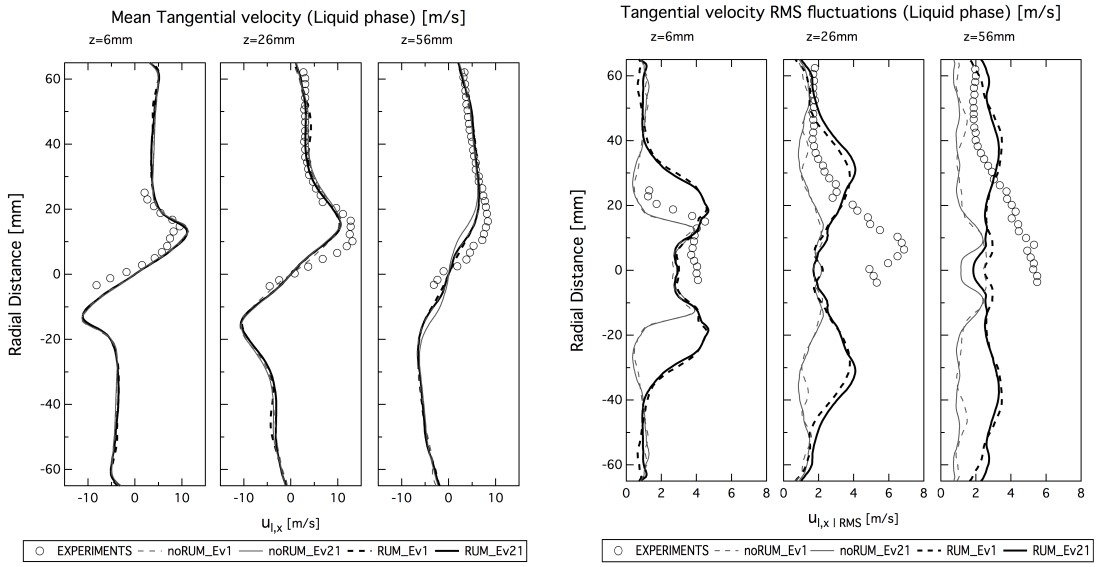

(a) (b)

Figure G.4: *Mean (a) and RMS (b) liquid tangential velocity profiles.*

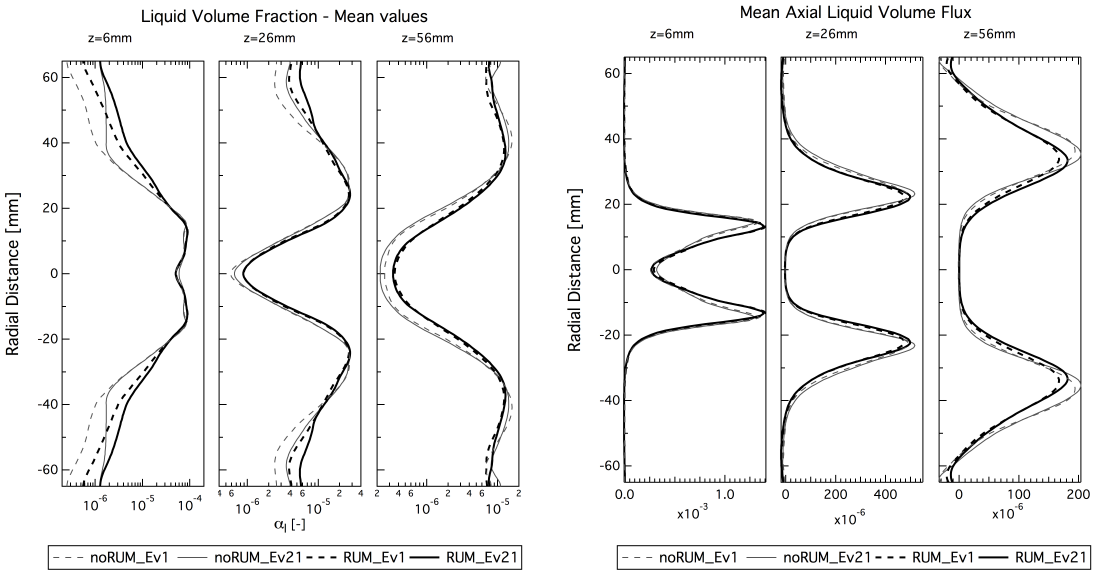

(a) (b)

Figure G.5: *Mean liquid volume fraction (a) and liquid volume flux (b).*